ATHENA Code Manual
Volume I: Code Structure, System Models and Solution Methods

The RELAP5-3D$^{©}$ Code Development Team

Idaho National Engineering and Environmental Laboratory
Bechtel BWXT Idaho, LLC

ATHENA CODE MANUAL
VOLUME I: CODE STRUCTURE, SYSTEM MODELS, AND SOLUTION METHODS

The RELAP5-3D© Code Development Team

Original Manuscript Completed:
February 1999
Revision 2.3 Completed:
December 2004

Idaho National Engineering and Environmental Laboratory
Idaho Falls, Idaho 83415

The ATHENA manuals are living documents and are being corrected and updated continuously. A printed version of the manuals is frozen and archived when a code version is released. This version of the manual corresponds to ATHENA version 2.3, released December 2004.

ABSTRACT

The ATHENA code has been developed for best-estimate transient simulation of light water reactor coolant systems during postulated accidents. The code models the coupled behavior of the reactor coolant system and the core for loss-of-coolant accidents and operational transients such as anticipated transient without scram, loss of offsite power, loss of feedwater, and loss of flow. A generic modeling approach is used that permits simulating a variety of thermal hydraulic systems. Control system and secondary system components are included to permit modeling of plant controls, turbines, condensers, and secondary feedwater systems.

ATHENA code documentation is divided into six volumes: Volume I presents modeling theory and associated numerical schemes; Volume II details instructions for code application and input data preparation; Volume III presents the results of developmental assessment cases that demonstrate and verify the models used in the code; Volume IV discusses in detail ATHENA models and correlations; Volume V presents guidelines that have evolved over the past several years through the use of the ATHENA code; and Volume VI discusses the numerical scheme used in ATHENA.

ACKNOWLEDGMENTS

EXECUTIVE SUMMARY

The RELAP5 series of codes has been developed at the Idaho National Engineering and Environmental Laboratory (INEEL) under sponsorship of the U.S. Department of Energy, the U.S. Nuclear Regulatory Commission, members of the International Code Assessment and Applications Program (ICAP), members of the Code Applications and Maintenance Program (CAMP), and members of the International RELAP5 Users Group (IRUG). Specific applications of the code have included simulations of transients in light water reactor (LWR) systems such as loss of coolant, anticipated transients without scram (ATWS), and operational transients such as loss of feedwater, loss of offsite power, station blackout, and turbine trip. ATHENA, the latest in the series of RELAP5 codes, is a highly generic code that, in addition to calculating the behavior of a reactor coolant system during a transient, can be used for simulation of a wide variety of hydraulic and thermal transients in both nuclear and nonnuclear systems involving mixtures of vapor, liquid, noncondensable gases, and nonvolatile solute.

The mission of the ATHENA development program was to develop a code version suitable for the analysis of all transients and postulated accidents in fusion reactor transient applications. Additional capabilities include space reactor simulations, gas cooled reactor applications, fast breeder reactor modeling, and cardiovascular bloodflow simulations.

The ATHENA code is based on a nonhomogeneous and nonequilibrium model for the two-phase system that is solved by a fast, partially implicit numerical scheme to permit economical calculation of system transients. The objective of the ATHENA development effort from the outset was to produce a code that included important first-order effects necessary for accurate prediction of system transients but that was sufficiently simple and cost effective so that parametric or sensitivity studies were possible.

The code includes many generic component models from which general systems can be simulated. The component models include pumps, valves, pipes, heat releasing or absorbing structures, reactor kinetics, electric heaters, jet pumps, turbines, separators, annuli, pressurizers, feedwater heaters, ECC mixers, accumulators, and control system components. In addition, special process models are included for effects such as form loss, flow at an abrupt area change, branching, choked flow, boron tracking, and noncondensable gas transport.

The system mathematical models are coupled into an efficient code structure. The code includes extensive input checking capability to help the user discover input errors and inconsistencies. Also included are free-format input, restart, renodalization, and variable output edit features. These user conveniences were developed in recognition that generally the major cost associated with the use of a system transient code is in the engineering labor and time involved in accumulating system data and developing system models, while the computer cost associated with generation of the final result is usually small.

The development of the models and code versions that constitute ATHENA has spanned more than two decades from the early stages of RELAP5 numerical scheme development (circa 1976) to the present. ATHENA represents the aggregate accumulation of experience in modeling reactor core behavior during

accidents, two-phase flow processes, and LWR systems. The code development has benefited from extensive application and comparison to experimental data in the LOFT, PBF, Semiscale, ACRR, NRU, and other experimental programs.

The ATHENA version contains several important enhancements over previous versions of the code. Enhancements include a new matrix solver, new thermodynamic properties for water, and improved time advancement for greater robustness. The new Border Profiled Lower Upper (BPLU) matrix solver is used to efficiently solve sparse linear systems of the form AX = B. BPLU is designed to take advantage of pipelines, vector hardware, and shared-memory parallel architecture to run fast. BPLU is most efficient for solving systems that correspond to networks, such as pipes, but is efficient for any system that it can permute into border-banded form.

The ATHENA code manual consists of six separate volumes. The modeling theory and associated numerical schemes are described in Volume I, to acquaint the user with the modeling base and thus aid in effective use of the code. Volume II contains more detailed instructions for code application and specific instructions for input data preparation.

Volume III presents the results of developmental assessment cases run with ATHENA to demonstrate and validate the models used in the code. The assessment matrix contains phenomenological problems, separate-effects tests, and integral systems tests.

Volume IV contains a detailed discussion of the models and correlations used in ATHENA. It presents the user with the underlying assumptions and simplifications used to generate and implement the base equations into the code so that an intelligent assessment of the applicability and accuracy of the resulting calculations can be made. Thus, the user can determine whether ATHENA is capable of modeling his or her particular application, whether the calculated results will be directly comparable to measurement or whether they must be interpreted in an average sense, and whether the results can be used to make quantitative decisions.

Volume V provides guidelines for users that have evolved over the past several years from applications of the ATHENA code at the Idaho National Engineering and Environmental Laboratory, at other national laboratories, and by users throughout the world.

Volume VI discusses the numerical scheme in ATHENA.

NOMENCLATURE

A	cross-sectional area (m^2), coefficient matrix in hydrodynamics, coefficient in pressure and velocity equations
A$_1$	coefficient in heat conduction equation at boundaries
A$_t$	throat area (m^2)
a	speed of sound (m/s), interfacial area per unit volume (m^{-1}), coefficient in gap conductance, coefficient in heat conduction equation, absorption coefficient
B	coefficient matrix, drag coefficient, coefficient in pressure and velocity equations
B$_1$	coefficient in heat conduction equation at boundaries
b	coefficient in heat conduction equation, source vector in hydrodynamics
B$_x$	body force in x coordinate direction (m/s^2)
B$_y$	body force in y coordinate direction (m/s^2)
C	coefficient of virtual mass, general vector function, coefficient in pressure and velocity equations, delayed neutron precursors in reactor kinetics, concentration, pressure-dependent coefficient in Unal's correlation (1/K•s)
C$_o$	coefficient in noncondensable specific internal energy equation (J/kg•K)
C$_0$, C$_1$	constants in drift flux model
C$_D$	drag coefficient
C$_p$	specific heat at constant pressure (J/kg•K)
C$_v$	specific heat at constant volume (J/kg•K), valve flow coefficient
c	coefficient in heat conduction equation, coefficient in new-time volume-average velocity equation, constant in CCFL model
D	coefficient of relative Mach number, diffusivity, pipe diameter or equivalent diameter (hydraulic diameter) (m), heat conduction boundary condition matrix, coefficient in pressure and velocity equations
D$_o$	coefficient in noncondensable specific internal energy equation (J/kg•K^2)
D$_1$	coefficient of heat conduction equation at boundaries
d	coefficient in heat conduction equation, droplet diameter (m)
DISS	energy dissipation function (W/m^3)
E	specific total energy (U + v^2/2) (J/kg), emissivity, Young's modulus, term in iterative heat conduction algorithm, coefficient in pressure equation
e	interfacial roughness
F	term in iterative heat conduction algorithm, gray-body factor with subscript, frictional loss coefficient, vertical stratification factor

FA	force per unit volume
FIF, FIG	interphase drag coefficients (liquid, vapor/gas) (s^{-1})
FI	interphase drag coefficient (m^3/kg•s)
FWF, FWG	wall drag coefficients (liquid, vapor/gas) (s^{-1})
f	interphase friction factor, vector for liquid velocities in hydrodynamics
G	mass flux (kg/m^2-s), shear stress, gradient, coefficient in heat conduction, vector quantity, fraction of delayed neutrons in reactor kinetics
GC	dynamic pressure for valve (Pa)
Gr	Grashof number
g	gravitational constant (m/s^2), temperature jump distance (m), vector for vapor/gas velocities in hydrodynamics
H	elevation (m), volumetric heat transfer coefficient (W/K•m^3), head (m)
HLOSSF, HLOSSG	form or frictional losses (liquid, vapor/gas) (m/s)
h	specific enthalpy (J/kg), heat transfer coefficient (W/m^2•K), energy transfer coefficient for Γ_g, head ratio
h_L	dynamic head loss (m)
I	identity matrix, moment of inertia (N-m-s^2)
J	junction velocity (m/s)
j	superficial velocity
K	energy form loss coefficient
K_s	Spring constant
Ku	Kutateladze number
k	thermal conductivity (W/m•K)
k_B	Boltzmann constant
L	length, limit function, Laplace capillary length
M	Mach number, molecular weight, pump two-phase multiplier, mass transfer rate, mass (kg)
m	constant in CCFL model
N	number of system nodes, number density (#/m^3), pump speed (rad/s), nondimensional number
Nu	Nusselt number
n	unit vector, order of equation system
P_{BP}	valve closing back pressure (Pa)

P	pressure (Pa), reactor power (W), channel perimeter (m), turbine power (W)
P_D	nitrogen pressure in accumulator dome (Pa)
P_f	relates reactor power to heat generation rate in heat structures
P_o	atmospheric pressure (Pa)
p	wetted perimeter (m), particle probability function
PCV	specified pressure required to close a valve (Pa)
Pr	Prandtl number
Q	volumetric heat addition rate (W/m^3), space dependent function, volumetric flow rate (m^3/s)
Q_D	total heat transfer rate to vapor dome (W)
q	heat transfer rate (W), heat flux (W/m^2)
R	radius (m), surface roughness in gap conductance, radiation resistance term, nondimensional stratified level height
Re	Reynolds number
Re_p	the particle Reynolds number
R_n, R_s	gas constants (noncondensable, vapor) (N•m/kg•K)
r	reaction fraction for turbine, radial position, ratio of volume centered boron density gradients
S	Chen's boiling suppression factor, stress gradient, specific entropy (J/kg•K), shape factor, real constant, source term in heat conduction or reactor kinetics (W)
s	surface, Laplace transform variable
T	temperature (K), trip
T_c	critical temperature (K)
T_R	reduced temperature (K)
T_t	specified time-dependent function in heat conduction
t	time (s)
U	specific internal energy (J/kg), vector of dependent variables
u	radial displacement in gap conductance (m)
V	volume (m^3), specific volume (m^3/kg), control quantity
V_D	volume of noncondensable in accumulator dome (m^3)
VFDP, VGDP	coefficient for pressure change in momentum equations (liquid, vapor/gas) (m/s-Pa)
VIS	numerical viscosity terms in momentum equations (m^2/s^2)

VISF, VISG	numerical viscosity terms in momentum equations (liquid, vapor/gas) (m^2/s^2)
VUNDER, VOVER	separator model parameters (liquid, vapor/gas)
v	mixture velocity (m/s), phasic velocity (m/s), flow ratio, liquid surge line velocity (m/s)
v_c	choking velocity (m/s)
W	weight of valve disk, weighting function in reactor kinetics, relaxation parameter in heat conduction, shaft work per unit mass flow rate, mass flow rate
W_{crit}	critical Weber number
We	Weber number
w	humidity ratio
X	flow quality, static quality, mass fraction, conversion from MeV/s to watts
x	spatial coordinate (m), vector of hydrodynamic variables
Y	control variable
Z	two-phase friction correlation factor, function in reactor kinetics
ΔZ	height of volume
z	elevation change coordinate (m)

Symbols

α	void fraction, subscripted volume fraction, angular acceleration (rad/s^2), coefficient for least-squares fit, speed ratio
β	coefficient of isobaric thermal expansion (K^{-1}), effective delayed neutron fraction in reactor kinetics
Γ	volumetric mass exchange rate ($kg/m^3 \bullet s$)
γ	exponential function in decay heat model
ΔP_f	dynamic pressure loss (Pa)
ΔP_s	increment in vapor pressure (Pa)
ΔV_s	increment in specific volume of vapor (m^3/kg)
Δt	increment in time variable (s)
Δt_c	Courant time step (s)
Δx	increment in spatial variable (m)
δ	area ratio, truncation error measure, film thickness (m), impulse function, Deryagin number
ε	coefficient, strain function, emissivity, tabular function of area ratio, surface roughness, wall vapor generation/condensation flag

ζ	diffusion coefficient, multiplier, or horizontal stratification terms
η	efficiency, bulk/saturation enthalpy flag
θ	relaxation time in correlation for Γ, angular position (rad), discontinuity detector function
κ	coefficient of isothermal compressibility (Pa^{-1})
Λ	prompt neutron generation time, Baroczy dimensionless property index
λ	eigenvalue, interface velocity parameter, friction factor, decay constant in reactor kinetics
μ	viscosity (kg/m•s)
ν	kinematic viscosity (m^2/s), Poisson's ratio
ξ	exponential function, RMS precision
π	3.141592654
ρ	density (kg/m^3), reactivity in reactor kinetics (dollars)
Σ_f	fission cross-section
Σ'	depressurization rate (Pa/s)
σ	surface tension (J/m^2), stress, flag used in heat conduction equations to indicate transient or steady-state
τ	shear stresses (N), torque (N-m)
υ	specific volume (m^3/kg)
ϕ	donored property, Lockhart-Martinelli two-phase parameter, neutron flux in reactor kinetics, angle of inclination of valve assembly, velocity-dependent coefficient in Unal's correlation
Φ	Roe's superbee gradient limiter
χ	Lockhart-Martinelli function
ψ	coefficient, fission rate (number/s)
ω	angular velocity, constant in Godunov solution scheme

Subscripts

AM	annular mist to mist flow regime transition
a	average value
ann	liquid film in annular mist flow regime
BS	bubbly-to-slug flow regime transition
b	bubble, boron

bulk	bulk fluid
CHF	value at critical heat flux condition
c	vena contract, continuous phase, cladding, critical property, cross-section, condensation
cm	cladding midpoint
co	carryover
core	vapor/gas core in annular-mist flow regime
cr, crit	critical property or condition
cu	carryunder
D	drive line, vapor dome, discharge passage of mechanical separator
DE	value at lower end of slug to annular-mist flow regime transition
d	droplet, delay in control component
drp	droplet
e	equilibrium, equivalent quality in hydraulic volumes, valve ring exit, elastic deformation, entrainment
ent	entrainment
F	wall friction, fuel
FB, FBB	film boiling, Bromley film boiling
f	liquid phase, flooding, film, flow
fg	phasic difference (i.e., vapor/gas term-liquid term)
flow	flow
fp	onset of vapor/gas pull-through
fr	frictional
front	value at thermal stratification front
g	vapor/gas phase, gap
ge	incipient liquid entrainment
H	head
HE	homogeneous equilibrium
h, hy, hydro	hydraulic
I	interface
IAN	inverted annular flow regime
i	interface, index

in	volume inlets
iso	isothermal
j, j+1, j-1	spatial noding indices for junctions
K	spatial noding index for volumes
k	iteration index in choking model
L	spatial noding index for volume, laminar
lev, level	value at two-phase level
l	left boundary in heat conduction
M	rightmost boundary in heat conduction, spatial noding index for volume
m	mixture property, motor, mesh point
min	minimum value
NOZ	nozzle
n	noncondensable component of vapor/gas phase
o	reference value
out	volume outlets
p	partial pressure of vapor, particle, projected
pipe	cross-section of flow channel
R	rated values
r	relative Mach number, right boundary in heat structure mesh
ref	reference value
rms	root mean square
S	suction region
SA	value at upper end of slug to annular-mist flow regime transition
s	vapor component of vapor/gas phase, superheated
sat	saturated quality
sb	small bubbles
sr	surface of heat structure
st	stratified
std	standard precision
T	point of minimum area, turbulent
TB	transition boiling

Tb	Taylor bubble
t	total pressure, turbulent, tangential, throat
up	upstream quantity
v	mass mean Mach number, vapor/gas quantity, valve
w	wall, water
wall	wall
wg, wf	wall to vapor/gas, wall to liquid
1	upstream station, multiple junction index, vector index
1ϕ	single-phase value
2	downstream station, multiple junction index, vector index
2ϕ	two-phase value
τ	torque
μ	viscosity
∞	infinity
~	vector
$\approx$	Matrix

Superscripts

B	bulk liquid
b	boundary gradient weight factor in heat conduction, vector quantities
exp	old time terms in velocity equation, used to indicate explicit velocities in choking
m-1, m, m+1	mesh points in heat conduction finite difference equation or mean value
n, n+l	time level index
n+1/2	an average of quantities with superscripts n and n+1
o	initial value
R	real part of complex number, right boundary in heat conduction
s	saturation property, space gradient weight factor in heat conduction
v	volume gradient weight factor in heat conduction
W	wall
1	vector index, coefficient in velocity equation
2	vector index

*	total derivative of a saturation property with respect to pressure, local variable, bulk/saturation property
'	derivative
-	vector, average quantity
.	donored quantity
~	unit momentum for mass exchange, intermediate time variable
^	linearized quantity, quality based on total mixture mass

CONTENTS

FIGURES

TABLES

1 Introduction

The RELAP5 series of codes has been developed at the Idaho National Engineering and Environmental Laboratory (INEEL) under sponsorship of the U.S. Department of Energy, the U.S. Nuclear Regulatory Commission, members of the International Code Assessment and Applications Program (ICAP), members of the Code Applications and Maintenance Program (CAMP), and members of the International RELAP5 Users Group (IRUG). Specific applications of the code have included simulations of transients in light water reactor (LWR) systems, such as loss of coolant, anticipated transients without scram (ATWS), and operational transients such as loss of feedwater, loss of offsite power, station blackout, and turbine trip. ATHENA, the latest code version in the series of RELAP5 codes, is a highly generic code that, in addition to calculating the behavior of a reactor coolant system during a transient, can be used for simulation of a wide variety of hydraulic and thermal transients in both nuclear and nonnuclear systems involving mixtures of vapor, liquid, noncondensable gas, and nonvolatile solute.

1.1 Development of ATHENA

The ATHENA code is a successor to the RELAP5/MOD3 code[1.1-1] which was developed for the Nuclear Regulatory Commission. Department of Energy sponsors of the code extensions in ATHENA include the DOE Office of Fusion Energy Sciences, Savannah River Laboratory, Bettis Atomic Power Laboratory, the International RELAP5 Users Group (IRUG), and the Laboratory Directed Research and Development Program at the INEEL. The ATHENA version contains several important enhancements over previous versions of the code. Enhancements include a new matrix solver, new thermodynamic properties of water, and improved time advancement for greater robustness. The new Border Profiled Lower Upper (BPLU) matrix solver is used to efficiently solve sparse linear systems of the form $AX = B$. BPLU is designed to take advantage of pipelines, vector hardware, and shared-memory parallel architecture to run fast. BPLU is most efficient for solving systems that correspond to networks, such as pipes, but is efficient for any system that it can permute into border-banded form.

1.1.1 References

1.1-1.   The RELAP5 Development Team, *RELAP5/MOD3 Code Manual, Volumes 1 and 2*, NUREG/CR-5535, INEL-95/0174, Idaho National Engineering Laboratory, August 1995.

1.2 Quality Assurance

ATHENA is maintained under a strict code-configuration system that provides a historical record of the changes in the code. Changes are made using a version control system that allows separate identification of improvements made to each successive version of the code. Modifications and improvements to the coding are reviewed and checked as part of a formal quality program for software. In addition, the theory and implementation of code improvements are validated through assessment calculations that compare the code-predicted results to idealized test cases or experimental results.

2 Code Architecture

Modeling flexibility, user-convenience, computer efficiency, and design for future growth were primary considerations in the selection of the basic architecture of the code. The following sections cover computer adaptability, code top level organization, input processing, and transient operation.

2.1 Computer Adaptability

ATHENA is written in FORTRAN 77 for a variety of 64-bit and 32-bit computers. Here, a 64-bit computer is one in which floating point, integer, and logical quantities use 64-bit words; a 32-bit machine uses 32-bit words for those same quantities but also allows 64-bit floating point operations. Examples of 64-bit computers are Cray and Cyber-NOS-VE mainframes, DEC Alpha workstations, and SGI workstations. Examples of 32-bit computers include IBM mainframes, such as a 3090; DEC, HP, IBM, SGI, and SUN workstations; and personal computers.

A common source is maintained for all computer versions. The common source is conditioned for a particular computer and operating system through the use of two precompilers maintained as part of ATHENA. The first precompiler processes compile time options such as machine and operating system dependencies. Through the use of standard Fortran and a widely used standard for bit operations, there is very little hardware dependence. The primary hardware dependence is in matrix factoring routines where details of the floating point characteristics are needed to monitor roundoff error. A future full conversion to the Fortran90 standard should remove all hardware dependencies. ATHENA is developed and maintained at INEEL on computers using the UNIX operating system. Some user-convenient features have been incorporated into the code based on UNIX, but these are under compile time option. The code does not depend on any particular operating system. The installation scripts distributed with the code are UNIX based, and control language to install and execute the code must be developed by the user for other operating systems. The source code appears to be written only for 64-bit machines. The second precompiler, however, converts the code for 32-bit computers by converting floating point variables to double precision, changing floating point literals to double precision, and adding an additional subscript to integer and logical arrays that are equivalenced to double precision floating point arrays such that they index as 64-bit quantities even though only 32-bit integer arithmetic and logical operations are used. As an example of the additional subscript, an integer statement would be changed from INTEGER IA(1000000) to INTEGER IA(2,1000000).

Transmittals of the code usually show the installation and execution of sample problems on several machines. The machines used depend on the machines currently available to the development staff.

2.2 Top Level Organization

ATHENA is coded in a modular fashion using top-down structuring. The various models and procedures are isolated in separate subroutines. The top level structure is shown in **Figure 2.2-1** and consists of input (INPUTD), transient/steady-state (TRNCTL), and stripping (STRIP) blocks.

```
          ┌─────────┐
          │ RELAP5  │
          └────┬────┘
     ┌─────────┼─────────┐
┌────┴───┐ ┌───┴────┐ ┌──┴─────┐
│ INPUTD │ │ TRNCTL │ │ STRIP  │
└────────┘ └────────┘ └────────┘
```
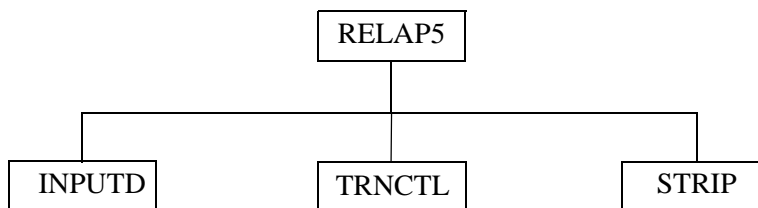
Figure 2.2-1 ATHENA top level structure.

The input block (INPUTD) processes input, checks input data, and prepares required data blocks for all program options and is discussed in more detail in Section 2.3.

The transient/steady-state block (TRNCTL) handles both transient and the steady-state options. The steady-state option determines the steady-state conditions if a properly posed steady-state problem is presented. Steady-state is obtained by running an accelerated transient until the time derivatives approach zero. Thus, the steady-state option is very similar to the transient option but contains convergence testing algorithms to determine satisfactory steady-state, divergence from steady-state, or cyclic operation. If the transient technique alone were used, approach to steady-state from an initial condition would be identical to a plant transient from that initial condition. Pressures, densities, and flow distributions would adjust quickly, but thermal effects would occur more slowly. To reduce the transient time required to reach steady-state, the steady-state option artificially accelerates heat conduction by reducing the thermal capacity of the conductors. The transient/steady-state block is discussed in more detail in Section 2.4.

The strip block (STRIP) extracts simulation data from a restart-plot file for convenient passing of ATHENA simulation results to other computer programs.

2.3 Input Processing Overview

ATHENA provides detailed input checking for all system models using three input processing phases. The first phase reads all input data, checks for punctuation and typing errors (such as multiple decimal points and letters in numerical fields), and stores the data keyed by card number such that the data are easily retrieved. A list of the input data is provided, and punctuation errors are noted.

During the second phase, restart data from a previous simulation are read if the problem is a RESTART type, and all input data are processed. Some processed input is stored in fixed common blocks, but the majority of the data are stored in dynamic data (common) blocks that are created only if needed by a problem and sized to the particular problem. In a NEW-type problem, dynamic blocks must be created. In RESTART problems, dynamic blocks may be created, deleted, added to, partially deleted, or modified as modeling features and components within models are added, deleted, or modified. Extensive input checking is done, but at this level, checking is limited to new data from the cards being processed. Relationships with other data cannot be checked because the latter may not yet be processed. As an

illustration of this level of checking, junction data are checked to determine if they are within the appropriate range (such as positive, nonzero, or between zero and one) and volume connection codes are checked for proper format. No attempt is made at this point to check whether or not referenced volumes exist in the problem until all input data are processed.

The third phase of processing begins after all input data have been processed. Since all data have been placed in fixed common or dynamic data (common) blocks during the second phase, complete checking of interrelationships can proceed. Examples of cross-checking are existence of hydrodynamic volumes referenced in junctions and heat structure boundary conditions; entry or existence of material property data specified in heat structures; and validity of variables selected for minor edits, plotting, or used in trips and control systems. As the cross-checking proceeds, cross-linking of the data blocks is done so that it need not be repeated at every time step. The initialization required to prepare the model for the start of the transient advancement is done at this level.

Input data editing and diagnostic messages can be generated during the second and/or third phases. Input processing for most models generates output and diagnostic messages during both phases. Thus, input editing for these models appears in two sections.

As errors are detected, various recovery procedures are used so that input processing can be continued and a maximum amount of diagnostic information can be furnished. Recovery procedures include supplying default or benign data, marking the data as erroneous so that other models do not attempt use of the data, or deleting the bad data. The recovery procedures sometimes generate additional diagnostic messages. Often after attempted correction of input, different diagnostic messages appear. These can be due to continued incorrect preparation of data, but the diagnostics may result from the more extensive testing permitted as previous errors are eliminated.

2.4 Transient Overview

Figure 2.4-1 shows the functional modular structure for the transient calculations, while **Figure 2.4-2** shows the second-level structures for the transient/steady-state blocks or subroutines.

The subroutine TRNCTL shown in **Figure 2.4-2** consists only of the logic to call the next lower level routines. Subroutine TRNSET performs final cross-linking of information between data blocks, sets up arrays to control the sparse matrix solution, establishes scratch work space, and returns unneeded computer memory. Subroutine TRAN, the driver, controls the transient advancement of the solution. Nearly all the execution time is spent in this block, and this block is the most demanding of memory. Nearly all the dynamic data blocks must be in the central memory, and the memory required for instruction storage is high, since coding to advance all models resides in this block. When transient advances are terminated, the subroutine TRNFIN releases space for the dynamic data blocks that are no longer needed.

A description is next presented of the functions of all of the modules (subroutines) driven by TRAN (see **Figure 2.4-2**).
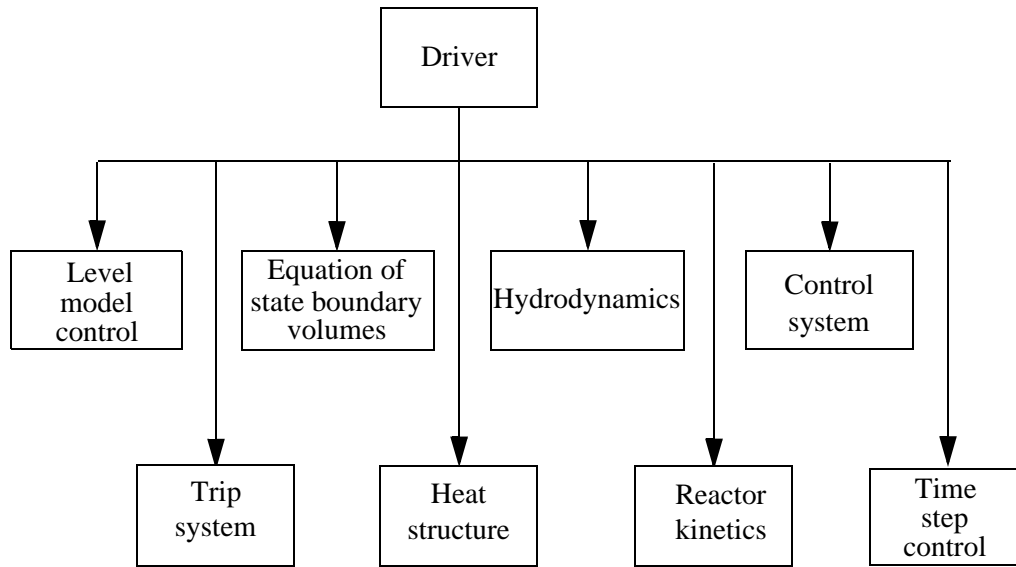
Figure 2.4-1 Modular structures of transient calculations in ATHENA.
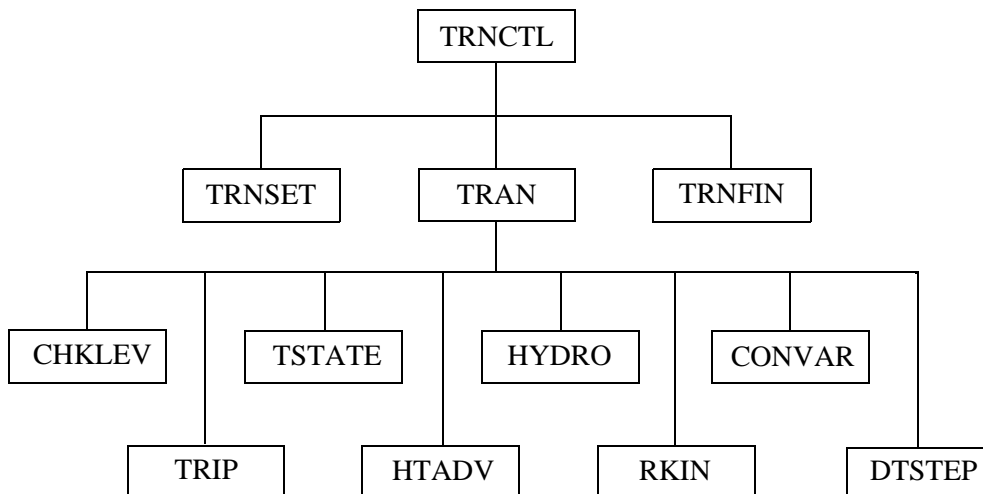
Figure 2.4-2 Transient/steady-state block structure.

The level module (CHKLEV) controls the movement of two-phase levels between volumes.

The trip system module (TRIP) evaluates logical statements. Each trip statement is a simple logical statement that has a true or false result. The decision of what action is needed resides within the components in other modules. For example, valve components are provided that open or close the valve based on trip values; pump components test trip status to determine whether a pump electrical breaker has tripped.

The equation of state boundary volume module (TSTATE) calculates the thermodynamic state of the fluid in each hydrodynamic boundary volume (time-dependent volume). This subroutine also computes velocities for the time-dependent junctions.

The heat structure module (HTADV) advances heat conduction/transfer solutions. It calculates heat transferred across solid boundaries of hydrodynamic volumes.

The hydrodynamics module (HYDRO) advances the hydrodynamic solution.

The reactor kinetics module (RKIN) advances the reactor kinetics of the code. It computes the power behavior in a nuclear reactor using the space-independent or point kinetics approximation, which assumes that power can be separated into space and time functions.

The control system module (CONVAR) provides the capability of simulating control systems typically used in hydrodynamic systems. It consists of several types of control components. Each component defines a control variable as a specific function of time-advanced quantities. The time-advanced quantities include quantities from hydrodynamic volumes, junctions, pumps, valves, heat structures, reactor kinetics, trip quantities, and the control variables themselves. This permits control variables to be developed from components that perform simple, basic operations.

The time step control module (DTSTEP) determines the time step size, controls output editing, and determines whether the transient advancements should be terminated. During program execution, this module displays such information as CPU time, problem time, time step size, and advancement number on the standard output, usually a terminal screen.

In the next sections of this volume of the manual, the various transient modules will be discussed. These are in the following order: hydrodynamics, heat structures, trips, control system, reactor kinetics, and special techniques (includes time step control).

3 Hydrodynamic Model

The ATHENA hydrodynamic model is a transient, two-fluid model for flow of a two-phase vapor/gas-liquid mixture that can contain noncondensable components in the vapor/gas phase and/or a soluble component in the liquid phase.

The ATHENA hydrodynamic model contains several options for invoking simpler hydrodynamic models. These include homogeneous flow, thermal equilibrium, and frictionless flow models. These options can be used independently or in combination. The homogeneous and equilibrium models were included primarily to be able to compare code results with calculations from the older codes based on the homogeneous equilibrium model.

The two-fluid equations of motion that are used as the basis for the ATHENA hydrodynamic model are formulated in terms of volume and time-averaged parameters of the flow. Phenomena that depend upon transverse gradients, such as friction and heat transfer, are formulated in terms of the bulk properties using empirical transfer coefficient formulations. In situations where transverse gradients cannot be represented within the framework of empirical transfer coefficients, such as subcooled boiling, additional models specially developed for the particular situation are employed. The system model is solved numerically using a semi-implicit finite-difference technique. The user can select an option for solving the system model using a nearly-implicit finite-difference technique, which allows violation of the material Courant limit. This option is suitable for steady-state calculations and for slowly varying, quasi-steady transient calculations.

The basic two-fluid differential equations possess complex characteristic roots that give the system a partially elliptic character and thus constitute an ill-posed initial boundary value problem. In ATHENA, the numerical problem is rendered well-posed by the introduction of artificial viscosity terms in the difference equation formulation that damp the high frequency spatial components of the solution. This is discussed further in **Reference 3.0-4** (Chapter 9). The ill-posed character of the two-fluid model is a result of the spatial averaging process and neglect of higher-order physical effects in the momentum formulation. Ransom and Hicks[3.0-5,3.0-6] have studied several formulations in which two pressures (one for each fluid) are included in the model, and these models are totally hyperbolic and thus constitute well-posed problems. A curious feature of the two-pressure approach, that was pointed out by Trapp and Ransom,[a] is that a well-posed problem is obtained without the addition of any viscous effects, which are known to be responsible for physical stabilization in real flows. Trapp and Ransom[a] indicated that in this case, a well-posed problem is obtained as a result of an unphysically large transverse inertia at short wave lengths. In addition, the two-pressure model was developed for stratified flows having a simple interfacial geometry, and it is unclear how to extend this concept to more general interfacial geometries. Limited numerical studies by Ransom and Scofield[3.0-7] have shown that solutions for the two-pressure model compare very well to that for the single-pressure model with damping (i.e., artificial viscosity). In general,

---

a. Personal communication, J. A. Trapp and V. H. Ransom to R. A. Riemke, January 1990.

the differences are significant only for short wavelength components of the solution where numerical truncation error is dominant. Thus, either approach provides a valid numerical simulation at solution component wavelengths of interest in most reactor safety problems. The simpler formulation of the single-pressure model favors using that approach.

Ramshaw and Trapp[3.0-8] developed a model in which surface tension was included such that the phasic pressures were, in general, different. They found this model to also be well-posed and investigated the characteristics of the model by dispersion analysis. Relative to numerical considerations they found that, in order to achieve a stable model at the macroscale of a practical discretization interval, an artificially large surface tension is required. They did not advocate the addition of surface tension as a means of achieving a stable numerical model, but offered this model as a means of providing insight to the ill-posed nature of the basic model. As with the two-pressure model, the surface tension model was developed for stratified flows having a simple interfacial geometry, and it is unclear how to extend this concept to more general interfacial geometries.

Trapp[3.0-9] has investigated a differential model in which the Reynolds stress-like terms that appear in the averaged formulation, but have usually been omitted, are modeled using the criterion that all unstable behavior be eliminated. This approach results in a well-posed problem, but the model has yet to be applied.

Ransom and Mousseau[3.0-10,3.0-11] have shown that the ATHENA implementation of the two-fluid model is consistent, stable, and convergent. In particular it was shown that the use of the ill-posed differential operator does not lead to instabilities or divergent behavior even for finer nodalization than is practical to use in applications. In fact the behavior of the ill-posed model was shown to be very similar to that of the well-posed two-pressure model, which is also consistent, stable, and convergent. When contemporary constitutive models for two-phase flow are included and the model was applied to a physical problem, convergence is obtained for a practical range of discretization interval. In no case was there an indication of divergent or unbounded behavior. Trapp[3.0-12] pointed out that no one has found a case where a growing mode has been traced to the complex characteristics feature of the model. This is discussed further in Volume VI (Section 4) of the manual, in **Reference 3.0-4** (Chapter 9), and in **Reference 3.0-13**.

The semi-implicit numerical solution scheme uses a direct sparse matrix solution technique for time step advancement. It is an efficient scheme and results in an overall grind time per node on the CRAY XMP/24 of ~0.00053 seconds, on the DEC Alpha 3000 of ~0.00057 seconds, and on the DECstation 5000 of ~0.00259 seconds. The method has a material Courant time step stability limit. However, this limit is implemented in such a way that single-node Courant violations are permitted without adverse stability effects. Thus, single small nodes embedded in a series of larger nodes will not adversely affect the time step and computing cost. The nearly-implicit numerical solution scheme also uses a direct sparse matrix solution technique for time step advancement. This scheme has a grind time that is 25 to 60% greater than the semi-implicit scheme but allows violation of the material Courant limit for all nodes.

3.0.1 References

3.0-1.   J. A. Trapp and V. H. Ransom, *RELAP5 Hydrodynamic Model: Progress Summary - Field Equations*, SRD-126-76, Idaho National Engineering Laboratory, June 1976.

3.0-2.   V. H. Ransom and J. A. Trapp, *RELAP5 Hydrodynamic Model: Progress Summary - PILOT Code*, PG-R-76-013, Idaho National Engineering Laboratory, December 1976.

3.0-3.   V. H. Ransom and J. A. Trapp, *RELAP5 Progress Summary-PILOT Code Hydrodynamic Model and Numerical Scheme*, CDAP-TR-005, Idaho National Engineering Laboratory, January 1978.

3.0-4.   V. H. Ransom, *Course A-Numerical Modeling of Two-Phase Flows for Presentation at Ecole d'Ete d'Analyse Numerique,* EGG-EAST-8546, Idaho National Engineering Laboratory, May 1989.

3.0-5.   V. H. Ransom and D. L. Hicks, "Hyperbolic Two-Pressure Models for Two-Phase Flow," *Journal of Computational Physics, 53,* 1984, pp. 124-151.

3.0-6.   V. H. Ransom and D. L. Hicks, "Hyperbolic Two-Pressure Models for Two-Phase Flow Revisited," *Journal of Computational Physics, 75,* 1988, pp. 489-504.

3.0-7.   V. H. Ransom and M. P. Scofield, *Two-Pressure Hydrodynamic Model for Two-Phase Separated Flow,* SRD-50-76, Idaho National Engineering Laboratory, February 1976.

3.0-8.   J. D. Ramshaw and J. A. Trapp, "Characteristics, Stability, and Short-Wavelength Phenomena in Two-Phase Flow Equation Systems," *Nuclear Science and Engineering, 66,* 1978, pp. 93-102.

3.0-9.   J. A. Trapp, "The Mean Flow Character of Two-Phase Flow Equations," *International Journal of Multiphase Flow, 12,* 1986, pp. 263-276.

3.0-10.   V. H. Ransom and V. A. Mousseau, "Convergence and Accuracy Expectations for Two-Phase Flow Simulations," *Canadian Nuclear Society International Conference on Simulation Methods in Nuclear Engineering, Montreal, Canada, April 18-20, 1990.*

3.0-11.   V. H. Ransom and V. A. Mousseau, "Convergence and Accuracy of the RELAP5 Two-Phase Flow Model," *International ANS Topical Meeting on the Advances in Mathematics, Computation, and Reactor Physics, Pittsburgh, PA, April 28-May 2, 1991.*

3.0-12.   J. A. Trapp, "Numerical Methods for Two-Phase Flow Simulation: Some Observations," *International ANS Topical Meeting on the Advances in Mathematics, Computation, and Reactor Physics, Pittsburgh, PA, April 28-May 2, 1991.*

3.0-13.   A. S.-L. Shieh, R. Krishnamurthy, and V. H. Ransom, "Stability, Accuracy, and Convergence of the Numerical Methods in RELAP5/MOD3," *Nuclear Science and Engineering, 116,* 1994, pp. 227-244.

3.1 Field Equations

The ATHENA thermal-hydraulic model solves eight field equations for eight primary dependent variables. The primary dependent variables are pressure (P), phasic specific internal energies (U_g, U_f), vapor/gas volume fraction (void fraction) (α_g), phasic velocities (v_g, v_f), noncondensable quality (X_n), and boron density (ρ_b). The independent variables are time (t) and distance (x). Noncondensable quality is defined as the ratio of the noncondensable gas mass to the total vapor/gas phase mass, i.e., $X_n = \dfrac{M_n}{M_n + M_s}$, where M_n is the mass of noncondensable in the vapor/gas phase and M_s is the mass of the vapor in the vapor/gas phase. The secondary dependent variables used in the equations are phasic densities (ρ_g, ρ_f), phasic temperatures (T_g, T_f), saturation temperature (T^s), and noncondensable mass fraction in noncondensable gas phase (X_{ni}) for the i-th noncondensable species, i.e.,

$$X_{ni} = \frac{M_{ni}}{\sum_{i=1}^{N} M_{ni}} = \frac{M_{ni}}{M_n} \tag{3.1-1}$$

where M_{ni} is the mass of the i-th noncondensable in the vapor/gas phase, M_n is the total mass of noncondensable gas in the vapor/gas phase, and N is the number of noncondensables.

The basic two-fluid differential equations that form the basis for the hydrodynamic model are next presented. This discussion will be followed by the development of a convenient form of the differential equations that is used as the basis for the numerical solution scheme. The modifications necessary to model horizontal stratified flow are also discussed. Subsequently, the semi-implicit scheme difference equations and the associated time-advancement scheme are discussed. Next, the nearly-implicit scheme difference equations and the associated time-advancement scheme are presented. Finally, the volume average velocity formulations, implicit hydrodynamic/heat structure coupling, and the boron transport equation numerical solution are presented.

3.1.1 Basic Differential Equations

The differential form of the one-dimensional transient field equations is first presented for a one-component system. The modifications necessary to consider noncondensables as a component of the vapor/gas phase and boron as a nonvolatile solute component of the liquid phase are discussed separately.

3.1.1.1 Vapor/Liquid System. The basic field equations for the two-fluid nonequilibrium model consist of two phasic continuity equations, two phasic momentum equations, and two phasic energy equations. The equations are recorded in differential stream tube form with time and one space dimension as independent variables and in terms of time and volume-average dependent variables.[a] The development of such equations for the two-phase process has been recorded in several references[3.1-1],[3.1-2],[3.1-3] and is not repeated here. The equations are cast in the basic form with discussion of those terms that may differ

from other developments. Manipulations required to obtain the form of the equations from which the numerical scheme was developed are described in Section 3.1.2.

Mass Continuity

The phasic continuity equations are

$$\frac{\partial}{\partial t}(\alpha_g \rho_g) + \frac{1}{A}\frac{\partial}{\partial x}(\alpha_g \rho_g v_g A) = \Gamma_g \tag{3.1-2}$$

$$\frac{\partial}{\partial t}(\alpha_f \rho_f) + \frac{1}{A}\frac{\partial}{\partial x}(\alpha_f \rho_f v_f A) = \Gamma_f \quad . \tag{3.1-3}$$

These equations come from the one-dimensional phasic mass equations [Equation (8.12)] in **Reference 3.1-1** as follows: Equation (8.12) can be written in area average notation wherein the term $\frac{L}{V}$ has been reduced to $\frac{1}{A}$. The vapor continuity Equation (3.1-2) then is the same as Equation (8.12) using $k = g$. The liquid continuity Equation (3.1-3) then is the same as Equation (8.12) using $k = f$. This derivation is discussed in Chapter 8 of **Reference 3.1-1**.

Generally, the flow does not include mass sources or sinks, and overall continuity consideration yields the requirement that the liquid generation term be the negative of the vapor generation, that is,

$$\Gamma_f = -\Gamma_g \quad . \tag{3.1-4}$$

The interfacial mass transfer model assumes that total mass transfer can be partitioned into mass transfer at the vapor/liquid interface in the bulk fluid (Γ_{ig}) and mass transfer at the vapor/liquid interface in the thermal boundary layer near the walls (Γ_w); that is,

$$\Gamma_g = \Gamma_{ig} + \Gamma_w \quad . \tag{3.1-5}$$

The Γ_{ig} term will be developed in the following sections, and the Γ_w term is determined as part of the wall heat transfer computation (Section 3.3.10).

Momentum Conservation

---

a. In all the field equations shown herein, the correlation coefficients[3.1-1] are assumed to be unity so the average of a product of variables is equal to the product of the averaged variables.

The phasic conservation of momentum equations are used, and recorded here, in an expanded form and in terms of momenta per unit volume using the phasic primitive velocity variables v_g and v_f. The spatial variation of momentum term is expressed in terms of v_g^2 and v_f^2. This form has the desirable feature that the momentum equation reduces to Bernoulli's equations for steady, incompressible, and frictionless flow. A guiding principle used in the development of the ATHENA momentum formulation is that momentum effects are secondary to mass and energy conservation in reactor safety analysis and a less exact formulation (compared to mass and energy conservation) is acceptable, especially since nuclear reactor flows are dominated by large sources and sinks of momentum (i.e., pumps, abrupt area change). A primary reason for use of the expanded form is that is it more convenient for development of the numerical scheme. The momentum equation for the vapor/gas phase is

$$
\begin{aligned}
\alpha_g \rho_g A \frac{\partial v_g}{\partial t} + \frac{1}{2} \alpha_g \rho_g A \frac{\partial v_g^2}{\partial x} = &- \alpha_g A \frac{\partial P}{\partial x} + \alpha_g \rho_g B_x A - (\alpha_g \rho_g A) FWG(v_g) \\
&+ \Gamma_g A (v_{gI} - v_g) - (\alpha_g \rho_g A) FIG(v_g - v_f) \\
&- C \alpha_g \alpha_f \rho_m A \left[\frac{\partial (v_g - v_f)}{\partial t} + v_f \frac{\partial v_g}{\partial x} - v_g \frac{\partial v_f}{\partial x} \right]
\end{aligned}
\tag{3.1-6}
$$

and for the liquid phase is

$$
\begin{aligned}
\alpha_f \rho_f A \frac{\partial v_f}{\partial t} + \frac{1}{2} \alpha_f \rho_f A \frac{\partial v_f^2}{\partial x} = &- \alpha_f A \frac{\partial P}{\partial x} + \alpha_f \rho_f B_x A - (\alpha_f \rho_f A) FWF(v_f) \\
&- \Gamma_g A (v_{fI} - v_f) - (\alpha_f \rho_f A) FIF(v_f - v_g) \\
&- C \alpha_f \alpha_g \rho_m A \left[\frac{\partial (v_f - v_g)}{\partial t} + v_g \frac{\partial v_f}{\partial x} - v_f \frac{\partial v_g}{\partial x} \right] \; .
\end{aligned}
\tag{3.1-7}
$$

These equations come from the one-dimensional phasic momentum equations [Equation (8.13)] in **Reference 3.1-1** with the following simplifications: the Reynolds stresses are neglected, the phasic pressures are assumed equal, the interfacial pressure is assumed equal to the phasic pressures (except for stratified flow), the covariance terms are universally neglected (unity assumed for covariance multipliers), interfacial momentum storage is neglected, phasic viscous stresses are neglected, the interface force terms consist of both pressure and viscous stresses, and the normal wall forces are assumed adequately modeled by the variable area momentum flux formulation. The phasic continuity equations are multiplied by the corresponding phasic velocity, and the resulting equations are subtracted from the momentum equations. The vapor/gas momentum Equation (3.1-6) is the same as the resulting vapor/gas momentum equation from Equation (8.13) using k = g; the liquid momentum Equation (3.1-7) is the same as the resulting liquid momentum equation from Equation (8.13) using k = f. This is discussed in Chapter 8 of **Reference 3.1-1**.

The force terms on the right sides of Equations (3.1-6) and (3.1-7) are, respectively, the pressure gradient, the body force (i.e., gravity and pump head), wall friction, momentum transfer due to interface

mass transfer, interface frictional drag, and force due to virtual mass. The terms FWG and FWF are part of the wall frictional drag, which are linear in velocity, and are products of the friction coefficient, the frictional reference area per unit volume, and the magnitude of the fluid bulk velocity. The interfacial velocity in the interface momentum transfer term is the unit momentum with which phase appearance or disappearance occurs. The coefficients FIG and FIF are part of the interface frictional drag; two different models (drift flux and drag coefficient) are used for the interface friction drag, depending on the flow regime. The coefficient of virtual mass is based on that used by Anderson[3.1-4] in the RISQUE code, where the value for C depends on the flow regime. A value of $C > 1/2$ has been shown to be appropriate for bubbly or dispersed flows,[3.1-5, 3.1-6] while $C = 0$ may be appropriate for a separated or stratified flow. At present, a value of $C > 1/2$ is used for all flow regimes. This is discussed in Section 3.3.

The virtual mass term listed in Equations (3.1-6) and (3.1-7) is the same objective formulation[3.1-7, 3.1-8] used in RELAP5/MOD1. In the ATHENA coding, however, this term is simplified. In particular, the spatial derivative portion of the term is neglected. The reason for this change is that inaccuracies in approximating the spatial derivative portion of the term for the relatively coarse nodalizations used in system representations can lead to nonphysical characteristics in the numerical solution. The primary effect of the virtual mass term is on the mixture sound speed; thus, the simplified form is adequate, since critical flows are calculated in ATHENA using an integral model[3.1-9] in which the sound speed is based on an objective formulation for the added mass terms.

Conservation of momentum at the interface requires that the force terms associated with interface mass and momentum exchange sum to zero, and is shown as

$$
\begin{aligned}
&\Gamma_g A v_{gI} - (\alpha_g \rho_g A) FIG(v_g - v_f) - C\alpha_g\alpha_f\rho_m A\left[\frac{\partial(v_g - v_f)}{\partial t}\right] \\
&- \Gamma_g A v_{fI} - (\alpha_f \rho_f A) FIF(v_f - v_g) - C\alpha_f\alpha_g\rho_m A\left[\frac{\partial(v_f - v_g)}{\partial t}\right] = 0
\end{aligned}
\tag{3.1-8}
$$

where the spatial derivatives have been eliminated as explained above.

This particular form for interface momentum balance results from consideration of the momentum equations in unexpanded form. The force terms associated with virtual mass acceleration in Equation (3.1-8) sum to zero identically as a result of the particular form chosen. In addition, it is usually assumed (although not required by any basic conservation principle) that the interface momentum transfer due to friction and due to mass transfer independently sum to zero, that is,

$$
v_{gI} = v_{fI} = v_I
\tag{3.1-9}
$$

and

$$\alpha_g \rho_g FIG \;=\; \alpha_f \rho_f FIF \;=\; \alpha_g \alpha_f \rho_g \rho_f FI \;\;. \tag{3.1-10}$$

These conditions are sufficient to ensure that Equation (3.1-8) is satisfied.

<u>Energy Conservation</u>

The phasic thermal energy equations are

$$\frac{\partial}{\partial t}(\alpha_g \rho_g U_g) + \frac{1}{A}\frac{\partial}{\partial x}(\alpha_g \rho_g U_g v_g A) \;=\; -\,P\frac{\partial \alpha_g}{\partial t} \;-\; \frac{P}{A}\frac{\partial}{\partial x}(\alpha_g v_g A)$$
$$+\; Q_{wg} + Q_{ig} + \Gamma_{ig} h_g^{*} + \Gamma_w h_g^{'} + DISS_g \tag{3.1-11}$$

$$\frac{\partial}{\partial t}(\alpha_f \rho_f U_f) + \frac{1}{A}\frac{\partial}{\partial x}(\alpha_f \rho_f U_f v_f A) \;=\; -\,P\frac{\partial \alpha_f}{\partial t} \;-\; \frac{P}{A}\frac{\partial}{\partial x}(\alpha_f v_f A)$$
$$+\; Q_{wf} + Q_{if} - \Gamma_{ig} h_f^{*} - \Gamma_w h_f^{'} + DISS_f \;\;. \tag{3.1-12}$$

These equations come from the one-dimensional phasic thermal energy equations [Equation (8.16)] in **Reference 3.1-1** with the following simplifications: the Reynolds heat flux is neglected, the covariance terms are universally neglected (unity assumed for covariance multipliers), interfacial energy storage is neglected, and internal phasic heat transfer is neglected. The vapor/gas thermal energy Equation (3.1-11) is the same as the resulting vapor/gas thermal energy equation from Equation (8.16) using k = g; the liquid thermal energy Equation (3.1-12) is the same as the resulting liquid thermal energy equation from Equation (8.16) using k = f. This derivation is discussed in Chapter 8 of **Reference 3.1-1**.

In the phasic energy equations, Q_{wg} and Q_{wf} are the phasic wall heat transfer rates per unit volume (see Section 3.3.9). These phasic wall heat transfer rates satisfy the equation

$$Q \;=\; Q_{wg} + Q_{wf} \tag{3.1-13}$$

where Q is the total wall heat transfer rate to the fluid per unit volume.

The phasic specific enthalpies (h_g^{*}, h_f^{*}) associated with bulk interface mass transfer in Equations (3.1-11) and (3.1-12) are defined in such a way that the interface energy jump conditions at the liquid-vapor interface are satisfied. In particular, the h_g^{*} and h_f^{*} are chosen to be h_g^{s} and h_f, respectively, for the case of vaporization and h_g and h_f^{s}, respectively, for the case of condensation. The same is true for the phasic specific enthalpies $(h_g^{'}, h_f^{'})$ associated with wall (thermal boundary layer) interface mass transfer. The logic for this choice will be further explained in the development of the mass transfer (vapor generation) model.

Vapor Generation

The vapor generation (or condensation) consists of two parts, vapor generation which results from energy exchange in the bulk fluid (Γ_{ig}) and energy exchange in the thermal boundary layer near the wall (Γ_w) [see Equation (3.1-5)]. Each of the vapor generation (or condensation) processes involves interface heat transfer effects. The interface heat transfer terms (Q_{ig} and Q_{if}) appearing in Equations (3.1-11) and (3.1-12) include heat transfer from the fluid states to the interface due to interface energy exchange in the bulk and in the thermal boundary layer near the wall. The vapor generation (or condensation) rates are established from energy balance considerations at the interface.

The discussion that follows assumes there is one wall (heat structure) that is next to the fluid. In some applications, there can be multiple walls (heat structures) next to the fluid. For this case, there can be flashing in the thermal boundary layer near some walls (i.e., hot walls) and condensation in the thermal boundary layer near the other walls (i.e., cold walls). The case of multiple walls is discussed in Section 3.1.7 of this volume of the manual as well as in Volume IV.

The summation of Equations (3.1-11) and (3.1-12) produces the mixture energy equation, from which it is required that the interface transfer terms sum to zero, that is,

$$Q_{ig} + Q_{if} + \Gamma_{ig}(h_g^* - h_f^*) + \Gamma_w(h_g' - h_f') = 0 \quad . \tag{3.1-14}$$

The interface heat transfer terms (Q_{ig} and Q_{if}) consist of two parts, that is, interface heat transfer in the bulk (Q_{ig}^B and Q_{if}^B) and interface heat transfer in the thermal boundary layer near the wall (Q_{ig}^W and Q_{if}^W). This is one situation where the assumption of no transverse gradients needs to be supplemented by a special model. The interface heat transfer terms are shown in **Figure 3.1-1** for the case of subcooled boiling.

The two parts are additive, that is,

$$Q_{ig} = Q_{ig}^B + Q_{ig}^W \tag{3.1-15}$$

and

$$Q_{if} = Q_{if}^B + Q_{if}^W \quad . \tag{3.1-16}$$

The bulk interface heat transfer is at the vapor-liquid interface in the bulk. This represents thermal energy exchange between the fluid interface (at the saturation temperature T^s corresponding to the total pressure P) and the bulk fluid state.
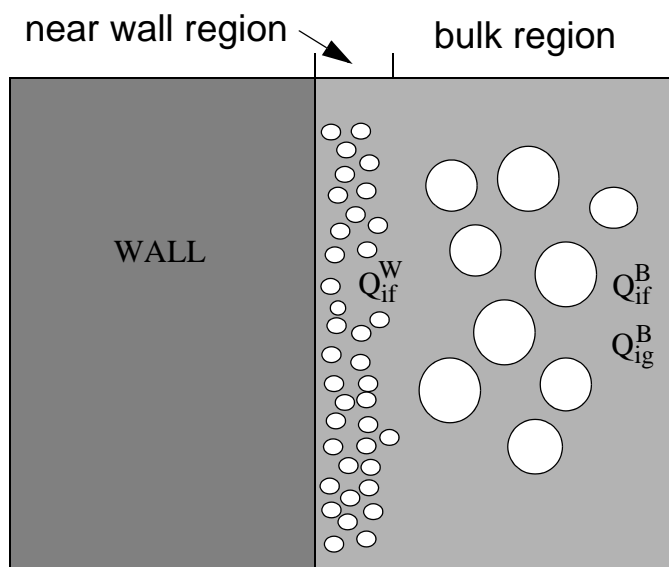
Figure 3.1-1 Interface heat transfer in the bulk and near the wall for subcooled boiling.

For vapor, the bulk interface heat transfer is given by

$$Q_{ig}^{B} = H_{ig}(T^{s} - T_{g}) \tag{3.1-17}$$

where H_{ig} is the vapor interface heat transfer coefficient per unit volume and T_{g} is the vapor temperature.

For liquid, the bulk interface heat transfer is given by

$$Q_{if}^{B} = H_{if}(T^{s} - T_{f}) \tag{3.1-18}$$

where H_{if} is the liquid interface heat transfer coefficient per unit volume and T_{f} is the liquid temperature.

The Q_{ig}^{W} and Q_{if}^{W} terms are the interface heat transfer rates near the wall and will be defined in terms of the wall vapor generation (or condensation) process. This is discussed in more detail in Volume IV. Inserting Equations (3.1-17) and (3.1-18) into Equations (3.1-15) and (3.1-16) gives

$$Q_{ig} = H_{ig}(T^{s} - T_{g}) + Q_{ig}^{W} \tag{3.1-19}$$

and

$$Q_{if} = H_{if}(T^s - T_f) + Q_{if}^W \quad . \tag{3.1-20}$$

Although it is not a fundamental requirement, it is assumed that Equation (3.1-14) will be satisfied by requiring that the bulk interface energy exchange terms and the near wall interface energy exchange terms each sum to zero independently. Thus,

$$H_{ig}(T^s - T_g) + H_{if}(T^s - T_f) + \Gamma_{ig}(h_g^* - h_f^*) = 0 \tag{3.1-21}$$

and

$$Q_{ig}^W + Q_{if}^W + \Gamma_w(h_g' - h_f') = 0 \quad . \tag{3.1-22}$$

In addition, since it is assumed that vapor appears at saturation, it follows that $Q_{ig}^W = 0$ for boiling processes in the boundary layer near the wall. Equation (3.1-22) can then be used to solve for the interface vaporization rate in the boundary layer near the walls, which is

$$\Gamma_w = \frac{-Q_{if}^W}{h_g' - h_f'} \quad . \tag{3.1-23}$$

Similarly, since it is assumed that liquid appears at saturation, it follows that $Q_{if}^W = 0$ for condensation processes in the boundary layer near the wall. Equation (3.1-22) can then be used to solve for the interface condensation rate in the boundary layer near the walls, which is

$$\Gamma_w = \frac{-Q_{ig}^W}{h_g' - h_f'} \quad . \tag{3.1-24}$$

Solving Equation (3.1-23) and (3.1-24) for Q_{if}^W and Q_{ig}^W, and substituting these terms into Equations (3.1-19) and (3.1-20), the interface energy transfer terms, Q_{ig} and Q_{if}, can thus be expressed in a general way as

$$Q_{ig} = H_{ig}(T^s - T_g) - \left(\frac{1-\varepsilon}{2}\right)\Gamma_w(h_g' - h_f') \tag{3.1-25}$$

and

$$Q_{if} = H_{if}(T^s - T_f) - \left(\frac{1 + \varepsilon}{2}\right)\Gamma_w(h_g' - h_f') \ , \tag{3.1-26}$$

where $\varepsilon = 1$ for boiling in the boundary layer near the wall, and $\varepsilon = -1$ for condensation in the boundary layer near the wall. Finally, Equation (3.1-14) can be used to solve for the interface vaporization (or condensation) rate in the bulk fluid, which is

$$\Gamma_{ig} = -\frac{Q_{ig} + Q_{if}}{h_g^* - h_f^*} - \Gamma_w\frac{(h_g' - h_f')}{h_g^* - h_f^*} \ , \tag{3.1-27}$$

which, upon substitution of Equations (3.1-25) and (3.1-26), becomes

$$\Gamma_{ig} = -\frac{H_{ig}(T^s - T_g) + H_{if}(T^s - T_f)}{h_g^* - h_f^*} \quad . \tag{3.1-28}$$

The phase change process that occurs at the interface is envisioned as a process in which bulk fluid is heated or cooled to the saturation temperature and phase change occurs at the saturation state. The interface energy exchange process from each phase must be such that at least the sensible energy change to reach the saturation state occurs. Otherwise, it can be shown that the phase change process implies energy transfer from a lower temperature to a higher temperature. Such conditions can be avoided by the proper choice of the variables h_g^* and h_f^* for bulk interface mass transfer and h_g' and h_f' for near wall interface mass transfer. In particular, it can be shown that h_g^* and h_f^* should be

$$h_g^* = \frac{1}{2}[(h_g^s + h_g) + \eta(h_g^s - h_g)] \tag{3.1-29}$$

and

$$h_f^* = \frac{1}{2}[(h_f^s + h_f) - \eta(h_f^s - h_f)] \tag{3.1-30}$$

where

$$\eta \quad = \quad 1 \text{ for } \Gamma_{ig} \geq 0$$

$$= \quad -1 \text{ for } \Gamma_{ig} < 0.$$

It can also be shown that $h_g^{'}$ and $h_f^{'}$ should be

$$h_g^{'} = \frac{1}{2}[(h_g^s + h_g) + \varepsilon(h_g^s - h_g)]$$ (3.1-31)

and

$$h_f^{'} = \frac{1}{2}[(h_f^s + h_f) - \varepsilon(h_f^s - h_f)]$$ (3.1-32)

where

$$\varepsilon \qquad = \qquad 1 \text{ for } \Gamma_w \geq 0$$

$$= \qquad -1 \text{ for } \Gamma_w < 0.$$

Substituting Equation (3.1-28) into Equation (3.1-5) gives the final expression for the total interface mass transfer as

$$\Gamma_g = -\frac{H_{ig}(T^s - T_g) + H_{if}(T^s - T_f)}{h_g^* - h_f^*} + \Gamma_w \quad .$$ (3.1-33)

Volume IV of the manual discusses the energy partitioning in more detail.

Dissipation Terms

The phasic energy dissipation terms, DISS_g and DISS_f, are the sums of wall friction, pump, and turbine effects. The dissipation effects due to interface mass transfer, interface friction, and virtual mass are neglected. This is a reasonable assumption since these terms are small in magnitude in the energy equation. In the mass and momentum equations, interface mass transfer, interface friction, and virtual mass are important and are not neglected. The wall friction dissipations are defined as

$$\text{DISS}_g = \alpha_g \rho_g \, \text{FWG} \, v_g^2$$ (3.1-34)

and

$$\text{DISS}_f = \alpha_f \rho_f \, \text{FWF} \, v_f^2 \quad .$$ (3.1-35)

The phasic energy dissipation terms satisfy the relation

$$\text{DISS} = \text{DISS}_g + \text{DISS}_f \tag{3.1-36}$$

where DISS is the energy dissipation. When a pump component is present, the associated energy dissipation is also included in the dissipation terms (see Section 3.5.4). When a turbine component is present, an appropriate heat source is used which is also included in the dissipation terms (see Section 3.5.5).

3.1.1.2 Noncondensables in the Vapor/Gas Phase. The basic, two-phase, single-component model just discussed can be extended to include a noncondensable component in the vapor/gas phase. The noncondensable component is assumed to move with the same velocity and have the same temperature as the vapor phase, so that

$$v_n = v_g \tag{3.1-37}$$

and

$$T_n = T_g \tag{3.1-38}$$

where the subscript, n, is used to designate the noncondensable component. The vapor/noncondensable mixture conditions can still be nonhomogeneous and nonequilibrium compared to the liquid and saturation conditions.

The general approach for inclusion of the noncondensable component consists of assuming that all properties of the vapor/gas phase (subscript g) are mixture properties of the vapor/noncondensable mixture. The static quality, X, is likewise defined as the mass fraction based on the mass of the vapor/gas phase. Thus, the two basic continuity equations [Equations (3.1-2) and (3.1-3)] are unchanged. However, it is necessary to add an additional mass conservation equation for the total noncondensable component, given by

$$\frac{\partial}{\partial t}(\alpha_g \rho_g X_n) + \frac{1}{A}\frac{\partial}{\partial x}(\alpha_g \rho_g X_n v_g A) = 0 \tag{3.1-39}$$

where

$\quad X_n \qquad = \qquad$ total noncondensable mass fraction in the vapor/gas phase

$$= \frac{\sum\limits_{i=1}^{N} M_{ni}}{\sum\limits_{i=1}^{N} M_{ni} + M_s} = \frac{M_n}{M_n + M_s} \qquad (3.1\text{-}40)$$

M_{ni} =   mass of i-th noncondensable gas

M_n =   total mass of noncondensable gas in the vapor/gas phase

M_s =   mass of vapor in the vapor/gas phase

N =   number of noncondensables.

For each noncondensable specie, the mass conservation equation is

$$\frac{\partial}{\partial t}(\alpha_g \rho_g X_n X_{ni}) + \frac{1}{A}\frac{\partial}{\partial x}(\alpha_g \rho_g X_n X_{ni} v_g A) = 0 \qquad (3.1\text{-}41)$$

where X_{ni} is defined in Equation (3.1-1). Only N-1 of the noncondensable gas specie equations need to be solved since the mass fraction of the N-th specie can be found as the difference between the total noncondensable gas mass fraction and the sum of the N-1 noncondensable gas specie mass fractions.

The energy equations are modified to include the sensible interface (direct) heating term Q_{gf}. This term is necessary because the interfacial terms use saturation temperature based on the bulk vapor partial pressure rather than saturation temperature based on the local (interface) vapor partial pressure. This is another situation in which the assumption of no transverse gradients in the one-dimensional formulation of the conservation equations needs to be supplemented by a special model. The energy field equations have the form

$$\frac{\partial}{\partial t}(\alpha_g \rho_g U_g) + \frac{1}{A}\frac{\partial}{\partial x}(\alpha_g \rho_g U_g v_g A) = -P\frac{\partial \alpha_g}{\partial t} - \frac{P}{A}\frac{\partial}{\partial x}(\alpha_g v_g A)$$
$$+ Q_{wg} + Q_{ig} + \Gamma_{ig} h_g^* + \Gamma_w h_g' - Q_{gf} + DISS_g \qquad (3.1\text{-}42)$$

$$\frac{\partial}{\partial t}(\alpha_f \rho_f U_f) + \frac{1}{A}\frac{\partial}{\partial x}(\alpha_f \rho_f U_f v_f A) = -P\frac{\partial \alpha_f}{\partial t} - \frac{P}{A}\frac{\partial}{\partial x}(\alpha_f v_f A)$$
$$+ Q_{wf} + Q_{if} - \Gamma_{ig} h_f^* - \Gamma_w h_f' + Q_{gf} + DISS_f \ . \qquad (3.1\text{-}43)$$

The term Q_{gf} in Equations (3.1-42) and (3.1-43) is the sensible heat transfer rate per unit volume. This is the heat transfer at the noncondensable gas-liquid interface, and it represents thermal energy

exchange between the bulk fluid states themselves when noncondensable gas is present. This term is given by

$$Q_{gf} = \left(\frac{P - P_s}{P}\right)H_{gf}(T_g - T_f) = \frac{P_n}{P}H_{gf}(T_g - T_f)$$

(3.1-44)

where H_{gf} is the sensible (direct) heat transfer coefficient per unit volume. This makes use of Dalton's law ($P = P_s + P_n$), where P_n is the noncondensable gas partial pressure. This term is similar to the heat conduction term in the accumulator model (see Section 3.5.7.2). The multiplier based on the difference in the total pressure and the partial pressure of vapor is an ad-hoc function used to turn off this term when there is no noncondensable gas in the volume. The value of the heat transfer coefficient depends upon the configuration of the interface (i.e., flow regime) between the liquid and the noncondensable gas just like the situation for the vapor-liquid interface.

The interfacial heat transfer and mass transfer terms are also modified when noncondensables are present. The vapor/gas bulk interface heat transfer [Equation (3.1-17)] now has the form

$$Q_{ig}^B = \frac{P_s}{P}H_{ig}[T^s(P_s) - T_g] \ ,$$

(3.1-45)

where the fluid interface is assumed to be at the saturation temperature $T^s(P_s)$ corresponding to the partial pressure of vapor (P_s).

Thus, the total vapor/gas interfacial heat transfer [Equation (3.1-19)] now has the form

$$Q_{ig} = \frac{P_s}{P}H_{ig}[T^s(P_s) - T_g] + Q_{ig}^W \ \ .$$

(3.1-46)

The assumption that the bulk interface exchange terms sum to zero [Equation (3.1-21)], now has the form

$$\frac{P_s}{P}H_{ig}[T^s(P_s) - T_g] + H_{if}[T^s(P_s) - T_f] + \Gamma_{ig}(h_g^* - h_f^*) = 0 \ \ .$$

(3.1-47)

Thus, the total vapor/gas interface energy transfer term [Equation (3.1-25)] is now expressed as

$$Q_{ig} = \frac{P_s}{P}H_{ig}[T^s(P_s) - T_g] - \left(\frac{1-\varepsilon}{2}\right)\Gamma_w(h_g' - h_f') \ \ .$$

(3.1-48)

The bulk interface mass transfer rate [Equation (3.1-28)] now has the form

$$\Gamma_{ig} = -\frac{\frac{P_s}{P}H_{ig}[T^s(P_s) - T_g] + H_{if}[T^s(P_s) - T_f]}{h_g^* - h_f^*} \qquad (3.1\text{-}49)$$

and the total interface mass transfer rate [Equation (3.1-33)] now has the form

$$\Gamma_g = -\frac{\frac{P_s}{P}H_{ig}[T^s(P_s) - T_g] + H_{if}[T^s(P_s) - T_f]}{h_g^* - h_f^*} + \Gamma_w \qquad . \qquad (3.1\text{-}50)$$

Volume IV of the manual discusses the energy partitioning in more detail.

The vapor saturation specific enthalpy h_g^s used for the vapor specific enthalphy h_g^*, and the liquid saturation specific enthalpy h_f^s used for the liquid specific enthalpy h_f^*, which are used in the energy field equations and in the mass transfer Γ_g, are based on the partial pressure of vapor instead of the total pressure when noncondensables are present.

The momentum field equations are unchanged when noncondensables are present. In all the equations, the vapor/gas field properties are now evaluated for the vapor/noncondensable mixture. The modifications appropriate to the state relationships are discussed in Section 3.2.3.

3.1.1.3 Boron Concentration in the Liquid Field. An Eulerian boron tracking model is used in ATHENA that simulates the transport of a dissolved component (solute) in the liquid phase (solvent). The solution is assumed to be sufficiently dilute that the following assumptions are valid:

- Liquid (solvent) properties are not altered by the presence of the solute.

- Solute is transported only in the liquid phase (solvent) and at the velocity of the liquid phase (solvent).

- Energy transported by the solute is negligible.

- Inertia of the solute is negligible.

Under these assumptions, only an additional field equation for the conservation of the solute (i.e., boron) is required. In differential form, the added equation is

$$\frac{\partial \rho_b}{\partial t} + \frac{1}{A}\frac{\partial (\rho_b v_f A)}{\partial x} = 0 \qquad\qquad (3.1\text{-}51)$$

where the spatial boron density, ρ_b, is defined as

$$\rho_b = \alpha_f \rho_f C_b = \rho_m (1 - X) C_b \quad . \qquad\qquad (3.1\text{-}52)$$

C_b is the concentration of boron (mass of boron per mass of liquid), ρ_b is the spatial boron density (mass of boron per total volume of liquid and vapor/gas), and X is the static quality.

3.1.1.4 Radionuclide Transport Model

An Eulerian radionuclide transport model is used in ATHENA to simulate the transport of radioactive or fertile nuclides in the reactor coolant systems (fertile nuclides are those nuclides that can be made radioactive by neutron capture). The model can be used in connection with the nuclear detector model to describe the response of the control and safety systems to the presence of radioactive species in the coolant systems. The radionuclide species may be transported by either the liquid or vapor/gas phases. A radioactive species may be created by neutron absorption in a fertile specie (i.e., nitrogen 16 may be created by an (n,p) reaction with the oxygen 16 in the water coolant in the reactor core) or may be injected into the coolant system using general tables or control variables. For example, general tables or control variables may be used to model the release of a radionuclide specie from fuel rods due to bursting during a transient or through pinhole leaks that develop due to erosion, fretting, or manufacturing defects in the fuel rod cladding or through leaching of the nuclide from the structural material in the reactor system (i.e., cobalt 59 is leached out of steel in the reactor system by the cooant and becomes available to be transmuted to cobalt 60 through neutron capture as it circulates through the reactor core). A radionuclide specie may also be destroyed by neutron absorption (i.e., transmuted to a radioactive or nonradioactive daughter specie). The concentration of radionuclide species are assumed to be sufficiently dilute that assumptions similar to those for the boron transport model are valid:

- The fluid properties (liquid of vapor/gas) are not altered by the presence of radionuclide species.

- Energy absorbed by the transporting phase from the decay of radionuclide species is negligable.

- The radionuclide species are well mixed with the transporting phase so that they are transported at the phase velocity.

Under these assumptions, the equation for the conservation of mass for a radionuclide specie is

$$\frac{\partial C}{\partial t} + \frac{1}{A}\frac{\partial}{\partial x}(CvA) = S \tag{3.1-53}$$

where C is the number density of the radionuclide specie in atoms per unit volume, v is the velocity of the transporting phase, A is the cross sectional area of the flow duct, and S is the source of the radionuclide specie in units of atoms per unit volume per second. The number density C may be converted to the mass density as

$$\rho = \frac{CMw}{N_a}$$

where ρ is the mass density of the radionuclide specie in units of mass per unit volume (i.e., kg/m^3), N_a is Avogradro's number (atoms per kg-mole), and Mw is the moelcular weight of the radionuclide specie (kg/kg-mole).

3.1.1.5 Stratified Flow. Flow at low velocity in a horizontal pipe can be stratified as a result of buoyancy forces caused by density differences between vapor/gas and liquid. When the flow is stratified, the area average pressures are affected by nonuniform transverse distribution of the phases. Appropriate modifications to the basic field equations when stratified flow exists are obtained by considering separate area average pressures for the vapor/gas and liquid phases and the interfacial pressure between them. Using this model, the pressure gradient force terms of Equations (3.1-6) and (3.1-7) become

$$-\alpha_g A\frac{\partial P}{\partial x} \quad \rightarrow \quad -\alpha_g A\frac{\partial P_g}{\partial x} + (P_I - P_g)A\frac{\partial \alpha_g}{\partial x} \tag{3.1-54}$$

and

$$-\alpha_f A\frac{\partial P}{\partial x} \quad \rightarrow \quad -\alpha_f A\frac{\partial P_f}{\partial x} + (P_I - P_f)A\frac{\partial \alpha_f}{\partial x} \quad . \tag{3.1-55}$$

The area average pressure for the entire cross-section of the flow is expressed in terms of the phasic area average pressures by

$$P = \alpha_g P_g + \alpha_f P_f \quad . \tag{3.1-56}$$

With these definitions, the sum of the phasic momentum equations, written in terms of the cross-section average pressure (see Section 3.1.2) remains unchanged. However, the difference of the phasic momentum equations (see Section 3.1.2), contains the following additional terms on the right side

$$\left(\frac{\rho}{\alpha_g\alpha_f\rho_g\rho_f}\right)\left[-\alpha_f\frac{\partial(\alpha_gP_g)}{\partial x}+\alpha_g\frac{\partial(\alpha_fP_f)}{\partial x}+P_I\frac{\partial\alpha_g}{\partial x}\right]\quad. \tag{3.1-57}$$

The interface and phasic cross-sectional average pressures, P_I, P_g, and P_f, can be found by means of the assumption of a transverse hydrostatic pressure in a round pipe. For a pipe having diameter D, pressures P_I, P_g, and P_f are given by

$$P_g = P_I - \rho_g B_y D\left(\frac{\sin^3\theta}{3\pi\alpha_g}-\frac{\cos\theta}{2}\right) \tag{3.1-58}$$

$$P_f = P_I - \rho_f B_y D\left(\frac{\sin^3\theta}{3\pi\alpha_f}-\frac{\cos\theta}{2}\right) \tag{3.1-59}$$

where B_y equals the transverse body force (ordinarily equal to -g).

The central angle, θ, is defined by the void fraction, as illustrated in **Figure 3.1-2**. The algebraic relationship between α_g and θ is
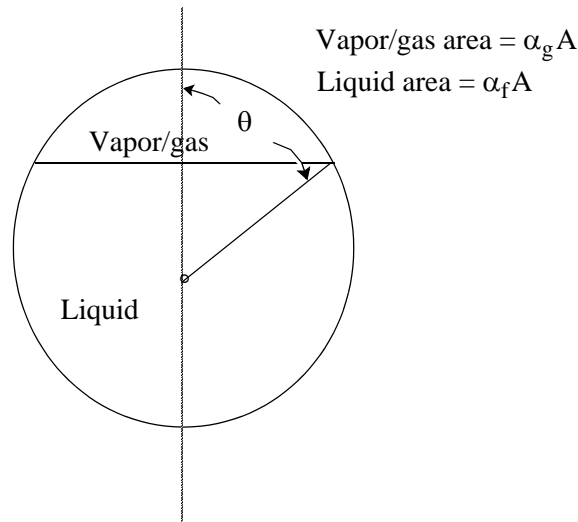
Figure 3.1-2 Relation of central angle θ to void fraction α_g.

$$\alpha_g\pi = \theta - \sin\theta\cos\theta\ . \tag{3.1-60}$$

The additional terms in the difference of the momentum equations [Equation (3.1-57)] can be simplified using Equations (3.1-58), (3.1-59), and (3.1-60) to obtain the term

$$-\left(\frac{\rho_m}{\rho_g\rho_f}\right)(\rho_f - \rho_g)\left(\frac{\pi D B_y}{4\sin\theta}\right)\frac{\partial\alpha_g}{\partial x}$$ (3.1-61)

where θ is related to the void fraction using Equation (3.1-60).

This equation can be rearranged to show more explicitly the dependence on the liquid level y as measured from the bottom of the pipe. Using Equation (3.1-60) along with

$$y = \frac{D}{2}(1 + \cos\theta) \,,$$ (3.1-62)

the term (3.1-61) becomes

$$\left(\frac{\rho_m}{\rho_g\rho_f}\right)(\rho_f - \rho_g)B_y\frac{\partial y}{\partial x} \quad.$$ (3.1-63)

For the phasic momentum Equations (3.1-6) and (3.1-7), the additional term takes the form

$$+\left[\frac{\alpha_g\alpha_f(\rho_f - \rho_g)}{\alpha_f\rho_f - \alpha_g\rho_g}\right]\rho_m B_y A\frac{\partial y}{\partial x}$$ (3.1-64)

for the vapor/gas momentum equation and

$$-\left[\frac{\alpha_g\alpha_f(\rho_f - \rho_g)}{\alpha_f\rho_f - \alpha_g\rho_g}\right]\rho_m B_y A\frac{\partial y}{\partial x}$$ (3.1-65)

for the liquid momentum equation. The preceding two equations are listed for informational purposes only, since the sum and difference of the phasic momentum equations is used in the numerical scheme.

To model a pipe of varying diameter, the liquid level is measured with respect to the center of the pipe rather than the bottom of the pipe. Equations (3.1-63), (3.1-64), and (3.1-65) are still valid; however, Equation (3.1-63) is replaced by

$$y = \frac{D}{2}\cos\theta \quad.$$ (3.1-66)

This new reference point is then at constant elevation in a horizontal pipe. For a varying area or constant area pipe, Equation (3.1-63) behaves correctly in that there is no head if the absolute level of the liquid is constant.

To take account of possible orifices, a junction diameter is estimated and the horizontal volume liquid levels are restrained to be within the range of this diameter. Thus, in the limit of a closed junction there will be no driving head term.

A ATHENA horizontal pipe need not be absolutely horizontal; it can have a slope of angle ϕ_{elev}, the elevation angle. There may also be a change of slope at the junction between two volumes. The modeling for this does not have a firm physical basis but has appropriate limiting behavior. The volume liquid levels are multiplied by $\cos\phi_{elev}$ which is unity for a horizontal volume. If the slopes of the two volumes are different then an extra term is added to the level difference. This term is proportional to the sine of the difference of the absolute values of the two slope angles. The sign and magnitude of the "constant" of proportionality are such that the following two conditions are met:

1. When a vertical volume is above a horizontal volume, the liquid level difference term is zero.

2. When a vertical volume is below a horizontal volume, the liquid level difference term is as if the liquid level in the vertical volume is at the bottom of the connecting orifice.

The above two limits ensure that liquid is not pushed upward, but can drain if required. When non-horizontal volumes have a significant liquid content, the normal head terms will be dominant.

The additional force term that arises for a stratified flow geometry in horizontal pipes is added to the basic equation when the flow is established to be stratified from flow regime considerations. Note that the additional force term was derived assuming a round pipe. If the cross-section is rectangular, this assumption is not valid.

A similar term is added when there is stratified flow in a series of cells defined as vertically oriented but are cross-connected in the horizontal direction. Equations (3.1-63), (3.1-64), and (3.1-65) are still used; however, Equation (3.1-62) is replaced with

$$y = \frac{1 - 2\alpha_g}{2}|\Delta z| \qquad\qquad\qquad (3.1\text{-}67)$$

where Δz is the elevation of the volume.

In order to provide for a smooth transition between stratified and nonstratified flow situations, this term is activated in all flow regimes. Since this term is small compared to other terms in the momentum equation when the flow is nonstratified, this is a reasonable assumption.

3.1.2 Numerically Convenient Set of Differential Equations

A more convenient set of differential equations upon which to base the numerical scheme is obtained from the expanded momentum difference equations [Equations (3.1-6) and (3.1-7)] and by expanding the time derivative (using the product rule) in the basic density and energy differential equations [Equations (3.1-2), (3.1-3), (3.1-39), (3.1-42), and (3.1-43)]. When the product rule is used to evaluate the time derivative, we will refer to this form as the expanded form. The mass and momentum equations are used as sum and difference equations in the numerical scheme and are recorded here in that form. The reason for using this form is ease of degeneration of the model to the single-phase case.

A sum density equation is obtained by expanding the time derivative in the phasic density equations, Equations (3.1-2) and (3.1-3), adding these two new equations, and using the relation

$$\frac{\partial \alpha_f}{\partial t} = -\frac{\partial \alpha_g}{\partial t} \quad . \tag{3.1-68}$$

This gives

$$\alpha_g \frac{\partial \rho_g}{\partial t} + \alpha_f \frac{\partial \rho_f}{\partial t} + (\rho_g - \rho_f)\frac{\partial \alpha_g}{\partial t} + \frac{1}{A}\frac{\partial}{\partial x}(\alpha_g \rho_g v_g A + \alpha_f \rho_f v_f A) = 0 \quad . \tag{3.1-69}$$

A difference density equation is obtained by expanding the time derivative in the phasic density equations, Equations (3.1-2) and (3.1-3), subtracting these two new equations, again using the relation

$$\frac{\partial \alpha_f}{\partial t} = -\frac{\partial \alpha_g}{\partial t} \tag{3.1-70}$$

and substituting Equation (3.1-50) for Γ_g. This gives

$$\alpha_g \frac{\partial \rho_g}{\partial t} - \alpha_f \frac{\partial \rho_f}{\partial t} + (\rho_g + \rho_f)\frac{\partial \alpha_g}{\partial t} + \frac{1}{A}\frac{\partial}{\partial x}(\alpha_g \rho_g v_g A - \alpha_f \rho_f v_f A)$$

$$= -\frac{2\left[\frac{P_s}{P}H_{ig}(T^s - T_g) + H_{if}(T^s - T_f)\right]}{h_g^* - h_f^*} + 2\Gamma_w \quad . \tag{3.1-71}$$

The time derivative of the total noncondensable density equation, Equation (3.1-39), is expanded to give

$$\rho_g X_n \frac{\partial \alpha_g}{\partial t} + \alpha_g X_n \frac{\partial \rho_g}{\partial t} + \alpha_g \rho_g \frac{\partial X_n}{\partial t} + \frac{1}{A}\frac{\partial}{\partial x}(\alpha_g \rho_g X_n v_g A) = 0 \quad .$$

(3.1–72)

The time derivative of the individual noncondensable density equation, Equation (3.1-41), is not expanded, since the individual noncondensable quality, X_{ni}, will be obtained from the unexpanded equation (Section 3.1.4.1).

The momentum equations are also rearranged into a sum and difference form. The sum momentum equation is obtained by direct summation of Equations (3.1-6) and (3.1-7) with the interface conditions [Equations (3.1-8) through (3.1-10)] substituted where appropriate and the cross-sectional area canceled throughout. The resulting sum equation is

$$\alpha_g \rho_g \frac{\partial v_g}{\partial t} + \alpha_f \rho_f \frac{\partial v_f}{\partial t} + \frac{1}{2}\alpha_g \rho_g \frac{\partial v_g^2}{\partial x} + \frac{1}{2}\alpha_f \rho_f \frac{\partial v_f^2}{\partial x} = -\frac{\partial P}{\partial x} + \rho_m B_x$$
$$- \alpha_g \rho_g FWG v_g - \alpha_f \rho_f FWF v_f - \Gamma_g(v_g - v_f) \quad .$$

(3.1–73)

The difference of the phasic momentum equations is obtained by first dividing the vapor/gas and liquid phasic momentum equations [Equations (3.1-6) and (3.1-7)] by $\alpha_g \rho_g A$ and $\alpha_f \rho_f A$, respectively, and subtracting. Here again, the interface conditions are used, and the common area is divided out. As previously discussed, the virtual mass term is simplified by neglecting the spatial derivative portion and the additional stratified force term (see Section 3.1.1.5) is added. The resulting equation is

$$\frac{\partial v_g}{\partial t} - \frac{\partial v_f}{\partial t} + \frac{1}{2}\frac{\partial v_g^2}{\partial x} - \frac{1}{2}\frac{\partial v_f^2}{\partial x} = -\left(\frac{1}{\rho_g} - \frac{1}{\rho_f}\right)\frac{\partial P}{\partial x}$$
$$- FWG v_g + FWF v_f$$
$$+ \frac{\Gamma_g[\rho_m v_I - (\alpha_f \rho_f v_g + \alpha_g \rho_g v_f)]}{\alpha_g \rho_g \alpha_f \rho_f} - \rho_m FI(v_g - v_f)$$
$$- C\frac{\rho_m^2}{\rho_g \rho_f}\frac{\partial(v_g - v_f)}{\partial t} + \left(\frac{\rho_m}{\rho_g \rho_f}\right)(\rho_f - \rho_g)B_y\frac{\partial y}{\partial x}$$

(3.1-74)

where the interfacial velocity, v_I, is defined as

$$v_I = \lambda v_g + (1 - \lambda)v_f \quad .$$

(3.1-75)

This definition for v_I has the property that if $\lambda = 1/2$ the interface momentum transfer process associated with mass transfer is reversible. This value leads to either an entropy sink or source, depending on the sign of Γ_g. However, if λ is chosen to be 0 for positive values of Γ_g and +1 for negative values of Γ_g

(that is, a donor formulation), the mass exchange process is always dissipative. The latter model for v_I is the most realistic for the momentum exchange process and is used for the numerical scheme development.

To develop an expanded form of the vapor/gas energy equation, the time derivative of the vapor/gas energy Equation (3.1-42) is expanded, Q_{ig} Equation (3.1-48) and the Γ_{ig} Equation (3.1-49) are substituted, and the H_{ig}, H_{if}, $\dfrac{\partial \alpha_g}{\partial t}$, and convective terms are collected. This gives the desired form for the vapor/gas energy equation, which is

$$
(\rho_g U_g + P)\frac{\partial \alpha_g}{\partial t} + \alpha_g U_g \frac{\partial \rho_g}{\partial t} + \alpha_g \rho_g \frac{\partial U_g}{\partial t} + \frac{1}{A}\left[\frac{\partial}{\partial x}(\alpha_g \rho_g U_g v_g A) + P\frac{\partial}{\partial x}(\alpha_g v_g A)\right]
$$

$$
= -\left(\frac{h_f^*}{h_g^* - h_f^*}\right)\frac{P_s}{P}H_{ig}(T^s - T_g) - \left(\frac{h_g^*}{h_g^* - h_f^*}\right)H_{if}(T^s - T_f) - \left(\frac{P - P_s}{P}\right)H_{gf}(T_g - T_f) \tag{3.1-76}
$$

$$
+ \left[\left(\frac{1+\varepsilon}{2}\right)h_g' + \left(\frac{1-\varepsilon}{2}\right)h_f'\right]\Gamma_w + Q_{wg} + DISS_g \ .
$$

To develop an expanded form of the liquid energy equation, the time derivative of the liquid energy Equation (3.1-43) is expanded, the Q_{if} Equation (3.1-26) and the Γ_{ig} Equation (3.1-49) are substituted, and

$$
\frac{\partial \alpha_f}{\partial t} = -\frac{\partial \alpha_g}{\partial t} \tag{3.1-77}
$$

is used. Then the H_{ig}, H_{if}, $\dfrac{\partial \alpha_g}{\partial t}$, and convective terms are collected. This gives the desired form for the liquid energy equation, which is

$$
-(\rho_f U_f + P)\frac{\partial \alpha_g}{\partial t} + \alpha_f U_f \frac{\partial \rho_f}{\partial t} + \alpha_f \rho_f \frac{\partial U_f}{\partial t} + \frac{1}{A}\left[\frac{\partial}{\partial x}(\alpha_f \rho_f U_f v_f A) + P\frac{\partial}{\partial x}(\alpha_f v_f A)\right]
$$

$$
= \left(\frac{h_f^*}{h_g^* - h_f^*}\right)\frac{P_s}{P}H_{ig}(T^s - T_g) + \left(\frac{h_g^*}{h_g^* - h_f^*}\right)H_{if}(T^s - T_f) + \left(\frac{P - P_s}{P}\right)H_{gf}(T_g - T_f) \tag{3.1-78}
$$

$$
- \left[\left(\frac{1+\varepsilon}{2}\right)h_g' + \left(\frac{1-\varepsilon}{2}\right)h_f'\right]\Gamma_w + Q_{wf} + DISS_f \ .
$$

The basic density and energy differential equations are, at times, used in unexpanded form in the back substitution part of the numerical scheme. When the product rule is not used to evaluate the time derivative, we will refer to this form as the *unexpanded* form. There are situations after a phase has appeared in a volume, where unphysical energies are calculated by the expanded form of the energy

equations. It was found that the unexpanded form, when used in the back substitution step, gave more physical temperatures because there is no linearization error in the time derivative when using the unexpanded form of the energy equations.

The vapor/gas, liquid, and noncondensable density equations, Equations (3.1-2), (3.1-3), and (3.1-39), are in unexpanded form. The Γ_g, Equation (3.1-50), is not substituted into the vapor/gas and liquid density equations. (The reason will be apparent in Section 3.1.4.) The vapor/gas energy equation, Equation (3.1-42), is altered by substituting Equation (3.1-48) for Q_{ig}, substituting Equation (3.1-49) for Γ_{ig}, and collecting the H_{ig}, H_{if}, and convective terms. This gives

$$
\frac{\partial}{\partial t}(\alpha_g \rho_g U_g) + \frac{1}{A}\left[\frac{\partial}{\partial x}(\alpha_g \rho_g U_g v_g A) + P\frac{\partial}{\partial x}(\alpha_g \rho_g A)\right]
$$

$$
= -P\frac{\partial \alpha_g}{\partial t} - \left(\frac{h_f^*}{h_g^* - h_f^*}\right)\frac{P_s}{P}H_{ig}(T^s - T_g) - \left(\frac{h_g^*}{h_g^* - h_f^*}\right)H_{if}(T^s - T_f) - \left(\frac{P - P_s}{P}\right)H_{gf}(T_g - T_f) \qquad (3.1\text{-}79)
$$

$$
+ \left[\left(\frac{1+\varepsilon}{2}\right)h_g' + \left(\frac{1-\varepsilon}{2}\right)h_f'\right]\Gamma_w + Q_{wg} + DISS_g \ .
$$

The liquid energy equation, Equation (3.1-43), is also altered by substituting Equation (3.1-26) for Q_{if}, substituting Equation (3.1-49) for Γ_{ig}, using Equation (3.1-77), and collecting the H_{ig}, H_{if}, and convective terms. This gives

$$
\frac{\partial}{\partial t}(\alpha_f \rho_f U_f) + \frac{1}{A}\left[\frac{\partial}{\partial x}(\alpha_f \rho_f U_f v_f A) + P\frac{\partial}{\partial x}(\alpha_f v_f A)\right]
$$

$$
= P\frac{\partial \alpha_g}{\partial t} + \left(\frac{h_f^*}{h_g^* - h_f^*}\right)\frac{P_s}{P}H_{ig}(T^s - T_g) + \left(\frac{h_g^*}{h_g^* - h_f^*}\right)H_{if}(T^s - T_f) + \left(\frac{P - P_s}{P}\right)H_{gf}(T_g - T_f) \qquad (3.1\text{-}80)
$$

$$
- \left[\left(\frac{1+\varepsilon}{2}\right)h_g' + \left(\frac{1-\varepsilon}{2}\right)h_f'\right]\Gamma_w + Q_{wf} + DISS_f \ .
$$

3.1.3 Semi-Implicit Scheme Difference Equations

The semi-implicit numerical solution scheme is based on replacing the system of differential equations with a system of finite difference equations partially implicit in time. The terms evaluated implicitly are identified as the scheme is developed. In all cases, the implicit terms are formulated to be linear in the dependent variables at new time. This results in a linear time-advancement matrix that is solved by direct inversion using the default border-profile LU solver.[3.1-10] The previously used sparse matrix solver[3.1-11] can also be used and is activated by the user in the input data. An additional feature of the scheme is that implicitness is selected such that the field equations can be reduced to a single difference equation per fluid control volume or mesh cell, which is in terms of the hydrodynamic pressure. Thus, only

an N x N system of equations must be solved simultaneously at each time step. N is the total number of control volumes used to simulate the fluid system.

It is well known[3.1-4,3.1-12] that the system of differential equations constitutes an ill-posed, initial-value problem. This fact is of little concern physically, since the addition of any second-order differential effect (regardless of how small), such as viscosity or surface tension, results in a well-posed problem.[3.1-13] However, the ill-posedness is of some concern numerically, since it is necessary that the numerical problem be well-posed. The approximations inherent in any numerical scheme modify the solution somewhat (truncation error); these effects can be either stabilizing or destabilizing. The resulting numerical scheme must be stable for mesh sizes of practical interest.

A well-posed and stable numerical algorithm results from employing several stabilizing techniques. These include the selective implicit evaluation of spatial gradient terms at the new time, donor formulations for the mass and energy flux terms, and use of a donor-like formulation for the momentum flux terms. Donor-like formulations for these flux terms are used because of the well-known instability of an explicit centered finite difference scheme. The term *donor-like* is used because the momentum flux formulation consists of a centered formulation for the spatial velocity gradient plus a numerical viscosity term. These two terms are similar to the form obtained when the momentum flux terms are donored with the unexpanded form of the momentum equations. The well-posedness of the final numerical scheme, as well as its accuracy, has been demonstrated for practical cell sizes by extensive numerical testing (see Volume VI).

The difference equations are based on the concept of a control volume (or mesh cell) in which mass and energy are conserved by equating accumulation to the rate of mass and energy in through the cell boundaries minus the rate of mass and energy out through the cell boundaries plus the source terms. This model results in defining mass and energy volume average properties and requiring knowledge of velocities at the volume boundaries. The velocities at boundaries are most conveniently defined through use of momentum control volumes (cells) centered on the mass and energy cell boundaries. This approach results in a numerical scheme having a staggered spatial mesh. The scalar properties (pressure, specific internal energies, and void fraction) of the flow are defined at cell centers, and vector quantities (velocities) are defined on the cell boundaries. The resulting one-dimensional spatial noding is illustrated in **Figure 3.1-3**. The term <u>cell</u> means an increment in the spatial variable, x, corresponding to the mass and energy control volume.

The difference equations for each cell are obtained by integrating the mass and energy equations [Equations (3.1-69), (3.1-71), (3.1-72), (3.1-76), and (3.1-78)] with respect to the spatial variable, x, from the junction at x_j to x_{j+1}. The momentum equations [Equations (3.1-73) and (3.1-74)] are integrated with respect to the spatial variable from cell center to adjoining cell center (x_K to x_L, **Figure 3.1-3**). The equations are listed for the case of a pipe with no branching and only one wall (heat structure) next to the cell. The numerical technique for the difference equations requires the volume be equal to the volume flow area times the length.
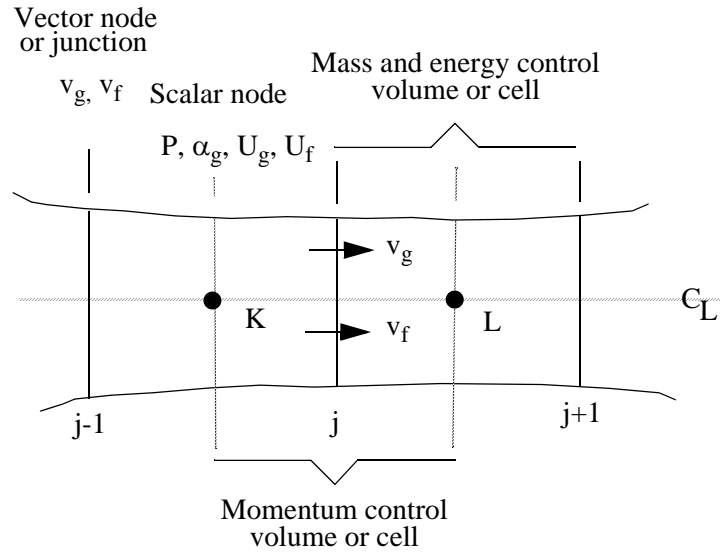
Figure 3.1-3 Difference equation nodalization schematic.

When the mass and energy equations [Equations (3.1-69), (3.1-71), (3.1-72), (3.1-76), and (3.1-78)] are integrated with respect to the spatial variable from junction j to j+1, differential equations in terms of cell-average properties and cell boundary fluxes are obtained. The subscripts and superscripts indicate integration limits for the enclosed quantity.

The sum density Equation (3.1-69) becomes

$$V\left[\alpha_g\frac{\partial\rho_g}{\partial t} + \alpha_f\frac{\partial\rho_f}{\partial t} + (\rho_g - \rho_f)\frac{\partial\alpha_g}{\partial t}\right] + (\alpha_g\rho_g v_g A)_{x_j}^{x_{j+1}} + (\alpha_f\rho_f v_f A)_{x_j}^{x_{j+1}} = 0 \quad . \tag{3.1-81}$$

The difference density Equation (3.1-71) becomes

$$V\left[\alpha_g\frac{\partial\rho_g}{\partial t} - \alpha_f\frac{\partial\rho_f}{\partial t} + (\rho_g + \rho_f)\frac{\partial\alpha_g}{\partial t}\right] + (\alpha_g\rho_g v_g A)_{x_j}^{x_{j+1}} - (\alpha_f\rho_f v_f A)_{x_j}^{x_{j+1}}$$

$$= V\left\{-\frac{2\left[\frac{P_s}{P}H_{ig}(T^s - T_g) + H_{if}(T^s - T_f)\right]}{h_g^* - h_f^*} + 2\Gamma_w\right\} \quad . \tag{3.1-82}$$

The total noncondensable density Equation (3.1-72) becomes

$$V\left[\rho_g X_n \frac{\partial \alpha_g}{\partial t} + \alpha_g X_n \frac{\partial \rho_g}{\partial t} + \alpha_g \rho_g \frac{\partial X_n}{\partial t}\right] + (\alpha_g \rho_g X_n v_g A)_{x_j}^{x_{j+1}} = 0 \quad .$$

(3.1-83)

The vapor/gas energy Equation (3.1-76) becomes

$$V\left[(\rho_g U_g + P)\frac{\partial \alpha_g}{\partial t} + \alpha_g U_g \frac{\partial \rho_g}{\partial t} + \alpha_g \rho_g \frac{\partial U_g}{\partial t}\right] + (\alpha_g \rho_g U_g v_g A)_{x_j}^{x_{j+1}} + P(\alpha_g v_g A)_{x_j}^{x_{j+1}}$$

$$= V\left\{-\left(\frac{h_f^*}{h_g^* - h_f^*}\right)\frac{P_s}{P}H_{ig}(T^s - T_g) - \left(\frac{h_g^*}{h_g^* - h_f^*}\right)H_{if}(T^s - T_f) - \left(\frac{P - P_s}{P}\right)H_{gf}(T_g - T_f)\right.$$

(3.1-84)

$$\left. + \left[\left(\frac{1+\varepsilon}{2}\right)h_g' + \left(\frac{1-\varepsilon}{2}\right)h_f'\right]\Gamma_w + Q_{wg} + DISS_g \right\} \quad .$$

The liquid energy Equation (3.1-78) becomes

$$V\left[-(\rho_f U_f + P)\frac{\partial \alpha_g}{\partial t} + \alpha_f U_f \frac{\partial \rho_f}{\partial t} + \alpha_f \rho_f \frac{\partial U_f}{\partial t}\right] + (\alpha_f \rho_f U_f v_f A)_{x_j}^{x_{j+1}} + P(\alpha_f v_f A)_{x_j}^{x_{j+1}}$$

$$= V\left\{\left(\frac{h_f^*}{h_g^* - h_f^*}\right)\frac{P_s}{P}H_{ig}(T^s - T_g) + \left(\frac{h_g^*}{h_g^* - h_f^*}\right)H_{if}(T^s - T_f) + \left(\frac{P - P_s}{P}\right)H_{gf}(T_g - T_f)\right.$$

(3.1-85)

$$\left. - \left[\left(\frac{1+\varepsilon}{2}\right)h_g' + \left(\frac{1-\varepsilon}{2}\right)h_f'\right]\Gamma_w + Q_{wf} + DISS_f \right\} \quad .$$

As discussed in Section 3.1.1, the phasic energy dissipation terms, $DISS_g$ and $DISS_f$, contain the sums of the wall friction and pump effects. These dissipation terms should also contain both the code calculated abrupt area change dissipation terms and the user-supplied loss coefficient dissipation terms. However these terms were removed in RELAP5/MOD2 because of temperature problems (i.e., overheating). Thus, they are not present in the default ATHENA code. They can be activated by the user in the input deck, however the user is cautioned that temperature problems may occur.

The sum and difference momentum equations [Equations (3.1-73) and (3.1-74)] are integrated from cell center to cell center to obtain

$$\frac{V}{A}\left(\alpha_g \rho_g \frac{\partial v_g}{\partial t} + \alpha_f \rho_f \frac{\partial v_f}{\partial t}\right) + \frac{1}{2}\alpha_g \rho_g (v_g^2)_{x_K}^{x_L} + \frac{1}{2}\alpha_f \rho_f (v_f^2)_{x_K}^{x_L}$$

$$= -(P)_{x_K}^{x_L} + \rho_m B_x(x_L - x_K) - (\alpha_g \rho_g FWG v_g + \alpha_f \rho_f FWF v_f)(x_L - x_K)$$

(3.1-86)

$$- \Gamma_g(v_g - v_f)(x_L - x_K) - \alpha_g \rho_g \, HLOSSG \, v_g - \alpha_f \rho_f \, HLOSSF \, v_f$$

and

$$\left(\frac{V}{A}\right)\left(1 + \frac{C\rho_m^2}{\rho_g\rho_f}\right)\left(\frac{\partial v_g}{\partial t} - \frac{\partial v_f}{\partial t}\right) + \frac{1}{2}(v_g^2)_{x_K}^{x_L} - \frac{1}{2}(v_f^2)_{x_K}^{x_L}$$

$$= -\left(\frac{1}{\rho_g} - \frac{1}{\rho_f}\right)(P)_{x_K}^{x_L} - (FWGv_g - FWFv_f)(x_L - x_K)$$

$$+ \Gamma_g \frac{\rho_m v_I - (\alpha_f\rho_f v_g + \alpha_g\rho_g v_f)}{\alpha_g\rho_g\alpha_f\rho_f}(x_L - x_K) - HLOSSG\ v_g + HLOSSF\ v_g \tag{3.1-87}$$

$$- \rho_m FI(v_g - v_f)(x_L - x_K)$$

$$+ \left(\frac{\rho_m}{\rho_g\rho_f}\right)(\rho_f - \rho_g)B_y(y_L - y_K)\ .$$

Here, the common area term, A, has been factored from most terms. The quantities shown in brackets with limits are evaluated at the indicated limits, while the coefficients are averaged over the cell or integration interval. The indicated derivatives are now derivatives of cell average quantities. Since the integration interval is centered on the junction, the coefficient averages are approximated by the junction values. In all cases, the correlation coefficients for averaged products are taken as unity, so averaged products are replaced directly with products of averages. The HLOSSG and HLOSSF terms contain both code calculated abrupt area change loss terms and user-specified loss terms. This is discussed further in this section when the full finite difference momentum equations are discussed.

Several general guidelines were followed in developing numerical approximations for Equations (3.1-81) through (3.1-87). These guidelines are summarized below.

- Mass and energy inventories are very important quantities in water reactor safety analysis. The numerical scheme should be consistent and conservative in these quantities. [A greater degree of approximation for momentum effects is considered acceptable, especially since nuclear reactor flows are dominated by large sources and sinks of momentum (i.e., pump, abrupt area change)]. Both mass and energy are convected from the same cell, and each is evaluated at the same time level; that is, mass density is evaluated at old time level, so energy density is also evaluated at old time.

- To achieve fast execution speed, implicit evaluation is used only for those terms responsible for the sonic wave propagation time step limit and those phenomena known to have small time constants. Thus, implicit evaluation is used for the velocity in the mass and energy transport terms, the pressure gradient in the momentum equations, and the interface mass and momentum exchange terms.

- To further increase computing speed, time-level evaluations are selected so the resulting implicit terms are linear in the new time variables. Where it is necessary to retain nonlinearities, Taylor series expansions about old time values are used to obtain a

formulation linear in the new time variables. (Higher-order terms are neglected.) Linearity results in high computing speed by eliminating the need to iteratively solve systems of nonlinear equations.

• To allow easy degeneration to homogeneous, or single-phase, formulations, the momentum equations are used as a sum and a difference equation. The particular difference equation used is obtained by first dividing each of the phasic momentum equations by $\alpha_g \rho_g$ and $\alpha_f \rho_f$, for the vapor/gas and liquid phase equations, respectively, and then subtracting.

Using the above guidelines, the finite difference equations for the mass and energy balances, corresponding to Equations (3.1-81) through (3.1-85), are listed below. Some of the terms are intermediate time variables, which are written with a tilde (~). The reason for their use is explained in Section 3.1.4.

The sum continuity equation is

$$
\begin{aligned}
V_L[\alpha_{g,L}^n(\tilde{\rho}_{g,L}^{n+1} - \rho_{g,L}^n) &+ \alpha_{f,L}^n(\tilde{\rho}_{f,L}^{n+1} - \rho_{f,L}^n) + (\rho_{g,L}^n - \rho_{f,L}^n)(\tilde{\alpha}_{g,L}^{n+1} - \alpha_{g,L}^n)] \\
&+ (\dot{\alpha}_{g,j+1}^n\dot{\rho}_{g,j+1}^n v_{g,j+1}^{n+1}A_{j+1} - \dot{\alpha}_{g,j}^n\dot{\rho}_{g,j}^n v_{g,j}^{n+1}A_j)\Delta t \\
&+ (\dot{\alpha}_{f,j+1}^n\dot{\rho}_{f,j+1}^n v_{f,j+1}^{n+1}A_{j+1} - \dot{\alpha}_{f,j}^n\dot{\rho}_{f,j}^n v_{f,j}^{n+1}A_j)\Delta t = 0 \ .
\end{aligned}
\tag{3.1-88}
$$

The difference continuity equation is

$$
\begin{aligned}
V_L[\alpha_{g,L}^n(\tilde{\rho}_{g,L}^{n+1} - \rho_{g,L}^n) &- \alpha_{f,L}^n(\tilde{\rho}_{f,L}^{n+1} - \rho_{f,L}^n) + (\rho_{g,L}^n + \rho_{f,L}^n)(\tilde{\alpha}_{g,L}^{n+1} - \alpha_{g,L}^n)] \\
&+ (\dot{\alpha}_{g,j+1}^n\dot{\rho}_{g,j+1}^n v_{g,j+1}^{n+1}A_{j+1} - \dot{\alpha}_{g,j}^n\dot{\rho}_{g,j}^n v_{g,j}^{n+1}A_j)\Delta t \\
&- (\dot{\alpha}_{f,j+1}^n\dot{\rho}_{f,j+1}^n v_{f,j+1}^{n+1}A_{j+1} - \dot{\alpha}_{f,j}^n\dot{\rho}_{f,j}^n v_{f,j}^{n+1}A_j)\Delta t
\end{aligned}
$$
$$
= -\left(\frac{2}{h_g^* - h_f^*}\right)_L^n V_L\Delta t\left[\frac{P_{s,L}^n}{P_L^n}H_{ig,L}^n(\tilde{T}_L^{s,n+1} - \tilde{T}_{g,L}^{n+1}) + H_{if,L}^n(\tilde{T}_L^{s,n+1} - \tilde{T}_{f,L}^{n+1})\right] + 2V_L\Delta t\Gamma_{w,L}^n \ .
\tag{3.1-89}
$$

The total noncondensable continuity equation is

$$
\begin{aligned}
V_L[\rho_{g,L}^n X_{n,L}^n(\tilde{\alpha}_{g,L}^{n+1} - \alpha_{g,L}^n) &+ \alpha_{g,L}^n X_{n,L}^n(\tilde{\rho}_{g,L}^{n+1} - \rho_{g,L}^n) + \alpha_{g,L}^n\rho_{g,L}^n(\tilde{X}_{n,L}^{n+1} - X_{n,L}^n)] \\
&+ (\dot{\alpha}_{g,j+1}^n\dot{\rho}_{g,j+1}^n\dot{X}_{n,j+1}^n v_{g,j+1}^{n+1}A_{j+1} - \dot{\alpha}_{g,j}^n\dot{\rho}_{g,j}^n\dot{X}_{n,j}^n v_{g,j}^{n+1}A_j)\Delta t = 0 \ .
\end{aligned}
\tag{3.1-90}
$$

The vapor/gas thermal energy equation is

$$V_L \left[\left(\rho_{g,L}^n U_{g,L}^n + P_L^n \right) \left(\tilde{\alpha}_{g,L}^{n+1} - \alpha_{g,L}^n \right) + \alpha_{g,L}^n U_{g,L}^n \left(\tilde{\rho}_{g,L}^{n+1} - \rho_{g,L}^n \right) + \alpha_{g,L}^n \rho_{g,L}^n \left(\tilde{U}_{g,L}^{n+1} - U_{g,L}^n \right) \right]$$

$$+ \left[\dot{\alpha}_{g,j+1}^n \left(\dot{\rho}_{g,j+1}^n \dot{U}_{g,j+1}^n + P_L^n \right) v_{g,j+1}^{n+1} A_{j+1} - \dot{\alpha}_{g,j}^n \left(\dot{\rho}_{g,j}^n \dot{U}_{g,j}^n + P_L^n \right) v_{g,j}^{n+1} A_j \right] \Delta t$$

$$= \left\{ -\left(\frac{h_f^*}{h_g^* - h_f^*} \right)_L^n \frac{P_{s,L}^n}{P_L^n} H_{ig,L}^n \left(\tilde{T}_L^{s,n+1} - \tilde{T}_{g,L}^{n+1} \right) - \left(\frac{h_g^*}{h_g^* - h_f^*} \right)_L^n H_{if,L}^n \left(\tilde{T}_L^{s,n+1} - \tilde{T}_{f,L}^{n+1} \right) \right.$$

$$\left. - \left(\frac{P_L^n - P_{s,L}^n}{P_L^n} \right) H_{gf,L}^n \left(\tilde{T}_{g,L}^{n+1} - \tilde{T}_{f,L}^{n+1} \right) + \left[\left(\frac{1+\varepsilon}{2} \right) h_{g,L}^{',n} + \left(\frac{1-\varepsilon}{2} \right) h_{f,L}^{',n} \right] \Gamma_{w,L}^n + Q_{wg,L}^n + DISS_{g,L}^n \right\} V_L \Delta t \ . \tag{3.1-91}$$

The liquid thermal energy equation is

$$V_L \left[-\left(\rho_{f,L}^n U_{f,L}^n + P_L^n \right) \left(\tilde{\alpha}_{g,L}^{n+1} - \alpha_{g,L}^n \right) + \alpha_{f,L}^n U_{f,L}^n \left(\tilde{\rho}_{f,L}^{n+1} - \rho_{f,L}^n \right) + \alpha_{f,L}^n \rho_{f,L}^n \left(\tilde{U}_{f,L}^{n+1} - U_{f,L}^n \right) \right]$$

$$+ \left[\dot{\alpha}_{f,j+1}^n \left(\dot{\rho}_{f,j+1}^n \dot{U}_{f,j+1}^n + P_L^n \right) v_{f,j+1}^{n+1} A_{j+1} - \dot{\alpha}_{f,j}^n \left(\dot{\rho}_{f,j}^n \dot{U}_{f,j}^n + P_L^n \right) v_{f,j}^{n+1} A_j \right] \Delta t$$

$$= \left\{ \left(\frac{h_f^*}{h_g^* - h_f^*} \right)_L^n \frac{P_{s,L}^n}{P_L^n} H_{ig,L}^n \left(\tilde{T}_L^{s,n+1} - \tilde{T}_{g,L}^{n+1} \right) + \left(\frac{h_g^*}{h_g^* - h_f^*} \right)_L^n H_{if,L}^n \left(\tilde{T}_L^{s,n+1} - \tilde{T}_{f,L}^{n+1} \right) \right.$$

$$\left. + \left(\frac{P_L^n - P_{s,L}^n}{P_L^n} \right) H_{gf,L}^n \left(\tilde{T}_{g,L}^{n+1} - \tilde{T}_{f,L}^{n+1} \right) - \left[\left(\frac{1+\varepsilon}{2} \right) h_{g,L}^{',n} + \left(\frac{1-\varepsilon}{2} \right) h_{f,L}^{',n} \right] \Gamma_{w,L}^n + Q_{wf,L}^n + DISS_{f,L}^n \right\} V_L \Delta t \ . \tag{3.1-92}$$

The quantities having a dot overscore are donored quantities based on the junction velocities, $v_{g,j}$ and $v_{f,j}$. The donored quantities are volume average scalar quantities defined analytically as

$$\dot{\phi}_j = \frac{1}{2} \left(\phi_K + \phi_L \right) + \frac{1}{2} \frac{|v_j|}{v_j} \left(\phi_K - \phi_L \right) \tag{3.1-93}$$

where $\dot{\phi}_j$ is any of the donored properties, and v_j is the appropriate velocity (that is, vapor/gas or liquid). This equation holds for the case $v_j \neq 0$. For the case $v_j = 0$ and $P_K > P_L$,

$$\dot{\phi}_j = \phi_K \ . \tag{3.1-94}$$

For the case $v_j = 0$ and $P_K < P_L$,

ATHENA/2.3

$$\dot{\phi}_j = \phi_L \ .$$ (3.1-95)

For the degenerate case $v_j = 0$ and $P_K = P_L$, a density-weighted average formulation is used,

$$\dot{\phi}_j = \frac{\rho_K \phi_K + \rho_L \phi_L}{\rho_K + \rho_L}$$ (3.1-96)

for all donored properties except for densities (which use a simple average). In this equation, ρ_K and ρ_L are the appropriate densities (e.g., vapor/gas or liquid). Where donored values are not used at junctions, linear interpolations between neighboring cell values are used. It is not required that $\dot{\alpha}_{gj}$ and $\dot{\alpha}_{fj}$ sum to 1; this can occur in counter-current flow.

The provisional advanced time phasic densities used in Equations (3.1-88) through (3.1-92) are obtained by linearizing the phasic density state relations about the old time values (see Section 3.2), these are

$$\tilde{\rho}_{g,L}^{n+1} = \rho_{g,L}^n + \left(\frac{\partial \rho_g}{\partial P}\right)_L^n \left(P_L^{n+1} - P_L^n\right) + \left(\frac{\partial \rho_g}{\partial X_n}\right)_L^n \left(\tilde{X}_{n,L}^{n+1} - X_{n,L}^n\right) + \left(\frac{\partial \rho_g}{\partial U_g}\right)_L^n \left(\tilde{U}_{g,L}^{n+1} - U_{g,L}^n\right)$$ (3.1–97)

$$\tilde{\rho}_{f,L}^{n+1} = \rho_{f,L}^n + \left(\frac{\partial \rho_f}{\partial P}\right)_L^n \left(P_L^{n+1} - P_L^n\right) + \left(\frac{\partial \rho_f}{\partial U_f}\right)_L^n \left(\tilde{U}_{f,L}^{n+1} - U_{f,L}^n\right) \ .$$ (3.1-98)

The method of obtaining the phasic density state derivatives used in Equations (3.1-97) and (3.1-98) is also indicated in Section 3.2.

The provisional advanced time phasic interface heat transfer rates can be written using the finite difference form of Equations (3.1-48) and (3.1-26) after evaluating the extrapolated temperature $\tilde{T}^{n+1}$; these are

$$\tilde{Q}_{ig,L}^{n+1} = \frac{P_{s,L}^n}{P_L^n} H_{ig,L}^n (\tilde{T}_L^{s,n+1} - \tilde{T}_{g,L}^{n+1}) - \left(\frac{1-\varepsilon}{2}\right) \Gamma_{w,L}^n (h_{g,L}^{',n} - h_{f,L}^{',n})$$ (3.1-99)

$$\tilde{Q}_{if,L}^{n+1} = H_{if,L}^n (\tilde{T}_L^{s,n+1} - \tilde{T}_{f,L}^{n+1}) - \left(\frac{1+\varepsilon}{2}\right) \Gamma_{w,L}^n (h_{g,L}^{',n} - h_{f,L}^{',n}) \ .$$ (3.1-100)

The provisional advanced time temperatures are obtained by linearizing the temperature state relations about the old time values (see Section 3.2); these are

$$\tilde{T}_L^{s,\,n+1} = T_L^{s,\,n} + \left(\frac{\partial T^s}{\partial P}\right)_L^n (P_L^{n+1} - P_L^n) + \left(\frac{\partial T^s}{\partial X_n}\right)_L^n (\tilde{X}_{n,\,L}^{n+1} - X_{n,\,L}^n) + \left(\frac{\partial T^s}{\partial U_g}\right)_L^n (\tilde{U}_{g,\,L}^{n+1} - U_{g,\,L}^n) \qquad (3.1\text{-}101)$$

$$\tilde{T}_{g,\,L}^{n+1} = T_{g,\,L}^n + \left(\frac{\partial T_g}{\partial P}\right)_L^n (P_L^{n+1} - P_L^n) + \left(\frac{\partial T_g}{\partial X_n}\right)_L^n (\tilde{X}_{n,\,L}^{n+1} - X_{n,\,L}^n) + \left(\frac{\partial T_g}{\partial U_g}\right)_L^n (\tilde{U}_{g,\,L}^{n+1} - U_{g,\,L}^n) \qquad (3.1\text{-}102)$$

$$\tilde{T}_{f,\,L}^{n+1} = T_{f,\,L}^n + \left(\frac{\partial T_f}{\partial P}\right)_L^n (P_L^{n+1} - P_L^n) + \left(\frac{\partial T_f}{\partial U_f}\right)_L^n (\tilde{U}_{f,\,L}^{n+1} - U_{f,\,L}^n) \quad . \qquad (3.1\text{-}103)$$

The method used in Equations (3.1-101) through (3.1-103) to obtain the temperature state derivatives is also indicated in Section 3.2.

The previously stated guidelines are also used to obtain the finite-difference equations for the phasic momentum equations. In this case, volume-average properties for the momentum control volume are taken as junction properties (that is, linear interpolations between mass and energy control volume centers). The momentum flux terms are approximated using a donor-like formulation that results in a centered velocity gradient term and a viscous-like term (numerical viscosity, artificial viscosity). The finite difference equations for the sum and difference momentum equations, Equations (3.1-86) and (3.1-87), are

$$
\begin{aligned}
&(\alpha_g \rho_g)_j^n (v_g^{n+1} - v_g^n)_j \Delta x_j + (\alpha_f \rho_f)_j^n (v_f^{n+1} - v_f^n)_j \Delta x_j \\
&+ \frac{1}{2}(\alpha_g \rho_g)_j^n [(v_g^2)_L^n - (v_g^2)_K^n]\Delta t + \frac{1}{2}(\alpha_f \rho_f)_j^n [(v_f^2)_L^n - (v_f^2)_K^n]\Delta t \\
&\quad - \frac{1}{2}[(\dot{\alpha}_g \dot{\rho}_g)_j^n VISG_j^n + (\dot{\alpha}_f \dot{\rho}_f)_j^n VISF_j^n]\Delta t \\
&= -(P_L - P_K)^{n+1}\Delta t + [(\rho_m)_j^n B_x - (\alpha_g \rho_g)_j^n FWG_j^n (v_g)_j^{n+1} \\
&\quad - (\alpha_f \rho_f)_j^n FWF_j^n (v_f)_j^{n+1} - (\Gamma_g)_j^n (v_g - v_f)_j^{n+1}]\Delta x_j \Delta t \\
&- [(\dot{\alpha}_g \dot{\rho}_g)_j^n HLOSSG_j^n v_{g,\,j}^{n+1} + (\dot{\alpha}_f \dot{\rho}_f)_j^n HLOSSF_j^n v_{f,\,j}^{n+1}]\Delta t
\end{aligned}
\qquad (3.1\text{-}104)
$$

and

$$
\left(1 + \frac{C\rho_m^2}{\rho_g\rho_f}\right)_j^n [(v_g^{n+1} - v_g^n) - (v_f^{n+1} - v_f^n)]_j \Delta x_j
$$

$$
+ \frac{1}{2}\left(\frac{\dot{\alpha}_g\dot{\rho}_g}{\alpha_g\rho_g}\right)_j^n [(v_g^2)_L^n - (v_g^2)_K^n]\Delta t - \frac{1}{2}\left(\frac{\dot{\alpha}_g\dot{\rho}_g}{\alpha_g\rho_g}\right)_j^n VISG_j^n \Delta t
$$

$$
- \frac{1}{2}\left(\frac{\dot{\alpha}_f\dot{\rho}_f}{\alpha_f\rho_f}\right)_j^n [(v_f^2)_L^n - (v_f^2)_K^n]\Delta t + \frac{1}{2}\left(\frac{\dot{\alpha}_f\dot{\rho}_f}{\alpha_f\rho_f}\right)_j^n VISF_j^n \Delta t = -\left(\frac{\rho_f - \rho_g}{\rho_f\rho_g}\right)_j^n (P_L - P_K)^{n+1}\Delta t
$$

$$
- \left\{ FWG_j^n (v_g)_j^{n+1} - FWF_j^n (v_f)_j^{n+1} - \left[\frac{\Gamma_g^n(\rho_m^n v_I^{n+1} - \alpha_f^n\rho_f^n v_g^{n+1} - \alpha_g^n\rho_g^n v_f^{n+1})}{(\alpha_g\rho_g\alpha_f\rho_f)^n} \right]_j \right.
$$

$$
\left. + (\rho_m FI)_j^n (v_g^{n+1} - v_f^{n+1})_j \right\} \Delta x_j \Delta t - \left[\left(\frac{\dot{\alpha}_g\dot{\rho}_g}{\alpha_g\rho_g}\right)_j^n HLOSSG_j^n v_{g,j}^{n+1} \right.
$$

$$
- \left(\frac{\dot{\alpha}_f\dot{\rho}_f}{\alpha_f\rho_f}\right)_j^n HLOSSF_j^n v_{f,j}^{n+1}]\Delta t
$$

$$
+ \left(\frac{\rho_m}{\rho_g\rho_f}\right)_j^n (\rho_f - \rho_g)_j^n B_y (y_L^n - y_K^n)\Delta t
$$

(3.1-105)

where the viscous-like terms (numerical viscosity, artificial viscosity) are defined as

$$
VISG_j^n = \frac{1}{2}\left\{ |v_{g,L}^n| \left[(v_g^n)_{j+1}\frac{A_{j+1}}{A_j} - (v_g^n)_j \right] - |v_{g,K}^n| \left[(v_g^n)_j - (v_g^n)_{j-1}\frac{A_{j-1}}{A_j} \right] \right\}
$$

(3.1-106)

and

$$
VISF_j^n = \frac{1}{2}\left\{ |v_{f,L}^n| \left[(v_f^n)_{j+1}\frac{A_{j+1}}{A_j} - (v_f^n)_j \right] - |v_{f,K}^n| \left[(v_f^n)_j - (v_f^n)_{j-1}\frac{A_{j-1}}{A_j} \right] \right\} \quad .
$$

(3.1-107)

The viscous-like terms vanish for steady, incompressible, one-dimensional flow. The coding for the finite difference form of the difference momentum equation is programmed as the difference of the liquid and vapor/gas momentum equations instead of the difference of the vapor/gas and liquid momentum equations as is shown in Equation (3.1-105).

In momentum Equations (3.1-104) and (3.1-105), the scalar or thermodynamic variables needed at the junctions are either linear interpolations between the neighboring cell values or donored quantities. Terms that are shown multiplied by Δx_j are interpolated between neighboring cell values based on the length of each half cell. The volume-centered velocities are defined in terms of the velocities in the junctions attached to the volume (see Section 3.1.6). The $HLOSSG_j$ and $HLOSSF_j$ terms contain both code-calculated abrupt area change loss terms (Section 3.4.3) and user-specified loss terms (Section 3.4.4).

These terms are given by

$$HLOSSG_j^n = \frac{1}{2}(K_g^n + K_{in})|v_{g,j}^n| \qquad (3.1\text{-}108)$$

and

$$HLOSSF_j^n = \frac{1}{2}(K_f^n + K_{in})|v_{f,j}^n| \qquad (3.1\text{-}109)$$

The code-calculated abrupt area change loss coefficients are K_g^n and K_f^n, where K_g^n is the vapor/gas loss coefficient and K_f^n is the liquid loss coefficient. The user-specified loss coefficient is K_{in}, where K_{in} is either the forward (K_F) or reverse (K_R) inputted user-specified loss coefficient, depending on the phasic velocity direction.

Using the same averaging techniques, the unexpanded form of the mass and energy equations [Equations (3.1-2), (3.1-3), (3.1-39), (3.1-41), (3.1-79), and (3.1-80)] are next presented in their final finite difference form.

The unexpanded vapor/gas density Equation (3.1-2) becomes

$$V_L[(\alpha_g\rho_g)_L^{n+1} - (\alpha_g\rho_g)_L^n] + (\dot{\alpha}_{g,j+1}^n\rho_{g,j+1}^n v_{g,j+1}^{n+1}A_{j+1} - \dot{\alpha}_{g,j}^n\rho_{g,j}^n v_{g,j}^{n+1}A_j)\Delta t = \tilde{\Gamma}_{g,L}^{n+1}V_L\Delta t \qquad (3.1\text{-}110)$$

The provisional advancement time variable, $\tilde{\Gamma}_{g,L}^{n+1}$, is obtained using the finite difference form of Equation (3.1-50) and is written

$$\tilde{\Gamma}_{g,L}^{n+1} = -\frac{\dfrac{P_{s,L}^n}{P_L^n}H_{ig,L}^n(\tilde{T}_L^{s,n+1} - \tilde{T}_{g,L}^{n+1}) + H_{if,L}^n(\tilde{T}_L^{s,n+1} - \tilde{T}_{f,L}^{n+1})}{h_{g,L}^{*,n} - h_{f,L}^{*,n}} + \Gamma_{w,L}^n \qquad (3.1\text{-}111)$$

The unexpanded liquid density Equation (3.1-3) becomes

$$V_L[(\alpha_f\rho_f)_L^{n+1} - (\alpha_f\rho_f)_L^n] + (\dot{\alpha}_{f,j+1}^n\rho_{f,j+1}^n v_{f,j+1}^{n+1}A_{j+1} - \dot{\alpha}_{f,j}^n\rho_{f,j}^n v_{f,j}^{n+1}A_j)\Delta t = -\tilde{\Gamma}_{g,L}^{n+1}V_L\Delta t \qquad (3.1\text{-}112)$$

The unexpanded total noncondensable density Equation (3.1-39) becomes

$$V_L[(\alpha_g\rho_gX_n)_L^{n+1} - (\alpha_g\rho_gX_n)_L^n] + (\dot{\alpha}_{g,j+1}^n\dot{\rho}_{g,j+1}^n \check{X}_{n,j+1}^n v_{g,j+1}^{n+1}A_{j+1} - \dot{\alpha}_{g,j}^n\dot{\rho}_{g,j}^n \check{X}_{n,j}^n v_{g,j}^{n+1}A_j)\Delta t$$
$$= 0 \qquad (3.1\text{-}113)$$

The unexpanded density equation for the i-th noncondensable species, Equation (3.1-41), becomes

$$V_L[(\alpha_g \rho_g X_n X_{ni})_L^{n+1} - (\alpha_g \rho_g X_n X_{ni})_L^n] + \dot{\alpha}_{g,j+1}^n \dot{\rho}_{g,j+1}^n \dot{X}_{n,j+1}^n \dot{X}_{ni,j+1}^n v_{g,j+1}^{n+1} A_{j+1}$$
$$-\dot{\alpha}_{g,j}^n \dot{\rho}_{g,j}^n \dot{X}_{n,j}^n \dot{X}_{ni,j}^n v_{g,j}^{n+1} A_j) \Delta t = 0 \quad . \tag{3.1-114}$$

The unexpanded vapor/gas thermal energy Equation (3.1-79) becomes

$$V_L[(\alpha_g \rho_g U_g)_L^{n+1} - (\alpha_g \rho_g U_g)_L^n] + [\dot{\alpha}_{g,j+1}^n (\dot{\rho}_{g,j+1}^n \dot{U}_{g,j+1}^n + P_L^n) v_{g,j+1}^{n+1} A_{j+1}$$
$$- \dot{\alpha}_{g,j}^n (\dot{\rho}_{g,j}^n \dot{U}_{g,j}^n + P_L^n) v_{g,j}^{n+1} A_j] \Delta t = -V_L P_L^n (\tilde{\alpha}_{g,L}^{n+1} - \alpha_{g,L}^n)$$
$$+ \left\{ -\left(\frac{h_f^*}{h_g^* - h_f^*}\right)_L^n \frac{P_{s,L}^n}{P_L^n} H_{ig,L}^n (\tilde{T}_L^{s,n+1} - \tilde{T}_{g,L}^{n+1}) - \left(\frac{h_g^*}{h_g^* - h_f^*}\right)_L^n H_{if,L}^n (\tilde{T}_L^{s,n+1} - \tilde{T}_{f,L}^{n+1}) \right. \tag{3.1-115}$$
$$-\left(\frac{P_L^n - P_{s,L}^n}{P_L^n}\right) H_{gf,L}^n (\tilde{T}_{g,L}^{n+1} - \tilde{T}_{f,L}^{n+1}) + \left[\left(\frac{1+\varepsilon}{2}\right) h_{g,L}^{\prime,n} + \left(\frac{1-\varepsilon}{2}\right) h_{f,L}^{\prime,n}\right] \Gamma_{w,L}^n + Q_{wg,L}^n + DISS_{g,L}^n \right\} V_L \Delta t \quad .$$

The variables $\tilde{\alpha}_{g,L}^{n+1}$, $\tilde{T}_L^{s,n+1}$, $\tilde{T}_{g,L}^{n+1}$, and $\tilde{T}_{f,L}^{n+1}$ are written with a tilde (~) to indicate they are provisional advancement time variables. The unexpanded liquid thermal energy Equation (3.1-80) becomes

$$V_L[(\alpha_f \rho_f U_f)_L^{n+1} - (\alpha_f \rho_f U_f)_L^n] + [\dot{\alpha}_{f,j+1}^n (\dot{\rho}_{f,j+1}^n \dot{U}_{f,j+1}^n + P_L^n) v_{f,j+1}^{n+1} A_{j+1}$$
$$- \dot{\alpha}_{f,j}^n (\dot{\rho}_{f,j}^n \dot{U}_{f,j}^n + P_L^n) v_{f,j}^{n+1} A_j] \Delta t = V_L P_L^n (\tilde{\alpha}_{g,L}^{n+1} - \alpha_{g,L}^n)$$
$$+ \left\{ \left(\frac{h_f^*}{h_g^* - h_f^*}\right)_L^n \frac{P_{s,L}^n}{P_L^n} H_{ig,L}^n (\tilde{T}_L^{s,n+1} - \tilde{T}_{g,L}^{n+1}) + \left(\frac{h_g^*}{h_g^* - h_f^*}\right)_L^n H_{if,L}^n (\tilde{T}_L^{s,n+1} - \tilde{T}_{f,L}^{n+1}) \right. \tag{3.1-116}$$
$$+\left(\frac{P_L^n - P_{s,L}^n}{P_L^n}\right) H_{gf,L}^n (\tilde{T}_{g,L}^{n+1} - \tilde{T}_{f,L}^{n+1}) - \left[\left(\frac{1+\varepsilon}{2}\right) h_{g,L}^{\prime,n} + \left(\frac{1-\varepsilon}{2}\right) h_{f,L}^{\prime,n}\right] \Gamma_{w,L}^n + Q_{wf,L}^n + DISS_{f,L}^n \right\} V_L \Delta t \quad .$$

3.1.4 Time Advancement for the Semi-Implicit Scheme

The solution scheme will be discussed with regard to the state of the fluid in a control volume for two successive time steps. There are four possible cases:

1. Two-phase to two-phase, where two-phase conditions exist at both old time (n) and new time (n+1).

2.   One-phase to one-phase, where one-phase conditions (either pure vapor/gas or pure liquid) exist at both old time (n) and new time (n+1).

3.   Two-phase to one-phase (disappearance), where two-phase conditions exist at old time (n), and one-phase conditions exist at new time (n+1).

4.   One-phase to two-phase (appearance), where one-phase conditions exist at old time (n), and two-phase conditions exist at new time (n+1).

The solution scheme will first be presented for the two-phase to two-phase case, because it is the most general. The solution scheme for the other three cases will then be presented.

3.1.4.1   Two-Phase To Two-Phase. First, the density and temperature Equations (3.1-97), (3.1-98), (3.1-101), (3.1-102) and (3.1-103) are substituted into the five expanded density and energy difference Equations (3.1-88) through (3.1-92). The equations are then ordered so that the noncondensable density equation is first, the vapor/gas energy equation is second, the liquid energy equation is third, the difference density equation is fourth, and the sum density equation is fifth. The five unknowns are expressed as differences, and the order is

$$(\tilde{X}_{n,L}^{n+1} - X_{n,L}^{n}), (\tilde{U}_{g,L}^{n+1} - U_{g,L}^{n}), (\tilde{U}_{f,L}^{n+1} - U_{f,L}^{n}), (\tilde{\alpha}_{g,L}^{n+1} - \alpha_{g,L}^{n}), \text{ and } (P_L^{n+1} - P_L^{n}) \quad . \tag{3.1-117}$$

The tilde (~) is used for X_n, U_g, U_f, and α_g to indicate that these are provisional new time variables and do not represent the final new time variables for the two-phase to two-phase case. The ordering of the variables and equations was selected so that a given equation is dominated by its corresponding variable (e.g., the vapor/gas energy equation is second and the vapor/gas specific internal energy variable U_g is also second). The noncondensable equation is placed first for ease of degeneration when a noncondensable component is not specified in the problem, and the pressure variable is placed last for numerical convenience in the pressure solution. The five equations are then each divided by the volume V_L. The system of equations has the following form, where the matrix $\underset{\sim}{A}$ and the vectors $\underset{\sim}{b}, \underset{\sim}{g}^1, \underset{\sim}{g}^2, \underset{\sim}{f}^1, \underset{\sim}{f}^2$ contain only old time level variables (the subscript L and the superscript n has been dropped for the listing of the matrix and vectors):

$$\underset{\sim}{A}\underset{\sim}{x} = \underset{\sim}{b} + \underset{\sim}{g}^1 v_{g,j+1}^{n+1} + \underset{\sim}{g}^2 v_{g,j}^{n+1} + \underset{\sim}{f}^1 v_{f,j+1}^{n+1} + \underset{\sim}{f}^2 v_{f,j}^{n+1} \tag{3.1-118}$$

where

$$
\underline{\underline{A}} \quad = \quad
\begin{bmatrix}
A_{11} & A_{12} & 0 & A_{14} & A_{15} \\
A_{21} & A_{22} & A_{23} & A_{24} & A_{25} \\
A_{31} & A_{32} & A_{33} & A_{34} & A_{35} \\
A_{41} & A_{42} & A_{43} & A_{44} & A_{45} \\
A_{51} & A_{52} & A_{53} & A_{54} & A_{55}
\end{bmatrix}
\qquad
\underline{x} =
\begin{bmatrix}
\tilde{X}_{n,L}^{n+1} - X_{n,L}^{n} \\
\tilde{U}_{g,L}^{n+1} - U_{g,L}^{n} \\
\tilde{U}_{f,L}^{n+1} - U_{f,L}^{n} \\
\tilde{\alpha}_{g,L}^{n+1} - \alpha_{g,L}^{n} \\
P_{L}^{n+1} - P_{L}^{n}
\end{bmatrix}
\tag{3.1-119}
$$

$$
\underline{b} \quad = \quad
\begin{bmatrix} 0 \\ b_2 \\ b_3 \\ b_4 \\ 0 \end{bmatrix}
\qquad
\underline{g}^1 =
\begin{bmatrix} g_1^1 \\ g_2^1 \\ 0 \\ g_4^1 \\ g_5^1 \end{bmatrix}
\qquad
\underline{g}^2 =
\begin{bmatrix} g_1^2 \\ g_2^2 \\ 0 \\ g_4^2 \\ g_5^2 \end{bmatrix}
\qquad
\underline{f}^1 =
\begin{bmatrix} 0 \\ 0 \\ f_3^1 \\ f_4^1 \\ f_5^1 \end{bmatrix}
\qquad
\underline{f}^2 =
\begin{bmatrix} 0 \\ 0 \\ f_3^2 \\ f_4^2 \\ f_5^2 \end{bmatrix}
\tag{3.1-120}
$$

$$
A_{11} \quad = \quad \alpha_g \left(X_n \frac{\partial \rho_g}{\partial X_n} + \rho_g \right)
\tag{3.1-121}
$$

$$
A_{12} \quad = \quad \alpha_g X_n \frac{\partial \rho_g}{\partial U_g}
\tag{3.1-122}
$$

$$
A_{14} \quad = \quad \rho_g X_n
\tag{3.1-123}
$$

$$
A_{15} \quad = \quad \alpha_g X_n \frac{\partial \rho_g}{\partial P}
\tag{3.1-124}
$$

$$
A_{21} \quad = \quad
\begin{aligned}
& \alpha_g U_g \frac{\partial \rho_g}{\partial X_n} + \left(\frac{h_f^*}{h_g^* - h_f^*} \right) \Delta t \frac{P_s}{P} H_{ig} \left(\frac{\partial T^s}{\partial X_n} - \frac{\partial T_g}{\partial X_n} \right) \\
& + \left(\frac{h_g^*}{h_g^* - h_f^*} \right) \Delta t H_{if} \frac{\partial T^s}{\partial X_n} + \Delta t \left(\frac{P - P_s}{P} \right) H_{gf} \frac{\partial T_g}{\partial X_n}
\end{aligned}
\tag{3.1-125}
$$

$$
A_{22} \quad = \quad
\begin{aligned}
& \alpha_g \left(U_g \frac{\partial \rho_g}{\partial U_g} + \rho_g \right) + \left(\frac{h_f^*}{h_g^* - h_f^*} \right) \Delta t \frac{P_s}{P} H_{ig} \left(\frac{\partial T^s}{\partial U_g} - \frac{\partial T_g}{\partial U_g} \right) \\
& + \left(\frac{h_g^*}{h_g^* - h_f^*} \right) \Delta t H_{if} \frac{\partial T^s}{\partial U_g} + \Delta t \left(\frac{P - P_s}{P} \right) H_{gf} \frac{\partial T_g}{\partial U_g}
\end{aligned}
\tag{3.1-126}
$$

$$A_{23} \quad = \quad -\left(\frac{h_g^*}{h_g^* - h_f^*}\right)\Delta t H_{if}\frac{\partial T_f}{\partial U_f} - \Delta t\left(\frac{P - P_s}{P}\right)H_{gf}\frac{\partial T_f}{\partial U_f} \tag{3.1-127}$$

$$A_{24} \quad = \quad \rho_g U_g + P \tag{3.1-128}$$

$$A_{25} \quad = \quad \begin{aligned} &\alpha_g U_g \frac{\partial \rho_g}{\partial P} + \left(\frac{h_f^*}{h_g^* - h_f^*}\right)\Delta t \frac{P_s}{P}H_{ig}\left(\frac{\partial T^s}{\partial P} - \frac{\partial T_g}{\partial P}\right) \\ &+ \left(\frac{h_g^*}{h_g^* - h_f^*}\right)\Delta t H_{if}\left(\frac{\partial T^s}{\partial P} - \frac{\partial T_f}{\partial P}\right) + \Delta t\left(\frac{P - P_s}{P}\right)H_{gf}\left(\frac{\partial T_g}{\partial P} - \frac{\partial T_f}{\partial P}\right) \end{aligned} \tag{3.1-129}$$

$$A_{31} \quad = \quad \begin{aligned} &-\left(\frac{h_f^*}{h_g^* - h_f^*}\right)\Delta t \frac{P_s}{P}H_{ig}\left(\frac{\partial T^s}{\partial X_n} - \frac{\partial T_g}{\partial X_n}\right) - \left(\frac{h_g^*}{h_g^* - h_f^*}\right)\Delta t H_{if}\frac{\partial T^s}{\partial X_n} \\ &- \Delta t\left(\frac{P - P_s}{P}\right)H_{gf}\frac{\partial T_g}{\partial X_n} \end{aligned} \tag{3.1-130}$$

$$A_{32} \quad = \quad \begin{aligned} &-\left(\frac{h_f^*}{h_g^* - h_f^*}\right)\Delta t \frac{P_s}{P}H_{ig}\left(\frac{\partial T^s}{\partial U_g} - \frac{\partial T_g}{\partial U_g}\right) - \left(\frac{h_g^*}{h_g^* - h_f^*}\right)\Delta t H_{if}\frac{\partial T^s}{\partial U_g} \\ &- \Delta t\left(\frac{P - P_s}{P}\right)H_{gf}\frac{\partial T_g}{\partial U_g} \end{aligned} \tag{3.1-131}$$

$$A_{33} \quad = \quad \alpha_f\left(U_f\frac{\partial \rho_f}{\partial U_f} + \rho_f\right) + \left(\frac{h_g^*}{h_g^* - h_f^*}\right)\Delta t H_{if}\frac{\partial T_f}{\partial U_f} + \Delta t\left(\frac{P - P_s}{P}\right)H_{gf}\frac{\partial T_f}{\partial U_f} \tag{3.1-132}$$

$$A_{34} \quad = \quad -\rho_f U_f - P \tag{3.1-133}$$

$$A_{35} \quad = \quad \begin{aligned} &\alpha_f U_f \frac{\partial \rho_f}{\partial P} - \left(\frac{h_f^*}{h_g^* - h_f^*}\right)\Delta t \frac{P_s}{P}H_{ig}\left(\frac{\partial T^s}{\partial P} - \frac{\partial T_g}{\partial P}\right) \\ &- \left(\frac{h_g^*}{h_g^* - h_f^*}\right)\Delta t H_{if}\left(\frac{\partial T^s}{\partial P} - \frac{\partial T_f}{\partial P}\right) - \Delta t\left(\frac{P - P_s}{P}\right)H_{gf}\left(\frac{\partial T_g}{\partial P} - \frac{\partial T_f}{\partial P}\right) \end{aligned} \tag{3.1-134}$$

$$A_{41} \quad = \quad \alpha_g\frac{\partial \rho_g}{\partial X_n} + \left(\frac{2}{h_g^* - h_f^*}\right)\Delta t \frac{P_s}{P}H_{ig}\left(\frac{\partial T^s}{\partial X_n} - \frac{\partial T_g}{\partial X_n}\right) + \left(\frac{2}{h_g^* - h_f^*}\right)\Delta t H_{if}\frac{\partial T^s}{\partial X_n} \tag{3.1-135}$$

$$A_{42} \quad = \quad \alpha_g \frac{\partial \rho_g}{\partial U_g} + \left(\frac{2}{h_g^* - h_f^*}\right)\Delta t \frac{P_s}{P} H_{ig}\left(\frac{\partial T^s}{\partial U_g} - \frac{\partial T_g}{\partial U_g}\right) + \left(\frac{2}{h_g^* - h_f^*}\right)\Delta t H_{if}\frac{\partial T^s}{\partial U_g} \qquad (3.1\text{-}136)$$

$$A_{43} \quad = \quad -\alpha_f \frac{\partial \rho_f}{\partial U_f} - \left(\frac{2}{h_g^* - h_f^*}\right)\Delta t H_{if}\frac{\partial T_f}{\partial U_f} \qquad (3.1\text{-}137)$$

$$A_{44} \quad = \quad \rho_g + \rho_f \qquad (3.1\text{-}138)$$

$$A_{45} \quad = \quad \begin{aligned} &\alpha_g \frac{\partial \rho_g}{\partial P} - \alpha_f \frac{\partial \rho_f}{\partial P} + \left(\frac{2}{h_g^* - h_f^*}\right)\Delta t \frac{P_s}{P} H_{ig}\left(\frac{\partial T^s}{\partial P} - \frac{\partial T_g}{\partial P}\right) \\ &+ \left(\frac{2}{h_g^* - h_f^*}\right)\Delta t H_{if}\left(\frac{\partial T^s}{\partial P} - \frac{\partial T_f}{\partial P}\right) \end{aligned} \qquad (3.1\text{-}139)$$

$$A_{51} \quad = \quad \alpha_g \frac{\partial \rho_g}{\partial X_n} \qquad (3.1\text{-}140)$$

$$A_{52} \quad = \quad \alpha_g \frac{\partial \rho_g}{\partial U_g} \qquad (3.1\text{-}141)$$

$$A_{53} \quad = \quad \alpha_f \frac{\partial \rho_f}{\partial U_f} \qquad (3.1\text{-}142)$$

$$A_{54} \quad = \quad \rho_g - \rho_f \qquad (3.1\text{-}143)$$

$$A_{55} \quad = \quad \alpha_g \frac{\partial \rho_g}{\partial P} + \alpha_f \frac{\partial \rho_f}{\partial P} \qquad (3.1\text{-}144)$$

$$b_2 \quad = \quad \begin{aligned} &-\left(\frac{h_f^*}{h_g^* - h_f^*}\right)\Delta t \frac{P_s}{P} H_{ig}(T^s - T_g) - \left(\frac{h_g^*}{h_g^* - h_f^*}\right)\Delta t H_{if}(T^s - T_f) \\ &-\Delta t\left(\frac{P - P_s}{P}\right)H_{gf}(T_g - T_f) + \Delta t \Gamma_w\left[\left(\frac{1-\varepsilon}{2}\right)h_f' + \left(\frac{1+\varepsilon}{2}\right)h_g'\right] + Q_{wg}\Delta t \\ &+ DISS_g\Delta t \end{aligned} \qquad (3.1\text{-}145)$$

$$b_3 = \left(\frac{h_f^*}{h_g^* - h_f^*}\right)\Delta t \frac{P_s}{P} H_{ig}(T^s - T_g) + \left(\frac{h_g^*}{h_g^* - h_f^*}\right)\Delta t H_{if}(T^s - T_f)$$
$$+ \Delta t\left(\frac{P - P_s}{P}\right)H_{gf}(T_g - T_f) - \Delta t\Gamma_w\left[\left(\frac{1-\varepsilon}{2}\right)h_f' + \left(\frac{1+\varepsilon}{2}\right)h_g'\right] + Q_{wf}\Delta t$$
$$+ DISS_f\Delta t$$
(3.1-146)

$$b_4 = -\left(\frac{2}{h_g^* - h_f^*}\right)\Delta t\frac{P_s}{P}H_{ig}(T^s - T_g) - \left(\frac{2}{h_g^* - h_f^*}\right)\Delta t H_{if}(T^s - T_f) + 2\Gamma_w\Delta t$$
(3.1-147)

$$g_1^1 = -(\dot{\alpha}_g\dot{\rho}_g\dot{X}_n A)_{j+1}\frac{\Delta t}{V}$$
(3.1-148)

$$g_2^1 = -[\dot{\alpha}_{g,j+1}(\dot{\rho}_{g,j+1}\dot{U}_{g,j+1} + P_L)A_{j+1}]\frac{\Delta t}{V}$$
(3.1-149)

$$g_4^1 = -(\dot{\alpha}_g\dot{\rho}_g A)_{j+1}\frac{\Delta t}{V}$$
(3.1-150)

$$g_5^1 = -(\dot{\alpha}_g\dot{\rho}_g A)_{j+1}\frac{\Delta t}{V}$$
(3.1-151)

$$g_1^2 = (\dot{\alpha}_g\dot{\rho}_g\dot{X}_n A)_j\frac{\Delta t}{V}$$
(3.1-152)

$$g_2^2 = [\dot{\alpha}_{g,j}(\dot{\rho}_{g,j}\dot{U}_{g,j} + P_L)A_j]\frac{\Delta t}{V}$$
(3.1-153)

$$g_4^2 = (\dot{\alpha}_g\dot{\rho}_g A)_j\frac{\Delta t}{V}$$
(3.1-154)

$$g_5^2 = (\dot{\alpha}_g\dot{\rho}_g A)_j\frac{\Delta t}{V}$$
(3.1-155)

$$f_3^1 = -[\dot{\alpha}_{f,j+1}(\dot{\rho}_{f,j+1}\dot{U}_{f,j+1} + P_L)A_{j+1}]\frac{\Delta t}{V}$$
(3.1-156)

$$f_4^1 = (\dot{\alpha}_f\dot{\rho}_f A)_{j+1}\frac{\Delta t}{V}$$
(3.1-157)

$$f_5^1 \qquad = \qquad -(\dot{\alpha}_f\dot{\rho}_fA)_{j+1}\frac{\Delta t}{V} \qquad\qquad\qquad\qquad (3.1\text{-}158)$$

$$f_3^2 \qquad = \qquad [\dot{\alpha}_{f,j}(\dot{\rho}_{f,j}\dot{U}_{f,j} + P_L)A_j]\frac{\Delta t}{V} \qquad\qquad\qquad (3.1\text{-}159)$$

$$f_4^2 \qquad = \qquad -(\dot{\alpha}_f\dot{\rho}_fA)_j\frac{\Delta t}{V} \qquad\qquad\qquad\qquad (3.1\text{-}160)$$

$$f_5^2 \qquad = \qquad (\dot{\alpha}_f\dot{\rho}_fA)_j\frac{\Delta t}{V}. \qquad\qquad\qquad\qquad (3.1\text{-}161)$$

A solver[a],[3.1-14] is used to obtain the bottom row of $\underset{\sim}{A}^{-1}$. The solver uses LU factorization without pivoting and factors the matrix into upper and lower triangular matrices (LU factors) using triangular decomposition.

Multiplying Equation (3.1-118) by $\underset{\sim}{A}^{-1}$, one can verify that just the bottom row of $\underset{\sim}{A}^{-1}$ is needed to obtain an equation that involves only the unknown variables $(P_L^{n+1} - P_L^n)$, $v_{g,j+1}^{n+1}$, $v_{g,j}^{n+1}$, $v_{f,j+1}^{n+1}$, and $v_{f,j}^{n+1}$. Substituting the velocity equations [after solving momentum Equations (3.1-104) and (3.1-105) for $v_{g,j}^{n+1}$ and $v_{f,j}^{n+1}$] into this equation results in a single equation involving pressures. This is done for each volume, giving rise to an N x N system of linear equations for the new time pressures in a system containing N volumes. Next, the default border-profile LU solver[3.1-10] is used to obtain $(P_L^{n+1} - P_L^n)$ for each volume. Then, the pressure differences $(P_L^{n+1} - P_L^n)$ are substituted into the velocity equations to obtain the new time velocities.

Now, the new time velocities are substituted back into Equation (3.1-118) to obtain a single vector on the right side. The LU factors are used to obtain the provisional time variables $\tilde{X}_{n,L}^{n+1}$, $\tilde{U}_{g,L}^{n+1}$, $\tilde{U}_{f,L}^{n+1}$, and $\tilde{\alpha}_{g,L}^{n+1}$.

A mixture density, $\rho_{m,L}^{n+1}$, is then calculated from the unexpanded form of the mixture continuity equation which is numerically mass preserving. The mixture density $\rho_{m,L}^{n+1}$ is calculated by adding the phasic density Equations, (3.1-2) and (3.1-3), to give the mixture continuity equation, which is

---

a. Personal communication, E. S. Marwill to J. A. Trapp, January 1983.

$$\frac{\partial \rho_m}{\partial t} + \frac{1}{A}\frac{\partial}{\partial x}(\alpha_g \rho_g v_g A + \alpha_f \rho_f v_f A) = 0 \quad .$$

(3.1-162)

The mass-preserving finite difference approximation is

$$V_L(\rho_{m,L}^{n+1} - \rho_L^n) + (\dot{\alpha}_{g,j+1}^n \dot{\rho}_{g,j+1}^n v_{g,j+1}^{n+1} A_{j+1} - \dot{\alpha}_{g,j}^n \dot{\rho}_{g,j}^n v_{g,j}^{n+1} A_j)\Delta t$$
$$+ (\dot{\alpha}_{f,j+1}^n \dot{\rho}_{f,j+1}^n v_{f,j+1}^{n+1} A_{j+1} - \dot{\alpha}_{f,j}^n \dot{\rho}_{f,j}^n v_{f,j}^{n+1} A_j)\Delta t = 0$$

(3.1-163)

from which $\rho_{m,L}^{n+1}$ is obtained. The density $\rho_{m,L}^{n+1}$ is compared with the mixture density, ρ_L^{n+1}, which is calculated from the state relations. The difference between these two mixture densities is used to provide a time step control based on truncation in the calculation of the mixture density (see Section 8.1).

Next, $\tilde{\Gamma}_{g,L}^{n+1}$ is calculated using Equation (3.1-111), where $\tilde{T}_L^{s,n+1}$, $\tilde{T}_{g,L}^{n+1}$, and $\tilde{T}_{f,L}^{n+1}$ are obtained from Equations (3.1-101) through (3.1-103) using the newly calculated variables P_L^{n+1}, $\tilde{U}_{g,L}^{n+1}$, $\tilde{U}_{f,L}^{n+1}$, and $\tilde{X}_{n,L}^{n+1}$.

To obtain the new time variables $X_{n,L}^{n+1}$, $X_{ni,L}^{n+1}$, $U_{g,L}^{n+1}$, $U_{f,L}^{n+1}$, and $\alpha_{g,L}^{n+1}$, the unexpanded difference equations, Equations (3.1-110), (3.1-112), (3.1-113), (3.1-114), (3.1-115), and (3.1-116) are used. In the discussion introducing the unexpanded difference equations, motives were given for use of the unexpanded form. Extensive numerical testing has shown the benefits of the following procedures.

Using the phasic convective terms along with $\tilde{\Gamma}_{g,L}^{n+1}$ from Equation (3.1-111), the unexpanded phasic density Equations (3.1-110) and (3.1-112) are used to obtain $(\alpha_g \rho_g)_L^{n+1}$ and $(\alpha_f \rho_f)_L^{n+1}$.

Next, the unexpanded total noncondensable density Equation (3.1-113) is used to calculate $(\alpha_g \rho_g X_n)_L^{n+1}$, which is then divided by $(\alpha_g \rho_g)_L^{n+1}$ to obtain $X_{n,L}^{n+1}$.

The unexpanded individual noncondensable density Equation (3.1-114) is then used to calculate $(\alpha_g \rho_g X_n X_{ni})_L^{n+1}$, which is divided by $(\alpha_g \rho_g X_n)_L^{n+1}$ to obtain $X_{ni,L}^{n+1}$.

Following this, the unexpanded vapor/gas energy Equation (3.1-115) is used with the vapor/gas energy source and convective terms from the expanded equation as well as the provisional time variables $\tilde{T}^{s,n+1}$, $\tilde{T}_g^{n+1}$, and $\tilde{T}_f^{n+1}$ to obtain $(\alpha_g \rho_g U_g)_L^{n+1}$, which is divided by $(\alpha_g \rho_g)_L^{n+1}$ to give $U_{g,L}^{n+1}$. Analogously, the unexpanded liquid energy Equation (3.1-116) is used to obtain $(\alpha_f \rho_f U_f)_L^{n+1}$, which is divided by $(\alpha_f \rho_f)_L^{n+1}$ to give $U_{f,L}^{n+1}$.

Finally, $\alpha_{g,L}^{n+1}$ is calculated from $(\alpha_f \rho_f)_L^{n+1}$ using the equation

$$\alpha_{g,L}^{n+1} = 1 - \alpha_{f,L}^{n+1} = 1 - \frac{(\alpha_f \rho_f)_L^{n+1}}{\hat{\rho}_{f,L}^{n+1}} \tag{3.1-164}$$

where $\hat{\rho}_{f,L}^{n+1}$ is obtained using a linearized state relation Equation (3.1-98) and the new time variables P_L^{n+1} and $U_{f,L}^{n+1}$. The equation for $\hat{\rho}_{f,L}^{n+1}$ has the form

$$\hat{\rho}_{f,L}^{n+1} = \rho_{f,L}^n + \left(\frac{\partial \rho_f}{\partial P}\right)_L^n (P_L^{n+1} - P_L^n) + \left(\frac{\partial \rho_f}{\partial U_f}\right)_L^n (U_{f,L}^{n+1} - U_{f,L}^n) \quad . \tag{3.1-165}$$

The unexpanded equations are used in all two-phase to two-phase cases, except when the provisional void fraction $\tilde{\alpha}_{g,L}^{n+1}$ is less than 0.001 and $\tilde{\alpha}_{g,L}^{n+1} < \alpha_{g,L}^n$. For this case, the provisional new time variables are taken to be the new time variables.

3.1.4.2 One-Phase to One-Phase. For this case, the pressure calculation remains the same as in the two-phase to two-phase case. For the densities and energies, however, the unexpanded equations are not used, and the provisional new time variables obtained from the expanded equations are taken to be the new time variables. For the phase that is not present, the interfacial heat transfer coefficient for that phase is computed as if the void fraction was approximately 10^{-5} instead of zero. This results in the specific internal energy of that phase being computed very close to saturation conditions. Slight numerical variations from saturation occur due to linearization; and the phasic specific internal energy, temperature, and density of the missing phase are reset to the saturation values in the state relations subroutine. This ensures agreement with saturation conditions. For the phase that is present, a value of 0.0 for the interfacial heat transfer coefficient is used, since there is no mass transfer occurring.

3.1.4.3 Two-Phase to One-Phase (Disappearance). For this case, the calculation is carried out in the same way as in the two-phase to two-phase case, where expanded calculations followed by unexpanded calculations are used (except for the case $\tilde{\alpha}_{g,L}^{n+1} < 0.001$ and $\tilde{\alpha}_{g,L}^{n+1} < \alpha_{g,L}^n$). Then, for the phase that disappears, the phasic specific internal energy, temperature, and density are reset to saturation values in the state relations subroutine, as is done with the one-phase to one-phase case. Sometimes when a phase disappears, the calculated void fraction and/or noncondensable quality is less than zero or greater than one. When this occurs, the void fraction and/or noncondensable quality is then reset to zero or one, respectively. If the calculated void fraction and/or noncondensable quality is too much less than zero or too much greater than one (amount determined through extensive testing, which is consistent with the mass error check), an error is assumed to have occurred, and the time step is reduced and repeated.

3.1.4.4 One-Phase to Two-Phase (Appearance). Here, the calculation proceeds in the same way as in the one-phase to one-phase case. For the phase that is not present, the large interfacial heat transfer coefficient for that phase is computed as if the void fraction was approximately 10^{-5} instead of

zero. This results in the specific internal energy and temperature of that phase being computed very close to saturation conditions. Because the phase that is appearing is assumed to appear at saturation conditions, an error can be made if, in reality, the phase appeared by convection from a neighboring volume that was at a temperature different from saturation. The magnitude of the potential error is controlled by letting the phase appear at saturation but restricting the amount that can appear by time step control. If more than the limiting amount (amount determined through extensive testing) appears, an error is assumed to have occurred, and the time step is reduced and repeated.

3.1.5 Difference Equations and Time Advancement for the Nearly-Implicit Scheme

For problems where the flow is expected to change very slowly with time, it is possible to obtain adequate information from an approximate solution based on very large time steps. This would be advantageous if a reliable and efficient means could be found for solving difference equations treating all terms (i.e., phase exchanges, pressure propagation, and convection) by implicit differences. Unfortunately, the state of the art is less satisfactory here than in the case of semi-implicit (convection-explicit) schemes. For illustration, a fully implicit scheme for the six-equation model of a 100-volume problem would require the solution of 600 coupled algebraic equations. If these equations were linearized for a pipe with no branching, inversion of a block tri-diagonal, 600 x 600 matrix with 6 x 6 blocks would be required. This would yield a matrix of bandwidth 23 containing ~13,800 nonzero elements, resulting in an extremely costly time-advancement scheme. Note that the tri-diagonal shape is limited to a pipe with no branching problem.

To reduce the number of calculations required for solving fully implicit difference schemes, fractional step (sometimes called multiple step) methods have been tried. The equations can be split into fractional steps based upon physical phenomena. This is the basic idea in the nearly-implicit scheme. Fractional step methods for two-phase flow problems have been developed.[3.1-15,3.1-16] These earlier efforts have been used to guide the development of the present nearly-implicit scheme. The fractional step method described here[3.1-17] differs significantly from prior efforts in the reduced number of steps used to evaluate the momentum equations.

The nearly-implicit scheme consists of two steps. The first step solves all seven conservation equations, treating all interface exchange processes, the pressure propagation process, and the momentum convection process implicitly. These finite difference equations are exactly the expanded ones [Equations (3.1-88) through (3.1-92), (3.1-104), and (3.1-105)] solved in the semi-implicit scheme with one major change. The convective terms in the momentum Equations (3.1-104) and (3.1-105) are evaluated implicitly (in a linearized form) instead of in an explicit donored fashion as is done in the semi-implicit scheme. The second step consists of solving the unexpanded form of the mass and energy equations. As is done for the semi-implicit scheme, the equations are listed for the case of a pipe with no branching and only one wall (heat structure) next to the wall.

3.1.5.1 First Step of the Nearly-Implicit Scheme. The linearized implicit technique used for the convective terms in the momentum equations in the first step is illustrated for the convective term in

ATHENA/2.3

the vapor/gas part of the sum momentum Equation (3.1-86). An analogous result occurs for the liquid part as well as for the difference momentum Equation (3.1-87). The vapor/gas convective term is

$$\frac{1}{2}\alpha_g\rho_g(v_g^2)_{x_K}^{x_L} \quad .$$

(3.1-166)

In the nearly-implicit scheme formulation, the VISF [Equation (3.1-107)] and VISG [Equation (3.1-106)] terms that result from the donor-like formulation are not used because they are not needed for stability purposes. Evaluating the velocities at new time gives the finite difference form of the vapor/gas convective term as

$$\frac{1}{2}(\dot\alpha_g\dot\rho_g)_j^n[(v_{g,L}^{n+1})^2 - (v_{g,K}^{n+1})^2] \quad .$$

(3.1-167)

This term can be rewritten as

$$\frac{1}{2}(\dot\alpha_g\dot\rho_g)_j^n[(v_{g,L}^{n+1} - v_{g,L}^n)^2 + 2v_{g,L}^n(v_{g,L}^{n+1} - v_{g,L}^n) + (v_{g,L}^n)^2$$
$$- (v_{g,K}^{n+1} - v_{g,K}^n)^2 - 2v_{g,K}^n(v_{g,K}^{n+1} - v_{g,K}^n) - (v_{g,K}^n)^2] \quad .$$

(3.1-168)

Assuming that the leading quadratic term for L and K is small (small temporal changes in velocity) compared to the others results in the term

$$\frac{1}{2}(\dot\alpha_g\dot\rho_g)_j^n[2v_{g,L}^n(v_{g,L}^{n+1} - v_{g,L}^n) + (v_{g,L}^n)^2 - 2v_{g,K}^n(v_{g,K}^{n+1} - v_{g,K}^n) - (v_{g,K}^n)^2] \quad .$$

(3.1-169)

Using this linearized implicit form, the convective (momentum flux) terms in the sum momentum finite difference Equation (3.1-104) are replaced by

$$\frac{1}{2}(\dot\alpha_g\dot\rho_g)_j^n[2v_{g,L}^n(v_{g,L}^{n+1} - v_{g,L}^n) + (v_{g,L}^n)^2 - 2v_{g,K}^n(v_{g,K}^{n+1} - v_{g,K}^n) - (v_{g,K}^n)^2]\Delta t$$
$$+ \frac{1}{2}(\dot\alpha_f\dot\rho_f)_j^n[2v_{f,L}^n(v_{f,L}^{n+1} - v_{f,L}^n) + (v_{f,L}^n)^2 - 2v_{f,K}^n(v_{f,K}^{n+1} - v_{f,K}^n) - (v_{f,K}^n)^2]\Delta t \quad .$$

(3.1−170)

Similarly, for the difference momentum finite difference Equation (3.1-105), the convective (momentum flux) terms are replaced by

$$\frac{1}{2}\left(\frac{\dot{\alpha}_g\dot{\rho}_g}{\alpha_g\rho_g}\right)_j^n [2v_{g,L}^n(v_{g,L}^{n+1} - v_{g,L}^n) + (v_{g,L}^n)^2 - 2v_{g,K}^n(v_{g,K}^{n+1} - v_{g,K}^n) - (v_{g,K}^n)^2]\Delta t$$

$$-\frac{1}{2}\left(\frac{\dot{\alpha}_f\dot{\rho}_f}{\alpha_f\rho_f}\right)_j^n [2v_{f,L}^n(v_{f,L}^{n+1} - v_{f,L}^n) + (v_{f,L}^n)^2 - 2v_{f,K}^n(v_{f,K}^{n+1} - v_{f,K}^n) - (v_{f,K}^n)^2]\Delta t \ .$$

(3.1–171)

Just like the semi-implicit scheme, the coding for the finite difference form of the difference momentum equation [Equation (3.1-105) with convective (momentum flux) terms from Equation (3.1-171)] is programmed as the difference of the liquid and vapor/gas momentum equations instead of the difference of the vapor/gas and the liquid momentum equations [as shown in Equation (3.1-105)] in the nearly-implicit scheme.

The volume-centered velocities are defined in terms of the velocities in the junctions attached to the volume (see Section 3.1.6). Thus, the new time volume-averaged velocities have the form

$$v_{f,L}^{n+1} = \sum_{j=1}^{Jin} c_{f,j}^n v_{f,j}^{n+1} + \sum_{j=1}^{Jout} c_{f,j}^n v_{f,j}^{n+1}$$

(3.1-172)

and

$$v_{g,L}^{n+1} = \sum_{j=1}^{Jin} c_{g,j}^n v_{g,j}^{n+1} + \sum_{j=1}^{Jout} c_{g,j}^n v_{g,j}^{n+1}$$

(3.1-173)

where $c_{f,j}^n$ and $c_{g,j}^n$ contain all old time quantities, and the equations have the same form as those in Section 3.1.6 except that the junction velocities are at new time values.

Although this additional implicitness involves only the momentum flux terms, it has a large impact on the algebraic solution algorithm in the first step of the nearly-implicit scheme. In the semi-implicit scheme, Equations (3.1-88) through (3.1-92) are solved locally to give a single equation of the form

$$P_L^{n+1} = Av_{g,j+1}^{n+1} + Bv_{g,j}^{n+1} + Cv_{f,j+1}^{n+1} + Dv_{f,j}^{n+1} + E$$

(3.1-174)

for pressure, where A, B, C, D, and E contain only n time level variables (see **Figure 3.1-3** for cell indexes). In the semi-implicit scheme, the momentum equations [Equations (3.1-104) and (3.1-105)] are also solved locally to obtain

$$v_{g,j}^{n+1} = A^1(P_L^{n+1} - P_K^{n+1}) + C^1$$

(3.1-175)

$$v_{f,j}^{n+1} = B^1(P_L^{n+1} - P_K^{n+1}) + D^1 \tag{3.1-176}$$

where A^1, B^1, C^1, and D^1 contain only n time level variables. If the momentum Equations (3.1-175) and (3.1-176) are used to eliminate the n+1 time level junction velocities from Equation (3.1-174), we get the pressure equation used in the semi-implicit scheme to obtain all the n+1 time level pressures. For the previous example of a 100 volume straight pipe with no branching problem, this results in a 100 x 100 tri-diagonal matrix system to solve for all the P^{n+1}.

In the nearly-implicit scheme, because the momentum flux terms are implicit [junction velocities are at new time (n+1)], the momentum Equations (3.1-104) and (3.1-105) [using the convective terms from Equations (3.1-170) and (3.1-171)] cannot be locally solved to get Equations (3.1-175) and (3.1-176). The new time convective terms bring in the n+1 time level upstream and downstream junction velocities, e.g., $v_{g,j-1}^{n+1}$, $v_{g,j+1}^{n+1}$, $v_{f,j-1}^{n+1}$, and $v_{f,j+1}^{n+1}$. The gravity head and the horizontal stratification force terms are also implicit [volume void fractions are at new time (n+1)]. Thus, in the nearly implicit scheme, the momentum equations are now of the form

$$A^1 v_{g,j-1}^{n+1} + B^1 v_{f,j-1}^{n+1} + C^1 v_{g,j}^{n+1} + D^1 v_{f,j}^{n+1} + E^1 v_{g,j+1}^{n+1} + F^1 v_{f,j+1}^{n+1} =$$
$$G^1(P_L^{n+1} - P_K^{n+1}) + H^1(\alpha_{g,L}^{n+1} - \alpha_{g,K}^{n+1}) + I^1 \tag{3.1-177}$$

$$J^1 v_{g,j-1}^{n+1} + K^1 v_{f,j-1}^{n+1} + L^1 v_{g,j}^{n+1} + M^1 v_{f,j}^{n+1} + N^1 v_{g,j+1}^{n+1} + O^1 v_{f,j+1}^{n+1} =$$
$$P^1(P_L^{n+1} - P_K^{n+1}) + Q^1(\alpha_{g,L}^{n+1} - \alpha_{g,K}^{n+1}) + R^1 \tag{3.1-178}$$

where A^1, B^1, C^1, D^1, E^1, F^1, G^1, H^1, I^1, J^1, K^1, L^1, M^1, N^1, P^1, Q^1, and R^1 contain only n time level variables.

Equations (3.1-88) through (3.1-92) are still used to obtain Equation (3.1-174). In the nearly-implicit scheme, Equation (3.1-174) is used to eliminate the n+1 time level pressure terms from Equations (3.1-177) and (3.1-178). An equation describing the void fraction in a volume in terms of the phasic velocoties in the junctions attached to the volume [similar to Equation (3.1-177)] can be derived from the solution of the phasic mass and energy equations. The equation for volume L is of the form

$$\alpha_{g,L}^{n+1} = S v_{g,j+1}^{n+1} + T v_{g,j}^{n+1} + U v_{f,j+1}^{n+1} + V v_{f,j}^{n+1} + W \tag{3.1-179}$$

where S, T, U, V, and W contain only n time level variables. In the nearly-implicit scheme, Equation (3.1-179) and a similar equation for the void fraction in volume K are used to eliminate the n+1 time level void fraction terms from Equations (3.1-177) and (3.1-178) to obtain a pair of coupled momentum equations involving only n+1 time level junction velocities. Because of the n+1 time level momentum flux terms, this is a globally coupled system. For a pipe with no branching of 100 junctions, a 200 x 200 matrix

system is obtained. By partitioning the matrix into 2 x 2 submatrices (or blocks), the matrix is in block tri-diagonal form. This system is next preconditioned in order to enhance the diagonal dominance of the matrix.[3.1-18] This system of equations is then solved using the default border-profile LU matrix solution algorithm.[3.1-10] Once the v_f^{n+1} and v_g^{n+1} solution is obtained, P^{n+1} is obtained by substitution into Equation (3.1-174). Using Equations (3.1-88) through (3.1-92), provisional new time values for α_g, U_g, U_f, and X_n, denoted by $\tilde{\alpha}_g^{n+1}$, $\tilde{U}_g^{n+1}$, $\tilde{U}_f^{n+1}$, and $\tilde{X}_n^{n+1}$, can also be obtained. The void fraction substitution makes the nearly-implicit solution algorithm more implicit and leads to enhanced numerical stability.

3.1.5.2 Second Step of the Nearly-Implicit Scheme. The second step in the nearly-implicit scheme is used to stabilize the convective terms in the mass and energy balance equations. This step uses the final n+1 time level junction velocities from the first step along with the interface exchange terms resulting from the provisional variables of the first step, i.e., the interface heat and mass exchanges for step two are calculated using P^{n+1}, $\tilde{U}_g^{n+1}$, $\tilde{U}_f^{n+1}$, and $\tilde{X}_n^{n+1}$ from step one. The phasic continuity and energy equations in this second step have the convected variables evaluated at the n+1 time level, i.e. implicitly, as compared to their explicit evaluation in the first step.

The vapor/gas density equation is

$$V_L[(\alpha_g\rho_g)_L^{n+1} - (\alpha_g\rho_g)_L^n] + [(\dot{\alpha\rho})_{g,j+1}^{n+1} v_{g,j+1}^{n+1} A_{j+1} - (\dot{\alpha\rho})_{g,j}^{n+1} v_{g,j}^{n+1} A_j]\Delta t = \tilde{\Gamma}_{g,L}^{n+1} V_L \Delta t \qquad . \qquad (3.1\text{-}180)$$

The liquid density equation is

$$V_L[(\alpha_f\rho_f)_L^{n+1} - (\alpha_f\rho_f)_L^n] + [(\dot{\alpha\rho})_{f,j+1}^{n+1} v_{f,j+1}^{n+1} A_{j+1} - (\dot{\alpha\rho})_{f,j}^{n+1} v_{f,j}^{n+1} A_j]\Delta t = -\tilde{\Gamma}_{g,L}^{n+1} V_L \Delta t \qquad . \qquad (3.1\text{-}181)$$

In Equations (3.1-180) and (3.1-181), the interfacial mass exchange $\tilde{\Gamma}_g^{n+1}$ is evaluated using the provisional values from the first step and is written

$$\tilde{\Gamma}_{g,L}^{n+1} = -\frac{\dfrac{P_{s,L}^n}{P_L^n}H_{ig,L}^n(\tilde{T}_L^{s,n+1} - \tilde{T}_{g,L}^{n+1}) + H_{if,L}^n(\tilde{T}_L^{s,n+1} - \tilde{T}_{f,L}^{n+1})}{h_{g,L}^{*,n} - h_{f,L}^{*,n}} + \Gamma_{w,L}^n \qquad (3.1\text{-}182)$$

where the provisional temperatures $\tilde{T}^{n+1}$ are evaluated as functions of $\tilde{U}_g^{n+1}$, $\tilde{U}_f^{n+1}$, $\tilde{X}_n^{n+1}$, and P^{n+1} from the linearized state relation [Equations (3.1-101), (3.1-102), and (3.1-103)].

The total noncondensable density equation is

$$V_L[(\alpha_g \rho_g X_n)_L^{n+1} - (\alpha_g \rho_g X_n)_L^n] + [(\alpha_g \dot{\rho}_g X_n)_{j+1}^{n+1} v_{g,j+1}^{n+1} A_{j+1}$$
$$- (\alpha_g \dot{\rho}_g X_n)_j^{n+1} v_{g,j}^{n+1} A_j]\Delta t = 0 . \tag{3.1-183}$$

The density equation for the i-th noncondensable species is

$$V_L[(\alpha_g \rho_g X_n X_{ni})_L^{n+1} - (\alpha_g \rho_g X_n X_{ni})_L^n] + [(\alpha_g \rho_g \dot{X}_n X_{ni})_{j+1}^{n+1} v_{g,j+1}^{n+1} A_{j+1}$$
$$- (\alpha_g \rho_g \dot{X}_n X_{ni})_j^{n+1} v_{g,j}^{n+1} A_j]\Delta t = 0 . \tag{3.1-184}$$

The vapor/gas thermal energy equation is given by

$$V_L[(\alpha_g \rho_g U_g)_L^{n+1} - (\alpha_g \rho_g U_g)_L^n] + [(\alpha \dot{\rho} U)_{g,j+1}^{n+1} v_{g,j+1}^{n+1} A_{j+1} - (\alpha \dot{\rho} U)_{g,j}^{n+1} v_{g,j}^{n+1} A_j]\Delta t$$

$$= -V_L P_L^n(\tilde{\alpha}_{g,L}^{n+1} - \alpha_{g,L}^n) - P_L^n(\dot{\alpha}_{g,j+1}^n v_{g,j+1}^{n+1} A_{j+1} - \dot{\alpha}_{g,j}^n v_{g,j}^{n+1} A_j)\Delta t$$

$$+ \left\{ -\left(\frac{h_f^*}{h_g^* - h_f^*}\right)_L^n \frac{P_{s,L}^n}{P_L^n} H_{ig,L}^n(\tilde{T}_L^{s,n+1} - \tilde{T}_{g,L}^{n+1}) - \left(\frac{h_g^*}{h_g^* - h_f^*}\right)_L^n H_{if,L}^n(\tilde{T}_L^{s,n+1} - \tilde{T}_{f,L}^{n+1}) \right. \tag{3.1-185}$$

$$\left. - \left(\frac{P_L^n - P_{s,L}^n}{P_L^n}\right) H_{gf,L}^n(\tilde{T}_{g,L}^{n+1} - \tilde{T}_{f,L}^{n+1}) + \left[\left(\frac{1+\varepsilon}{2}\right)h_{g,L}^{',n} + \left(\frac{1-\varepsilon}{2}\right)h_{f,L}^{',n}\right]\Gamma_{w,L}^n + Q_{wg,L}^n + DISS_{g,L}^n \right\} V_L \Delta t$$

The liquid thermal energy equation is given by

$$V_L[(\alpha_f \rho_f U_f)_L^{n+1} - (\alpha_f \rho_f U_f)_L^n] + [(\alpha \dot{\rho} U)_{f,j+1}^{n+1} v_{f,j+1}^{n+1} A_{j+1} - (\alpha \dot{\rho} U)_{f,j}^{n+1} v_{f,j}^{n+1} A_j]\Delta t$$

$$= V_L P_L^n(\tilde{\alpha}_{g,L}^{n+1} - \alpha_{g,L}^n) - P_L^n(\dot{\alpha}_{f,j+1}^n v_{f,j+1}^{n+1} A_{j+1} - \dot{\alpha}_{f,j}^n v_{f,j}^{n+1} A_j)\Delta t$$

$$+ \left\{ \left(\frac{h_f^*}{h_g^* - h_f^*}\right)_L^n \frac{P_{s,L}^n}{P_L^n} H_{ig,L}^n(\tilde{T}_L^{s,n+1} - \tilde{T}_{g,L}^{n+1}) + \left(\frac{h_g^*}{h_g^* - h_f^*}\right)_L^n H_{if,L}^n(\tilde{T}_L^{s,n+1} - \tilde{T}_{f,L}^{n+1}) \right. \tag{3.1-186}$$

$$\left. + \left(\frac{P_L^n - P_{s,L}^n}{P_L^n}\right) H_{gf,L}^n(\tilde{T}_{g,L}^{n+1} - \tilde{T}_{f,L}^{n+1}) - \left[\left(\frac{1+\varepsilon}{2}\right)h_{g,L}^{',n} + \left(\frac{1-\varepsilon}{2}\right)h_{f,L}^{',n}\right]\Gamma_{w,L}^n + Q_{wf,L}^n + DISS_{f,L}^n \right\} V_L \Delta t .$$

The second step uses the mass and energy balance equations. If the structure of Equations (3.1-180), (3.1-181), (3.1-183), (3.1-184), (3.1-185), and (3.1-186) is examined, it is seen that each equation involves only one unknown variable:

• Vapor/gas density Equation (3.1-180) $(\alpha\rho)_g^{n+1}$.

- Liquid density Equation (3.1-181) $(\alpha\rho)_f^{n+1}$.

- Total noncondensable density Equation (3.1-183) $(\alpha_g\rho_g X_n)^{n+1}$.

- Individual noncondensable density Equation (3.1-184) $(\alpha_g\rho_g X_n X_{ni})^{n+1}$.

- Vapor/gas energy Equation (3.1-185) $(\alpha\rho U)_g^{n+1}$.

- Liquid energy Equation (3.1-186) $(\alpha\rho U)_f^{n+1}$.

This is because the new time velocities, v_g^{n+1} and v_f^{n+1}, are known from step one, and provisional n+1 values from step one are used in the exchange terms. Hence, each equation is uncoupled from the others and can be solved independently. In addition, the equations involving the vapor/gas phase, Equations (3.1-180), (3.1-183), (3.1-184), and (3.1-185), have the same structural form for the convective terms, i.e., each equation convects with velocity v_g^{n+1}. The coefficient matrix generated by Equation (3.1-180) is inverted once, and then this inverse is used with different right sides to solve Equations (3.1-183), (3.1-184), and (3.1-185). Hence, for the pipe without branching problem of 100 cells, only one 100 x 100 tri-diagonal system is inverted to obtain $(\alpha\rho)_g^{n+1}$, $(\alpha_g\rho_g X_n)^{n+1}$, $(\alpha_g\rho_g X_n X_{ni})^{n+1}$, and $(\alpha\rho U)_g^{n+1}$. In like manner, the liquid phase Equations (3.1-181) and (3.1-186) have the same structure and require only one inversion to be carried out to solve both equation sets, giving $(\alpha\rho)_f^{n+1}$ and $(\alpha\rho U)_f^{n+1}$.

With the above new time variables known, we obtain X_n^{n+1}, X_{ni}^{n+1}, U_g^{n+1}, and U_f^{n+1} from

$$X_n^{n+1} = \frac{(\alpha_g\rho_g X_n)^{n+1}}{(\alpha_g\rho_g)^{n+1}} \tag{3.1-187}$$

$$X_{ni}^{n+1} = \frac{(\alpha_g\rho_g X_n X_{ni})^{n+1}}{(\alpha_g\rho_g X_n)^{n+1}} \tag{3.1-188}$$

$$U_g^{n+1} = \frac{(\alpha_g\rho_g U_g)^{n+1}}{(\alpha_g\rho_g)^{n+1}} \tag{3.1-189}$$

$$U_f^{n+1} = \frac{(\alpha_f \rho_f U_f)^{n+1}}{(\alpha_f \rho_f)^{n+1}} \quad . \tag{3.1-190}$$

The void fraction, α_g^{n+1}, is obtained from

$$\alpha_g^{n+1} = \frac{\rho_m^{n+1} - \hat{\rho}_f^{n+1}}{\hat{\rho}_g^{n+1} - \hat{\rho}_f^{n+1}} = \frac{(\alpha\rho)_g^{n+1} + (\alpha\rho)_f^{n+1} - \hat{\rho}_f^{n+1}}{\hat{\rho}_g^{n+1} - \hat{\rho}_f^{n+1}} \tag{3.1-191}$$

where

ρ_m^{n+1} =   the overall mixture density

$\hat{\rho}_f^{n+1}$ =   the liquid density, which is calculated from the linearized state relation [Equation (3.1-98)] using P^{n+1} and U_f^{n+1}

$\hat{\rho}_g^{n+1}$ =   the vapor/gas density, which is calculated from the linearized state relationship [Equation (3.1-97)] using P^{n+1}, X_n^{n+1}, and U_g^{n+1} .

Up to this point of this section on the nearly-implicit scheme, the difference equations have been presented along with the time advancement for the case of two-phase to two-phase only. As indicated in Section 3.1.4, there are three other possible transition cases (one-phase to one-phase, two-phase to one-phase, and one-phase to two-phase). These three cases will now be described for the nearly-implicit scheme.

For the one-phase to one-phase case, both the first step and the second step are carried out as in the two-phase to two-phase case. For the phase that is not present, a large interfacial heat transfer coefficient consistent with the interfacial heat transfer coefficients computed from the correlation for a void fraction of 10^{-5} is used. For the phase that is present, a value of 0.0 is used for the interfacial heat transfer coefficient. For the phase that is not present, α is zero, and thus $(\alpha\rho)^{n+1}$ equals zero for that phase. The provisional n+1 value of the corresponding variable is used in order to avoid the division by zero in Equations (3.1-187) through (3.1-190). As with the semi-implicit time advancement, phasic specific internal energy, temperature, and density of the missing phase are reset to the saturation values in the state relations subroutine.

For the two-phase to one-phase case (disappearance), the calculation is carried out the same as in the two-phase to two-phase case. Then, for the phase that is missing, the phasic specific internal energy, temperature, and density of the missing phase are reset to saturation values in the state relations subroutine as is done with the one-phase to one-phase case. Sometimes when a phase disappears, the calculated void

fraction and/or noncondensable quality is less than zero or greater than one. When this occurs, the void fraction and/or noncondensable quality is then reset to zero or one, respectively. If the calculated void fraction and/or noncondensable quality is too much less than zero or too much greater than one (amount determined through extensive testing, which is consistent with the mass error check), an error is assumed to have occurred, and the time step is reduced and repeated. This is the same approach used in the semi-implicit scheme time advancement.

For the one-phase to two-phase case (appearance), the first step quantities are used for the appearing phase. A large interfacial heat transfer coefficient, consistent with the interfacial heat transfer coefficients from the correlations, as if the void fraction were 10^{-5}, is used for the appearing phase, resulting in the energy and temperature of that phase being very close to saturation. Because the phase that is appearing is assumed to appear at saturation conditions, an error can be made if, in reality, the phase appeared by convection from a neighboring volume that was at a temperature different from saturation. The magnitude of the potential error is controlled by letting the phase appear at saturation but restricting the amount that can appear by time step control. If more than the limiting amount appears, an error is assumed to have occurred, and the time step is reduced and repeated. This is the same approach used in the semi-implicit scheme time advancement.

In summary, the second step stabilizes the convective terms in the mass and energy equations, and it does so with very little computational effort due to the fractional step nature of the scheme. As an example, if the nearly-implicit method is compared with the fully implicit method for a pipe without branching problem of 100 cells, we have the following efficiency estimates. The fully implicit method requires the inversion of a banded block tri-diagonal 600 x 600 matrix of bandwidth 23 containing 13,800 nonzero elements. The nearly-implicit method requires the inversion of one block tri-diagonal 200 x 200 matrix with 2 x 2 blocks and bandwidth 7 containing 1,400 nonzero elements plus two 100 x 100 tri-diagonal matrices with 300 nonzero elements. The nearly-implicit method thus requires about 1/10 the number of storage locations required by the fully implicit method. If the computational efficiency is estimated by counting the number of multiplications in the forward part of a Gaussian elimination algorithm, then the fully implicit method for this problem requires about 450,000 multiplications, whereas the nearly-implicit method requires about 2,000 multiplications. Thus, the nearly-implicit method requires about 1/200 (based on the number of multiplications) of the computational time per time step needed for a fully implicit scheme.

3.1.6 Volume-Average Velocities

The previous development of the difference equations considered a pipe consisting of a series of singly connected volumes without branching. In ATHENA, each volume may have zero, one or more junctions attached to its inlet end in the normal flow direction, and, zero, one, or more junctions attached to its outlet end in the normal flow direction. The same can be true for the two crossflow directions (see Section 3.4.5). Therefore, the flux terms at the inlet or outlet end of a volume for the normal or crossflow directions consist of a summation over all of the junctions attached to that end of the volume.

Volume-average velocities are required for the momentum flux calculation, evaluation of the wall frictional forces, evaluation of the wall heat transfer, evaluation of the interfacial heat transfer, and the Courant time step limit. In a simple constant area passage, the arithmetic average between the inlet and outlet is a satisfactory approximation. At branch volumes, however, with multiple inlets and/or outlets or for volumes with abrupt area change, use of the arithmetic average results in nonphysical behavior.

The liquid and vapor/gas velocities in the normal or crossflow directions in the volume cells are calculated by a method that averages the phasic mass flows over the volume cell inlet and outlet junctions in the normal or crossflow directions. A cell volume is shown in **Figure 3.1-4**, where the rectangular box represents a cell volume. Each of the arrow vectors into or out of the box represents the liquid mass flow through an inlet or outlet junction, respectively, in the normal or crossflow directions. The variable Jin is the number of inlet junctions, and Jout is the number of outlet junctions. This discussion will be for liquid velocity; the vapor/gas velocity derivation is the same.
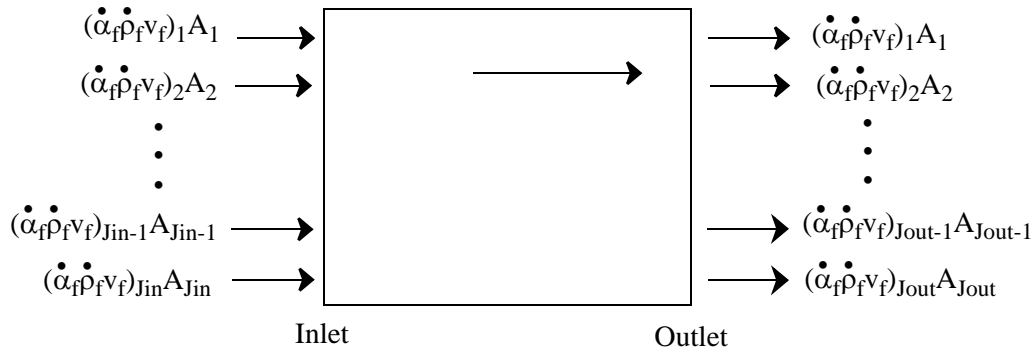
Figure 3.1-4 Schematic of a volume cell showing multiple inlet and outlet junction mass flows.

At the inlet side of the volume, the total mass flow rate into the volume is given by

$$M_{f,\,in} = \sum_{j\,=\,1}^{Jin} \dot{\alpha}_{f,\,j} \dot{\rho}_{f,\,j} v_{f,\,j} A_j \tag{3.1-192}$$

where $M_{f,in}$ is the mass flow rate of liquid into the volume.

The average inlet liquid volume fraction can be defined as

$$\overline{\alpha}_{f,\,in} = \frac{\displaystyle\sum_{j\,=\,1}^{Jin} \dot{\alpha}_{f,\,j}A_j}{\displaystyle\sum_{j\,=\,1}^{Jin} A_j} \quad . \tag{3.1-193}$$

The average inlet liquid density can be defined as

$$\overline{\rho}_{f,\,in} = \frac{\displaystyle\sum_{j\,=\,1}^{Jin} \dot{\alpha}_{f,\,j}\dot{\rho}_{f,\,j}A_j}{\displaystyle\sum_{j\,=\,1}^{Jin} \dot{\alpha}_{f,\,j}A_j} \quad . \tag{3.1-194}$$

The average inlet liquid velocity with respect to the total inlet junction cross-sectional area can be defined as

$$\overline{v}_{f,\,in} = \frac{\displaystyle\sum_{j\,=\,1}^{Jin} \dot{\alpha}_{f,\,j}\dot{\rho}_{f,\,j}v_{f,\,j}A_j}{\displaystyle\sum_{j\,=\,1}^{Jin} \dot{\alpha}_{f,\,j}\dot{\rho}_{f,\,j}A_j} \quad . \tag{3.1-195}$$

The total inlet junction cross-sectional area is

$$A_{in} = \sum_{j\,=\,1}^{Jin} A_j \quad . \tag{3.1-196}$$

Equation (3.1-192) can be expressed in terms of the average inlet conditions as

$$M_{f,\,in} = \sum_{j\,=\,1}^{Jin} \dot{\alpha}_{f,\,j}\dot{\rho}_{f,\,j}v_{f,\,j}A_j = \overline{\alpha}_{f,\,in}\overline{\rho}_{f,\,in}\overline{v}_{f,\,in}A_{in} \quad . \tag{3.1-197}$$

In terms of the volume cross-sectional area, A_L, the mass flow rate can be written as

$$M_{f,\,in} = \overline{\alpha}_{f,\,in}\overline{\rho}_{f,\,in}\overline{v}_{f,\,in}^L A_L \tag{3.1-198}$$

where $\bar{v}^L_{f,\,in}$ is the liquid volume inlet velocity. By equating Equations (3.1-197) and (3.1-198), canceling terms and rearranging, the liquid volume inlet velocity can be expressed as

$$\bar{v}^L_{f,\,in} \;=\; \bar{v}_{f,\,in}\frac{A_{in}}{A_L} \quad . \tag{3.1-199}$$

Substituting Equations (3.1-195) and (3.1-196) into Equation (3.1-199) gives

$$\bar{v}^L_{f,\,in} \;=\; \frac{\left(\sum\limits_{j=1}^{Jin}\dot{\alpha}_{f,j}\dot{\rho}_{f,j}v_{f,j}A_j\right)\left(\sum\limits_{j=1}^{Jin}A_j\right)}{\sum\limits_{j=1}^{Jin}\dot{\alpha}_{f,j}\dot{\rho}_{f,j}A_j}\frac{}{A_L} \quad . \tag{3.1-200}$$

Similarly, the liquid volume outlet velocity can be expressed as

$$\bar{v}^L_{f,\,out} \;=\; \frac{\left(\sum\limits_{j=1}^{Jout}\dot{\alpha}_{f,j}\dot{\rho}_{f,j}v_{f,j}A_j\right)\left(\sum\limits_{j=1}^{Jout}A_j\right)}{\sum\limits_{j=1}^{Jout}\dot{\alpha}_{f,j}\dot{\rho}_{f,j}A_j}\frac{}{A_L} \quad . \tag{3.1-201}$$

In RELAP5/MOD1, the total liquid momentum of the volume was expressed in terms of the momentum of the inlet and outlet halves of the volume as (assuming density changes are small)

$$\rho_{f,\,L}V_L v_{f,\,L} \;=\; \frac{1}{2}\rho_{f,\,L}V_L\bar{v}^L_{f,\,in} + \frac{1}{2}\rho_{f,\,L}V_L\bar{v}^L_{f,\,out} \quad . \tag{3.1-202}$$

Thus,

$$v_{f,\,L} \;=\; \frac{1}{2}(\bar{v}^L_{f,\,in} + \bar{v}^L_{f,\,out}) \quad . \tag{3.1-203}$$

Substitution of Equations (3.1-200) and (3.1-201) into Equation (3.1-203) yields

$$v_{f,L}^n = \frac{1}{2} \frac{\left(\sum_{j=1}^{Jin} \dot{\alpha}_{f,j}^n \dot{\rho}_{f,j}^n v_{f,j}^n A_j\right)\left(\sum_{j=1}^{Jin} A_j\right)}{A_L \sum_{j=1}^{Jin} \dot{\alpha}_{f,j}^n \dot{\rho}_{f,j}^n A_j} + \frac{1}{2} \frac{\left(\sum_{j=1}^{Jout} \dot{\alpha}_{f,j}^n \dot{\rho}_{f,j}^n v_{f,j}^n A_j\right)\left(\sum_{j=1}^{Jout} A_j\right)}{A_L \sum_{j=1}^{Jout} \dot{\alpha}_{f,j}^n \dot{\rho}_{f,j}^n A_j} \tag{3.1-204}$$

where old time levels (n) are used for time varying quantities. This arithmetic average of the averaged inlet and averaged outlet velocities was used in RELAP5/MOD1.[3.1-19]

The use of the 1/2 factor in front of the inlet and outlet average velocities sometimes resulted in unphysical results in the convective term of the momentum equations (momentum flux), which uses the volume average velocities. One example occurred in a vertical pipe that is vertically stratified. Sometimes the liquid velocity was calculated to be unphysical. Using the liquid and the inlets as an example, the 1/2 factor used in RELAP5/MOD1 was replaced in subsequent versions of ATHENA by

$$\frac{\sum_{j=1}^{Jin} (\dot{\alpha}_f \dot{\rho}_f)_j^n A_j}{\sum_{j=1}^{Jin+Jout} (\dot{\alpha}_f \dot{\rho}_f)_j^n A_j} . \tag{3.1-205}$$

This is also done for the liquid outlets, as well as the vapor/gas inlets and outlets. This approach resolves the above problem, and it gives a liquid velocity that is similar to the liquid velocity in the junction below.

Using the modification discussed above, the ATHENA volume-average velocity formulas then have the form

$$
\begin{aligned}
(v_f)_L^n &= \frac{\left(\sum_{j=1}^{Jin} (\dot{\alpha}_f \dot{\rho}_f v_f)_j^n A_j\right)\left(\sum_{j=1}^{Jin} A_j\right)}{A_L \sum_{j=1}^{Jin+Jout} (\dot{\alpha}_f \dot{\rho}_f)_j^n A_j} + \frac{\left(\sum_{j=1}^{Jout} (\dot{\alpha}_f \dot{\rho}_f v_f)_j^n A_j\right)\left(\sum_{j=1}^{Jout} A_j\right)}{A_L \sum_{j=1}^{Jin+Jout} (\dot{\alpha}_f \dot{\rho}_f)_j^n A_j} \\
&= \sum_{j=1}^{Jin} c_{f,j}^n v_{f,j}^n + \sum_{j=1}^{Jout} c_{f,j}^n v_{f,j}^n
\end{aligned} \tag{3.1-206}
$$

and

$$(v_g)_L^n = \frac{\left(\sum_{j=1}^{Jin}(\dot{\alpha}_g\dot{\rho}_g v_g)_j^n A_j\right)\left(\sum_{j=1}^{Jin}A_j\right)}{A_L\sum_{j=1}^{Jin+Jout}(\dot{\alpha}_g\dot{\rho}_g)_j^n A_j} + \frac{\left(\sum_{j=1}^{Jout}(\dot{\alpha}_g\dot{\rho}_g v_g)_j^n A_j\right)\left(\sum_{j=1}^{Jout}A_j\right)}{A_L\sum_{j=1}^{Jin+Jout}(\dot{\alpha}_g\dot{\rho}_g)_j^n A_j} \qquad (3.1\text{-}207)$$

$$= \sum_{j=1}^{Jin}c_{g,j}^n v_{g,j}^n + \sum_{j=1}^{Jout}c_{g,j}^n v_{g,j}^n$$

where $c_{f,j}^n$ and $c_{g,j}^n$ contain only old time quantities (no velocities).

Equations (3.1-206) and (3.1-207) are used for the momentum flux calculation, evaluation of the interfacial heat transfer, and the Courant time step limit. For the evaluation of the wall frictional forces and the wall heat transfer, different formulas are used.

For the evaluation of the wall frictional forces, the magnitude of the volume velocities is needed. An obvious way to compute this magnitude is to take just the absolute value of the result from Equations (3.1-206) and (3.1-207). A problem can occur when the magnitude is zero because the inlet velocity is equal and opposite to the outlet velocity. To avoid this case, the calculation of the magnitude of the volume velocities used in the wall friction uses the same form as Equations (3.1-206) and (3.1-207), with the magnitude of the junction velocities used in the formulas. Thus, the equations used in the wall friction evaluation are

$$|v_f|_L^n = \frac{\left(\sum_{j=1}^{Jin}(\alpha_f\rho_f|v_f|)_j^n A_j\right)\left(\sum_{j=1}^{Jin}A_j\right)}{A_L\sum_{j=1}^{Jin+Jout}(\alpha_f\rho_f)_j^n A_j} + \frac{\left(\sum_{j=1}^{Jout}(\alpha_f\rho_f|v_f|)_j^n A_j\right)\left(\sum_{j=1}^{Jout}A_j\right)}{A_L\sum_{j=1}^{Jin+Jout}(\alpha_f\rho_f)_j^n A_j} \qquad (3.1\text{-}208)$$

$$|v_g|_L^n = \frac{\left(\sum_{j=1}^{Jin}(\dot{\alpha}_g\dot{\rho}_g|v_g|)_j^n A_j\right)\left(\sum_{j=1}^{Jin}A_j\right)}{A_L\sum_{j=1}^{Jin+Jout}(\dot{\alpha}_g\dot{\rho}_g)_j^n A_j} + \frac{\left(\sum_{j=1}^{Jout}(\dot{\alpha}_g\dot{\rho}_g|v_g|)_j^n A_j\right)\left(\sum_{j=1}^{Jout}A_j\right)}{A_L\sum_{j=1}^{Jin+Jout}(\dot{\alpha}_g\dot{\rho}_g)_j^n A_j} \quad . \qquad (3.1\text{-}209)$$

For the evaluation of the wall heat transfer rate, a simpler version of Equations (3.1-206) and (3.1-207) is used for the volume average velocities. This arose during the implementation of the Groeneveld CHF (see Volume IV) correlation into ATHENA, where it was observed that the total volume

mass flux G_L, which is based on the volume velocities, was not well behaved for the purpose of wall heat transfer. The mass flux G_L is given by

$$G_L = (\alpha_g \rho_g v_g)_L + (\alpha_f \rho_f v_f)_L \ .$$ (3.1-210)

It was found that the volume mass flux using Equations (3.1-206) and (3.1-207) for v_{gL} and v_{fL} was as much as 30% below the volumes' inlet mass flux and outlet mass flux in ATHENA simulations of Bennett's CHF experiments (steady-state boiling of water in a heated tube). This Bennett experiment is discussed in Volume III of this manual. As a result of the problem exhibited in Bennett's problem, a simpler version of the volume velocities is used instead for wall heat transfer.

Here, the average inlet phase velocity with respect to the total inlet junction cross-sectional area is

$$\bar{v}_{f,in} = \frac{\displaystyle\sum_{j=1}^{Jin} \dot{\alpha}_{f,j} \dot{\rho}_{f,j} v_{f,j} A_j}{\alpha_{f,L} \rho_{f,L} \displaystyle\sum_{j=1}^{Jin} A_j} \ .$$ (3.1-211)

Substitution into Equation (3.1-199) yields the volume inlet liquid velocity, which is given by

$$\bar{v}_{f,in}^L = \frac{\displaystyle\sum_{j=1}^{Jin} \dot{\alpha}_{f,j} \dot{\rho}_{f,j} v_{f,j} A_j}{\alpha_{f,L} \rho_{f,L} A_L} \ .$$ (3.1-212)

Similarly, the volume outlet liquid velocity is given by

$$\bar{v}_{f,out}^L = \frac{\displaystyle\sum_{j=1}^{Jout} \dot{\alpha}_{f,j} \dot{\rho}_{f,j} v_{f,j} A_j}{\alpha_{f,L} \rho_{f,L} A_L} \ .$$ (3.1-213)

Thus, using Equation (3.1-203), the volume liquid velocity used in the wall heat transfer rate calculation is

$$v_{f,L}^n = \frac{\dfrac{1}{2}\displaystyle\sum_{j=1}^{Jin} (\dot{\alpha}_f \dot{\rho}_f v_f)_j^n A_j + \dfrac{1}{2}\displaystyle\sum_{j=1}^{Jout} (\dot{\alpha}_f \dot{\rho}_f v_f)_j^n A_j}{\alpha_{f,L}^n \rho_{f,L}^n A_L} \ .$$ (3.1-214)

Similarly, the volume vapor/gas velocity used in the wall heat transfer rate calculation is

$$v_{g,L}^n = \frac{\frac{1}{2}\sum_{j=1}^{Jin}(\dot{\alpha}_g\dot{\rho}_g v_g)_j^n A_j + \frac{1}{2}\sum_{j=1}^{Jout}(\dot{\alpha}_g\dot{\rho}_g v_g)_j^n A_j}{\alpha_{g,L}^n\rho_{g,L}^n A_L} \quad . \tag{3.1-215}$$

These forms of the volume average velocity produce the same mass flux at steady-state for the volume as well as for its inlet and outlet junctions, which is the desired result.

At branch volumes with multiple inlets and/or outlets, the viscous-like term (artificial viscosity) discussed in Section 3.1.3 has a more general form. This is most easily shown by recasting the finite difference momentum equations into a donor form for the momentum flux terms. The difference equations for the sum and difference momentum equations are

$$
\begin{aligned}
&(\alpha_g\rho_g)_j^n(v_g^{n+1} - v_g^n)_j\Delta x_j + (\alpha_f\rho_f)_j^n(v_f^{n+1} - v_f^n)_j\Delta x_j \\
&\quad + \frac{1}{2}(\dot{\alpha}_g\dot{\rho}_g)_j^n[(v_g)_L^n(\dot{v}_g)_L^n - (v_g)_K^n(\dot{v}_g)_K^n]\Delta t \\
&\quad + \frac{1}{2}(\dot{\alpha}_f\dot{\rho}_f)_j^n[(v_f)_L^n(\dot{v}_f)_L^n - (v_f)_K^n(\dot{v}_f)_K^n]\Delta t \\
&= -(P_L - P_K)^{n+1}\Delta t + [(\rho_m)_j^n B_x - (\alpha_g\rho_g)_j^n FWG_j^n(v_g)_j^{n+1} \\
&\quad - (\alpha_f\rho_f)_j^n FWF_j^n(v_f)_j^{n+1} - (\Gamma_g)_j^n(v_g - v_f)_j^{n+1}]\Delta x_j\Delta t \\
&\quad - [(\dot{\alpha}_g\dot{\rho}_g)_j^n HLOSSG_j^n v_{g,j}^{n+1} + (\dot{\alpha}_f\dot{\rho}_f)_j^n HLOSSF_j^n v_{f,j}^{n+1}]\Delta t
\end{aligned}
\tag{3.1-216}
$$

and

$$\left(1 + \frac{C\rho_m^2}{\rho_g\rho_f}\right)_j^n [(v_g^{n+1} - v_g^n) - (v_f^{n+1} - v_f^n)]_j \Delta x_j$$

$$+ \frac{1}{2}\left(\frac{\dot{\alpha}_g\dot{\rho}_g}{\alpha_g\rho_g}\right)_j^n [(v_g)_L^n(\dot{v}_g)_L^n - (v_g)_K^n(\dot{v}_g)_K^n]\Delta t$$

$$- \frac{1}{2}\left(\frac{\dot{\alpha}_f\dot{\rho}_f}{\alpha_f\rho_f}\right)_j^n [(v_f)_L^n(\dot{v}_f)_L^n - (v_f)_K^n(\dot{v}_f)_K^n]\Delta t = -\left(\frac{\rho_f - \rho_g}{\rho_f\rho_g}\right)_j^n (P_L - P_K)^{n+1}\Delta t$$

$$- \left\{ FWG_j^n(v_g)_j^{n+1} - FWF_j^n(v_f)_j^{n+1} - \left[\frac{\Gamma_g^n(\rho_m^n v_I^{n+1} - \alpha_f^n\rho_f^n v_g^{n+1} - \alpha_g^n\rho_g^n v_f^{n+1})}{(\alpha_g\rho_g\alpha_f\rho_f)^n}\right]_j \right\} \qquad (3.1\text{-}217)$$

$$+ (\rho_m FI)_j^n(v_g^{n+1} - v_f^{n+1})_j \} \Delta x_j \Delta t - \left[\left(\frac{\dot{\alpha}_g\dot{\rho}_g}{\alpha_g\rho_g}\right)_j^n HLOSSG_j^n v_{g,j}^{n+1}\right.$$

$$- \left(\frac{\dot{\alpha}_f\dot{\rho}_f}{\alpha_f\rho_f}\right)_j^n HLOSSF_j^n v_{f,j}^{n+1}\right]\Delta t$$

$$+ \left(\frac{\rho_m}{\rho_g\rho_f}\right)_j^n (\rho_f - \rho_g)_j^n B_y(y_L^n - y_K^n)\Delta t$$

where the donored volume liquid velocity for the L volume is from

$$(\dot{v}_f)_L^n = \frac{1}{2}(\bar{v}_{f,in}^L + \bar{v}_{f,out}^L) + \frac{1}{2}\frac{|(v_f)_L^n|}{(v_f)_L^n}(\bar{v}_{f,in}^L - \bar{v}_{f,out}^L) \quad . \qquad (3.1\text{-}218)$$

Here, $\bar{v}_{f,in}^L$ is from Equation (3.1-200), $\bar{v}_{f,out}^L$ is from Equation (3.1-201), and $(v_f)_L^n$ is from Equation (3.1-206). Similarly, the donored volume vapor/gas velocity for the L volume is from

$$(\dot{v}_g)_L^n = \frac{1}{2}(\bar{v}_{g,in}^L + \bar{v}_{g,out}^L) + \frac{1}{2}\frac{|(v_g)_L^n|}{(v_g)_L^n}(\bar{v}_{g,in}^L - \bar{v}_{g,out}^L) \quad . \qquad (3.1\text{-}219)$$

The donored volume liquid and vapor/gas velocities for the K volume are similar. The momentum flux terms that use the velocities shown here default to the equation shown in Section 3.1.3 for a pipe with no branching.

3.1.7 Multiple Heat Structures

Heat structures represent the solid structures bounding hydrodynamic volumes (i.e., pipe walls) or solid structures internal to hydrodynamic volumes (i.e., fuel pins).

In previous subsections [see Equations (3.1-5) and (3.1-13)], the quantities, Γ_w, Q_{wg}, and Q_{wf}, which are related to heat and mass transfer at and near the wall surface, were introduced. These were discussed as

if only one wall surface could be attached to a volume. Similar to the possibility of multiple junctions being connected to the ends of a volume, multiple wall surfaces representing quite different heat transfer situations can be attached to a volume. Thus the Γ_w, Q_{wg}, and Q_{wf} quantities involve summations over the surfaces attached to a volume. Details of the summations are shown in Volume IV.

The previous subsections combined boiling and condensation in the Γ_w quantity, but showed a difference in the two situations through the factor ε [Equations (3.1-31) and (3.1-32)]. That notation is correct for one heat structure connected to a volume and relies on the wall surface possibly boiling, or condensing, but not both simultaneously. With multiple heat structures, some might be boiling and others could be condensing. Accordingly, boiling mass transfer, Γ_w, and condensing mass transfer, Γ_c, are separated. Thus, the total mass transfer consists of mass transfer in the bulk fluid (Γ_{ig}) and mass transfer in the boundary layers near the walls (Γ_w and Γ_c); that is,

$$\Gamma_g = \Gamma_{ig} + \Gamma_w + \Gamma_c \ . \tag{3.1-220}$$

Both the logic for multiple heat structures and the logic of some heat structures in boiling, and some heat structures in condensing are used for both the semi-implicit scheme and the nearly-implicit scheme.

3.1.8 Implicit Hydrodynamic and Heat Structure Coupling

An option exists to implicitly couple the time advancement of the hydrodynamic and heat structure models. One-dimensional heat conduction (non-reflood) and two-dimensional heat conduction (reflood) are used to compute temperature distributions within heat structures. Hydrodynamic and heat structure conditions are coupled through heat structure boundary conditions. The solution matrix for the set of simultaneous equations resulting from the implicit coupling of hydrodynamic and heat structure advancement contains the same number of nonzero elements as discussed in the previous sections but with some of the elements having additional terms. In addition, the total set of simultaneous equations includes an equation from each mesh point of each heat structure attached to the hydrodynamic volumes. The heat conduction equations have additional terms related to fluid temperatures introduced in the boundary conditions. This larger set of simultaneous equations, however, is solved with only a modest increase in computations compared to the explicit coupling. This implicit coupling can be used with either the semi-implicit or nearly-implicit advancement.

The purpose of the implicit coupling of hydrodynamic and heat structure time advancement is to more accurately model the exchange of energy between the structures and fluid in the volumes, to avoid numerical instabilities due to explicit coupling, and to achieve reduction of computing time through larger time steps.

The purpose of the remainder of this section is to show the additional terms added to the hydrodynamic equations because of the implicit coupling. A complete understanding of the implicit coupling requires information from Section 4 describing numerical techniques for heat structures,

information from Section 3.3.10 describing heat transfer correlations, and information from Volume IV, describing relationships between heat transfer from structures, heat added to volumes, and mass transfer near the wall associated with wall heat transfer. Equations (3.1-223) through (3.1-226) follow directly from the material in Volume IV.

With implicit hydrodynamic and heat structure coupling, some source terms in the mass and energy equations for the semi-implicit and nearly-implicit schemes become implicit. In the continuity equations, $\Gamma_w + \Gamma_c$ becomes $\tilde{\Gamma}_{w,L}^{n+1} + \tilde{\Gamma}_{c,L}^{n+1}$. In the vapor/gas energy equations, terms involving $\Gamma_w + \Gamma_c$ and Q_{wg} become

$$\tilde{\Gamma}_{w,L}^{n+1} h_{g,L}^{s,n} + \tilde{\Gamma}_{c,L}^{n+1} h_{f,L}^{s,n} + \tilde{Q}_{wg,L}^{n+1} \quad . \tag{3.1-221}$$

In the liquid energy equations, terms involving $\Gamma_w + \Gamma_c$ and Q_{wf} become

$$-\tilde{\Gamma}_{w,L}^{n+1} h_{g,L}^{s,n} - \tilde{\Gamma}_{c,L}^{n+1} h_{f,L}^{s,n} + \tilde{Q}_{wf,L}^{n+1} \quad . \tag{3.1-222}$$

The wall heat transfer and mass transfer terms can be written as

$$\begin{aligned}
\tilde{Q}_{wf}^{n+1} &= Q_{wf0}^n + Q_{wff}^n(\tilde{T}_f^{n+1} - T_f^n) + Q_{wfg}^n(\tilde{T}_g^{n+1} - T_g^n) + Q_{wft}^n(\tilde{T}_t^{s,n+1} - T_t^{s,n}) \\
&\quad + Q_{wfp}^n(\tilde{T}^{s,n+1} - T^{s,n})
\end{aligned} \tag{3.1-223}$$

$$\begin{aligned}
\tilde{Q}_{wg}^{n+1} &= Q_{wg0}^n + Q_{wgf}^n(\tilde{T}_f^{n+1} - T_f^n) + Q_{wgg}^n(\tilde{T}_g^{n+1} - T_g^n) + Q_{wgt}^n(\tilde{T}_t^{s,n+1} - T_t^{s,n}) \\
&\quad + Q_{wgp}^n(\tilde{T}^{s,n+1} - T^{s,n})
\end{aligned} \tag{3.1-224}$$

$$\begin{aligned}
\tilde{\Gamma}_w^{n+1} = \tilde{\Gamma}_{wf}^{n+1} &= \Gamma_{wf0}^n + \Gamma_{wff}^n(\tilde{T}_f^{n+1} - T_f^n) + \Gamma_{wfg}^n(\tilde{T}_g^{n+1} - T_g^n) + \Gamma_{wft}^n(\tilde{T}_t^{s,n+1} - T_t^{s,n}) \\
&\quad + \Gamma_{wfp}^n(\tilde{T}^{s,n+1} - T^{s,n})
\end{aligned} \tag{3.1-225}$$

$$\begin{aligned}
\tilde{\Gamma}_c^{n+1} = \tilde{\Gamma}_{wg}^{n+1} &= \Gamma_{wg0}^n + \Gamma_{wgf}^n(\tilde{T}_f^{n+1} - T_f^n) + \Gamma_{wgg}^n(\tilde{T}_g^{n+1} - T_g^n) + \Gamma_{wgt}^n(\tilde{T}_t^{s,n+1} - T_t^{s,n}) \\
&\quad + \Gamma_{wgp}^n(\tilde{T}^{s,n+1} - T^{s,n}) \quad .
\end{aligned} \tag{3.1-226}$$

The variables $\tilde{T}^{s,n+1}$, $\tilde{T}_g^{n+1}$, and $\tilde{T}_f^{n+1}$ are given by Equations (3.1-101) through (3.1-103), where T^s is the saturation temperature. When noncondensables are present, this T^s is based on the partial pressure of vapor $[T^s(P_s)]$. Some of the heat transfer terms, when noncondensables are present, use the saturation

temperature based on the total pressure P $(= P_s + P_n)$. In Equations (3.1-223) through (3.1-226), the saturation temperature based on P_s is denoted by $T^s(P_s)$ and the saturation temperature based on P is denoted by $T_t^s(P)$. Thus, $\tilde{T}_{t,L}^{s,n+1}(P)$ is given by

$$\tilde{T}_{t,L}^{s,n+1}(P) = T_{t,L}^{s,n}(P) + \left(\frac{dT_t^s}{dP}\right)_L^n (P_L^{n+1} - P_L^n) \quad . \tag{3.1-227}$$

It should be pointed out that when the explicit coupling of the hydrodynamics and the heat structures is used, only the first term in Equations (3.1-223) through (3.1-226) is used. These first terms use wall temperature at new time and fluid temperature at old time.

When the implicit coupling of the hydrodynamics and the heat slabs is used, additional terms are added to some of the terms of the $\underset{\sim}{A}$ matrix in Equation (3.1-118). These additional terms are next shown as additions to the $\underset{\sim}{A}$ matrix elements listed in Equations (3.1-121) through (3.1-144).

$$A_{21} = A_{21} - \Delta t(Q_{wgg} + \Gamma_{wfg}h_g^s + \Gamma_{wgg}h_f^s)\frac{\partial T_g}{\partial X_n} - \Delta t(Q_{wgp} + \Gamma_{wfp}h_g^s + \Gamma_{wgp}h_f^s)\frac{\partial T^s}{\partial X_n} \tag{3.1-228}$$

$$A_{22} = A_{22} - \Delta t(Q_{wgg} + \Gamma_{wfg}h_g^s + \Gamma_{wgg}h_f^s)\frac{\partial T_g}{\partial U_g} - \Delta t(Q_{wgp} + \Gamma_{wfp}h_g^s + \Gamma_{wgp}h_f^s)\frac{\partial T^s}{\partial U_g} \tag{3.1-229}$$

$$A_{23} = A_{23} - \Delta t(Q_{wgf} + \Gamma_{wff}h_g^s + \Gamma_{wgf}h_f^s)\frac{\partial T_f}{\partial U_f} \tag{3.1-230}$$

$$A_{25} = A_{25} - \Delta t(Q_{wgf} + \Gamma_{wff}h_g^s + \Gamma_{wgf}h_f^s)\frac{\partial T_f}{\partial P} - \Delta t(Q_{wgg} + \Gamma_{wfg}h_g^s + \Gamma_{wgg}h_f^s)\frac{\partial T_g}{\partial P}$$
$$- \Delta t(Q_{wgp} + \Gamma_{wfp}h_g^s + \Gamma_{wgp}h_f^s)\frac{\partial T^s}{\partial P} - \Delta t(Q_{wgt} + \Gamma_{wft}h_g^s + \Gamma_{wgt}h_f^s)\frac{dT_t^s}{dP} \tag{3.1-231}$$

$$A_{31} = A_{31} - \Delta t(Q_{wfg} - \Gamma_{wfg}h_g^s - \Gamma_{wgg}h_f^s)\frac{\partial T_g}{\partial X_n} - \Delta t(Q_{wfp} - \Gamma_{wfp}h_g^s - \Gamma_{wgp}h_f^s)\frac{\partial T^s}{\partial X_n} \tag{3.1-232}$$

$$A_{32} = A_{32} - \Delta t(Q_{wfg} - \Gamma_{wfg}h_g^s - \Gamma_{wgg}h_f^s)\frac{\partial T_g}{\partial U_g} - \Delta t(Q_{wfp} - \Gamma_{wfp}h_g^s - \Gamma_{wgp}h_f^s)\frac{\partial T^s}{\partial U_g} \tag{3.1-233}$$

$$A_{33} = A_{33} - \Delta t (Q_{wff} - \Gamma_{wff} h_g^s - \Gamma_{wgf} h_f^s) \frac{\partial T_f}{\partial U_f} \qquad (3.1\text{-}234)$$

$$A_{35} = A_{35} - \Delta t (Q_{wff} - \Gamma_{wff} h_g^s - \Gamma_{wgf} h_f^s) \frac{\partial T_f}{\partial P} - \Delta t (Q_{wfg} - \Gamma_{wfg} h_g^s - \Gamma_{wgg} h_f^s) \frac{\partial T_g}{\partial P}$$
$$- \Delta t (Q_{wfp} - \Gamma_{wfp} h_g^s - \Gamma_{wgp} h_f^s) \frac{\partial T^s}{\partial P} - \Delta t (Q_{wft} - \Gamma_{wft} h_g^s - \Gamma_{wgt} h_f^s) \frac{dT_t^s}{dP} \qquad (3.1\text{-}235)$$

$$A_{41} = A_{41} - 2\Delta t (\Gamma_{wfg} + \Gamma_{wgg}) \frac{\partial T_g}{\partial X_n} - 2\Delta t (\Gamma_{wfp} + \Gamma_{wgp}) \frac{\partial T^s}{\partial X_n} \qquad (3.1\text{-}236)$$

$$A_{42} = A_{42} - 2\Delta t (\Gamma_{wfg} + \Gamma_{wgg}) \frac{\partial T_g}{\partial U_g} - 2\Delta t (\Gamma_{wfp} + \Gamma_{wgp}) \frac{\partial T^s}{\partial U_g} \qquad (3.1\text{-}237)$$

$$A_{43} = A_{43} - 2\Delta t (\Gamma_{wff} + \Gamma_{wgf}) \frac{\partial T_f}{\partial U_f} \qquad (3.1\text{-}238)$$

$$A_{45} = A_{45} - 2\Delta t (\Gamma_{wff} + \Gamma_{wgf}) \frac{\partial T_f}{\partial P} - 2\Delta t (\Gamma_{wfg} + \Gamma_{wgg}) \frac{\partial T_g}{\partial P}$$
$$- 2\Delta t (\Gamma_{wfp} + \Gamma_{wgp}) \frac{\partial T^s}{\partial P} - 2\Delta t (\Gamma_{wft} + \Gamma_{wgt}) \frac{dT_t^s}{dP} \ . \qquad (3.1\text{-}239)$$

3.1.9 Numerical Solution of Boron Transport Equation

The boron field and its attendant modeling assumptions were discussed in Section 3.1.1.3. The default numerical scheme for boron solute tracking is the upwind difference scheme; a second-order accurate Godunov scheme can also be used and is activated by the user in the input deck. These two schemes will next be discussed.

3.1.9.1 Upward Difference Scheme. Applying the upwind difference scheme to the boron differential Equation (3.1-51) for the semi-implicit scheme, gives

$$V_L (\rho_{b,L}^{n+1} - \rho_{b,L}^n) + (\dot{\rho}_{b,j+1}^n v_{f,j+1}^{n+1} A_{j+1} - \dot{\rho}_{b,j}^n v_{f,j}^{n+1} A_j) \Delta t = 0 \ . \qquad (3.1\text{-}240)$$

Figure 3.1-5 shows the meaning of the subscripts. Here, the boron densities in the convective terms are evaluated at old time.

.
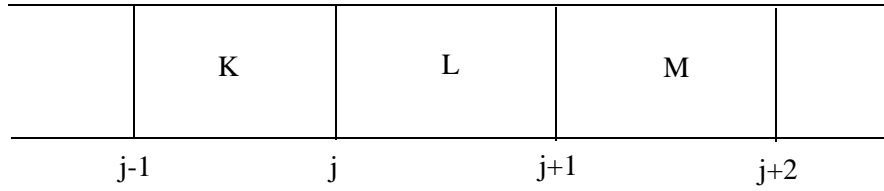
Figure 3.1-5 Nodalization for boron numerics.

Applying the upwind scheme to the boron differential Equation (3.1-51) for the nearly-implicit scheme gives

$$V_L(\rho_{b,L}^{n+1} - \rho_{b,L}^n) + (\dot{\rho}_{b,j+1}^{n+1} v_{f,j+1}^{n+1} A_{j+1} - \dot{\rho}_{b,j}^{n+1} v_{f,j}^{n+1} A_j)\Delta t = 0 \quad . \tag{3.1-241}$$

Here, the boron densities in the convective terms are evaluated at new time. The coefficient matrix generated by the liquid continuity Equation (3.1-181) is used.

3.1.9.2 Godunov Scheme. Accurate calculation of the boron field is required to simulate the coupled hydrodynamics and neutron behavior of a reactor. Recent advances in shock-capturing schemes or the TVD schemes (the oscillation-suppression strategy of the total-variation diminishing scheme) achieve impressive results for the numerical solution of the advective transport equations.[3.1-20],[3.1-21],[3.1-22],[3.1-23] These schemes use locally varying positive artificial diffusion or viscosity (first order upwind) to suppress oscillations combined with local negative viscosity (such as first order downwinding) to compress or steepen the front. Rider and Woodruff[3.1-24] reported that an algorithm using a second-order accurate Godunov method with a highly compressive limiter can adequately solve the advective transport equation for solute tracking. This method is chosen to solve the boron transport Equation (3.1-51) because it is consistent with ATHENA numerics and is applicable to complex geometry.

A second-order accurate Godunov method to solve the boron transport equation was implemented in ATHENA. The new method significantly improves the results as compared with that using the highly diffusive first-order upwind difference previously used.

The equation governing boron transport, Equation (3.1-51), can be rewritten in a control volume (V) with surface area $\underset{\sim}{A}$ as

$$\int_V \frac{\partial \rho_b}{\partial t} dV + \int_A \rho_b \underset{\sim}{v}_f \bullet d\underset{\sim}{A} = 0 \quad . \tag{3.1-242}$$

The use of the second-order accurate Godunov method to solve Equation (3.1-242) is well documented by Rider and Woodruff[3.1-23]. The essential numerics are summarized below.

The numerical solution of Equation (3.1-242) can be written as

$$\rho_{b,L}^{n+1} = \rho_{b,L}^{n} + \frac{\Delta t}{V_L} A_j F_j^n - \frac{\Delta t}{V_L} A_{j+1} F_{j+1}^n \tag{3.1-243}$$

where **Figure 3.1-5** shows the meaning of the subscripts.

The flux F_{j+1}^n in junction j+1 is written as

$$F_{j+1}^n = \frac{1}{2}\left[v_{f,j+1}^{n+\frac{1}{2}} (\rho_{b,j+1}^{n,L} + \rho_{b,j+1}^{n,M}) + \left| v_{f,j+1}^{n+\frac{1}{2}} \right| (\rho_{b,j+1}^{n,L} - \rho_{b,j+1}^{n,M}) \right], \tag{3.1-244}$$

where volumes L and M are the volumes to the left and right of junction j+1. The time-centered velocity in junction j+1 is given by

$$v_{f,j+1}^{n+\frac{1}{2}} = v = \frac{1}{2}(v_{f,j+1}^{n+1} + v_{f,j+1}^{n}) \, . \tag{3.1-245}$$

The boron density in junction j+1 (extrapolated from the left and from the right) is expressed as

$$\rho_{b,j+1}^{n,L} = \rho_{b,L}^{n} + \left(\frac{1}{2}\Delta x_L\right)\left(1 - \frac{v\Delta t}{\Delta x_L}\right)\bar{S}_L \tag{3.1-246}$$

and

$$\rho_{b,j+1}^{n,M} = \rho_{b,M}^{n} - \left(\frac{1}{2}\Delta x_M\right)\left(1 + \frac{v\Delta t}{\Delta x_M}\right)\bar{S}_M \tag{3.1-247}$$

where $\bar{S}_L$ and $\bar{S}_M$ are volume-centered limited gradients in volumes L and M.

A similar equation can be written for F_j^n (using volumes K and L instead of volumes L and M).

The volume-centered limited gradient in volume L, $\bar{S}_L$, is given as

$$\overline{S}_L = (1 + \theta_L \omega_L) \Phi(r, 1) S_{j+1} = (1 + \theta_L \omega_L) \Phi(r, 1) \left(\frac{\rho_{b,M}^n - \rho_{b,L}^n}{\Delta x_{j+1}} \right) \ . \tag{3.1-248}$$

Similar equations can be written for $\overline{S}_K$ and $\overline{S}_M$.

Note that both the superbee limiter of Roe[3.1-25] $\Phi(r, 1)$ and an artificial compression factor[3.1-26] $(1 + \theta_L \omega_L)$ are used in the computation of the volume-centered limited gradient. The superbee limiter is needed to ensure that the boron density is always positive and the artificial compression factor is used because the number of grid points in modeling the reactor system tend to be relatively small. These factors also ensure that the method is a TVD scheme.[3.1-22] The superbee limiter is defined as

$$\Phi(r, 1) = \max[0, \min(2r, 1), \min(r, 2)] \tag{3.1-249}$$

where

$$r = \frac{S_j}{S_{j+1}} \tag{3.1-250}$$

$$S_j = \frac{\rho_{b,L}^n - \rho_{b,K}^n}{\Delta x_j} \tag{3.1-251}$$

and

$$S_{j+1} = \frac{\rho_{b,M}^n - \rho_{b,L}^n}{\Delta x_{j+1}} \ . \tag{3.1-252}$$

In the artificial compression factor $(1 + \theta_L \omega_L)$, the discontinuity detector θ_L is given as

$$\theta_L = \frac{|1 - r|}{1 + |r|} \ . \tag{3.1-253}$$

The parameter ω_L is chosen to be a function of the local Courant number $\nu_L = \frac{\nu_L \Delta t}{\Delta x_L}$, and is given by

$$\omega_L = \min(\nu_L, 1 - \nu_L) \ . \tag{3.1-254}$$

Note that both the superbee limiter of Roe and the artificial compression factor are written as functions of the ratio of the gradients of the boron density across the junctions at the left and right sides of volume L.

In modeling a reactor system, there are components containing volumes to which multiple junctions are connected to form a multi-dimensional flow network. The cell-centered limited gradient $\overline{S}_L$ is set to zero in these volumes and the Godunov scheme reverts to the upwind difference scheme for these volumes.

The above numerical solution is used when the semi-implicit scheme is chosen to solve the field equations. If the nearly-implicit scheme is employed to solve the field equations, the time-step used in the scheme may be greater than the material Courant limit. A subcycling calculation of the boron transport is implemented for the nearly-implicit scheme. In the method, the boron transport is integrated within each large time step taken by the advancement of the field equations. The time step used in the boron calculation is limited by the Courant condition. The liquid velocity used in the boron calculation is interpolated from the results of the field equations. The boron transport is calculated in such a fashion such that solutions of the field equations and boron transport are synchronized in the same large time step.

3.1.10 Numerical Solution of Radionuclide Transport Equations

The radionuclide transport model and its attendant modeling assumptions were discussed in Section 3.1.1.4. The numerical scheme for radionuclide transport is the upwind difference scheme discussed in Section 3.1.9.1 for the boron transport equation.

3.1.10.1 Semi-Implicit Solution Algorithm. Applying the upwind difference scheme to the radionuclide transport differential equation for the semi-implicit numerical solution scheme gives

$$V_L(C_{i,L}^{n+1} - C_{i,L}^n) + (\dot{C}_{i,j+1}^n v_{k,j+1}^{n+1} A_{j+1} - \dot{C}_{i,j}^n v_{k,j}^{n+1} A_j)\Delta t = \Delta t V_L S_{i,L}^n \qquad (3.1\text{-}255)$$

where C_i is the number density of radionuclide specie i, subscript k is either f or g depending upon which phase transports radionuclide specie i, and **Figure 3.1-5** shows the meaning of the other subscripts.

The source term in Equation (3.1-255) represents several different processes that may produce or destroy a radionuclide specie. The production processes include addition of the specie from an external source (modelled in ATHENA using general tables or control variables) and production of the radionuclide specie by neutron capture in a parent radionuclide specie. The processes that destroy a radionuclide specie are radioactive decay of the specie and neutron absorption in the specie. The source term is given by the sum of these processes

$$S_{i,L}^n = X_{i,L}^n + P_{i,L}^n - D_{i,L}^n - A_{i,L}^n \ . \qquad (3.1\text{-}256)$$

The external source is given by

$$X_{i,L}^n = \frac{F_{i,L} N_a}{M w_i V_L}$$
(3.1-257)

where $F_{i,L}$ is the flow rate of an external source of radionuclide i into volume L in kg/sec obtained from a general table or control variable, N_a is Avogadro's number, and Mw_i is the molecular weight of radionuclide specie in kg/kg-mole.

The production source by neutron capture in a parent nuclide is given by

$$P_{i,L}^n = C_{p,L}^n \sum_{g=1}^{N_g} \sigma_{p,g} \frac{V_L}{V_{L,T}} W_i \Phi_{L,T}^g$$
(3.1-258)

where

$\qquad C_{p,L}^n \qquad = \qquad$ number density of parent radionuclide p of radionuclide i in volume L,

$\qquad \sigma_{p,g} \qquad = \qquad$ neutron production cross section in parent radionuclide p of radionuclide specie i for neutron energy group g,

$\qquad N_g \qquad = \qquad$ number of neutron energy group in the nodal kinetics model,

$\qquad V_{L,T} \qquad = \qquad$ total volume of hydraulic volumes in neutron kinetics zone to which volume L belongs,

$\qquad W_i \qquad = \qquad$ user input weight factor, and

$\qquad \Phi_{L,T}^g \qquad = \qquad$ flux-volume integral in neutron energy group g in neutron kinetics zone to which volume L belongs.

The flux-volume intergal and the volume ratio need further explanation. The neutron kinetics model solves for the neutron flux in a set of kinetics nodes that are different from but that overlay the hydraulic volumes and the heat structures in the reactor code. The overlap is defined by zones. A zone is a collection of hydraulic volumes and heat structures and a hydraulic volume or heat structure may belong to one and only one zone. The average fluid properties and structural temperatures are computed as a weighted sum of the properties in the volumes and heat structures in the zone, and these average properties are used to compute the neutron cross sections in the neutron kinetics nodes that overlap the zone. The neutron flux can then be computed in the kinetics nodes. The absorption and production processes need to know the neutron flux-integral in the hydraulic volume, but the code only computes it in the kinetics nodes. The flux-volume integral in the hydraulic volume is computed as the flux-volume integral in the kinetics nodes that comprise the zone (computed as the sum of the product of the fluxes in the kinetics nodes and the volume

of the kinetics nodes) to which the particular volume belongs multiplied by the ratio of the volume in the particular volume to the total volume in all of the volumes belonging to the zone and a user input weight factor. The weight factor is used to account for the fact that the kinetics nodes overlap the heat structures as well as the hydraulic volumes (see Section 7.2.5 of this volume of the manual for a more complete discussion of kinetics nodes and zones).

The decay source (actually a sink) is given by,

$$D_{i,L}^n = \lambda_i C_{i,L}^n \tag{3.1-259}$$

where λ_i is the decay constant for radionuclide specie i given by

$$\lambda_i = \frac{\ln 2}{T_i} \tag{3.1-260}$$

and T_i is the half-life of radionuclide specie i in seconds.

The neutron absorption source $A_{i,L}^n$ (actually a sink) is given by an equation similar to Equation (3.1-258) except that the neutron cross section is a summation over the production cross sections for all radionuclides for which radionuclide i is the parent. It is given by

$$A_{i,L}^n = C_{i,L}^n \sum_{g=1}^{N_g} \frac{V_L}{V_{L,T}} W_i \Phi_{L,T}^g \sum_{k=1}^{N_k} \sigma_{k,g} \tag{3.1-261}$$

where the summation over k denotes the fact that radionuclide specie i may be the parent specie for multiple daughter radionuclide species and N_k is the number of radionuclide species for which radionuclide specie i is the parent.

3.1.10.2 *Nearly-implicit Solution Algorithm.* The nearly-implicit solution of the radionuclide transport equations is similar to the semi-implicit solutions except that the time level of several terms in the equation have been changed. The conservation equation is given by

$$V_L(C_{i,L}^{n+1} - C_{i,L}^n) + (\dot{C}_{i,j+1}^{n+1} v_{k,j+1}^{n+1} A_{j+1} - \dot{C}_{i,j}^{n+1} v_{k,j}^{n+1} A_j)\Delta t = \Delta t V_L(S_{i,L}^{1,n} - S_{i,L}^{2,n+1}) \tag{3.1-262}$$

where the source term has been divided into two parts, a part that is evaluated at the beginning of the time step (i.e, explicitly) and a part that the evaluated implicitly (i.e., at the end of the time step). The explicit parts of the source are the external source, the production source, and the absorption source. The explicit source is given by given by

$$S_{i,L}^{1,n} = X_{i,L}^{n} + P_{i,L}^{n} - A_{i,L}^{n}$$

where the three terms are given by Equations (3.1-257), (3.1-258), and (3.1-261) respectively. The implicit part of the source is the decay source and is given by

$$S_{i,L}^{2,n+1} = D_{i,L}^{n+1} \tag{3.1-263}$$

where the implicit decay source is given by

$$D_{i,L}^{n+1} = \lambda_i C_{i,L}^{n+1} . \tag{3.1-264}$$

The resulting equation contains contributions for the neighboring volumes in the flux terms just like the solution equations for the second step of the nearly-implicit solution algorithm for the hydraulic volumes. These equations are assembled into a closed system of equations and are solved in the same way that the hydraulic equations are solved in the second step of the nearly-implicit solution algorithm.

3.1.11 References

3.1-1.   V. H. Ransom, *Course A-Numerical Modeling of Two-Phase Flows for Presentation at Ecole d'Ete d'Analyse Numerique,* EGG-EAST-8546, Idaho National Engineering Laboratory, May 1989.

3.1-2.   M. Ishii, *Thermo-Fluid Dynamic Theory of Two-Phase Flow,* Collection de la Direction des Etudes d'Recherches of Electricute de France, 1975.

3.1-3.   F. H. Harlow and A. A. Amsden, "Flow of Interpenetrating Material Phases," *Journal of Computational Physics, 18,* 1975, pp. 440-464.

3.1-4.   P. S. Anderson, P. Astrup, L. Eget, and O. Rathman, "Numerical Experience with the Two-Fluid Model RISQUE," *Proceedings from Topical Meeting on Thermal Reactor Safety, Sun Valley, ID, July 31-August 4, 1977.*

3.1-5.   N. Zuber, "On the Dispersed Two-Phase Flow in the Laminar Flow Regime," *Chemical Engineering Science, 19,* 1964, pp. 897-917.

3.1-6.   L. Van Wijngaarden, "Hydrodynamic Interaction between Gas and Bubbles in Liquid," *Journal of Fluid Mechanics, 77,* 1, 1976, pp. 27-44.

3.1-7.   R. T. Lahey, Jr., "RPI Two-Phase Flow Modeling Program," *Fifth Water Reactor Safety Research Information Meeting, Washington, D.C., November 7-11, 1977.*

3.1-8.   D. A. Drew, L. Y. Cheng, and R. T. Lahey, Jr., "The Analysis of Virtual Mass Effects in Two-Phase Flow," *International Journal of Multiphase Flow, 5,* 1979, pp. 233-242.

3.1-9.   J. A. Trapp and V. H. Ransom, "A Choked-Flow Calculation Criterion for Nonhomogeneous, Nonequilibrium Two-Phase Flows," *International Journal of Multiphase Flow, 8,* 6, 1982, pp. 669-681.

3.1-10.   G. L. Mesina, "Border-Profile LU Solver for RELAP5-3D*," 1998 RELAP5 International Users Seminar, College Station, Texas, May 17-21, 1998.*

3.1-11.   A. R. Curtis and J. K. Reid, *FORTRAN Subroutines for the Solution of Sparse Sets of Linear Equations,* AERE-R6844, Atomic Energy Research Establishment Harwell, June 1971.

3.1-12.   D. Gidaspow (Chairman), "Modeling of Two-Phase Flow," *Proceedings of Round Table Discussion RT-1-2 at the Fifth International Heat Transfer Conference, Tokyo, Japan, September 3-7, 1974, also in ASME Journal of Heat Transfer, 3,* 1974.

3.1-13.   J. D. Ramshaw and J. A. Trapp, "Characteristics, Stability, and Short-Wavelength Phenomena in Two-Phase Flow Equation Systems," *Nuclear Science and Engineering, 66,* 1978, pp. 93-102.

3.1-14.   J. J. Dongarra, C. B. Moler, J. R. Bunch, and G. W. Stewart, *LINPACK User's Guide,* Philadelphia: SIAM, 1979.

3.1-15.   H. B. Stewart, "Fractional Step Methods for Thermohydraulic Calculations," *Journal of Computational Physics, 40,* 1981, pp. 77-90.

3.1-16.   J. H. Mahaffy, "A Stability-Enhancing Two-Step Method for Fluid Flow Calculations," *Journal of Computational Physics, 46,* 1982, pp. 329-341.

3.1-17.   J. A. Trapp and R. A. Riemke, "A Nearly-Implicit Hydrodynamic Numerical Scheme for Two-Phase Flows," *Journal of Computational Physics, 66,* 1986, pp. 62-68.

3.1-18.   A. S. Shieh and R. A. Riemke, "Diagonally Dominant Enhancement Methods for Matrix Solvers in RELAP5," *Nuclear Science and Engineering, 105,* 1990, pp. 404-408.

3.1-19.   V. H. Ransom et al., *RELAP5/MOD1 Code Manual,* NUREG/CR-1826, EGG-2070, Idaho National Engineering Laboratory, March 1982.

3.1-20.   H. C. Yee, *Upwind and Symmetric Shock-Capturing Schemes,* NASA Technical Memorandum 1000916, Ames Research Center, 1987.

3.1-21.   B. P. Leonard, *Universal Limiter for Transient Interpolation Modeling of the Advective Transport Equation: The ULTIMATE Conservative Difference Scheme,* NASA Technical Memorandum 1000916, Ames Research Center, 1988.

3.1-22.   W. J. Rider, *Design of High Resolution Upwind Shock-Capturing Methods,* LA-12327-T, Los Alamos National Laboratory, 1992.

3.1-23.   R. J. LeVeque, *Numerical Methods for Conservation Laws*, Lectures in Mathematics, ETH Zurich, Basel: Birkhauser Verlag, 1992.

3.1-24.   W. J. Rider and S. B. Woodruff, *High-Order Solute Tracking in Two-Phase Thermal Hydraulics,* LA-UR-91-2263, Los Alamos National Laboratory, 1991.

3.1-25.   P. L. Roe, "Some Contributions to the Modeling of Discontinuous Flow," *Lectures in Applied Mathematics, 22,* Part 2, 1975, pp. 163-193.

3.1-26.   H. C. Yee and R. F. Warming, "Implicit Total Variation Diminishing (TVD) Schemes for Steady-State Calculations," *Journal of Computational Physics, 57,* 1985, pp. 327-360.

3.2 State Relationships

The six-equation model uses five independent state (thermodynamic fluid) variables with an additional equation for the noncondensable gas component. The independent state variables are chosen to be P, α_g, U_g, U_f, and X_n. All the remaining thermodynamic fluid variables (temperatures, densities, partial pressures, qualities, etc.) are expressed as functions of these five independent state variables. In addition to these variables, several state derivatives are needed for some of the linearizations used in the numerical scheme. This section contains three parts. The first discusses the state property derivatives needed in the numerical scheme. The second section develops the appropriate derivative formulas for the single component case. The third section does the same for the two-phase, two-component case.

3.2.1 State Equations

To expand the time derivatives of the phasic densities in terms of these independent state variables using two-term Taylor series expansions, the following derivatives of the phasic densities are needed:

$$\left(\frac{\partial \rho_g}{\partial P}\right)_{U_g, X_n}, \quad \left(\frac{\partial \rho_g}{\partial U_g}\right)_{P, X_n}, \quad \left(\frac{\partial \rho_g}{\partial X_n}\right)_{P, U_g}, \quad \left(\frac{\partial \rho_f}{\partial P}\right)_{U_f}, \quad \left(\frac{\partial \rho_f}{\partial U_f}\right)_{P} \quad .$$

The interphase mass and heat transfer models use an implicit (linearized) evaluation of the temperature potentials T_I - T_f and T_I - T_g. The quantity T_I is the temperature that exists at the phase interface. For a single-component mixture, we have

$$T_I = T^s(P) \tag{3.2-1}$$

where the superscript s denotes a saturation value. In the presence of a noncondensable mixed with the vapor, we assume[3.2-1]

$$T_I = T^s(P_s) \tag{3.2-2}$$

where P_s is the partial pressure of the vapor in the vapor/gas phase. The vapor/gas phase properties for a two-component mixture can be described with three independent properties.[3.2-2] In particular, the vapor partial pressure, P_s, can be expressed as

$$P_s = P_s (P, X_n, U_g) \quad . \tag{3.2-3}$$

Substituting Equation (3.2-3) into Equation (3.2-2) gives the interface temperature, T_I, as the desired function of P, X_n, and U_g.[a] The implicit (linearized) evaluation of the temperature potentials in the numerical scheme requires the following derivatives of the phasic and interface temperatures:

$$\left(\frac{\partial T_g}{\partial P}\right)_{U_g, X_n}, \left(\frac{\partial T_g}{\partial U_g}\right)_{P, X_n}, \left(\frac{\partial T_g}{\partial X_n}\right)_{P, U_g}, \left(\frac{\partial T_f}{\partial P}\right)_{U_f}, \left(\frac{\partial T_f}{\partial U_f}\right)_{P}, \left(\frac{\partial T^s}{\partial P}\right)_{U_g, X_n}, \left(\frac{\partial T^s}{\partial U_g}\right)_{P, X_n}, \left(\frac{\partial T^s}{\partial X_n}\right)_{P, U_g} \quad .$$

If we have a single component, the X_n derivatives are zero and

$$\left(\frac{\partial T^s}{\partial U_g}\right)_P = 0 \tag{3.2-4}$$

since T^s is only a function of P for this case.

In addition to these derivatives, the basic phasic properties as functions of P, U_g, U_f, and X_n are needed, along with the homogeneous equilibrium sound speed for the critical flow model.

The basic properties for light water are calculated from default thermodynamic tables[3.2-3,3.2-4,3.2-5] that tabulate saturation properties as a function of temperature, saturation properties as a function of pressure, and single-phase properties as a function of pressure and temperature. These tables are based on the 1967 ASME Steam Tables, which are calculated using the 1967 International Formulation Committee (IFC) Formulation for Industrial Use and is known as IFC-67. The properties and derivatives in the tables are saturation pressure, saturation temperature, specific volume (υ), specific internal energy, and three derivatives [the isobaric thermal expansion coefficient (β), the isothermal compressibility (κ), and the specific heat at constant pressure (C_p)]. The accuracy of the default thermodynamic tables can be improved (under the penalty of increased storage requirements) by increasing the number of pressure and temperature points in the input data to the thermodynamic table generation subroutine. This can sometimes improve code performance by reducing mass error.

The basic properties for light water can also be calculated from optional (activated by the user in the input deck) thermodynamic tables[3.2-6] that tabulate saturation properties as a function of temperature, saturation properties as a function of pressure, and single-phase properties as a function of pressure and specific internal energy. These tables are based on the 1984 U. S. National Bureau of Standards and the National Research Council of Canada (NBS/NRC) Steam Tables. The properties and derivatives in the tables are saturation pressure, saturation temperature, specific volume (υ), temperature, and three derivatives [the isobaric thermal expansion coefficient (β), the isothermal compressibility (κ), and the specific heat at constant pressure (C_p)]. The accuracy of these optional thermodynamic tables can be improved (under the penalty of increased storage requirements) by increasing the number of pressure and specific internal energy points in the input data to the thermodynamic table generation subroutine. This can sometimes improve code performance by reducing mass error.

a. The properties ρ_g and T_g could have initially been written with P_s, X_n, U_g as the independent arguments. Equation (3.2-3) would then be used to write ρ_g and T_g, with P, X_n, and U_g as the independent variables.

The basic properties for light water can also be calculated from optional (activated by the user in the input deck) thermodynamic tables[3.2-7] that tabulate saturation properties as a function of temperature, saturation properties as a function of pressure, and single-phase properties as a function of pressure and temperature. These tables are based on the 1995 Steam Tables from the International Association for the Properties of Water and Steam (IAPWS); it is known as IAPWS-95. IAPWS also released an industrial formulation in 1997 (known as IAPWS-97), which is not as accurate, but more efficient than the 1995 formulation. Since the steam tables in ATHENA are only built once (during installation), the code uses IAPWS-95 because it is more accurate. The properties and derivatives in the tables are saturation pressure, saturation temperature, specific volume (υ), specific internal energy, and three derivatives [the isobaric thermal expansion coefficient (β), the isothermal compressibility (κ), and the specific heat at constant pressure (C_p)]. The accuracy of these thermodynamic tables can be improved (under the penalty of increased storage requirements) by increasing the number of pressure and temperature points in the input data to the thermodynamic table generation subroutine. This can sometimes improve code performance by reducing mass error.

3.2.2 Single-Component, Two-Phase Mixture

For the purposes of this manual, a single-component, two-phase mixture is referred to as Case 1. Case 1 is straightforward. Liquid properties are obtained from the thermodynamic tables, given P and U_f. All the desired density and temperature derivatives can then be obtained from the derivatives κ_f, β_f, and C_{pf}.[3.2-8] The desired derivatives are given as

$$\left(\frac{\partial \rho_f}{\partial U_f}\right)_P = -\frac{\upsilon_f \beta_f}{(C_{pf} - \upsilon_f \beta_f P)\upsilon_f^2} \tag{3.2-5}$$

$$\left(\frac{\partial T_f}{\partial U_f}\right)_P = \frac{1}{C_{pf} - \upsilon_f \beta_f P} \tag{3.2-6}$$

$$\left(\frac{\partial \rho_f}{\partial P}\right)_{U_f} = \frac{C_{pf}\upsilon_f \kappa_f - T_f(\upsilon_f \beta_f)^2}{(C_{pf} - \upsilon_f \beta_f P)\upsilon_f^2} \tag{3.2-7}$$

$$\left(\frac{\partial T_f}{\partial P}\right)_{U_f} = -\frac{P\upsilon_f \kappa_f - T_f \upsilon_f \beta_f}{C_{pf} - \upsilon_f \beta_f P} \quad . \tag{3.2-8}$$

Parallel formulae hold for the vapor phase, with P and U_g as the independent variables.

For the default case, the only nonstandard feature involved in the evaluation of the formulae in Equations (3.2-5) through (3.2-8) is the calculation of υ, T, κ, β, and C_p if the vapor is subcooled or the

liquid is superheated, i.e., metastable states. A constant pressure extrapolation from the saturation state is used for the temperature and specific volume for metastable states. Using the first two terms of a Taylor series, this gives

$$T \approx T^s(P) + \frac{1}{C_p^s(P) - P\upsilon^s(P)\beta^s(P)}[U - U^s(P)] \tag{3.2-9}$$

$$\upsilon \approx \upsilon^s(P) + \upsilon^s(P)\beta^s(P)[T - T^s(P)] \quad . \tag{3.2-10}$$

In these Equations, (3.2-9) and (3.2-10), the argument P indicates a saturation value.

To obtain the properties β, κ, and C_p corresponding to the extrapolated υ and T, the extrapolation formulas are differentiated. Taking definitions and the appropriate derivatives of Equation (3.2-9) and (3.2-10) gives

$$C_p(P, T) \triangleq \left(\frac{\partial h}{\partial T}\right)_P = \left(\frac{\partial U}{\partial T}\right)_P + P\left(\frac{\partial \upsilon}{\partial T}\right)_P = C_p^s(P) \tag{3.2-11}$$

$$\beta(P, T) \triangleq \frac{1}{\upsilon}\left(\frac{\partial \upsilon}{\partial T}\right)_p = \frac{\upsilon^s(P)\beta^s(P)}{\upsilon(P, T)} \tag{3.2-12}$$

$$\kappa(P, T) \triangleq -\frac{1}{\upsilon}\left(\frac{\partial \upsilon}{\partial P}\right)_T = \{\upsilon^s(P) + [T - T^s(P)]\upsilon^s(P)\beta^s(P)\}\frac{\kappa^s(P)}{\upsilon(P, T)}$$
$$- [T - T^s(P)]\frac{\upsilon^s(P)}{\upsilon(P, T)}\left\{\frac{d\beta^s(P)}{dP} + [\beta^s(P)]\frac{dT^s(P)}{dP}\right\} \quad . \tag{3.2-13}$$

Equation (3.2-11) shows that the extrapolated C_p is equal to the saturation value $C_p^s(P)$. Equation (3.2-12) gives the extrapolated β as a function of the saturation properties and the extrapolated υ. Equation (3.2-13) gives the extrapolated κ as a function of the extrapolated properties and saturation properties. The extrapolated κ in Equation (3.2-13) involves a change of saturation properties along the saturation line. In particular, $\frac{d\beta^s(P)}{dP}$ involves a second derivative of specific volume. Since no second-order derivatives are available from the thermodynamic property tables, this term was approximated for the vapor/gas phase by assuming that the fluid behaves as an ideal gas. With this assumption, the last term in Equation (3.2-13) vanishes and the appropriate formula for the vapor phase (subcooled vapor) κ is

$$\kappa_g (P, T_g) = \kappa_g^s(P) \tag{3.2-14}$$

where Equation (3.2-10) has been used to simplify the results.

For the liquid phase extrapolation (superheated liquid), a hand calculation shows that the $\dfrac{d\beta^s(P)}{dP}$ term in Equation (3.2-13) is the largest of the correction terms. Since this term cannot be obtained from the thermodynamic property tables, only the first term in Equation (3.2-13) is retained, i.e.,

$$\kappa_f(P, T_f) = \frac{\upsilon_f^s(P)\kappa_f^s(P)}{\upsilon_f(P, T_f)} \ . \tag{3.2-15}$$

For the 1984 optional case, the 1984 NBS/NRC Steam Tables[3.2-6] contain metastable properties for water and steam; thus, the extrapolation is not needed. For the 1995 optional case (IAPWS-95 Steam Tables[3.2-7]), extrapolation similar to the default case is used for the metastable properties.

The homogeneous sound speed (a) for a two-phase mixture is calculated from a standard homogeneous equilibrium formula (see Volume IV, Section 7, Appendix 7A) using the appropriate saturation values for T, υ, κ, β and C_p. For equilibrium flow, the quality is assumed to change during the flow. Here the liquid vaporizes or the vapor condenses, and the liquid and vapor are always in equilibrium. The sound speed formula given by

$$a^2 = \frac{\upsilon^2\left(\dfrac{dP^s}{dT}\right)^2}{X_e\left[\dfrac{C_{pg}^s}{T^s} + \upsilon_g^s\dfrac{dP^s}{dT}\left(\kappa_g^s\dfrac{dP^s}{dT} - 2\beta_g^s\right)\right] + (1 - X_e)\left[\dfrac{C_{pf}^s}{T^s} + \upsilon_f^s\dfrac{dP^s}{dT}\left(\kappa_f^s\dfrac{dP^s}{dT} - 2\beta_f^s\right)\right]} \tag{3.2-16}$$

is used, where from Clapeyron's equation

$$\frac{dP^s}{dT} = \frac{h_g^s - h_f^s}{T^s(\upsilon_g^s - \upsilon_f^s)} \ , \tag{3.2-17}$$

$$\upsilon = X_e\upsilon_g^s + (1 - X_e)\upsilon_f^s \tag{3.2-18}$$

and X_e is the equilibrium quality used in the sound speed, which is given by

$$X_e = \frac{[XU_g + (1-X)U_f] - U_f^s}{U_g^s - U_f^s} \quad , \tag{3.2-19}$$

where $X = \hat{X}_g = (\alpha_g \rho_g)/(\alpha_g \rho_g + \alpha_f \rho_f)$ is the static quality. It is noted that the derivative $\frac{dT^s}{dP}$ used in the numerical solution scheme is given by the reciprocal of Equation (3.2-17)

The homogeneous sound speed for both single-phase liquid ($X_e = 0$) and single-phase vapor ($X_e = 1$) is calculated from a standard homogeneous frozen formula (see Volume IV, Section 7, Appendix 7A). For frozen flow, the quality is assumed to not change during the flow. Here the liquid is assumed not to vaporize, the vapor is assumed not to condense, and the liquid and vapor are not in equilibrium. It is given by

$$a = \upsilon \left\{ \frac{\left(\frac{C_P}{T \upsilon \beta}\right)}{\upsilon \left[\kappa \left(\frac{C_P}{T \upsilon \beta}\right) - \beta \right]} \right\}^{1/2} \tag{3.2-20}$$

and the thermodynamic properties and derivatives are either liquid or vapor quantities, depending on the phase present.

For this Case 1, the transport properties phasic viscosities μ_g, μ_f, phasic thermal conductivities k_g, k_f, and surface tension σ are evaluated as functions of the local thermodynamic properties. For the default case, correlations from the 1967 ASME Steam Tables[3.2-3] and Schmidt[3.2-9] are used for these transport properties for steam and liquid water. For the 1984 optional case, correlations from the 1984 NBS/NRC Steam Tables[3.2-6] are used for these transport properties for steam and liquid water. For the 1995 optional case, tables based on correlations from the IAPWS-95 Steam Tables[3.2-7] are used for these transport properties for steam and liquid water.

3.2.3 Two-Component, Two-Phase Mixture

This case is referred to as Case 2. The liquid phasic properties and derivatives are calculated in exactly the same manner as described in Case 1 (see Section 3.2.2); we assume that the noncondensable component is present only in the vapor/gas phase.

The properties for the vapor/gas phase are calculated assuming a modified Gibbs-Dalton mixture of vapor (real gas from thermodynamic table data) and an ideal noncondensable gas. The modified Gibbs-Dalton mixture is based upon the following assumptions:

$$P_n = \sum_{i=1}^{N} P_{ni} \qquad\qquad (3.2\text{-}21)$$

$$P = P_n + P_s \qquad\qquad (3.2\text{-}22)$$

$$U_g = X_n U_n + (1 - X_n) U_s \qquad\qquad (3.2\text{-}23)$$

$$\upsilon_g = X_n \upsilon_n = (1 - X_n) \upsilon_s \qquad\qquad (3.2\text{-}24)$$

where P_s and P_{ni} are the partial pressures of the vapor and the individual noncondensable components, respectively. The specific internal energies, U_s, U_n, and the specific volumes, υ_s, υ_n, are evaluated at the vapor/gas temperature and the respective partial pressures. The vapor/gas properties are obtained from the thermodynamic tables, and the noncondensable state equations are

$$P_n \upsilon_n = R_n T_g \qquad\qquad (3.2\text{-}25)$$

and

$$U_n = \begin{cases} U_o + C_o T_g & T_g < T_0 \\ U_o + C_o T_g + \dfrac{1}{2}D_o(T_g - T_o)^2 + \dfrac{1}{3}E_o(T_g - T_o)^3 + \dfrac{1}{4}F_o(T_g - T_o)^4 & T_g \geq T_0 \end{cases} \qquad (3.2\text{-}26)$$

where

$$R_n \quad = \quad \sum_{i=1}^{N} R_{ni} X_{ni} \qquad\qquad (3.2\text{-}27)$$

$$C_o \quad = \quad \sum_{i=1}^{N} C_{o,ni} X_{ni} \qquad\qquad (3.2\text{-}28)$$

$$D_o \quad = \quad \sum_{i=1}^{N} D_{o,ni} X_{ni} \qquad\qquad (3.2\text{-}29)$$

$$E_o \quad = \quad \sum_{i=1}^{N} E_{o,ni} X_{ni} \qquad\qquad (3.2\text{-}30)$$

$$F_o \quad = \quad \sum_{i=1}^{N} F_{o,ni} X_{ni} \qquad\qquad (3.2\text{-}31)$$

$$U_o \quad = \quad \sum_{i=1}^{N} U_{o,ni} X_{ni} \qquad\qquad (3.2\text{-}32)$$

$$T_o \quad = \quad 250 \text{ K}. \qquad\qquad (3.2\text{-}33)$$

An alternate but equivalent method of defining the specific internal energy of a mixture of noncondensable gases [See Equation (3.2-26)] is as follows. The specific internal energy of each individual noncondensable gas is expressed as

$$U_{n,i} = \begin{cases} U_{o,ni} + C_{o,ni} T_g & T_g < T_0 \\ U_{o,ni} + C_{o,ni} T_g + \dfrac{1}{2} D_{o,ni}(T_g - T_o)^2 + \dfrac{1}{3} E_{o,ni}(T_g - T_o)^3 + \dfrac{1}{4} F_{o,ni}(T_g - T_o)^4 & T_g \geq T_0 \end{cases} \qquad (3.2\text{-}34)$$

and the specific internal energy of a mixture of noncondensable gases is defined as

$$U_n = \sum_{i=1}^{N} U_{n,i} X_{ni} \qquad\qquad (3.2\text{-}35)$$

Table 3.2-1 lists the values used by the code for R_{ni}, $C_{o,ni}$, $D_{o,ni}$, $E_{o,ni}$, $F_{o,ni}$, and $U_{o,ni}$ in SI units. The values for R_{ni} are given as the universal gas constant 8,314.3 J/kg-mole•K divided by the molecular weight (kg/kg-mole). The temperature T_o is the upper limit at which the ideal specific heat is no longer applicable, and the higher order effects have to be taken into account. For the first eight noncondensable gases, $C_{o,ni}$ is the ideal specific heat at constant volume, i.e., $C_{o,ni} = 1.5 R_{ni}$ for a monatomic gas, and $C_{o,ni} = 2.5 R_{ni}$ for a diatomic gas, the values of $D_{o,ni}$ and $U_{o,ni}$ are obtained by least-squares fitting to the data reported by Reynolds[3.2-10] for 250 K to 700 K, and the values of $E_{o,ni}$ and $F_{o,ni}$ are zero. For the last three noncondensable gases, the values of the constants $C_{o,ni}$, $D_{o,ni}$, $E_{o,ni}$, and $F_{o,ni}$ were determined by the method of least squares using values from Rivken[3.2-11] for temperatures between 250 K and 289 K and from Avallone[3.2-12] for temperatures between 289 K and 3,000 K. The fitted values of $C_{o,ni}/R_{ni}$ are 2.46 for oxygen and 2.34 for carbon monoxide, which are close to the 2.5 value derived from kinetic theory for

rigid diatomic molecules (Zucrow and Hoffman[3.2-13]). The fitted value of $C_{o,ni}/R_{ni}$ for carbon dioxide is 3.49, which is reasonably close to the theoretical value of 3.0 for rigid polyatomic molecules.

Table 3.2-1 Values of R_{ni}, $C_{o,ni}$, $D_{o,ni}$, $E_{o,ni}$, $F_{o,ni}$, and $U_{o,ni}$ for various noncondensable gases.

Gas	R_{ni} (J/kg•K)	$C_{o,ni}$ (J/kg•K)	$D_{o,ni}$ (J/kg•K^2)	$E_{o,ni}$ (J/kg•K^3)	$F_{o,ni}$ (J/kg•K^4)	$U_{o,ni}$ (J/kg)
Helium	8,314.3/4.002598	3,115.839	0.003455924	0.0	0.0	13,256.44
Hydrogen	8,314.3/2.01593	10,310.75	0.522573	0.0	0.0	182,783.4
Nitrogen	8,314.3/28.01403	741.9764	0.1184518	0.0	0.0	145,725.884
Krypton	8,314.3/83.800	148.824	0.0035	0.0	0.0	122,666.5
Xenon	8,314.3/131.300	94.9084	0.0035	0.0	0.0	122,666.5
Air	8,314.3/28.963	715.0	0.10329037	0.0	0.0	158,990.52
Argon	8,314.3/39.948	312.192	0.003517	0.0	0.0	122,666.5
SF$_6$	8,314.3/146.05	793.399	0.000001	0.0	0.0	0.0
Oxygen	8,314.3/32.000	639.8541	0.3537302	-1.613807×10^{-4}	2.923424×10^{-8}	1,641.42
Carbon Dioxide	8,314.3/44.010	658.7377	0.7563373	-3.726885×10^{-4}	6.513268×10^{-8}	-41,467.2
Carbon Monoxide	8,314.3/28.010	693.2758	0.3421647	-1.216078×10^{-4}	1.503636×10^{-8}	14,231.1

Given P, U_g, and X_n, we must solve Equations (3.2-21) through (3.2-24) implicitly to find the state of the vapor/gas phase. If Equation (3.2-22) is used to eliminate P_n, and Equation (3.2-25) is used for υ_n, Equations (3.2-23) and (3.2-24) can be written as

$$f_1 = (1 - X_n)U_s + X_n U_n[T_g(U_s, P_s)] - U_g = 0 \qquad (3.2\text{-}36)$$

and

$$f_2 = (1 - X_n)\left[\frac{\upsilon_s(U_s, P_s)P_s}{T_g(U_s, P_s)}\right](P - P_s) - X_n R_n P_s = 0, \qquad (3.2\text{-}37)$$

where Equation (3.2-24) was divided by the temperature and multiplied by the partial pressures to obtain Equation (3.2-37). If P, U_g, and X_n are known, Equations (3.2-36) and (3.2-37) implicitly determine U_s and P_s.

To obtain the derivatives needed in the numerical scheme, we must evaluate the derivatives of U_s and P_s with respect to P, U_g, and X_n. These derivatives can be obtained from Equations (3.2-36) and (3.2-37) by the use of the chain rule and implicit differentiation, along with using $\left(\dfrac{\partial f_1}{\partial P}\right)_{U_g, X_n} = 0$, $\left(\dfrac{\partial f_1}{\partial U_g}\right)_{P, X_n} = 0$, $\left(\dfrac{\partial f_1}{\partial X_n}\right)_{P, U_g} = 0$, $\left(\dfrac{\partial f_2}{\partial P}\right)_{U_g, X_n} = 0$, $\left(\dfrac{\partial f_2}{\partial U_g}\right)_{P, X_n} = 0$, and $\left(\dfrac{\partial f_2}{\partial X_n}\right)_{P, U_g} = 0$. For example, taking the derivative of Equations (3.2-36) and (3.2-37) with respect to P using $\left(\dfrac{\partial f_1}{\partial P}\right)_{U_g, X_n} = 0$ and $\left(\dfrac{\partial f_2}{\partial P}\right)_{U_g, X_n} = 0$, and recalling that $P_s = P_s(P, U_g, X_n)$ and $U_s = U_s(P, U_g, X_n)$, we obtain

$$
\begin{bmatrix}
X_n\left(\dfrac{dU_n}{dT_g}\right)\left(\dfrac{\partial T_g}{\partial P_s}\right)_{U_s} & 1 - X_n + X_n\left(\dfrac{dU_n}{dT_g}\right)\left(\dfrac{\partial T_g}{\partial U_s}\right)_{P_s} \\
\\
\begin{array}{c} -X_n R_n - (1 - X_n)R_s \\ + \text{TERM1} \end{array} & \text{TERM2}
\end{bmatrix}
\bullet
\begin{bmatrix}
\left(\dfrac{\partial P_s}{\partial P}\right)_{U_g, X_n} \\
\\
\left(\dfrac{\partial U_s}{\partial P}\right)_{U_g, X_n}
\end{bmatrix}
=
\begin{bmatrix}
0 \\
\\
-(1 - X_n)R_s
\end{bmatrix}
\tag{3.2-38}
$$

as a linear system of two equations determining

$$\left(\frac{\partial P_s}{\partial P}\right)_{U_g, X_n} \text{ and } \left(\frac{\partial U_s}{\partial P}\right)_{U_g, X_n} .$$

In Equation (3.2-38),

$$R_s = \frac{P_s \upsilon_s}{T_g} \tag{3.2-39}$$

is the equivalent gas constant for the vapor,

$$\text{TERM1} = (1 - X_n)P_n R_s\left[\frac{1}{P_s} + \frac{1}{\upsilon_s}\left(\frac{\partial \upsilon_s}{\partial P_s}\right)_{U_s} - \frac{1}{T_g}\left(\frac{\partial T_g}{\partial P_s}\right)_{U_s}\right] \tag{3.2-40}$$

and

$$\text{TERM2} = (1 - X_n)P_n R_s\left[\frac{1}{\upsilon_s}\left(\frac{\partial \upsilon_s}{\partial U_s}\right)_{P_s} - \frac{1}{T_g}\left(\frac{\partial T_g}{\partial U_s}\right)_{P_s}\right] . \tag{3.2-41}$$

To obtain the derivatives of P_s and U_s with respect to U_g and X_n, we repeat the above development taking derivatives of Equations (3.2-36) and (3.2-37) with respect to U_g and X_n. In each case, linear equations parallel to those in Equation (3.2-38) are obtained. In fact, the left side matrix is exactly the same, and the right side vector changes.

Having obtained all the derivatives of P_s and U_s, it is relatively easy to obtain the temperature derivatives needed for the vapor/gas phase. From the chain rule, we have

$$\left(\frac{\partial T_g}{\partial P}\right)_{U_g, X_n} = \left(\frac{\partial T_g}{\partial P_s}\right)_{U_s}\left(\frac{\partial P_s}{\partial P}\right)_{U_g, X_n} + \left(\frac{\partial T_g}{\partial U_s}\right)_{P_s}\left(\frac{\partial U_s}{\partial P}\right)_{U_g, X_n} \tag{3.2-42}$$

$$\left(\frac{\partial T_g}{\partial U_g}\right)_{P, X_n} = \left(\frac{\partial T_g}{\partial P_s}\right)_{U_s}\left(\frac{\partial P_s}{\partial U_g}\right)_{P, X_n} + \left(\frac{\partial T_g}{\partial U_s}\right)_{P_s}\left(\frac{\partial U_s}{\partial U_g}\right)_{P, X_n} \tag{3.2-43}$$

$$\left(\frac{\partial T_g}{\partial X_n}\right)_{P, U_g} = \left(\frac{\partial T_g}{\partial P_s}\right)_{U_s}\left(\frac{\partial P_s}{\partial X_n}\right)_{P, U_g} + \left(\frac{\partial T_g}{\partial U_s}\right)_{P_s}\left(\frac{\partial U_s}{\partial X_n}\right)_{P, U_g} \tag{3.2-44}$$

where

$$\left(\frac{\partial T_g}{\partial P_s}\right)_{U_s} \text{ and } \left(\frac{\partial T_g}{\partial U_s}\right)_{P_s}$$

are the standard phasic derivatives for the vapor phase (see Case1, Section 3.2.2, vapor phase). Equations (3.2-42) through (3.2-44) give all the desired vapor/gas temperature derivatives. The interface temperature derivatives are obtained from Clapeyron's equation and the known P_s derivatives, i.e.,

$$\left(\frac{\partial T_I}{\partial P}\right)_{U_g, X_n} = \frac{dT_I}{dP_s}\left(\frac{\partial P_s}{\partial P}\right)_{U_g, X_n} \tag{3.2-45}$$

$$\left(\frac{\partial T_I}{\partial U_g}\right)_{P, X_n} = \frac{dT_I}{dP_s}\left(\frac{\partial P_s}{\partial U_g}\right)_{P, X_n} \tag{3.2-46}$$

$$\left(\frac{\partial T_I}{\partial X_n}\right)_{P, U_g} = \frac{dT_I}{dP_s}\left(\frac{\partial P_s}{\partial X_n}\right)_{P, U_g} \tag{3.2-47}$$

where $\dfrac{dT_I}{dP_s}$ is given by the reciprocal of Equation (3.2-17). The phasic enthalpies and phasic specific volumes in Equation (3.2-17) are evaluated at P_s.

The derivatives of the densities can be obtained from $\upsilon_g = X_n \upsilon_n$ or $\upsilon_g = (1 - X_n) \upsilon_s$, as these two formulae for the vapor/gas specific volume are equivalent [see Equation (3.2-24)]. A symmetric formula can be obtained by eliminating X_n from the above two formulae, giving

$$\upsilon_g = \frac{\upsilon_s \upsilon_n}{\upsilon_s + \upsilon_n} \quad . \tag{3.2-48}$$

Using Equation (3.2-48), we have for the derivatives of ρ_g with respect to P

$$\left(\frac{\partial \rho_g}{\partial P}\right)_{U_g, X_n} = -\frac{1}{\upsilon_n^2}\left(\frac{\partial \upsilon_n}{\partial P}\right)_{U_g, X_n} - \frac{1}{\upsilon_s^2}\left(\frac{\partial \upsilon_s}{\partial P}\right)_{U_g, X_n} \quad . \tag{3.2-49}$$

Similar formulas are obtained when either U_g or X_n is the independent variable. The partial derivatives on the right side of Equation (3.2-49) are obtained from formulae exactly parallel to those in Equations (3.2-42) through (3.2-44) with T_g replaced by υ_s or υ_n. When taking the derivatives of υ_n, we use

$$\upsilon_n = \frac{R_n T_g(P_s, \upsilon_s)}{P - P_s} \quad . \tag{3.2-50}$$

Hence, an additional term appears in the parallel formula for Equation (3.2-42) due to the direct dependence of υ_n on P.

The liquid properties and derivatives are obtained as above for Case 1. To obtain the vapor/gas properties, Equations (3.2-36) and (3.2-37) must be solved iteratively. A global Newton iteration in two variables is used.[3.2-14] The iteration variables are P_s and U_s. The thermodynamic table subroutine is called once during each iteration to obtain all the needed vapor properties, and Equations (3.2-25) and (3.2-26) are used to obtain the noncondensable properties. Once the iteration has converged, the vapor/gas properties and derivatives are determined from the formulas in this section.

The homogeneous equilibrium sound speed (a) for a noncondensable-vapor-liquid mixture is[3.2-2] taken from

$$a^2 = \frac{\upsilon^2}{-\left(\frac{\partial \upsilon}{\partial P}\right)_{S, \hat{X}_n}} \tag{3.2-51}$$

where

$$\left(\frac{\partial \upsilon}{\partial P}\right)_{S,\hat{X}_n} = (1 - \hat{X}_f)\left\{X_n^2\upsilon_n\left[\left(\beta_n\frac{1}{P'_s} + \kappa_n\right)\left(\frac{\partial P_s}{\partial P}\right)_{S,\hat{X}_n} - \kappa_n\right] + X_s^2\upsilon_s\left(\beta_s\frac{1}{P'_s} - \kappa_s\right)\left(\frac{\partial P_s}{\partial P}\right)_{S,\hat{X}_n}\right\}$$

$$+ \hat{X}_f\upsilon_f\left[\beta_f\frac{1}{P'_s}\left(\frac{\partial P_s}{\partial P}\right)_{S,\hat{X}_n} - \kappa_f\right] + (\upsilon_g - \upsilon_f)\left(\frac{\partial \hat{X}_s}{\partial P}\right)_{S,\hat{X}_n} \tag{3.2-52}$$

$$P'_s = \frac{dP^s}{dT} = \frac{h_s^s - h_f^s}{T^s(\upsilon_s^s - \upsilon_f^s)} = \frac{S_s^s - S_f^s}{\upsilon_s^s - \upsilon_f^s} \quad . \tag{3.2-53}$$

Equation (3.2-52) can be shown to be equivalent to Equation (18) in **Reference 3.2-2**, where the relation

$$\left(\frac{\partial T}{\partial P}\right)_{S,X_n} = \frac{1}{P'_s}\left(\frac{\partial P_s}{\partial P}\right)_{S,X_n} \tag{3.2-54}$$

is used. Equation (3.2-53) is the inverse of Equation (22) (Clausius-Clapeyron relation) in **Reference 3.2-2**. The quantities $\left(\frac{\partial P_s}{\partial P}\right)_{S,\hat{X}_n}$ and $\left(\frac{\partial \hat{X}_s}{\partial P}\right)_{S,\hat{X}_n}$ in Equation (3.2-52) are obtained from the following matrix equation:

$$\begin{bmatrix} \hat{X}_n\upsilon_n\beta_n - \hat{X}_s\upsilon_s\beta_s & S_s - S_f \\ + \frac{1}{P'_s}\left[(\hat{X}_nC_{pn} + \hat{X}_sC_{ps})\frac{1}{T_g} + \hat{X}_fC_{pf}\frac{1}{T_f}\right] & \\ \hat{X}_n\upsilon_n\left(\kappa_n + \beta_n\frac{1}{P'_s}\right) + \hat{X}_s\upsilon_s\left(\kappa_s - \beta_s\frac{1}{P'_s}\right) & -\upsilon_s \end{bmatrix} \bullet \begin{bmatrix} \left(\frac{\partial P_s}{\partial P}\right)_{S,\hat{X}_n} \\ \\ \left(\frac{\partial \hat{X}_s}{\partial P}\right)_{S,\hat{X}_n} \end{bmatrix} = \begin{bmatrix} \hat{X}_n\upsilon_n\beta_n + \hat{X}_f\upsilon_f\beta_f \\ \\ \hat{X}_n\upsilon_n\kappa_n \end{bmatrix} . \tag{3.2-55}$$

Equation (3.2-55) is from the first and third equations in Equation (19) in **Reference 3.2-2**, where Equation (3.2-54) is used as well as

$$\hat{X}_n\upsilon_n = \hat{X}_s\upsilon_s = \hat{X}_g\upsilon_g \quad . \tag{3.2-56}$$

In the above formulae, $\hat{X}_s$, $\hat{X}_n$, $\hat{X}_g$, and $\hat{X}_f$ are, respectively, mass qualities for vapor, noncondensable, vapor/gas, and liquid based on the total mixture mass; X_s and X_n are the mass qualities for vapor and noncondensable based on the vapor/gas mixture mass. Thus, their definitions are

$$\hat{X}_s = \frac{M_s}{M_s + M_n + M_f} \tag{3.2-57}$$

$$\hat{X}_n = \frac{M_n}{M_s + M_n + M_f} \tag{3.2-58}$$

$$\hat{X}_g = X = \frac{M_s + M_n}{M_s + M_n + M_f} = \frac{M_g}{M_g + M_f} \tag{3.2-59}$$

$$\hat{X}_f = \frac{M_f}{M_s + M_n + M_f} = \frac{M_f}{M_g + M_f} \tag{3.2-60}$$

$$X_s = \frac{M_s}{M_s + M_n} \tag{3.2-61}$$

$$X_n = \frac{M_n}{M_s + M_n}, \tag{3.2-62}$$

where

M_s	=	the mass of the vapor in the vapor/gas phase
M_n	=	the mass of the noncondensable in the vapor/gas phase
$M_g(=M_s+M_n)$	=	the mass of the vapor/gas phase
M_f	=	the mass of the liquid phase.

The variable $X\ (=\hat{X}_g)$ is usually referred to as the static quality.

In Equations (3.2-52) and (3.2-55), the variables β_s, κ_s, and C_{ps} are the vapor variables β_g, κ_g, and C_{pg}, discussed in the single component Section 3.2.2. The variables β_n, κ_n, and C_{pn} are determined using the standard formulas for the ideal noncondensable gas Equations (3.2-25) and (3.2-26), that is

$$\beta_n = \frac{1}{T_g} \tag{3.2-63}$$

$$\kappa_n = \frac{1}{P_n} \tag{3.2-64}$$

$$C_{pn} = \begin{cases} C_o + R_n & T_g < T_o \\ C_o + D_o(T_g - T_o) + E_o(T_g - T_o)^2 + F_o(T_g - T_o)^3 + R_n & T_g \geq T_o \end{cases} \tag{3.2-65}$$

The homogeneous sound speed for single-phase vapor/gas is calculated from the same standard homogeneous frozen formula (see Volume IV, Section 7, Appendix 7A) used for Case 1 [vapor phase, Equation (3.2-20)]. The thermodynamic properties and derivatives are vapor/gas quantities. The specific volume (υ_g) is calculated from Equation (3.2-48). The properties β_g, κ_g, and C_{pg} are calculated from the definitions shown in Case 1 [Equations (3.2-11), (3.2-12), and (3.2-13)], where the vapor/gas mixture derivatives in these equations are obtained from the mixture derivatives from this section of manual (Case 2) using the chain rule.

Evaluation of the sound speed formulas at the saturated equilibrium state requires a second iteration. To avoid this extra iteration, the sound speed formulas were evaluated using the nonequilibrium state properties.

For this Case 2, the transport phasic viscosities μ_g, μ_f, phasic thermal conductivities k_g, k_f, and surface tension σ are evaluated as functions of the local thermodynamic properties. For the default case, correlations from the 1967 ASME Steam Tables[3.2-3] and Schmidt[3.2-9] are used for these transport properties for steam and liquid water. For the 1984 optional case, correlations from the 1984 NBS/NRC Steam Tables[3.2-6] are used for these transport properties for steam and liquid water. For the 1995 optional case, tables based on correlations from the IAPWS-95 Steam Tables[3.2-7] are used for these transport properties of steam and liquid water. The presence of noncondensables in the vapor/gas phase is accounted for by using Wilke's semi-empirical formula[3.2-15] for μ_g, and by using Mason and Saxena's analogous method[3.2-16] (with approved modification by Bird, Stewart, and Lightfoot[3.2-17]) for k_g. Using Wilke's formula and Mason and Saxena's method requires values of the viscosity and thermal conductivity for the various noncondensable gases listed in **Table 3.2-1**. The formula used for the viscosity of an individual noncondensable gas is a simple two-constant Sutherland equation[3.2-18], and is given by

$$\mu_{ni} = \frac{\mu_{oni}T_g^{1.5}}{T_g + T_{refni}} \tag{3.2-66}$$

where a plot of $\dfrac{T_g^{1.5}}{\mu_{ni}}$ versus T_g is a straight line with a slope of $\dfrac{1}{\mu_{oni}}$ and a intercept of $\dfrac{T_{refni}}{\mu_{oni}}$ (T_{refni} is referred to as the Sutherland constant). **Table 3.2-2** lists the values used by the code for μ_{oni} and T_{refni} in SI units. For the last three noncondensable gases, the values of μ_{oni} and T_{refni} were obtained by fitting the data of Lemmon et. al[3.2-19].

Table 3.2-2 Values of μ_{oni}, T_{refni}, A_{ni}, and B_{ni} .

Noncondensable gas	μ_{oni} $(kg/m{\cdot}s{\cdot}K^{0.5})$	T_{refni} (K)	A_{ni} $(W/m{\cdot}K^{1+B_{ni}})$	B_{ni} (-)
Helium	1.473×10^{-6}	80.3	2.639×10^{-3}	0.7085
Hydrogen	6.675×10^{-7}	83.0	1.097×10^{-3}	0.8785
Nitrogen	1.381×10^{-6}	102.7	5.314×10^{-4}	0.6898
Krypton	2.386×10^{-6}	188.0	8.247×10^{-5}	0.8363
Xenon	2.455×10^{-6}	252.01	4.351×10^{-5}	0.8616
Air	1.492×10^{-6}	114.0	1.945×10^{-4}	0.8586
Argon	1.935×10^{-6}	147.0	2.986×10^{-4}	0.7224
SF_6	2.306654×10^{-6}	0.0	2.374568×10^{-2}	0.0
Oxygen	1.826×10^{-6}	169.0	1.766×10^{-4}	0.8824
Carbon Dioxide	1.651×10^{-6}	268.0	3.110×10^{-5}	1.1136
Carbon Monoxide	1.463×10^{-6}	138.0	5.050×10^{-4}	0.6954

The formula used for the thermal conductivity of an individual noncondensable gas is a simple two-constant equation from MATPRO[3.2-20], and is given by

$$k_{ni} = A_{ni} T_g^{B_{ni}} .$$ (3.2-67)

Table 3.2-2 lists the values used by the code for A_{ni} and B_{ni} in SI units. For the last three noncondensables, the values of and were obtained by fitting the data of Lemmon et. al[3.2-19].

3.2.4 References

3.2-1.   J. G. Collier, *Convective Boiling and Condensation,* 2nd Edition, New York: McGraw-Hill, 1981.

3.2-2.   V. H. Ransom and J. A. Trapp, "Sound Speed Models for a Noncondensable Gas-Steam-Water Mixture," *Proceedings Japan-U.S. Seminar on Two-Phase Flow Dynamics, Lake Placid, NY, July 29-August 3, 1984.*

3.2-3.   C. A. Meyer, R. G. McClintock, G. J. Silvestri, and R. C. Spencer, Jr., *1967 ASME Steam Tables--Thermodynamic and Transport Properties of Steam,* New York: The American Society of Mechanical Engineers, 1967.

3.2-4.   K. V. Moore, *ASTEM--A Collection of FORTRAN Subroutines to Evaluate the 1967 ASME Equations of State for Water/Steam and Derivatives of These Equations,* ANCR-1026, Aerojet Nuclear Company, National Reactor Testing Station, October 1971.

3.2-5.   R. J. Wagner, "STH2O, A Subroutine Package to Compute the Thermodynamic Properties of Water," and R. J. Wagner, "STH2X Water Property Subroutines," in: *NRTS Environmental Subroutine Manual,* EG&G Idaho, Idaho National Engineering Laboratory, 1977. Improvements and extensions to these subroutines by D. K. Patel and S. W. James are internally documented.[a,b]

3.2-6.   L. Haar, J. S. Gallagher, and G. S. Kell, *NBS/NRC Steam Tables: Thermodynamic and Transport Properties and Computer Programs for Vapor and Liquid States of Water in SI Units,* New York: Hemisphere, 1984.

3.2-7.   A. H. Harvey, A. P. Peskin, and S. A. Klein, *NIST/ASME Steam Properties*, Version 2.2, Users' Guide, National Institute of Standards and Technology, U. S. Department of Commerce, NIST Standard Reference Database 10, March 2000.

3.2-8.   P. W. Bridgman, *Thermodynamics of Electrical Phenomena in Metals and a Condensed Collection of Thermodynamic Formulas,* New York: Dover Publications, 1961.

3.2-9.   E. Schmidt, *Properties of Water and Steam in SI Units,* New York: Springer-Verlag, 1969.

3.2-10.   W. C. Reynolds, *Thermodynamic Properties in SI,* Palo Alto: Stanford University, 1979.

3.2-11.   S. L. Rivken, *Thermodynamic Properties of Gases*, 4th Edition (Revised), New York: Hemisphere, 1988.

3.2-12.   E. A. Avallone, *Mark's Standard Handbook for Mechanical Engineers*, 9th Edition, New York: McGraw-Hill, 1987.

---

a. EG&G Idaho, Inc., Idaho National Engineering Laboratory, Interoffice Correspondence, "Water Property Interpolation Improvements," DKP-2-77, November 18, 1977.

b. EG&G Idaho, Inc., Idaho National Engineering Laboratory, Interoffice Correspondence, "Documentation for Water Properties Extension," SWJ-2-84, February 29, 1984.

3.2-13.   M. J. Zucrow and J. D. Hoffman, *Gas Dynamics*, Volume I, New York: Wiley, 1976.

3.2-14.   J. Dennis and R. Schnabel, *Quasi-Newton Methods for Unconstrained Nonlinear Problems,* Englewood Cliffs, NJ: Prentice-Hall, 1983.

3.2-15.   C. R. Wilke, "A Viscosity Equation for Gas Mixtures," *Journal of Chemical Physics, 18,* 1950, pp. 517-519.

3.2-16.   E. A. Mason and S. C. Saxena, "Approximate Formula for the Thermal Conductivity of Gas Mixtures," *The Physics of Fluids, 1,* 1958, pp. 361-369.

3.2-17.   R. B. Bird, W. E. Stewart, and E. N. Lightfoot, *Transport Properties,* New York: Wiley, 1960.

3.2-18.   R. C. Reid and T. K. Sherwood, *The Properties of Gases and Liquids*, New York: McGraw-Hill, 1966.

3.2-19.   E. W. Lemmon, M. O. McLinden, and M. L. Huber, *REFPROP Reference Fluid Thermodynamic and Transport Properties*, Version 7.0, Beta Version, National Institute of Standards and Technology, U. S. Department of Commerce, NIST Standard Reference Database 23, June 2002.

3.2-20.   The SCDAP/RELAP5-3D[©] Development Team, *SCDAP/RELAP5-3D[©] Code Manual, MATPRO - A Library of Materials Properties for Light-Water-Reactor Accident Analysis*, Volume IV, INEEL/EXT-02-00589, Idaho National Engineering and Environmental Laboratory, May 2002.

3.3 Constitutive Models

The constitutive relations include models for defining flow regimes and flow-regime-related models for interphase friction, the coefficient of virtual mass, wall friction, wall heat transfer, interphase heat and mass transfer, and direct (sensible) heat transfer. Heat transfer regimes are defined and used for wall heat transfer. For the virtual mass, a formula based on the void fraction is used.

In RELAP5/MOD2, all constitutive relations were evaluated using volume-centered conditions; junction parameters, such as interfacial friction coefficients, were obtained as volume-weighted averages of the volume-centered values in the volumes on either side of a junction. The procedure for obtaining junction parameters as averages of volume parameters was adequate when the volumes on either side of a junction were in the same flow regime and the volume parameters were obtained using the same flow regime map (i.e., both volumes were horizontal volumes or both volumes were vertical volumes). Problems were encountered when connecting horizontal volumes to vertical volumes.

These problems have been eliminated in ATHENA by computing the junction interfacial friction coefficient using junction properties so that the interfacial friction coefficient would be consistent with the state of the fluid being transported through the junction. The approach has been used successfully in the TRAC-B code.[3.3-1,3.3-2,3.3-3] The independent variables in the flow regime maps for the volumes and junctions are somewhat different as a result of the finite-difference scheme and staggered mesh used in the numerical scheme.

The volume and junction flow regime maps will be discussed separately, followed by a discussion of the interphase friction, coefficient of virtual mass, wall friction, wall heat transfer models, interphase heat and mass transfer, and direct (sensible) heat transfer. Volume I presents an overview of the constitutive models, and Volume IV presents more details of the constitutive models.

The volume map is based on volume quantities. It is used for interphase heat and mass transfer, wall friction, and wall heat transfer. The constitutive relations, in general, include flow regime effects for which simplified mapping techniques have been developed to control the use of constitutive relation correlations. The flow regime maps are based on the work of Taitel and Dukler[3.3-4,3.3-5] and Ishii.[3.3-6,3.3-7,3.3-8]

Taitel and Dukler have simplified flow regime classifications and developed semi-empirical relations to describe flow regime transitions. However, some of their transition criteria are quite complex, and further simplification has been carried out in order to efficiently apply these criteria in ATHENA. In addition, post-critical heat flux (CHF) regimes as suggested by Ishii[3.3-6] are included.

Four flow regime maps are used: a horizontal map for flow in pipes; a vertical map for flow in pipes, annuli, and bundles; a high mixing map for flow in pumps; and an ECC mixer map for flow in the horizontal pipe near the ECC injection port.

3.3.1 Vertical Volume Flow Regime Map

The vertical flow regime map (for both up and down flow) is for volumes whose inclination (vertical) angle ϕ is such that $60 \le |\phi| \le 90$ degrees. An interpolation region between vertical and horizontal flow regimes is used for volumes whose absolute value of the inclination (vertical) angle is between 30 and 60 degrees. This map is modeled as nine regimes--four for pre-CHF heat transfer, four for post-CHF heat transfer, and one for vertical stratification. For pre-CHF heat transfer, the regimes modeled are the bubbly, slug, annular-mist, and mist-pre-CHF regimes. Formulations for the first three regimes were utilized by Vince and Lahey[3.3-9] to analyze their data. The mist-pre-CHF regime was added for smoothness. For post-CHF heat transfer, the bubbly, slug, and annular-mist regimes are transformed to the inverted annular, inverted slug, and mist regimes, respectively, as suggested by Ishii.[3.3-6] The mist-post-CHF regime was added for symmetry with the mist-pre-CHF regime. The mist flow regimes consist of pure droplet flow where all of the available liquid is assumed to be entrained and there is no liquid film on the wall. Unheated components are also modeled, utilizing the pre-CHF map. A schematic representing the pre-CHF, post-CHF, and transition regimes of the vertical flow regime map is shown in **Figure 3.3-1**. The schematic is three-dimensional, to illustrate flow regime transitions as functions of void fraction α_g, average mixture velocity v_m, and boiling regime (pre-CHF, transition, and post-dryout) where

$$v_m = \frac{G_m}{\rho_m} \tag{3.3-1}$$

$$G_m = \alpha_g \rho_g |v_g| + \alpha_f \rho_f |v_f| \tag{3.3-2}$$

$$\rho_m = \alpha_g \rho_g + \alpha_f \rho_f \ . \tag{3.3-3}$$

The map consists of bubbly, slug, annular-mist, and dispersed (droplet or mist) flows in the pre-CHF regime; inverted annular, inverted slug, and dispersed (droplet or mist) flows in post-dryout; and vertically stratified for sufficiently low mixture velocity v_m. Transition regions provided in the code are shown. The flow regime identifiers which appear in the printed output are shown in parenthesis for each of the regimes. The criteria for defining the boundaries for transition from one regime to another are given by the following correlations.

For the bubbly-to-slug transition, Taitel and Dukler[3.3-4,3.3-5] suggested that bubbly flow may not exist in tubes of small diameter where the rise velocity of small bubbles exceeds the rise velocity of Taylor bubbles. The small bubble rise velocity is given by the correlation[3.3-5]

$$v_{sb} = 1.53 \left[\frac{g(\rho_f - \rho_g)\sigma}{\rho_f^2} \right]^{1/4} = 1.53 \left[\frac{D^* \sigma}{D \rho_f} \right]^{1/2} \tag{3.3-4}$$
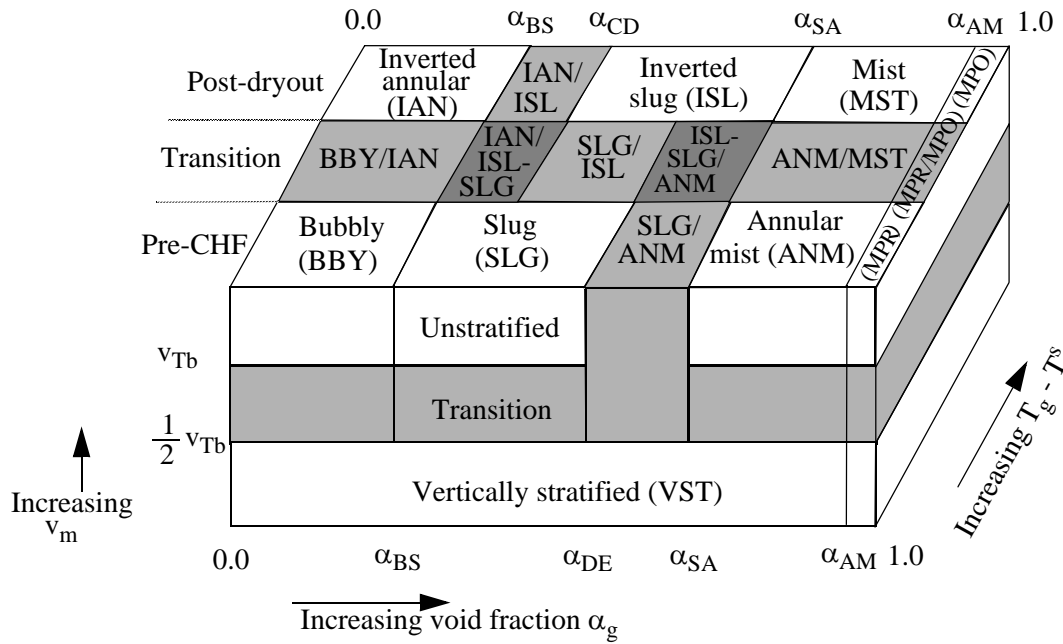
Figure 3.3-1 Schematic of vertical flow regime map with hatchings indicating transitions.

and the Taylor bubble rise velocity is given by the correlation[3.3-10]

$$v_{Tb} = 0.35\left[\frac{gD(\rho_f - \rho_g)}{\rho_f}\right]^{1/2} = 0.35D^*\left[\frac{\sigma}{D\rho_f}\right]^{1/2} \quad , \tag{3.3-5}$$

where D^* is the dimensionless tube diameter (Bond number) and is given by

$$D^* = D\left[\frac{g(\rho_f - \rho_g)}{\sigma}\right]^{1/2} \quad . \tag{3.3-6}$$

(Note: in **Reference 3.3-5**, ρ_f - ρ_g is approximated as ρ_f; see also **Reference 3.3-7** and **Reference 3.3-11**.) Accordingly, the limiting dimensionless tube diameter allowing the presence of bubbly flow is

$$D^* \geq 19.11 \ . \tag{3.3-7}$$

In the coding, 19.11 has been modified to 22.22 where this value was chosen based on comparisons with data during the developmental assessment of RELAP5/MOD2.[3.3-12] This is discussed further in Volume IV of this manual.

Equation (3.3-6) is the dimensionless ratio of tube diameter to film thickness times the Deryagin number, where the Deryagin number is the ratio of film thickness to the Laplace capillary constant length. Also, in the limit, as the fluid properties approach the thermodynamic critical pressure, $D^* = D$.

For tubes with diameters satisfying the condition of Equation (3.3-7), the bubble-slug transition occurs at a void fraction $\alpha_g = 0.25$ for low mass fluxes of $G \leq 2000$ kg/m^2•s. By combining this void criterion with Equation (3.3-7) and using 22.22 instead of 19.11, the bubble-slug transition criterion can be defined such that

$$\alpha_g = 0.25 \, \min\left[1.0, \left(\frac{D^*}{22.22}\right)^8\right] . \tag{3.3-8}$$

Hence, if the local void fraction, α_g, exceeds the criterion of Equation (3.3-8), then bubbly flow cannot exist, since the rise velocity of small bubbles exceeds that of Taylor bubbles. The exponential power of 8 is used to provide a smooth variation of α_L as D^* decreases.

For bundles, the bubbly-slug transition (α_{BS}) is constrained from being less than 0.25. This was necessary to obtain good results in the developmental assessment.

At high mass fluxes of $G_m \geq 3,000$ kg/m^2•s, bubbly flow with finely dispersed bubbles can exist up to a void fraction, α_g, of 0.5. Then, if the criterion is linearly interpolated between the upper and lower void limits, the bubbly-slug transition criterion can be written as

$$\alpha_{BS} = \alpha_L \tag{3.3-9}$$

for mass fluxes of $G_m \leq 2,000$ kg/m^2•s,

$$\alpha_{BS} = \alpha_L + 0.001 \, (0.5 - \alpha_L) \, (G_m - 2000) \tag{3.3-10}$$

for mass fluxes of $2,000 < G_m < 3,000$ kg/m^2•s, and

$$\alpha_{BS} = 0.5 \tag{3.3-11}$$

for mass fluxes of $G_m \geq 3,000$ kg/m^2·s. The flow regime can therefore be said to be in the bubbly regime if $\alpha_g < \alpha_{BS}$ and in the slug regime if $\alpha_g \geq \alpha_{BS}$.

The bubble-slug transition defined by Equations (3.3-9) to (3.3-11) is similar to that given by Taitel and Dukler,[3.3-5] except that their void fraction relation is converted into a form based on liquid and vapor/gas superficial velocities, and finely dispersed bubbles are also distinguished from ordinary bubbles.

For the slug to annular transition, Taitel et al.[3.3-5] and Mishima and Ishii[3.3-13] indicate that the annular flow transition for upflow is principally governed by criteria of the form

$$ j_g^* = \frac{\alpha_g v_g}{\left[gD \frac{(\rho_f - \rho_g)}{\rho_g} \right]^{1/2}} \geq j_{g,\,crit}^* \tag{3.3-12} $$

and

$$ Ku_g = \frac{\alpha_g v_g}{\left[g\sigma \frac{(\rho_f - \rho_g)}{\rho_g^2} \right]^{1/4}} \geq Ku_{g,\,crit} \tag{3.3-13} $$

with the first criterion (flow reversal) controlling the transition in small tubes and the second criterion (droplet entrainment) controlling the transition in large tubes. McQuillan and Whalley[3.3-14,3.3-15] considered the above criteria using

$$ j_{g,\,crit}^* = 1 \tag{3.3-14} $$

and

$$ Ku_{g,crit} = 3.2 \tag{3.3-15} $$

and obtained good predictions of the annular flow boundary in each case. Putney[3.3-16] has found that better agreement can be obtained if annular flow occurs when either criterion is satisfied. In terms of the slug-to-annular transition void fraction α_{SA}, Putney indicates that these criteria take on the form

$$ \alpha_{SA} = min(\alpha_{crit}^f, \alpha_{crit}^e) \tag{3.3-16} $$

where

$$\alpha_{crit}^f \quad = \quad \frac{1}{v_g}\left[\frac{gD(\rho_f-\rho_g)}{\rho_g}\right]^{1/2} \quad \text{for upflow} \tag{3.3-17}$$

$$= \quad 0.75 \text{ for downflow and countercurrent flow} \tag{3.3-18}$$

and

$$\alpha_{crit}^e = \frac{3.2}{v_g}\left[\frac{g\sigma(\rho_f-\rho_g)}{\rho_g^2}\right]^{1/4} \tag{3.3-19}$$

where the void fraction for flow reversal, α_{crit}^f, is found by combining Equations (3.3-12) and (3.3-14) and the void fraction for droplet entrainment, α_{crit}^f, is found by combining Equations (3.3-13) and (3.3-15).

The transition region between the slug flow and annular mist flow regimes is defined by α_{DE} and α_{SA} where

$$\alpha_{DE} = \max(\alpha_{BS}, \alpha_{SA} - 0.05) \tag{3.3-20}$$

The minimum void fraction for annular mist flow, α_{SA}, is constrained to lie between 0.5 and 0.9. For bundles, the minimum void fraction for annular mist flow (α_{SA}) is constrained from being greater than 0.8. This was necessary to obtain good results in the developmental assessment.

For the transition between annular mist and mist pre-CHF (regime MPR in **Figure 3.3-1**), the value of α_{AM} is

$$\alpha_{AM} = 0.9999 \ . \tag{3.3-21}$$

where all of the available liquid is assumed to be in the form of droplets in the mist regimes.

If the hydrodynamic volume has heat flux from a surrounding wall to the vapor/gas or the reflood model is turned on for that wall, and the vapor/gas temperature is more than 1 $^{\circ}$K superheated, then the flow regime is a post-CHF regime. For post-CHF heat transfer, the above formulations are also used to define the regimes. Equations (3.3-9) through (3.3-11) define the inverted annular to inverted slug regime transition, Equation (3.3-16) defines the inverted slug to mist regime transition, and Equation (3.3-21) defines the mist to mist post-CHF (regime MPO in **Figure 3.3-1**) regime transition. The transition region between inverted slug flow and inverted annular flow regimes is defined by α_{BS} and α_{CD} where

$$\alpha_{CD} = \alpha_{BS} + 0.2 \ . \tag{3.3-22}$$

At low mass fluxes, the possibility exists for vertically stratified conditions. In ATHENA, vertical flow in a volume cell is considered to be stratified if the following criteria are met:

- The void fraction for the volume above is > 0.7, and the difference between the void fractions in the volume in question and the void fraction in the volume above or below is > 0.2. This criterion is the same as the level detection logic for a normal profile from TRAC-B.[3.3-1,3.3-2] If more than one junction is connected to the top, the volume above with the smallest void fraction will be treated as the "above volume;" if more than one junction is connected to the bottom, the volume below with the largest void fraction will be treated as the "below volume."

- The magnitude of the volume average mixture mass flux is less than the Taylor bubble rise velocity mass flux. The Taylor bubble criterion is based on the Taylor bubble rise velocity given by Equation (3.3-5) such that

$$G_m < \rho_m v_{Tb} \tag{3.3-23}$$

where v_{Tb} is the Taylor bubble rise velocity. Hence, if Equation (3.3-23) is true, then transition to vertical stratification exists; and if Equation (3.3-23) is false, then transition to vertical stratification does not exist. Fixed numbers are not shown on **Figure 3.3-1** for the mass flux limits for the vertical stratification region because these depend on v_{Tb}. The lower transition limit is $\frac{1}{2}v_{Tb}$. The vertical stratification model does not calculate a mixture level position and is not intended to be a mixture level model. A more mechanistic level tracking model is described in Section 3.4.8.

3.3.2 Horizontal Volume Flow Regime Map

The horizontal flow regime map is for volumes whose inclination (vertical) angle ϕ is such that $0 \leq |\phi| \leq 30$ degrees. An interpolation region between vertical and horizontal flow regimes is used for volumes whose absolute value of the inclination (vertical) angle is between 30 and 60 degrees. This map is similar to the vertical flow regime map except that the post-CHF regimes are not included, and a horizontally stratified regime replaces the vertically stratified regime. The horizontal flow regime map therefore consists of horizontally stratified, bubbly, slug, annular-mist, and mist pre-CHF regimes. A schematic for the horizontal flow regime map is shown in **Figure 3.3-2**. The transition criteria for the bubbly to slug and the slug to annular mist regimes are somewhat similar to those for the vertical map.

The bubbly-slug transition criterion is

$$\alpha_{BS} = 0.25 \qquad G_m \leq 2{,}000 \ \text{kg/m}^2\text{-s} \tag{3.3-24}$$
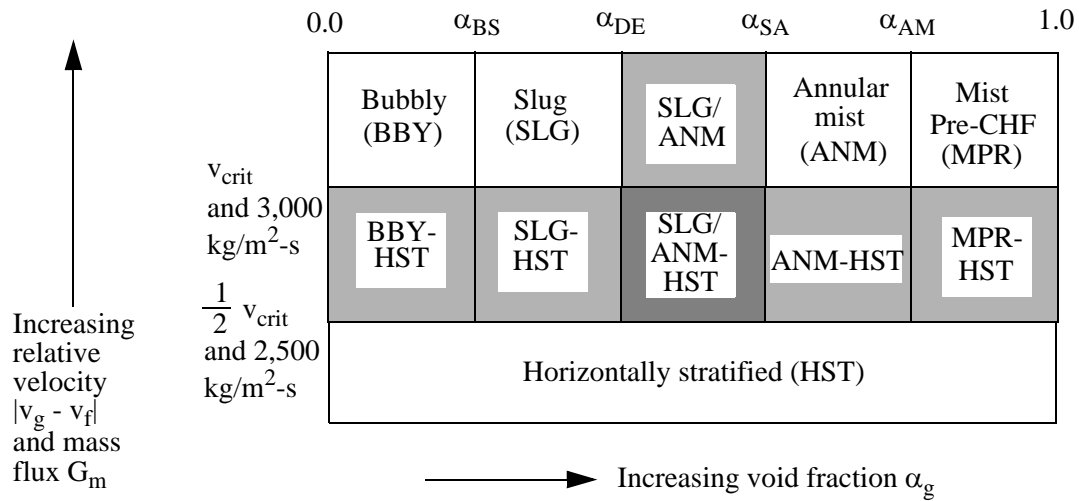
Figure 3.3-2 Schematic of horizontal flow regime map with hatchings indicating transition regions.

$$= 0.25 + 0.00025 \, (G_m - 2,000) \quad 2,000 < G_m < 3,000 \text{ kg/m}^2\text{-s}$$

$$= 0.5 \quad G_m \geq 3,000 \text{ kg/m}^2\text{-s},$$

the minimum void fraction for annular mist flow, α_{SA}, is a constant

$$\alpha_{SA} = 0.8, \tag{3.3-25}$$

and the transition region between slug flow and annular mist flow regimes is defined by α_{DE} and α_{SA} where

$$\alpha_{DE} = 0.75 \ . \tag{3.3-26}$$

The annular mist to mist pre-CHF transition criterion is

$$\alpha_{AM} = 0.9999 \ . \tag{3.3-27}$$

The criterion defining the horizontally stratified regime is based on the one developed by Taitel and Dukler.[3.3-4] According to Taitel and Dukler, the flow field is horizontally stratified if the vapor/gas velocity satisfies the condition

$$|v_g| < v_{crit} \tag{3.3-28}$$

where v_{crit} is the vapor/gas velocity above which waves on the horizontal interface will begin the grow and is given by

$$v_{crit} = \frac{1}{2}\left[\frac{(\rho_f - \rho_g)g\alpha_g A}{\rho_g D \sin\theta}\right]^{\frac{1}{2}}(1 - \cos\theta) \tag{3.3-29}$$

where θ is given by the solution of Equation (3.1-60). The angle θ (see **Figure 3.1-2**) is related to the liquid level with respect to the bottom of the volume.

This condition is modified in the code to handle situations where the flow is stratified but the liquid is not stagnant as was assumed by Taitel and Dukler.[3.3-4] The flow is horizontally stratified if the phasic velocity difference satisfies the condition

$$|v_g - v_f| < v_{crit} \tag{3.3-30}$$

and the mass flux satisfies the condition

$$G_m < 3{,}000 \text{ kg/m}^2\text{-s} . \tag{3.3-31}$$

If the horizontal stratification conditions of Equations (3.3-30) and (3.3-31) are met, then the flow field undergoes a transition to the horizontally stratified flow regime. If the conditions of Equations (3.3-30) and (3.3-31) are not met, then the flow field undergoes a transition to the bubbly, slug, annular mist, or mist pre-CHF flow regime. The lower transition limit for $|v_g - v_f|$ is (1/2) v_{crit} and for G_m is 2,500 kg/m^2-s.

3.3.3 High Mixing Volume Flow Regime Map

The high mixing flow regime map (used in pumps and compressors) is based on vapor/gas void fraction, α_g, and consists of a bubbly regime for $\alpha_g \leq 0.5$, a mist regime for $\alpha_g \geq 0.95$, and a transition regime for $0.5 < \alpha_g < 0.95$. The transition regime is modeled as a mixture of bubbles dispersed in liquid and droplets dispersed in vapor/gas. A schematic for the high mixing flow regime map is shown in **Figure 3.3-3**.
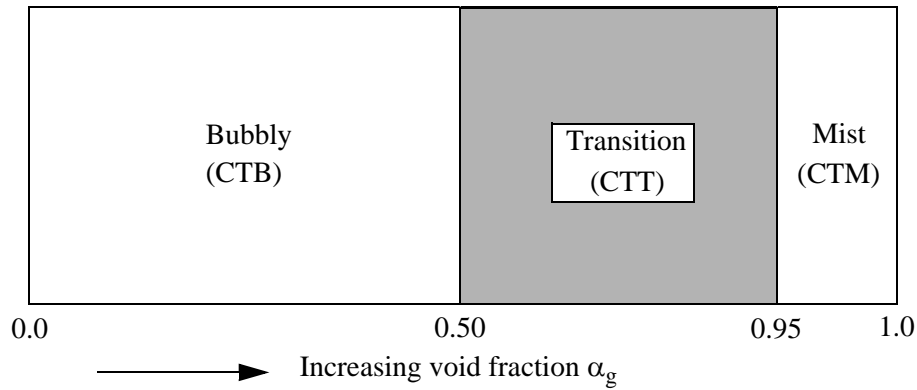
Figure 3.3-3 Schematic of high mixing volume flow regime map.

3.3.4 ECC Mixer Volume Flow Regime Map

Prior to the introduction of the ECCMIX component into RELAP5/MOD3, RELAP5 included the three previously discussed flow regime maps, as described in the RELAP5/MOD2 manual[3.3-17] and in the RELAP5/MOD2 models and correlations report.[3.3-18] None of those, however, would apply specifically to the condensation process in a horizontal pipe near the emergency core coolant (ECC) injection port. A flow regime map for condensation inside horizontal tubes is reported by Tandon et al.,[3.3-19] and it was considered a more suitable basis for the interfacial heat transfer calculation in condensation for this geometry. According to **Reference 3.3-19**, the two-phase flow patterns during condensation inside a horizontal pipe may be identified in terms of the local volumetric ratio of liquid and vapor/gas, $\frac{1-\alpha_g}{\alpha_g}$, and the nondimensional vapor/gas velocity, v_g^*, where

$$v_g^* = \frac{X_{flow}G}{[gD\rho_g(\rho_f-\rho_g)]^{1/2}}$$

$$X_{flow} = \frac{\alpha_g\rho_g v_g}{\alpha_g\rho_g v_g + \alpha_f\rho_f v_f}$$

$$G = \alpha_g\rho_g v_g + \alpha_f\rho_f v_f$$

and D is the diameter of the channel.

Although the condensation flow regime map of Tandon et al.[3.3-19] does not include any zone for bubbly flow, the existence of a bubbly flow regime at very low void fractions cannot be logically excluded, particularly in a highly turbulent liquid flow. For this reason, a region of bubbly flow was included for void fractions less than 20% ($\alpha_g \leq 0.2$). Furthermore, to protect against failure of the numerical solution, it is

necessary to specify some reasonable flow pattern for every combination of the volumetric ratio and v_g^* and to include transition zones around some of the boundaries between different flow patterns. The transition zones are needed for interpolation between the calculated values of the correlations for the interfacial heat transfer and friction that apply for the different flow patterns. These interpolations prevent discontinuities that would otherwise exist and that could make the numerical solutions very difficult. With these considerations, the flow regime map of **Reference 3.3-19** was modified, as shown in **Figure 3.3-4**. The modified condensation flow regime map comprises eleven different zones that include six basic patterns and five interpolation zones. **Table 3.3-1** shows a list of the basic flow patterns and the interpolation zones for the ECCMIX component, with their acronyms and flow regime numbers, that are printed out in the ATHENA output.

$$v_g^* = \frac{X_{flow}G}{\sqrt{gD\rho_g(\rho_f - \rho_g)}}$$
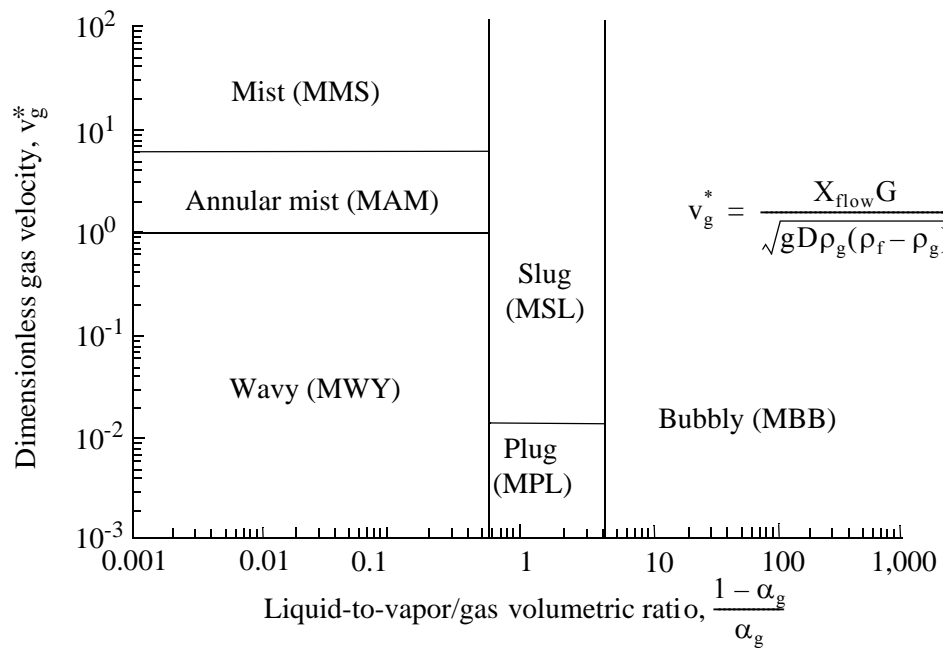
Figure 3.3-4 Schematic of ECC mixer volume flow regime map (modified Tandon et al.[3.3-19]).

Table 3.3-1 List of flow regimes in the ECCMIX component.

Flow regime number[a]	Flow regime	Acronym	Remarks
16[a]	Wavy	MWY	Basic pattern

Table 3.3-1 List of flow regimes in the ECCMIX component. (Continued)

Flow regime number[a]	Flow regime	Acronym	Remarks
17	Wavy/annular mist	MWA	Transition between wavy and annular mist flows
18	Annular mist	MAM	Basic pattern
19	Mist	MMS	Basic pattern
20	Wavy/slug	MWS	Transition between wavy and slug flows
21	Wavy/plug/slug	MWP	Transition between wavy, plug, and slug flows
22	Plug	MPL	Basic pattern
23	Plug/slug	MPS	Transition between plug and slug flows
24	Slug	MSL	Basic pattern
25	Plug/bubbly	MPB	Transition between plug and bubbly flows
26	Bubbly	MBB	Basic pattern

a. Flow regime numbers 1 through 15 are used in ATHENA for flow patterns in other components.

The variable names that are used in the coding for the coordinates of the condensation flow regime map are

$$\text{voider} = \frac{1 - \alpha_g}{\alpha_g} \tag{3.3-32}$$

$$\text{stargj} = v_g^* = \frac{X_{flow}G}{[gD\rho_g(\rho_f - \rho_g)]^{1/2}} \quad . \tag{3.3-33}$$

In terms of these variables, the different zones of the flow regime map are as follows:

If voider > 4.0, bubbly flow, MBB.

If 3.0 < voider ≤ 4.0 and stargj < 0.01, transition, MPB.

If 0.5 < voider ≤ 4.0 and stargj > 0.0125, slug flow, MSL.

If 0.625 < voider ≤ 4.0, and 0.01 < stargj ≤ 0.0125, transition, MPS.

If 0.5 < voider ≤ 3.0, and stargj ≤ 0.01, plug flow, MPL.

If 0.5 < voider ≤ 0.625, and 0.01 < stargj ≤ 0.0125, transition, MWP.

If 0.5 < voider ≤ 0.625, and 0.0125 < stargj ≤ 1.0, transition, MWS.

If voider ≤ 0.5 and stargj ≤ 1.0, wavy flow, MWY.

If voider ≤ 0.5, and 1.0 < stargj ≤ 1.125, transition, MWA.

If voider ≤ 0.5, and 1.125 < stargj ≤ 6.0, annular mist, MAM.

If voider ≤ 0.5, and stargj > 6.0, mist flow, MMS.

In the coding, each one of these regions is identified by a flow pattern identification flag, MFLAG, whose value varies from 1 for wavy flow to 11 for bubbly flow. The flow regime number in **Table 3.3-1** is MFLAG + 15.

In addition to the transition zones that are shown on **Figure 3.3-4** and listed in **Table 3.3-1**, there are two other transitions, namely:

- Transition between wavy and plug flows.

- Transition between annular mist and mist (or droplet) flows.

Interpolations between the interfacial friction, interfacial heat transfer, and the wall friction rates for these transitions are performed through the gradual changes in the interfacial area in the first case and the droplet entrainment fraction in the second case. Hence, there was no need for specifying transition zones for these on the flow regime map.

3.3.5 Junction Flow Regime Map

The junction map is based on both junction and volume quantities. It is used for the interphase drag and shear, as well as the coefficient of virtual mass. The flow regime maps used for junctions are the same as used for the volumes and are based on the work of Taitel and Dukler,[3.3-4,3.3-5,3.3-20] Ishii,[3.3-6,3.3-8] and Tandon et al.[3.3-19]

Junction quantities used in the map decisions are junction phasic velocities, donored (based on phasic velocities) phasic densities, and donored (based on mixture superficial velocity) surface tension.

The junction void fraction, $\alpha_{g,j}^*$, is calculated from either of the volume void fractions of the neighboring volumes, $\alpha_{g,K}$ or $\alpha_{g,L}$, using a donor direction based on the mixture superficial velocity, j_m. A cubic spline weighting function is used to smooth the void fraction discontinuity across the junction when $|j_m| < 0.465$ m/s. The purpose of this method is to use a void fraction that is representative of the real junction void fraction. This is assumed to have the form

$$\alpha_{g,j}^* = w_j \bullet \alpha_{g,K} + (1 - w_j) \bullet \alpha_{g,L} \tag{3.3-34}$$

where

$$w_j \quad = \quad 1.0 \qquad\qquad \text{when } j_m > 0.465 \text{ m/s} \tag{3.3-35}$$

$$w_j \quad = \quad x_1^2(3 - 2x_1) \qquad \text{when } -0.465 \text{ m/s} \le j_m \le 0.465 \text{ m/s} \tag{3.3-36}$$

$$w_j \quad = \quad 0 \qquad\qquad \text{when } j_m < -0.465 \text{ m/s} \tag{3.3-37}$$

$$x_1 \quad = \quad \frac{j_m + 0.465}{0.93} \tag{3.3-38}$$

$$j_m \quad = \quad \dot{\alpha}_{g,j}v_{g,j} + \dot{\alpha}_{f,j}v_{f,j}. \tag{3.3-39}$$

For horizontal stratified flow, the void fraction from the entrainment/pullthrough (or offtake) model is used (see Section 3.4.2). The case of vertical stratified flow will be discussed in Section 3.3.6.7. The junction mass flux is determined from

$$G_j = \dot{\alpha}_{g,j}\dot{\rho}_{g,j}|v_{g,j}| + \dot{\alpha}_{f,j}\dot{\rho}_{f,j}|v_{f,j}| \quad . \tag{3.3-40}$$

The methods for calculating $\alpha_{g,j}^*$ and G_j are the same ones that are used in TRAC-B.[3.3-1,3.3-2]

As with the volumes, four junction flow regime maps are used. They are a horizontal map for flow in pipes; a vertical map for flow in pipes, annuli, and bundles; a high mixing map for flow in pumps; and an ECC mixer map for flow in the horizontal pipe near the ECC injection port. These will not be discussed in any detail because they are similar to the volumes flow regime maps. The decision of whether a junction is in the horizontal or vertical junction flow regime is done slightly differently than for a volume. The junction inclination (vertical) angle is determined from either of the volume inclination (vertical) angles, ϕ_K or ϕ_L, based on input by the user using a donor direction based on the mixture superficial velocity, j_m. The formula used is similar to that used for the junction void fraction, however, it uses the sine of the angle. It is given by

$$\sin \phi_j \ = \ w_j \sin \phi_K + (1 - w_j)\sin \phi_L \ .$$ (3.3-41)

The vertical flow regime map is for junctions whose junction inclination (vertical) angle ϕ_j is such that $60 \leq |\phi_j| \leq 90$ degrees. The horizontal flow regime map is for junctions whose junction inclination (vertical) angle ϕ_j is such that $0 \leq |\phi_j| \leq 30$ degrees. An interpolation region between vertical and horizontal flow regimes is used for junctions whose junction inclination (vertical) angle ϕ_j is such that $30 < |\phi_j| < 60$ degrees. This interpolation region is used to smoothly change between vertical and horizontal flow regimes.

3.3.6 Interphase Friction

The interface friction per unit volume in the phasic momentum equations [Equations (3.1-6) and (3.1-7)] is expressed in terms of phasic interfacial friction coefficients as

$$F_{ig} \ = \ \alpha_g \rho_g FIG \ (v_g - v_f)$$ (3.3-42)

and

$$F_{if} \ = \ \alpha_f \rho_f FIF \ (v_g - v_f)$$ (3.3-43)

where F_{ig} is the magnitude of the interfacial friction force per unit volume on the vapor/gas and F_{if} is the magnitude of the interfacial friction force per unit volume on the liquid. The magnitude of the interfacial friction force per unit volume on the liquid is assumed to be equal to the magnitude of the interfacial friction on the vapor/gas phase. This assumption leads to the condition [Equation (3.1-10)]

$$\alpha_g \rho_g FIG \ = \ \alpha_f \rho_f FIF \ = \ \alpha_g \rho_g \alpha_f \rho_f FI$$ (3.3-44)

where a global interfacial friction coefficient FI is defined in terms of the phasic interfacial friction coefficients (FIG and FIF).

The interfacial friction force term in the difference momentum equation [Equation (3.1-74)] is given by

$$\frac{F_{ig}}{\alpha_g \rho_g} + \frac{F_{if}}{\alpha_f \rho_f} \ = \ (FIG + FIF)(v_g - v_f)$$ (3.3-45)

which becomes

$$\frac{F_{ig}}{\alpha_g \rho_g} + \frac{F_{if}}{\alpha_f \rho_f} = \rho_m FI(v_g - v_f)$$ (3.3-46)

where the phasic interfacial friction coefficients (FIG and FIF) are represented in terms of the global interfacial friction coefficient FI using Equation (3.3-44). This relation can be rearranged to give a constitutive relation for the global interfacial friction coefficient, which is given by

$$FI = \frac{\left(\dfrac{F_{ig}}{\alpha_g \rho_g} + \dfrac{F_{if}}{\alpha_f \rho_f}\right)}{\rho_m(v_g - v_f)} \quad .$$ (3.3-47)

Once the phasic interfacial friction forces per unit volume (F_{ig} and F_{if}) have been computed, the global interfacial friction coefficient FI can be determined.

ATHENA uses two different models for the phasic interfacial friction force computation, the drift flux method and the drag coefficient method. The basis of each of these methods will be described in the following sections. Once the two methods have been explained, the final form of the difference momentum equation incorporating a framework within which both methods have been implemented will be presented. Finally, the drift flux and drag coefficient correlations used in the several flow regimes will be presented.

3.3.6.1 Drift Flux Method. The drift flux approach is used in the bubbly and slug flow regimes for vertical flow. The drift flux model specifies the distribution coefficient and the vapor/gas drift velocity. These two quantities must be converted into a constitutive relation for the interfacial frictional force per unit volume. The objective of this conversion is to compute the global interfacial friction coefficient FI, which leads to a relative velocity consistent with the relative velocity computed directly from the drift flux parameters, when used in the phasic momentum equations in conjunction with the other force terms such as the wall friction and buoyancy force terms. This conversion is accomplished in two steps. The first step considers the effect of the phasic wall frictional force per unit volume on the relative velocity between the phases, and the second step computes the interfacial friction force per unit volume from the drift flux parameters.

The first step begins by writing the steady-state phasic momentum equations in symbolic form and neglecting the virtual mass force and the momentum flux terms. The simplified equations are

$$0 = -\alpha_g \frac{dP}{dx} - F_{ig} - F_{wg} - \alpha_g \rho_g g$$

$$0 = -\alpha_f \frac{dP}{dx} + F_{if} - F_{wf} - \alpha_f \rho_f g \quad .$$ (3.3-48)

If we multiply the first equation by α_f and the second by α_g and subtract the second equation from the first, the pressure gradient term is eliminated. The resulting equation can be rearranged to give

$$\alpha_f F_{ig} + \alpha_g F_{if} = \alpha_f \alpha_g (\rho_f - \rho_g) \, g - \alpha_f F_{wg} + \alpha_g F_{wf} \qquad (3.3\text{-}49)$$

which can be simplified by remembering that the magnitudes of the interfacial force per unit volume on the two phases are equal to give

$$F_i = \alpha_f \alpha_g (\rho_f - \rho_g) \, g - \alpha_f F_{wg} + \alpha_g F_{wf} \qquad (3.3\text{-}50)$$

where

$$F_{ig} = F_{if} = F_i.$$

Equation (3.3-50) states that the interfacial frictional force per unit volume is balanced by buoyancy and wall friction forces per unit volume. Equation (3.3-50) could be used directly to compute the interfacial friction force coefficient FI. However, there are several problems with Equation (3.3-50) as it stands. First, the interfacial friction force F_i might have a negative value at high void fraction and high flow rates where the magnitude of the wall frictional force is high and where most of the wall frictional force acts on the vapor/gas phase. The factor $\alpha_f F_{wg}$ may be larger than the sum of the buoyance force term and the fraction of the wall force which acts on the liquid phase, leading to a negative value for the interfacial force. A negative value for the interfacial force violates the assumption that interfacial friction is a retarding force tending to decrease the relative velocity between the phases. The second problem with Equation (3.3-50) is that it implies the interfacial force coefficient is a function of the magnitude of the individual phasic flow rates (through the phasic wall friction) rather than a function of the relative velocity between the phases. Experimental evidence shows that the drift flux parameters, and hence the interfacial friction coefficient, do not depend upon the magnitude of the phasic flow rates, being constant in a given flow regime. Finally, consider the case of a very large tank for which the wall friction is negligible. In this case, the interfacial friction force is balanced by only the buoyance force. For these reasons, we remove the wall friction terms from Equation (3.3-50) before proceeding. This can be accomplished by partitioning the total wall frictional force per unit volume between the phases based on the phasic volume fractions (also see Anderson[3.3-21] and Ishii[3.3-22, 3.3-23]) rather than by the use of the Chisholm model (see Section 3.3.8). That is, we want,

$$\begin{aligned} F_{wg} &= \alpha_g F_{wt} \\ F_{wf} &= \alpha_f F_{wt} \end{aligned} \qquad (3.3\text{-}51)$$

where F_{wt} is the total wall frictional force per unit volume on the two-phase mixture.

Substitution of Equation (3.3-51) into Equation (3.3-50) gives

$$F_i = \alpha_f \alpha_g (\rho_f - \rho_g) \, g \qquad (3.3\text{-}52)$$

where the interfacial frictional force per unit volume is balanced by the buoyancy force per unit volume. Recalling that the total wall frictional force on the two-phase mixture is given by

$$F_{wt} = \alpha_f \rho_f \, FWF \, v_f + \alpha_g \rho_g FWG \, v_g, \tag{3.3-53}$$

the desired wall frictional force per unit volume on the phases is given by

$$F_{wf} = \alpha_f(\alpha_f \rho_f FWF \, v_f + \alpha_g \rho_g FWG \, v_g)$$
$$F_{wg} = \alpha_g(\alpha_f \rho_f FWF \, v_f + \alpha_g \rho_g FWG \, v_g) \; . \tag{3.3-54}$$

Comparing these phasic wall frictional terms to the wall friction terms already included in the phasic momentum equations shows that additional terms must be added to the right hand side of the phasic momentum equations to effect the changing of the partitioning of the wall frictional force per unit volume. These extra terms are

$$\alpha_g \alpha_f \rho_f FWF \, v_f \; - \; \alpha_f \alpha_g \rho_g FWG \, v_g \tag{3.3-55}$$

for the liquid momentum equation and

$$- \, \alpha_g \alpha_f \rho_f FWF \, v_f \; + \; \alpha_f \alpha_g \rho_g FWG \, v_g \tag{3.3-56}$$

for the vapor/gas momentum equation. These terms can be simplified by defining

$$f_{wg} = \alpha_f \alpha_g \rho_g FWG$$
$$f_{wf} = \alpha_g \alpha_f \rho_f FWF \tag{3.3-57}$$

so that the extra terms in the liquid momentum equations can be written as

$$f_{wf} \, v_f \; - \; f_{wg} \, v_g \tag{3.3-58}$$

and for the vapor/gas momentum equations as

$$f_{wg} \, v_g \; - \; f_{wf} \, v_f \; . \tag{3.3-59}$$

A means of removing the extra terms when the interfacial frictional force per unit volume model is not being determined from the drift flux correlations has been implemented by multiplying the extra terms by a parameter f_x which is defined as $f_x = 1$ when the drift flux model is being used to determine the

interfacial friction force per unit volume and is defined as $f_x = 0$ when the drag coefficient model is being used to determine the interfacial friction force per unit volume. This parameter is interpolated from one to zero in the interpolation region between flow regimes using the drift flux model and those using the two-fluid model for the determination of the interfacial friction force per unit volume.

The second step is next described. The interfacial friction force per unit volume relation specified by Equation (3.3-52) does not constitute a constitutive relation for the interfacial friction force per unit volume since it does not provide a relationship between the friction interfacial force per unit volume and the relative velocity. Such a relation can be found by assuming that the interfacial friction force per unit volume is given by

$$F_i = C_i |v_R| v_R \tag{3.3-60}$$

where C_i is a unknown coefficient and v_R is the relative velocity between the phases. Within the context of the drift flux model, the relative velocity between the phases in not the difference between the phasic velocities but is a weighted difference between the phase velocities given by

$$v_R = C_1 v_g - C_0 v_f \tag{3.3-61}$$

where C_0 is given by the drift flux correlations and C_1 is given by

$$C_1 = \frac{1 - \alpha_g C_0}{1 - \alpha_g} \quad . \tag{3.3-62}$$

Substituting these relations into Equation (3.3-60) gives the interfacial friction force per unit volume in terms of the phasic velocities, given by

$$F_i = C_i \left| C_1 v_g - C_0 v_f \right| (C_1 v_g - C_0 v_f) \tag{3.3-63}$$

with the coefficient C_i undetermined as yet. The drift flux model also specifies that the relative velocity v_R can be written as the ratio of the vapor/gas drift velocity and the liquid volume fraction, and is given by

$$v_R = \frac{v_{gj}}{\alpha_f} \tag{3.3-64}$$

where the vapor/gas drift velocity v_{gj} is given by the drift flux correlations. Substituting this value of the relative velocity into Equation (3.3-60) and combining the resulting equation with Equation (3.3-52) allows the coefficient C_i to be determined from

$$C_i = \frac{\alpha_g \alpha_f^3 (\rho_f - \rho_g) g}{v_{gj}^2} \quad .$$

(3.3-65)

We are now in a position to determine the global interfacial friction coefficient FI by modifying Equation (3.3-47) to take into account the different definition of the relative velocity in the drift flux model,

$$FI = \frac{\left(\dfrac{F_{ig}}{\alpha_g \rho_g} + \dfrac{F_{if}}{\alpha_f \rho_f} \right)}{\rho_m (C_1 v_g - C_0 v_f)}$$

(3.3-66)

and by modifying the definition of the relative velocity in the interfacial friction term in the difference momentum equation accordingly. The interfacial friction force per unit volume F_i is computed from Equation (3.3-63) from which the global interfacial friction coefficient FI can be computed using Equation (3.3-66), using the relation $F_{ig} = F_{if} = F_i$.

3.3.6.2 Drag Coefficient Method. The drag coefficient method is used in all flow regimes except for bubbly and slug flows in vertical components. The model uses correlations for drag coefficients and for the computation of the interfacial area density and is the model used by previous versions of ATHENA for all flow regimes.

The constitutive relation for the frictional force on a body moving relative to a fluid is given by

$$F = \frac{1}{2} \rho v^2 C_D A$$

(3.3-67)

where

F	=	drag force
ρ	=	fluid density
v	=	velocity of body relative to the fluid
C_D	=	drag coefficient
A	=	projected area of the body.

Expressing the frictional force for a group of bodies moving relative to a fluid (e.g., bubbles moving through liquid or droplets moving through vapor/gas) in terms of the frictional force for each body leads to the following constitutive relation for the interfacial frictional force per unit volume:

$$F_i = \frac{1}{8}\rho_c|v_g - v_f|(v_g - v_f)C_DS_Fa_{gf} = C_i|v_g - v_f|(v_g - v_f) \qquad (3.3\text{-}68)$$

where

F_i = interfacial friction force per unit volume

C_i = $\frac{1}{8}\rho_cC_DS_Fa_{gf}$

ρ_c = density of continuous phase

a_{gf} = interfacial area per unit volume

S_F = shape factor.

The additional factor of 1/4 comes from the conversion of the projected area of spherical particles (i.e., πr^2) into the interfacial area (i.e., $4\pi r^2$) and the shape factor is included to account for non-spherical particles. The drag coefficient model for the global interfacial friction coefficient has been reduced to the specification of the continuous density, drag coefficient, interfacial area density, and shape factor for the several flow regimes. Once these quantities have been computed, the interfacial friction force per unit volume F_i is computed from Equation (3.3-68) from which the global interfacial friction coefficient FI can be computed using Equation (3.3-47), using the relation $F_{ig} = F_{if} = F_i$.

3.3.6.3 Difference Momentum Equation. The finite difference form of the one dimensional difference momentum equation for the semi-implicit solution scheme [Equation (3.1-105)] must be modified to incorporate a framework under which the additional wall friction terms which appear when the drift flux model is used for the computation of the interfacial friction force can be included as well as accommodate the drift flux definition of the relative velocity. This framework uses a parameter f_x which is used to select either the drift flux model or the drag coefficient model for the interfacial friction force. The value of this parameter is selected on the basis of the flow regime in a junction. The drift flux model is used for bubbly and slug flows in vertical components, and the drag coefficient model is used for all other flow regimes. The finite difference form of the difference momentum equation becomes

$$\left(1 + \frac{C\rho_m^2}{\rho_g\rho_f}\right)_j^n [(v_g^{n+1} - v_g^n) - (v_f^{n+1} - v_f^n)]_j \Delta x_j$$

$$+ \frac{1}{2}\left(\frac{\alpha_g\dot{\rho}_g}{\alpha_g\rho_g}\right)_j^n [(v_g^2)_L^n - (v_g^2)_K^n]\Delta t - \frac{1}{2}\left(\frac{\alpha_g\dot{\rho}_g}{\alpha_g\rho_g}\right)_j^n VISG_j^n \Delta t$$

$$- \frac{1}{2}\left(\frac{\alpha_f\dot{\rho}_f}{\alpha_f\rho_f}\right)_j^n [(v_f^2)_L^n - (v_f^2)_K^n]\Delta t + \frac{1}{2}\left(\frac{\alpha_f\dot{\rho}_f}{\alpha_f\rho_f}\right)_j^n VISF_j^n \Delta t = -\left(\frac{\rho_f - \rho_g}{\rho_f\rho_g}\right)_j^n (P_L - P_K)^{n+1}\Delta t$$

$$- \left(FWG_j^n(v_g)_j^{n+1} - FWF_j^n(v_f)_j^{n+1} - \left[\frac{\Gamma_g^n(\rho_m^n v_I^{n+1} - \alpha_f^n\rho_f^n v_g^{n+1} - \alpha_g^n\rho_g^n v_f^{n+1})}{(\alpha_g\rho_g\alpha_f\rho_f)^n}\right]\right)_j \quad (3.3\text{-}69)$$

$$- (f_x)_j^n\left(\frac{1}{\alpha_g\rho_g} + \frac{1}{\alpha_f\rho_f}\right)_j^n [(f_{wg})_j^n(v_g)_j^{n+1} - (f_{wf})_j^n(v_f)_j^{n+1}]$$

$$+ (\rho_m FI)_j^n\{[1 + f_x(C_1 - 1)]_j^n(v_g)_j^{n+1} - [1 + f_x(C_0 - 1)]_j^n(v_f)_j^{n+1}\})\Delta x_j \Delta t$$

$$- \left[\left(\frac{\alpha_g\dot{\rho}_g}{\alpha_g\rho_g}\right)_j^n HLOSSG_j^n v_{g,j}^{n+1} - \left(\frac{\alpha_f\dot{\rho}_f}{\alpha_f\rho_f}\right)_j^n HLOSSF_j^n v_{f,j}^{n+1}\right]\Delta t$$

$$+ \left(\frac{\rho_m}{\rho_g\rho_f}\right)_j^n (\rho_f - \rho_g)_j^n B_y(y_L^n - y_K^n)\Delta t$$

3.3.6.4 Dispersed Flow. The bubbly, mist, mist pre-CHF, and mist post-CHF flow regimes are considered as dispersed flow. For vertical bubbly flow, the drift flux model is used for which $f_x = 1$. For non-vertical bubbly flow and all droplet (mist, mist pre-CHF, mist post-CHF) flow situations, the drag coefficient model is used for which $f_x = 0$.

The drag coefficient model will first be discussed. According to Wallis[3.3-24] and Shapiro,[3.3-25] the dispersed bubbles or droplets can be assumed to be spherical particles with a size distribution of the Nukiyama-Tanasawa[3.3-24] form. The Nukiyama-Tanasawa distribution function in nondimensional form is

$$p^* = 4d^{*2}e^{-2d^*} \quad (3.3\text{-}70)$$

where $d^* = \frac{d}{d'}$, d' is the most probable particle diameter, and p^* is the probability of particles with nondimensional diameter d^*. With this distribution, it can be shown that the average particle diameter $d_o = 1.5\,d'$, and the surface area per unit volume is

$$a_{gf} = \frac{6\bar{\alpha}}{d'} - \frac{\int d^{*2}p^*dd^*}{\int d^{*3}p^*dd^*} = \frac{2.4\bar{\alpha}}{d'} \quad (3.3\text{-}71)$$

where $\bar{\alpha} = \alpha_g$ for bubbles and $\bar{\alpha} = \alpha_f$ for droplets. In terms of the average diameter, d_o, the interfacial area per unit volume, a_{gf}, is

$$a_{gf} = \frac{3.6\bar{\alpha}}{d_o} \quad .$$

(3.3-72)

The average diameter d_o is obtained by assuming that $d_o = (1/2)d_{max}$. The maximum diameter, d_{max}, is related to the critical Weber number, We, by

$$We = \frac{d_{max}\rho_c(v_g - v_f)^2}{\sigma}$$

(3.3-73)

where σ is the surface tension. The values for We are presently taken as We = 10.0 for bubbly flow, We = 3.0 for mist-pre-CHF flow, and We = 12.0 for mist and mist-post-CHF flow.

The drag coefficient to be used in non-vertical bubbly flow and all droplet flow situations is given by Ishii and Chawla[3.3-7] for the viscous regime as

$$C_D = \frac{24(1.0 + 0.1\,Re_p^{0.75})}{Re_p}$$

(3.3-74)

where the particle Reynolds number, Re_p, is defined as

$$Re_p = \frac{|v_g - v_f|d_o\rho_c}{\mu_m} \quad .$$

(3.3-75)

The density, ρ_c, is for the continuous phase, and is given by ρ_f for bubbles and ρ_g for drops. The mixture viscosity, μ_m, is for the continuous phase, and is given by $\mu_m = \frac{\mu_f}{\alpha_f}$ for bubbles and $\mu_m = \frac{\mu_g}{(\alpha_g)^{2.5}}$ for mist pre-CHF. For mist and mist post-CHF droplets, $\mu_m = \mu_g$ is used.

For vertical bubbly flow, the drift flux model is used for which $f_x = 1$. The drift flux parameters are calculated using drift flux correlations from the literature based on Putney's

work.[3.3-26,3.3-27,3.3-28,3.3-29,3.3-30] **Table 3.3-2** indicates which correlations are used for different

Table 3.3-2 Drift flux void fraction correlations for vertical bubbly-slug flow.

Flow rates	Rod bundles	Narrow rectangular channels	Small pipes $D \leq 0.018m$	Intermediate pipes $0.018m < D \leq 0.08m$	Large pipes $0.08m < D$
High upflow rates $G \geq 100$ kg/m^2•s	EPRI (2) (eprij)	Griffith (2) (griftj)	EPRI (3) (eprij)	EPRI (9) (eprij)	Churn-turbulent bubbly flow (14) Transition (15) Kataoka-Ishii (16) (katokj)
Medium upflow rates 50 kg/m^2•s $< G <$ 100 kg/m^2•s			Transition^a (5)	Transition^a (13)	
Low upflow, downflow, and countercurrent flow rates - 50 kg/m^2•s $\leq G \leq$ 50 kg/m^2•s			Zuber-Findlay slug flow (4) (zfslgj)	Churn-turbulent bubbly flow (10) Transition (11) Kataoka-Ishii (12) (katokj)	
Medium downflow rates - 100 kg/m^2•s $< G$ $< $ - 50 kg/m^2•s			Transition^a (5)	Transition^a (13)	
High downflow rates $G \leq$ -100 kg/m^2•s			EPRI (3) (eprij)	EPRI (9) (eprij)	

a. Interpolation is applied between different flow rates in pipes.

geometry and flow conditions. The number in parenthesis is the value of the minor edit/plot variable IREGJ, the vertical bubbly/slug flow junction flow regime number. The name in parenthesis is the subroutine used to calculate the correlation. It should be noted that the EPRI correlation implemention has some differences between bundles and pipes; this is discussed in Volume IV.

The correlation labeled EPRI is by Chexal and Lellouche.[3.3-31] The correlation has been recently modified[3.3-32,3.3-33] and many of the changes have been incorporated into ATHENA. The distribution coefficient C_0 is calculated from

$$C_0 = \frac{L(\alpha_g, P)}{K_0 + (1 - K_0)\alpha_g{}^r} \tag{3.3-76}$$

where

$$L(\alpha_g, P) \quad = \quad \frac{1 - \exp(-C_1\alpha_g)}{1 - \exp(-C_1)} \tag{3.3-77}$$

$$C_1 \quad = \quad \left|\frac{4P_{crit}^2}{P(P_{crit} - P)}\right| \tag{3.3-78}$$

$$P_{crit} \quad = \quad \text{critical pressure}$$

$$K_0 \quad = \quad B_1 + (1 - B_1)\left(\frac{\rho_g}{\rho_f}\right)^{1/4} \tag{3.3-79}$$

$$B_1 \quad = \quad \min(0.8, A_1) \tag{3.3-80}$$

$$A_1 \quad = \quad \frac{1}{1 + \exp\left[-\left(\frac{Re}{60,000}\right)\right]} \tag{3.3-81}$$

$$Re \quad = \quad Re_g \qquad \text{if } Re_g > Re_f \text{ or } Re_g < 0 \tag{3.3-82}$$

$$\quad = \quad Re_f \qquad \text{otherwise} \tag{3.3-83}$$

$$Re_f \quad = \quad \text{local liquid superficial Reynolds number}$$

$$\quad = \quad \frac{\rho_f j_f D_h}{\mu_f} \tag{3.3-84}$$

$$Re_g \quad = \quad \text{local vapor/gas superficial Reynolds number}$$

$$\quad = \quad \frac{\rho_g j_g D_h}{\mu_g} \tag{3.3-85}$$

$$r \quad = \quad \frac{1 + 1.57\left(\frac{\rho_g}{\rho_f}\right)}{1 - B_1} \; . \tag{3.3-86}$$

The sign of j_k is positive if phase k flows upwards and negative if it flows downwards. This convention determines the sign of Re_g, Re_f, and Re.

The vapor/gas drift velocity, v_{gj}, for the Chexal-Lellouche correlation is calculated from

$$v_{gj} = 1.41 \left[\frac{(\rho_f - \rho_g)\sigma g}{\rho_f^2} \right]^{1/4} C_1 C_2 C_3 C_4 \tag{3.3-87}$$

where

$$C_1 \quad = \quad (1 - \alpha_g)^{B_1} \quad \text{if } Re_g \geq 0 \tag{3.3-88}$$

$$= \quad (1 - \alpha_g)^{0.5} \quad \text{if } Re_g < 0. \tag{3.3-89}$$

$$C_2 \quad = \quad 1 \quad \text{if } \frac{\rho_f}{\rho_g} \geq 18 \text{ and } C_5 \geq 1 \tag{3.3-90}$$

$$= \quad 1 \quad \text{if } \frac{\rho_f}{\rho_g} \geq 18 \text{ and } C_5 < 1 \text{ and } C_6 \geq 85 \tag{3.3-91}$$

$$= \quad \frac{1}{1 - \exp(-C_6)} \quad \text{if } \frac{\rho_f}{\rho_g} \geq 18 \text{ and } C_5 < 1 \text{ and } C_6 < 85 \tag{3.3-92}$$

$$= \quad 0.4757 \left[\ln\left(\frac{\rho_f}{\rho_g}\right) \right]^{0.7} \quad \text{if } \frac{\rho_f}{\rho_g} < 18 \tag{3.3-93}$$

$$C_5 \quad = \quad \left[150\left(\frac{\rho_g}{\rho_f}\right) \right]^{1/2} \tag{3.3-94}$$

$$C_6 \quad = \quad \frac{C_5}{1 - C_5} \tag{3.3-95}$$

$$C_4 \quad = \quad 1 \quad \text{if } C_7 \geq 1 \tag{3.3-96}$$

$$= \quad \frac{1}{1 - \exp(-C_8)} \quad \text{if } C_7 < 1 \tag{3.3-97}$$

$$C_7 \quad = \quad \left(\frac{D_2}{D}\right)^{0.6} \tag{3.3-98}$$

$$D_2 \quad = \quad 0.09144 \text{ m (normalizing diameter)}$$

$$C_8 \quad = \quad \frac{C_7}{1 - C_7} \tag{3.3-99}$$

The parameter C_3 depends on the directions of the vapor/gas and liquid flows:

Upflow (both j_g and j_f are positive)

$$C_3 = \max\left[0.50,\, 2\exp\left(-\frac{|Re_f|}{300,000}\right)\right] \ . \tag{3.3-100}$$

Downflow (both j_g and j_f are negative)

$$C_3 = \left(\frac{C_{10}}{2}\right)^{B_2} \tag{3.3-101}$$

$$B_2 = \frac{1}{1 + 0.05\left|\dfrac{Re_f}{350,000}\right|^{0.4}} \tag{3.3-102}$$

$$C_{10} = 2\exp\left[\left(\frac{|Re_f|}{350,000}\right)^{0.4}\right] - 1.7|Re_f|^{0.035}\exp\left[\frac{-|Re_f|}{60,000}\left(\frac{D_1}{D}\right)^2\right] + \left(\frac{D_1}{D}\right)^{0.1}|Re_f|^{0.001} \tag{3.3-103}$$

$$D_1 = 0.0381 \text{ m (normalizing diameter)}. \tag{3.3-104}$$

Countercurrent Flow (j_g is positive, j_f is negative)

$$C_3 = \left(\frac{C_{10}}{2}\right)^{B_2} \tag{3.3-105}$$

$$B_2 = \frac{1}{1 + 0.05\left|\dfrac{Re_f}{350,000}\right|^{0.4}} \tag{3.3-106}$$

$$C_{10} = 2\exp\left[\left(\frac{|Re_f|}{350,000}\right)^{0.4}\right] - 1.7|Re_f|^{0.035}\exp\left[\frac{-|Re_f|}{60,000}\left(\frac{D_1}{D}\right)^2\right] + \left(\frac{D_1}{D}\right)^{0.1}|Re_f|^{0.001} \tag{3.3-107}$$

$D_1 = 0.0381$ (normalizing diameter). (3.3-108)

The parameters C_1, C_2, C_3, C_4, ..., C_{10} are from the Chexal-Lellouche correlation.[3.3-31, 3.3-32,3.3-33]

The correlation labelled Griffith is for vertical narrow rectangular channels. The distribution parameter is given by Ishii[3.3-23]

$$C_0 = 1.35 - 0.35 \sqrt{\frac{\rho_g}{\rho_f}}$$ (3.3-109)

and the drift velocity is given by Griffith[3.3-34]

$$v_{gj} = \left(0.23 + 0.13\frac{W}{S}\right)\left(\frac{(\rho_f - \rho_g)gS}{\rho_f}\right)^{1/2}$$ (3.3-110)

where W is the channel width (pitch, gap, short dimension) perpendicular to the flow and S is the channel length (span, long dimension) perperdicular to the flow.

The correlation labeled Zuber-Findlay Slug Flow is by Zuber and Findlay.[3.3-35,3.3-36] The distribution parameter is given by

$$C_0 = 1.2$$ (3.3-111)

and the drift velocity is given by

$$v_{gj} = 0.35\left[\frac{(\rho_f - \rho_g)gD}{\rho_f}\right]^{1/2} \quad .$$ (3.3-112)

The correlation labeled Kataoka-Ishii is by Kataoka and Ishii.[3.3-37] The distribution parameter is given by the modified Rouhani correlation[3.3-38] used in TRAC-BF1,[3.3-3] that is

$$C_0 = C_\infty - (C_\infty - 1)\left(\frac{\rho_g}{\rho_f}\right)^{1/2}$$ (3.3-113)

$$C_\infty = 1 + 0.2\left[\frac{\rho_f(gD)^{1/2}}{|G| + 0.001}\right]^{1/2}$$ (3.3-114)

and the drift velocity is given by

$$v_{gj} = 0.0019(D^*)^{0.809}\left(\frac{\rho_g}{\rho_f}\right)^{-0.157} N_{\mu f}^{-0.562}\left[\frac{\sigma g(\rho_f - \rho_g)}{\rho_f^2}\right]^{1/4} \quad \text{for } D^* \le 30 \tag{3.3-115}$$

$$v_{gj} = 0.030\left(\frac{\rho_g}{\rho_f}\right)^{-0.157} N_{\mu f}^{-0.562}\left[\frac{\sigma g(\rho_f - \rho_g)}{\rho_f^2}\right]^{1/4} \quad \text{for } D^* > 30 \tag{3.3-116}$$

where D^* is the Bond number given by Equation (3.3-6) and the viscosity number, $N_{\mu f}$, is given by

$$N_{\mu f} = \frac{\mu_f}{\left\{\rho_f \sigma\left[\frac{\sigma}{g(\rho_f - \rho_g)}\right]^{1/2}\right\}^{1/2}} \quad . \tag{3.3-117}$$

The correlation labeled Churn Turbulent Bubbly Flow is by Zuber and Findlay.[3.3-35,3.3-36] The distribution parameter is given by the modified Rouhani correlation[3.3-38] used in TRAC-BF1,[3.3-3] Equations (3.3-113) and (3.3-114), and the drift velocity is given by

$$v_{gj} = 1.41\left[\frac{\sigma g(\rho_f - \rho_g)}{\rho_f^2}\right]^{1/4} \quad . \tag{3.3-118}$$

For intermediate pipes (for low upflow, downflow, and countercurrent flow rates) and large pipes (all cases), the churn turbulent bubbly flow correlation is applied when

$$j_g^+ = \frac{j_g}{\left[\frac{\sigma g(\rho_f - \rho_g)}{\rho_f^2}\right]^{\frac{1}{4}}} \le j_{g1}^+ = 0.5 \quad .$$

The Kataoka-Ishii correlation is applied when

$$j_g^+ \ge j_{g2}^+ \tag{3.3-119}$$

where $j_{g2}^+ = 2.5$. Linear interpolation is used between the two correlations.

Putney has also placed a countercurrent flow limitation (CCFL) on the drift flux parameters. The limitation is based on the Kutateladze condition (see Section 3.4.7), that is

$$|Ku_g|^{1/2} + m|Ku_f|^{1/2} = Ku_{crit}^{1/2} \tag{3.3-120}$$

where

$$Ku_g = \frac{\alpha_g v_g \rho_g^{\frac{1}{2}}}{[\sigma g(\rho_f - \rho_g)]^{\frac{1}{4}}} \tag{3.3-121}$$

$$Ku_f = \frac{\alpha_f v_f \rho_f^{\frac{1}{2}}}{[\sigma g(\rho_f - \rho_g)]^{\frac{1}{4}}} \tag{3.3-122}$$

$$m = 1 \tag{3.3-123}$$

and Ku_{crit} (using linear interpolation) is given by **Table 3.3-3**. This table for Ku_{crit} as a function of D^* is from Wallis and Makkenchery.[3.3-39] This has been used successfully in the RELAP-UK code.[3.3-40] The value of m = 1 was also used in the RELAP-UK code.

Table 3.3-3 Values of Ku_{crit}.

D^*	Ku_{crit}
≤ 2	0
4	1.0
10	2.1
14	2.5
20	2.8
28	3.0
≥ 50	3.2

On the flooding curve, the drift flux parameters satisfy the relationship

$$v_{gj} = \frac{(1 - \alpha_g C_0) C_0 K u_{crit} \left[\frac{(\rho_f - \rho_g) g \sigma}{\rho_f^2} \right]^{1/4}}{\alpha_g C_0 \left(\frac{\rho_g}{\rho_f} \right)^{1/2} + m^2 (1 - \alpha_g C_0)} \quad .$$

(3.3-124)

This flooding limit for v_{gj} is applied for mass fluxes (G) larger than 100 kg/m^2•s and for $\alpha_g \geq 0.5$. Linear interpolation is used down to a mass flux of 50 kg/m^2•s and to $\alpha_g = 0.3$, at which point the normal drift flux correlations are used.

3.3.6.5 Slug Flow. For vertical slug flow, the drift flux model is used. For non-vertical slug flow, the drag coefficient model is used.

The drag coefficient model will first be discussed. Slug flow for non-vertical geometry is modeled as a series of Taylor bubbles separated by liquid slugs containing small bubbles. A sketch of a slug flow pattern is shown in **Figure 3.3-5**. The Taylor bubble has a diameter nearly equal to the pipe diameter and a length varying from 1 to 100 pipe diameters.
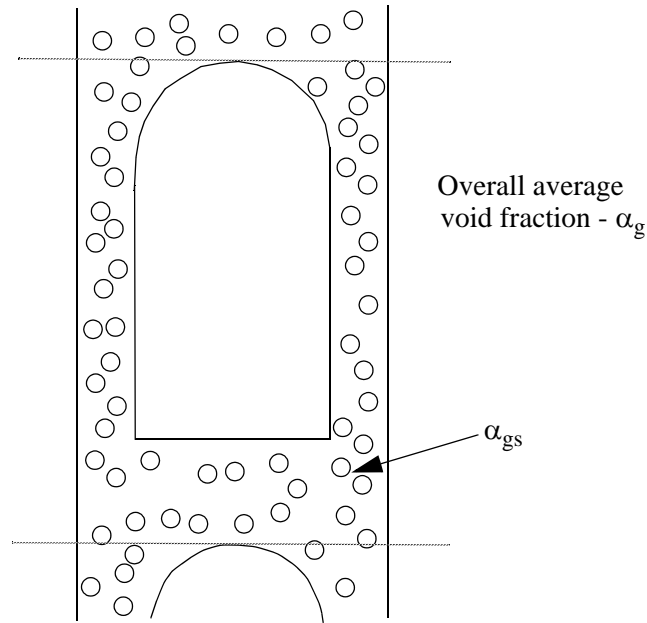
Figure 3.3-5 Slug flow pattern.

Let α_{gs} be the average void fraction in the liquid film and slug region. The void fraction of a single Taylor bubble, α_b, in the total mixture is then

$$\alpha_b = \frac{\alpha_g - \alpha_{gs}}{1 - \alpha_{gs}} \quad . \tag{3.3-125}$$

The Taylor bubble frontal area per unit volume is $\frac{\alpha_b}{L}$, where L is the cell length. Consequently, the interfacial area per unit volume, a_{gf}, for slug flow is

$$a_{gf} = \frac{\alpha_b}{L} + \left(\frac{3.6\alpha_{gs}}{d_o}\right)(1 - \alpha_b) \quad . \tag{3.3-126}$$

To provide a smooth transition into and out of slug flow, α_{gs} in Equation (3.3-125) is considered as a free parameter varying from α_{BS} at the bubbly-to-slug flow regime transition to nearly zero at the slug-to-annular-mist flow regime transition. The variation is represented by the exponential expression

$$\alpha_{gs} = \alpha_{BS}\exp\left[-8\left(\frac{\alpha_g - \alpha_{BS}}{\alpha_{SA} - \alpha_{BS}}\right)\right] \quad . \tag{3.3-127}$$

The drag coefficient for Taylor bubbles in non-vertical slug flow is given by Ishii and Chawla[3.3-7] as

$$C_D = 10.9\left(\frac{D'}{D}\right)(1 - \alpha_b)^3 \tag{3.3-128}$$

where D' is the Taylor bubble diameter and α_b is given by combining Equations (3.3-125) and (3.3-127).

The drag coefficient for small bubbles in non-vertical slug flow is given by Ishii and Chawla[3.3-7] by Equation (3.3-74).

For vertical slug flow, the interphase drag and shear terms are calculated using the same drift flux correlations that are used in vertical bubbly flow.

3.3.6.6 Annular-Mist Flow. Annular-mist flow is characterized by a liquid film along the wall and a vapor/gas core containing entrained liquid droplets. Let α_{ff} be the average liquid volume fraction of the liquid film along the wall. Then, from simple geometric considerations, the interfacial area per unit volume can be shown to be

$$a_{gf} = \left(\frac{4C_{ann}}{D}\right)(1 - \alpha_{ff})^{1/2} + \left(\frac{3.6\alpha_{fd}}{d_o}\right)(1 - \alpha_{ff}) \tag{3.3-129}$$

where C_{ann} is a roughness parameter introduced to account for waves in the liquid wall film, α_{fd} is the average liquid volume fraction in the vapor/gas core, for which

$$\alpha_{fd} = \frac{\alpha_f - \alpha_{ff}}{1 - \alpha_{ff}} \tag{3.3-130}$$

and d_o is the average diameter of the drops. For an annulus component, all the liquid is in the film and there are no drops. Thus, $\alpha_{ff} = \alpha_f$ and $\alpha_{fd} = 0$ are used for an annulus. This was necessary to get downcomer penetration following a cold leg break. This is discussed more in Volume IV.

A simple relation based on the flow regime transition criterion and liquid Reynolds number is used to correlate the average liquid film volume fraction. For vertical flow regimes, the entrainment relation is

$$\alpha_{ff} = \alpha_f C_f \exp\left[-7.5\times10^{-5}\left(\frac{\alpha_g v_g}{u_c}\right)^6\right] \tag{3.3-131}$$

where u_c is the critical entrainment superficial velocity given by the combination of Equations (3.3-13) and (3.3-15).

For horizontal flow regimes, the entrainment relation is

$$\alpha_{ff} = \alpha_f C_f \exp\left[-4.0\times10^{-5}\left(\frac{|v_g - v_f|}{v_{gL}}\right)^6\right] \tag{3.3-132}$$

where v_{gL} is the horizontal stratification critical velocity given by Equation (3.3-29). The term C_f is expressed as

$$C_f = 1.0 - 10^{-4}\left(\alpha_f \rho_f |v_f| \frac{D}{\mu_f}\right)^{0.25}. \tag{3.3-133}$$

The interfacial friction factor, f_i, for the liquid film takes the place of C_D in Equation (3.3-68), and is described by a standard correlation in the laminar region and is based on Wallis' correlation in the turbulent region.[3.3-24] In the turbulent region, the Wallis correlation was modified to use the factor 0.02 rather than 0.005. This is the value used in RELAP5/MOD1,[3.3-41] and it was selected because of the RELAP5/MOD3 assessment (see Volume IV of the manual for details). It is based on the vapor/gas Reynolds number defined as

$$Re_g = \frac{\rho_g |v_g - v_f| D_g}{\mu_g} \qquad (3.3\text{-}134)$$

where

$D_g \qquad = \qquad \alpha_g^{1/2} D$ is the equivalent wetted diameter $\qquad\qquad (3.3\text{-}135)$

$\mu_g \qquad = \qquad$ viscosity of the vapor/gas phase. $\qquad\qquad\qquad (3.3\text{-}136)$

The values of f_i are

$f_i \qquad = \qquad \dfrac{64}{Re_g} \qquad$ for $Re_g \leq 500$

$$= \qquad \left(\frac{1{,}500 - Re_g}{1{,}000}\right)\frac{64}{Re_g} + \left(\frac{Re_g - 500}{1{,}000}\right)0.02\{1 + 150[1 - (1 - \alpha_{ff})^{1/2}]\} \quad ,$$

for $500 < Re_g < 1{,}500$

$$= \qquad 0.02\{1 + 150[1\text{-}(1 - \alpha_{ff})^{1/2}]\} \text{ for} \qquad Re_g \geq 1{,}500. \qquad (3.3\text{-}137)$$

The interfacial drag coefficient C_D for the drops is given by Ishii and Chawla[3.3-7] from Equation (3.3-74).

For bundles in vertical annular-mist flow or in vertical slug/annular-mist transition flow, a maximum of the interphase drag coefficient from the EPRI drift flux correlation (bubbly-slug flow) and the interphase drag coefficient from annular-mist flow (friction factor/drag coefficient previously discussed). This was necessary to remove inaccurate low void predictions in rod bundles. This is discussed more in Volume IV.

For an annulus component and a multid component (no drops option), all the liquid is in the film (i.e., no drops) when in the annular mist flow regime.

3.3.6.7 Vertical Stratified Flow. For the junction above the vertically stratified volume (junction j in **Figure 3.3-6**), the interphase drag is based on the void fraction in the volume above (volume L). This is consistent with the junction-based interphase drag. This is obtained as follows: The void fraction $\alpha_{g,j}^*$ used in the junction j for the junction-based interphase drag is given by

$$\alpha_{g,j}^* = w_j \bullet \alpha_{g,K}^* + (1 - w_j) \bullet \alpha_{g,L} \qquad (3.3\text{-}138)$$
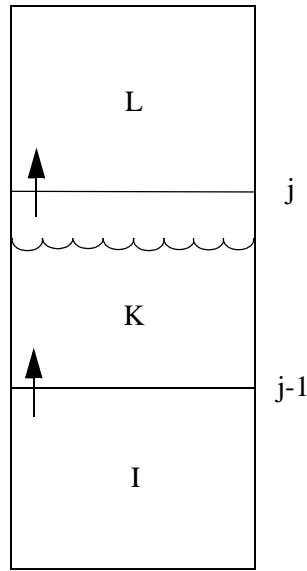
Figure 3.3-6 Three vertical volumes with the middle volume being vertically stratified.

and is similar to Equation (3.3-34) except that $\alpha_{g,K}$ is replaced by $\alpha_{g,K}^{*}$. This void fraction is given by

$$\alpha_{g,K}^{*} \;=\; \text{strat} \bullet \alpha_{g,L} + (1 - \text{strat}) \bullet \alpha_{g,K} \qquad\qquad (3.3\text{-}139)$$

where strat takes on values from 0 to 1. For a vertically stratified volume, strat = 1, $\alpha_{g,K}^{*} = \alpha_{g,L}$ and $\alpha_{g,j}^{*} = \alpha_{g,L}$. For a non-vertically stratified volume, strat = 0, $\alpha_{g,K}^{*} = \alpha_{g,K}$, and $\alpha_{g,j}^{*}$ is given by Equation (3.3-34). The smoothing parameter strat is given by

$$\text{strat} \;=\; \text{strat1} \bullet \text{strat2} \qquad\qquad (3.3\text{-}140)$$

where

$$\text{strat1} \;=\; 1 - e^{-0.5\alpha_{f,L}} \qquad\qquad (3.3\text{-}141)$$

$$\text{strat2} \;=\; 2\!\left(1 - \frac{v_m}{v_{Tb}}\right) \quad . \qquad\qquad (3.3\text{-}142)$$

Both strat1 and strat2 are limited to values between 0 and 1. Equation (3.3-141) for strat1 is a modification of the approach used in RELAP5/MOD2. The variable strat1 exponentially turns off the stratification effect when the volume above (volume L) becomes empty of liquid. When $\alpha_{f,L} = 0.01$, strat1

= 0.005. For strat2, the variables v_m and v_{Tb} are the mixture velocity based on the volume centered velocities and Taylor bubble rise velocity given by Equation (3.3-5).

A different method is used at junction j-1 below the vertically stratified volume. Equations (3.3-138), (3.3-139), (3.3-140), and (3.3-142) are used, however, strat1 is given by

$$strat1 = 20 \, (\alpha_{level} - 0.05) \tag{3.3-143}$$

where

$$\alpha_{level} \quad = \quad \frac{\alpha_{g,\,L} - \alpha_{g,\,K}}{\alpha_{g,\,L} - \alpha_{g,\,I}}. \tag{3.3-144}$$

The variable α_{level} is an implied non-dimensional mixture level position within volume K. The coding is generalized to handle the case where the volumes and junctions are oriented downward. The vertical stratification model is not intended to be a mixture level model, and a more mechanistic level tracking model is described in Section 3.4.8.

If more than one junction is connected to the top, the volume above with the smallest void fraction will be treated as the "above volume;" if more than one junction is connected to the bottom, the volume below with the largest void fraction will be treated as the "below volume."

3.3.6.8 Horizontal Stratified Flow. By simple geometric consideration, one can show that the interfacial area per unit volume is

$$a_{gf} = 4C_{st}\frac{\sin\theta}{\pi D} \tag{3.3-145}$$

where C_{st} is a roughness parameter introduced to account for surface waves and is set to 1 at the present time. (See **Figure 3.1-2** for the definition of angle θ).

The interface Reynolds number is defined with the vapor/gas properties and regarding liquid as the continuous phase for which

$$Re_i = \frac{\rho_g |v_g - v_f| D_i}{\mu_g} \tag{3.3-146}$$

where the equivalent wetted diameter, D_i, for the interface is

$$D_i = \frac{\alpha_g \pi D}{\theta + \sin \theta} \quad .$$ (3.3-147)

The interfacial friction factor, f_i, replaces C_D in Equation (3.3-68) and is obtained by assuming typical friction factor relationships for which

$$f_i = \max\left(\frac{64}{Re_i}, \frac{0.3164}{Re_i^{0.25}}\right) \quad .$$ (3.3-148)

3.3.6.9 Inverted Flow Regimes. These regimes arise when there is hot vapor/gas in the cell and either hot walls or the reflood model is on. The interphase drag relationships for post-CHF inverted flow regimes are treated in a similar fashion to the corresponding pre-CHF flow regimes, except that the roles of vapor/gas and liquid are interchanged.

3.3.6.9.1 Inverted Annular Flow--Immediately downstream of a quench front or CHF position, there may be an inverted annular flow region if the combination of liquid flow and subcooling are high enough. The physical concept in the model is the presence of vapor/gas bubbles in the liquid core (just as there are liquid drops in the vapor/gas core region for annular-mist flow) and an annular vapor/gas layer between the walls and the core. The drag term [f_{gf} in Equation (3.3-68)] is the sum of the drag between the bubbles and the liquid in the core and the drag between the vapor/gas annulus and the outer surface of the core.

The drag coefficient for the bubbles is the Ishii-Chawla correlation given by Equation (3.3-74), and the interfacial area is

$$\alpha_{gf} = \frac{3.6\alpha_{gb}}{d_o}(1 - \alpha_B)$$ (3.3-149)

where

α_{gb} = the vapor/gas void fraction in the liquid core

d_o = the bubble diameter

α_B = the fraction of the total area occupied by the vapor/gas annulus.

The Weber number used to solve for the bubble diameter is 10. The annulus vapor/gas void fraction is an exponential function of the total vapor/gas void fraction, similar to Equation (3.3-127), and is presented in Volume IV of the ATHENA manuals. The core vapor/gas void fraction is

$$\alpha_{gb} = \frac{V_{gas,\,core}}{V_{core}} = \frac{V_{gas,\,tot} - V_{gas,\,ann}}{V_{tot} - V_{gas,\,ann}} = \frac{\alpha_g - \alpha_B}{1 - \alpha_B}$$
(3.3-150)

where

V_{core} = volume of the liquid core including bubbles

V_{tot} = volume of control volume.

The annular shear force uses the Bharathan et al.[3.3-42] equation for the drag coefficient

$$C_D = 4[0.005 + A(\delta^*)^B]$$
(3.3-151)

where

$$\log_{10} A = -0.56 + \frac{9.07}{D^*}$$
(3.3-152)

$$B = 1.63 + \frac{4.74}{D^*}$$
(3.3-153)

$$\delta^* = \delta\left[\frac{(\rho_f - \rho_g)g}{\sigma}\right]^{1/2}.$$
(3.3-154)

The term δ^* is the liquid wall film Deryagin number for which δ is the film thickness, and D^* is the dimensionless diameter Bond number given by Equation (3.3-6). The film thickness δ is defined in Volume IV.

The interfacial area of the vapor/gas annular film per unit length in a pipe is

$$a_{gf,\,ann} = \frac{\pi D'}{\frac{\pi}{4}D^2} = \frac{4D'}{D^2}$$
(3.3-155)

where

D' = inner diameter of annulus

D = diameter of pipe.

$$\frac{V_{core}}{V_{tot}} = \frac{\frac{\pi}{4}D'^2}{\frac{\pi}{4}D^2} = \frac{D'^2}{D^2} = 1 - \alpha_B \qquad (3.3\text{-}156)$$

where

V_{core} = idealized volume of the vapor/gas core per unit length

V_{tot} = volume of control volume per unit length.

Solving for the ratio $\frac{D'}{D}$ from Equation (3.3-156) and putting it into Equation (3.3-155) yields

$$a_{gf, ann} = \frac{4}{D}(1 - \alpha_B)^{1/2} \quad . \qquad (3.3\text{-}157)$$

3.3.6.9.2 Inverted Slug Flow--The inverted slug flow regime as envisioned by DeJarlais and Ishii[3.3-43] consists of bubble-impregnated liquid droplets (see **Figure 3.3-7**). The coded interfacial friction coefficients recognize the liquid droplets, vapor/gas blanket, and liquid slugs, but not the presence of bubbles in the slugs. Contributions to the interfacial friction are recognized then, as coming from two sources: (a) the liquid droplet interfaces in the vapor/gas annulus and (b) the liquid slug/annulus interface. It is assumed that the liquid slugs are so long that any contributions to interfacial friction at their ends are negligible.
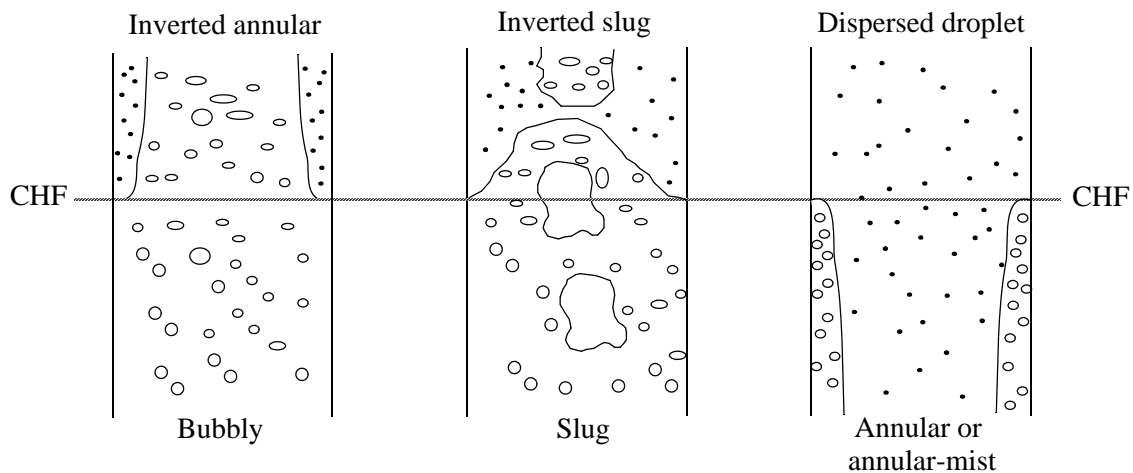
Figure 3.3-7 Flow regimes before and after the critical heat flux (CHF) transition.

The interfacial areas for the annulus/droplet portion and the slug/annulus portion are derived analogously to those for nonvertical slug flow (Section 3.3.6.5). The void fraction of the liquid slug, α_B, is analogous to that for a Taylor bubble, α_{Tb}, and the average droplet void fraction in the vapor/gas blanket, α_{drp}, is analogous to the average void fraction, α_{gs}, in the liquid annulus for slug flow. That is, the interfacial areas are computed for inverted slug flow by simply reversing the liquid and vapor/gas phases from slug flow. The droplet void fraction, α_{drp}, in the vapor/gas annulus is an expression that exponentially increases the portion of α_f due to droplets as α_g increases until the transition void fraction, α_{SA}, is reached, at which point all of the liquid is appropriately assumed to be in droplet form. The value for the Weber number used is 12.0.

The drag coefficients for the annulus/droplet portion and the slug/annulus portion are analogous to those for non-vertical slug flow, except that the liquid and vapor/gas phases are reversed.

3.3.6.9.3 *Mist Flow*--The mist flow regime is discussed in Section 3.3.6.4, Dispersed Flow.

For mist pre-CHF, We = 3.0 and $\mu_m = \dfrac{\mu_g}{(\alpha_g)^{2.5}}$; for mist and mist post-CHF, We = 12.0 and $\mu_m = \mu_g$.

3.3.7 Coefficient of Virtual Mass

The coefficient of virtual mass is determined based on the junction flow regime map. The calculation of the drag due to the virtual mass effect (dynamic drag) is based on an objective and symmetric formulation of the relative acceleration.[3.3-44] The inertial drag force per unit volume in the phasic momentum equations is written as

$$FA_{gf} = -C\alpha_g(1-\alpha_g)\rho\left[\frac{\partial}{\partial t}(v_g - v_f)\right]$$
(3.3-158)

where

$$\rho \quad = \quad \alpha_g\rho_g + (1 - \alpha_g)\rho_f$$
(3.3-159)

$$FA_{gf} \quad = \quad \text{force per unit volume due to dynamic drag.}$$

The factor, $C\alpha_g(1 - \alpha_g)\rho$, is chosen to ensure a smooth transition between $\alpha_g = 0$ and $\alpha_g = 1.0$. This factor also gives the proper limit, $C\alpha_g\rho_f$ in the thinly dispersed bubbly flow, and $C(1 - \alpha_g)\rho_g$ in the dispersed droplet flow. The virtual mass coefficient, C, is given[3.3-45] as

$$C = \frac{1}{2}\frac{(1 + 2\alpha_g)}{(1 - \alpha_g)} \quad \text{for } 0 \le \alpha_g \le 1/2$$
(3.3-160)

$$C = \frac{1}{2}\frac{(3 - 2\alpha_g)}{\alpha_g} \quad \text{for } 1/2 \leq \alpha_g \leq 1 \ . \tag{3.3-161}$$

It may be appropriate to assume that $C = 0$ should be used for separated or stratified flow. At present, the value of C defined by Equations (3.3-160) and (3.3-161) is used without regard to the flow regime.

3.3.8 Wall Friction

The wall friction is determined based on the volume flow regime map. The wall friction force terms include only wall shear effects. Losses due to abrupt area change are calculated using mechanistic form-loss models. Other losses due to elbows or complicated flow passage geometry are modeled using energy-loss coefficients that must be input by the user.

Emphasis was placed on obtaining reasonable values for wall friction in all flow regimes in the development of the wall friction model. The flow regime models are discussed in Section 3.3.1 through Section 3.3.4.

The wall friction model is based on a two-phase multiplier approach in which the two-phase multiplier is calculated from the Heat Transfer and Fluid Flow Service (HTFS)-modified Baroczy correlation.[3.3-46] The individual phasic wall friction components are calculated by apportioning the two-phase friction between the phases using a technique derived by Chisholm[3.3-47] from the Lockhart-Martinelli[3.3-48] model. The partitioning model is based on the assumption that the frictional pressure drop may be calculated using a quasi-steady form of the momentum equation. As discussed in Section 3.3.6, this wall friction partitioning model is used with the drag coefficient method of the interphase friction model. The drift flux method of the interphase friction model uses a wall friction model that partitions the total wall friction force to the phases based on the phasic volume fraction rather than using the Chisholm partition model.

3.3.8.1 The Two-Phase Friction Multiplier Approach. The Lockhart-Martinelli model computes the overall two-phase friction pressure drop in terms of the liquid-alone wall friction pressure drop, that is

$$\left(\frac{dP}{dx}\right)_{2\phi} = \phi_f^2 \left(\frac{dP}{dx}\right)_f \tag{3.3-162}$$

or in terms of the vapor/gas-alone wall friction pressure drop, that is

$$\left(\frac{dP}{dx}\right)_{2\phi} = \phi_g^2 \left(\frac{dP}{dx}\right)_g \tag{3.3-163}$$

where ϕ_f and ϕ_g are the liquid-alone and vapor/gas-alone two-phase Darcy-Weisbach friction multipliers, respectively. The phasic wall friction pressure gradients are expressed as

$$\left(\frac{dP}{dx}\right)_f = \frac{\lambda_f'(Re_f')M_f^2}{2D\rho_f A^2} \qquad (3.3\text{-}164)$$

for the liquid alone, and

$$\left(\frac{dP}{dx}\right)_g = \frac{\lambda_g'(Re_g')M_g^2}{2D\rho_g A^2} \qquad (3.3\text{-}165)$$

for the vapor/gas alone, where the prime indicates the liquid and vapor/gas-alone Darcy-Weisbach friction factors, respectively, calculated at the respective Reynolds numbers, given by

$$Re_f' = \frac{M_f D}{\mu_f A} \qquad (3.3\text{-}166)$$

and

$$Re_g' = \frac{M_g D}{\mu_g A} \quad . \qquad (3.3\text{-}167)$$

The liquid and vapor/gas mass flow rates, respectively, are defined as

$$M_f = \alpha_f \rho_f v_f A \qquad (3.3\text{-}168)$$

and

$$M_g = \alpha_g \rho_g v_g A \quad . \qquad (3.3\text{-}169)$$

Throughout the current literature, the overall two-phase friction pressure gradient is calculated using two-phase friction multiplier correlations. However, regardless of the correlation used, the multipliers may be interrelated using Equations (3.3-162) through (3.3-165) and the Lockhart-Martinelli[3.3-48] ratio defined as

$$\chi^2 = \frac{\left(\dfrac{dP}{dx}\right)_f}{\left(\dfrac{dP}{dx}\right)_g} = \frac{\phi_g^2}{\phi_f^2} \quad . \tag{3.3-170}$$

3.3.8.2 The HTFS Two-Phase Friction Multiplier Correlation. The HTFS correlation[3.3-46] is used to calculate the two-phase friction multipliers. This correlation was chosen because it is correlated to empirical data over very broad ranges of phasic volume fractions, phasic flow rates and phasic flow regimes. The correlation has also been shown to give good agreement with empirical data.

The HTFS correlation for the two-phase friction multiplier[3.3-46] is expressed as

$$\phi_f^2 = 1 + \frac{C}{\chi} + \frac{1}{\chi^2} \tag{3.3-171}$$

for the liquid-alone multiplier, or

$$\phi_g^2 = \chi^2 + C\chi + 1 \tag{3.3-172}$$

for the vapor/gas-alone multiplier, where C is the correlation coefficient and χ is the Lockhart-Martinelli ratio given by Equation (3.3-170). The correlation coefficient, C, is expressed in terms of scalar mass flux, G, and the Baroczy dimensionless property index, Λ, such that

$$C = -2 + f_1 (G) \, T_1 (\Lambda, G) \tag{3.3-173}$$

where

$$f_1 (G) \quad = \quad 28 - 0.3 \sqrt{G} \tag{3.3-174}$$

$$T_1 (\Lambda, G) = \quad \exp\left[-\frac{(\log_{10}\Lambda + 2.5)^2}{2.4 - G(10^{-4})} \right] \tag{3.3-175}$$

$$\Lambda \quad = \quad \frac{\rho_g}{\rho_f}\left(\frac{\mu_f}{\mu_g}\right)^{0.2} . \tag{3.3-176}$$

The terms ρ, μ, α, and v denote the density, viscosity, volume fraction, and velocity, respectively.

If the HTFS correlation is combined with the wall friction formulations by combining Equations (3.3-162) through (3.3-165), (3.3-168) through (3.3-170), and (3.3-172), then

$$\left(\frac{dP}{dx}\right)_{2\phi} = \phi_f^2\left(\frac{dP}{dx}\right)_f = \phi_g^2\left(\frac{dP}{dx}\right)_g = \frac{1}{2D}\{\lambda_f'\rho_f(\alpha_f v_f)^2 + C[\lambda_f'\rho_f(\alpha_f v_f)^2 \lambda_g'\rho_g(\alpha_g v_g)^2]^{1/2}$$
$$+ \lambda_g'\rho_g(\alpha_g v_g)^2\} \ . \tag{3.3-177}$$

3.3.8.3 Partitioning of Wall Friction. Two-phase friction can be modeled in terms of two-phase friction multipliers and known friction factors using the method developed by Lockhart-Martinelli.[3.3-48] Chisholm[3.3-47] also developed a theoretical basis for the Lockhart-Martinelli model that provides a rationale for partitioning the overall wall friction between the phases which is independent of the model for interfacial friction. As discussed previously, this method is used with the drag coefficient method of the interphase friction model.

From the theoretical basis developed by Chisholm, the phasic momentum equations can be expressed in scalar form as

$$\alpha_f A\left(\frac{dP}{dx}\right)_{2\phi} - \tau_f p_f + S_{FI} = 0 \tag{3.3-178}$$

for the liquid, and

$$\alpha_g A\left(\frac{dP}{dx}\right)_{2\phi} - \tau_g p_g - S_{FI} = 0 \tag{3.3-179}$$

for the vapor/gas, where τ_f and τ_g are the liquid and vapor/gas wall shear stresses, respectively, p_f and p_g are the liquid and vapor/gas wetted perimeters, respectively, and S_{FI} is a stress gradient due to interphase friction. Eliminating the overall pressure gradient between these two equations determines the interfacial friction term in terms of the ratio of the phasic shear stresses and phasic wetted perimeters. The result is

$$\frac{1 + S_R\left(\frac{\alpha_g}{\alpha_f}\right)}{(1 - S_R)} = \frac{\left(\frac{\tau_f p_f}{\alpha_f}\right)}{\left(\frac{\tau_g p_g}{\alpha_g}\right)} = Z^2 \tag{3.3-180}$$

where the interphase friction term, S_R, is defined as

$$S_R = \cfrac{S_{FI}}{\alpha_g A \left(\cfrac{dP}{dx}\right)_{2\phi}} \quad .$$ (3.3-181)

Equation (3.3-180) can be rearranged to give a relation for the interfacial shear stress gradient in terms of the ratio of the phasic wall shear forces. This relation can then be substituted into the quasi-static momentum balances to give a relation for the individual phasic wall shear force gradients in terms of the overall wall friction and the ratio of the phasic wall shear stresses. These are

$$\tau_f p_f = \alpha_f \left.\frac{dP}{dx}\right|_{2\phi} \left(\frac{Z^2}{\alpha_g + \alpha_f Z^2}\right)$$ (3.3-182)

and

$$\tau_g p_g = \alpha_g \left.\frac{dP}{dx}\right|_{2\phi} \left(\frac{1}{\alpha_g + \alpha_f Z^2}\right) \quad .$$ (3.3-183)

These relations are nothing more than a rearrangement of the quasi-static momentum equations and have only eliminated one unknown, the interfacial shear stress in terms of another unknown, Z^2, the ratio of the phasic wall friction gradients. Chisholm postulated that the liquid wall shear stress could be determined using the liquid Darcy-Weisbach friction factor computed from the liquid Reynolds number based on liquid properties as

$$\tau_f = \frac{\lambda(Re_f)\rho_f v_f^2}{4} \frac{\rho_f v_f^2}{2}$$ (3.3-184)

where

$\lambda(Re_f)$	=	liquid Darcy friction factor	(3.3-185)
Re_f	=	liquid Reynolds number	(3.3-186)
	=	$\dfrac{\rho_f v_f D_f}{\mu_f}$	(3.3-187)
D_f	=	liquid hydraulic diameter	(3.3-188)

$$= \frac{4A_f}{p_f} \tag{3.3-189}$$

$$A_f \quad = \quad \text{liquid flow area} \tag{3.3-190}$$

$$= \quad \alpha_f A \tag{3.3-191}$$

$$p_f \quad = \quad \text{liquid wetted perimeter} \tag{3.3-192}$$

$$= \quad \alpha_{fw} p \tag{3.3-193}$$

where α_{fw} is the liquid fraction on the wall. The vapor/gas shear stress is defined in an analogous manner based on vapor/gas properties. Substituting the liquid shear stress from Equation (3.3-184) and the liquid wetted perimeter from Equation (3.3-193) and the analogous expressions for the vapor/gas friction factor and wetted perimeter, defines the unknown parameter Z^2 by the expression

$$Z^2 = \frac{\lambda_f(Re_f)\rho_f v_f^2 \frac{\alpha_{fw}}{\alpha_f}}{\lambda_g(Re_g)\rho_g v_g^2 \frac{\alpha_{gw}}{\alpha_g}} \quad . \tag{3.3-194}$$

Substituting Equation (3.3-194) into the relations for the phasic wall friction forces Equations (3.3-182) and (3.3-183) yields equations which determine the magnitude of the phasic wall friction force in terms of the overall wall friction force and the ratio of the phasic wall frictional forces, independent of the formulation for the interfacial shear forces and independent of the particular model for the overall wall frictional force.

It should be noted that the calculation of the phasic friction factors using the Reynolds numbers defined above and the assumption that two-phase flows behave similarly to single-phase flows in the laminar, transition, and turbulent regimes provides the rationale relating Equations (3.3-182) and (3.3-183) to empirical data. It is this same rationale that allows the correlating term Z^2 to be expressed in terms of friction factors that are independent of interphase friction as given by Equation (3.3-180). It is this equation that forms the basis for apportioning the overall two-phase wall friction between the phases.

3.3.8.4 ATHENA Wall Friction Coefficients. The ATHENA phasic momentum equations, Equations (3.1-6) and (3.1-7) can be written in a quasi-static form similar to Equations (3.3-178) and (3.3-179), except that the wall friction terms are in terms of the ATHENA wall friction coefficients instead of phasic wall shear stresses. Comparison of these two forms of the momentum equations provides a definition of the ATHENA phasic wall friction coefficients as

$$FWF(\alpha_f \rho_f v_f)A = \tau_f p_f = \alpha_f \left(\frac{dP}{dx}\right)\bigg|_{2\phi} \left(\frac{Z^2}{\alpha_g + \alpha_f Z^2}\right)A \tag{3.3-195}$$

and

$$FWG(\alpha_g \rho_g v_g)A = \tau_g p_g = \alpha_g \left(\frac{dP}{dx}\right)\bigg|_{2\phi} \left(\frac{1}{\alpha_g + \alpha_f Z^2}\right)A \quad . \tag{3.3-196}$$

Taking the sum of these two equations gives the overall quasi-static, two-phase wall friction pressure gradient as

$$FWF(\alpha_f \rho_f v_f)A + FWG(\alpha_g \rho_g v_g)A = \left(\frac{dP}{dx}\right)\bigg|_{2\phi} A \quad . \tag{3.3-197}$$

3.3.8.5 Flow Regime Factors for Phasic Wall Friction. Phasic wall friction is expressed in terms of wall shear stress, which, in turn, requires knowledge of the surface area wetted by each phase. From the flow regime model discussed in Section 3.3.1 through Section 3.3.4 expressions for the wall film phasic volume fractions can be derived. Using these expressions, the phasic wall friction factor that appears in Equations (3.3-184) may then be computed.

In the flow regime map, eight flow regimes are modeled, which are: for pre-CHF heat transfer, the bubbly, slug, and annular-mist; for post-CHF heat transfer, the inverted-annular, inverted-slug and mist; and for stratified flow, the vertically and horizontally stratified. For the transition regime between pre- and post-CHF heat transfer, an interpolation scheme is also implemented in the code.

To implement flow regime effects in the two-phase wall friction model, first consider the wall liquid and vapor/gas volume fractions. These terms are

$$\frac{p_f}{p} = \alpha_{fw}, \tag{3.3-198}$$

which represents the liquid volume fraction in the wall film, and

$$\frac{p_g}{p} = \alpha_{gw}, \tag{3.3-199}$$

which represents the vapor/gas volume fraction in the wall film, where the terms p_f, p_g, and p are the perimeters wetted by the liquid, vapor/gas, and mixture, respectively. Then, from the flow regime model, these are formulated for all of the flow regimes as follows:

For the bubbly regime,

$$\alpha_{fw} = \alpha_f \text{ and } \alpha_{gw} = \alpha_g \tag{3.3-200}$$

where α_f, α_g are the overall liquid and vapor/gas volume fractions, respectively.

For the slug regime,

$$\alpha_{fw} = 1 - \alpha_{gs} \text{ and } \alpha_{gw} = \alpha_{gs} \tag{3.3-201}$$

where α_{gs} is given by Equation (3.3-127).

For the annular-mist regime,

$$\alpha_{fw} = (\alpha_{ff})^{1/4} \text{ and } \alpha_{gw} = 1 - (\alpha_{ff})^{1/4} \tag{3.3-202}$$

where α_{ff} is given by Equation (3.3-132).

For the inverted-annular regime,

$$\alpha_{fw} = 1 - (\alpha_{gg})^{1/4} \text{ and } \alpha_{gw} = (\alpha_{gg})^{1/4} \tag{3.3-203}$$

where α_{gg} is the inverted form of Equation (3.3-132).

For the inverted-slug regime,

$$\alpha_{fw} = \alpha_{fs} \text{ and } \alpha_{gw} = 1 - \alpha_{fs} \tag{3.3-204}$$

where α_{fs} is the inverted form of Equation (3.3-127).

For the mist regime,

$$\alpha_{fw} = \alpha_f \text{ and } \alpha_{gw} = \alpha_g \tag{3.3-205}$$

similar to the bubbly regime.

For the vertically stratified regime,

$$\alpha_{fw} = \alpha_f \text{ and } \alpha_{gw} = \alpha_g \ . \tag{3.3-206}$$

For the horizontally stratified regime,

$$\alpha_{fw} = 1 - \frac{\Theta}{\pi} \text{ and } \alpha_{gw} = \frac{\Theta}{\pi} \tag{3.3-207}$$

where θ results from the solution of Equation (3.1-61).

3.3.8.6 *The Friction Factor Model.* In ATHENA the Darcy-Weisbach friction factor is computed from correlations for laminar and turbulent flows with interpolation in the transition regime.There are two turbulent flow friction factor models. The first model computes the turbulent friction factor using an engineering approximation to the Colebrook-White correlation,[3.3-49] while the second model uses an exponential function with users' input coefficients.

The friction factor model is simply an interpolation scheme linking the laminar, laminar-turbulent transition, and turbulent flow regimes. The laminar friction factor is calculated as

$$\lambda_L = \frac{64}{Re\Phi_S} \text{ for } 0 \le Re \le 2,200 \tag{3.3-208}$$

where Re is the Reynolds number and Φ_S is a user-input shape factor for noncircular flow channels. For a noncircular flow channel such as a concentric annulus, the shape factor is given by[3.3-50]

$$\Phi_S = \frac{1 + \left(\frac{D_i}{D_o}\right)^2 + \frac{1 - \left(\frac{D_i}{D_o}\right)^2}{\ln\left(\frac{D_i}{D_o}\right)}}{\left(1 - \frac{D_i}{D_o}\right)^2} \ . \tag{3.3-209}$$

where D_i is the inner diameter of the annulus and D_o is the outer diameter of the annulus. As D_i becomes larger and approaches D_o, the shape factor Φ_S approaches 2/3. Other noncircular flow channels are discussed in **Reference 3.3-51**.

The friction factor in the transition region between laminar and turbulent flows is computed by reciprocal interpolation as

$$\lambda_{L,T} = \left(3.75 - \frac{8,250}{Re}\right)(\lambda_{T,3000} - \lambda_{L,2200}) + \lambda_{L,2200} \qquad \text{for } 2,200 < Re < 3,000 \qquad (3.3\text{-}210)$$

where $\lambda_{L,2200}$ is the laminar factor at a Reynolds number of 2,200, $\lambda_{T,3000}$ is the turbulent friction factor at a Reynolds number of 3,000, and the interpolation factor is defined to lie between zero and one.

The turbulent friction factor is given by the Zigrang-Sylvester approximation[3.3-52] to the Colebrook-White correlation,[3.3-49] which is

$$\frac{1}{\sqrt{\lambda_T}} = -2\log_{10}\left\{\frac{\varepsilon}{3.7D} + \frac{2.51}{Re}\left[1.14 - 2\log_{10}\left(\frac{\varepsilon}{D} + \frac{21.25}{Re^{0.9}}\right)\right]\right\} \qquad \text{for } 3,000 \leq Re \qquad (3.3\text{-}211)$$

where ε is the surface roughness, and the other variables have been defined previously. The Zigrang-Sylvester equation, Equation (3.3-211), has the advantage that it is an explicit relation for the friction factor, while the Colebrook-White correlation is a transcendental function requiring iteration for the determination of the friction factor. **Reference 3.3-52**[a] incorrectly uses 1.114 rather than the correct value 1.14.

3.3.8.7 Heated Wall Effect.
The friction model as described above applies to unheated surfaces. The user may correct the isothermal friction factor for the variation of the fluid viscosity near a heated surface using the relationship used in the VIPRE code.[3.3-53] This relation is given by

$$\frac{f}{f_{iso}} = 1 + \frac{P_H}{P_W}\left[\left(\frac{\mu_{wall}}{\mu_{bulk}}\right)^D - 1\right] \qquad (3.3\text{-}212)$$

where f_{iso} is the friction factor evaluated with properties at the bulk fluid temperature, P_H is the heated perimeter of the surface, P_W is the wetted perimeter of the volume, μ_{wall} is the viscosity evaluated at the surface temperature, μ_{bulk} is the viscosity evaluated at the bulk fluid temperature, and the exponent D is a user-input constant (viscosity ratio exponent). The default value in the code for the viscosity ratio exponent D is 0, which results in no viscosity variation effect on wall friction. Kays and Perkins[3.3-54] indicate a range of values for tubes from the literature for the exponent D. The values are 0.50 to 0.58 for liquid

---

a. Personal communication, D. J. Zigrang to R. A. Riemke, October 1993.

laminar flow, 0.25 for liquid turbulent flow, 1.0 to 1.35 for vapor/gas laminar flow, and -0.1 for vapor/gas turbulent flow. Kays and Perkins[3.3-54] use the term T_{wall}/T_{bulk} rather than the term μ_{wall}/μ_{bulk} for vapor/gas in Equation (3.3-212). Errors of ~ 5 % result because of this.

3.3.9 Wall Heat Transfer Models

In ATHENA the total wall heat flux (q''_{total}) is the heat flux to the vapor/gas plus the heat flux to the liquid. The general expression for the total wall heat flux is

$$q''_{total} = h_{wgg}(T_w - T_g) + h_{wgspt}(T_w - T_{spt}) + h_{wgspp}(T_w - T_{spp})$$
$$+ h_{wff}(T_w - T_f) + h_{wfspt}(T_w - T_{spt})$$

(3.3-213)

where

h_{wgg} = heat transfer coefficient to vapor/gas, with the vapor/gas temperature as the reference temperature (W/m^{2}K)

h_{wgspt} = heat transfer coefficient to vapor/gas, with the saturation temperature based on the total pressure as the reference temperature (W/m^{2}K)

h_{wgspp} = heat transfer coefficient to vapor/gas, with the saturation temperature based on the vapor partial pressure as the reference temperature (W/m^{2}K)

h_{wff} = heat transfer coefficient to liquid, with the liquid temperature as the reference temperature (W/m^{2}K)

h_{wfspt} = heat transfer coefficient to liquid, with the saturation temperature based on the total pressure as the reference temperature (W/m^{2}K)

T_w = wall temperature (K)

T_g = vapor/gas temperature (K)

T_f = liquid temperature (K)

T_{spt} = saturation temperature based on the total pressure (K)

T_{spp} = saturation temperature based on the partial pressure of vapor in the bulk (K).

A code user may flag a heat transfer structure as a reflood structure. Structures flagged as reflood structures employ axial conduction. ATHENA uses a slightly different wall heat transfer logic for reflood flagged surfaces than it does for other surfaces.

A boiling curve is used in ATHENA to govern the selection of the wall heat transfer correlations when the wall surface temperature is above the saturation temperature (superheated relative to the saturation temperature based on total pressure). When a hydraulic volume is voided and the adjacent surface temperature is subcooled, vapor condensation on the surface is predicted. If noncondensable gases are present, the phenomena is more complex because while boiling is a function of the wall superheat based on the total pressure, condensation is based on the partial pressure of vapor. When the wall temperature is less than the saturation temperature based on total pressure, but greater than the saturation temperature based on vapor partial pressure, a convection condition exists. **Figure 3.3-8** illustrates these three regions.
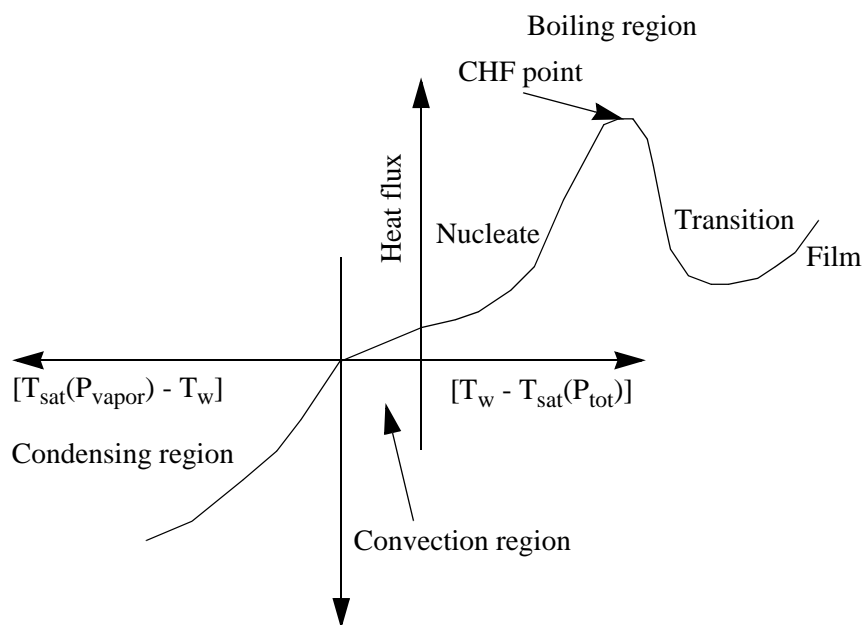
Figure 3.3-8 ATHENA boiling and condensing curves.

There are many factors to consider when deciding which convective heat transfer coefficient correlation to use. Relative factors that are addressed by the ATHENA logic are: (a) is the pressure above the critical pressure, (b) is the wall temperature above the saturation temperature, (c) is a noncondensable gas present, (d) is the fluid liquid, two-phase, or vapor/gas, (e) is the heat flux above the critical heat flux (CHF), and (f) is the film boiling heat flux greater than the transition boiling heat flux? The decision logic in ATHENA leads to the selection of the appropriate correlation for the heat transfer coefficient that is used to find the heat flux.

The heat transfer mode number is a code output parameter used to inform users of the heat transfer regime or correlation selected by the code. Twelve mode numbers from 0 to 11 are possible, as shown in **Figure 3.3-9**, where

T	=	TRUE
F	=	FALSE
P	=	total pressure
P_{crit}	=	critical pressure
X_n	=	noncondensable mass quality
X_e	=	equilibrium quality used in wall heat transfer (based on phasic specific enthalpies and mixture specific enthalpy, with the mixture specific enthalpy calculated using the flow quality)
	=	$$\frac{[X_{flow}h_g + (1 - X_{flow})h_f] - h_f^s}{h_g^s - h_f^s}$$
X_{flow}	=	flow quality
	=	$$\frac{\alpha_g \rho_g v_g}{\alpha_g \rho_g v_g + \alpha_f \rho_f v_f}$$
α_g	=	vapor/gas void fraction
T_w	=	wall temperature
T_{spt}	=	vapor saturation temperature based on total pressure
T_{spp}	=	vapor saturation temperature based on vapor partial pressure
T_f	=	liquid temperature
CHF	=	critical heat flux
q''	=	heat flux
q''_{NB}	=	nucleate boiling heat flux
q''_{FB}	=	film boiling heat flux
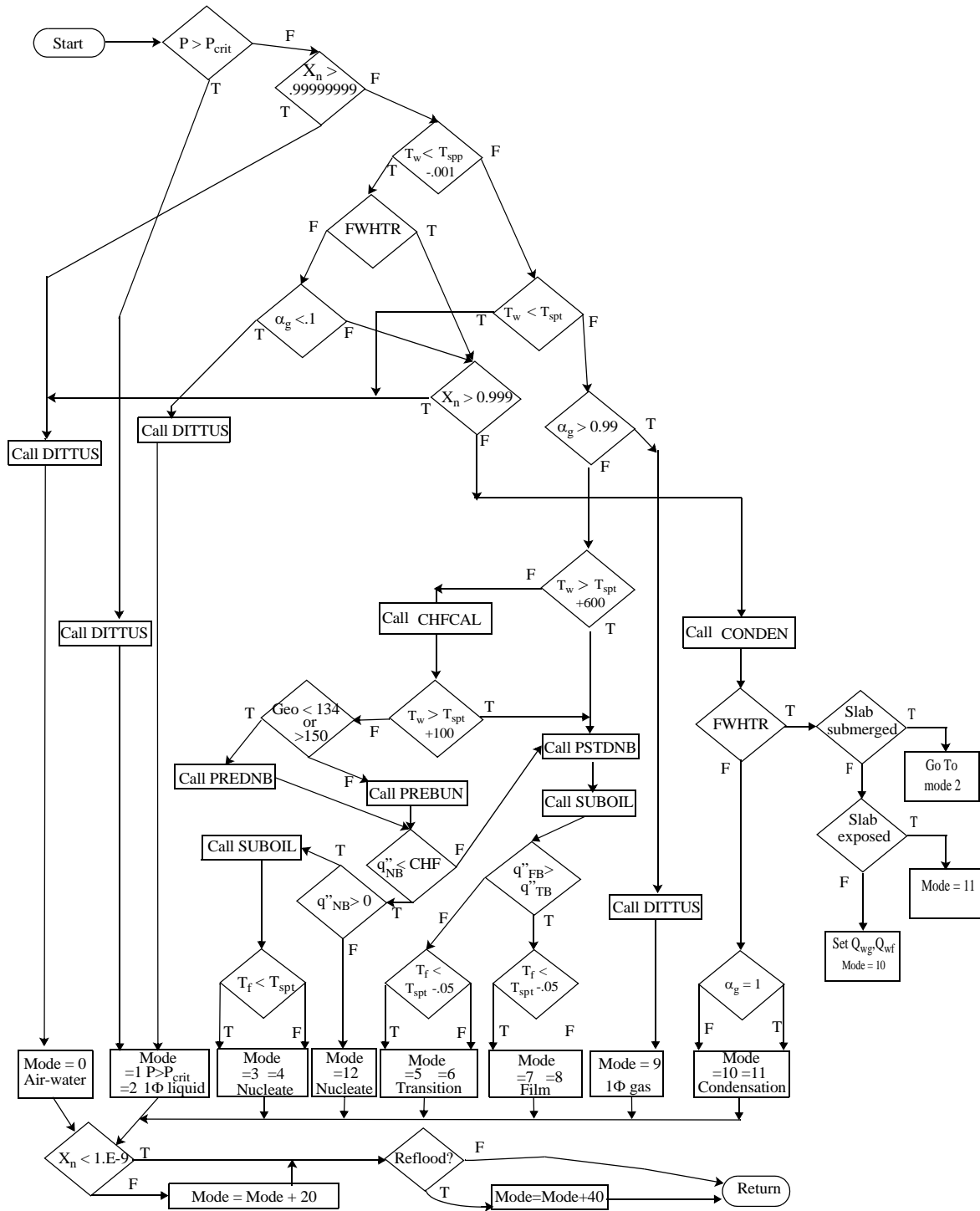
Figure 3.3-9 ATHENA wall heat transfer flow chart.

q''_{TB} =   transition boiling heat flux

Geom   =   type of hydraulic cell

1Φ =   single-phase.

If a noncondensable gas is present, 20 is added to the mode number; and another 40 is added if the surface is a reflood surface. Most of this logic is built into the HTRC1 subroutine. The heat transfer coefficients are determined in one of five subroutines: DITTUS, PREDNB, PREBUN, PSTDNB, and CONDEN. Subroutine CONDEN calculates the coefficients when the wall temperature is below the saturation temperature based on the partial pressure of vapor. Subroutine DITTUS is called for single-phase liquid or vapor/gas conditions. Subroutine PREDNB contains the nucleate boiling correlations for all surfaces except horizontal bundles and subroutine PREBUN is used for the outer surface of horizontal bundles of rods or tubes. Subroutine PSTDNB has the transition and film boiling correlations. Subroutine CHFCAL determines the critical heat flux. If reflood is on, subroutine CHFCAL has been called prior to the call to subroutine HTRC1, and thus it is not called from subroutine HTRC1. Subroutine SUBOIL calculates the vapor generation rate in the superheated liquid next to a superheated wall.

ATHENA wall heat transfer correlations are based mainly on internal flow in pipes. Additional geometries considered in the logic are vertical parallel plates, vertical and horizontal tube bundles, and horizontal flat plates.

3.3.10 Wall Heat Transfer Correlations

The boiling curve uses the Chen[3.3-55] boiling correlation up to the critical heat flux point. A table lookup method[3.3-56] developed by Groeneveld, Cheng, and Doan is used for the prediction of the critical heat flux. Code users also have the option of using a critical heat flux correlation developed by the Czech Republic.[3.3-57] When the wall superheat exceeds the critical value, the heat flux for both the transition boiling and the film boiling regimes are calculated and the maximum value is used. This eliminates the need for a prediction of a minimum film boiling temperature. The Chen-Sundaram-Ozkaynak correlation[3.3-58] is used for transition boiling and a modified Bromley correlation[3.3-59] is used for film boiling.

To obtain the fraction of the boiling heat flux which causes vapor generation near a superheated wall, the Lahey method[3.3-60] is used. The expression for the mass transfer rate per unit volume near a wall, Γ_w, is

$$\Gamma_w = \frac{q'' A_w}{V(h_g' - h_f')} Mul \tag{3.3-214}$$

where

q'' = total wall heat flux

A_w = wall surface area

V = cell volume

Mul = multiplier.

The multiplier is defined as

$$Mul = \frac{h_f - h_{cr}}{(h_f^s - h_{cr})(1 + \varepsilon_P)}$$
(3.3-215)

where

h_{cr} = critical specific enthalpy for net voids calculated using the Saha-Zuber[3.3-61] correlation (see Volume IV)

ε_P = the pumping term

$$= \frac{\rho_f[h_f^s - \min(h_f, h_f^s)]}{\rho_g h_{fg}} \ .$$
(3.3-216)

Convection mode calculations rely on evaluating forced turbulent convection, forced laminar convection, and natural convection and selecting the maximum of these three. The correlations are by Dittus-Boelter,[3.3-62] Kays,[3.3-63] and Churchill-Chu,[3.3-64] respectively.

For parallel plates the Petukhov correlation[3.3-65] is used in place of the Dittus-Boelter correlation, and the Elenbaas[3.3-66] correlation is used instead of the Churchill-Chu correlation.

ATHENA treats vertical bundles differently than pipes. The turbulent convection coefficient is multiplied by the tube pitch-to-diameter ratio as suggested by Inayatov.[3.3-67]

Horizontal bundles in ATHENA differ from pipes in their nucleate boiling, critical heat flux, and natural convection prediction methods. Nucleate boiling predictions follow the Polley-Ralston-Grant method,[3.3-68] and prediction of critical heat flux uses the Folkin-Goldberg method.[3.3-69] Horizontal bundles use the Churchill-Chu[3.3-70] horizontal cylinder correlation for natural circulation.

Except for the FWHTR component, the heat transfer coefficient in the condensation mode uses the maximum of the Nusselt[3.3-71](laminar) and Shah[3.3-72](turbulent) correlations for vertical or inclined surfaces and the maximum of the Chato[3.3-73] (laminar) and Shah[3.3-72] (turbulent) correlations for horizontal surfaces. When noncondensable gases are present, the Colburn-Hougen[3.3-74] iteration method is used to solve for the interface temperature between the vapor/gas and liquid and this value is used in the heat flux calculation. For the right side (outside diameter) of heat slabs associated with a FWHTR component, the condensation heat transfer coefficient is that from Chen[3.3-75], and is applied to that fraction of the heat slab above the water level. For the fraction of the heat slab below the water level, the heat transfer is based on the maximum of liquid forced turbulent convection, forced laminar convection, and natural convection in a horizontal bundle.

ATHENA has a reflood heat transfer model developed by the Paul Scherrer Institute in Switzerland.[3.3-76]

Details of heat transfer coefficient correlations and implementation are given in Volume IV.

3.3.11 Interphase Mass Transfer

The interphase mass transfer is modeled according to the volume flow regime discussed in Section 3.3.1 through Section 3.3.4. It is used to determine the phasic interfacial area and to select the interphase heat transfer correlation for superheated liquid (SHL), subcooled liquid (SCL), superheated vapor/gas (SHG), and subcooled vapor/gas (SCG).

The mass transfer model is formulated so that the net interfacial mass transfer rate is composed of two components; the mass transfer rate in the bulk fluid, and the mass transfer rate near the wall. It is expressed as

$$\Gamma_g = \Gamma_{ig} + \Gamma_w \tag{3.3-217}$$

where Γ_{ig} is given by Equation (3.1-49) and Γ_w is discussed briefly in Section 3.3.10 and is presented in more detail in Volume IV.

For components not modeling wall heat transfer and for the general bulk mass transfer processes, the interfacial mass transfer model in the bulk fluid depends on the volume flow regime. In the bubbly flow regime for a condition of superheated liquid, interfacial mass transfer is the larger of either the model for bubble growth developed by Plesset and Zwick[3.3-77] or the model for convective heat transfer for a spherical bubble (modified Lee and Ryley).[3.3-78] For the bubbly flow regime with a condition of superheated vapor/gas, an interphase heat transfer coefficient is assumed that is high enough that the vapor/gas temperature will relax toward the equilibrium (saturation) condition. Analogously, in the mist flow regime for the condition of superheated vapor/gas, a convective heat transfer model for a spherical

droplet[3.3-78] is used for the interphase heat transfer coefficient. For mist flow with superheated liquid, an interphase heat transfer coefficient is assumed that is high enough that the liquid temperature will relax toward the equilibrium (saturation) condition. In the bubbly flow regime for the subcooled liquid condition, the interfacial mass transfer is calculated by the modified Unal bubble collapse model[3.3-79,3.3-80] and the Lahey model.[3.3-60] In the annular-mist flow regime for the subcooled liquid condition, the interfacial mass transfer is calculated by the modified Brown droplet model[3.3-81] for the drops and the modified Theofanous interfacial condensation model[3.3-82] for the film. Correlations used to calculate the coefficients in the interfacial mass transfer in the bulk fluid are summarized in **Table 3.3-4**. For bubbles and drops, the critical Weber number shown is reduced by 50% in the coded value to reflect the fact that the code uses the Weber to calculate a particle size that is half the maximum size. Volume IV of this manual, from which this table was extracted and simplified, contains a more detailed description of the correlations used in each flow regime.

Table 3.3-4 ATHENA interfacial mass transfer in bulk fluid.

Bubbly Flow

SHL (superheated liquid, $\Delta T_{sf} < 0$)

$$H_{if} = \max \begin{bmatrix} -\dfrac{k_f}{d_b}\dfrac{12}{\pi}\Delta T_{sf}\dfrac{\rho_f C_{pf}}{\rho_g h_{fg}}\beta & \text{(Plesset – Zwick)} \\ \dfrac{k_f}{d_b}(2.0 + 0.74 Re_b^{0.5}) & \text{(modified Lee-Ryley)} \end{bmatrix} a_{gf}$$

where

$$\Delta T_{sf} \quad = \quad T^S - T_f$$

$$Re_b \quad = \quad \frac{(1 - \alpha_{bub})\rho_f v_{fg} d_b}{\mu_f} = \frac{We\sigma(1 - \alpha_{bub})}{\mu_f (v_{fg}^2)^{1/2}}$$

$$d_b \quad = \quad \text{average bubble diameter } (= 1/2\ d_{max})$$

$$= \quad \frac{We\sigma}{\rho_f v_{fg}^2}, \quad We = 5, We\sigma = \max(We\sigma, 10^{-10}\ N/m))$$

$$\beta \quad = \quad 1.0 \text{ for bubbly flow}$$

$$a_{gf} \quad = \quad \text{interfacial area per unit volume}$$

$$= \frac{3.6\alpha_{bub}}{d_b}$$

$$\alpha_{bub} = \max(\alpha_g, 10^{-5})$$

$$v_{fg} = v_g - v_f.$$

SCL (subcooled liquid, $\Delta T_{sf} > 0$)

$$H_{if} = \frac{F_5 h_{fg} \rho_g \rho_f \alpha_g}{\rho_f - \rho_g} \text{ (modified Unal, Lahey)} \qquad \alpha_g > 0.0$$

$$= 0.0 \qquad\qquad\qquad\qquad \alpha_g = 0.0$$

where

$$F_5 = 0.075 \qquad \alpha_{bub} \geq 0.25$$

$$= 1.8\phi C \exp(-45\alpha_{bub}) + 0.075 \qquad \alpha_{bub} < 0.25$$

$$C = 65.0 - 5.69 \times 10^{-5} (P - 1.0 \times 10^5) \frac{1}{K \bullet s} \qquad P \leq 1.1272 \times 10^6 \text{ Pa}$$

$$= \frac{2.5 \times 10^9}{P^{1.418}} \frac{1}{K \bullet s} \qquad P > 1.1272 \times 10^6 \text{ Pa}$$

$$P = \text{pressure (Pa)}$$

$$\phi = 1.0 \qquad |v_f| \leq 0.61 \text{ m/s}$$

$$= [1.639344|v_f|]^{0.47} \qquad |v_f| > 0.61 \text{ m/s}.$$

SHG (superheated vapor/gas, $\Delta T_{sg} < 0$)

$$H_{ig} = h_{ig} a_{gf}$$

where

$$h_{ig} = 10^4 \text{ W/m}^2\text{-K}$$

a_{gf} is as for bubbly SHL.

SCG (subcooled vapor/gas, $\Delta T_{sg} > 0$)

H_{ig} is as for bubbly SHG.

<div align="center">

Slug Flow

</div>

SHL (superheated liquid, $\Delta T_{sf} < 0$)

$$H_{if} = H_{if,Tb} + H_{if,bub}$$

where

$\qquad H_{if,Tb} \qquad = \qquad 3\times10^6 a_{gf,\,Tb}^* \alpha_{Tb}$

where

$\qquad a_{gf,\,Tb}^* \qquad = \qquad$ volumetric interfacial area $= \left(\dfrac{4.5}{D}\right)$ (2.0), where 2.0 is a roughness factor

$\qquad \alpha_{Tb} \qquad = \qquad$ Taylor bubble void fraction $= \dfrac{\alpha_g - \alpha_{gs}}{1 - \alpha_{gs}}$

$\qquad\qquad\qquad\quad = \qquad$ Taylor bubble volume/total volume

$\qquad \alpha_{gs} \qquad = \qquad$ the average void fraction in the liquid film and slug region

$\qquad\qquad\qquad\quad = \qquad \alpha_{BS} F_9$

$\qquad F_9 \qquad = \qquad \exp\left[-8\left(\dfrac{\alpha_g - \alpha_{BS}}{\alpha_{SA} - \alpha_{BS}}\right)\right]$

$\qquad \alpha_{BS} \qquad = \qquad \alpha_g$ for bubbly-slug transition (see Section 3.3.1)

$\qquad \alpha_{SA} \qquad = \qquad \alpha_g$ for slug-annular mist transition (see Section 3.3.1)

and

$\qquad H_{if,bub}$ is as for H_{if} for bubbly SHL with the following modifications:

$\qquad \alpha_{bub} \qquad = \qquad \alpha_{AB} F_9$

$\qquad v_{fg} \qquad = \qquad (v_g - v_f) F_9^2$

$$a_{gf,bub} \quad = \quad (a_{gf})_{bub} \, (1 - \alpha_{Tb}) \, F_9$$

$$\beta \quad = \quad F_9.$$

SCL (subcooled liquid, $\Delta T_{sf} > 0$)

$$H_{if} \; = \; H_{if,Tb} + H_{if,bub}$$

where

$$H_{if,Tb} \quad = \quad 1.18942 Re_f^{0.5} Pr_f^{0.5} \frac{k_f}{D} a_{gf,\,Tb}^{*} \alpha_{Tb}$$

where

α_{Tb} and $a_{gf,\,Tb}^{*}$ are as for slug SHL

$$Pr_f \quad = \quad \frac{C_{pf}\mu_f}{k_f}$$

$$Re_f \quad = \quad \frac{\rho_f |v_f - v_g| D}{\mu_f}$$

and

$H_{if,bub}$ is as for bubbly SCL.

SHG (superheated vapor/gas, $\Delta T_{sg} < 0$)

$$H_{ig} \; = \; H_{ig,Tb} + H_{ig,bub}$$

where

$$H_{ig,Tb} \quad = \quad (2.2 + 0.82 Re_g^{0.5}) \frac{k_g}{D} a_{gf,\,Tb}^{*} \alpha_{Tb}$$

where

$a_{gf,\,Tb}^{*}$ and α_{Tb} are as for slug SHL

$$Re_g \quad = \quad \frac{\rho_g |v_f - v_g| D}{\mu_g}$$

and

$$H_{ig,bub} = h_{ig} (1 - \alpha_{Tb}) a_{gf,bub}$$

where

α_{Tb} and $a_{gf,bub}$ are as for slug SHL

and

h_{ig} is as for bubbly SHG.

SCG (subcooled vapor/gas, $\Delta T_{sg} > 0$)

$$H_{ig} = H_{ig,Tb} + H_{ig,bub}$$

where

$$H_{ig,Tb} \quad = \quad h_{ig} \, \alpha_{Tb} \, a^*_{gf, Tb}$$

where α_{Tb} and $a^*_{gf, Tb}$ are as for slug SHL.

h_{ig} is as for bubbly SHG

and

$H_{ig,bub}$ is as for slug SHG.

Annular Mist Flow

SHL (superheated liquid, $\Delta T_{sf} < 0$)

$$H_{if} = H_{if,ann} + H_{if,drp}$$

where

$$H_{if,ann} \quad = \quad 3.0 \times 10^6 \, a_{gf,ann}$$

where

$$a_{gf,ann} = \left(\frac{4C_{ann}}{D}\right)(1 - \alpha_{ff})^{1/2}$$

$$C_{ann} = (30\alpha_{ff})^{1/8}\,(2.5), \text{2.5 is a roughness factor}$$

$$\alpha_{ff} = \alpha_f F_{11}$$

$$F_{11} = (1\text{-}G^*)\exp(-C_e \times 10^{-5}\lambda^6)$$

$$C_e = 4.0 \text{ horizontal}$$

$$= 7.5 \text{ vertical}$$

$$\lambda = \frac{|v_g - v_f|}{v_{crit}} \text{ horizontal flow}$$

$$= \frac{\alpha_g v_g}{v_{crit}} \text{ vertical flow}$$

$$v_{crit}\text{ (horizontal)} = 0.5\left[\frac{(\rho_f - \rho_g)g\alpha_g A_{pipe}}{\rho_g D \sin\theta}\right]^{1/2}(1 - \cos\theta)\ , \text{[see Equation (3.3-29)]}$$

$$v_{crit}\text{ (vertical)} = \frac{3.2[\sigma g(\rho_f - \rho_g)]^{1/4}}{\rho_g^{1/2}}\ , \text{[see Equation (3.3-19)]}$$

$$G^* = 10^{-4}\,Re_f^{0.25}$$

$$Re_f = \frac{\alpha_f \rho_f |v_f| D}{\mu_f}$$

$$H_{if,drp} = \frac{k_f}{d_d}F_{13}a_{gf,\,drp}$$

$$d_d = \frac{We\,\sigma}{\rho_g v_{fg}^2}\,, \text{We} = 1.5, \text{We}\,\sigma = \max(\text{We}\,\sigma, 10^{-10}\,\text{N/m})$$

$$v_{fg} = v_g - v_f$$

$$\alpha_{fd} = \max\left[\frac{\alpha_f - \alpha_{ff}}{1 - \alpha_{ff}}, (1 - \alpha_{AM})\right]$$

$$F_{13} = 2.0 + 7.0\min\left[1.0 + \frac{C_{pf}\max(0.0, \Delta T_{sf})}{h_{fg}}, 8.0\right]$$

$$a_{gf,drp} = \frac{3.6\alpha_{fd}}{d_d}(1 - \alpha_{ff}).$$

For an annulus component, $\alpha_{ff} = \alpha_f$ and $\alpha_{fd} = 0$.

SCL (subcooled liquid, $\Delta T_{sf} > 0$)

$$H_{if} = H_{if,ann} + H_{if,drp}$$

where

$$H_{if,ann} = 10^{-3}\,\rho_f C_{pf}\,|v_f|\,a_{gf,ann} \text{ (modified Theofanous)}$$

where

$a_{gf,ann}$ is as for annular mist SHL

and

$$H_{if,drp} = \frac{k_f}{d_d}F_{13}a_{gf,\,drp} \text{ (modified Brown)}$$

where

$a_{gf,drp}$, F_{13}, and d_d are as for annular mist SHL.

For an annulus component, $\alpha_{ff} = \alpha_f$ and $\alpha_{fd} = 0$.

SHG (superheated vapor/gas, $\Delta T_{sg} < 0$)

$$H_{ig} = H_{ig,ann} + H_{ig,drp}$$

where

$$H_{ig,ann} = \frac{k_g}{D} 0.023 Re_g^{0.8} a_{gf,\,ann}$$

where

$$Re_g = \frac{\alpha_g \rho_g |v_g - v_f| D}{\mu_g}$$

$a_{gf,ann}$ is as for annular mist SHL, and

$$H_{ig,\,drp} = \frac{k_g}{d_d}(2.0 + 0.5 Re_d^{0.5}) a_{gf,\,drp} \quad \text{(Lee-Riley)}$$

where

d_d is as for annular mist SHL

$$Re_d = \frac{(1 - \alpha_{f,\,d})^{2.5} \rho_g v_{fg} d_d}{\mu_g} = \frac{We\sigma(1 - \alpha_{f,\,d})^{2.5}}{\mu_g v_{fg}} \text{, where } We = 1.5$$

$a_{gf,drp}$, $\alpha_{f,d}$, and v_{fg} are as for annular mist SHL.

For an annulus component, $\alpha_{ff} = \alpha_f$ and $\alpha_{fd} = 0$.

SCG (subcooled vapor/gas, $\Delta T_{sg} > 0$)

$$H_{ig} = H_{ig,ann} + H_{ig,drp}$$

where

$$H_{ig,ann} = h_{ig} a_{gf,ann}$$

where h_{ig} is as for bubbly SHG and $a_{gf,ann}$ is as for annular mist SHL

and

$$H_{ig,drp} = h_{ig}\, a_{gf,drp}$$

where

h_{ig} is as for bubbly SHG and

$a_{gf,drp}$ is as for annular mist SHG.

For an annulus component, $\alpha_{ff} = \alpha_f$ and $\alpha_{fd} = 0$.

Inverted Annular Flow

SHL (superheated liquid, $\Delta T_{sf} < 0$)

$$H_{if} = H_{if,bub} + H_{if,ann}$$

where

$H_{if,bub}$ is as for H_{if} for bubbly with the following modifications:

$$v_{fg} \quad = \quad (v_g - v_f)F_{16}^2$$

where

$$F_{16} \quad = \quad 1 - F_{17}$$

$$F_{17} \quad = \quad \exp\left[\frac{-8(\alpha_{BS} - \alpha_{IAN})}{\alpha_{BS}}\right]$$

$$\alpha_{IAN} \quad = \quad \alpha_g \text{ inverted annular}$$

$$= \quad \alpha_{AB} \text{ IAN/ISL transition (see \textbf{Figure 3.3-1})}$$

$$\beta \quad = \quad F_{16}$$

$$\alpha_g \quad = \quad \alpha_{bub}$$

$$\alpha_{bub} \quad = \quad \frac{(\alpha_{IAN} - \alpha_B)}{(1 - \alpha_B)}$$

$$\alpha_B \quad = \quad F_{17}\,\alpha_{IAN}$$

$$a_{gf,bub} \quad = \quad \frac{3.6\alpha_{bub}}{d_b}(1 - \alpha_B)F_{16}$$

and

$$H_{if,ann} \quad = \quad 3 \times 10^6 \, a_{gf,ann}$$

where

$$a_{gf,ann} \quad = \quad \frac{4}{D} \, F_{15} \,(2.5), \text{ where 2.5 is a roughness factor}$$

$$F_{15} \quad = \quad (1 - \alpha_B)^{1/2}.$$

SCL (subcooled liquid, $\Delta T_{sf} > 0$)

$$H_{if} \;=\; H_{if,bub} + H_{if,ann}$$

where

$H_{if,bub}$ is as for bubbly SCL

and

$$H_{if,ann} \quad = \quad \frac{k_f}{D} 0.023 \, Re_{IAN}^{0.8} a_{gf,\,ann}$$

where

$$Re_{IAN} \quad = \quad (1 - \alpha_{IAN})\frac{\rho_f |v_f - v_g|}{\mu_f}$$

$a_{gf,ann}$ and α_{IAN} are as for inverted annular SHL.

SHG (superheated vapor/gas, $\Delta T_{sg} < 0$)

$$H_{ig} \;=\; H_{ig,bub} + H_{ig,ann}$$

where

$$H_{ig,bub} \quad = \quad h_{ig} \, a_{gf,bub}$$

where

h_{ig} is as for bubbly SHG and $a_{gf,bub}$ is as for inverted annular SHL

and

$$H_{ig,ann} \quad = \quad \frac{k_g}{D} \, a_{gf,ann}$$

where

$a_{gf,ann}$ is as for inverted annular SHL.

SCG (subcooled vapor/gas, $\Delta T_{sg} > 0$)

H_{ig} is as for inverted annular SHG.

<div align="center">

Inverted Slug Flow

</div>

SHL (superheated liquid, $\Delta T_{sf} < 0$)

$$H_{if} \; = \; H_{if,ann} + H_{if,drp}$$

where

$$H_{if,ann} \quad = \quad \frac{k_f}{D} \, F_{13} \, a_{gf,ann}$$

where

$$a_{gf,ann} \quad = \quad \frac{4.5}{D} \, \alpha_B(2.5), \text{ where 2.5 is a roughness factor}$$

$$\alpha_B \quad = \quad \frac{\alpha_f - \alpha_{drp}}{1 - \alpha_{drp}}$$

$$\alpha_{drp} \quad = \quad (1 - \alpha_{AM}) \, F_{21}$$

$$F_{21} \quad = \quad \exp\left[-\frac{(\alpha_{AM} - \alpha_g)}{(\alpha_{AM} - \alpha_{BS})}\right]$$

and

$$H_{if,drp} \quad = \quad \frac{k_f}{d_d} \, F_{13} \, a_{gf,drp}$$

where

$$a_{gf,drp} \quad = \quad \frac{3.6\alpha_{drp}}{d_d}(1 - \alpha_B)$$

$$d_d \quad = \quad \text{characteristic droplet diameter}$$

$$= \quad \frac{We\sigma}{\rho_g v_{fg}^2}, \text{ where } We = 6.0$$

$$v_{fg} \quad = \quad (v_g - v_f)\, F_{21}^2.$$

SCL (subcooled liquid, $\Delta T_{sf} > 0$)

$$H_{if} = H_{if,ann} + H_{if,drp}$$

where

$$H_{if,ann} \quad = \quad \frac{k_f}{D}\, F_{13}\, a_{gf,ann}$$

where

F$_{13}$ is as for annular-mist SCL

$a_{gf,ann}$ is as for inverted slug SHL

and

$$H_{if,drp} \quad = \quad \frac{k_f}{d_d}\, F_{13}\, a_{gf,drp}$$

where

$a_{gf,drp}$ is as for inverted slug SHL.

SHG (superheated vapor/gas, $\Delta T_{sg} < 0$)

$$H_{ig} = H_{ig,ann} + H_{ig,drp}$$

where

$$H_{ig,ann} \quad = \quad \frac{k_g}{D} a_{gf,ann}$$

where

$a_{gf,ann}$ is as for inverted slug SHL

and

$$H_{ig,drp} \quad = \quad \frac{k_g}{d_d} (2.0 + 0.5 \, Re_{drp}^{0.5}) a_{gf,drp}$$

where

d_d and $a_{gf,drp}$ are as for inverted slug SHL

and

$$Re_{drp} \quad = \quad \frac{\rho_g v_{fg} d_d}{\mu_g}.$$

SCG (subcooled vapor/gas, $\Delta T_{sg} > 0$)

H_{ig} is as for inverted slug SHG.

Dispersed (Droplet, Mist) Flow

SHL (superheated liquid, $\Delta T_{sf} < 0$)

$$H_{if} = \frac{k_f}{d_d} F_{13} a_{gf}$$

where

$$a_{gf} \quad = \quad \frac{3.6 \alpha_f}{d_d}$$

$$d_d \quad = \quad \frac{We \sigma}{\rho_g v_{fg}^2}, \text{ where } We = 1.5 \text{ for pre-CHF and } 6.0 \text{ for post-CHF}$$

$$v_{fg} \quad = \quad v_g - v_f.$$

SCL (subcooled liquid, $\Delta T_{sf} > 0$)

$$H_{if} = \frac{k_f}{d_d} a_{gf}$$

where

F$_{13}$ is as for annular mist SCL

a_{gf} is as for dispersed SHL.

SHG (superheated vapor/gas, $\Delta T_{sg} < 0$)

$$H_{ig} = \frac{k_g}{d_d}(2.0 + 0.5\,\mathrm{Re}_{drp}^{0.5})a_{gf} \qquad \alpha_f > 0.0$$

$$= 0.0 \qquad\qquad\qquad \alpha_f = 0.0$$

where d_d and a_{gf} are as for dispersed SHL and

$$\mathrm{Re}_{drp} = \frac{(1 - \alpha_f)^{2.5}\rho_g v_{fg} d_d}{\mu_g} = \frac{\mathrm{We} \bullet \sigma(1 - \alpha_f)^{2.5}}{\mu_g v_{fg}} \quad \text{pre-CHF and post-CHF.}$$

SCG (subcooled vapor/gas, $\Delta T_{sg} > 0$)

$$H_{ig} = 0.0 \qquad\qquad \alpha_f = 0.0 \text{ and } P_s < P_{\text{triple point}}$$

$$= h_{ig}\, a_{gf} \qquad \text{otherwise}$$

where

h_{ig} is as for bubbly SHG and

a_{gf} is as for dispersed SHG.

Horizontally Stratified Flow

$$H_{if} = 0 \text{ unless } \alpha_g > 0 \text{ or } \Delta T_{sf} < \text{-1 K}$$

$$H_{ig} = 0 \text{ unless } \alpha_f > 0 \text{ or } \Delta T_{sg} > 0.2 \text{ K}$$

otherwise:

SHL (superheated liquid, $\Delta T_{sf} < 0$)

$$H_{if} = \frac{k_f}{D_{hf}}\left[0.023\,Re_f^{0.8} - 3.81972\frac{\Delta T_{sf}\rho_f C_{pf}}{\rho_g h_{fg}\max(4\alpha_g,\,1)}\right]a_{gf}$$

where

    D_{hf} =   liquid phase hydraulic diameter

           = $\dfrac{\pi\alpha_f D}{\pi - \theta + \sin\theta}$ (see **Figure 3.1-2** for definition of θ)

    Re_f = $\dfrac{\alpha_f\rho_f|v_g - v_f|D}{\mu_f}$

    a_{gf} = $\dfrac{4\sin\theta}{\pi D}F_{27}$

    F_{27} = $1 + \left|\dfrac{v_g - v_f}{v_{crit}}\right|^{1/2}$.

SCL (subcooled liquid, $\Delta T_{sf} > 0$)

$$H_{if} = \frac{k_f}{D_{hf}}(0.023\,Re_f^{0.8})a_{gf}$$

where

    D_{hf}, Re_f and a_{gf} are as for horizontally stratified SHL.

SHG (superheated vapor/gas, $\Delta T_{sg} < 0$)

$$H_{ig} = \frac{k_g}{D_{hg}}[0.023\,Re_g^{0.8} + 4h_{ig}\max(0.0,\,0.25 - \alpha_g)]a_{gf}$$

where

    D_{hg} =   vapor/gas phase hydraulic diameter

$$= \frac{\pi \alpha_g D}{\theta + \sin \theta}$$

$$Re_g = \frac{\alpha_g \rho_g |v_g - v_f| D}{\mu_g}$$

h_{ig} is as for bubbly SHG, and a_{gf} is as for horizontally stratified SHL.

SCG (subcooled vapor/gas, $\Delta T_{sg} > 0$)

$$H_{ig} = h_{ig} \, a_{gf}$$

where

h_{ig} is as for bubbly SHG and

a_{gf} is as for horizontally stratified SHL.

<p align="center">**Vertically Stratified Flow**</p>

SHL (superheated liquid, $\Delta T_{sf} < 0$)

$$H_{if} = H_{if,REG}$$

where

REG = flow regime of flow when not vertically stratified, which can be BBY, SLG, SLG/ANM, ANM, MPR, IAN, IAN/ISL, ISL, MST, MPO, BBY/IAN, IAN/ISL-SLG, SLG/ISL, ISL-SLG/ANM, ANM/MST, MPR/MPO, (see flow regime map, **Figure 3.3-1**).

SCL (subcooled liquid, $\Delta T_{sf} > 0$)

$$H_{if} = Nu_f \frac{k_f}{D} a_{gf} \quad (McAdams)$$

where

$$a_{gf} = \frac{A}{V} = \frac{A}{AL} = \frac{1}{L}$$

L = length of volume cell

$$Nu_f \quad = \quad 0.27\,(Gr_fPr_f)^{0.25}$$

SHG (superheated vapor/gas, $\Delta T_{sg} < 0$)

$$H_{ig} = Nu_g\frac{k_g}{D}a_{gf} \text{ (McAdams)}$$

where

$$Nu_g \quad = \quad 0.27\,(Gr_gPr_g)^{0.25}$$

$$a_{gf} \quad = \quad \frac{A}{V} = \frac{A}{AL} = \frac{1}{L}$$

a_{gf} is as for vertically stratified SHL.

SCG (subcooled vapor/gas, $\Delta T_{sg} > 0$)

$$H_{ig} = H_{ig,REG}.$$

3.3.12 Direct Heating

The direct (sensible) heating between the noncondensable gas and liquid becomes important when there is noncondensable present (see Section 3.1.1.2). This occurs when $P_s < P$. The direct heat transfer coefficient is

$$H_{gf} = \begin{cases} H_{ig}(T_g > T^s) & T_g > T^s \\ H_{ig}(T_g = T^s) & T_g \le T^s \end{cases}. \tag{3.3-218}$$

Thus, when the noncondensable gas is subcooled, H_{gf} uses the value of H_{ig} at saturation.

3.3.13 References

3.3-1.   W. L. Weaver et al., *TRAC-BF1 Manual: Extensions to TRAC-BD1/MOD1,* NUREG/CR-4391, EGG-2417, Idaho National Engineering Laboratory, August 1986.

3.3-2.   M. M. Giles et al., *TRAC-BF1/MOD1: An Advanced Best Estimate Computer Program for BWR Accident Analysis*, NUREG/CR-4356, EGG-2626, Idaho National Engineering Laboratory, June 1992 and August 1992.

3.3-3.   S. Z. Rouhani et al., *TRAC-BF1/MOD1 Models and Correlations*, NUREG/CR-4391, EGG-2680, Idaho National Engineering Laboratory, August 1992.

3.3-4.   Y. Taitel and A. E. Dukler, "A Model of Predicting Flow Regime Transitions in Horizontal and Near Horizontal Gas-Liquid Flow," *AIChE Journal, 22,* 1976, pp. 47-55.

3.3-5.   Y. Taitel, D. Bornea, and A. E. Dukler, "Modeling Flow Pattern Transitions for Steady Upward Gas-Liquid Flow in Vertical Tubes," *AIChE Journal, 26,* 1980, pp. 345-354.

3.3-6.   M. Ishii and G. De Jarlais, "Inverted Annular Flow Modeling," *Advanced Code Review Group Meeting, Idaho Falls, ID, July 27, 1982.*

3.3-7.   M. Ishii and T. C. Chawla, *Local Drag Laws in Dispersed Two-Phase Flow,* NUREG/CR-1230, ANL-79-105, Argonne National Laboratory, December 1979.

3.3-8.   M. Ishii and K. Mishima, *Study of Two-Fluid Model and Interfacial Area,* NUREG/CR-1873, ANL-80-111, Argonne National Laboratory, December 1980.

3.3-9.   M. A. Vince and R. T. Lahey, Jr., "On the Development of An Objective Flow Regime Indicator," *International Journal of Multiphase Flow, 8,* 1982, pp. 93-124.

3.3-10.   M. Ishii, *Thermo-Fluid Dynamic Theory of Two-Phase Flow,* Collection de la Direction des Etudes d'Recherches of Electricute de France, 1975.

3.3-11.   D. T. Dumitrescu, "Stomung an einer Luftblase in senkrechten Rohr," *Z. Angel Math. Mech. 23,* 1943, p. 139.

3.3-12.   V. H. Ransom et al., *RELAP5/MOD2 Code Manual, Volume 3; Developmental Assessment Problems,* EGG-TFM-7952, Idaho National Engineering Laboratory, December 1987.

3.3-13.   K. Mishima and M. Ishii, "Flow Regime Transition Criteria for Upward Two-Phase Flow in Vertical Tubes," *International Journal of Heat and Mass Transfer, 27,* 1984, pp. 723-737.

3.3-14.   K. W. McQuillan and P. B. Whalley, *Flow Patterns in Vertical Two-Phase Flow,* AERE-R 11032, 1983.

3.3-15.   K. W. McQuillan and P. B. Whalley, "Flow Patterns in Vertical Two-Phase Flow," *International Journal of Multiphase Flow, 11,* 1985, pp. 161-175.

3.3-16.   J. M. Putney, *An Assessment of the Annular Flow Transition Criteria and Interphase Friction Models in RELAP5/MOD2,* CERL Report RD/L/3451/R89, PWR/HTWG/P(88)653, February 1989.

3.3-17.   V. H. Ransom et al., *RELAP5/MOD2 Code Manual,* NUREG/CR-4312, EGG-2396, Idaho National Engineering Laboratory, August 1985 and December 1985, revised March 1987.

3.3-18.   R. A. Dimenna et al., *RELAP5/MOD2 Models and Correlations,* NUREG/CR-5194, EGG-2531, Idaho National Engineering Laboratory, August 1988.

3.3-19.   T. N. Tandon, H. K. Varma, and C. P. Gupta, "A New Flow Regime Map for Condensation Inside Horizontal Tubes," *Journal of Heat Transfer, 104,* November 1982, pp. 763-768.

3.3-20.   Y. Taitel, N. Lee, and A. E. Dukler, "Transient Gas-Liquid Flow in Horizontal Pipes: Modeling Flow Pattern Transitions," *AIChE Journal, 24,* 5, 1978, pp. 920-934.

3.3-21.   J. G. M. Anderson and K. H. Chu, *BWR Refill-Reflood Program Task 4.7--Constitutive Correlations for Shear and Heat Transfer for the BWR Version of TRAC,* NUREG/CR-2134, EPRI NP-1582, 1981.

3.3-22.   M. Ishii, T. Chawla, and N. Zuber, "Constitutive Equation for Vapor Drift Velocity in Two Phase Annular Flow," *AIChE Journal, 22,* 1976, pp. 283-289.

3.3-23.   M. Ishii, *One-dimensional Drift-flux Model and Constitutive Equations for Relative Motion Between Phases in Various Two-phase Flow Regimes,* ANL-77-47, Argonne National Laboratory, September 1977.

3.3-24.   G. B. Wallis, *One-dimensional Two-phase Flow,* New York: McGraw-Hill, 1969.

3.3-25.   A. H. Shapiro and A. J. Erickson, *Transactions of ASME, 79,* 1957, p. 775.

3.3-26.   J. M. Putney, *Proposals for Improving Interphase Drag Modeling for the Bubbly and Slug Regimes in RELAP5,* CERL Report RD/L/3306/R88, PWR/HTWG/P(88)622, June 1988.

3.3-27.   J. M. Putney, *Implementation of a New Bubbly-Slug Interphase Drag Model in RELAP5/MOD2,* CERL Report RD/L/3369/R88, PWR/HTWG/P(88)597, November 1988.

3.3-28.   J. M. Putney, *Equations for Calculating Interfacial Drag and Shear from Void Fraction Correlations,* CERL Report RD/L/3429/R88, PWR/HTWG/P(88)630, December 1988.

3.3-29.   J. M. Putney, *Development of a New Bubbly-Slug Interfacial Friction Model for RELAP5--Final Report,* National Power Report ESTD/L/0075/R89, PWR/HTWG/P(89)722, October 1989.

3.3-30.   J. M. Putney, "Development of a New Bubbly-Slug Interfacial Friction Model for RELAP5," *Nuclear Engineering and Design, 131,* 1991, pp. 223-240.

3.3-31.   B. Chexal and G. Lellouche, *A Full-Range Drift-Flux Correlation for Vertical Flows (Revision 1),* EPRI NP-3989-SR, September 1986.

3.3-32.   B. Chexal et al., *The Chexal-Lellouche Void Fraction Correlation for Generalized Applications,* Electric Power Research Institute, NSAC-139, April 1991.

3.3-33.   B. Chexal et al., *Void Fraction Technology for Design and Analysis*, Electric Power Research Institute, TR-106326, March 1997.

3.3-34.   P. Griffith, "The Prediction of Low-Quality Boiling Voids," *Transactions of the ASME, Journal of Heat Transfer, 86,* 1964, pp. 327-333.

3.3-35.   N. Zuber and J. A. Findlay, "Average Volumetric Concentrations in Two-Phase Flow Systems," *Transactions of the ASME*, *Journal of Heat Transfer, 87,* 1965, pp. 453-568.

3.3-36.   N. Zuber et al., *Steady-State and Transient Void Fraction in Two-Phase Flow Systems,* General Electric Company, GEAP-5417, 1967.

3.3-37.   I. Kataoka and M. Ishii, "Drift Flux Model for Large Diameter Pipe and New Correlation for Pool Void Fraction," *International Journal of Heat and Mass Transfer, 30,* 1987, pp. 1927-1939.

3.3-38.   S. Z. Rouhani, *Modified Correlations for Void and Pressure Drop,* AB Atomenergi, Sweden, Internal Report AE-RTC 841, March 1969.

3.3-39.   G. B. Wallis and S. Makkenchery, "The Hanging Film Phenomenon in Vertical Annular Two-Phase Flow," *Transactions of the ASME, Journal of Fluids Engineering, 96,* 1974, p. 297-298.

3.3-40.   J. A. Holmes, "Description of the Drift Flux Model in the LOCA Code RELAP-UK," *I. Mech. E.,* C206/77, 1977.

3.3-41.   V. H. Ransom et al., *RELAP5/MOD1 Code Manual,* NUREG/CR-1826, EGG-2070, Idaho National Engineering Laboratory, March 1982.

3.3-42.   D. Bharathan, G. B. Wallis, and H. J. Richter, *Air-Water Counter-Current Annular Flow,* EPRI/NP-1165, 1979.

3.3-43.   G. DeJarlais and M. Ishii, *Inverted Annular Flow Experimental Study,* NUREG/CR-4277, ANL-85-31, Argonne National Laboratory, April 1985.

3.3-44.   N. Zuber, "On the Dispersed Two-Phase Flow in the Laminar Flow Regime," *Chemical Engineering Science, 19,* 1964, pp. 897-917.

3.3-45.   D. A. Drew, L. Y. Cheng, and R. T. Lahey, Jr., "The Analysis of Virtual Mass Effects in Two-Phase Flow," *International Journal of Multiphase Flow, 5,* 1979, pp. 233-242.

3.3-46.   K. T. Claxton, J. G. Collier, and J. A. Ward, *H.T.F.S. Correlation for Two-Phase Pressure Drop and Void Fraction in Tubes,* HTFS Proprietary Report HTFS-DR-28, AERE-R7162, November 1972.

3.3-47.   D. Chisholm, "A Theoretical Basis for the Lockhart-Martinelli Correlation for Two-Phase Flow," *International Journal of Heat and Mass Transfer, 10,* 1967, pp. 1767-1778.

3.3-48.   R. W. Lockhart and R. C. Martinelli, "Proposed Correlation of Data for Isothermal Two-Phase, Two-Component Flow in Pipes," *Chemical Engineering Progress, 45,* 1, 1949, pp. 39-48.

3.3-49.   C. F. Colebrook, "Turbulent Flow in Pipes with Particular Reference to the Transition Region Between Smooth and Rough Pipe Laws," *Journal of Institute of Civil Engineers, 11,* 1939, pp. 133-156.

3.3-50.   J. G. Knudsen and D. L. Katz, *Fluid Dynamics and Heat Transfer,* New York: McGraw-Hill, 1958.

3.3-51.   F. M. White, *Viscous Fluid Flow,* New York: McGraw-Hill, 1974.

3.3-52.   D. J. Zigrang and N. D. Sylvester, "A Review of Explicit Friction Factor Equations," *Transactions of ASME, Journal of Energy Resources Technology, 107,* 1985, pp. 280-283.

3.3-53.   C. W. Stewart et al., *VIPRE-01: A Thermal-Hydraulic Code for Reactor Cores,* EPRI NP-2511-CCM, Pacific Northwest Laboratory, July 1985.

3.3-54.   W. M. Kays and H. C. Perkins, "Forced Convection, Internal Flow in Ducts," in: W. M. Rohsenow, J. P. Hartnett, and E. N. Ganic (eds.), *Handbook of Heat Transfer Fundamentals,* New York: McGraw-Hill, 1985.

3.3-55.   J. C. Chen, "A Correlation for Boiling Heat Transfer to Saturated Fluids in Convective Flow," *Process Design and Development, 5,* 1966, pp. 322-327.

3.3-56.   D. C. Groeneveld, S. C. Cheng, and T. Doan, "1986 AECL-UO Critical Heat Flux Lookup Table," *Heat Transfer Engineering, 7,* 1-2, 1986, pp. 46-62.

3.3-57.   R. Pernicia and J. Cizek, "General Correlation for Prediction of Critical Heat Flux Ratio," *Proceedings of the 7th International Meeting on Nuclear Reactor Thermal-Hydraulics, NURETH-7, Saratoga Springs, NY, September 10 - 15, 1995,* NUREG/CP-0142, Vol. 4.

3.3-58.   J. C. Chen, R. K. Sundaram, and F. T. Ozkaynak, *A Phenomenological Correlation for Post-CHF Heat Transfer,* NUREG-0237, June 1977.

3.3-59.   L. A. Bromley, "Heat Transfer in Stable Film Boiling," *Chemical Engineering Progress, 46,* 1950, pp. 221-227.

3.3-60.   R. T. Lahey, "A Mechanistic Subcooled Boiling Model," *Proceedings Sixth International Heat Transfer Conference, Toronto, Canada, August 7-11*, *1978, Volume 1*, pp. 293-297.

3.3-61.   P. Saha and N. Zuber, "Point of Net Vapor Generation and Vapor Void Fraction in Subcooled Boiling," *Proceedings Fifth International Heat Transfer Conference, Tokyo, Japan, September 3-7, 1974, Volume 4,* pp. 175-179.

3.3-62.   F. W. Dittus and L. M. K. Boelter, "Heat Transfer in Automobile Radiators of the Tubular Type," *Publications in Engineering, 2,* University of California, Berkeley, 1930, pp. 443-461.

3.3-63.   W. M. Kays, "Numerical Solution for Laminar Flow Heat Transfer in Circular Tubes," *Transactions of the ASME, 77,* 1955, pp. 1265-1274.

3.3-64.   S. W. Churchill and H. H. S. Chu, "Correlating Equations for Laminar and Turbulent Free Convection from a Vertical Plate," *International Journal of Heat and Mass Transfer, 18,* 1975, pp. 1323-1329.

3.3-65.   B. S. Petukhov, "Heat Transfer and Friction in Turbulent Pipe Flow with Variable Physical Properties," *Advances in Heat Transfer,* New York: Academic Press, 1970, pp. 503-565.

3.3-66.   F. P. Incropera and D. P. DeWitt, *Introduction to Heat Transfer,* New York: Wiley, 1990, p. 501.

3.3-67.   A. Y. Inayatov, "Correlation of Data on Heat Transfer Flow Parallel to Tube Bundles at Relative Tube Pitches of 1.1 < s/d < 1.6," *Heat Transfer-Soviet Research, 7,* 3, May-June 1975.

3.3-68.   G. T. Polley, T. Ralston, and I. D. R. Grant, "Forced Crossflow Boiling in an Ideal In-line Tube Bundle," *ASME 80-HT-46,* 1981.

3.3-69.   B. S. Folkin and Y. N. Goldberg, "Simulation of Free Convection Boiling Crisis In Vapor Blanketing of a Horizontal Tube Bundle," *Heat Transfer Soviet Research, 12,* 3, 1980, pp.77-81.

3.3-70.   S. W. Churchill and H. H. S. Chu, "Correlating Equations for Laminar and Turbulent Free Convection from a Horizontal Cylinder," *International Journal of Heat and Mass Transfer, 18,* 1975, p. 1049-1053.

3.3-71.   W. Nusselt, "Die Oberflachenkondensation des Wasserdampfes," *Zieschrift Ver. Deutsch. Ing., 60,* 1916, pp. 541-546 and 569-575.

3.3-72.   M. M. Shah, "A General Correlation for Heat Transfer during Film Condensation Inside Pipes," *International Journal of Heat and Mass Transfer, 22,* 1979, pp. 547-556.

3.3-73.   J. C. Chato, "Laminar Condensation Inside Horizontal and Inclined Tubes, "*American Society of Heating, Refrigeration, and Air Conditioning Journal*, *4*, 1962, pp. 52-60.

3.3-74.   A. P. Colburn and O. A. Hougen, "Design of Cooler Condensers for Mixtures of Vapors with Non-Condensing Gases," *Industrial and Engineering Chemistry, 26,* 1934, pp. 1178-1182.

3.3-75.   M. M. Chen,"An Analytical Study of Laminar Film Condensation: Part 2 - Single and Multiple Horizontal Tubes," *Transactions of the ASME, Journal of Heat Transfer, 83*, 1961, pp. 55-60.

3.3-76.   G. Th. Analytis, "Developmental Assessment of RELAP5/MOD3.1 with Separate Effect and Integral Test Experiments: Model Changes and Options," *Nuclear Engineering and Design, 163,* 1996, pp. 125-148.

3.3-77. M. S. Plesset and S. A. Zwick, "Growth of Vapor Bubbles in Superheated Liquids," *Journal of Applied Physics, 25,* 4, 1954, pp. 493-500.

3.3-78. K. Lee and D. J. Ryley, "The Evaporation of Water Droplets in Superheated Steam," *Transactions of the ASME, Journal of Heat Transfer,* November 1968, pp. 445-456.

3.3-79. H. C. Unal, "Maximum Bubble Diameter, Maximum Bubble-Growth Time and Bubble-Growth Rate During the Subcooled Nucleate Flow Boiling of Water up to 17.7 MN/m^2," *International Journal of Heat and Mass Transfer, 19,* 1976, pp. 643-649.

3.3-80. R. A. Riemke, "Modification to Unal's Subcooled Flow Boiling Bubble Model," *Nuclear Technology, 102,* 1993, pp. 416-417.

3.3-81. G. Brown, "Heat Transmission by Condensation of Steam on a Spray of Water Drops," *Institute of Mechanical Engineers,* 1951, pp. 49-52.

3.3-82. T. G. Theofanous, "Modeling of Basic Condensation Processes," *The Water Reactor Safety Research Workshop on Condensation, Silver Springs, MD, May 24-25, 1979.*

3.4 Special Process Models

Certain models in ATHENA have been developed to simulate special processes. Special process models are used in ATHENA to model those processes which are so complex in nature that they must be modeled by quasi-steady emperical models. Choking, stratification entrainment/pull-through, abrupt area change, and counter-current flow limitation are examples of such processes.

The use of quasi-stready models for choking and abrupt area change results in considerable savings in computer time since it is not necessary to use fine nodalization at such points. The fluid dynamic and thermodynamic processes for such phenomena are approximated by steady flow relations, which can be solved to provide lumped parameter data and/or boundary condition data for the transient solution. This results is direct savings since fewer fluid volumes are required and indirect savings due to the ability to use larger time steps. A decisive advantage for the use of a choking model results when choking at points of abrupt area change occurs, such as at double-ended pipe breaks or at a sudden contraction due to an orifice. It is not possible to construct one-dimensional grids at such points that will result is meaningful self-choking results, because of the discontinuous variation of flow area with length.

These models are described in the following subsections.

3.4.1 Choked Flow

A choked-flow model developed by Ransom and Trapp[3.4-1,3.4-2] is included primarily for calculation of the mass discharge from the system at a pipe break or a nozzle. Generally, the flow at the break or nozzle is choked until the system pressure nears the containment pressure. The choked-flow model is used to predict if the flow is choked at a break or nozzle and, if it is, to establish the discharge boundary condition. In addition, the choked-flow model can be used to predict existence of and calculate choked flow at internal points in the system.

Choking is defined as the condition wherein the mass flow rate becomes independent of the downstream conditions (that point at which further reduction in the downstream pressure does not change the mass flow rate). The fundamental reason that choking occurs is that acoustic signals can no longer propagate upstream. This occurs when the fluid velocity equals or exceeds the propagation velocity. The choked-flow model is based on a definition that is established by a characteristic analysis using time-dependent differential equations.

Consider a system of n first-order, quasi-linear, partial differential equations of the form

$$A(U)\frac{\partial U}{\partial t} + B(U)\frac{\partial U}{\partial x} + C(U) = 0 \quad .$$

(3.4-1)

The characteristic directions (or characteristic velocities) of the system are defined[3.4-3,3.4-4] as the roots,[a] $\lambda_i(i \leq n)$, of the characteristic polynomial

$$(A\lambda - B) = 0 \ . \tag{3.4-2}$$

The real part of any root, λ_i, gives the velocity of signal propagation along the corresponding characteristic path in the space/time plane. The imaginary part of any complex root, λ_i, gives the rate of growth or decay of the signal propagating along the respective path. For a hyperbolic system in which all the roots of Equation (3.4-2) are real and nonzero, the number of boundary conditions required at any boundary point equals the number of characteristic lines entering the solution region as time increases. If we consider the system [Equation (3.4-1)] for a particular region $0 \leq x \leq L$ and examine the boundary conditions at $x = L$, as long as any λ_i are less than zero, we must supply some boundary information to obtain the solution. If all λ_i are greater than or equal to zero, no boundary conditions are needed at $x = L$; and the interior solution is unaffected by conditions beyond this boundary.

A choked condition exists when no information can propagate into the solution region from the exterior. Such a condition exists at the boundary point, $x = L$, when

$$\lambda_j = 0 \text{ for some } j \leq n \tag{3.4-3}$$

$$\lambda_i \geq 0 \text{ for all } i \ \neq \ j \ . \tag{3.4-4}$$

These are the mathematical conditions satisfied by the equations of motion for a flowing fluid when reduction in downstream pressure ceases to result in increased flow rate. It is well known[3.4-5] that the choked condition for single-phase flow occurs when the fluid velocity just equals the local sound speed. For this case, one of the λ_i's is just equal to zero. For the two-phase case, it is possible for all λ_i's to be greater than zero under special conditions which can exist during discharge of a subcooled liquid.

Extensive investigation was carried out to determine a two-phase choked-flow criterion under two assumed conditions:[a] (a) thermal equilibrium between phases, and (b) adiabatic phases without phase change (frozen).[3.4-6] The frozen assumption was in poor agreement with data compared to the thermal equilibrium assumption. Therefore, the thermal equilibrium assumption with slip is used as the basis for the ATHENA choked-flow criterion when two phase conditions exist.

3.4.1.1 Choking Criterion for Nonhomogeneous, Equilibrium Two-Phase Flow. The two-fluid model for the conditions of thermal equilibrium (equilibrium interphase mass transfer) is

---

a. The number n is the number of differential equations comprising the system defined by Equation (3.4-1) and the number i designates any of the corresponding n roots.

a. The hydrodynamic model is not based on either of these assumptions. However, the purpose of this analysis is simply to establish a criterion for a choked flow; thus, there is no conflict with the basic hydrodynamic model.

described by the overall mass continuity equation, two-phasic momentum equations, and the mixture entropy equation. This system of equations is

$$\frac{\partial(\alpha_g\rho_g + \alpha_f\rho_f)}{\partial t} + \frac{\partial(\alpha_g\rho_g v_g + \alpha_f\rho_f v_f)}{\partial x} = 0 \qquad (3.4\text{--}5)$$

$$\alpha_g\rho_g\left(\frac{\partial v_g}{\partial t} + v_g\frac{\partial v_g}{\partial x}\right) + \alpha_g\frac{\partial P}{\partial x}$$

$$+ C\alpha_g\alpha_f\rho\left(\frac{\partial v_g}{\partial t} + v_f\frac{\partial v_g}{\partial x} - \frac{\partial v_f}{\partial t} - v_g\frac{\partial v_f}{\partial x}\right) = 0 \qquad (3.4\text{-}6)$$

$$\alpha_f\rho_f\left(\frac{\partial v_f}{\partial t} + v_f\frac{\partial v_f}{\partial x}\right) + \alpha_f\frac{\partial P}{\partial x}$$

$$+ C\alpha_f\alpha_g\rho\left(\frac{\partial v_f}{\partial t} + v_g\frac{\partial v_f}{\partial x} - \frac{\partial v_g}{\partial t} - v_f\frac{\partial v_g}{\partial x}\right) = 0 \qquad (3.4\text{-}7)$$

$$\frac{\partial(\alpha_g\rho_g S_g + \alpha_f\rho_f S_f)}{\partial t} + \frac{\partial(\alpha_g\rho_g S_g v_g + \alpha_f\rho_f S_f v_f)}{\partial x} = 0 \quad . \qquad (3.4\text{--}8)$$

The momentum equations include the interphase force terms due to relative acceleration.[3.4-7] These force terms have a significant effect on wave propagation velocity and consequently on the choked flow velocity. The particular form chosen is frame invariant and symmetrical; and the coefficient of virtual mass, $C\alpha_g\alpha_f\rho$, is chosen to ensure a smooth transition between pure vapor/gas and pure liquid. For a dispersed flow, the constant, C, has a theoretical value of 0.5; whereas for a separated flow, the value may approach zero. The energy equation is written in terms of mixture entropy, which is constant for adiabatic flow. (The energy dissipation associated with interphase mass transfer and relative phase acceleration is neglected.)

The nondifferential source terms, C(U), in Equation (3.4-1) do not enter into the characteristic analysis or affect the propagation velocities. For this reason, the source terms associated with wall friction, interphase drag, and heat transfer are omitted for brevity in Equations (3.4-5) through (3.4-8).

In the thermal equilibrium case, ρ_g, ρ_f, S_g, and S_f are known functions of the pressure only (the vapor/gas and liquid values along the saturation curve). The derivatives of these variables are designated by an asterisk as follows:

$$\rho_f^* = \frac{d\rho_f^s}{dP} , \rho_g^* = \frac{d\rho_g^s}{dP} \qquad (3.4\text{--}9)$$

$$S_f^* = \frac{dS_f^s}{dP} \ , S_g^* = \frac{dS_g^s}{dP} \ . \qquad (3.4\text{-}10)$$

The system of governing equations [Equations (3.4-5) through (3.4-8)] can be written in terms of the four dependent variables, α_g, P, v_g, and v_f, by application of the chain rule and the property derivatives [Equations (3.4-9) and (3.4-10)]. Thus, the system of equations can be written in the form of Equation (3.4-1) where the A and B are fourth-order square coefficient matrices.

The characteristic polynomial that results is fourth-order in λ, and factorization can only be carried out approximately to obtain the roots for λ and establish the choking criterion. The first two roots are

$$\lambda_{1,2} = \frac{\left(\begin{array}{l} \left\{ \alpha_f \rho_g + \frac{\rho C}{2} \pm \left[\left(\frac{\rho C}{2} \right)^2 - \alpha_g \alpha_f \rho_g \rho_f \right]^{1/2} \right\} v_g \\[4pt] + \left\{ \alpha_g \rho_f + \frac{\rho C}{2} \mp \left[\left(\frac{\rho C}{2} \right)^2 - \alpha_g \alpha_f \rho_g \rho_f \right]^{1/2} \right\} v_f \end{array} \right)}{\left(\alpha_f \rho_g + \frac{\rho C}{2} \right) + \left(\alpha_g \rho_f + \frac{\rho C}{2} \right)} \ . \qquad (3.4\text{--}11)$$

These two roots are obtained by neglecting the fourth-order factors relative to the second-order factors in $(\lambda - v_g)$ and $(\lambda - v_f)$. There are no first- or third-order factors. Inspection of Equation (3.4-11) shows that $\lambda_{1,2}$ have values between v_g and v_f; thus, the fourth-order factors, $(\lambda - v_g)$ and $(\lambda - v_f)$, are small (i.e., neglecting these terms is justified). The values for $\lambda_{1,2}$ may be real or complex depending on the sign of the quantity $\left[\left(\frac{\rho C}{2} \right)^2 - \alpha_g \alpha_f \rho_g \rho_f \right]$.

The remaining two roots are obtained by dividing out the quadratic factor containing $\lambda_{1,2}$, neglecting the remainder, and factoring the remaining quadratic terms. [This procedure can be shown to be analogous to neglecting the second- and higher-order terms in the relative velocity, $(v_g - v_f)$.] The remaining roots are

$$\lambda_{3,4} = v + D(v_g - v_f) \pm a \qquad (3.4\text{-}12)$$

where

$$v \qquad = \qquad \frac{\alpha_g \rho_g v_g + \alpha_f \rho_f v_f}{\rho} \qquad (3.4\text{-}13)$$

$$a = a_{HE} \left[\frac{C\rho^2 + \rho(\alpha_g\rho_f + \alpha_f\rho_g)}{C\rho^2 + \rho_g\rho_f} \right]^{1/2} \qquad (3.4\text{-}14)$$

and

$$D = 0.5 \left[\frac{(\alpha_g\rho_f - \alpha_f\rho_g)}{(\rho C + \alpha_f\rho_g + \alpha_g\rho_f)} + \frac{\rho_g\rho_f(\alpha_f\rho_f - \alpha_g\rho_g)}{\rho(\rho_g\rho_f + C\rho^2)} - a_{HE}^2 \frac{\rho(\alpha_g\rho_g^2 S_g^* + \alpha_f\rho_f^2 S_f^*)}{\rho_g\rho_f(S_g - S_f)} \right] \quad . \qquad (3.4\text{-}15)$$

The quantity, a_{HE}, is the homogeneous equilibrium speed of sound (see Volume IV). The roots, $\lambda_{3,4}$, have only real values.

The general nature and significance of these roots is revealed by applying the characteristic considerations. The speed of propagation of small disturbances is related to the values of the characteristic roots. In general, the velocity of propagation corresponds to the real part of a root, and the growth or attenuation is associated with the complex part of the root. Choking will occur when the signal, which propagates with the largest velocity relative to the fluid, is just stationary, i.e.,

$$\lambda_j^R = 0 \text{ for some } j \leq 4 \qquad (3.4\text{-}16)$$

and

$$\lambda_i^R \geq 0 \text{ for all } i \neq j \quad . \qquad (3.4\text{-}17)$$

The existence of complex roots for $\lambda_{1,2}$ makes the initial boundary value problem ill-posed. This problem has been discussed by many investigators,[3.4-8,3.4-9] and the addition of any small, second-order viscous effects renders the problem well-posed.[3.4-8,3.4-10] The whole phenomenon of systems with mixed orders of derivatives and a first-order system with the addition of a small, second-order term has been discussed and analyzed by Whitham.[3.4-4] He has shown that the second-order viscous terms give infinite characteristic velocities. However, very little information is propagated along these characteristic lines; and the bulk of the information is propagated along characteristic lines defined by the first-order system. We conclude that the ill-posed nature of Equations (3.4-5) through (3.4-8) can be removed by the addition of small, second-order viscous terms that have little effect upon the propagation of information. Therefore, the choking criterion for the two-phase flow system analyzed here is established from Equation (3.4-16).

The explicit character of the choking criterion for the two-phase flow model defined by Equations (3.4-5) through (3.4-8) is examined. Since the two roots, $\lambda_{1,2}$, are between the phase velocities, v_f and v_g, the choking criterion is established from the roots, $\lambda_{3,4}$, and Equation (3.4-16). The choking criterion is

$$v + D(v_g - v_f) = \pm a \ . \tag{3.4-18}$$

The choking criterion can be rewritten in terms of the mass mean and relative Mach numbers, which are

$$M_v = \frac{v}{a}, \qquad\qquad M_r = \frac{v_g - v_f}{a} \tag{3.4-19}$$

as

$$M_v + DM_r = \pm 1 \ . \tag{3.4-20}$$

This relation is similar to the choking criterion for single-phase flow where only the mass average Mach number appears and choking corresponds to a Mach number of unity.

The choking criterion [Equation (3.4-20)] is a function of the two parameters, D and a. In **Figure 3.4-1**, a is plotted as a function of the void fraction, α_g, for a typical steam/water system at 7.5 MPa, with C equal to zero (the stratified equilibrium sound speed), C equal to 0.5 (the typical value for a dispersed flow model), and in the limiting case when C becomes infinite (homogeneous equilibrium sound speed). From **Figure 3.4-1**, it is evident that the virtual mass coefficient has a significant effect upon the choked-flow dynamics in two-phase flow.[3.4-11]

To establish the actual choked-flow rate for two-phase flow with slip, the relative velocity term in Equation (3.4-20) must also be considered. The relative Mach number coefficient, D, is shown plotted in **Figure 3.4-2** for values of C equal to 0, 0.5, and infinity. It is evident from these results that the choked-flow velocity can differ appreciably from the mass mean velocity when slip occurs. It is significant that the variation of the choked-flow criterion from the homogeneous result is entirely due to velocity nonequilibrium, since these results have been obtained under the assumption of thermal equilibrium. The particular values of these parameters used in the model are further discussed later in this section.

3.4.1.2 Subcooled Choking Criterion. The previous analysis assumes two-phase conditions exist throughout the break flow process. However, initially and in the early phase of blowdown, the flow approaching the break or break nozzle will be subcooled liquid. Under most conditions of interest in LWR systems, the fluid undergoes a phase change at the break. The transition from single- to two-phase flow is accompanied by a discontinuous change in the fluid bulk modulus. This is especially true for the liquid-to-liquid/vapor/gas transition. For example, at 600 kPa, the ratio of the single- to two-phase sound speed at the liquid boundary is 339.4. This is discussed in Volume IV, Appendix 7A. Thus, considerable care must be exercised when analyzing a flow having transitions to or from a pure phase. (A discontinuity is also present at the vapor/gas boundary, but the ratio is only 1.0695.)
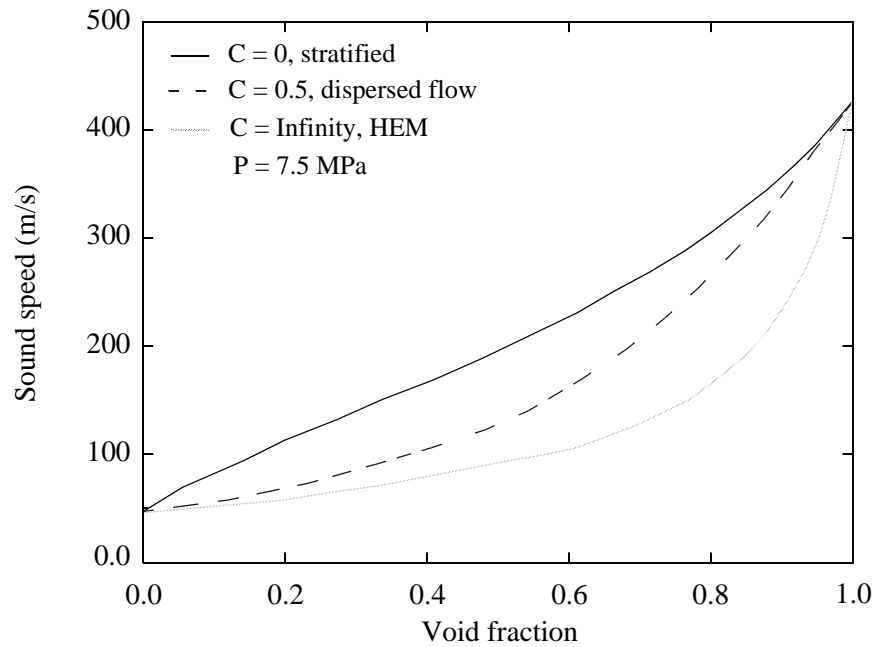
Figure 3.4-1 Equilibrium speed of sound as a function of void fraction and virtual mass coefficient.
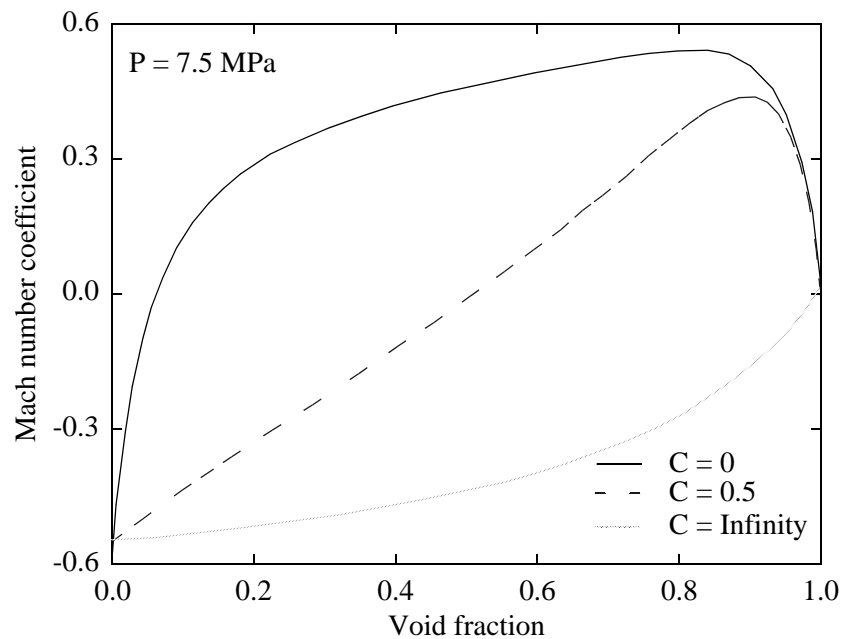
Figure 3.4-2 Coefficient of relative Mach number for thermal equilibrium flow as a function of void fraction and virtual mass coefficient.

To understand the physical process that occurs for subcooled upstream conditions, consider the flow through a converging/diverging nozzle connected to an upstream plenum with subcooled liquid at a high pressure. For a downstream pressure only slightly lower than the upstream pressure, subcooled liquid flow will exist throughout the nozzle. Under these conditions, the flow can be analyzed using Bernoulli's equation, which predicts a minimum pressure, P_t, at the throat.[a] As the downstream pressure is lowered further, a point is reached where the throat pressure equals the local saturation pressure, P_{sat}. If the downstream pressure is lowered further, vaporization will take place at the throat.[b] When this happens, the fluid sound speed lowers drastically; but continuity considerations dictate that the velocity, v_t, of the two-phase mixture (at the point of minuscule void fraction) just equals the velocity of the subcooled liquid slightly upstream of the throat. When this occurs, v_t in the subcooled region is less than the liquid sound speed; but in the two-phase region, v_t can be greater than the two-phase sound speed. Hence, the subcooled liquid has a Mach number (M) < 1, whereas the two-phase mixture at the throat has a Mach number > 1. Under these conditions (Mach numbers > 1 in the two-phase region), downstream pressure effects are not propagated upstream and the flow is choked. In particular, the supersonic two-phase fluid at the throat must increase in velocity, and the pressure must drop as it expands in the diverging section.[c] (Transition back to subsonic flow can occur in the nozzle as a result of a shock wave.) This choked condition is shown as case (a) in **Figure 3.4-3**. Contrary to the usual single-phase choked flow in a converging/diverging nozzle, there is no point in the flow field where M = 1. This is because in the homogeneous equilibrium model the fluid undergoes a discontinuous change in sound speed from single-phase subcooled conditions to two-phase conditions, although the fluid properties are continuous through the transition point.

When this condition prevails, the flow rate can be established from application of Bernoulli's equation $[(1/2)\rho(v_t^2 - v_{up}^2) = P_{up} - P_{sat}]$. For further decrease in the downstream pressure, no further increase in upstream fluid velocity will occur as long as the upstream conditions are maintained constant.

Now consider the process where a subcooled choked flow, as described above, initially exists (with a very low downstream pressure) and the upstream pressure is lowered as shown in cases (b) and (c) in **Figure 3.4-3**. As the upstream pressure decreases, the pressure at the throat will remain at P_{sat}, and Bernoulli's equation will give a smaller subcooled liquid velocity (v_t) at the throat. As P_{up} is lowered further, a point is reached where $v_t = a_{HE}$ and M = 1 on the two-phase side of the throat. (The Mach number in the subcooled portion upstream of the throat is much less than 1.) This situation is shown schematically in **Figure 3.4-3** as case (b).

---

a. For all practical cases of choking, the subcooled liquid can be considered incompressible with infinite sound speed.

b. An idealized one-dimensional homogeneous equilibrium model is assumed.

c. In a supersonic flow, a diverging nozzle implies an increase in velocity.
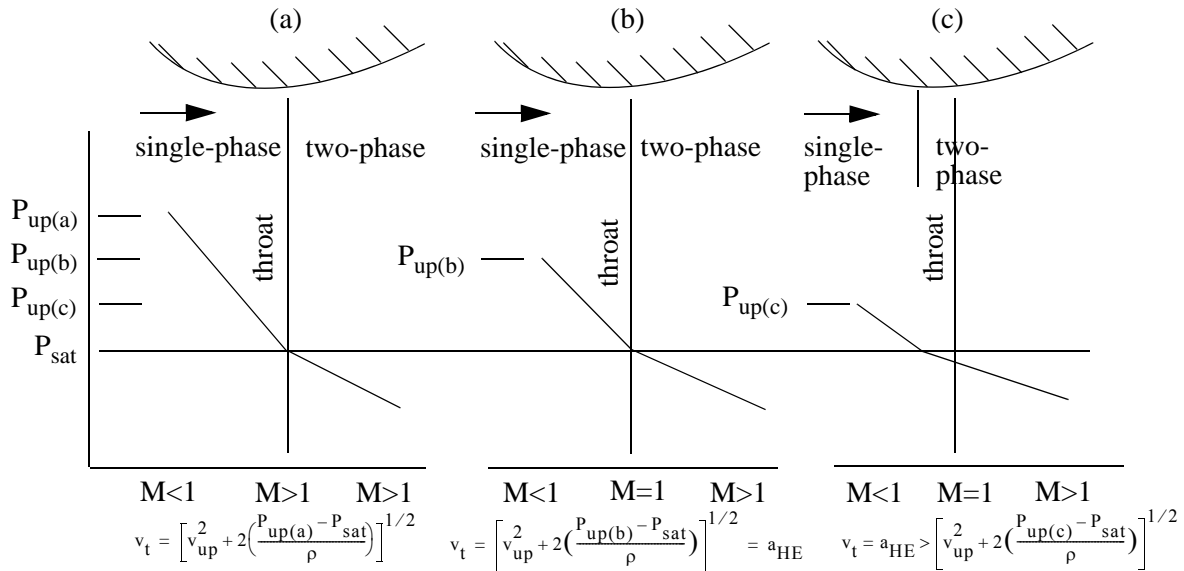
Figure 3.4-3 Subcooled choking process.

As the upstream pressure is lowered further, the point where the pressure reaches P_{sat} must move upstream of the throat. This is shown as case (c) in **Figure 3.4-3**. The subcooled liquid velocity at the P_{sat} location is smaller than the two-phase sound speed, and the flow is subsonic. In the two-phase region between the point at which P_{sat} is reached and the throat, the Mach number is less than 1 but increases to M = 1 at the throat; that is, the two-phase sonic velocity is reached at the throat (as in the case of choked flow having a continuous variation of sound speed with pressure). As P_{up} is lowered still further, the P_{sat} point moves upstream until the flow becomes completely two-phase.

The homogeneous assumption applied in the above subcooled choking description is very close to the real situation when vapor is first formed. However, nonequilibrium can result in a superheated liquid state at a throat pressure, P_t, much lower than the saturation pressure, P_{sat}. The onset of vaporization occurs at P_t instead of P_{sat}.

The pressure undershoot, P_{sat} - P_t, can be described by the Alamgir-Lienhard-Jones correlation,[3.4-12,3.4-13] which is

$$P_{sat} - P_t = \max(\Delta P, 0) \tag{3.4-21}$$

with

$$\Delta P = 0.258\sigma^{3/2}T_R^{13.76}\frac{(1 + 13.25R\Sigma'^{0.8})^{1/2}}{(k_B T_c)^{1/2}\left(1 - \dfrac{V_f}{V_g}\right)} - 0.069984\left(\frac{A_t}{A}\right)^2(\rho v_c^2) \quad . \tag{3.4-22}$$

The first term in ΔP represents the static depressurization effect and is derived by Alamgir and Lienhard[3.4-13] based on classical nucleation theory. For a steady flow in a nozzle, the depressurization rate, Σ', can be shown to be

$$\Sigma' = \frac{\rho v_c^3}{A_t}\left(\frac{dA}{dx}\right)_t \quad . \tag{3.4-23}$$

Note that in Equation (3.4-22), Σ' is in units of Matm/s, but in Equation (3.4-23), Σ' is in units of Pa/s. Here, $\left(\dfrac{dA}{dx}\right)_t$ is the variation of area with respect to axial length and is to be evaluated between the center of the upstream volume and the throat. The second term in ΔP [Equation (3.4-22)] represents the turbulence effect and is developed by Jones.[3.4-14]

The choking velocity, based upon the process shown in **Figure 3.4-3**, can be obtained in the following manner. The subcooled critical flow model is based on the assumption that flashing occurs at the throat of the nozzle or upstream of the throat. This assumption implies that critical flow of subcooled liquid must be accompanied by a minimum pressure drop, which we denote by ΔP_{min}. In this case $\Delta P_{min} = P_{up} - P_t$, where P_{up} is the pressure in the upstream volume and P_t is the throat pressure obtained from the Alamgir-Lienhard-Jones correlation. This leads to a condition on the fluid velocity at the throat, which is obtained from the Bernoulli equation. Assuming the fluid is incompressible and that frictional and gravitational forces are negligible, the Bernoulli equation is given by $\Delta P = \frac{1}{2}\rho(v_t^2 - v_{up}^2)$, where ΔP is the pressure drop from the upstream volume to the throat, v_t is the velocity at the throat, and v_{up} is the velocity in the upstream volume. Thus we obtain the condition $v_t > v_c$, where

$$v_c = \left[v_{up}^2 + 2\left(\frac{P_{up} - P_t}{\rho}\right)\right]^{1/2} \tag{3.4-24}$$

and P_t is to be computed from Equation (3.4-21).

For the process shown in **Figure 3.4-3** case (a), the choking velocity is given by Equation (3.4-24). For the processes shown in **Figure 3.4-3** case (b) and **Figure 3.4-3** case (c), the two-phase choking criterion applies, and the choking velocity is given by

$$v_c = a_{HE} \qquad\qquad (3.4\text{-}25)$$

where a_{HE} is the equilibrium sound speed of a two-phase mixture.

To determine which of the above situations exists, both v_c's are calculated, and the larger is used as the choking velocity to be imposed at the throat. This velocity is imposed numerically in exactly the same way as the choking criterion used for the two-phase condition described previously.

The equilibrium sound speed, a_{HE}, is calculated using thermodynamic conditions at the throat. Momentum and mechanical energy balances are used to calculate the pressure and specific internal energy at the throat and use the thermodynamic property tables to obtain the thermodynamic properties of a saturated liquid-vapor mixture at this pressure and specific internal energy. This method is consistent with the process of subcooled critical flow described in this section, and allows for the presence of a two-phase mixture at the throat. The precise equations used to determine the hydrodynamic conditions at the throat are presented in Volume IV. Note that in an earlier version of ATHENA, the quality of the two-phase mixture at the throat was not determined. Instead the throat was assumed to contain saturated liquid at the temperature of the subcooled liquid upstream. However, this assumption led to an abrupt change of the computed flowrate at the single-phase to two-phase transition.

The subcooled choking model is very similar in concept to the model proposed by Burnell[3.4-15] in that both models assume a Bernoulli expansion to the point of vapor inception at the choke plane. The criterion for transition from subcooled choking to two-phase choking is now better understood and is in agreement with the physics of two-phase flow. The model here is also in agreement with cavitating venturi experience (experimentally confirmed behavior)[3.4-12]. The ATHENA subcooled choking model is somewhat different than the model proposed by Moody[3.4-16] in that the Moody model assumes that an isentropic process occurs to the choke plane.

3.4.1.3 Implementation of Choked Flow Model. Ideally, the two-phase choking criterion [Equation (3.4-18)] can be used as a boundary condition for obtaining flow solutions. However, the applicability of Equation (3.4-18) has not been fully explored. Instead, an approximate criterion given by

$$\frac{\alpha_g \rho_f v_g + \alpha_f \rho_g v_f}{\alpha_g \rho_f + \alpha_f \rho_g} = \pm\, a_{HE} \qquad\qquad (3.4\text{-}26)$$

has been applied extensively and has produced good code/data comparisons. Equation (3.4-26) can be obtained from Equation (3.4-18) in the following manner[3.4-18]. Neglecting the third term in D, we obtain

$$\frac{\alpha_g \rho_g v_g + \alpha_f \rho_f v_f}{\rho} + 0.5 \left[\frac{(\alpha_g \rho_f - \alpha_f \rho_g)}{(\rho C + \alpha_f \rho_g + \alpha_g \rho_f)} + \frac{\rho_g \rho_f (\alpha_f \rho_f - \alpha_g \rho_g)}{\rho(\rho_g \rho_f + C\rho^2)} \right] (v_g - v_f)$$

$$= \pm a_{HE} \left[\frac{C\rho^2 + \rho(\alpha_g \rho_f - \alpha_f \rho_g)}{C\rho^2 + \rho_g \rho_f} \right]^{0.5} . \tag{3.4-27}$$

Then setting C = 0 (stratified) on the left side of Equation (3.4-27) and C = ∞ (homogeneous) on the right side of Equation (3.4-27) and computing the limits, we obtain the approximate criterion given by Equation (3.4-26). Because of the extensive experience with this approximate model, Equation (3.4-26) is currently used in ATHENA choked flow calculations.

In the ATHENA critical flow model, choking is assumed to occur at the narrowest part of the flow channel. This location is called the throat. Under critical flow conditions, the fluid velocity at the throat is equal to the two-phase speed of sound. The critical flow model includes two separate tests to determine if critical flow occurs: a choking test to determine if the hydrodynamic conditions lead to critical flow, and an unchoking test to determine if the hydrodynamic conditions can maintain critical flow. In the choking test [Equation (3.4-26)], the fluid velocity is compared to the local speed of sound, which is based on the hydrodynamic conditions at the throat. In the unchoking test, a momentum balance from the upstream volume center to the throat is used to determine whether the pressure drop is large enough to sustain choked flow. Ideally, choked flow occurs only if the fluid velocity exceeds the local speed of sound and the minimum pressure drop condition is satisfied. In the current implementation of the critical flow model, however, these conditions are relaxed so that choked flow occurs if either of the conditions in the previous sentence is true in order to prevent the computed solution from oscillating at the threshold between sonic and subsonic flow. The precise logic used to determine critical flow and a flowchart of the algorithm is presented in Volume IV.

At each time step and at each flow junction where two-phase cocurrent flow exists, the choking criterion [Equation (3.4-26)] is checked using explicitly calculated values. When choking occurs, Equation (3.4-26) uses new-time phasic velocities for v_g and v_f; it uses the throat pressure P_t to evaluate the old time sound speed $a_{HE,j}$. In Equation (3.4-26), the right hand side term $a_{HE,j}^{n+1}$ is approximated by

$$a_{HEj}^{n+1} = a_{HEj}^n + \left(\frac{\partial a_{HE}}{\partial P} \right)_j^n (P_K^{n+1} - P_K^n) \tag{3.4-28}$$

where P_K is the upstream volume pressure. As P_t is not needed in system calculations, we can eliminate $\frac{\partial P}{\partial x}$ from the vapor/gas and liquid momentum equations (see Volume IV) to obtain

$$\rho_g\left(\frac{\partial v_g}{\partial t} + \frac{1}{2}\frac{\partial v_g^2}{\partial x}\right) - \rho_f\left(\frac{\partial v_f}{\partial t} + \frac{1}{2}\frac{\partial v_f^2}{\partial x}\right)$$

$$= (\rho_g - \rho_f)B_x + \Gamma_g\left(\frac{v_I - \alpha_f v_g - \alpha_g v_f}{\alpha_f \alpha_g}\right) \quad (3.4\text{--}29)$$

$$- \rho_g v_g FWG + \rho_f v_f FWF - \rho_f \rho_g (v_g - v_f)FI - C\rho\frac{\partial(v_g - v_f)}{\partial t} \quad .$$

The finite-difference form of this equation is obtained by integrating with respect to the spatial variable from the upstream volume center to the junction. In this finite-difference equation, all junction velocities are evaluated implicitly.[3.4-18] . The HLOSSG$_j$ and HLOSSF$_j$ terms (code-calculated abrupt area change loss terms and user-defined loss terms) are not present in the finite-difference equation, because these losses are primarily important downstream of the junction. The finite-difference equations corresponding to Equations (3.4-26) and (3.4-29) can be solved for $v_{g,j}^{n+1}$ and $v_{f,j}^{n+1}$ in terms of P_K^{n+1} and old time values.

The unchoking test may be explained by reference to **Figure 3.4-4**, which illustrates the effect of downstream pressure on choked flow through a typical converging-diverging nozzle. In this case, a necessary condition for choked flow is $P_K > P_t$, where P_t is the pressure at the throat and P_K is the pressure in the upstream volume. The term M is the Mach number. However, we may have $P_t > P_L$ or $P_t < P_L$, where P_L is the pressure in the downstream volume. In some cases, shocks may occur in the diverging portion of the nozzle in order that the pressure of the fluid leaving the nozzle matches the downstream pressure. For choking we also require $\max(P_t, P_{Lcrit}) > P_L$ where $P_{Lcrit} = P_K - \Delta P_{min}$ and ΔP_{min}, is a minimum pressure difference needed to maintain choked flow. The quantity ΔP_{min} is calculated from a momentum balance which includes the effects of the variation of flow area, wall friction, and form loss. In particular, the calculation includes the following sequence of steps: (1) Use momentum and energy balances from the upstream volume center to the throat in order to obtain P_t and U_t. (2) Use the thermodynamic property tables to determine the thermodynamic state at the throat from which the two-phase sound speed is obtained. (3) Assuming the fluid velocity at the throat is equal to the two-phase sound speed, use a momentum balance from the upstream volume center to the downstream volume center in order to obtain the pressure drop due to a change in flow area, wall friction, and form loss downstream of the expansion. (This is a minimum pressure drop needed to sustain choked flow. We note that the static pressure increases in the diverging section of the nozzle because the fluid decelerates, but the total pressure decreases due to friction and form losses.) (4) Test for unchoking by comparing the actual pressure drop to the minimum pressure drop. We can justify this test by observing that for choked flow, an increase in the downstream pressure eventually leads to unchoking, and the critical value of the downstream pressure is $P_K - \Delta P_{min}$. This test is especially important for critical flow of subcooled liquid though an abrupt area change. Since an abrupt area change is accompanied by form loss downstream of the throat, the pressure drop must be large enough to accelerate the liquid to sonic velocity at the throat and overcome the form loss downstream of the throat.
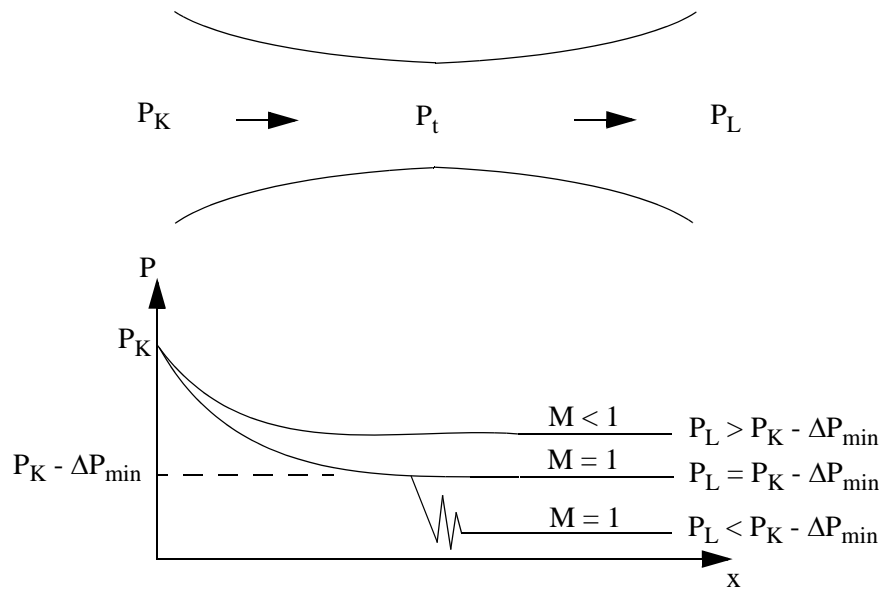
Figure 3.4-4 Pressure distribution for choked flow through a converging-diverging nozzle.

In general, there is a large drop in critical velocity when the fluid changes from a subcooled to a two-phase state. This sudden change often leads to unrealistic velocity oscillations and causes the time step to be reduced considerably. To provide a smooth transition from subcooled to two-phase, a transition region (transition region 1) is inserted between subcooled choking $(\alpha_{g,j} < 10^{-5})$ and two-phase choking $(\alpha_{g,j} > 0.10)$ in which the sound speed is interpolated between the subcooled choking sound speed and the two-phase sound speed, based on the donored value of the junction void fraction, $\dot{\alpha}_{g,j}$. The subcooled sound speed is computed from Equation (3.4-24) using a void fraction of 1.0 x 10^{-5}, and the two-phase sound speed is computed from thermodynamic relations using the homogeneous equilibrium model using a void fraction of 0.10. A void fraction of 0.10 was chosen so that it would require several time steps to traverse the interpolation region based on typical time step sizes and typical rates to change of void fraction per time step. To provide additional smoothing of the transition between subcooled and two-phase choking, the phase velocities obtained from the choking computation [i.e., the simultaneous solution of Equation (3.4-26) and the finite difference form of Equation (3.4-29)] are relaxed with the values from the previous time step, using a variable relaxation factor. The velocities are given by

$$v_{g,j}^{n+1} = v_{g,j}^{n} + R(v_{g,j}^{n+1} - v_{g,j}^{n}) \qquad (3.4\text{-}30)$$

$$v_{f,j}^{n+1} = v_{f,j}^{n} + R(v_{f,j}^{n+1} - v_{f,j}^{n}) \qquad (3.4\text{-}31)$$

where

R $\qquad$ = $\qquad$ 0.1 for $\alpha_{g,j} \leq 0.10$

$\qquad$ = $\qquad$ 0.9 for $\alpha_{g,j} \geq 0.15$ $\qquad$ (3.4-32)

and the relaxation factor R is interpolated between the two values of the junction void fraction. The region between 0.10 and 0.15 is transition region 2. A variable relaxation factor in transition region 2 is used to reduce the numerical noise that would result from an abrupt switch from the heavy under-relaxation in transition region 1 to very little under-relaxation for void fraction above transition region 2. This is discussed in further in Volume IV, Section 7.2.4.

3.4.2 Stratification Entrainment/Pullthrough Model

Under stratified conditions in horizontal and vertical components, the void fraction flowing through a junction may be different from the upstream volume void fraction. Consequently, the regular donoring scheme for the junction void fraction is no longer appropriate because vapor/gas may be pulled through the junction and liquid may also be entrained and pulled through the junction.

3.4.2.1 Horizontal Volumes. A model for this process of vapor/gas pullthrough and liquid entrainment for various conditions for horizontal volumes was developed by Ardron and Bryce[3.4-19] and implemented by Bryce.[3.4-20] This model is sometimes referred to as the offtake model. The correlation for the onset of pullthrough or entrainment is given by

$$h_b = \frac{KW_k^{0.4}}{\left[g\rho_k(\rho_f - \rho_g) \right]^{0.2}}$$ (3.4-33)

where

$\qquad$ h_b $\qquad$ = $\qquad$ the distance between the stratified liquid level and the junction at which pullthrough or entrainment first begins (i.e., the inception height)

$\qquad$ W_k $\qquad$ = $\qquad$ mass flow rate of the continuous phase k in the branch

$\qquad$ ρ_k $\qquad$ = $\qquad$ density of the continuous phase k in the branch

and K is a constant defined as follows: for a vertically upward branch, K = 1.67; for a vertically downward branch, K = 1.50; for vapor/gas pullthrough in a horizontal side branch, K = 0.75; and for liquid entrainment in a horizontal side branch, K = 0.69.

Once the liquid level is closer to the junction than the inception height, the flow quality through the junction is given by the following set of correlations:

For a vertically upward branch,

$$X = R^{3.25(1-R)^2}$$
(3.4-34)

where

$$R \quad = \quad \frac{h}{h_b}$$

$h \quad = \quad$ distance from the stratified liquid level to the junction.

For a vertically downward branch,

$$X = e^{-3.1R}(1 - R^2)^{3.5}$$
(3.4-35)

For a horizontal side branch,

$$X = X_o^{1+CR}[1 - 0.5R(1+R)X_o^{(1-R)}]^{0.5}$$
(3.4-36)

where

$$X_o \quad = \quad \frac{1.15}{1 + \left(\dfrac{\rho_f}{\rho_g}\right)^{1/2}} \, ,$$
(3.4-37)

$C = 1.09$ for gas pullthrough, and $C = 1.00$ for liquid entrainment. The flow quality is converted into a junction void fraction using the slip ratio in the junction from the previous time step.

The calculation of the junction void fraction is subject to several limitations to handle special situations (e.g., inception height greater than pipe radius for side branch or greater than pipe diameter for vertical branches) and to eliminate oscillations that would cause the time step to be reduced, thereby increasing code run time. The details of the implementation of the stratification entrainment/pullthrough model for horizontal volumes can be found in Volume IV of this manual, in Ardron and Bryce,[3.4-19] and in Bryce.[3.4-20]

3.4.2.2 Vertical Volumes. The entrainment/pullthrough model described above was developed for stratified flow in horizontal volumes. With the implementation of the mixture tracking model, the code is able to model stratified flow in vertical volumes. The control logic for the entrainment/pullthrough model for horizontal volumes was modified to allow for the entrainment/pullthrough at junctions attached to the sides of 'vertical' volumes. Vertical volumes are defined as one-dimensional volumes whose primary flow direction (i.e., the 'x' direction) is oriented in the vertical direction or as volumes in the

multi-dimensional component where the 'z' direction is oriented in the vertical direction. If a junction is attached to the 'y' or 'z' faces of a one-dimensional vertical volume or the 'x' or 'y' faces of a volume in the multi-dimensional component, the user may designate the junction as a 'side offtake' junction which activates the entrainment/pullthrough logic for side branches as described in the previous sections. The side junction is assumed to be attached the vertical volume at an elevation of half of the height of the vertical volume and the height of the stratified level relative to the side junction is determined by the two-phase level model.

3.4.3 Abrupt Area Change

The general reactor system contains piping networks with many sudden area changes and orifices. To apply the ATHENA hydrodynamic model to such systems, analytical models for these components have been developed.[3.4-21] The basic hydrodynamic model is formulated for slowly varying (continuous) flow area variations; therefore, special models are not required for this case.

The abrupt area change model, discussed here and developed in detail in **Reference 3.4-21**, is based on the Borda-Carnot[3.4-22] formulation for a sudden (i.e., sharp, blunt) enlargement and standard pipe flow relations, including the vena-contracta effect for a sudden (i.e., sharp, blunt) contraction or sharp-edge orifice or both. It does not include the case where an enlargement contraction or orifice is rounded or beveled. Quasi-steady continuity and momentum balances are employed at points of abrupt area change. The numerical implementation of these balances is such that hydrodynamic losses are independent of upstream and downstream nodalization. In effect, the quasi-steady balances are employed as jump conditions that couple fluid components having abrupt changes in cross-sectional area. This coupling process is achieved without change to the basic linear semi-implicit and nearly-implicit numerical time-advancement schemes.

3.4.3.1 Abrupt Area Change Modeling Assumptions. The basic assumption used for the transient calculation of two-phase flow in flow passages with points of abrupt area change is: the transient flow process can be approximated as a quasi-steady flow process that is instantaneously satisfied by the upstream and downstream conditions (that is, transient inertia, mass, and energy storage are neglected at abrupt area changes). However, the upstream and downstream flows are treated as fully transient flows.

There are several bases for the above assumption. A primary consideration is that available loss correlations are based on data taken during steady flow processes; however, transient investigations[3.4-23] have verified the adequacy of the quasi-steady assumption. The volume of fluid and associated mass, energy, and inertia at points of abrupt area change is generally small compared with the volume of upstream and downstream fluid components. The transient mass, energy, and inertia effects are approximated by lumping them into upstream and downstream flow volumes. Finally, the quasi-steady approach is consistent with modeling of other important phenomena in transient codes (that is, heat transfer, pumps, and valves).

3.4.3.2 Review of Single-Phase Abrupt Area Change Models. The modeling techniques used for dynamic pressure losses associated with abrupt area change in single-phase flow are reviewed

briefly before discussing the extension of these methods to two-phase flows. In a steady incompressible flow, losses at an area change are modeled by the inclusion of an appropriate dynamic head loss term, h_L, in the one-dimensional modified Bernoulli equation, that is

$$\left(\frac{v^2}{2} + \frac{P}{\rho}\right)_1 = \left(\frac{v^2}{2} + \frac{P}{\rho}\right)_2 + h_L \tag{3.4-38}$$

where h_L is of the form $h_L = (1/2)\ Kv^2$. The particular form of the dynamic head loss is obtained by employing the Borda-Carnot[3.4-22] assumption for calculating losses associated with the expansion part of the flow process at points of abrupt area change.

For the case of a one-dimensional branch, apportioned volume areas are calculated. This is discussed in Section 3.5.1.

3.4.3.2.1 Expansion--Consider a steady and incompressible flow undergoing a sudden increase in cross-sectional area (expansion) as shown in **Figure 3.4-5**. Here the flow is assumed to be from left to right with the upstream conditions denoted by the subscript 1 and the downstream condition by 2. Here the upstream and downstream conditions are assumed to be far enough removed from the point of area change that flow is one-dimensional, i.e., none of the two-dimensional effects of the abrupt area change exist. These locations can range from several diameters upstream to as many as 30 diameters downstream. However, for purposes of modeling the overall dynamic pressure loss, the entire process is assumed to occur as a discontinuous jump in flow condition at the point of abrupt area change. In this context, the stations 1 and 2 refer to locations immediately upstream and downstream of the abrupt area change.
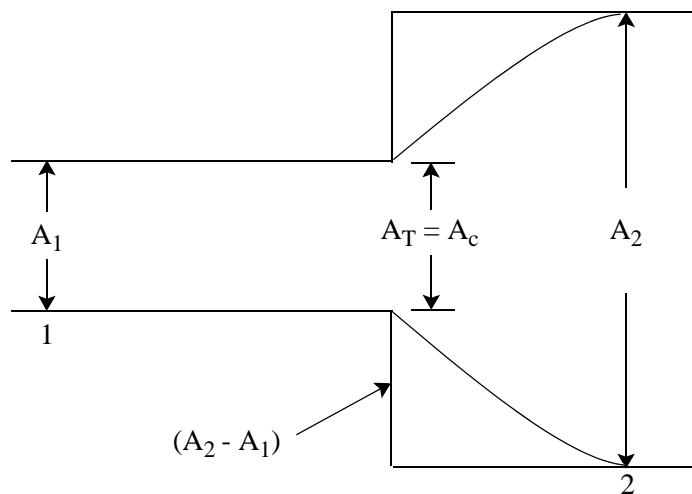
Figure 3.4-5 Abrupt expansion.

The dynamic head loss for the abrupt expansion shown in **Figure 3.4-5** can be obtained using the Borda-Carnot[3.4-22] assumption, i.e., the pressure acting on the "washer shaped" area, A_2 - A_1, is the upstream pressure, P_1. When this assumption is employed in an overall momentum balance, the head loss is

$$h_L = \frac{1}{2}\left(1 - \frac{A_1}{A_2}\right)^2 v_1^2 \quad . \tag{3.4-39}$$

The loss in the dynamic pressure associated with the area change is related to the head by

$$\Delta P_f = \rho h_L = \frac{1}{2}\rho\left(1 - \frac{A_1}{A_2}\right)^2 v_1^2 \quad . \tag{3.4-40}$$

3.4.3.2.2 Contraction--The flow process at a point of abrupt reduction in flow area (contraction) is idealized in much the same manner as for the expansion, except that an additional process must be considered. The flow continues to contract beyond the point of abrupt area reduction and forms a vena contracta, see **Figure 3.4-6**. The point of vena contracta is designated by c. The far-upstream and far-downstream conditions are designated by 1 and 2, respectively.
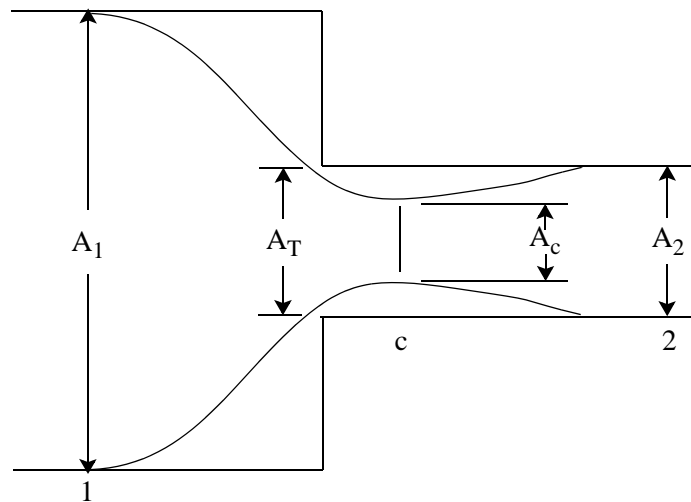
Figure 3.4-6 Abrupt contraction.

Consider a sudden contraction in a steady incompressible flow. The loss in dynamic pressure from the upstream station to the vena contracta is the smaller part of the total loss. Measurements[3.4-22] indicate

that the contracting flow experiences a loss no larger than $\Delta P_f = 0.046\left(\frac{1}{2}\rho v_c^2\right) = 0.12\left(\frac{1}{2}\rho v_2^2\right)$, where v_c is the velocity at the contracta. This loss is at most 24% of the total loss and is neglected in ATHENA. The dynamic pressure loss associated with the new expansion from the area at the vena contracta to the downstream area is modeled using the Borda-Carnot assumption with the condition at the vena contracta as the upstream condition, that is

$$\Delta P_f = \frac{1}{2}\rho\left(1 - \frac{A_c}{A_2}\right)^2 v_c^2 \ , \tag{3.4-41}$$

where from continuity considerations for incompressible flow

$$v_c = \frac{A_2 v_2}{A_c} \ . \tag{3.4-42}$$

The contraction ratio, $\frac{A_c}{A_2}$, is a function of $\frac{A_2}{A_1}$. This is based on a synthesis of analytical approaches and generally accepted experimental information.[3.4-22] The function in **Reference 3.4-22** is in the form of a table. This table has been approximated in ATHENA as the function equation $\frac{A_c}{A_2} = 0.62 + 0.38\left(\frac{A_2}{A_1}\right)^3$. Volume IV discusses this approximation in more detail.

Combining Equations (3.4-41) and (3.4-42) leads to

$$\Delta P_f = \frac{1}{2}\rho\left(1 - \frac{A_2}{A_c}\right)^2 v_2^2 \tag{3.4-43}$$

as the dynamic pressure loss for a contraction.[3.4-22]

        *3.4.3.2.3 Abrupt Area Change With an Orifice--*The most general case of an abrupt area change is a contraction with an orifice at the point of contraction. Such a configuration is shown in **Figure 3.4-7**. In this case, an additional flow area, the orifice flow area, must be specified. Conditions at the orifice throat station will be designated by a subscript T. Three area ratios are used throughout this development. The first is the contraction area ratio at the vena-contracta relative to the minimum physical area, $\varepsilon_c = \frac{A_c}{A_T}$. The second is the ratio of the minimum physical area to the upstream flow area, $\varepsilon_T = \frac{A_T}{A_1}$. The third is the ratio of the downstream to upstream area, $\varepsilon = \frac{A_2}{A_1}$.
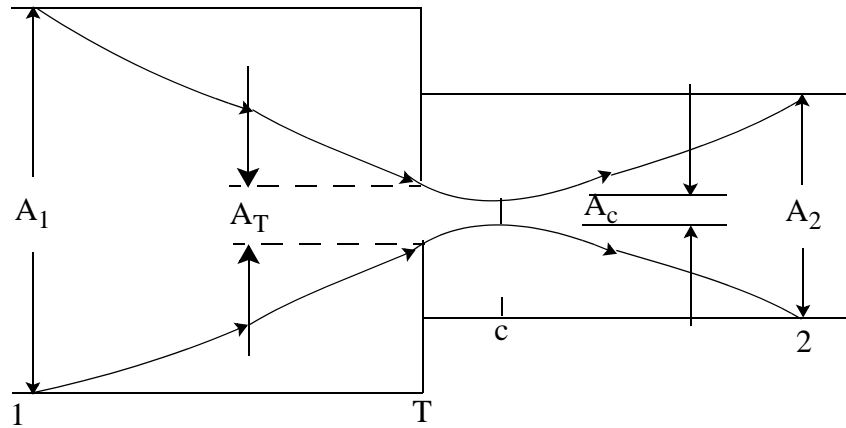
Figure 3.4-7 Orifice at abrupt area change.

The dynamic pressure loss for an abrupt area contraction combined with an orifice is analyzed in a manner parallel to that for a simple contraction. The loss associated with the contracting fluid stream from Station 1 to c (the point of vena-contracta) is neglected. The dynamic pressure loss associated with the expansion from the vena-contracta to the downstream section is given by

$$\Delta P_f = \frac{1}{2}\rho\left(1 - \frac{A_c}{A_2}\right)^2 v_c^2 \quad . \tag{3.4-44}$$

The contraction ratio, $\varepsilon_c = \dfrac{A_c}{A_T}$, is a function of $\varepsilon_T = \dfrac{A_T}{A_1}$. The code uses the same function equation as is used for a contraction. The function equation ε_c has the form $\varepsilon_c = 0.62 + 0.38\,(\varepsilon_T)^3$. Using the continuity equations, $v_c = \dfrac{A_T v_T}{A_c} = \dfrac{v_T}{\varepsilon_c}$ and $v_T = \dfrac{A_2 v_2}{A_T} = \dfrac{\varepsilon}{\varepsilon_T} v_2$, Equation (3.4-44) can be written as

$$\Delta P_f = \frac{1}{2}\rho\left(1 - \frac{\varepsilon}{\varepsilon_c \varepsilon_T}\right)^2 v_2^2 \tag{3.4–45}$$

where $K_f = K_g = \left(1 - \dfrac{\varepsilon}{\varepsilon_c \varepsilon_T}\right)^2$.

Equation (3.4-45) is a generalization applicable to all the cases previously treated. For a pure expansion, $\varepsilon_T = 1$, $\varepsilon_c = 1$, and $\varepsilon > 1$; for a contraction, $\varepsilon_T = \varepsilon < 1$ and $\varepsilon_c < 1$. Each of these is a special case of Equation (3.4-45).

The two-phase dynamic pressure loss model is based on an adaptation of the general single-phase head loss given by Equation (3.4-45). It is described is the next section.

3.4.3.3 Two-Phase Abrupt Area Change Model. The two-phase flow through an abrupt area change is modeled in a manner very similar to that for single-phase flow by defining phasic flow areas. The two phases are coupled through the interphase drag, a common pressure gradient, and the requirement that the phases coexist in the flow passage. As with the single-phase case, apportioned volume areas are calculated for a one-dimensional branch. This is discussed in Section 3.5.1.

The one-dimensional phasic stream-tube momentum equations are given in Section 3.1.1. The flow at points of abrupt area change is assumed to be quasi-steady and incompressible. In addition, the terms in the momentum equations due to body force, wall friction, and mass transfer are assumed to be small in the region affected by the area change. The interphase drag terms are retained, since the gradient in relative velocity can be large at points of abrupt area changes. The interphase drag is increased for co-current horizontal stratified abrupt area changes in order to ensure more homogeneous flow.

Equations (3.1-7) and (3.1-8) can be integrated approximately for a steady incompressible, smoothly varying flow to obtain modified Bernoulli-type equations for each phase, that is

$$\left(\frac{1}{2}\rho_f v_f^2 + P\right)_1 = \left(\frac{1}{2}\rho_f v_f^2 + P\right)_2 + \left(\frac{FI'}{\alpha_f}\right)_1 (v_{f1} - v_{g1})L_1 + \left(\frac{FI'}{\alpha_f}\right)_2 (v_{f2} - v_{g2})L_2 \tag{3.4-46}$$

and

$$\left(\frac{1}{2}\rho_g v_g^2 + P\right)_1 = \left(\frac{1}{2}\rho_g v_g^2 + P\right)_2 + \left(\frac{FI'}{\alpha_g}\right)_1 (v_{g1} - v_{f1})L_1 + \left(\frac{FI'}{\alpha_g}\right)_2 (v_{g2} - v_{f2})L_2 \tag{3.4-47}$$

where L_1 and L_2 are the lengths from the upstream condition to the throat and from the throat to the downstream condition respectively and where $FI' = \alpha_f \alpha_g \rho_f \rho_g FI$. The term FI is determined from Equation (3.3-47). The interphase drag is divided into two parts, which are associated with the upstream and downstream parts of the flow affected by the area change.

3.4.3.4 General Model. Consider the application of Equations (3.4-46) and (3.4-47) to the flow of a two-phase fluid through a passage having a generalized abrupt area change. The flow passage is shown in **Figure 3.4-8**.[a] Here, the area A_T is the throat or minimum area associated with an orifice located at the point of the abrupt area change. Since each phase is governed by a modified Bernoulli-type equation, it is reasonable to assume that losses associated with changes in the phasic flow area can be modeled by separate dynamic pressure loss terms for both the liquid and vapor/gas phases. Hence, it is assumed that the liquid sustains a loss as if it alone (except for interphase drag) were experiencing an area change from α_{f1} A_1 to α_{fT} A_T to α_{f2} A_2; and the vapor/gas phase experiences a loss as if it alone were flowing through an area change from α_{g1} A_1 to α_{gT} A_T to α_{g2} A_2. The area changes for each phase are the phasic area changes

(see **Figure 3.4-8**). When the losses for these respective area changes [based on the Borda-Carnot model and given by Equation (3.4-45)] are added to Equations (3.4-46) and (3.4-47), the following phasic momentum equations are obtained:
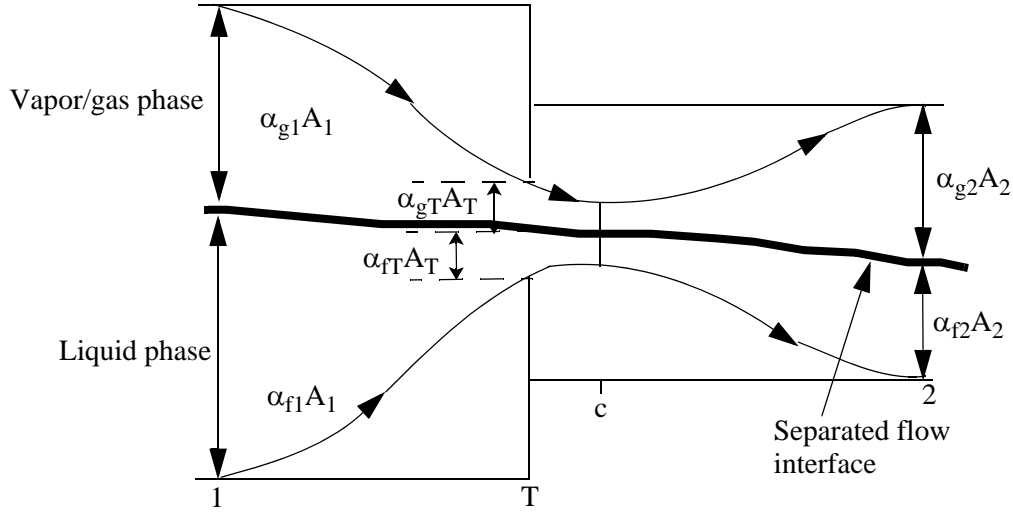
Figure 3.4-8 Schematic flow of two-phase mixture at abrupt area change.

$$\left(\frac{1}{2}\rho_f v_f^2 + P\right)_1 = \left(\frac{1}{2}\rho_f v_f^2 + P\right)_2 + \frac{1}{2}\rho_f\left(1 - \frac{\alpha_{f2}\varepsilon}{\alpha_{fT}\varepsilon_{fc}\varepsilon_T}\right)^2 (v_{f2})^2$$
$$+ \left(\frac{FI'}{\alpha_f}\right)_1 (v_{f1} - v_{g1})L_1 + \left(\frac{FI'}{\alpha_f}\right)_2 (v_{f2} - v_{g2})L_2$$

(3.4-48)

and

$$\left(\frac{1}{2}\rho_g v_g^2 + P\right)_1 = \left(\frac{1}{2}\rho_g v_g^2 + P\right)_2 + \frac{1}{2}\rho_g\left(1 - \frac{\alpha_{g2}\varepsilon}{\alpha_{gT}\varepsilon_{gc}\varepsilon_T}\right)^2 (v_{g2})^2$$
$$+ \left(\frac{FI'}{\alpha_g}\right)_1 (v_{g1} - v_{f1})L_1 + \left(\frac{FI'}{\alpha_g}\right)_2 (v_{g2} - v_{f2})L_2$$

(3.4-49)

---

a. In **Figure 3.4-8**, the flow is shown as a separated flow for clarity. The models developed are equally
applicable to separated and dispersed flow regimes, as evidenced by the calculations performed when the
abrupt area change model was incorporated into ATHENA.[3.4-21] The model was verified on single-phase
expansions, contractions, and orifices. Three two-phase problems were also run: (1) expansion case with the
interphase drag equal to zero, which simulates separated flow, (2) expansion case with the interphase drag
appropriate for dispersed flow, and (3) contraction case with the interphase drag appropriate for dispersed
flow.

where $K_f = \left(1 - \dfrac{\alpha_{f2}\varepsilon}{\alpha_{fT}\varepsilon_{fc}\varepsilon_T}\right)^2$ and $K_g = \left(1 - \dfrac{\alpha_{g2}\varepsilon}{\alpha_{gT}\varepsilon_{gc}\varepsilon_T}\right)^2$.

These phasic momentum equations are used across an abrupt area change. In Equations (3.4-48) and (3.4-49), ε_{fc} and ε_{gc} are the same tabular function of area ratio as in the single-phase case, except the area ratios used are the phasic area ratios, given by

$$\varepsilon_{fT} = \frac{\alpha_{fT}}{\alpha_{f1}}\varepsilon_T \qquad (3.4-50)$$

and

$$\varepsilon_{gT} = \frac{\alpha_{gT}}{\alpha_{g1}}\varepsilon_T \qquad (3.4-51)$$

respectively. The area ratios, $\varepsilon = \dfrac{A_2}{A_1}$ and $\varepsilon_T = \dfrac{A_T}{A_1}$, are the same as for single-phase flow.

The HLOSSG_j^n and HLOSSF_j^n terms in Section 3.1.3 momentum Equations (3.1-104) and (3.1-105) are of the form $\mathrm{HLOSSG}_j^n = \dfrac{1}{2}(K_g^n + K_{in})\left|v_{g,j}^n\right|$ and $\mathrm{HLOSSF}_j^n = \dfrac{1}{2}(K_f^n + K_{in})\left|v_{f,j}^n\right|$, where K_g^n and K_f^n are defined after Equations (3.4-48) and (3.4-49). The user-specified loss coefficient K_{in} is discussed in Section 3.4.4.

The interphase drag effects in Equations (3.4-48) and (3.4-49) are important. These terms govern the amount of slip induced by an abrupt area change; and, if they are omitted, the model will always predict a slip at the area change appropriate to a completely separated flow situation and give erroneous results for a dispersed flow.

3.4.3.5 Model Application. A few remarks concerning the way Equations (3.4-48) and (3.4-49) are applied to expansions and contractions, both with and without an orifice, are necessary. In a single-phase, steady flow situation and given the upstream conditions v_1 and P_1, one can solve for v_2 and P_2 by using the continuity equation ($v_1 A_1 = v_2 A_2$) and Equation (3.4-38). Equations (3.4-48) and (3.4-49), along with the two phasic continuity equations, can be used in a similar manner except that now the downstream void fraction is an additional unknown which must be determined.

3.4.3.5.1 Expansion--For the purpose of explanation, consider the case of an expansion ($\alpha_{fT} = \alpha_{f1}$, $\alpha_{gT} = \alpha_{g1}$, $\varepsilon > 1$, $\varepsilon_T = 1$, $\varepsilon_{fc} = \varepsilon_{gc} = 1$, $\mathrm{FI}_1' = 0$, $L_1 = 0$) for which Equations (3.4-48) and (3.4-49) reduce to

$$\left(\frac{1}{2}\, \rho_f v_f^2 + P\right)_1 = \left(\frac{1}{2}\, \rho_f v_f^2 + P\right)_2 + \frac{1}{2}\, \rho_f\left(1 - \frac{\alpha_{f2}\varepsilon}{\alpha_{f1}}\right)^2 (v_{f2})^2 + \left(\frac{FI'}{\alpha_f}\right)_2 (v_{f2} - v_{g2})L_2 \tag{3.4-52}$$

and

$$\left(\frac{1}{2}\, \rho_g v_g^2 + P\right)_1 = \left(\frac{1}{2}\, \rho_g v_g^2 + P\right)_2 + \frac{1}{2}\, \rho_g\left(1 - \frac{\alpha_{g2}\varepsilon}{\alpha_{g1}}\right)^2 (v_{g2})^2 + \left(\frac{FI'}{\alpha_g}\right)_2 (v_{g2} - v_{f2})L_2 \quad . \tag{3.4-53}$$

These two equations with the two incompressible continuity equations, given by

$$\alpha_{f1}v_{f1}A_1 = \alpha_{f2}v_{f2}A_2 \tag{3.4-54}$$

and

$$\alpha_{g1}v_{g1}A_1 = \alpha_{g2}v_{g2}A_2 \tag{3.4-55}$$

are a system of four equations having four unknowns, α_{f2} ($\alpha_{g2} = 1 - \alpha_{f2}$), v_{f2}, v_{g2}, and P_2, given the upstream conditions, α_{f1} ($\alpha_{g1} = 1 - \alpha_{f1}$), v_{f1}, v_{g1}, and P_1. (The interphase drag, FI', is a known function of the flow properties.) It is important to note that the downstream value of the liquid fraction (α_{f2}) is an additional unknown compared with the single-phase case and is determined (with the downstream velocities and pressure) by simultaneous solution of Equations (3.4-52) through (3.4-55) without additional assumptions. It is reassuring that by taking a proper linear combination of Equations (3.4-48) and (3.4-49), the usual overall momentum balance obtained using the Borda-Carnot[3.4-22] assumption can be obtained.[3.4-24,3.4-25]

If, as in the cited literature,[3.4-24,3.4-25,3.4-26,3.4-27] only the overall momentum balance is used at an expansion, there will be an insufficient number of equations to determine all the downstream flow parameters, α_{f2}, v_{f2}, v_{g2}, and P_2. The indeterminacy has been overcome in cited works by means of several different assumptions concerning the downstream void fraction.[a] In the model developed here [Equations (3.4-52) and (3.4-53)], division of the overall loss into liquid and vapor/gas parts, respectively, results in sufficient conditions to determine all downstream flow variables, including α_{f2}. In addition, the present model includes force terms due to interphase drag in Equations (3.4-52) and (3.4-53), which are necessary to predict the proper amount of slip and void redistribution that occurs at points of area change.

---

a. J. G. Collier[3.4-24] mentions three different assumptions that have been used: (1) $a_{f2} = a_{f1}$, (2) a_{f2} is given by a homogeneous model, and (3) a_{f2} is given by the Hughmark void fraction correlation.

3.4.3.5.2 Contraction--Consider the application of Equations (3.4-48) and (3.4-49) to a contraction. To determine both the downstream conditions and throat conditions from the upstream values of $\alpha_{f1}(\alpha_{g1})$, v_{f1}, v_{g1}, and P_1, an additional consideration needs to be made. To obtain the throat values, apply the momentum equations valid for the contracting section of flow (where the L_1 portion of the interphase force is associated with the contraction). This results in

$$\left(\frac{1}{2}\,\rho_f v_f^2 + P\right)_1 = \left(\frac{1}{2}\,\rho_f v_f^2 + P\right)_T + \left(\frac{FI'}{\alpha_f}\right)_1 (v_{f1} - v_{g1})L_1 \tag{3.4-56}$$

$$\left(\frac{1}{2}\,\rho_g v_g^2 + P\right)_1 = \left(\frac{1}{2}\,\rho_g v_g^2 + P\right)_T + \left(\frac{FI'}{\alpha_g}\right)_1 (v_{g1} - v_{f1})L_1 \quad . \tag{3.4-57}$$

The two incompressible continuity equations are

$$\alpha_{f1} v_{f1} A_1 = \alpha_{fT} v_{fT} A_T \tag{3.4-58}$$

$$\alpha_{g1} v_{g1} A_1 = \alpha_{gT} v_{gT} A_T \quad . \tag{3.4-59}$$

These four equations are solved simultaneously for the values of $\alpha_{fT}(\alpha_{gT})$, v_{fT}, v_{gT}, and P_T at the throat section (the minimum physical area). No additional or special assumptions are made concerning the throat conditions, since they follow as a direct consequence of the unique head loss models for each phase. After the throat values have been obtained, the conditions, at the point of vena-contracta are established, assuming the void fraction is the same as at the throat. Thus, ε_{fc} and ε_{gc} are established using the single-phase contraction function equation and the throat area ratios, ε_{fT} and ε_{gT}, defined by Equations (3.4-50) and (3.4-51). The functions are $\varepsilon_{fc} = 0.62 + 0.38(\varepsilon_{fT})^3$ and $\varepsilon_{gc} = 0.62 + 0.38(\varepsilon_{gT})^3$. To determine the downstream values, Equations (3.4-48) and (3.4-49) can be applied directly from Stations 1 to 2 with the throat values known, or the expansion loss equations can be used from the throat section to Station 2. Both approaches produce identical downstream solutions. As in the case of an expansion, because the proper upstream and downstream interphase drag is included, this modeling approach establishes the phase slip and resulting void redistribution. An orifice at an abrupt area change is treated exactly as the contraction explained above (that is, with two separate calculations to establish first the throat and then the downstream flow variables).

3.4.3.5.3 Countercurrent Flow--The preceding development implicitly assumed a cocurrent flow. For countercurrent flow, Equations (3.4-48) and (3.4-49) are applied exactly as in cocurrent flow except that the upstream sections for the respective phases are located on different sides of the abrupt area change. The difference appears in how the throat and downstream volume fractions are determined. To determine the throat properties, equations similar to Equations (3.4-56) through (3.4-59) are used with the upstream values appropriate for each phase. These four equations are then solved for

$\alpha_{fT}(\alpha_{gT})$, v_{fT}, v_{gT}, and P_T. To determine the downstream values for each phase, only the head loss terms are needed for the downstream volume fractions. (The downstream v_f, v_g, and P do not appear.) For countercurrent flow, these volume fractions are set such that the downstream volume fraction of each phase plus the upstream volume fraction of the opposite phase adds to 1. (Both phases together must fill the flow channel.) With the throat and downstream volume fractions now known, Equations (3.4-48) and (3.4-49) can be used directly to determine the total loss for each phase at the abrupt area change.

3.4.4 User-Specified Form Loss

In the calculation of the total form loss, partitioning of the form friction losses between the liquid and the vapor/gas phases are implemented based on the phasic volume fractions. However, there are many practical situations for the users of using flow condition dependent form loss coefficients in order to represent the friction loss close to experimental values. This section documents the implementation of the general user-specified form loss coefficients.

The $HLOSSG_j^n$ and $HLOSSF_j^n$ terms in Section 3.1.3 momentum Equations (3.1-104) and (3.1-105) are of the form

$$HLOSSG_j^n = \frac{1}{2}(K_g^n + K_{in})\left|v_{g,j}^n\right|$$ (3.4-60)

$$HLOSSF_j^n = \frac{1}{2}(K_f^n + K_{in})\left|v_{f,j}^n\right|$$ (3.4-61)

where the user-specified loss term K_{in} is either the forward (K_F) or reverse (K_R) inputted user-specified loss, depending on the phasic velocity direction. The code-calculated abrupt area loss terms K_g^n and K_f^n are discussed in Section 3.4.3.

In many cases the form loss coefficient is a function of the Reynolds number. Thus it is suggested that the user-specified form loss coefficients can be generally expressed as

$$K_F = A_F + B_F \, Re^{-C_F}$$ (3.4-62)

$$K_R = A_R + B_R \, Re^{-C_R}$$ (3.4-63)

where K_F and K_R are the forward and reverse user-specified form loss coefficients; A_F, A_R, B_F, B_R, C_F, and C_R are the constants that are user-specified and Re is the Reynolds number based on mixture fluid properties. To prevent a divide by a small number or a potential divide by zero in low speed flow, the Reynolds number is limited to values greater than or equal to 50 as is done in the wall friction model (see

Volume IV). There are several different ways of defining the mixture Reynolds number based on the way the mixture viscosity is computed.[3.4-28] In ATHENA, the mixture viscosity μ_m defined by Cicchitti[3.4-29] is implemented for calculating the mixture Reynolds number, and is given by

$$\mu_m = X \mu_g + (1 - X) \mu_f \qquad (3.4\text{-}64)$$

where μ_g is the vapor/gas viscosity, μ_f is the liquid viscosity, and X is the static quality. The mixture Reynolds number is then computed from

$$Re = \frac{|\alpha_g \rho_g v_g + \alpha_f \rho_f v_f| \cdot D}{\mu_m} \qquad (3.4\text{-}65)$$

3.4.5 Crossflow Junction

The ATHENA numerical scheme is generally formulated using one-dimensional elements. However, there are several applications where an approximate treatment of crossflow provides an improved physical simulation. This is discussed further in Volume II. Three different applications for a crossflow formulation are described in the following paragraphs.

The first application concerns a small crossflow between two essentially axial flow streams. This situation is typical of regions such as a reactor core or a steam generator, because the component geometry provides a large resistance (i.e., small flow rate) to crossflow and a small resistance (i.e., large flow rate) to axial flow. Hence, simplified crossflow momentum equations can be used to couple a hot flow channel to a bulk flow channel.

The second application of a crossflow junction is to provide a tee model. In this case, the momentum flux in the side branch is assumed to be perpendicular to the main stream; thus, the main stream momentum flux does not contribute to the crossflow momentum formulation.

The third application is modeling of leak flow paths. In this case, the flow is small and governed primarily by pressure differential, gravity, and flow resistance.

The vapor/gas momentum finite difference equation used in the basic numerical scheme is

$$
\begin{aligned}
(\alpha_g \rho_g)_j^n (v_g^{n+1} &- v_g^n)_j \Delta x_j + \frac{1}{2} (\alpha_g \rho_g)_j^n [(v_g^2)_L^n - (v_g^2)_K^n] \Delta t + \text{VISCOUS\ TERMS} \\
&= -\alpha_{g,j}^n (P_L^{n+1} - P_K^{n+1}) \Delta t - (\alpha_g \rho_g)_j^n (\text{FWG}_j^n \Delta x_j + \text{HLOSSG}_j^n) v_{g,j}^{n+1} \Delta t \\
&\quad - (\alpha_g \rho_g)_j^n \text{FIG}_j^n (v_{g,j}^{n+1} - v_{f,j}^{n+1}) \Delta x_j \Delta t + (\alpha_g \rho_g)_j^n B_x \Delta x_j \Delta t \\
&\quad + \text{VIRTUAL MASS} + \text{MASS TRANSFER MOMENTUM} \\
&\qquad + \text{STRATIFIED PRESSURE GRADIENT EFFECT}
\end{aligned}
\qquad (3.4\text{-}66)
$$

where

$$\Delta x_j \qquad = \qquad \frac{1}{2}(\Delta x_K + \Delta x_L) \ . \qquad\qquad\qquad (3.4\text{-}67)$$

A parallel equation holds for the liquid phase. It should be noted that the momentum Equation (3.4-66) is in reality the sum of half the K cell momentum plus half the L cell momentum. This is the reason for Equation (3.4-67).

In crossflow junctions, just as in the normal junctions, the transverse momentum advection terms are neglected, i.e., there is no transport of x-direction momentum due to the flow in the transverse direction.

For the case of a small crossflow junction between two axial flow streams (J_2 in **Figure 3.4-9**) all the geometric input (area, length, elevation change) for both of the volumes relates to the axial flow direction, as do the wall drag and code-calculated form losses.

The crossflow area and the length scale can be either user-specified or code-calculated values. When code-calculated values are used, the volume geometries are defaulted for the case of a cylindrical pipe, and the appropriate length scale and flow area are used in the code. When user-specified values are used, the user should provide the representative crossflow area and length scale in the input deck. The length scale can be calculated as the volume divided by the crossflow area.
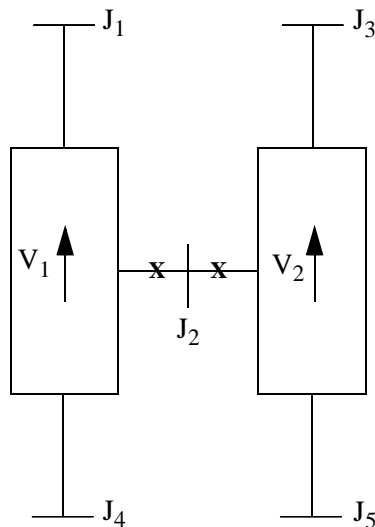
Figure 3.4-9 Modeling of crossflows or leak.

Since the connecting K and L volumes are assumed to be predominantly axial flow volumes, the crossflow junction momentum flux (related to the axial volume velocity in K and L) can be neglected (by using a junction flag) along with the associated numerical viscous term.

The resulting vapor/gas momentum finite difference equation (when the momentum flux is neglected using a junction flag) for a crossflow junction between two axial flow streams is

$$(\alpha_g \rho_g)_j^n (v_g^{n+1} - v_g^n)_j \Delta x_j = -\alpha_{g,j}^n (P_L - P_K)^{n+1} \Delta t - (\alpha_g \rho_g)_j^n HLOSSG_g^n v_{g,j}^{n+1} \Delta t$$
$$- (\alpha_g \rho_g)_j^n FIG_j^n (v_{g,j}^{n+1} - v_{f,j}^{n+1}) \Delta x_j \Delta t + (\alpha_g \rho_g)_j^n B_x \Delta x_j \Delta t$$
$$+ \text{VIRTUAL MASS} + \text{MASS TRANSFER MOMENTUM}$$
$$+ \text{STRATIFIED PRESSURE GRADIENT EFFECT} \ . \tag{3.4-68}$$

A similar equation can be written for the liquid phase. The Δx_j term that is used to estimate the inertial length associated with crossflow is defined using the diameters of volumes K and L, is given by

$$\Delta x_j = \frac{1}{2}[D(K) + D(L)] \tag{3.4-69}$$

if the default is used. If user-specified lengths are input, they are used instead of D(K) and D(L).

The crossflow option can be used with the crossflow junction perpendicular to the axial flow in volume L (or K) but parallel to the axial flow in volume K (or L) (see **Figure 3.4-10**). Here, the situation regarding the half cell momentum contribution in volume L is the same as described above. The half cell momentum contribution associated with volume K is the same as for a normal junction. This type of crossflow modeling can be used for a 90-degree tee simulation.
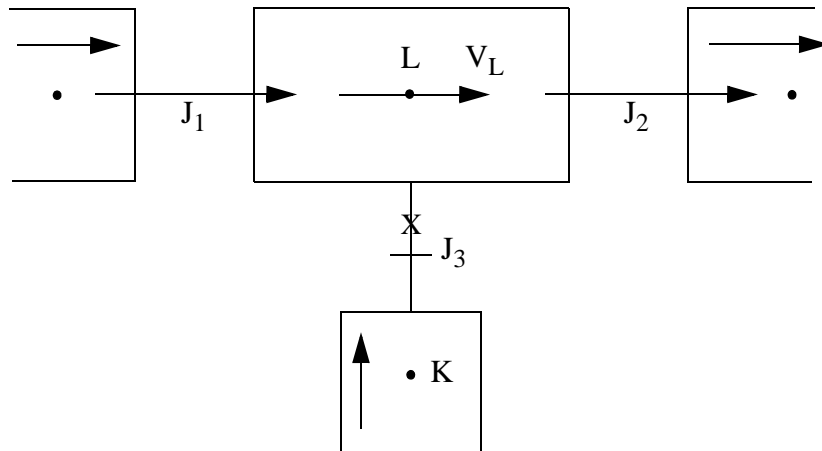
Figure 3.4-10 Simplified tee crossflow.

The resulting vapor/gas momentum finite difference equation for a crossflow junction perpendicular to the axial flow in volume L but parallel to the axial flow in volume K is

$$
\begin{aligned}
&(\alpha_g \rho_g)_j^n (v_g^{n+1} - v_g^n)_j \Delta x_j + \frac{1}{2}(\alpha_g \rho_g)_j^n [-(v_g^2)_K^n] \Delta t + (\text{VISCOUS TERM})_K \\
&= -\alpha_{g,j}^n (P_L^{n+1} - P_K^{n+1}) \Delta t - (\alpha_g \rho_g)_j^n [FWG_j^n \Delta x_j + HLOSSG_j^n] v_{g,j}^{n+1} \Delta t \\
&\quad - (\alpha_g \rho_g)_j^n FIG_j^n (v_{g,j}^{n+1} - v_{f,j}^{n+1}) \Delta x_j \Delta t + (\alpha_g \rho_g)_j^n B_x \Delta x_j \Delta t \\
&\quad + \text{VIRTUAL MASS} + \text{MASS TRANSFER MOMENTUM} \\
&\qquad + \text{STRATIFIED PRESSURE GRADIENT EFFECT}
\end{aligned}
\tag{3.4-70}
$$

where the momentum flux in volume L is neglected by using a junction flag.

A similar equation can be written for the liquid phase. The Δx_j term has the form

$$
\Delta x_j = \frac{1}{2}[\Delta x_K + D(L)]
\tag{3.4-71}
$$

if the default is used. If a user-specified length is input for the L volume, it is used instead of D(L).

For leak flows and minor flow paths, the modeling approach shown in **Figure 3.4-11** is recommended. Here, J_3 is the normal flow path, whereas junction J_1, volume M, and junction J_2 represent the leak flow path. Junctions J_1 and J_2 should be modeled as <u>tee</u> junctions described above. The only reason for using volume M is to obtain a correct representation of the gravity head from K to L. If a crossflow junction were modeled directly between volumes K and L, then there would be no gravity head in the leak flow junction equation. Leak paths may also be modeled using a crossflow junction that is perpendicular to both the K and L volumes when the leak flow is between volumes having the same volume center elevation.

3.4.6 Water Packing Mitigation Scheme

Large pressure spikes that cannot be explained by known physical phenomena are at times encountered when Eulerian-type computer codes are used to analyze integral systems tests or reactor accidents. These fictitious pressure spikes are sometimes calculated when vapor/gas is disappearing from, and liquid is about to fill, a control volume. The situation is often referred to as water packing. This section discusses the situation for water packing where water is the working fluid. These same equations are used in ATHENA when other working fluids are specified.

The cause of the anomalous pressure spikes is the discontinuous change in compressibility between a two-phase mixture of small void fraction and a pure liquid phase, and approximations inherent in the discrete momentum equations. The same problems are seen using a two-fluid model or the homogeneous
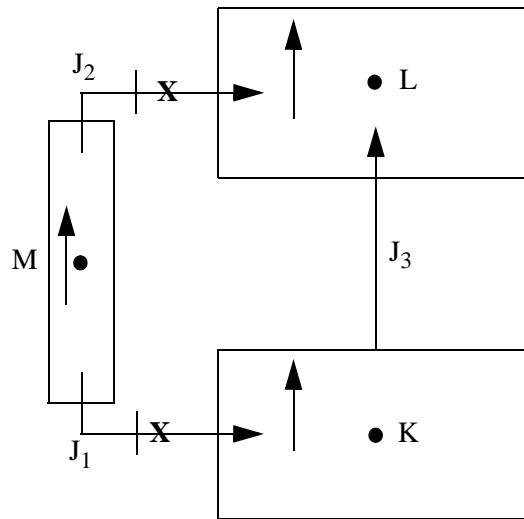
Figure 3.4-11 Leak flow modeling.

equilibrium model. Consider the homogeneous equilibrium case and a cell that is nearly full of liquid with a net influx of mass. The density-pressure relationship used to calculate the new time pressure is based upon the beginning of time step values for the state properties and derivatives. The compressibility of this low void fraction cell is dominated by the mass transfer. The equivalent mixture corresponds to a highly compressible fluid, i.e., significant volume changes can easily occur with very little change in pressure. This high compressibility can allow significant continuing influx of liquid with very little pressure rise. In fact, in some cases the net volume influx of liquid during the time step can be larger than the initial vapor/gas volume in the cell. This filling of the cell is accompanied by only slight pressure changes. This small change in pressure may do little to slow down or reverse the liquid influx momentum. If this is the case, the following time step will be taken with a liquid full cell and large liquid influx momentum existing at the beginning of the time step. Because the liquid is nearly incompressible, this large influx of liquid momentum will cause a large increase in pressure during this following time step.

In the neighborhood of these spurious numerical pressure spikes, the calculated phasic velocities may increase substantially, and smaller time-step sizes are needed to satisfy the material Courant stability limit. Thus, the computational efficiency is greatly reduced by the presence of water packing. Of course, the computed pressure spikes are unphysical. Furthermore, water packing may severely distort the transient solution by changing the void distribution or driving the liquid completely out of an open system.

A water packing scheme has been installed to mitigate these spikes. The water packing scheme closely follows the method used in the TRAC code.[3.4-30],[3.4-31] It involves a detection scheme to determine when a pressure change occurs in a volume containing mostly liquid. It then imposes changes to the liquid momentum equation, followed by a recalculation of the time step with the same time step size.

The detection logic used in the water packing scheme evolved from experience gained in running a vertical fill problem.[3.4-32] The detection logic requires the following formula for the pressure:

$$P_K^{n+1} \geq P_K^n + 0.0023 P_K^n \tag{3.4-72}$$

where volume K is the volume that water packs and volume L is the next volume (see **Figure 3.4-12**). In volume K, the detection scheme also requires a void fraction $(\alpha_g) \leq 0.12$, the liquid temperature (T_f) to be less than the saturation temperature (T^s), the volume to be flagged as vertically stratified, and the next volume above to be highly voided. Thus, a legitimate water hammer situation would not be eliminated by the water packing scheme.

The next part of the scheme involves altering the liquid momentum equation so that only small pressure changes will occur when the volume fills with liquid. The scheme involves modifying the coefficient that multiplies the pressure change in the filling volume. The modification multiplies this coefficient by a large number and is discussed in more detail in the next paragraph.

The finite difference form of the liquid momentum equation used can be written as

$$v_{f,j}^{n+1} = v_{f,j}^{n,exp} - (VFDP)_j^n [(P_L^{n+1} - P_L^n) - (P_K^{n+1} - P_K^n)] \tag{3.4-73}$$

where $v_{f,j}^{n,exp}$ contains all the old time terms and $(VFDP)_j^n$ contains all the terms that multiply the pressure change. Consider the filling example in **Figure 3.4-12**, where volume K is full of liquid and volume L is full of vapor/gas. The first change to the liquid momentum equation is to set $v_{f,j}^{n,exp}$ to 0.01 m/s to insure the explicit liquid velocity is going from the K volume to the L volume. The second change to the liquid momentum equation is to multiply the $(P_K^{n+1} - P_K^n)$ terms by a large number (FACTOR), which forces P_K^{n+1} to be approximately the same as P_K^n. Thus, the liquid-filled K volume will not show a pressure spike. The K liquid momentum equation then has the form

$$v_{f,j}^{n+1} = 0.01 - (VFDP)_j^n (P_L^{n+1} - P_L^n) + (VFDP)_j^n (FACTOR)(P_K^{n+1} - P_K^n) \quad . \tag{3.4-74}$$

The term FACTOR is pressure dependent because the density is pressure dependent. A pressure-dependent linear ramp is used that begins ramping FACTOR from a highest value of 10^6 at 1,500 psia (10.342 x 10^6 Pa) to a lowest value of 10^4 at 1,250 psia (8.618 x 10^6 Pa).

3.4.7 Countercurrent Flow Limitation Model

There are several structures internal to RCSs where gravity drainage of liquid can be impeded by upward flowing vapor/gas. These include the upper core tie plate, downcomer annulus, steam generator tube support plates, and the entrance to the tube sheet in the steam generator inlet plenum. A completely mechanistic approach to determine the onset of flow limiting for all structural configurations is impractical. Both the Wallis and Kutateladze forms of the general flooding limit equation have been found
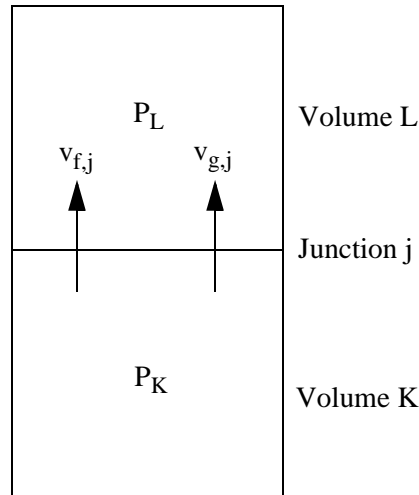
Figure 3.4-12 Two vertical vapor/gas/liquid volumes.

to provide acceptable results when constants applicable to specific geometries are used in conjunction with them. Wallis[3.4-28] discusses the phenomenon of flooding, which can occur when liquid is falling in a vertical structure and vapor/gas is moving upward. For a specified liquid downflow rate, there is a certain vapor/gas upward flow rate at which very large waves appear on the interface, the flow becomes chaotic, vapor/gas pressure drop increases, and liquid flows upward. **Figure 3.4-13** is a reproduction of Wallis' Figure 11.11 and shows this phenomena for water and gas. Wallis points out that the flooding point is not approached as the limit of a continuous process (which occurs in drops or bubbles), but it is the result of a marked instability.

A general countercurrent flow limitation (CCFL) model is implemented[3.4-33] that allows the user to select the Wallis form, the Kutateladze form, or a form in between the Wallis and Kutateladze forms. This general form was proposed by Bankoff et al.[3.4-34] and is used in the TRAC-PF1 code.[3.4-35] It has the structure

$$H_g^{1/2} + mH_f^{1/2} = c \qquad (3.4-75)$$

where H_g is the dimensionless vapor/gas flux, H_f is the dimensionless liquid flux, c is the vapor/gas intercept (value of $H_g^{1/2}$ when $H_f = 0$, i.e., complete flooding), and m is the "slope", that is the vapor/gas intercept divided by the liquid intercept (the value of $H_f^{1/2}$ when $H_g = 0$). A typical plot of $H_g^{1/2}$ versus $H_f^{1/2}$ is shown in **Figure 3.4-14**. Quotes are used around the word "slope" because in a strict mathematical sense, the slope is negative for Equation (3.4-75) and m = -slope. The constant m will be called the slope in
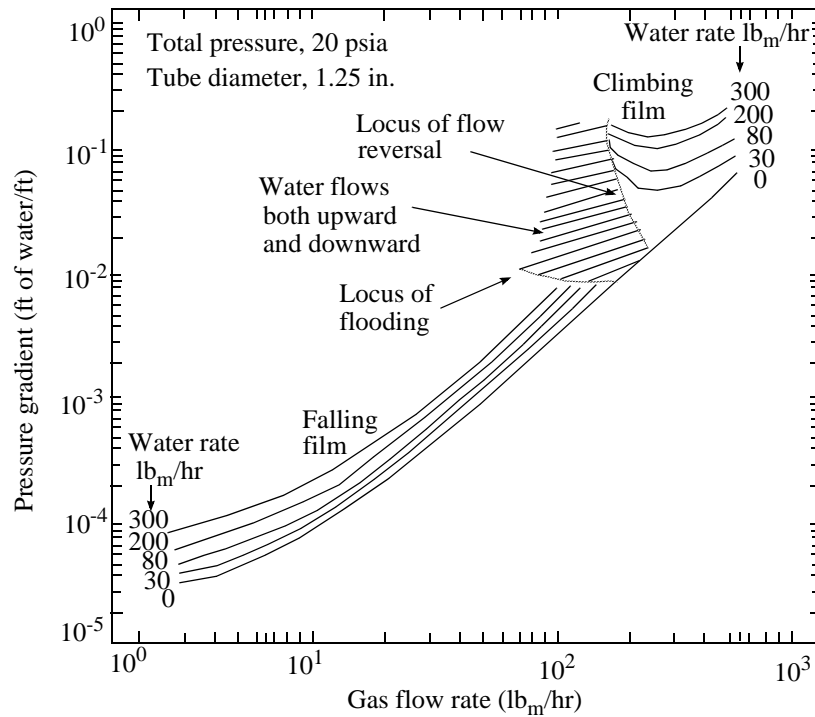
Figure 3.4-13 Pressure-drop characteristics near the boundary between countercurrent and cocurrent flow.

this section of the manual and in the input cards and output edit, but one should think of this as the negative of the true slope. The dimensionless fluxes have the form

$$H_g = j_g \left[\frac{\rho_g}{gw(\rho_f - \rho_g)} \right]^{1/2} \qquad (3.4\text{-}76)$$

$$H_f = j_f \left[\frac{\rho_f}{gw(\rho_f - \rho_g)} \right]^{1/2} \qquad (3.4\text{-}77)$$

where j_g is the vapor/gas superficial velocity ($\alpha_g v_g$), j_f is the liquid superficial velocity ($\alpha_f v_f$), ρ_g is the vapor/gas density, ρ_f is the liquid density, α_g is the vapor/gas volume fraction, α_f is the liquid volume fraction, g is the gravitational acceleration, and w is the length scale and is given by the expression

$$w = D_j^{1-\beta} L^\beta \qquad (3.4\text{-}78)$$

where β is a user-input constant.
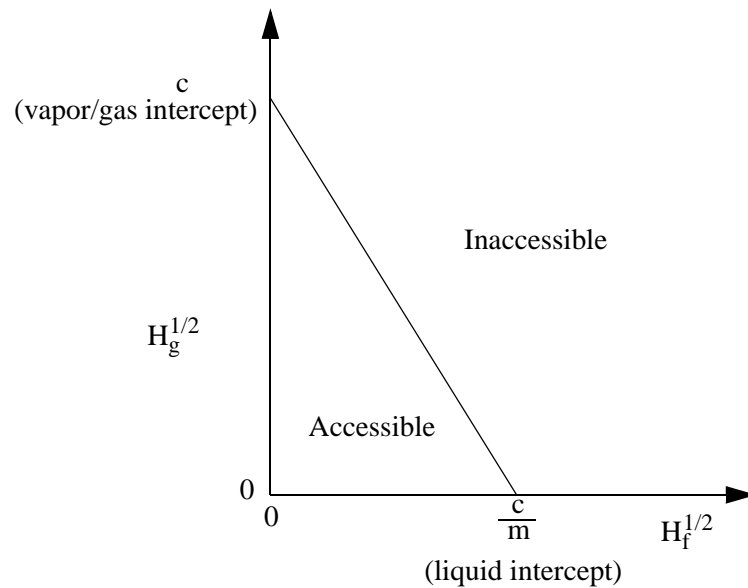
Figure 3.4-14 Plot of $H_g^{1/2}$ versus $H_f^{1/2}$ for a typical CCFL correlation.

In Equation (3.4-78), D_j is the junction hydraulic diameter and L is the Laplace capillary length constant, given by

$$L = \left[\frac{\sigma}{g(\rho_f - \rho_g)}\right]^{1/2} \quad . \tag{3.4-79}$$

In Equation (3.4-78), β can be a number from 0 to 1. For $\beta = 0$, the Wallis form of the CCFL equation is obtained; and for $\beta = 1$, the Kutateladze form of the CCFL equation is obtained. For $0 < \beta < 1$, a form in between the Wallis and Kutateladze forms is obtained; and Bankoff[3.4-34] suggests that β be correlated to data for the particular geometry of interest. He has included a possible function for β, although it is somewhat restrictive. The form of Equations (3.4-75) through (3.4-79) is general enough to allow the Wallis or Kutateladze form to appear at either small or large diameters. Other approaches (e.g., Tien, et. al.[3.4-36]) appear to be more restrictive by defaulting to the Wallis form at small diameters and the Kutateladze form at large diameters.

With regard to the solution method, if the CCFL model is requested by the user, the coding checks if countercurrent flow exists and if the liquid downflow exceeds the limit imposed by Equation (3.4-75). If this is true, the sum momentum equation [Equation (3.1-104)] and the flooding limit equation are applied. This approach was suggested by Trapp,[a] who observed that the CCFL model is similar to the choking model in that both place limits on the momentum equations. He observed that since the flooding

phenomenon can be incorporated by altering the interphase friction (as is done in TRAC-PF1), it can also be incorporated by replacing the code's difference momentum equation [Equation (3.1-105)] with the flooding limit equation. The difference equation contains the interphase friction, whereas the sum equation does not. (In the choking model, the sum momentum equation is replaced with the choking limit equation.) This method is advantageous in that the phasic velocities still must satisfy the sum momentum equation, which contains gravity and pressure terms. The numerical form of Equation (3.4-75) needed by the code is obtained by letting $c_g = \dfrac{H_g}{v_g}$ and $c_f = \dfrac{H_f}{v_f}$, solving for $mH_f^{1/2}$, and squaring the equation, which results in

$$m^2 c_{f,j}^n v_{f,j}^{n+1} = c^2 - 2c(c_{g,j}^n)^{1/2}(v_{g,j}^{n+1})^{1/2} + c_{g,j}^n v_{g,j}^{n+1} \quad . \tag{3.4-80}$$

Linearization of $(v_{g,j}^{n+1})^{1/2}$ gives

$$(v_{g,j}^{n+1})^{1/2} = (v_{g,j}^n)^{1/2} + \frac{1}{2}(v_{g,j}^n)^{-1/2}(v_{g,j}^{n+1} - v_{g,j}^n) \tag{3.4-81}$$

and substitution into Equation (3.4-80) gives

$$m^2 c_{f,j}^n v_{f,j}^{n+1} + [c(c_{g,j}^n)^{1/2}(v_{g,j}^n)^{-1/2} - c_{g,j}^n]v_{g,j}^{n+1} = c^2 - c(c_{g,j}^n)^{1/2}(v_{g,j}^n)^{1/2} \quad . \tag{3.4-82}$$

3.4.8 Mixture Level Tracking Model

Accurate tracking of liquid levels is essential for modeling gravity-driven cooling systems. In modeling a reactor system using ATHENA, a set of large hydrodynamic volumes are used to model the various components. Because the discretization of the governing equations uses mean void fractions in each control volume, a fine nodalization is required to resolve a large change in void fraction, such as is associated with a liquid level. Even that may not be adequate to model the phenomena because ATHENA uses a highly diffusive upwind difference scheme to discretize the advection terms. To compensate for the inherent limitation of the finite-difference scheme used in ATHENA and to allow a coarser nodalization to reduce the computational cost, a mixture level tracking model is implemented in ATHENA.

The mixture level tracking model is intended to model situations in which the void fraction increases in the vertical direction. In places where there is a flow restriction such as a grid spacer or tie plate in a rod bundle, liquid may pool on the flow restriction leading to an inverted void profile (void fraction decreasing in the vertical direction) and multiple mixture levels may appear. An inverted void profile may also appear when vapor/gas is injected below the surface of a subcooled pool and the vapor condenses as it rises due to

a. Personal communication, J. A. Trapp to R. A. Riemke, January 1987.

buoyancy. To handle multiple mixture levels and inverted void profiles, ATHENA divides the vertical flow passages in the user input into "level stacks" of volumes and allows only one mixture level per level stack. Level stacks are built during the input processing phase of a computation. They are defined as a set of volume singly connected in the vertical direction containing no flow restrictions between the volumes. Junctions which have been input as "abrupt" constitute flow restrictions for the purposes of the mixture level tracking model. The level tracking model ignores multiple junctions connected to the sides of volumes for the purpose of building level stacks. The code searches for the head of a level stack by moving from volume to volume to find a volume which has no vertical junction on its top face, or has an abrupt junction attached to it top face, or is attached to a volume through the junction attached to its top face in which the mixture level model has been deactivated by user input. If a volume has multiple junctions attached to its top or bottom faces, it is treated as if the user had deactivated the level tracking model in the volume. Multiple vertical connections on the top or bottom faces of a volume is not allowed by the mixture level tracking model because the level appearance logic examines the void distribution over three adjacent volumes to determine whether a void discontinuity exists. If there is more than one volume "above" or "below" the current volume, the model has no way to determine whether a void discontinuity exists because it has no way of determining which volume is "above" or "below". The code searches for a mixture level beginning at the head of a level stack and continuing down until a mixture level is found or the bottom of the stack is found. Once a level has been found in a stack, the level is propagated from volume to volume within the stack as fluid conditions dictate and another level cannot be initiated in the stack until the original mixture level disappears from the stack. A mixture level can disappear only by propagation out of the top or bottom of the stack. If a level stack contains no mixture level, it is searched from the top down each time advancement until a mixture level is initiated in the stack and then the level is propagated as described above. The stack is searched from the top down so that the mixture level, if found, is placed as high in the stack as possible.

The mixture level tracking model implemented in ATHENA is based on TRAC-BF1/MOD1.[3.4-37] The mixture level is defined as the location where a sharp change of the void fraction distribution exists. This sharp change is associated with the change in flow regime. The model consists of five parts.

1. Detection of the mixture level appearance.

2. Calculation of mixture level parameters that are necessary to describe a mixture level, such as the position and velocity of the level, and the void fractions above and below the level.

3. Movement of the mixture level from volume to volume.

4. Modification of the mass and energy equations of ATHENA to accurately convect void fractions above and below the mixture level, and modification of the density terms, the pressure gradient, and the momentum flux terms in the momentum equation according to the location of the mixture level.

5. Modification of the heat transfer calculation according to the mixture level.

The details of the model and its implementation in ATHENA are presented in the next subsections.

3.4.8.1 Detection of Level Appearance. The mixture level is the location of an abrupt change in void fraction that is associated with a change in flow regime. There are two types of mixture levels, normal and inverted. With a normal mixture level (void profile), the void fraction increases in the upward axial direction, while with an inverted void profile, the void fraction decreases in the upward axial direction. These situations are illustrated in **Figure 3.4-15**, **Figure 3.4-16**, and **Figure 3.4-17**. Two situations that give rise to a normal void profile are heating along a vertical flow path and depressurization in a vertical column. Inverted void profiles typically arise as the result of liquid pooling in the upper and lower tie plates of a BWR pressure vessel. If more than one junction is connected to the top or if more than one junction is connected to the bottom, the mixture level model is not used and is turned off.
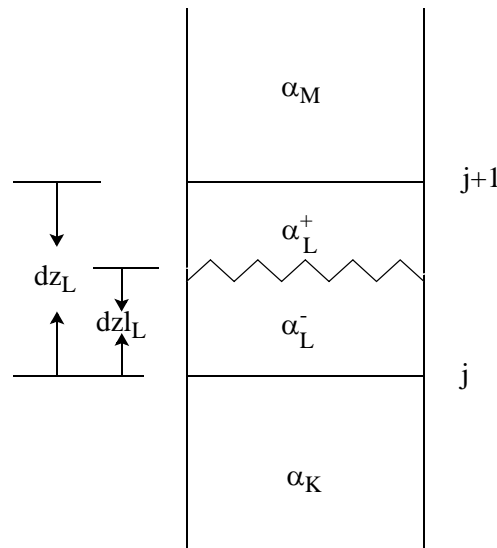
Figure 3.4-15 Mixture level in normal void profile.

The logic for the detection of a mixture level appearance in a computational cell is based on BWR experimental data and numerical experiments.[3.4-37,3.4-38,3.4-39] The logic for detecting a mixture level is different for the two different kinds of mixture levels.

The level detection logic for a normal void profile, **Figure 3.4-15**, is

$$\alpha_M - \alpha_L > \delta\alpha_c \text{ (default} = 0.2)\tag{3.4-83}$$

or
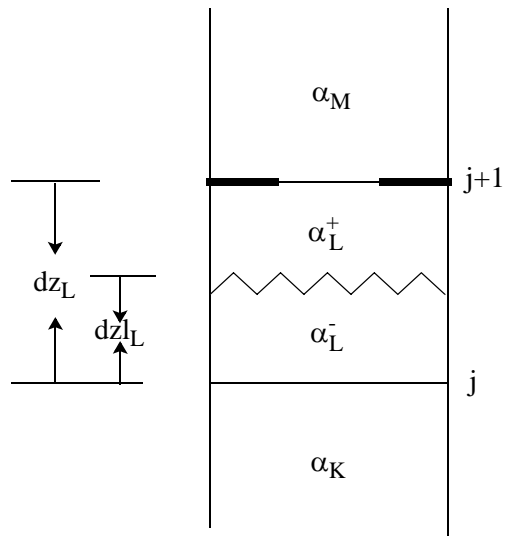
Figure 3.4-16 Mixture level in a volume below a void fraction inversion.
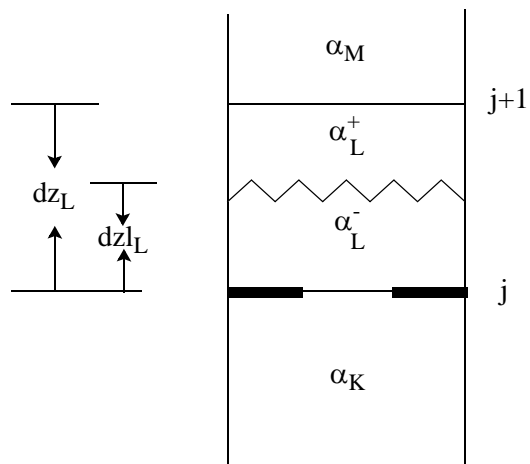
Figure 3.4-17 Mixture level in a volume above a void fraction inversion.

$\alpha_L - \alpha_K > \delta\alpha_c$ (default = 0.2) (3.4-84)

and

$$\alpha_M > \alpha_c \text{ (default = 0.7)} \ . \tag{3.4-85}$$

Here, α_c is the minimum allowable void fraction in the cell above a normal mixture level, and $\delta\alpha_c$ is the smallest change that signals the presence of a normal mixture level. The values in parentheses are the default values used in ATHENA and are recommended by Cheung et al.[3.4-38] The notation α or α_g is used for volume vapor/gas fraction (void fraction). The notation α_f is used for volume liquid fraction.

The logic for an inverted void profile depends on whether a particular cell is above or below a void inversion. A mixture level is defined as being below a void profile inversion **Figure 3.4-16** if

$$\alpha_L - \alpha_M > \delta\alpha_j \text{ (default = 0.1)} \ . \tag{3.4-86}$$

If a mixture level is above a void profile inversion (**Figure 3.4-17**), the criteria becomes

$$\alpha_K - \alpha_L > \delta\alpha_j \text{ (default = 0.1)} \ . \tag{3.4-87}$$

The void inversion logic is activated if there is an orifice at the junction. The level detection logic is summarized in block diagrams as shown in **Figure 3.4-18**, **Figure 3.4-19**, **Figure 3.4-20**, and **Figure 3.4-21**.

3.4.8.2 Calculation of Level Parameters. The parameters that describe the mixture level are:

1. The void fraction above and below the level α_L^+ and α_L^- .

2. The location of the level (dzl).

3. The mixture level velocity (v_{lev}).

3.4.8.2.1 Determination of the Void Fraction Above and Below the Level--The correlations to calculate the void fraction above and below the level α_L^+ and α_L^-, respectively, are given below for the three cases:

1. Normal profile.

2. Void inversion above volume L or flow restriction at the top of volume L.

3. Void inversion below volume L or flow restriction at the bottom of volume L.
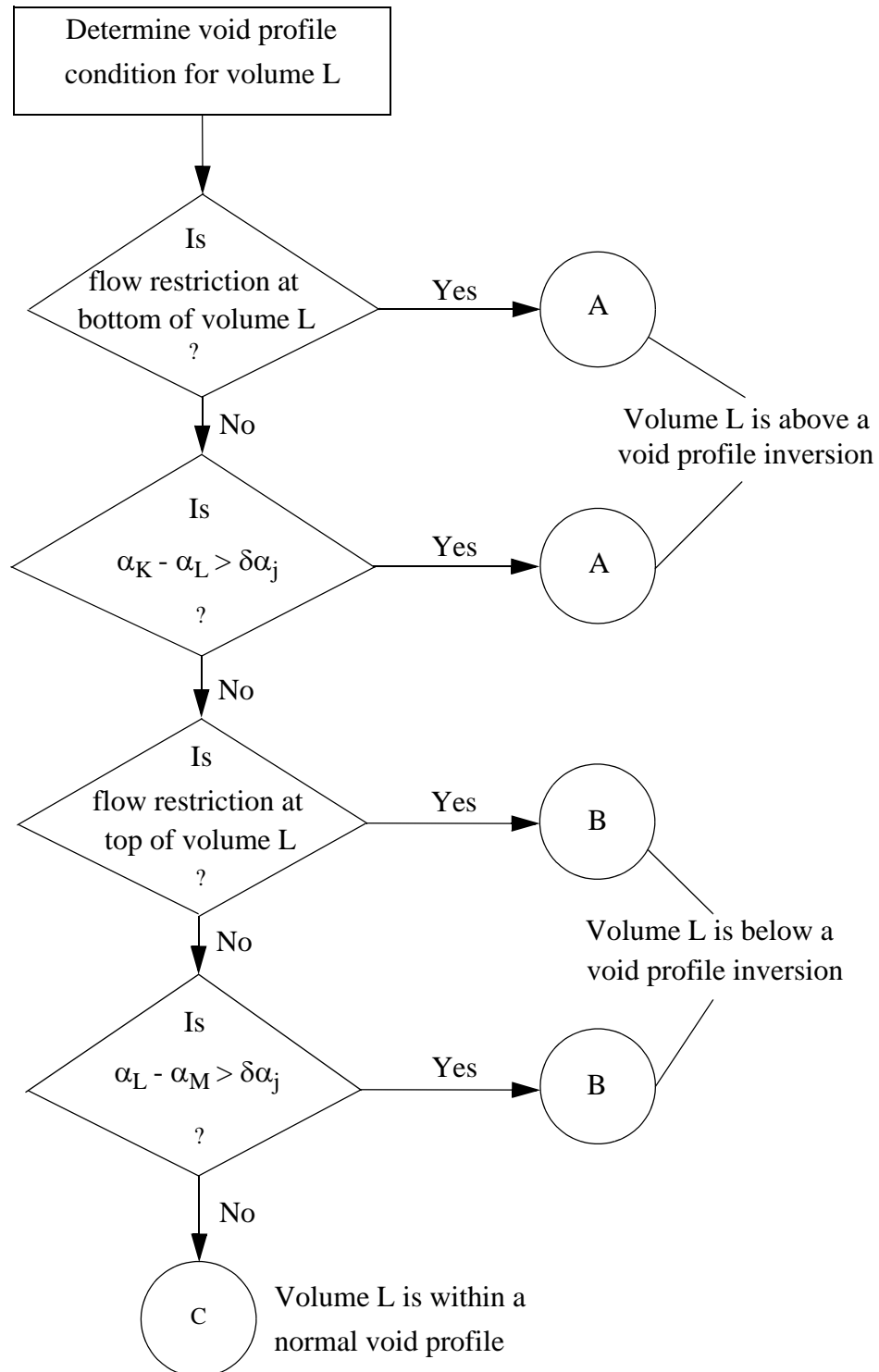
Figure 3.4-18 Level detection logic diagram for volume L.
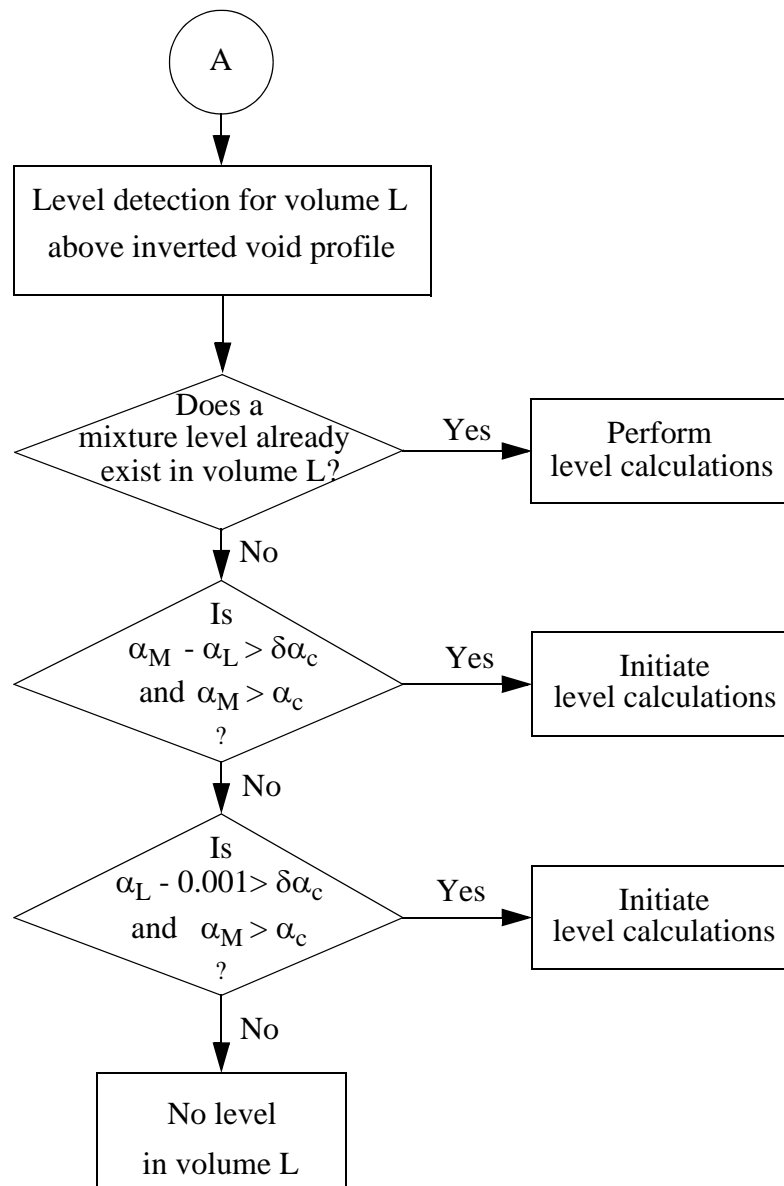
Figure 3.4-19 Level detection logic diagram for volume L above an inverted profile.
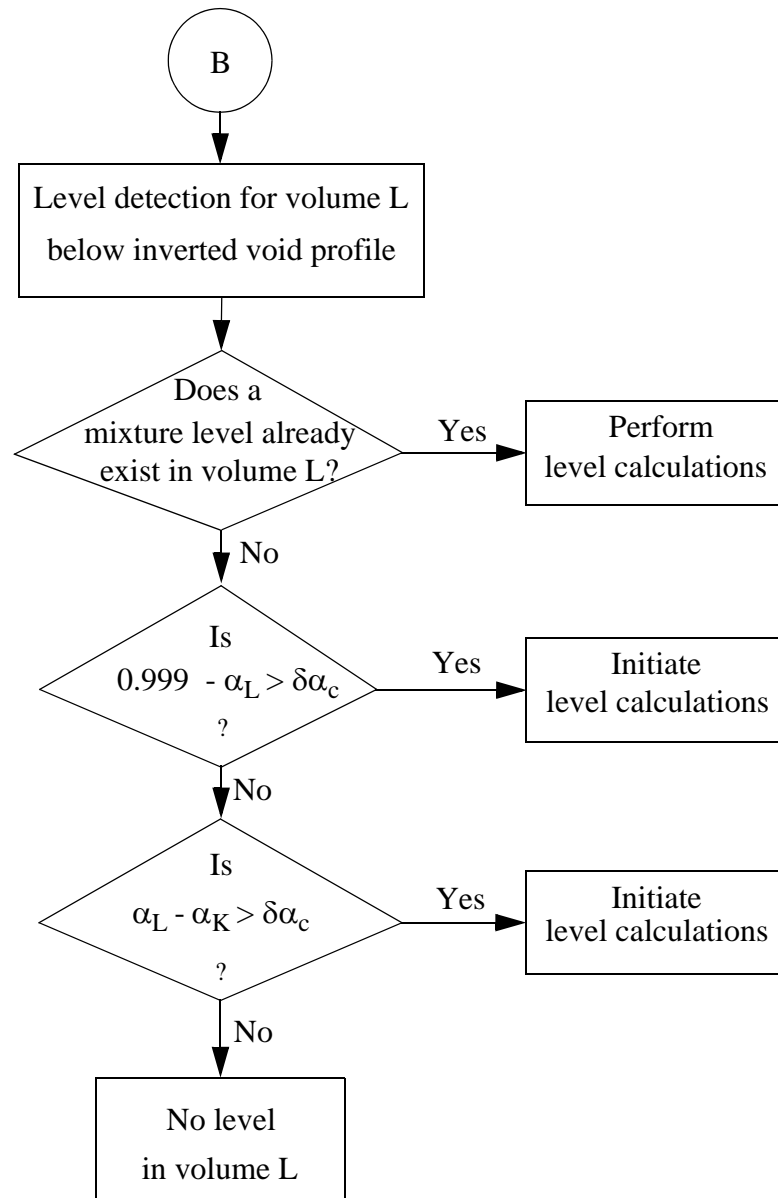
Figure 3.4-20 Level detection logic diagram for volume L below an inverted profile.

C

Level detection for volume L
normal void profile

Does a
mixture level already
exist in volume L? — Yes → Initiate level calculations

No

Is
$\alpha_M - \alpha_L > \delta\alpha_c$
and $\alpha_M > \alpha_c$
? — Yes → Initiate level calculations

No

Is
$\alpha_L - \alpha_K > \delta\alpha_c$
and $\alpha_M > \alpha_c$
? — Yes → Initiate level calculations

No

No level
in volume L
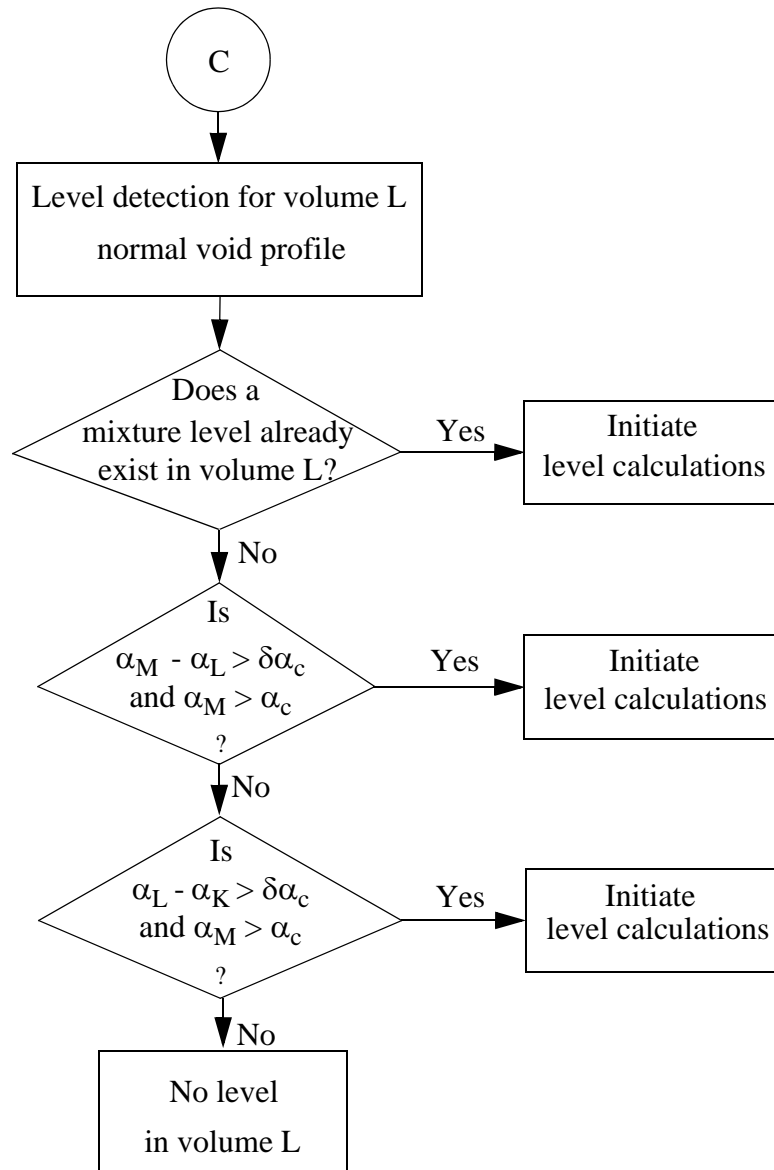
Figure 3.4-21 Level detection logic diagram for a normal profile.

Case 1: Normal Void Profile.

For a normal void profile, the void fraction below the level is assumed to equal the void fraction in volume K, i.e.,

$$\alpha_L^- = \alpha_K \; . \tag{3.4-88}$$

In the absence of entrainment of liquid from below the level, the void fraction above the level is given by

$$\alpha_L^+ = \alpha_M \; . \tag{3.4-89}$$

If the velocity at the cell junction is upward, the void fraction α_L^+ is derived from the correlation of the entrainment liquid mass flux (G_{lent}) developed by Rosen[3.4-40] as

$$\alpha_L^+ = 1 - \frac{G_{lent}}{\rho_f v_f} \tag{3.4-90}$$

and

$$v_f = v_{f,j+1}\left(\frac{A_{j+1}}{A_L}\right) \tag{3.4-91}$$

where

$\quad v_{f,j+1} \quad = \quad$ the junction liquid velocity

$\quad A_{j+1} \quad = \quad$ the junction area

$\quad A_L \quad = \quad$ the average area of the control volume.

The entrainment liquid mass flux (G_{lent}) is expressed by

$$G_{lent} = \left[3.0 \times 10^{-5}(CK^{0.5} + 530 \bullet CK^{2.1})\left(\frac{\rho_f - \rho_g}{\rho_g}\right)^{0.5}\right] j_g \rho_g \tag{3.4-92}$$

where

$$\text{CK} \quad = \quad \frac{2.0 \bullet \text{DMAX} \bullet j_g}{\left[\text{VCRIT} \bullet g \bullet \left(\frac{\sigma}{\rho_f - \rho_g} \right)^{0.5} \right]} \tag{3.4-93}$$

$$\text{VCRIT} \quad = \quad 2.0 \left[\frac{\sigma g (\rho_f - \rho_g)}{\rho_g^2} \right]^{0.25} \tag{3.4-94}$$

$$\text{DMAX} \quad = \quad 0.3375 \left[\frac{\rho_g v_g^2}{g(\rho_f - \rho_g)} \right] . \tag{3.4-95}$$

In the above expression, G_{lent} is calculated using donor cell-averaged values for ρ_f, ρ_g, and σ at cell L. The value of j_g is set equal to (for positive v_f)

$$j_g = \alpha_M v_g, \tag{3.4-96}$$

where

$$v_g = v_{g,j+1} \left(\frac{A_{j+1}}{A_L} \right) \tag{3.4-97}$$

and $v_{g,j+1}$ is the junction vapor/gas phasic velocity.

If either $v_{f,j+1}$ or $v_{g,j+1}$ is negative, α_L^+ is given by

$$\alpha_L^+ = \alpha_M . \tag{3.4-98}$$

Case 2: Void Inversion Above Volume L or Flow Restriction at the Top of Volume L.

The calculation of the void fraction above and below the level (α_L^+ and α_L^-) is similar to Case 1 except with the following modification.

The volumetric vapor/gas flux used in Equations (3.4-92) and (3.4-93) becomes

$$j_g = 0.999 v_g . \tag{3.4-99}$$

If $v_{g,j+1}$ is negative, then

$$\alpha_L^+ = 0.999 \ .$$

(3.4-100)

Case 3: Void Inversion Below Volume L or Flow Restriction at the Bottom of Volume L.

For a cell mixture level occurring above a void fraction inversion or bottom cell area reduction, the void fraction below the level α_L^- is calculated using the drift flux approximation, and is given by

$$\alpha_L^- = \frac{j_g^-}{C_o j^- + v_{gj}}$$

(3.4-101)

where

$$v_{gj} = 1.41\left[\frac{\sigma g(\rho_f - \rho_g)}{\rho_f^2}\right]^{\frac{1}{4}}$$

(3.4-102)

$$C_o = C_\infty - (C_\infty - 1)\sqrt{\frac{\rho_g}{\rho_f}}$$

(3.4-103)

$$C_\infty = 1.0 + 0.2\left[\frac{\rho_f(gD_h)^{\frac{1}{2}}}{|\alpha_g\rho_g v_g| + |\alpha_f\rho_f v_f|}\right]^{\frac{1}{2}} \ .$$

(3.4-104)

Rouhani's[3.4-41] correlation is used for C_∞. The parameters used in calculating C_∞ are based on cell-centered quantities. The volumetric fluxes j_g^- and j_f^- are calculated using junction-donored velocities from bottom cell j and void fractions of either α_K or α_L^-, depending on whether or not the phasic velocities are positive or negative, respectively. They are given by

$$j_g^- = \frac{1}{2}v_{g,j}'[(\alpha_{g,K} + \alpha_L^-) + \text{sgn}(v_{g,j}')(\alpha_{g,K} - \alpha_L^-)]$$

(3.4-105)

$$j_f^- = \frac{1}{2}v_{f,j}'\{[\alpha_{f,K} + (1 - \alpha_L^-)] + \text{sgn}(v_{f,j}')[\alpha_{f,K} - (1 - \alpha_L^-)]\}$$

(3.4-106)

$$j^- = j_f^- + j_g^-$$

(3.4-107)

where

$$v'_{f,j} = v_{f,j}\left(\frac{A_j}{A_L}\right) \tag{3.4-108}$$

$$v'_{g,j} = v_{g,j}\left(\frac{A_j}{A_L}\right) . \tag{3.4-109}$$

The logic and correlations used to calculate α_L^+ are the same as for the normal void profile scheme.

3.4.8.2.2 Location of the Mixture Level--Once the presence of a level is determined in a particular volume, a level flag is set and the level parameters are calculated. The position of the level (dzl_L) of a cell with length dz_L is given by

$$dzl_L = dz_L\left(\frac{\alpha_L^+ - \alpha_L}{\alpha_L^+ - \alpha_L^-}\right) \tag{3.4-110}$$

where the above and below mixture level void fractions are given above.

3.4.8.2.3 Velocity of Level Movement--The level velocity v_{lev} is obtained by forming a difference approximation to the time derivative of Equation (3.4-110) as

$$v_{lev} = \frac{dz_L\dfrac{d\alpha_L}{dt} - dzl_L\dfrac{d\alpha_L^+}{dt} - (dz_L - dzl_L)\dfrac{d\alpha_L^-}{dt}}{\alpha_L^+ - \alpha_L^-} . \tag{3.4-111}$$

3.4.8.3 Movement of Mixture Level Between Volumes. Once the position and velocity of a mixture level has been determined, its position at the end of the time advancement is estimated. If the mixture is predicted to lie outside of the volume in which it currently resides, the level is moved into the appropriate volume before the advancement is attempted. This is done to prevent pressure spikes and oscillations which would result from the discontinuous change in the flow regime in the junction through which the mixture level passes when moving from one volume to an adjacent volume. The algorithm for the movement of the mixture level from one volume into an adjacent volume is based on the level crossing algorithm originally developed at INEEL for the TRAC-BWR[3.4-37,3.4-39]code. This algorithm was then refined at Pennsylvania State University for the TRAC-BWR code[3.4-42,3.4-43,3.4-44].

The level crossing algorithm consists of three parts:

1.   Prediction of the position of the mixture level at the end of the advancement.

2.   Determination of the mixture level parameters in its new location.

3. Computation of the phasic velocities in the junction through which the mixture level passed when moving from one volume to an adjacent volume.

3.4.8.3.1 Prediction of Mixture Level Position--The prediction of the position of the mixture level is accomplished by a simple level velocity extrapolation as given by

$$dzl_j^{n+1} = dzl_j^n + v_{lev,j}^n \bullet dt^n \quad . \tag{3.4-112}$$

If the projected level position is negative, the mixture level is moved into the volume below the current volume if the volume below the current volume is within the same level stack or the volume below the current volume is the head of an adjacent level stack and no level exists in the adjacent level stack. If the projected level position is greater than the height of the current volume, the mixture level is moved into the volume above the current volume if the volume above the current volume lies in the same level stack or if the volume above the current volume is the bottom volume of an adjacent level stack and there is no mixture level in the adjacent level stack.

3.4.8.3.2 Determination of Level Parameters in New Location--Once the level has been determined to reside in a different volume from the current volume, the level parameters in the two volumes must be reset to reflect the new location. The level parameters which must be computed for its new location are the location of the level within its new volume, the above and below level void fractions, and the velocity of the mixture level in the new volume. The location of the level in the new volume is set to either the top or bottom of the volume depending upon whether the level enters the volume from above or below. The void fraction in the volume containing the mixture level is adjusted so that there is enough of the minor phase (the minor phase is vapor/gas if the mixture level lies at the top of the volume and the minor phase is liquid if the mixture level lies at the bottom of the volume) to support the presence of a mixture level. Finally the above and below level void fractions are determined. The equations used for these adjustments are shown below for the situation in which the mixture level moves down from volume L into volume K (See **Figure 3.4-15**):

$$dzl_K^n = dz_K \tag{3.4-113}$$

$$v_{lev,K}^n = v_{lev,L}^n \tag{3.4-114}$$

$$\left.\begin{array}{l} \alpha_K^n = \alpha_K^n + \varepsilon_\alpha \\[2mm] \alpha_L^n = \alpha_L^n - \dfrac{V_K(\rho_f-\rho_g)_K}{V_L(\rho_f-\rho_g)_L}\varepsilon_\alpha \end{array}\right\} \quad \text{if} \quad \alpha_K^n < \varepsilon_\alpha \tag{3.4-115}$$

$$\begin{array}{l} \alpha_K^+ = \alpha_L^+ \\[2mm] \alpha_K^- = \alpha_K^n \end{array} \quad . \tag{3.4-116}$$

3.4.8.3.3 Phase Velocity Adjustment--After the level parameters are determined for the new location of the level, the phase velocities in the junction connecting the two volumes must be recomputed. This is needed because the flow regime in the junction depends upon the mixture level location. If the mixture level is in the volume at the top of the junction (top with respect to gravity), the flow regime in the junction is the low void fraction bubbly flow regime and if the mixture level is in the volume at the bottom of the junction, the flow regime is the high void annular/mist or mist flow regime. The magnitude of the interfacial friction is very different in these two flow regimes which results in a different relative velocity between the phases and a different slip ratio. If the phase velocities were not recomputed to be consistent with the new flow regime in the junction, pressure spikes and oscillations would result as the phase velocities adjusted to the new flow regime. The velocity of the major phase in the junction, i.e. the vapor/gas velocity in annular/mist or mist flow and the liquid velocity in bubbly flow, is computed from a steady-state, zero phase change phasic mass balance [Equations (3.1-2) or (3.1-3)] for the volume from which the mixture level exited and the minor phase velocity is set equal to the major phase velocity. A flag is set for the junction to disable the under-relaxation of the interfacial friction coefficient so that the values from two different flow regimes (i.e., the flow regimes in the junction before and after level crossing) are not averaged together.

3.4.8.4 Modification of ATHENA Field Equations for Level Tracking. The following modifications will be made in solving the field equations in ATHENA:

1.   The donor cell void fraction based on the void fraction above and below the mixture level is used in the momentum equations and the mass and energy convective terms.

2.   The phasic density, pressure gradient, and momentum flux terms in the momentum equations are modified according to the location of the mixture level.

3.4.8.4.1 Donor Cell Volume Fraction Formulation--The donor volume fractions used at junctions j+1 and j in the momentum equations and convective terms of the mass and energy equations are given in **Table 3.4-1**. A positive velocity is for rising fluid.

Table 3.4-1 Logic for determining donor volume fraction.

Junction	v_g	$\dot{\alpha}_g$	v_f	$\dot{\alpha}_f$
j + 1 above level	> 0	α_L^+	> 0	$1 - \alpha_L^+$
j + 1 above level	< 0	α_M	< 0	$1 - \alpha_M$
j below level	> 0	α_K	> 0	$1 - \alpha_K$
j below level	< 0	α_L^-	< 0	$1 - \alpha_L^-$

The determination of the donor volume fraction is to ensure that the level is maintained as a sharp interface in ATHENA.

3.4.8.4.2 Modifications to the Momentum Equations--The density terms, pressure gradient, and momentum flux terms in the sum and difference momentum equations are modified to include the effect of a two-phase mixture level. The modifications to the individual terms of the momentum equations are done in such a way as to make the entire momentum cell appear to contain a single flow regime rather than containing two regions of dissimilar flow regimes. The flow regime for the momentum cell is that flow regime existing in the junction between the volumes. If the mixture level is in the upper half of the volume forming the lower portion of the momentum cell [See **Figure 3.4-22** (A-1)], the terms in the momentum equation are computed as if the mixture level were in the center of the volume forming the lower portion of the momentum cell [See **Figure 3.4-22** (A-2)]. If the mixture level in the lower half of the volume forming the upper portion of the momentum cell [See **Figure 3.4-22** (B-1)], the terms in the momentum equation are computed as if the mixture level was located in the center of the volume forming the upper portion of the momentum cell [See **Figure 3.4-22** (B-2)].

The averaged phasic densities in the momentum equation are a line average of the phasic densities on either side of the junction and are given by Equation (3.4-117) for the mixture level location shown in **Figure 3.4-22** (A-1) and by Equation (3.4-118) for the situation shown in **Figure 3.4-22** (B-1). These are

$$\bar{\rho}_{f,j} = \frac{\alpha_{f,K}^{+}\rho_{f,K}dz_K + \alpha_{f,L}\rho_{f,L}dz_L}{dz_K + dz_L} \tag{3.4-117}$$

$$\bar{\rho}_{f,j} = \frac{\alpha_{f,K}\rho_{f,K}dz_K + \alpha_{f,L}^{-}\rho_{f,L}dz_L}{dz_K + dz_L} \tag{3.4-118}$$

for the liquid densities, and the vapor/gas densities are computed similarly.

The pressure gradient in the momentum cell must also be modified to accommodate the presence of the mixture level. The pressure gradient in the momentum cell is computed as

$$\frac{dP}{dz} = \frac{P_L - P_K}{dz_j} \quad . \tag{3.4-119}$$

If there is a mixture level in the momentum cell, the pressure at one or the other end of the momentum cell is modified. The pressure at the K end of the momentum cell is modified if the mixture level is in the K volume, and the pressure at the L end of the momentum cell is modified if the mixture level is in the L volume. The pressures are modified by extrapolating the pressure gradient in the junction below the junction containing the mixture level. The junction below the one containing the mixture level is in bubbly flow which has a large pressure gradient. Extrapolation of a large pressure gradient leads to a better numerical performance since small errors in the computed pressure gradient leads to a smaller relative error than extrapolation of small pressure gradients found in the junctions above the mixture level. The pressures are modified as
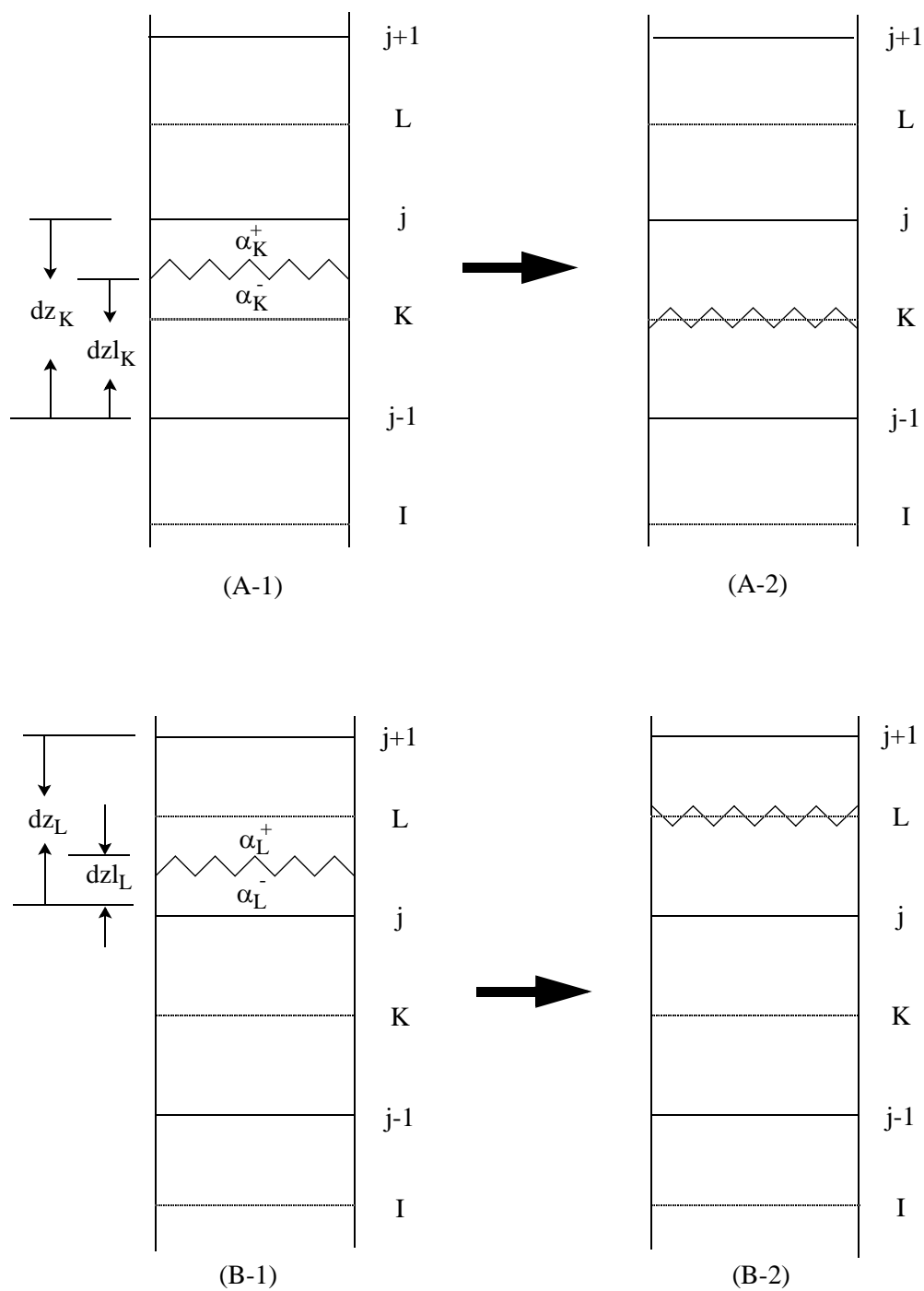
Figure 3.4-22 The control volume for momentum cell j.

$$P_K{}' = P_K + \left(dzl_K - \frac{dz_K}{2}\right)\frac{dP}{dz}\bigg|_{j-1} \tag{3.4-120}$$

$$P_L{}' = P_L + \left(\frac{dz_L}{2} - dzl_L\right)\frac{dP}{dz}\bigg|_{j-1} \tag{3.4-121}$$

where

$$\frac{dP}{dz}\bigg|_{j-1} = \frac{P_K - P_I}{dz_{j-1}} \tag{3.4-122}$$

for the situations shown in **Figure 3.4-22** (A-1) and **Figure 3.4-22** (B-1), respectively. If there is no junction at the bottom or top of the volume containing the mixture level, the pressure gradient due to gravity head is used to adjust the volume pressure.

The momentum flux terms are also modified in the momentum equations. These terms are set to zero for the junctions above and below the volume containing the mixture level.

3.4.8.5 Modification of Heat Transfer Calculation. When a heat structure is associated with a hydrodynamic volume where a mixture level exists, the heat transfer will be partitioned according the level location (**Figure 3.4-23**). The heat fluxes from the wall to the liquid phase and from the wall to the vapor/gas phase (q_{wf} and q_{wg}) are calculated as
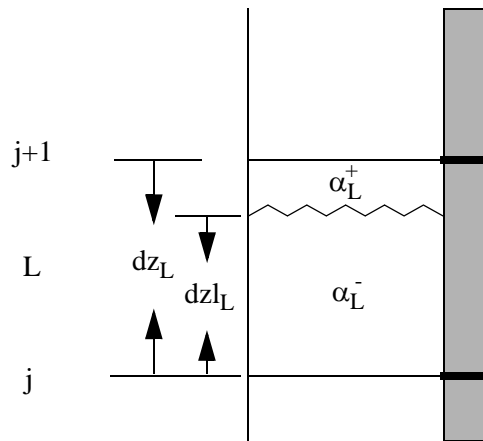
Figure 3.4-23 Hydrodynamic volume with heat structure.

$$q_{wg} = h_{wgg}(T_w - T_g)\left(1 - \frac{dzl_L}{dz_L}\right)$$ (3.4-123)

$$q_{wf} = h_{wff}(T_w - T_f)\left(\frac{dzl_L}{dz_L}\right)$$ (3.4-124)

where the heat transfer coefficient to the vapor/gas and the liquid (h_{wgg} and h_{wff}), wall temperature (T_w), and vapor/gas and liquid temperature (T_g and T_f) are the same as described in Section 3.3.9.

3.4.9 Thermal Stratification Model

A thermal stratification model is included to improve the accuracy of solutions when there is warm liquid appearing above cold liquid in a vertical stack of cells. In this case, there is a sharp thermal front between the two liquids because of the density differences between them. Because ATHENA uses a first-order upwind differencing scheme that has considerable numerical diffusion, there is significant artificial mixing of the hot and cold liquids. This has an unfavorable effect on the accuracy of the solution. Therefore, a model is included with the following features:

1.   A sharp temperature profile is maintained which separates the hot liquid from the cold liquid whenever thermal stratification occurs.

2.   Correct donoring of liquid specific internal energy at the junctions for the cell where the thermal stratification occurs.

3.   Only the hot liquid in a cell which contains the thermal front is allowed to flash.

In addition, the model is compatible with the mixture level model and when used in conjunction with the level model, it allows the code to predict the stratified behavior in a tank with considerable accuracy.

There are essentially two good choices to meet the requirements stated above. One possibility is to use a Godunov-type scheme with an artificial compression method to sharpen the temperature profile at the edge of the cell. The second approach is to use Harten's subcell resolution scheme,[3.4-45] to track the front in the interior of the cell. The problem with the first approach is that the front is tracked at the edge of the cell, whereas the front spends most of its time in the interior of the cell. Among other things, criteria 2 and 3 of the above may never be satisfied. This is not a serious problem for CFD codes where cell size tends to be fairly small. For engineering codes that use coarse nodalization, Harten's approach is the best approach if it is applicable to the problems in question.

It should be emphasized that although the proposed model can be viewed as an extension of Harten's method to the liquid specific internal energy for two-phase flow problems, the implementation of the model draws heavily from that of the mixture level model. Still, to have a deeper understanding of the range of applicability of the method, the reader is strongly encouraged to read Harten's paper. In the

thermal stratification model, the solution locally near the front is assumed to have a very simple profile. It is piecewise constant with the larger positive value appearing on top of a smaller value. Because ATHENA uses a simple first-order scheme with positive coefficients, it is therefore possible to determine the position of the front accurately using a simple calculation given in Section 3.4.9.3 below.

3.4.9.1 Overview of Software Design for the Thermal Stratification Model. The thermal front is defined as the location where a sharp change in the temperature of the liquid occurs. The thermal front tracking model implemented in ATHENA is analogous to the mixture level tracking model currently in ATHENA (see Section 3.4.8), both in its methodology and in its implementation. The model consists of four parts:

1.　　　Detection of the thermal front appearance and disappearance.

2.　　　Calculation of thermal front parameters that are necessary to describe a thermal front such as the position and velocity of the front, and the temperatures above and below the front.

3.　　　Modification of the liquid specific internal energy at the junctions to accurately convect the liquid specific internal energy above and below the front.

4.　　　Modification of the heat transfer calculation and vapor generation rate according to the position of the thermal front and temperature of the hot liquid in the cell that contains the thermal front.

3.4.9.2 Detection of Thermal Front Appearance and Disappearance. The thermal front is the location of an abrupt change in the liquid temperature. The logic for the detection of a thermal front appearance and disappearance in a computational cell is based on experimental data and numerical experiments. The density difference between the hot and cold liquid typically exceeds 3%. The thermal front detection logic for cell L in **Figure 3.4-24** is

$$\frac{|\rho_M - \rho_L|}{\rho_L} > 0.01 \tag{3.4-125}$$

or

$$\frac{|\rho_K - \rho_L|}{\rho_L} > 0.01 \tag{3.4-126}$$

provided that no thermal front exists in cell M or cell K and the liquid in the cells K, L, and M is stably stratified, or in other words, the specific internal energy of the liquid is a monotonically increasing from cell K to cell L to cell M. This is both a physical and mathematical necessity, since the computed dz1 at
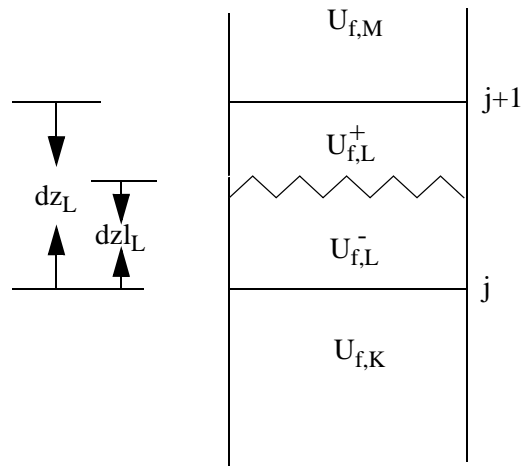
Figure 3.4-24 Thermal front in a tank.

cell L according to Equation **Figure 3.4-24** should be a positive number less than dz. See **Figure 3.4-25** for the logic diagram for the thermal front detection.

> **3.4.9.3 Calculation of Front Parameters.** The front parameters that describe the thermal front are

  1.   The specific internal energy of the liquid above and below the front $(U_{fL}^{+}$ and $U_{fL}^{-})$.

  2.   The location of the front (dzl_{L}).

  3.   The thermal front velocity (v_{front}).

> **3.4.9.3.1 Determination of the Specific Internal Energy Above and Below the Front--**The specific internal energy of the liquid below the front is set equal to the specific internal energy of the liquid in volume K, that is

$$U_{fL}^{-} \ = \ U_{f,K} \ , \tag{3.4-127}$$

while the specific internal energy of the liquid above the front is set equal to the specific internal energy of the liquid in volume M, that is

$$U_{fL}^{+} \ = \ U_{f,M} \ . \tag{3.4-128}$$

ATHENA/2.3
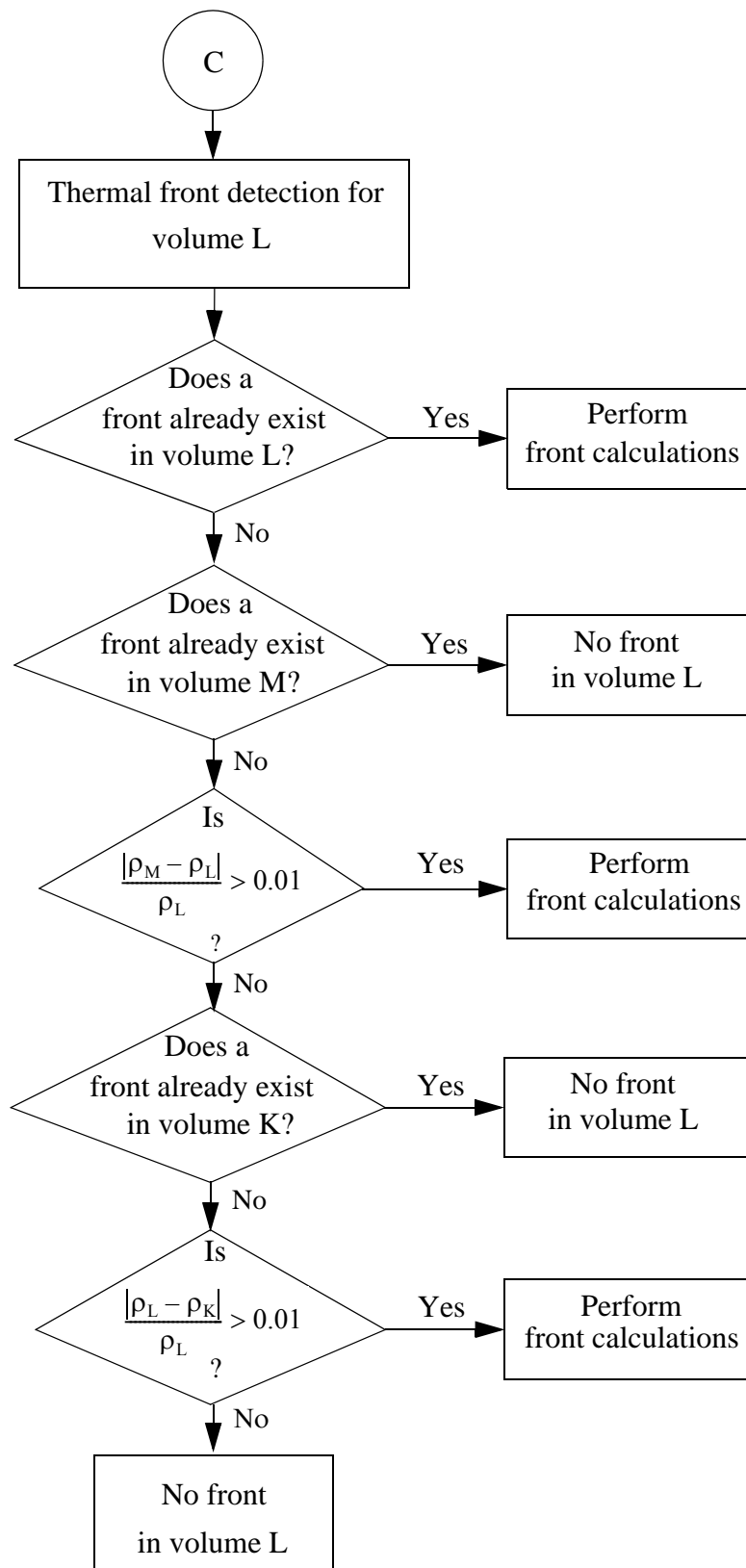
Figure 3.4-25 Thermal front detection logic diagram for volume L.

INEEL-EXT-98-00834-V1 3-232

3.4.9.3.2 Location of the Thermal Front--Once the presence of a thermal front is determined in a particular volume, a flag is set and the front parameters are calculated. The position of the thermal front ($dz1_L$) in a volume of length dz_L is given by

$$dz1_L = dz_L \left(\frac{U_{fL}^+ - U_{fL}}{U_{fL}^+ - U_{fL}^-} \right) \tag{3.4-129}$$

where U_{fL}^+ and U_{fL}^- are given by Equations (3.4-127) and (3.4-128). It is emphasized that this computation is performed only when $U_{fL}^+ > U_{fL} > U_{fL}^-$. This ensures that $dz1_L$ is a positive number less than dz_L.

3.4.9.3.3 Velocity of the Thermal Front--The velocity of the thermal front is computed from

$$v_{front} = \frac{dz1_L^n - dz1_L^{n-1}}{\Delta t} \ . \tag{3.4-130}$$

3.4.9.3.4 Modifications for Front Crossing--The criteria to determine if a thermal front will cross a cell boundary area

1.   For a rising front, $v_{front} > 0$,

$$\frac{|\rho_L - \rho_L^-|}{\rho_L} < 0.001 \tag{3.4-131}$$

or

$$\frac{dz1_L}{dz_L} \geq 0.98 \ . \tag{3.4-132}$$

This is the case when the thermal front is near the top of volume L and the densities ρ_L and ρ_L^- are very close.

2.   For a falling front, $v_{front} < 0$

$$\frac{|\rho_L^+ - \rho_L|}{\rho_L} < 0.001 \tag{3.4-133}$$

or

$$\frac{dz1_L}{dz_L} \leq 0.02 \quad .$$

(3.4-134)

This is the case when the thermal front is near the bottom of volume L and the densities ρ_L and ρ_L^+ are very close.

Figure 3.4-26 shows the logic diagram for the computation of thermal front parameters with modifications for front crossing.

3.4.9.4 Modification of ATHENA Field Equations for Front Tracking. The following modifications were made in solving the field equations in ATHENA:

1. The donor cell liquid specific internal energy based on the liquid specific internal energy above and below the thermal front will be used in the field equations.

2. The liquid temperature in the cell that contains the thermal front is modified in the computation of mass and energy transfer to indicate that only the hot liquid in the cell can undergo phase change (i.e., flash to vapor).

3. The liquid interphase heat transfer coefficient in the cell that contains the thermal front is modified to indicate that only the hot liquid in the cell can flash.
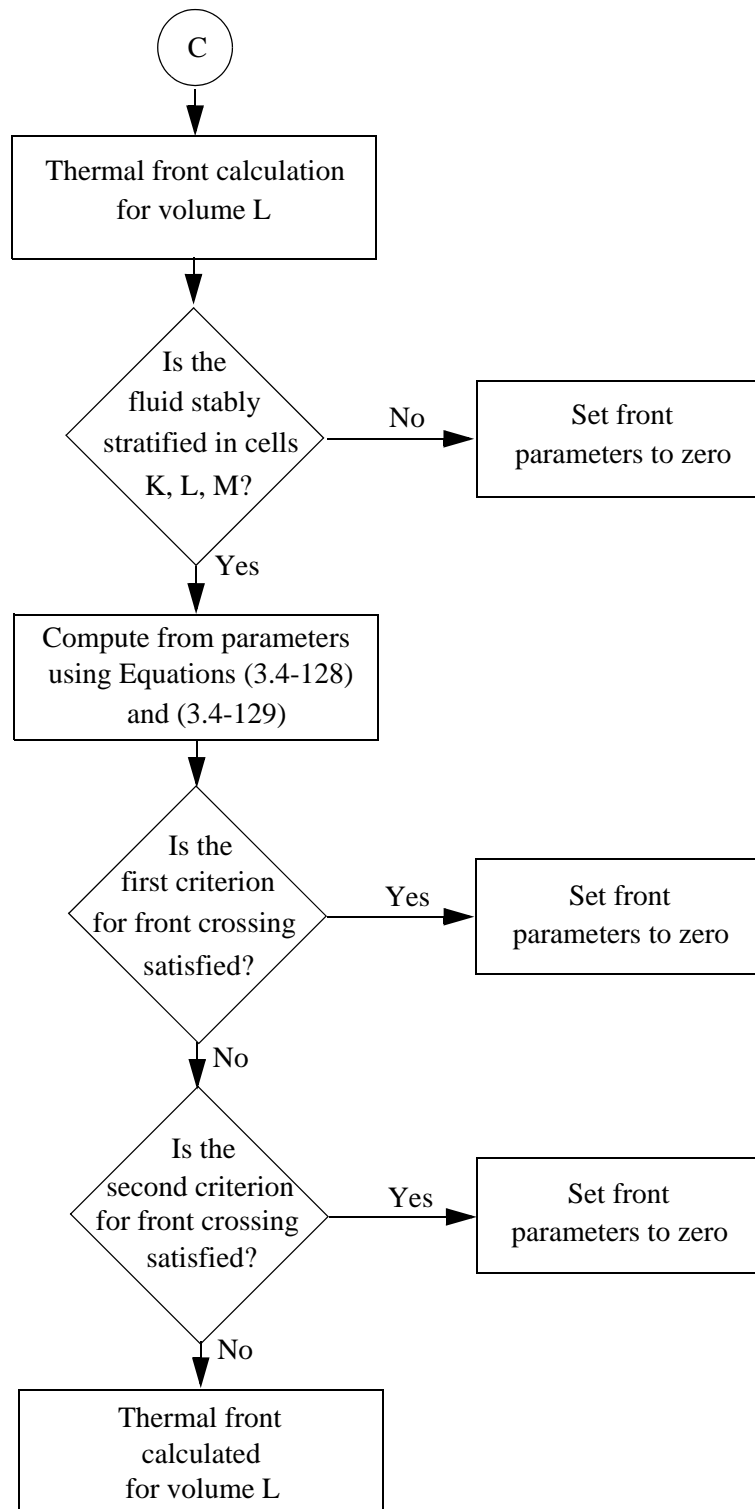
Figure 3.4-26 Computation of thermal front parameters logic diagram for volume L.

3.4.9.4.1 Donor Cell Internal Energy Formulation--The donor specific internal energies to be used at junctions j+1 and j in the field equations are given in **Table 3.4-2**. A positive velocity is for rising fluid**.**

Table 3.4-2 Logic for determining donor specific internal energy.

Junction	$\mathbf{v_g}$	$\dot{U}_g$	$\mathbf{v_f}$	$\dot{U}_f$
j+1 above front	> 0	$U_{g,L}$	> 0	$U_{f,M}$
j+1 above front	< 0	$U_{g,M}$	< 0	$U_{f,M}$
j below front	> 0	$U_{g,K}$	> 0	$U_{f,K}$
j below front	< 0	$U_{g,L}$	< 0	$U_{f,K}$

3.4.9.4.2 Modifications of Mass and Energy Transfer Calculation--Because only hot liquid in the cell that contains the thermal front can flash, the liquid interfacial heat transfer coefficient needs to be recalculated to reflect this. If the thermal front occurs at cell L, then H_{if} will be recomputed as

$$H_{if}^{new} = H_{if}\left(1 - \frac{dzl_L}{dz_L}\right) \quad .$$

(3.4-135)

The contribution to the vapor generation by the term H_{if} (T^s - T_{fL}) is then modified to be $H_{if}^{new}[T^s - T_f(U_{f,L}^+)]$, where $T_f(U_{f,L}^+)$ is the temperature of the hot liquid in the cell that contains the front (**Figure 3.4-27**).
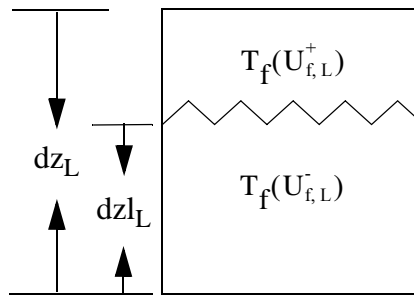
Figure 3.4-27 Hydrodynamic volume with thermal front.

3.4.10 Energy Conservation at an Abrupt Change

In special situations involving abrupt changes in either flow geometry (i.e., area changes) or flow conditions (i.e., shocks), predictions using the default ATHENA models do not conserve total energy. The situation usually involves significant pressure drops between ATHENA volumes. The primary interest in this is the simulation of the discharge at a break in the piping at a nuclear plant into the containment vessel. When the containment is modeled using normal ATHENA volumes (not time-dependent volumes), the lack of total energy conservation can result in the containment temperature being significantly under-predicted (by approximately 100 $^{\circ}$F).[a]

The thermal (internal) energy Equations (3.1-11) and (3.1-12) are equivalent to the total energy equations (i.e., energy is conserved) in the differential sense. This will not be true in the finite difference implementation because thermal energy equations cannot be expressed in so-called conservation law form as is possible for the total energy equations. Although the total energy equations can be implemented in the conservation form, there are some difficulties in the numerical implementation. These include the energy storage, energy flux, interfacial energy, and kinetic energy terms. The method used in ATHENA is to allow the user to correct the energy flux terms at points where they are known to be in error. This is done through a user junction input flag. The method used will next be described.

The vapor/gas thermal energy equation will be used to describe the method. The liquid thermal energy equation is similar. The nonexpanded vapor/gas thermal energy Equation (3.1-115) is of the finite difference form

$$
\begin{aligned}
V_L[(\alpha_g \rho_g U_g)_L^{n+1} - (\alpha_g \rho_g U_g)_L^n] &+ [\dot{\alpha}_{g,j+1}^n(\dot{\rho}_{g,j+1}^n \dot{U}_{g,j+1}^n + P_L^n)v_{g,j+1}^{n+1}A_{j+1} \\
&- \dot{\alpha}_{g,j}^n(\rho_{g,j}^n \dot{U}_{g,j}^n + P_L^n)v_{g,j}^{n+1}A_j]\Delta t = \text{RHS}
\end{aligned}
\tag{3.4-136}
$$

where RHS is the right-hand side terms. If the vapor/gas velocity is positive through junctions j and j+1, the pressure used in the energy flux term for junction j is P_K^n rather than P_L^n. Thus, Equation (3.4-136) becomes

$$
\begin{aligned}
V_L[(\alpha_g \rho_g U_g)_L^{n+1} - (\alpha_g \rho_g U_g)_L^n] &+ [\dot{\alpha}_{g,j+1}^n(\dot{\rho}_{g,j+1}^n \dot{U}_{g,j+1}^n + P_L^n)v_{g,j+1}^{n+1}A_{j+1} \\
&- \dot{\alpha}_{g,j}^n(\rho_{g,j}^n \dot{U}_{g,j}^n + P_K^n)v_{g,j}^{n+1}A_j]\Delta t = \text{RHS} \ .
\end{aligned}
\tag{3.4-137}
$$

For positive vapor/gas velocity in junction j, the donored density $\dot{\rho}_{g,j}$ and the donored specific internal energy $\dot{U}_{g,j}$, will also be from volume K. Thus, the energy flux term for junction j is really the

---

a. Personal communication, M. Van Haltern to R. A. Riemke, November 1991.

specific enthalpy from volume K. This modification results in using specific internal energy in the time derivative and specific enthalpy in the convective terms. This is the approach used in the containment code CONTAIN.[3.4-46] In the CONTAIN code, the total energy equation is the starting equation, but the kinetic energy is then ignored in the time derivative and convective terms because typical containment volumes are quite large. The resultant time derivative and convective terms are the same as shown in Equation (3.4-137). Using CONTAIN and the ATHENA modification to the energy flux give results that correctly match the containment temperature.

3.4.11 Jet Junction Model

Jet junctions are used where subcooled liquid is injected into the bottom of a pool in a vertical volume. The liquid from the jet causes a stirring action in the pool to increase the condensation rate on the surface of the pool. The surface turbulence intensity is a function of the distance of the surface from the jet, the pool diameter, the jet Reynolds number, and liquid properties such as the Prandtl and Jacob numbers. The details of the model are discussed in the closure relations section of Volume IV.

3.4.12 References

3.4-1. V. H. Ransom and J. A. Trapp, "The RELAP5 Choked Flow Model and Application to a Large Scale Flow Test," *Proceedings of the ANS/ASME/NRC International Topical Meeting on Nuclear Reactor Thermal-Hydraulics, Saratoga Springs, New York, October 5-8, 1980,* pp. 799-819.

3.4-2. J. A. Trapp and V. H. Ransom, "A Choked-Flow Calculation Criterion for Nonhomogeneous, Nonequilibrium, Two-Phase Flows," *International Journal of Multiphase Flow, 8,* 6, 1982, pp. 669-681.

3.4-3. P. R. Garabedian, *Partial Differential Equations,* New York: Wiley, 1964.

3.4-4. G. B. Whitham, *Linear and Nonlinear Waves,* New York: Wiley, 1974.

3.4-5. A. H. Shapiro, *The Dynamics and Thermodynamics of Compressible Fluid Flow, Volumes I and II,* New York: Ronald, 1953 and 1954.

3.4-6. V. H. Ransom and J. A. Trapp, *RELAP5 Progress Summary, Analytical Choking Criterion for Two-Phase Flow,* CDAP-TR-013, Idaho National Engineering Laboratory, April 1978.

3.4-7. D. A. Drew, L. Y. Cheng, and R. T. Lahey, Jr., "The Analysis of Virtual Mass Effects in Two-Phase Flow," *International Journal of Multiphase Flow, 5,* 1979, pp. 233-242.

3.4-8. P. S. Anderson, P. Astrup, L. Eget, and O. Rathman, "Numerical Experience with the Two-Fluid Model RISQUE," *Proceedings from Topical Meeting on Thermal Reactor Safety, Sun Valley, ID, July 31-August 4, 1977.*

3.4-9. D. Gidaspow (Chairman), "Modeling of Two-Phase Flow," *Proceedings of Round Table Discussion RT-1-2 at the Fifth International Heat Transfer Conference, Tokyo, Japan, September 3-7, 1974, also in ASME Journal of Heat Transfer, 3,* 1974.

3.4-10. J. D. Ramshaw and J. A. Trapp, "Characteristics, Stability, and Short-Wavelength Phenomena in Two-Phase Flow Equation Systems," *Nuclear Science and Engineering, 66,* 1978, pp. 93-102.

3.4-11. N. Zuber, "On the Dispersed Two-Phase Flow in the Laminar Flow Regime," *Chemical Engineering Science, 19,* 1964, pp. 897-917.

3.4-12. N. Abuaf, O. C. Jones, Jr., and B. J. C. Wu, *Critical Flashing Flows in Nozzles with Subcooled Inlet Conditions,* BNL-NUREG-27512, Brookhaven National Laboratory, March 1980.

3.4-13. M. D. Alamgir and J. H. Lienhard, "Correlation of Pressure Undershoot During Hot Water Depressurization," *Transactions of the ASME, Journal of Heat Transfer, 103,* 1981, pp. 52-73.

3.4-14. O. C. Jones, Jr., "Flashing Inception in Flowing Liquids," *Transactions of the ASME, Journal of Heat Transfer, 102,* 1980, pp. 439-444.

3.4-15. J. W. Burnell, "Flow of Boiling Water through Nozzles, Orifices, and Pipes," *Engineering,* 1947, pp. 572-576.

3.4-16. F. J. Moody, "Maximum Flow Rate of a Single-Component, Two-Phase Mixture," *Transactions of the ASME, Journal of Heat Transfer, 87,* 1965, pp. 134-142.

3.4-17. V. H. Ransom and J. A. Trapp, *RELAP5 Progress Summary-PILOT Code Hydrodynamic Model and Numerical Scheme. CDAP-TR-005,* Idahoo National Engineering Laboratory, January 1978.

3.4-18. W. M. Bryce, *Improvements to the RELAP5/MOD1/014 LOCA Code: The RELAP5/MOD1/WIN001 Code,* AEEW-R-1649, Atomic Energy Establishment Winfrith, May 1983, pp. 64-65.

3.4-19. K. H. Ardron and W. M. Bryce, *Assessment of Horizontal Stratification Entrainment Model in RELAP5/MOD3,* AEEW-R 2345, Atomic Energy Establishment Winfrith, April 1988.

3.4-20. W. M. Bryce, *Numerics and Implementation of the UK Horizontal Stratification Entrainment Off-Take Model into RELAP5/MOD3,* AEA-TRS-1050, AEEW-R 2501, Atomic Energy Establishment Winfrith, March 1991.

3.4-21. J. A. Trapp and V. H. Ransom, *RELAP5 Hydrodynamic Model Progress Summary-Abrupt Area Changes and Parallel Branching,* PG-R-77-92, Idaho National Engineering Laboratory, November 1977.

3.4-22. J. K. Vennard, "One-Dimensional Flow," in: V. L. Streeter (ed.), *Handbook of Fluid Dynamics,* 1st Edition, New York: McGraw Hill, 1961.

3.4-23.   J. Weisman, T. Ake, and R. Knott, "Two-Phase Pressure Drop Across Abrupt Area Changes in Oscillatory Flow," *Nuclear Science and Engineering, 61,* 1976, pp. 297-309.

3.4-24.   J. G. Collier, "Advanced Study Institute on Two-Phase Flows and Heat Transfer," *ASI Proceedings, Istanbul, Turkey, August 1976.*

3.4-25.   M. M. El-Wakil, *Nuclear Heat Transport,* Scranton: International Textbook, 1971.

3.4-26.   B. Harsch, A. Hussain, and J. Weisman, *Two-Phase Pressure Drop Across Restrictions and Other Abrupt Area Changes,* NUREG-0062, April 1976.

3.4-27.   P. A. Lottes, "Expansion Losses in Two-Phase Flows," *Nuclear Science and Energy, 9,* 1961, pp. 26-31.

3.4-28.   G. B. Wallis, *One-dimensional Two-phase Flow,* New York: McGraw-Hill, 1969, pp. 336-341.

3.4-29.   A. Cicchitti et al., "Two-Phase Cooling Experiments-Pressure Drop, Heat Transfer, and Burnout Measurements," *Energi Nucl., 7,* 1960, pp. 407-425.

3.4-30.   D. R. Liles et al., *TRAC-PF1/MOD1: Correlations and Models,* NUREG/CR-5069, LA-11208-MS, Los Alamos National Laboratory, December 1988.

3.4-31.   J. H. Mahaffy and D. R. Liles, "Numerically Induced Pressure Excursions in Two-Phase Flow Calculations," *2nd International Topical Meeting on Nuclear Reactor Thermal Hydraulics, Santa Barbara, CA, January 11-14, 1983.*

3.4-32.   V. H. Ransom et al., *RELAP5/MOD0 Code Description,* Volume 2, Code Development Update and Sample Problems, CDAP-TR-057, Idaho National Engineering Laboratory, May 1979.

3.4-33.   R. A. Riemke, "Countercurrent Flow Limitation Model for RELAP5/MOD3," *Nuclear Technology, 93,* 1991, pp. 166-173.

3.4-34.   S. G. Bankoff, R. S. Tankin, M. C. Yuen, and C. L. Hsieh, "Countercurrent Flow of Air/Water and Steam/Water Through a Horizontal Perforated Plate," *International Journal of Heat and Mass Transfer, 24,* 1981, pp. 1381-1385.

3.4-35.   M. W. Cappiello, *A Description of the TRAC-PF1/MOD1 CCFL Model,* LA-UR-87-294, Los Alamos National Laboratory, 1987.

3.4-36.   C. L. Tien, K. S. Chung, and C. P. Liu, *Flooding in Two-Phase Countercurrent Flows,* EPRI NP-1283, December 1979.

3.4-37.   S. Z. Rouhani et al., *TRAC-BF1/MOD1 Models and Correlations,* NUREG/CR-4391, EGG-2680, Idaho National Engineering Laboratory, August 1992.

3.4-38. Y. K. Cheung, V. Parameswaran, and J. C. Shaug, *BWR Refill-Reflood Program Task 4.7-Model Development, TRAC-BWR Component Models,* NUREG/CR-2574, EPRI NP-2376, GEAP-22052, April 1983.

3.4-39. D. D. Taylor, *1-D Level Tracking Model,* IS-NSMD-83-011, Idaho National Engineering Laboratory, April 1983.

3.4-40. A. Rosen et al., *Teploenergetikia,* 1976, Vol. 11, p. 59

3.4-41. S. Z. Rouhani, *Modified Correlations for Void and Pressure Drop,* AB Atomenergi, Sweden, Internal Report No. AE-RTV 841, March 1969.

3.4-42. B. Aktas, *Improvements to the Two-Phase Water Level Tracking Model of a Transient Reactor Analysis Code,* M.S. Thesis, Pennsylvania State University, 1994.

3.4-43. B. Aktas and J. H. Mahaffy, "A Two-Phase Level Tracking Method," *Nuclear Engineering and Design, 162,* 271-280, 1996.

3.4-44. B. Aktas and J. H. Mahaffy, "Enhanced Numerical Modeling of Manometer Based Oscillations by Discontinuity Tracking," *Transactions of the American Nuclear Society, San Francisco, CA, November, 1995*, 73, pp. 503-504.

3.4-45. A. Harten, "ENO Schemes with Subcell Resolution," *Journal of Computational Physics, 83,* 1989, pp. 148-184.

3.4-46. K. W. Washington et al., *Reference Manual for the CONTAIN 1.1 Code for Containment Severe Accident Analysis,* NUREG/CR-5715, SAND91-0835, Sandia National Laboratory, May 1991.

3.5 Component Models

ATHENA consists of a variety of generic models that are used to build system models. These include the pipe, annulus, branch, single-volume, single-junction, etc., and will be discussed in more detail in Volume II of this manual. The general philosophy has been to avoid system component models such as steam generator and core. However, certain subsystem components are unavoidable due to unique processes or performance. ATHENA contains models for subsystem components such as a branch, separator, jet mixer, pump, turbine, valve, accumulator, ECC mixer, annulus, pressurizer, and feedwater heater. A brief summary of each of these models is included here.

3.5.1 Branch

The branch component is a model designed for convenient interconnection of hydrodynamic components. The identical result can be obtained by using a single-volume component and several single-junction components. Thus, the branch is a separate component only in the input processing scheme.

The crossflow junction has been added in which the junction velocities are assumed to be normal to the one-dimensional flow path of the hydrodynamic volume. Thus, the branch component can include multiple connections at the inlet, outlet, or in the crossflow direction.

Specialized modeling considerations are applied to any volume having multiple junctions connected at either volume end. (The ends of a hydrodynamic volume are the inlet and outlet, as defined in Section 3.1.1.)

These special calculations include both the method for calculating the volume average velocities (See Section 3.1.6) and the method for partitioning the volume cross-sectional area between the multiple inlet or multiple outlet junctions (See Section 3.5.1.1). The partitioned volume cross-sectional areas are used both in the momentum equations source terms (i.e., wall friction, abrupt area loss, user-specified loss, etc.) and in the momentum equations time variation of momentum.

In applications, the multiple junction and crossflow models are used in three distinct ways to model branching flows. These are a one-dimensional branch, a tee branch, and a crossflow branch. A combination of the three basic branches may also occur. Each of the three basic models will be discussed in turn.

3.5.1.1   One-Dimensional Branch. This basic branch model is consistent with the one-dimensional approximation for a piping network and assumes that multidimensional effects at branches are small compared to system interaction effects. In the case of branched flows that occur in headers or plena, the model gives an accurate physical description of the flow division or merging process; and the one-dimensional branch model is intended primarily for use in modeling such branched flows. Examples of such situations in LWR systems are flow division at the core inlet if parallel flow paths through the core are modeled, steam generator inlet and outlet plena when several parallel tube groups are modeled (for the effect of tube height and length), or at a wye connection.

The partitioned volume cross-sectional areas for the one-dimensional branch are discussed. The partitioned volume cross-sectional area for a junction is the actual volume cross-sectional area divided in proportion to the volume flow of the junction divided by the total volume flow for all the junctions on that end of the volume. This method of apportioning the volume cross-sectional area satisfies continuity but does not conserve momentum, particularly for high velocity differences between the merging streams. (For flow spliting, however, the method does preserve momentum.) For this reason, the special jet mixer component was developed for merging flows having high relative velocities, such as in a jet pump. The jet mixer component can be used for one-dimensional mixing but this component model is limited to two inlet streams and a single outlet stream. (See Section 3.5.3 for a description of the jet mixer model).

The method for determining the partitioned volume cross-sectional area for a one-dimensional branch is illustrated in **Figure 3.5-1** for a volume having two inlet junctions and one outlet junction The junctions J_1 and J_2 are the inlet junctions, and junction J_3 is the outlet junction. The volume cross-sectional area for inlet junction j attached to volume V_K (where there are N junctions on the inlet) is given by:

.
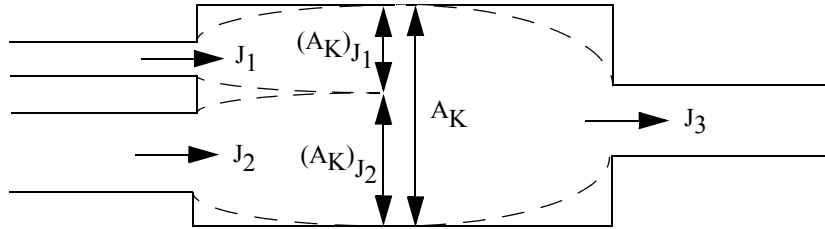
Figure 3.5-1 One-dimensional branch

$$(A_K)_j = \left\{ \frac{[\ |(\alpha_f)_j^n (v_f)_j^n| + |(\alpha_g)_j^n (v_g)_j^n|\ ] A_j}{\displaystyle\sum_{i=J_1}^{J_N} [\ |(\alpha_f)_i^n (v_f)_i^n| + |(\alpha_g)_i^n (v_g)_i^n|\ ] A_i} \right\} A_K \quad . \tag{3.5-1}$$

The dotted lines in **Figure 3.5-1** show the approximation to the stream tubes for the three junctions.

For the case of **Figure 3.5-1**, N = 2 and j takes the values of J_1 and J_2. A similar equation is used for multiple output junctions.

3.5.1.2 Tee Branch. The crossflow junction (see Section 3.4.5) is used to form a 90-degree tee, as shown in **Figure 3.4-10**. In this particular application, the side connection to the tee is modeled using a junction in which one-half of the junction momentum equation has the crossflow form. (The half of junction J_3 associated with volume V_L is a crossflow junction and is designated by an X, see **Figure 3.4-10**.)

No special component is provided to accomplish the input associated with a model, such as illustrated in **Figure 3.4-10**. The volume, V_L, may be specified as a branch with the associated junctions or as a single-volume with single-junctions used to specify the connecting junctions. In either case, junctions J_1 and J_2 should be specified as smooth unless actual abrupt changes in area occur at either junction. Junction J_3 should be specified as smooth with a user-specified form loss factor to account for the turning and entrance losses. In addition, junction J_3 must be specified so that the half of the junction associated with volume V_L is modeled as a crossflow junction and the half associated with volume V_K is a normal junction. These options are specified through input of junction control flags.

It is also possible to model a 90-degree tee without using a crossflow junction; however, unphysical numerical results have been obtained at times for reasons that are not fully understood. Thus, the 90-degree tee model using the crossflow junction is recommended and is a closer approximation to the actual fluid momentum interaction that occurs at a tee.

In some branching situations where the throughflow is small or where the flow is constrained by the geometry, body force effects may be significant. Examples that occur in PWR systems are the cold leg connections to the inlet annulus and downcomer and the hot leg connection to the upper plenum and core. This type of branched flow is modeled as shown in **Figure 3.5-2**. Here the vertical direction is modeled as the throughflow direction (indicated by the volume orientation arrows). The cold or hot leg connections are modeled by crossflow junctions. The throughflow direction of volume V_3 is chosen to correspond to the major flow path. In the case of a PWR inlet annulus, throughflow in the horizontal direction is inhibited by the annular structure; in the case of the upper-plenum-to-core connection, the area for flow in the vertical direction is large compared to the flow area in the horizontal direction. Some judgment is required to select the orientation. However, the crossflow branch connection will permit throughflow in the horizontal direction, but with some accompanying pressure rise and drop associated with the fact that the momentum flux terms can be neglected in the crossflow part of the junction.

The model illustrated in **Figure 3.5-2** has the additional advantage that the effect of vertical void gradients in the flow out of the horizontal connections may be more sharply defined as a result of the central volume, V_3, which has a vertical height equal to the diameter of branch volumes V_1 and V_4.

No special component model is provided for modeling the vertical tee, and either a branch or a single-volume may be used for volume V_3. The branch component is more convenient, since all junctions connecting to volume V_3 can be specified with the branch component.

3.5.1.3 Crossflow Branch. A third type of branched flow path can be created by the use of a crossflow junction to couple two volumes. This type of branch is used to model crossflow between parallel core channels and leak paths between volumes having centers at the same vertical elevation. The application of the crossflow junction for crossflow or leak path modeling is illustrated in **Figure 3.4-9**. The default length scale associated with the crossflow junction is one-half the diameter of the K volume plus one half the diameter of the L volume. This length is only used for modeling the fluid inertia terms in the momentum equation. The user has the option to input the length for a crossflow junction.
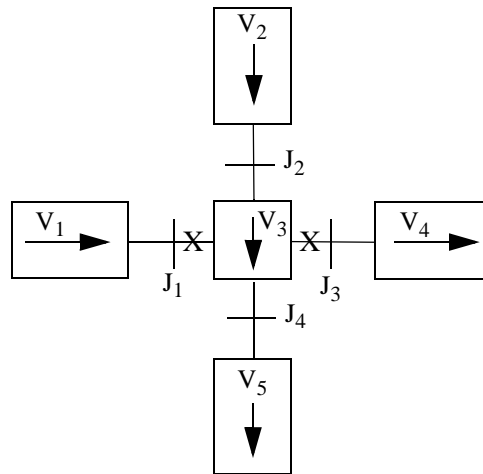
Figure 3.5-2 Gravity effects on a tee.

The pure crossflow branch is most easily modeled using a single-junction component for the crossflow junction. However, either volume V_1 or V_2 in **Figure 3.4-9** can be modeled using the branch component and specifying the coupling junctions with that component.

3.5.2 Separator

PWR and BWR nuclear power plants use a steam separator to increase the quality of steam prior to the generation of mechanical energy in the turbine. Typically in BWR's the quality of the steam is increased from 10-13% at the core output to at least 90% at the outlet of the separator. In addition, steam dryers are also used, which further increase the quality of the steam to at least 99.9%. By providing dry steam to the turbines the efficiency of the turbines in increased, wear is decreased, and radioactivity carried to the turbines is minimized. Water entrained with the steam is called carryover.

In addition to producing dry steam, the separators and dryers minimize the quality of the water removed from the dryed steam. The steam in the water removed from the dryed steam is called carryunder. The problems associated with excessive carryunder are that lower fluid density increases the chance of pump cavitation, it slightly increases the void supplied to the BWR core or PWR steam generator, and it slightly increases the pressure drop in the BWR core or PWR steam generator.

The physical situation being modeled is the removal of water from the two phase flow which is exiting either the core in a BWR or the steam generator in a PWR. There are usually three distinct regions common the both types of nuclear plants. The first is a centrifical type separator which causes the two phase flow to rotate rapidly either by injecting it into a cylinder either tangentially or from the bottom through turning vanes. As the mixture rotates, the denser liquid is thrown to the interior wall of the cylinder and drained while the less dense steam is removed from the center of the cylinder at the top. After

exiting the centrifical separator, the higher quailty steam-water mixture enters a gravity separator where the momentum of the flow is reduced such that the gravitational forces cause the water droplets to fall to the bottom where the liquid is drained into a downcomer while the steam mixture exits from the top. Finally the steam leaving from the top of the gravity separator enters a dryer. The dryer is a series of convoluted flow passages through chevron plates that cause the mixture to accelerate repeatedly. Water droplets entrained in the flow impinge on the plates where they are collected and drained while the steam continues on to the turbines.

The separator component model has two options, the simple separator model which was implemented in previous versions of ATHENA and a mechanistic separator model intended to model the centrifugal separators and chevron dryers in BWR reactors. The separator model determines the convected volume fractions in the liquid fall back junction and the vapor/gas outlet junction.

3.5.2.1 Simple Separator. The model is a nonmechanistic or black-box model consisting of a special volume with junction flows, as pictured in **Figure 3.5-3**. A vapor/gas-liquid inflowing mixture is separated by defining the volume fractions of the outflow streams using empirical functions. No attempt is made to model the actual separation process from first principles**.**
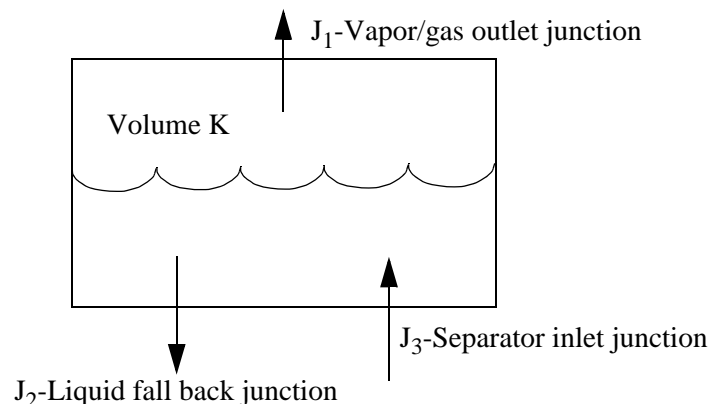
Figure 3.5-3 Typical separator volume and junctions.

The separator vapor/gas outlet performance is defined by means of a special function for the junction vapor/gas void fraction at J_1. The donored junction vapor/gas volume fraction used to flux mass through the vapor/gas outlet is related to the vapor/gas volume fraction in the separator volume using the curve in **Figure 3.5-4**. For separator volume vapor/gas volume fractions above the value of VOVER (an input parameter), a vapor/gas volume fraction of VGMAX (an input parameter) is fluxed out junction J_1. If VGMAX is 1.0, perfect vapor/gas separation occurs. For separator volume vapor /gas volume fractions less than VOVER, a two-phase mixture is fluxed out. The VOVER parameter helps govern the vapor/gas volume fraction of the outflow. If VOVER is small, the vapor/gas outflow corresponds to an ideal separator for vapor/gas if VGMAX is 1.0. If VOVER equals 1.0, the vapor/gas outlet junction behaves as a

normal junction, and the vapor/gas outlet junction volume fraction is equal to the separator volume vapor/gas volume fraction. A limit is placed on the vapor/gas volume fraction of the outflow, in that at most 99.9% of the vapor/gas present in the separator volume can be fluxed out junction J_1. This limit is used to prevent over extraction of vapor/gas.
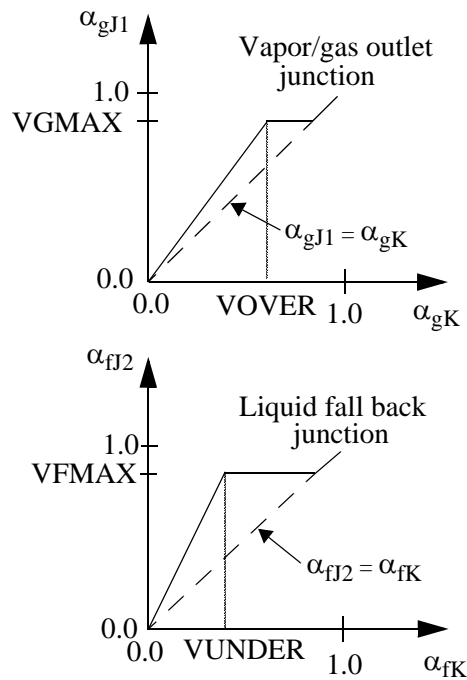
Figure 3.5-4 Donor junction volume fractions for outflow.

The flow of the separator liquid drain junction is modeled in a manner similar to the vapor/gas outlet except that a liquid volume fraction of VFMAX (an input parameter) is fluxed out junction J_2 when the volume liquid fraction is greater than the value of VUNDER (an input parameter) (see **Figure 3.5-4**). As with the vapor/gas output, if VFMAX is 1.0, perfect liquid separation occurs. As with the vapor/gas outlet, a 99.9% extraction limit is placed on the liquid drain. Normal donored fluxes are used for the separator inlet junction.

Although the volume fractions used in the flux of mass and energy from the separator volumes are modified, the normal junction momentum equations are used to calculate the flow velocities. It is not required that α_{gJ1} and α_{fJ1} sum to 1, nor is it required that α_{gJ2} and α_{fJ2} sum to 1. This can occur in counter-current flow.

3.5.2.2 *Mechanistic Separator.* The mechanistic separator component model is intended to model the centrifugal separators and chevron dryers in BWR reactors. Like the simple separator, the mechanistic separator consists of a special volume with three junction flows, as pictured in **Figure 3.5-3**. A

vapor/gas-liquid inflowing mixture is separated by defining the quality of the outflow streams using mechanistic models of the separating process in the separator and dryer components.

3.5.2.2.1 Centrifugal Separator Model--The model for the centrifugal separator was taken from the TRAC-BWR computer code and was developed by the General Electric Company as part of the joint USNRC- EPRI- General Electric Company sponsored BWR Refill-Reflood Program. Separators are made up of either two- or three-stages connected in series. The separator model determines the separating efficiency of a single-stage, feeding the output of one stage to the input of the next stage. The primary measures of separator performance are carryover of entrained liquid in the vapor/gas leaving the separator, carryunder of vapor/gas in the liquid leaving the discharge passage of the separator, and the separator pressure drop. A mechanistic model has been developed to calculate the carryover, carryunder, and separator pressure drop. The separator component volume as shown in **Figure 3.5-3** represents the physical volume in the separator barrel and discharge passages. The inlet junction J_3 represents the flow from the separator standpipe through the swirl vanes to the separator barrel. The vapor outlet junction J_1 represents the flow out of the top of the separating barrel from the last separating stage and the liquid outlet junction J_2 represents the combined discharge passages of all of the stages. The following description of the mechanistic separator model is adapted from **Reference 3.5-1**.

A separator component consists of three regions, a standpipe, the separator barrel, and the discharge passage. **Figure 3.5-5** shows a schematic of the first stage of a separator component. A two-phase mixture enters the separator barrel from the standpipe, passing through a set of stationary swirl vanes attached to the separator hub which acts as a bladed nozzle. These vanes produce a high rotational velocity component in the fluid flowing through the separator barrel. The resultant centrifugal force separates the vapor/gas-liquid mixture into a liquid vortex on the inner wall of the separating barrel and a vapor/gas vortex core. Separation is accomplished by directing the liquid layer on the wall into the discharge passage through pick-off rings at the exit of the separator barrel.

3.5.2.2.2 Assumptions and Model Equations--In this model, the following assumptions are made for the axial location near the pick-off ring*:*

1.   There is one uniform axial velocity in each of the flow regions, i.e.

$0 \leq r \leq r_f$: $v_a = v_{ag}$, uniform in vapor/gas core   (3.5-2)

$r_f \leq r \leq r_w$: $v_a = v_{af}$, uniform in liquid layer   (3.5-3)

where r_f is the inner radius of the liquid layer.

2.   The tangential velocity in each region is proportional to C which is related to the vortex strength, and is a function of r as follows:
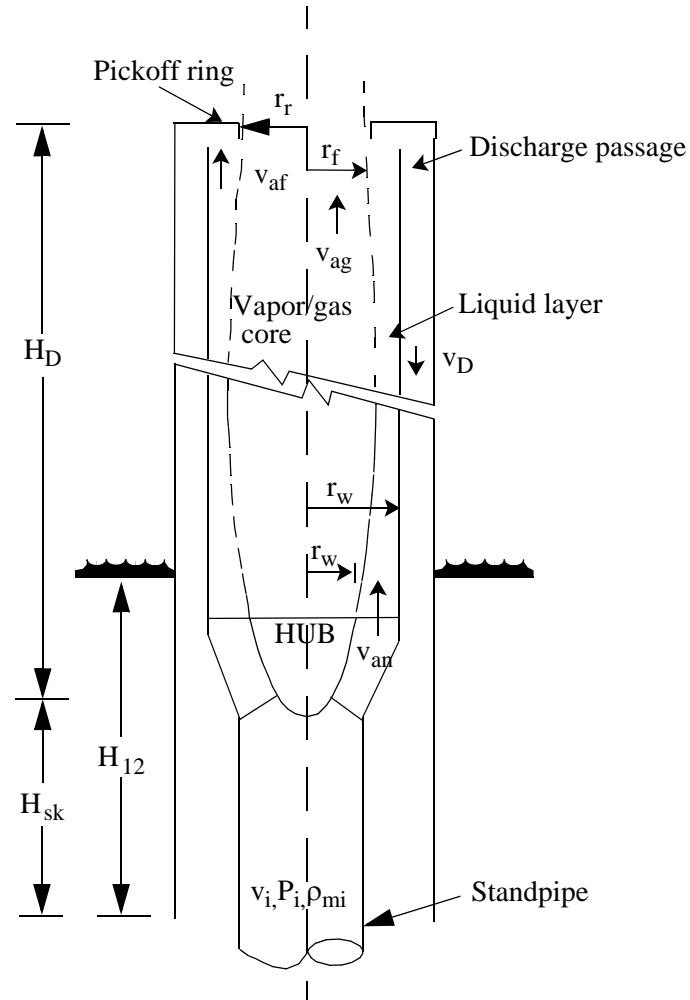
Figure 3.5-5 Schematic of first stage of mechanistic separator.

$$0 \le r \le r_f \quad : \qquad v_t = \frac{rC}{r_f^{3/2}} \qquad\qquad\qquad (3.5\text{-}4)$$

$$r_f \le r \le r_w \quad : \qquad v_t = \frac{C}{\sqrt{r}} \quad . \qquad\qquad\qquad (3.5\text{-}5)$$

3.   The vapor/gas void fraction profiles are assumed as follows:

$$0 \le r \le r_f \quad : \qquad \alpha_g = 1 - b\frac{r}{r_w} \tag{3.5-6}$$

$$r_f \le r \le r_w \quad : \qquad \alpha_g = a\left(\frac{r_w}{r} - 1\right) \tag{3.5-7}$$

and

$$a = AA\left(\frac{\sqrt{gr_w^2}}{C}\right)^{0.5} X_i^2 \qquad \text{for } X_i < 0.15 \tag{3.5-8}$$

$$a = AA\left(\frac{\sqrt{gr_w^2}}{C}\right)^{0.5} (0.09335)X_i^{0.75}, \qquad \text{for } X_i > 0.15 \tag{3.5-9}$$

$$b = BB\left(\frac{\sqrt{gr_w^2}}{C}\right)^{0.5} (1 - X_i)^3 \tag{3.5-10}$$

where X_i is the inlet flow quality, and AA and BB are parameters to be fitted with data.

4.　　　The pressure in the vapor/gas core (P_o) is assumed to be uniform radially and axially, and the pressure at the separator wall (P_w) is related to P_o by centrifugal force across the liquid layer.

For the first stage of the separator, a total of six unknowns are introduced in this model. These are v_{ag}, v_{af}, C, r_f, P_o, and P_w. The required equations are formulated from conservation of liquid mass, vapor/gas mass, axial momentum, and angular momentum entering and leaving the separating barrel, from centrifugal pressure drop across the liquid layer and from pressure drop in the discharge passage. The above unknowns can now be solved from given conditions of pressure, P_i, total flow rate, W_i, and flow quality at the swirl vane inlet, X_i.

The mass and momentum conservation equations for flows entering and leaving the separating barrel are

Liquid Mass

$$(1 - X_i)W_i = 2\pi \int (1 - \alpha_g)\rho_f v_a r dr = 2\pi \rho_f v_{ag} \frac{1}{3} b \frac{r_f}{r_w} r_f^2$$

$$+ 2\pi \rho_f v_{af} \left[\left(\frac{1+a}{2} \right) (r_w^2 - r_f^2) - a r_w (r_w - r_f) \right] \quad . \tag{3.5-11}$$

Vapor/Gas Mass

$$X_i W_i = 2\pi \int_0^{r_w} \alpha_g \rho_g v_g r dr = 2\pi \rho_g v_{ag} \left(\frac{1}{2} - \frac{1}{3} b \frac{r_f}{r_w} \right) r_f^2$$

$$+ 2\pi \rho_g v_{af} a \frac{1}{2} (r_w - r_f)^2 \quad . \tag{3.5-12}$$

Angular Momentum

$$\int_{r_h}^{r_w} V_{tn} r (2\pi r \rho_{mi} v_{an}) dr = \int_0^{r_w} v_t r (2\pi r \rho v_a) dr + F_t r_w \quad . \tag{3.5-13}$$

Axial Momentum

$$\pi r_h^2 P_o + 2\pi \int_0^{r_w} (\rho_{mi} v_{an}^2 + P_n) r dr = 2\pi \int_0^{r_w} (\rho v_a^2 + P) r dr + F_a \quad . \tag{3.5-14}$$

Assuming that the flow through the swirl vane passages is homogeneous and that the swirl vane passages act as a nozzle, the pressure and velocity entering the separating barrel are related to the conditions in the standpipe as follows:

$$W_i = \rho_{mi} v_i A_i = \rho_{mi} v_{an} A_n \tag{3.5-15}$$

$$P_i + \frac{1}{2} \rho_{mi} v_i^2 = P_n + \frac{1}{2} \rho_{mi} (v_{an}^2 + v_{tn}^2)(1 + C_{NOZ}) \tag{3.5-16}$$

$$\frac{v_{an}}{v_{tn}} = \tan\theta \tag{3.5-17}$$

where θ is the angle between the swirl vanes and the horizontal plane, ρ_{mi} is the inlet mixture density, and C_{NOZ} is the contraction loss coefficient defined as

$$C_{NOZ} = 0.5\left(1 - \frac{A_n}{A_i}\right) \tag{3.5-18}$$

where A_n is the swirl vane flow area and A_i is the standpipe flow area.

F_a and F_t in Equations (3.5-13) and (3.5-14) are the axial and tangential components of the frictional force on the swirling liquid layer, and are given by

$$F_a = F_f\left(\frac{v_{af}}{v_w}\right) \tag{3.5-19}$$

$$F_t = F_f\left(\frac{v_{tw}}{v_w}\right) \tag{3.5-20}$$

where v_{tw} is the tangential velocity on the wall, given by

$$v_{tw} = \frac{C}{\sqrt{r_w}} \tag{3.5-21}$$

and v_w is the resultant swirling velocity on the wall, given by

$$v_w = \sqrt{v_{tw}^2 + v_{af}^2} \tag{3.5-22}$$

F_f is the resultant frictional force, given by

$$F_f = \frac{1}{2}\rho_f C_F v_w^2 (2\pi r_w)H_D \quad . \tag{3.5-23}$$

Assuming that the liquid film is thin with respect to the radius of curvature of the separator barrel, the flow can be considered to be film flow over a flat plate. For turbulent flow over a flat plate, C_F is given by

$$C_F = \frac{0.455}{(\log_{10}Re_L)^{2.58}} \tag{3.5-24}$$

where Re_L is defined as

$$Re_L = \frac{\rho v_w}{\mu} \frac{H_D v_w}{V_{af}} \quad .$$ (3.5-25)

The radial pressure drop across the liquid layer due to centrifugal force is

$$\int_{P_0}^{P_w} dP = \int_{r_f}^{r_w} \rho \frac{v_t^2}{r} dr$$ (3.5-26)

or

$$P_o = P_w - [\rho_f + a(\rho_f - \rho_g)]C^2\left(\frac{1}{r_f} - \frac{1}{r_w}\right) + a(\rho_f - \rho_g)C^2\left(\frac{r_w}{r_f r_r}\frac{1}{r_w} - \frac{1}{r_w}\right) \quad .$$ (3.5-27)

The pressure drop in the discharge passage is

$$\frac{\int_{r_r}^{r_w}\left(\frac{1}{2}\rho v_a^2 + P\right)dA}{\int_{r_r}^{r_w} dA} = \frac{1}{2}\rho_{M,D}v_D^2\left[1 + 2C_F\left(\frac{H_D}{D_D} + EFFLD\right) + C_K\right]$$ (3.5-28)

$$+ [P_o + \rho_f g H_{12} - \rho_D g(H_D + H_{sk})]$$

where $\rho_{M,D}$ and v_D are the mixture density and mixture velocity in the discharge passage, H_D and D_D are the length of the separator barrel and hydraulic diameter of the discharge passage, EFFLD is the effective L/D coefficient at the pick-off ring, C_K is the total loss coefficient in the discharge passage, H_{12} is the height of the liquid pool surrounding the separator relative to the bottom of the discharge passage, and H_{sk} is the axial distance between the separator hub and the bottom of the discharge passage.

For the discharge passage,

$$C_F = \frac{0.079}{Re^{0.25}} \quad .$$ (3.5-29)

The vapor/gas and liquid flow rates discharged through the discharge passage are calculated as follows:

$$W_{g,\,cu} = 2\pi \int_{r_r}^{r_w} \alpha_g \rho_g v_a r dr$$

$$W_{f,\,cu} = \int_{r_r}^{r_w} (1 - \alpha_g) \rho_f v_a r dr \ .$$

(3.5-30)

For a liquid layer thicker than the gap between the pick-off ring and the separator barrel, i.e., $r_f < r_r$, the vapor/gas and liquid flow rates through the discharge passage are

$$W_{g,\,cu} = \pi \rho_g v_{af} a (r_w - r_w)^2$$

$$W_{f,\,cu} = \pi \rho_f v_{af} [(r_w^2 - r_r^2) - a(r_w - r_r)^2] \ .$$

(3.5-31)

For a water layer thinner than the gap between the pick-off ring and the separator barrel wall, i.e., $r_r < r_f$, the vapor/gas and liquid flow rates through the discharge passage are

$$W_{g,\,cu} = X_i W_i - 2\pi \rho_g v_{ag} \left(\frac{1}{2} - \frac{1}{3} b \frac{r_r}{r_w} \right) r_r^2$$

$$W_{f,\,cu} = (1 - X_i) W_i - 2\pi \rho_f v_{ag} r_r^2 \left(\frac{1}{3} \right) b \frac{r_r}{r_w} \ .$$

(3.5-32)

The vapor/gas and liquid flow rates leaving the present stage and entering the next stage are

$$W_{g,\,co} = (\text{vapor/gas flow rate})_{in} - W_{g,\,cu}$$

$$W_{f,\,co} = (\text{liquid flow rate})_{in} - W_{f,\,cu} \ .$$

(3.5-33)

The total discharge flow rate is

$$W_D = W_{g,cu} + W_{f,cu} \ .$$

(3.5-34)

Assuming homogeneous flow in the discharge passage, the mean vapor/gas void fraction is

$$\alpha_{g,\,cu} = \frac{W_{g,\,cu}}{W_{g,\,cu} + W_{f,\,cu}\dfrac{\rho_g}{\rho_f}}\ , \tag{3.5-35}$$

the mixture density in the discharge passage is

$$\rho_{M,D} = \alpha_{g,cu}\rho_g + (1 - \alpha_{g,cu})\rho_f \tag{3.5-36}$$

and the mixture velocity in the discharge passage is

$$v_D = \frac{W_D}{\rho_{M,D}A_D}\ . \tag{3.5-37}$$

In summary, for given swirl vane inlet conditions, P_i, X_i, and W_i, the unknowns v_{ag}, v_{af}, C, r_f, P_o, and P_w are calculated by solving Equations (3.5-11) to (3.5-28) simultaneously.

Similar equations can be written for the second- and third-stages. Since it is assumed that P_o is uniform axially, i.e., the vapor/gas core pressure drop in the axial direction is small, the axial momentum equation can be neglected in the solution for the upper stages. For these stages, the unknowns are reduced to v_{ag}, v_{af}, C, r_f, and P_w, and the equations are the conservation of liquid mass, vapor/gas mass, angular momentum, the pressure drop across the liquid layer, and the pressure drop in the discharge passage.

The right hand sides of Equations (3.5-11), (3.5-12), and (3.5-13) represent the liquid flow rate, vapor/gas flow rate, and angular momentum entering the separator barrel. For the second- and third-stages, these terms are modified as follows:

$$(\text{Liquid flow rate})_{in} = (W_{f,\,co})_{previous\ stage}$$
$$(\text{Vapor/gas flow rate})_{in} = (W_{g,\,co})_{previous\ stage}$$
$$(\text{Angular momentum})_{in} = \left[\int_o^{r_r} V_t r(2\pi\rho v_a)r dr\right]_{previous\ stage}\ . \tag{3.5-38}$$

3.5.2.2.3 Carryover and Carryunder--The total vapor/gas flow rate that is carried under consists of two parts; i.e., the vapor/gas flow through the first discharge passage which discharges its fluid below the liquid level and the vapor/gas entrained by the liquid discharged from higher stages. The exits of the discharge passages of the higher stages are located above the liquid level. It is assumed that the entrainment is proportional to the square of the total liquid flow discharged from the higher stages, i.e.,

$$(W_{g,\,cu})_{total} = (W_{g,\,cu})_1 + CC\left[\sum_{i=2}^{N}(W_{f,\,cu})_i\right] \qquad (3.5\text{-}39)$$

where

N   =   2 for a two-stage separator

         =   3 for a three-stage separator

and CC is a constant to be fitted with data.

The total liquid that is carried over consists of two parts, the liquid flow rate through the last stage and the liquid flow rate entrained by the vapor/gas discharged from the higher stages through their discharge passages. Similarly, the second part is assumed to be proportional to the square of the total vapor/gas flow discharged from the higher stages, i.e.,

$$(W_{f,\,co})_{total} = (W_{f,\,co})_N + DD\left[\sum_{i=2}^{N}(W_{g,\,cu})_i\right] \qquad (3.5\text{-}40)$$

where DD is a constant to be fitted with data.

The carryunder and carryover are defined as

$$CU = \frac{(W_{g,\,cu})_{total}}{\text{Total downward liquid flow rate}}$$

$$CO = \frac{(W_{f,\,co})_{total}}{\text{Total upward vapor/gas flow rate}} \; . \qquad (3.5\text{-}41)$$

The parameters AA, BB, CC, and DD were tuned to fit the available test data[3.5-2,3.5-3,3.5-4] for two- and three-stage separators. **Table 3.5-1** summarizes the values for these parameters.

Table 3.5-1 Summary of fitted parameters in a mechanistic separator model.

Parameter	2-Stage Separator		3-Stage Separator		
	1st Stage	2nd Stage	1st Stage	2nd Stage	3rd Stage
AA	110.	20.	110.	20.	20.
BB	0.5	0.25	0.5	0.25	0.55

Table 3.5-1 Summary of fitted parameters in a mechanistic separator model. (Continued)

Parameter	2-Stage Separator		3-Stage Separator		
	1st Stage	2nd Stage	1st Stage	2nd Stage	3rd Stage
CC	0.0004	---	0.0004	---	---
DD	0.009	---	0.11	---	---

3.5.2.2.4 Chevron Dryer Model--The vapor/gas dryer uses chevron vanes to remove the moisture which is discharged from the vapor/gas separators. The vanes provide a curved path which the liquid droplets must follow if they are to flow through the dryer. If the interfacial force is too low, it cannot drag the liquid droplets along the curved path due to their inertial and they hit the vanes, are de-entrained, and the resultant liquid film flows down the vanes under the force of gravity into collecting trays and then back to the liquid pool surrounding the separators. If the vapor/gas velocity is high, it exerts a larger interfacial force on the droplets and more of the entrained liquid gets through the dryer vanes. Thus the dryer efficiency depends on the vapor/gas velocity and the moisture content of the vapor/gas flow entering the dryer. For a given vapor/gas inlet velocity, there is a critical dryer inlet moisture. Good moisture separation is achieved if the inlet moisture is lower than the critical value. If the inlet moisture is above the critical value, the dryer separating capacity is exceeded and the moisture can pass through the dryer.

The dryer capacity is simulated by a capacity factor GDRY which is defined in the following way. For a given vapor/gas velocity v at the inlet to the dryer, the critical dryer inlet moisture CDIM is calculated as

$$CDIM \ = \ 1 \qquad\qquad\qquad v < VDRY1$$

$$= \ 1 - \frac{v - VDRY1}{VDRY2 - VDRY1} \qquad VDRY1 < v < VDRY2 \qquad\qquad (3.5\text{-}42)$$

$$= \ 0 \qquad\qquad\qquad VDRY2 < v$$

where CDIM is the critical inlet moisture, VDRY1 is the vapor/gas velocity below which any amount of moisture is assumed to be separated from the vapor/gas stream, and VDRY2 is the vapor/gas velocity above which no amount of moisture, however small, can be separated from the vapor/gas stream.

The dryer inlet moisture (DIM) is computed assuming homogeneous flow as

$$DIM \ = \ 1 - \frac{\alpha_g}{\alpha_g + (1 - \alpha_g)\dfrac{\rho_f}{\rho_g}} \qquad\qquad\qquad (3.5\text{-}43)$$

where α_g, ρ_f, and ρ_g are the vapor/gas void fraction, liquid density, and the vapor/gas density in the dryer.

The capacity factor GDRY is defined as

$$GDRY \; = \; 1 \qquad\qquad DIM < CDIM$$

$$= \; 1 + \frac{CDIM - DIM}{DELDIM} \qquad CDIM < DIM < (CDIM + DELDIM) \qquad (3.5\text{-}44)$$

$$= \; 0 \qquad\qquad (CDIM + DELDIM) < DIM$$

where DELDIM is the range of inlet moisture over which the dryer capacity goes from one to zero for a fixed vapor/gas inlet velocity. These relations are shown schematically in **Figure 3.5-6**.
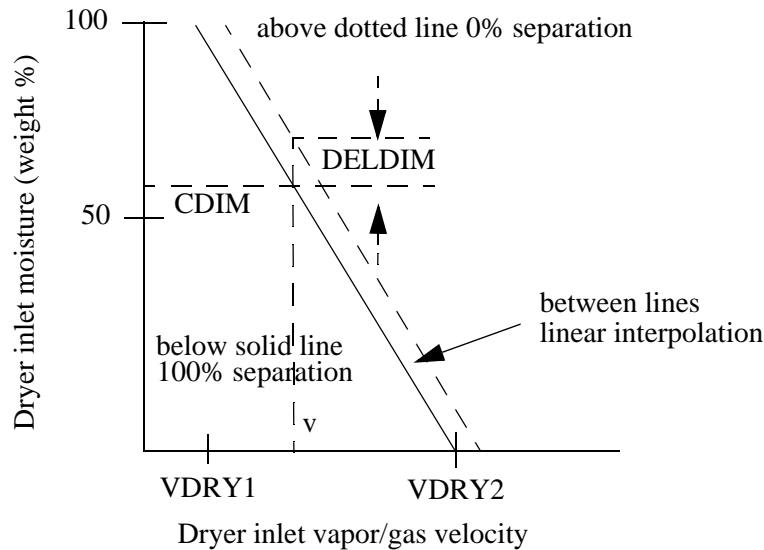
Figure 3.5-6 Dryer capacity.

The capacity factor GDRY is used to modify the void fraction in the dryer outlet junction such that if the dryer capacity is one, the donored void fraction is one; if the dryer capacity is zero, the regular donor void fraction is used, and if the dryer capacity is between zero and one, the void fraction is interpolated between the values for the capacities of zero and one.

3.5.3 Jet Mixer

There are several components in a typical reactor plant where the momentum effects due to the mixing of two parallel streams of fluid at different velocities may be important. An example of this is the

jet pump in a BWR. In this component, the pumping action is caused by the momentum transfer between the two fluid streams. Momentum effects may also be important for the aspirators present in some vapor/gas generators. The JETMIXER component was developed for these cases. Momentum effects may also be important for mixing at ECC injection points, and the ECCMIX component (Section 3.5.8) was developed for this case.

3.5.3.1 Basic Jet Mixing Model. The basic approach for modeling the jet mixing process is to superimpose a quasi-steady model for the mixing process on the normal volume-junction flow path representation used in ATHENA. To derive the momentum equations needed to model a jet mixing situation, consider the schematic shown in **Figure 3.5-7**, which illustrates a mixing volume connected to a drive and a suction volume.[a] The suction junction (with velocity vS and area AS) connects the last upstream suction region volume, KS, to the mixing volume, L. The drive junction (with velocity vD and area AD) connects the last upstream drive line volume, KD, to the mixing volume, L. **Figure 3.5-7** shows
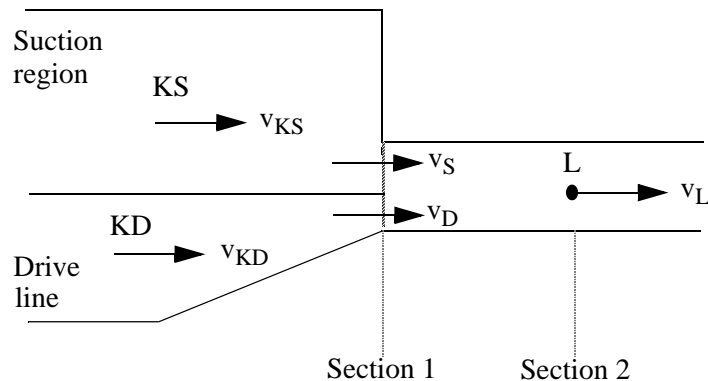
Figure 3.5-7 Schematic of mixing junctions.

the drive junction as a smooth junction and the suction junction as abrupt. The user can model either junction either way if the appropriate loss factors are included (see input guidelines in Volume II of this manual). Volume fractions and densities subscripted by a D or S are donored values; a subscript a indicates an average value.

The mixing of the drive and suction flows between cross-section 1 and 2 requires a reevaluation of the momentum flux terms. The wall drag, interphase drag, temporal acceleration, momentum exchange due to mass transfer, and gravity head terms for the drive and suction junctions are treated exactly as they are at any other junction. Only the pressure and momentum flux terms will be examined in the following momentum equation development.

---

a. The drive and suction junctions should be the high-speed and low-speed junctions respectively when the JETMIXER component is used for other than jet pump applications.

Consider a control volume in the mixing region between cross-sections 1 and 2 and assume the following: (a) steady single-phase flow; (b) one-dimensional flow at cross-sections 1 and 2; (c) equal pressures at junctions D and S; and (d) constant area in the mixing region. If we apply the conservation of momentum principle for this control volume with these assumptions, the momentum equation becomes

$$(P_L - P_1)A_L + \rho_L v_L^2 A_L - \rho_S v_S^2 A_S - \rho_D v_D^2 A_D = 0 \quad .$$
(3.5-45)

Conservation of mass applied with these same assumptions gives

$$\rho_L v_L A_L - \rho_S v_S A_S - \rho_D v_D A_D = 0 \quad .$$
(3.5-46)

Equation (3.5-46) can be used to write Equation (3.5-45) in an expanded form, obtaining

$$P_L - P_1 + \frac{\rho_S v_S A_S (v_L - v_S)}{A_L} + \frac{\rho_D v_D A_D (v_L - v_D)}{A_L} = 0 \quad .$$
(3.5-47)

Equation (3.5-47) gives the momentum equation (pressure and flux terms) for the upstream half of the mixing volume. To develop the momentum equation for the suction junction, a normal ATHENA half-cell momentum equation is written from KS to cross-section 1, i.e.,

$$P_1 - P_{KS} + \frac{1}{2}\rho_{KS}(v_S^2 - v_{KS}^2) = 0 \quad .$$
(3.5-48)

Adding this to the half cell momentum Equation (3.5-47) for cross-sections 1 to L (Section 2) gives

$$P_L - P_{KS} + \frac{1}{2}\rho_{KS}(v_S^2 - v_{KS}^2) + \frac{\rho_S v_S A_S (v_L - v_S)}{A_L} + \frac{\rho_D v_D A_D (v_L - v_D)}{A_L} = 0 \quad .$$
(3.5-49)

This equation shows how the pressure and momentum flux terms should be calculated for the suction junction equation.

If the suction junction were a normal junction, its momentum equation (pressure and flux terms) would be

$$P_L - P_{KS} + \frac{1}{2}\rho_S(v_L^2 - v_{KS}^2) = 0 \quad .$$
(3.5-50)

The velocity terms in Equation (3.5-50) must be replaced by the velocity terms in Equation (3.5-49) to correctly model the momentum equation at the suction junction. Similar equations for the drive junction can be obtained.

3.5.3.2 *Jet Mixing in Two-Phase Flows.* If a derivation similar to the previous section is carried out for the pressure and momentum flux terms in the two-phase case, the following equations are obtained for the liquid phase in the mixing region:

Conservation of momentum (from cross-section 1 to L),

$$\alpha_{fL}A_L(P_L - P_1) + \alpha_{fL}\rho_{fL}v_{fL}^2 A_L - \alpha_{fS}\rho_{fS}v_{fS}^2 A_S - \alpha_{fD}\rho_{fD}v_{fD}^2 A_D = 0 \quad . \tag{3.5-51}$$

Conservation of mass (from cross-section 1 to L),

$$\alpha_{fL}\rho_L v_{fL}A_L - \alpha_{fS}\rho_{fS}v_{fS}A_{fS} - \alpha_{fD}\rho_{fD}v_{fD}A_D = 0 \quad . \tag{3.5-52}$$

Using Equation (3.5-52) in Equation (3.5-51) and rewriting Equation (3.5-45) in expanded form yields

$$\alpha_{fL}(P_L - P_1) + \frac{\alpha_{fS}\rho_{fS}v_{fS}A_S(v_{fL} - v_{fs})}{A_L} + \frac{\alpha_{fD}\rho_{fD}v_{fD}A_D(v_{fL} - v_{fD})}{A_L} \quad . \tag{3.5–53}$$

Equation (3.5-53) can now be combined with the appropriate half-cell momentum equation for the upstream volume to obtain the final momentum equation for the liquid flow at the suction junction. A parallel development gives the vapor/gas phase momentum equation at the suction junction.

The momentum equations used consist of the sum of the phasic momentum equations and the difference of the phasic momentum equations. To derive the sum momentum equation (pressure and flux terms only) for the suction junction, Equation (3.5-53) for the liquid phase is added to a similar equation for the vapor/gas phase to obtain

$$P_L - P_1 + \frac{\alpha_{fS}\rho_{fS}v_{fS}A_S(v_{fL} - v_{fS})}{A_L} + \frac{\alpha_{fD}\rho_{fD}v_{fD}A_D(v_{fL} - v_{fD})}{A_L}$$
$$+ \frac{\alpha_{gS}\rho_{gS}v_{gS}A_S(v_{gL} - v_{gS})}{A_L} + \frac{\alpha_{gD}\rho_{gD}v_{gD}A_D(v_{gL} - v_{gD})}{A_L} = 0 \quad . \tag{3.5-54}$$

The normal half-cell sum momentum equation (pressure and flux terms only) for the upstream suction volume can then be added to Equation (3.5-54) to give

$$P_L - P_{KS} + \frac{\alpha_{fS}\rho_{fS}v_{fS}A_S(v_{fL} - v_{fS})}{A_L} + \frac{\alpha_{fD}\rho_{fD}v_{fD}A_D(v_{fL} - v_{fD})}{A_L}$$

$$+ \frac{\alpha_{gS}\rho_{gS}v_{gS}A_S(v_{gL} - v_{gS})}{A_L} + \frac{\alpha_{gD}\rho_{gD}v_{gD}A_D(v_{gL} - v_{gD})}{A_L} \qquad (3.5\text{-}55)$$

$$+ \frac{1}{2}\alpha_{fKS}\rho_{fKS}(v_{fS}^2 - v_{fKS}^2) + \frac{1}{2}\alpha_{gKS}\rho_{gKS}(v_{gS}^2 - v_{gKS}^2) = 0$$

as the final form for the pressure and momentum flux terms in the new sum momentum equation for the suction junction. The pressure term in this equation has exactly the same form as the pressure term in the normal sum momentum equation. A parallel equation holds for the drive junction. Hence, at the drive and suction mixing junctions, the normal momentum flux terms in the sum momentum equation must be replaced by those in Equation (3.5-55).

The difference momentum equation for the suction junction is derived by dividing the liquid momentum mixing Equation (3.5-53) by α_{fL} and adding it to the half-cell liquid momentum equation for the upstream suction volume (also divided by the appropriate volume fraction, α_{fKS}) to obtain

$$P_L - P_{KS} + \frac{\alpha_{fS}\rho_{fS}v_{fS}A_S(v_{fL} - v_{fS})}{\alpha_{fL}A_L} + \frac{\alpha_{fD}\rho_{fD}v_{fD}A_D(v_{fL} - v_{fD})}{\alpha_{fL}A_L}$$

$$+ \frac{1}{2}\frac{\alpha_{fKS}\rho_{fKS}}{\alpha_{fKS}}(v_{fS}^2 - v_{fKS}^2) = 0 \ . \qquad (3.5\text{-}56)$$

Next, Equation (3.5-56) is divided by the average junction liquid density, ρ_{fa}, and subtracted from the corresponding vapor/gas equation to obtain

$$\left(\frac{\rho_f - \rho_g}{\rho_f\rho_g}\right)_a (P_L - P_{KS}) + \frac{\alpha_{gS}\rho_{gS}v_{gS}A_S(v_{gL} - v_{gS})}{\alpha_{gL}\rho_{ga}A_L}$$

$$+ \frac{\alpha_{gD}\rho_{gD}v_{gD}A_D(v_{gL} - v_{gD})}{\alpha_{gL}\rho_{ga}A_L} + \frac{1}{2}\frac{\alpha_{gKS}\rho_{gKS}(v_{gS}^2 - v_{gKS}^2)}{\alpha_{gKS}\rho_{ga}}$$

$$- \frac{\alpha_{fS}\rho_{fS}v_{fS}A_S(v_{fL} - v_{fS})}{\alpha_{fL}\rho_{fa}A_L} - \frac{\alpha_{fD}\rho_{fD}v_{fD}A_D(v_{fL} - v_{fD})}{\alpha_{fL}\rho_{fa}A_L} \qquad (3.5\text{-}57)$$

$$- \frac{1}{2}\frac{\alpha_{fKS}\rho_{fKS}(v_{fS}^2 - v_{fKS}^2)}{\alpha_{fKS}\rho_{fa}} = 0$$

as the final difference momentum equation to be used at junction S. A parallel equation must be used at the drive junction. The pressure term in Equation (3.5-57) has exactly the same form as the pressure term in the normal difference momentum equation. Hence, at the drive and suction mixing junctions the normal

momentum flux terms in the difference momentum equation must be replaced by those in Equation (3.5-57).

Mathematically the α_{gKS} terms in the fourth term of Equation (3.5-57) cancel and the α_{fKS} terms in the seventh term of Equation (3.5-57) cancel. In a physical system, the velocity of the non-existent phase would be zero, contributing no momentum to the momentum balance. The ATHENA model of the non-existent phase, however, sets the phasic velocity to that of the existing phase. Hence the non-existent phase would contribute some erroneous momentum to the momentum balance if the α_{fKS} or α_{gKS} terms cancel. To fix this problem, the correct single phase limits are preserved in the coding by replacing the α_{gKS} in the denominator of the fourth term of Equation (3.5-57) by $\max(\alpha_{gKS},10^{-7})$ and by replacing the α_{fKS} in the denominator of the seventh term of Equation (3.5-57) by $\max(\alpha_{fKS},10^{-7})$.

The correct single phase limit is also protected in the second and third terms of Equation (3.5-57) by replacing the α_{gL} in the denominator by $\max(\alpha_{gL},10^{-7})$ and in the fifth and sixth terms of Equation (3.5-57) by replacing the α_{fL} in the denominator by $\max(\alpha_{fL},10^{-7})$.

3.5.3.3 Associated Flow Losses. The flow in the *mixing* region of volume L can in reality be either a true jet mixing or a flow split (for reverse flow). The flow split case is governed by different physics than the jet-mixing case considered in the previous discussions. The redistribution that occurs when the flow splits is primarily determined by the effective resistances downstream of the separation point in the suction and drive flow paths. The mixing terms derived above do not apply. For this reason, the additional mixing terms are applied only for the positive-drive flow regimes. The normal momentum flux calculations are used for the negative-drive flow regimes.

The junctions associated with the JETMIXER component can be modeled as smooth or abrupt. If the junctions are input as smooth, then the appropriate flow resistances should be calculated in a standard fashion and input as form loss coefficients at the appropriate junctions by the user.

If the junctions in the JETMIXER component are input as abrupt area changes, then the code will calculate form loss coefficients as usual except that (a) the forward loss coefficients at the drive and suction junctions are set to zero and (b) the reverse loss coefficients for the suction and drive junctions are those associated with the expansions from the junction areas to the suction or drive volume areas. The forward losses at these junctions are actually associated with the expansion from the vena-contracta to the downstream mixing volume flow area. For parallel mixing streams, this loss is no longer appropriate. The losses associated with any contraction from the mixing volume to the suction or drive junctions are neglected for the same reason.

If the above normal flow losses are used when the suction flow reverses, it will be found that jet pump performance (head ratio) in this regime is significantly below the experimental data. The reverse flow loss coefficient applied in the suction junction has a significant effect on the jet pump performance in this flow situation. This loss coefficient (in addition to the normal loss coefficient associated with the

expansion from A_S to area A_{KS}) represents all the irreversible losses associated with the turning and expansion of the flow from the drive junction. Because this flow regime is an important regime in the accident analysis of a BWR, it was decided to include an approximation for this flow-dependent loss in the jet mixing model.

This reverse suction flow loss was based upon the expansion losses experienced by the flow as it moves from the drive to the suction junction. Two flow situations with reversed suction flow and positive drive flow are possible, depending upon the flow direction in the mixing section (**Figure 3.5-8**). In the first situation, the expansion loss associated with the area change A_D to A_S, i.e.,

Regime 1   Regime 2
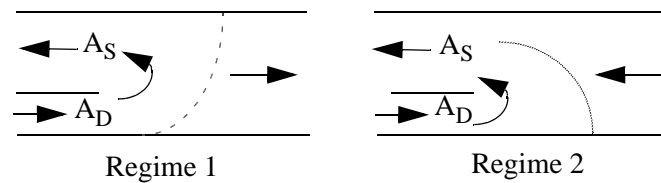
Figure 3.5-8 Flow regimes and dividing streamline.

$$K = \left(\frac{A_S}{A_D} - 1\right)^2 \tag{3.5-58}$$

is added to the user-specified reverse loss coefficient (or the standard abrupt area change loss factor if the junction is input as abrupt) for the suction junction. In the second situation, the effective area for the suction flow that comes from the drive junction is less than A_S because the discharge flow is reversed. In this situation, the effective areas for the expansion loss are A_D and $A_S\left|\frac{W_D}{W_S}\right|$. Hence, for the second situation, the loss coefficient given by

$$K = \left(\frac{A_S\left|\frac{W_D}{W_S}\right|}{A_D} - 1\right)^2 \tag{3.5-59}$$

is added to the user-specified reverse loss coefficient (or the abrupt area loss factor if the junction is input as abrupt) at the suction junction only if $A_S\left|\frac{W_D}{W_S}\right|$ is $> A_D$. If $A_S\left|\frac{W_D}{W_S}\right|$ is $< A_D$, the drive-to-suction flow is effectively a contraction, and the additional loss coefficient is set to zero.

Since the jet mixing and effective resistances are modeled by special terms in the suction and drive junction momentum equations, the normal losses associated with the partitioning of volume L are not included in these junction equations. However, the normal losses associated with the area ratios experienced by the flow upstream of the suction and drive junctions are retained in the junction momentum equations.

3.5.3.4 Numerical Implementation. The basic numerical algorithm used to evaluate the new momentum flux terms in Equations (3.5-55) and (3.5-57) is similar to the numerical evaluation of the normal momentum flux terms. The normal momentum flux terms are calculated explicitly at the n-th time level. The new momentum flux terms in Equations (3.5-55) and (3.5-57) are also explicitly evaluated, and the spatial location of each variable is indicated by its subscript.

3.5.4 Pump

The ATHENA pump model is almost identical to the RELAP5/MOD1 pump model,[3.5-5] which was originally adapted from the RELAP4 pump model.[3.5-6] The pump model was originally developed by Farman and Anderson[3.5-7] for the RELAP3 code, and then it became the accepted methodology in the RELAP4 and RELAP5 codes. The only significant difference is that in ATHENA, there is the added capability of linking the pump to a shaft component. The pump can be linked to a shaft component, and thus can be driven by either a motor or a turbine. The RELAP5/MOD1 options for a motor-driven pump were retained so that input changes to an existing plant model using the pump are not required unless it is desired to make use of the shaft coupling.

The basic approach to pump modeling is to superimpose a quasi-static model for pump performance on the ATHENA volume-junction flow path representation. The pump is a volume-oriented component, and the head developed by the pump is apportioned equally between the suction and discharge junctions that connect the pump volume to the system. The pump model is interfaced with the two-fluid hydrodynamic model by assuming the head developed by the pump is similar to a body force. Thus, the head term appears in the mixture momentum equation; but, like the gravity body force, it does not appear in the difference momentum equation used in ATHENA. The term that is added to the mixture momentum equation is $(1/2)\rho_m gH$, where H is the total head rise of the pump (m), ρ_m is the volume fluid density (kg/m^3), and g is the acceleration due to gravity (m/s^2). The factor 1/2 is needed because the term is applied at both the suction and discharge junctions.

In both the semi-implicit and nearly-implicit numerical schemes, the pump head is coupled implicitly to the velocities through its dependence on the volumetric flow rate, Q. The volumetric flow rate is defined as the volume mass flow rate divided by the volume density. It is assumed that the head depends on the volumetric flow rate, and can be approximated by a two-term Taylor series expansion given by

$$H^{n+1} = H^n + \left(\frac{dH}{dQ}\right)^n (Q^{n+1} - Q^n) \quad . \tag{3.5-60}$$

Thus, the numerical equivalent of the term $\rho g H$ in both schemes is

$$\frac{1}{2}\rho_m^n g H^n \Delta t + \frac{1}{2}\rho_m^n g\left(\frac{dH}{dQ}\right)^n (Q^{n+1} - Q^n)\Delta t \quad . \tag{3.5-61}$$

This term is added to the right side of the mixture momentum Equation (3.1-104). For the semi-implicit scheme, only one of the junction velocities is made implicit (the junction for which the new time velocity is calculated). For the nearly-implicit scheme, both junction velocities are made implicit simultaneously.

The pump energy dissipation is calculated for the pump volume as

$$\text{DISS} = \tau^n \omega^n - g H^n (\alpha_f^n \rho_f^n \bar{v}_f^n + \alpha_g^n \rho_g^n \bar{v}_g^n)A \tag{3.5-62}$$

where τ is the pump torque and ω is the pump angular rotation speed. This can be viewed as follows; the total pump power added to the fluid by the pump ($\tau\omega$) is separated into a hydraulic term $g H[(\alpha_f \rho_f v_f + \alpha_g \rho_g v_g)A]$ and a dissipation term (DISS). The dissipation term arises from turbulence in the pump and is added to the pump volume as heat. In a closed system, the hydraulic head from the pump is balanced by the sum of wall friction losses and form losses in the momentum equation. These losses should also appear as energy source terms in the energy equation, but only the wall friction terms are implemented in the default code. The default code should also add the form loss (code calculated abrupt area change loss and user-supplied loss) dissipation to the energy equation. This dissipation was removed in RELAP5/MOD2 because of temperature problems (i.e., overheating), and thus it is not present in ATHENA. The dissipation can be activated by the user in the input deck, however the user is cautioned that temperature problems may occur.

This term is evaluated explicitly in both the semi-implicit and nearly-implicit schemes, and it is partitioned between the liquid and vapor thermal energy equations in such a way that the rise in temperature due to dissipation is equal in each phase. (The details of the dissipation mechanism in a two-phase system are unknown, so the assumption is made that the mechanism acts in such a way that thermal equilibrium between the phases is maintained without phase change.) Thus, the terms that are added to the right sides of the liquid and vapor/gas thermal energy equations, Equations (3.1-91) and (3.1-92), for the pump volumes are

$$\text{DISS}_f = [\tau^n \omega^n - g H^n (\alpha_f^n \rho_f^n \bar{v}_f^n + \alpha_g^n \rho_g^n \bar{v}_g^n)A]\Delta t \left(\frac{\alpha_f^n \rho_f^n C_{pf}^n}{\alpha_f^n \rho_f^n C_{pf}^n + \alpha_g^n \rho_g^n C_{pg}^n}\right) \tag{3.5-63}$$

and

$$\text{DISS}_g = [\tau^n \omega^n - gH^n(\alpha_f^n \rho_f^n \bar{v}_f^n + \alpha_g^n \rho_g^n \bar{v}_g^n)A]\Delta t \left(\frac{\alpha_g^n \rho_g^n C_{pg}^n}{\alpha_f^n \rho_f^n C_{pf}^n + \alpha_g^n \rho_g^n C_{pg}^n} \right) \tag{3.5-64}$$

respectively.

The pump head, H, and torque, τ, are defined by means of an empirical homologous pump performance model, and the pump speed, ω, is defined by a pump drive model. The derivative of the pump head with respect to the volumetric flow rate, $\frac{dH}{dQ}$, is obtained from the empirical steady-state homologous pump performance model, using the assumption that the pump speed is constant.

3.5.4.1 *Centrifugal Pump Performance Model.*
The basic pump performance data must be generated experimentally. Analytical programs have been developed that are reasonably successful in predicting near-design pump performance for single-phase fluids. However, for off-design operation or for operation with a two-phase fluid, the problems of analytical pump performance prediction are nearly insurmountable. The basic parameters that characterize the pump performance are the rotational speed, ω, the volumetric flow, Q, the head rise, H, and the shaft torque, τ. The relationship between these four parameters can be uniquely displayed by a four-quadrant representation of such data. A typical four-quadrant curve is shown in **Figure 3.5-9**. Both positive and negative values for each of the four parameters are represented. The disadvantages in using such a data map for numerical purposes are the need for two-dimensional interpolation, the large number of points needed to define the entire range, and the fact that the map is infinite in extent. These objections can be largely overcome by use of a homologous transformation based on the centrifugal pump similarity relationships. Such a transformation collapses the four-quadrant data onto a single, bounded, dimensionless curve having eight octants. Typical homologous curves for the head and torque are illustrated in **Figure 3.5-10** and **Figure 3.5-11**, respectively, where ω_R, Q_R, H_R, and τ_R are the rated values for the pump speed, volumetric flow rate, head, and torque, respectively. Details on generating the homologous curves are presented in Volumes II and IV. The homologous transformation is not unique, and not all points of **Figure 3.5-9** lie on the curves of **Figure 3.5-10** and **Figure 3.5-11**. However, the data are closely grouped, and the single curve is a good approximation for pump performance. The pump model allows the user the option of accounting for two-phase degradation effects on pump performance.

The two-phase degradation model is based on experimental data. Available pump data from the 1-1/2 Loop Model Semiscale and Westinghouse Canada Limited (WCL) experiments were used in developing the two-phase pump model. The single-phase pump head (dimensionless) curves for the Semiscale pump are shown in **Figure 3.5-12**, and the fully degraded two-phase pump head curves for the Semiscale pump are shown in **Figure 3.5-13**. These represent complete pump characteristics (except for the reverse pump fully degraded region) for the Semiscale pump operating under two-phase conditions, with the average of the void fractions of the pump inlet and outlet mixtures between 0.2 and 0.9. The lines drawn through the data were determined by least-squares polynomial fits to the data using known constraints.
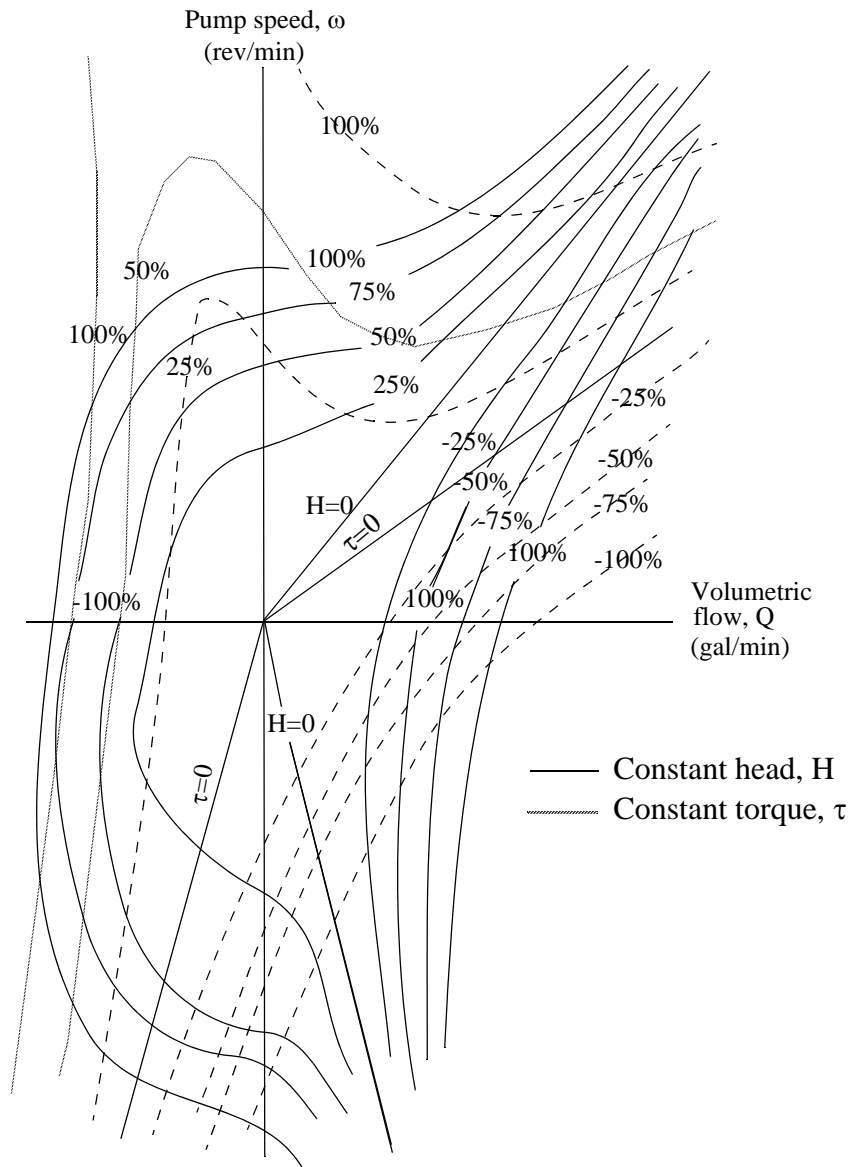
Figure 3.5-9 Typical pump characteristic four-quadrant curves.

A comparison of the two-phase data in **Figure 3.5-13** with the single-phase data in **Figure 3.5-12** shows that the two-phase dimensionless head ratio (h/v^2 or h/α^2) is significantly less than the single-phase dimensionless head ratio for the normal pump operation region (HAN and HVN). For negative ratios of v/α, such as those that occur in the HAD region, the pump flow becomes negative. When the pump flow is negative, the two-phase dimensionless head ratio is greater than the single-phase dimensionless head ratio. Two-phase flow friction losses are generally greater than single-phase losses, and friction is controlling in
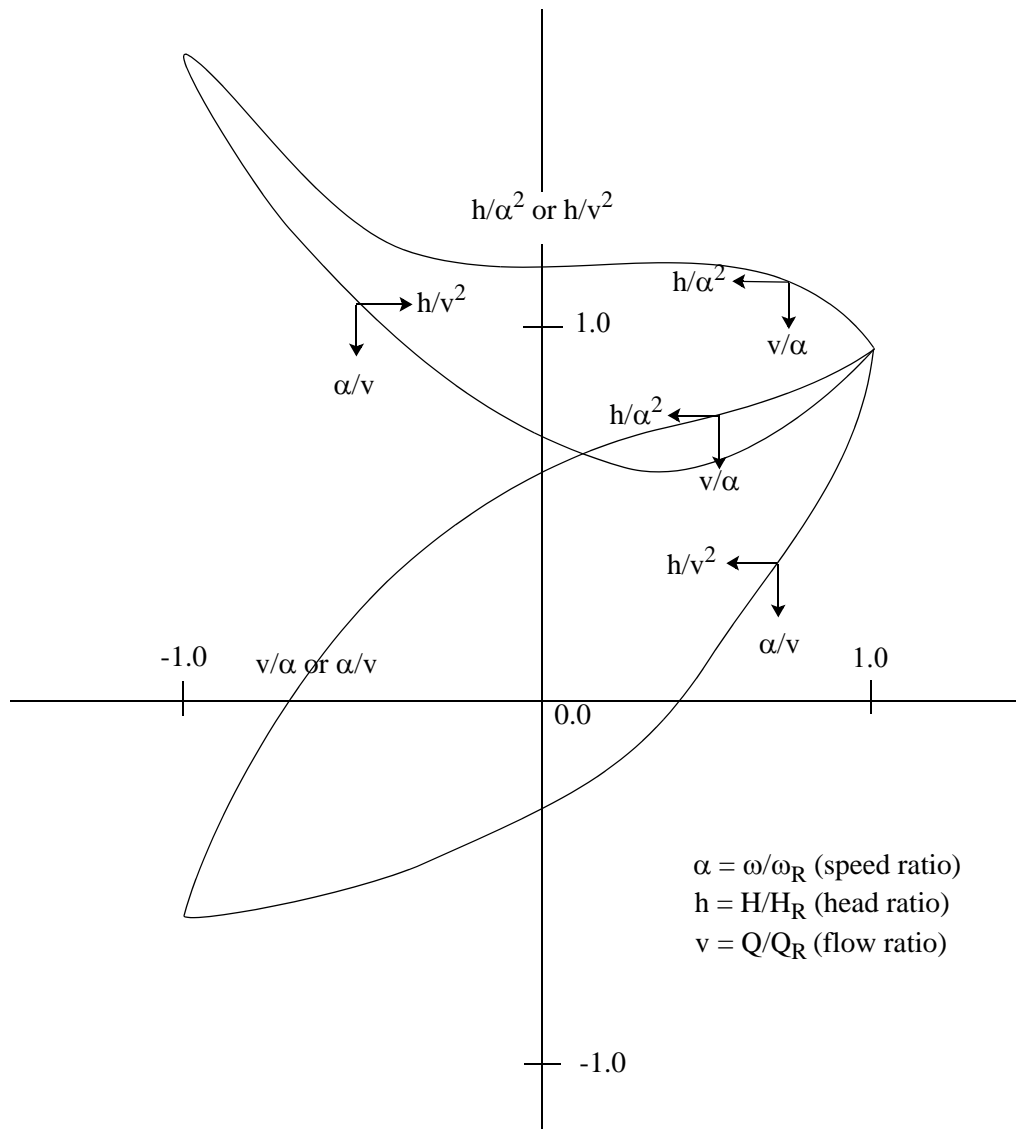
Figure 3.5-10 Typical pump homologous head curves.

this energy dissipation region (HAD). The other regions of two-phase dimensionless head ratio data show similar deviations from single-phase data, with the exception of regions HAR and HVR (show no deviations).

    Table 3.5-2 presents the difference between the single- and two-phase dimensionless head ratio data as a function of v/α and α/v for the various pumping regions shown in **Figure 3.5-12** and **Figure 3.5-13** where
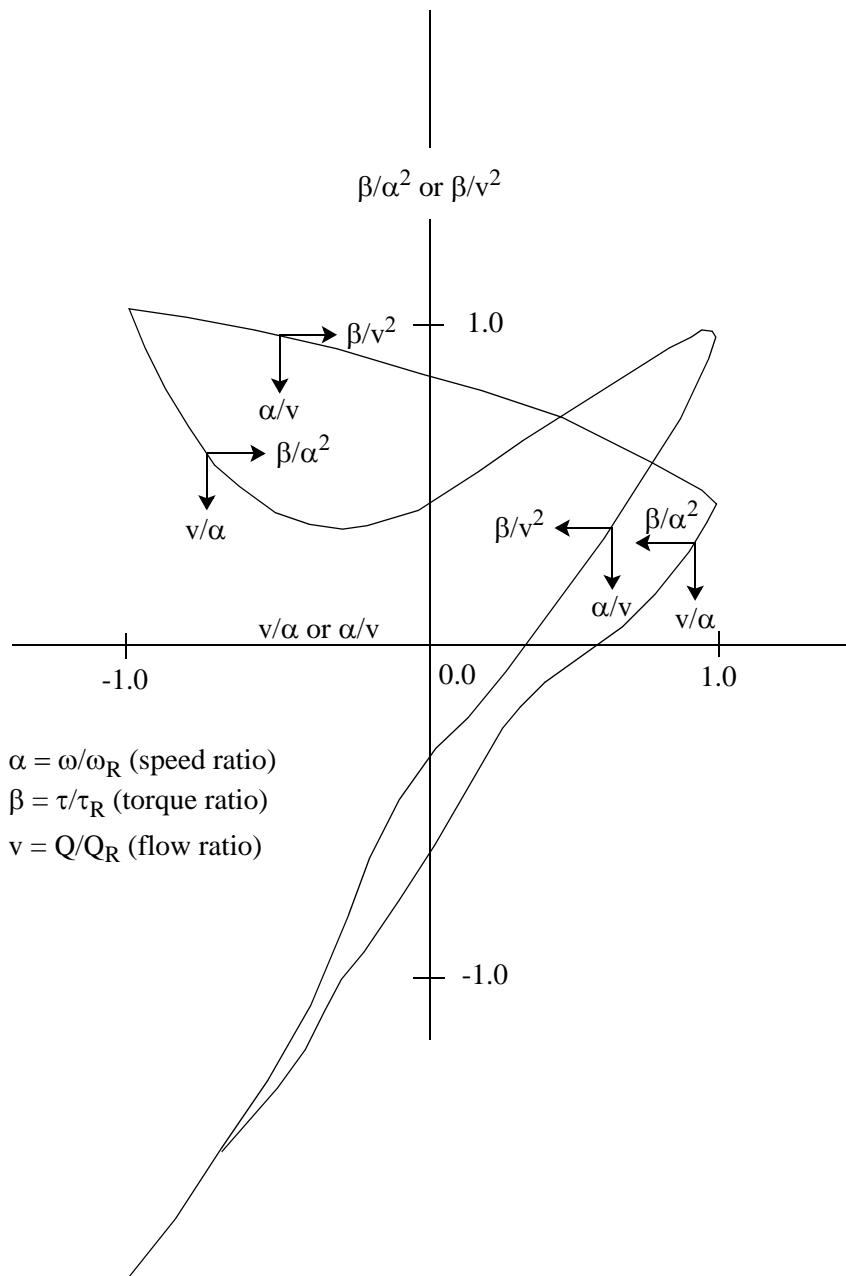
Figure 3.5-11 Typical pump homologous torque curves.

$$x = \frac{v}{\alpha} \text{ or } \frac{\alpha}{v}$$

$$y = \left(\left.\frac{h}{\alpha^2}\right|_{1\phi} - \left.\frac{h}{\alpha^2}\right|_{2\phi}\right) \text{ or } \left(\left.\frac{h}{v^2}\right|_{1\phi} - \left.\frac{h}{v^2}\right|_{2\phi}\right)$$

(3.5-65)

Normal pump $\quad (+ Q, + \omega)$ {HAN HVN

Energy dissipation $(- Q, + \omega)$ {HAD HVD

Normal turbine $\quad (- Q, - \omega)$ {HAT HVT

Reverse pump $\quad (+ Q, - \omega)$ {HAR HVR

Figure 3.5-12 Single-phase homologous head curves for 1-1/2 loop MOD1 Semiscale pumps.

The differences shown in **Table 3.5-2** are for the eight curve types used for determining pump head.
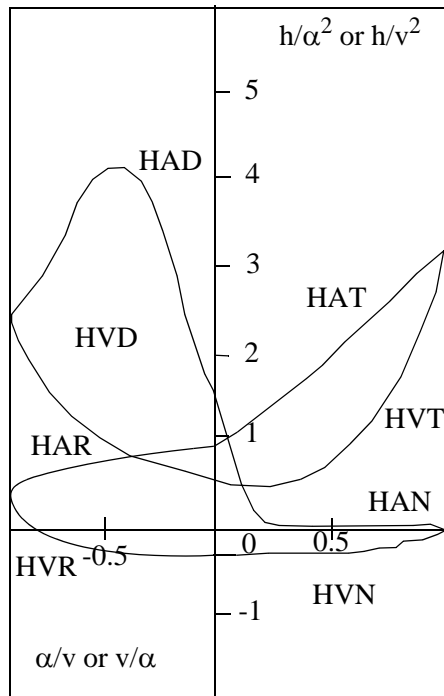
Figure 3.5-13 Fully degraded, two-phase homologous head curves for 1-1/2 loop MOD1 Semiscale pumps.

Table 3.5-2 Semiscale dimensionless head ratio difference data (single-phase minus two-phase).

Curve type	x	y	Curve type	x	y
1 (HAN)	0.00	0.00	4 (HVD)	-1.00	-1.16
	0.10	0.83		-0.90	-0.78
	0.20	1.09		-0.80	-0.50
	0.50	1.02		-0.70	-0.31
	0.70	1.01		-0.60	-0.17
	0.90	0.94		-0.50	-0.08
	1.00	1.00		-0.35	0.00
				-0.20	0.05
2 (HVN)	0.00	0.00		-0.10	0.08
	0.10	-0.04		0.00	0.11

Table 3.5-2 Semiscale dimensionless head ratio difference data (single-phase minus two-phase).

Curve type	x	y	Curve type	x	y
	0.20	0.00			
	0.30	0.10	5 (HAT)	0.00	0.00
	0.40	0.21		0.20	-0.34
	0.80	0.67		0.40	-0.65
	0.90	0.80		0.60	-0.93
	1.00	1.00		0.80	-1.19
				1.00	-1.47
3 (HAD)	-1.00	-1.16			
	-0.90	-1.24	6 (HVT)	0.00	0.11
	-0.80	-1.77		0.10	0.13
	-0.70	-2.36		0.25	0.15
	-0.60	-2.79		0.40	0.13
	-0.50	-2.91		0.50	0.07
	-0.40	-2.67		0.60	-0.04
	-0.25	-1.69		0.70	-0.23
	-0.10	-0.50		0.80	-0.51
	0.00	0.00		0.90	-0.91
				1.00	-1.47
			7 (HAR)	-1.00	0.00
				0.00	0.00
			8 (HVR)	-1.00	0.00
				0.00	0.00

The head multiplier, $M_H(\alpha_g)$, and void fraction data shown in **Table 3.5-3** were obtained in the following manner. The Semiscale and WCL pump data[3.5-6] were converted to dimensionless head ratios of h/α^2 or h/v^2. Values of the dimensionless head ratios were obtained for pump speeds and volumetric flow rates within 50% of the rated speed and flow rate for the pumps. The difference between the single- and two-phase dimensionless ratios was developed as a function of the average void fractions for the pump

inlet and outlet mixtures. The difference between the single- and two-phase dimensionless ratios was then normalized to a value between 0 and 1.0. The normalized result was tabulated as a function of the void fraction.

Table 3.5-3 Head multiplier and void fraction data.

α_g	$M_H(\alpha_g)$
0.000	0.00
0.070	0.00
0.080	0.74
0.165	1.00
0.900	1.00
1.000	0.00

If the two-phase option is selected, the pump head and torque are calculated from

$$H = H_{1\phi} - M_H(\alpha_g) (H_{1\phi} - H_{2\phi}) \tag{3.5-66}$$

$$\tau = \tau_{1\phi} - M_\tau(\alpha_g) (\tau_{1\phi} - \tau_{2\phi}) \tag{3.5-67}$$

where

    1ϕ =   single-phase value

    2ϕ =   two-phase, fully degraded value, $0.2 < \alpha_g < 0.9$

    M   =   multiplier on difference curve as a function of α_g.

Assumptions inherent in the pump model for two-phase flow include

- The head multiplier, $M_H(\alpha_g)$, determined empirically for the normal operating region of the pump, is also valid as an interpolating factor in all other operating regions.

- The relationship of the two-phase to the single-phase behavior of the Semiscale pump is applicable to large reactor pumps. This assumes that the pump model of two-phase flow is independent of pump specific speed.

3.5.4.2 Centrifugal Pump Drive Model. The pump torque is used to calculate the pump speed (ω) after the pump has been shut off by the input trip signal. The speed is calculated by the deceleration equation

$$I\frac{d\omega}{dt} = \tau \quad .$$

(3.5-68)

The finite difference approximation of this equation is

$$\omega_{t+\Delta t} = \omega_t + \frac{\tau\Delta t}{I}$$

(3.5-69)

where

τ = net torque

I = moment of inertia

t = time

Δt = time step

ω = angular velocity (pump speed).

The rate of energy addition to the pump system is given by $\tau\omega$ and has been used in Equation (3.5-62) to calculate the pump dissipation.

The total pump torque is calculated by considering the hydraulic torque from the homologous curves and the pump frictional torque. The net torque with the drive motor shut off is

$$\tau = \tau_{hy} + \tau_{fr}$$

(3.5-70)

where

τ_{hy} = hydraulic torque

τ_{fr} = frictional torque.

The hydraulic torque is calculated from the homologous curves by

$$\tau_{hy} = \tau_{ho}\left(\frac{\rho_m}{\rho_R}\right) \tag{3.5-71}$$

where τ_{ho} is the dimensional homologous curve torque, ρ_m is the fluid mixture density, and ρ_R is the rated fluid density.

The frictional torque is in the form of a constant or in the form of a four-term equation that depends on the speed ratio as described in the input manual (Volume II, Appendix A). The value of the frictional torque is also dependent on the sign of the pump speed. An option is available to specify whether reverse rotation of the pump is allowed.

The pump moment of inertia is in the form of a constant or in the form of a cubic equation that depends on the speed ratio as described in the input manual (Volume II, Appendix A).

The electric drive motor will affect the speed behavior of the pump while the motor remains connected to its power source. The net torque with the drive motor on is incorporated into the pump model by adding the value of motor torque, τ_m, to the torque summation

$$\tau = \tau_{hy} + \tau_{fr} - \tau_m \tag{3.5-72}$$

where the sign of the motor torque is the same as that of the hydraulic and frictional torque for steady operating conditions, that is, zero net torque.

Induction motors are used to drive primary coolant pumps. At constant voltage, the motor torque is an explicit function of speed. This torque/speed relationship is normally available from the motor manufacturer.

Motor torque is supplied to the pump model as a tabular function of torque versus speed as given by the manufacturer's data. A typical torque/speed curve for an induction motor is shown in **Figure 3.5-14**.

The capability to simulate a locked-rotor condition of the pump is included in ATHENA. This option provides for simulation of the pump rotor lockup as a function of input elapsed time, maximum forward speed, or maximum reverse speed. At the time the rotor locks (and at all times thereafter), the pump speed is set equal to zero.

3.5.5 Turbine

A turbine is a device that converts energy contained in high-pressure fluid to mechanical work. The complicated configuration of a turbine precludes a complete first-principles model, at least for the purpose of system transient calculations. A lumped-parameter turbine model is used in ATHENA wherein a sequence of turbine stages (henceforth referred to as a stage group) is treated as a single-junction and
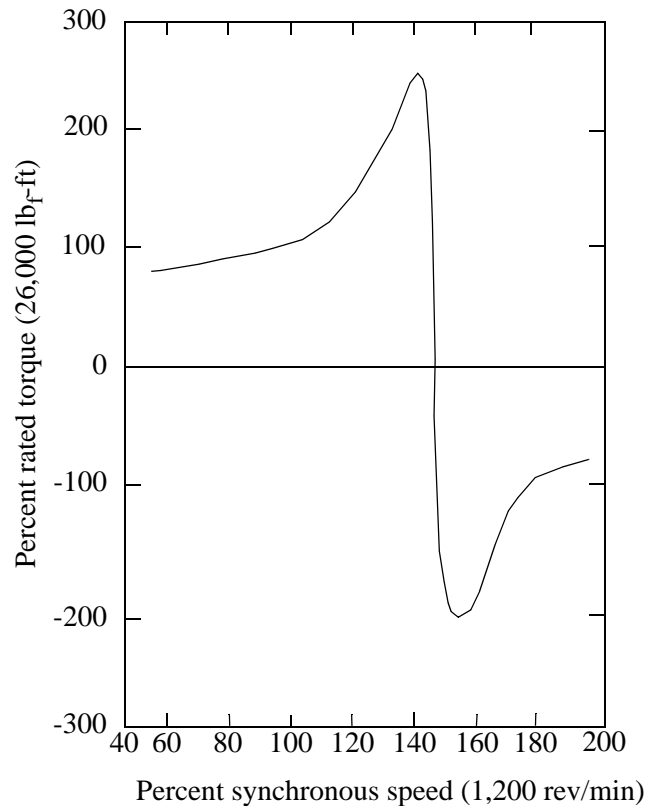
Figure 3.5-14 Torque versus speed, Type 93A pump motor (rated voltage).

single-volume. The stage group is then represented using modified energy, continuity, and momentum equations. An efficiency factor based upon simple momentum and energy considerations is used to represent the nonideal internal processes.

A turbine can be modeled using a single-stage group, i.e., a single-volume and single-junction, or several stage groups depending upon the resolution required. If turbine vapor/gas is extracted to preheat the feedwater, then several stage groups may be needed to obtain the correct vapor/gas properties at the feedwater heating bleed points. All such bleed points are modeled as crossflow junctions in the ATHENA model.

3.5.5.1 Model Design. The normal unmodified volume continuity equations are used for the stage group, with a representative nozzle throat area for the inlet junction and the last stator nozzle throat discharge area as the outlet junction area. It is important to use the same representative nozzle area at both junctions.

3.5.5.1.1 Momentum Equations--Unlike the continuity equations, the momentum equations are modified by the work extracted in the rotating blade system of each stage group. To develop the general form for the momentum equations, we first consider a steady-state total energy balance for a homogeneous

fluid passing through a stage group (**Figure 3.5-15**). We will subsequently extend this general form to that used for the two-fluid system**.**
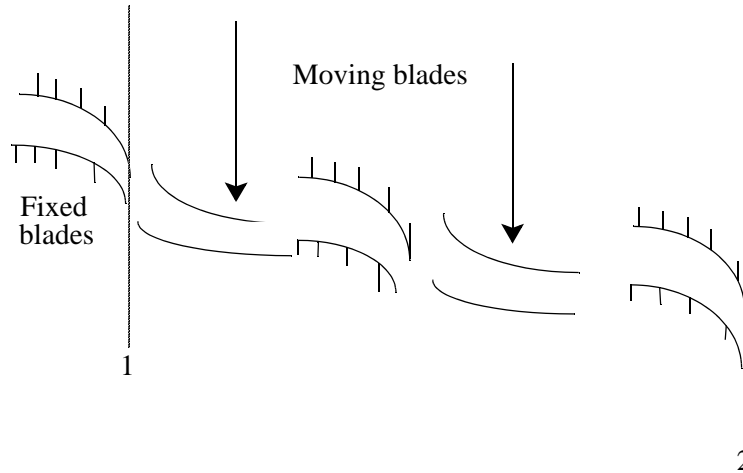
Figure 3.5-15 A schematic of a stage group with idealized flow path between Points 1 and 2.

Although the fluid particles follow a tortuous path through the turbine, we can still write a total energy balance between cross-sections 1 and 2 (**Figure 3.5-15**). For a steady-state situation, this gives

$$\left[\rho v A\left(\frac{1}{2}v^2 + h\right)\right]_1 = \left[\rho v A\left(\frac{1}{2}v^2 + h\right)\right]_2 + (\rho v A)_1 W \qquad (3.5-73)$$

where

ρ = the density

v = the velocity

h = the specific enthalpy

A = the cross-sectional area.

The term W represents the shaft work per unit mass extracted from the fluid. Heat loss is neglected in this ideal analysis. From continuity considerations, $\rho v A$ is constant. Dividing Equation (3.5-73) by $\rho v A$, we obtain

$$\frac{1}{2}v_2^2 - \frac{1}{2}v_1^2 = -(h_2 - h_1) - W \quad . \qquad (3.5-74)$$

In this way, the energy balance is converted into an equivalent force balance (power = force x velocity).

In this idealized process where external heat loss and internal dissipation are neglected, the process is isentropic and

$$dh = \frac{1}{\rho}dP \quad . \tag{3.5-75}$$

Integrating Equation (3.5-75) approximately (assuming constant density) between points 1 and 2 gives

$$h_2 - h_1 = \frac{1}{\rho}(P_2 - P_1) \tag{3.5-76}$$

where ρ is an average density.

The actual work per unit mass, W, produced by the fluid on the rotating blades as its momentum is changed, is usually written as an efficiency factor times the isentropic specific enthalpy change across the stage and becomes

$$W = -\eta \int_{S\,=\,const} dh = -\eta \int_{S\,=\,const} \frac{1}{\rho}dP \quad . \tag{3.5-77}$$

If a constant efficiency and density for the stage group is assumed, Equation (3.5-77) can be approximated as

$$W = -\eta\frac{1}{\rho}(P_2 - P_1) \quad . \tag{3.5-78}$$

When Equations (3.5-76) and (3.5-78) are substituted into Equation (3.5-74), we obtain

$$\frac{1}{2}v_2^2 - \frac{1}{2}v_1^2 = -\frac{(1-\eta)}{\rho}(P_2 - P_1) \tag{3.5-79}$$

as the momentum equation for this steady-state case. Equation (3.5-79) shows that only a small fraction, $(1 - \eta)$, of the pressure gradient contributes to changes in the kinetic energy of the fluid. The larger fraction, η, of the pressure gradient results in turbine work [Equation (3.5-78)].

Using Equation (3.5-79) as a prototype, the full two-fluid momentum equations which are used in the turbine model are (in differential form)

$$(\alpha_g\rho_g)\left(\frac{\partial v_g}{\partial t} + v_g\frac{\partial v_g}{\partial x}\right) = -\alpha_g(1-\eta)\frac{\partial P}{\partial x} - \alpha_g\rho_g\text{HLOSSG } v_g - \alpha_g\rho_g \text{ FIG}(v_g - v_f) \qquad (3.5\text{-}80)$$

$$(\alpha_f\rho_f)\left(\frac{\partial v_f}{\partial t} + v_f\frac{\partial v_f}{\partial x}\right) = -\alpha_f(1-\eta)\frac{\partial P}{\partial x} - \alpha_f\rho_f\text{HLOSSF } v_f - \alpha_f\rho_f \text{ FIF}(v_f - v_g) \qquad . \qquad (3.5\text{-}81)$$

The application guidelines will be summarized in Volume II of this report, but it seems appropriate at this point to mention three guidelines that are related to the momentum equation development:

1. In practice, a turbine does not usually contain significant liquid, and the tortuous path precludes accurate modeling of the interphase drag. Therefore, it is recommended that the homogeneous option be used at all axial turbine junctions. The effect of condensation could be included in the efficiency factor, if desired. At present, it is not included, as the effect is usually small.

2. The fluid path through the turbine volume is very tortuous. This, coupled with the large number of blades, makes the standard wall friction calculation meaningless. For this reason, the wall friction terms have not been shown in Equations (3.5-80) and (3.5-81). It is recommended that the turbine volume wall friction flag be set to use the zero wall friction option. If the user wants to include any momentum effects due to frictional or form losses, it should be done with an appropriate user-specified form loss.

3. The area changes in a turbine are gradual, so the smooth junction option should be used.

3.5.5.1.2 Energy Equations--The ATHENA turbine component conserves energy in that the power extracted from the fluid matches the power added to the shaft. An appropriate heat source is used that, when added to the turbine energy equation, causes the hydraulic and shaft powers to match.

For steady, single phase flow, the thermal energy equation can be written [see Equation (3.1-84)] as

$$(\dot{m}U)_j^{j+1} + \left(P\frac{\dot{m}}{\rho}\right)_j^{j+1} = \dot{Q} \qquad (3.5\text{-}82)$$

where $\dot{m}$ is the mass flow rate, U is the specific internal energy, P is the pressure, ρ is the density, $\dot{Q}$ is the power added to the volume due to heat transfer from structures, and j and j+1 refer to the two adjacent junctions. Using subscripts 1 and 2 to denote the inlet and outlet junctions and using the same pressure at both junctions [see Equations (3.1-91)], Equation (3.5-82) can be written as

$$U_2 - U_1 + P_2\left(\frac{1}{\rho_2} - \frac{1}{\rho_1}\right) = \frac{\dot{Q}}{\dot{m}} \tag{3.5-83}$$

Rewriting in terms of specific enthalpy, h, yields

$$h_2 - h_1 + \frac{P_1 - P_2}{\rho_1} = \frac{\dot{Q}}{\dot{m}} \tag{3.5-84}$$

Applying the same assumptions across the turbine, and neglecting the heat transfer term, the total energy equation can be written as (see **Reference 3.5-8**)

$$h_2 - h_1 + 0.5(v_2^2 - v_1^2) = -\frac{\dot{W}}{\dot{m}} = W \tag{3.5-85}$$

where v is the fluid velocity and $\dot{W}$ is the rate of work done by the fluid on the shaft. Equation (3.5-85) matches Equation (3.5-74). Equating Equations (3.5-84)and (3.5-85) and solving for $\dot{Q}$ yields

$$\dot{Q} = \dot{m}\left[\frac{P_1 - P_2}{\rho_1} + 0.5(v_2^2 - v_1^2)\right] - \dot{W} \tag{3.5-86}$$

The ATHENA turbine model approximates the shaft power as

$$\dot{W} = \frac{\eta(P_1 - P_2)}{0.5(\rho_1 + \rho_2)}\dot{m} \tag{3.5-87}$$

where the efficiency, η, is defined as the ratio of the actual to the isentropic power

$$\eta = \frac{\dot{W}_{act}}{\dot{W}_{isen}} = \frac{\dot{m}(h_1 - h_2)}{\dot{m}(h_1 - h_{2'})} = \frac{h_1 - h_2}{h_1 - h_{2'}} \tag{3.5-88}$$

and the prime denotes an isentropic expansion.

Combining Equations (3.5-86)and (3.5-87) yields

$$\dot{Q} = \dot{m}\left[\frac{P_1 - P_2}{\rho_1} + 0.5(v_1^2 - v_2^2)\right] - \frac{\eta(P_1 - P_2)}{0.5(\rho_1 + \rho_2)}\dot{m} \tag{3.5-89}$$

If one treats the density as constant, which is appropriate for relatively small changes in pressure, and neglects the kinetic energy term, Equation (3.5-89) becomes

$$\dot{Q} \approx \dot{m}\left(\frac{P_1 - P_2}{\rho}\right)(1 - \eta) \approx \frac{1 - \eta}{\eta}\dot{W}$$ (3.5-90)

Since turbine efficiencies are typically near 0.8, a relatively small fraction of the shaft power is added to the fluid. This heat source is analogous to the pump dissipation. Equation (3.5-84) shows that the change in specific enthalpy depends on the pressure difference, which is determined by the momentum equation. For consistency between the energy and momentum equations, the kinetic term in Equation (3.5-89) is evaluated using the velocity squared terms used in the calculation of the momentum flux. Specifically,

$$v^2 = |\bar{v}\dot{v}|$$ (3.5-91)

where $\bar{v}$ is the volume average velocity and $\dot{v}$ is the donor velocity. The donor velocity is calculated as

$$\dot{v} = \frac{v_j A_j}{\bar{A}}$$ (3.5-92)

where v_j and A_j are the velocity and flow area of the upwind junction and $\bar{A}$ is the flow area of the volume.

3.5.5.2 Efficiency Formulas. The basic efficiency formulas can be derived from velocity diagrams with assumed nozzle and blade efficiency factors. The derivations are fairly straightforward and are found in standard texts. The efficiency formulas recorded here were obtained from **Reference 3.5-9**. The efficiency factors for four turbine designs are described in the following paragraphs.

3.5.5.2.1 Single-Stage Turbine--The first model considered is the most general. This is called a Type 1 turbine in the input manual (Volume II, Appendix A). We consider a single-row fixed-blade system followed by a single-row rotating-blade system. Let r be the reaction fraction, i.e., the fraction of the stage energy released (enthalpy change) in the moving-blade system. If r is zero, we have a pure impulse stage with no pressure drop in the moving-blade system, i.e., the moving blades only change the fluid flow direction. A turbine stage with nonzero r at design conditions is commonly called a reaction stage. A value of r = 0.5 is a common design.

If all blading angles are ideal and all nozzle losses are zero, the ideal efficiency, as given in **Reference 3.5-9**, is

$$\eta = \{(vb - v_t) + [(vb - v_t)^2 + rv^2]^{1/2}\}\left(\frac{2v_t}{v^2}\right)$$ (3.5-93)

where v is the fluid velocity at the nozzle exit, v_t is the tangential or rim velocity of the moving blades, and

$$b = (1 - r)^{1/2} \ .$$ (3.5-94)

In general, due to nozzle losses, entrance effects, and nonideal blading angles, the efficiency is less than that given by Equation (3.5-93). The maximum efficiency ($\eta = 1.0$) given by Equation (3.5-93) can be found by differentiation to occur when

$$\frac{v_t}{v} = \frac{0.5}{(1-r)^{1/2}} \ .$$ (3.5-95)

For an impulse stage, the maximum efficiency occurs at $\frac{v_t}{v} = 0.50$. For a reaction turbine designed with r = 0.5, the maximum efficiency occurs at $\frac{v_t}{v} = 0.707$.

In general, the actual efficiency is less than the ideal value derived above. A first approximation to the actual efficiency (see **Reference 3.5-9**) is to include a constant factor, η_o, in Equation (3.5-93) that represents the actual efficiency at the maximum point, i.e.,

$$\eta = \eta_o \frac{2v_t}{v^2}\{(vb - v_t) + [(vb - v_t)^2 + rv^2]^{1/2}\} \ .$$ (3.5-96)

Equation (3.5-96) is the general efficiency formula that is applied to a single-row impulse or reaction turbine. This formula is applied to a stage group that may consist of a single-blade passage or multiple-blade passages. If the stage group contains multiple-blade passages, the efficiency represents some average value.

3.5.5.2.2 Two-Stage Impulse Turbine--The second turbine design considered is a two-row impulse stage, i.e., a nozzle, a moving constant-area blade passage, a fixed constant-area stationary passage, and a final constant-area moving blade passage. This is called a Type 0 turbine in the input manual (Volume II, Appendix A). This blading system is modeled as a single-stage group. This type of stage design is sometimes used as the first stage in a turbine for governing purposes. **Reference 3.5-9** records the efficiency formula for this design as

$$\eta = \eta_o \frac{8v_t}{v^2}(v - 2v_t) \quad .$$ (3.5-97)

3.5.5.2.3 Constant Efficiency--The third efficiency option that is included is a constant efficiency independent of the reaction, nozzle fluid velocity, and rim speed, i.e.,

$$\eta = \eta_o \quad .$$ (3.5-98)

This is called a Type 2 turbine in the input manual (Volume II, Appendix A).

It should be noted that a turbine stage, designed to operate with a given reaction fraction r at design conditions, will have a different reaction fraction for off-design conditions. The change in reaction fraction with $\frac{v_t}{v}$ can be calculated [**Reference 3.5-9**, p. 207, Equation (14)]. For reaction stages, the change is small. In all cases, this change in r is neglected in the above efficiency formulas.

3.5.5.2.4 User Specified Efficiency--A user specified efficiency turbine allows the user to specify turbine efficiency as a function of normalized speed and load (shaft power or rate of work done by the fluid on the shaft). This is called a Type 3 turbine in the input manual (Volume II, Appendix A). The efficiency is calculated as

$$\eta = \eta_R \left[a_0 + a_1 \left(\frac{\omega}{\omega_R} \right) + a_2 \left(\frac{\omega}{\omega_R} \right)^2 + a_3 \left(\frac{\omega}{\omega_R} \right)^3 \right] \left[b_0 + b_1 \left(\frac{\dot{W}}{\dot{W}_R} \right) + b_2 \left(\frac{\dot{W}}{\dot{W}_R} \right)^2 + b_3 \left(\frac{\dot{W}}{\dot{W}_R} \right)^3 \right]$$ (3.5-99)

where ω is the turbine speed and η_R, ω_R, $\dot{W}_R$, a0, a1, a2, a3, b0, b1, b2, and b3 are input data. The efficiency is limited between -100. and 1.0. The negative minimum efficiency allows for the possibility that the shaft does work on the fluid, which can occur if the fluid velocity is less than the tangential velocity. The negative efficiency was limited becasue code execution failures encountered during initial testing of the Type 0 turbine. As shown by Equation (3.5-97), the efficiency approaches negative infinity as the fluid velocity approaches zero. The large negative efficiency value caused the code to fail in test cases in which the initial fluid velocity was zero.

3.5.5.2.5 Power/Torque Output of Turbine--In general, the relationship between power and torque for a rotating shaft is

$$\dot{W} = \tau\omega,$$ (3.5-100)

where $\dot{W}$ is the power, τ is the torque, and ω is the shaft rotational velocity.

ATHENA/2.3

The power extracted from the fluid per mass flow rate for a given stage group is

$$\eta \int_{S=\text{const}} dh \qquad (3.5\text{-}101)$$

so we have for the torque

$$\tau = (\rho v A)\frac{\eta}{\rho}\frac{(P_2 - P_1)}{\omega} \qquad (3.5\text{-}102)$$

or

$$\tau = (\rho v A)\frac{\eta}{\rho}(P_2 - P_1)\frac{R}{v_t} \qquad (3.5\text{-}103)$$

where R is the mean stage radius at the nozzle and the approximation in Equation (3.5-78) has been used.

Equation (3.5-103) gives the torque that is extracted from a given stage group in terms of the stage efficiency, mean stage radius R, mean blade tangential velocity v_t, and pressure drop. This is the torque that is applied by the turbine component when it is coupled to the shaft component.

3.5.5.2.6 Inertia and Friction-- Turbine torque is used to calculate the turbine speed (ω) after the turbine is disconnected from the shaft. The speed is calculated by the deceleration equation

$$I\frac{d\omega}{dt} = \tau \qquad (3.5\text{-}104)$$

The finite difference approximation to this equation is

$$\omega_{t+\Delta t} = \omega_t + \frac{\tau \Delta t}{I} \qquad (3.5\text{-}105)$$

where

$$\tau \quad = \quad \text{net torque}$$

$$I \quad = \quad \text{moment of inertia}$$

$$t \quad = \quad \text{time}$$

Δt = time step

ω = angular velocity (turbine speed)

The total turbine torque is calculated by

$$\tau = \frac{\dot{W}}{\omega} - \tau_{fr} \tag{3.5-106}$$

where

$\dot{W}$ = shaft power from Equation (3.5-87)

τ_{fr} = frictional torque.

If the turbine stage is connected to the shaft, the torque for the stage group is obtained from the right hand side of Equation (3.5-106) and the turbine stage inertia is included in the total inertia of all the components connected to the shaft.

The frictional torque is in the form of a five-term equation that depends on the speed ratio as described in the input manual (Volume II, Appendix A). The value of the frictional torque is also dependent on the sign of the turbine speed.

The turbine moment of inertia is in the form of a constant or in the form of a cubic equation that depends on the speed ratio as described in the input manual (Volume II, Appendix A).

3.5.5.2.7 Numerical Implementation--As noted in the model design section, a stage group is modeled as a single-junction (j) and single-volume (L) (see **Figure 3.5-16**).
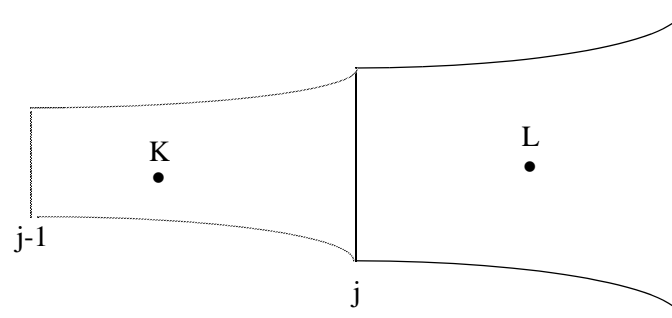
Figure 3.5-16 Schematic of lumped model for turbine stage group.

The continuity equation in Section 3.1 is unchanged from its standard form. The normal finite difference form of the momentum equations for junction j is modified in two ways:

1. The pressure gradient term in the sum and difference numerical equations is multiplied by $(1 - \eta)$.

2. The numerical differencing of the convective terms has been modified. At a normal junction, the convective terms are approximated as

$$v\frac{\partial v}{\partial x} = \frac{\frac{1}{2}v_L^2 - \frac{1}{2}v_K^2}{\Delta x} + \frac{1}{2}\frac{VIS}{\Delta x} \quad . \tag{3.5-107}$$

The small viscous term VIS is numerically calculated so as to give a donored formulation of the momentum flux term in a straight pipe. For a variable-area channel, it is formulated so that it vanishes for a variable-area channel with a constant density fluid. In a turbine, the area is slowly varying; but the fluid experiences large pressure changes (due to the work extraction), hence large density changes. A numerical simulation with the above convective terms used at the turbine junctions resulted in a viscous term that is larger than the kinetic energy terms. Because the normal viscous terms for a variable area channel are inaccurate in the turbine situation with large density changes and dominate the physical kinetic energy change, the momentum flux terms for a turbine junction are neglected and set to zero.

The normal finite difference form of the internal energy equation is modified by adding the dissipation heat source term from Equation (3.5-89).

The algebraic efficiency formulas in Equations (3.5-96) through (3.5-99) are coded with v, η_o, r, ω, and R (where $v_t = R\omega$) as arguments. The type of the turbine stage group is fixed at input time.

The stage torque that is applied to the shaft is calculated from Equation (3.5-103). The torques from each stage group are added using the SHAFT component that integrates the angular momentum equation. The power is calculated from Equation (3.5-100). This variable is not needed in the integration scheme but is printed in the major edits.

3.5.6 Valves

Valves are quasi-steady models that are used either to specify an option in a system model or to simulate control mechanisms in a hydrodynamic system. The valve models can be classified into two categories: valves that open or close instantly and valves that open or close gradually. Either type can be operated by control systems or by flow dynamics.

Valves in the first category are trip valves and check valves. The model for these valves does not include valve inertia or momentum effects. If the valve is used as a junction with an abrupt area change, then the abrupt area change model is used to calculate kinetic loss factors when the valve is open.

Valves in the second category are the inertial swing check valve, the motor valve, the servo valve, and the relief valve. The inertial valve and relief valve behavior is modeled using Newton's second law of motion. The abrupt area change model controls losses through these valves as the cross-sectional flow area varies with valve assembly movement. The motor and servo valve use differential equations to control valve movement. These two valves include the options to use the abrupt area change model to calculate losses across the valve or to use flow coefficients (C_v) specified by the user. The C_v's are converted to energy loss coefficients within the numerical scheme [see Equation (3.5-121)].

Valves are modeled as junction components. The types of valves are defined as follows.

3.5.6.1 Trip Valve. The operation of a trip valve is solely dependent on the trip selected. With an appropriate trip, an abrupt full opening or full closing of the valve will occur. A latch option is also included for latching the valve in the open or closed position.

3.5.6.2 Check Valve. The operation of a check valve can be specified to open or close by static differential pressure, to open by static differential pressure and close by flow reversal, or to open by static differential pressure and close by dynamic differential pressure.

All of the check valves will be opened based on static differential pressure across the junction according to

$$(P_K - \Delta P_{K_g}) - (P_L + \Delta P_{L_g}) - PCV > 0, \text{ valve opens} \qquad (3.5\text{-}108)$$

where

P_K, P_L = junction *from* and *to* volume thermodynamic pressures

$\Delta P_{K_g}, \Delta P_{L_g}$ = static pressure head due to gravity

PCV = back pressure required to close the valve (user input).

For a *static pressure* controlled check valve, the valve will open if Equation (3.5-108) becomes positive and will close if Equation (3.5-108) becomes negative. If Equation (3.5-108) is zero, the valve will remain as previously defined.

For a *flow* controlled check valve, the valve will open if Equation (3.5-108) is positive and will close only if a flow reversal occurs such that

$$\text{FFF} < 0 \tag{3.5-109}$$

where FFF is given as

$$\text{FFF} = \frac{1}{2}(\Delta x_K + \Delta x_L)(\alpha_f \rho_f v_f + \alpha_g \rho_g v_g)_j \ . \tag{3.5-110}$$

For a *dynamic pressure* controlled check valve, the valve opens if Equation (3.5-108) is greater than zero. Once the valve is open, the forces due to pressure differential and momentum hold the valve open until

$$(P_K - \Delta P_{K_g}) - (P_L + \Delta P_{L_g}) + GC - PCV < 0, \text{ valve closes,} \tag{3.5-111}$$

$$= 0, \text{ remains as previously defined}$$

where $GC = \frac{1}{2}(\alpha_f \rho_f v_f |v_f| + \alpha_g \rho_g v_g |v_g|)_j \ .$

The terms α_f and α_g are the junction liquid and vapor volume fractions, respectively; ρ_f and ρ_g are the junction liquid and vapor densities, respectively; and v_f and v_g are the junction liquid and vapor velocities, respectively.

Flow and *dynamic pressure* controlled valves exhibit a hysteresis effect with respect to the forces opening and closing the valve. The *static pressure* controlled valve, however, has no hysteresis effect.

All check valves may be initialized as either open or closed. Leakage is also allowed if the valve is closed, and the abrupt area change model is used to calculate the valve form losses.

3.5.6.3 *Inertial Valve.* This valve models the motion of the valve flapper assembly in an inertial-type check valve. The abrupt area change model is used to calculate kinetic form losses, assuming that the area between the flapper and the valve seat behaves as an orifice whose area changes in time as a function of the inertial valve geometry.

The motion of the flapper about the shaft axis is given by Newton's second law (angular version) as

$$\Sigma T = I \dot{\omega} \tag{3.5-112}$$

where

      T   =   torque

I	=	moment of inertia
$\dot{\omega}$	=	angular acceleration
ω	=	angular velocity $= \dot{\theta}$, counter-clockwise motion is positive
θ	=	disc angular position, $\theta = 0$ is fully closed.

Torque is defined as r x F; the cross-product of a force F and the distance from the hinge pivot point, r, to the force. Each particle of a rotating body has kinetic energy. Kinetic energy is defined as $0.5mV^2$ where m is the mass and V is the velocity. Since $V = r\omega$ where r is the distance to the particle and ω is the angular velocity, the kinetic energy of the particle is $0.5mr^2\omega^2$. The total kinetic energy of a rotating body is the sum of the kinetic energy of all of its particles. Since the angular velocity of all particles is the same, ω can be factored out to give:

$$\text{Kinetic Energy} = 0.5(\Sigma m_i r_i^2)\omega^2 \quad . \tag{3.5-113}$$

The term in parentheses is know as the moment of inertia, I.

A diagram of an inertial valve is shown in **Figure 3.5-17**. The valve flapper disc resides in a pipe and swings on a hinge pin. The valve are used to prevent backflow. The flapper position depends on factors such as flapper mass, gravity vector, moment of inertia, distance from the hinge pin to the center of mass, flapper area, pressure difference across the valve, viscous and Coulomb friction between the flapper and the pin, and lift and drag forces on the flapper. Only torque due to differential pressure, T_{DP}, Coulomb friction, T_F, and weight, T_W, are included in this model. These torques are given by

$$T_{DP} = (P_K - P_L) A_P L \tag{3.5-114}$$

$$T_F = \Delta P_F A_R L \tag{3.5-115}$$

$$T_W = - MgL\sin\theta \tag{3.5-116}$$

where

P_K	=	pressure in the hydraulic cell on the left
P_L	=	pressure in the hydraulic cell on the right
A_P	=	projected area of the disc
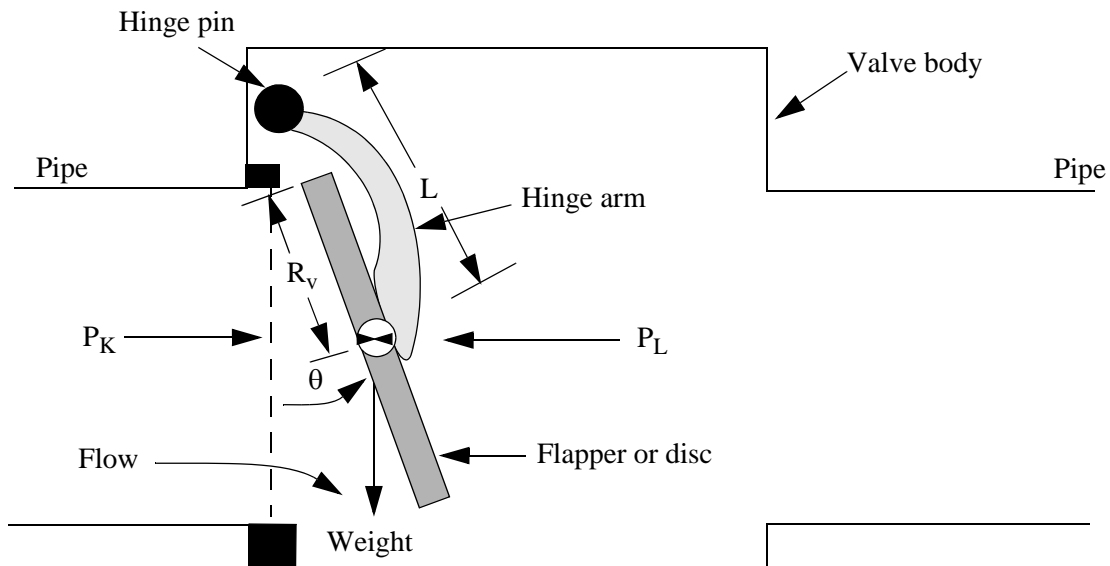
Figure 3.5-17 Diagram of inertial valve.

L	=	user input flapper moment arm length from the hinge to the center of inertia
A_R	=	area of disc $= \pi R_v^2$
R_v	=	user input disc radius
ΔP_F	=	user input value of minimum pressure difference across the valve required to initiate motion (cracking pressure)
g	=	acceleration due to gravity
M	=	mass of the flapper.

The differential pressure across the flapper faces decreases as the valve flapper swings into hydraulic cell on the right. To approximate this decrease, the projected area is used in the T_{DP} term (see **Figure 3.5-18**).The projected area of a circle is an ellipse with an area of $\pi R_v b$. Since $b = R_v \sin(\phi)$ where ϕ is 90-θ;

$$A_P = \pi R_v^2 \sin(90\text{-}\theta) = \pi R_v^2 \cos \theta . \tag{3.5-117}$$

.

Front view   Side view

Figure 3.5-18 Two views of a partially open flapper valve.

The angular acceleration is solved from Equation (3.5-112), resulting in

$$\dot{\omega}^n = \frac{\Sigma T}{I}$$
(3.5-118)

and the new time flapper velocity and angle are

$$\omega^n = \omega^{n-1} + \dot{\omega}^n \Delta t \ \ .$$
(3.5-119)

The new time angle is calculated from the angle at the previous time step and the average velocity during the time step, which is

$$\theta^n = \theta^{n-1} + 0.5(\omega^{n-1} + \omega^n)\,\Delta t$$
(3.5-120)

where superscript n stands for new time and n-1 indicates the previous time step value.

In order to obtain the correct velocity to compare with the sonic speed at the valve the vena-contracta is considered. The effective flow area is C_c times the actual open area, where C_c is the contraction coefficient (i.e., effective area/actual open area).

Table 3.5-4 gives the table of contraction coefficients.[3.5-10] C_c is less than one and has the effect of increasing the code calculated velocity in the valve opening. The table also shows the loss coefficient K_{loss}, which the abrupt area change model automatically calculates for the code users. Volume IV discusses this in more detail.

Table 3.5-4 Contraction coefficient table.

Area fraction open	0.0	0.1	0.2	0.3	0.4	0.5	0.6	0.7	0.8	0.9	1.0
C_c	0.617	0.624	0.632	0.643	0.659	0.681	0.712	0.755	0.813	0.892	1.0
K_{Loss}	0.38	0.36	0.34	0.31	0.27	0.22	0.16	0.10	0.05	0.02	0.0

Several options are allowed with the use of this valve, such as specifying minimum and maximum flapper angular positions when the valve is closed, specifying latch or no latch options, and specifying leakage area.

3.5.6.4 Motor Valve. This valve model has the capability of controlling the junction flow area between two control volumes as a function of time. The operation of the valve is controlled by two trips; one for opening the valve and a second for closing the valve. A constant rate parameter controls the speed at which the normalized valve area changes. The motor valve area variation can also be specified using a general table. When the general table is specified, the constant rate parameter controls the normalized valve stem position, and the general table relates the normalized stem position to the normalized valve flow area. Conversely, when the general table is not specified, the constant rate parameter controls the rate of change in the normalized valve area. If the normalized valve flow area has a value less than 1.0×10^{-10}, the valve is assumed to be closed.

The first option for the motor valve is to use the abrupt area change model to calculate kinetic form losses with respect to the valve area.

A second option allowed for the motor valve is the specification of valve flow coefficients, C_v, using the smooth area change model. These coefficients may be specified using a general table of C_v versus normalized stem position and the smooth junction option must be specified. The conversion of C_v to an energy loss coefficient, K, is done in the numerical scheme using the formula

$$K = 2C\frac{A_{valve}^2}{C_v^2 \rho_o} \tag{3.5-121}$$

where ρ_o is the density of liquid light water at 60.0 °F (288.71 K), 14.7 lb_f/in^2 (1.0×10^5 Pa). The value of the density ρ_o is 62.4 lb_m/ft^3 (999.09 kg/m^3). The value of C is $9.3409 \times 10^8 \dfrac{\left(\frac{gal}{min}\right)^2 lb_m}{ft^7 \frac{lb_f}{in^2}}$. Provisions also

exist for applying multipliers to both normalized stem position and C_v. The C_v term is entered in British units only.

3.5.6.5 Servo Valve. The servo valve operation is similar to that for the motor valve. However, the normalized valve area or normalized stem position is controlled by a control variable rather than by a specified rate parameter. The servo valve also has the same options as the motor valve.

3.5.6.6 Relief Valve. For thermal-hydraulic analysis of overpressure transients, it is necessary to simulate the effects of relief valves. In particular, it is desirable to model the valve dynamic behavior, including simulation of valve flutter and hysteresis effects.

To assist in understanding the relief valve model, three schematics of a typical relief valve are shown in **Figure 3.5-19**, **Figure 3.5-20**, and **Figure 3.5-21**. The three schematics represent the valve in the closed (**Figure 3.5-19**), partially open (**Figure 3.5-20**), and fully open (**Figure 3.5-21**) modes, respectively. In the schematics, the seven main components of a relief valve are shown, which are the valve housing, inlet, outlet, piston, rod assembly, spring, bellows, and valve adjusting ring assembly.

The numerical model of the valve simply approximates the fluid forces acting on the valve piston and the valve reaction to these forces. The model of the fluid forces is based on a quasi-steady-state form of the impulse momentum principle, and the valve reaction force is based on Newton's Second Law of motion.

A qualitative understanding of the operation of the relief valve can be gained by referring again to **Figure 3.5-19**, **Figure 3.5-20**, and **Figure 3.5-21**. If the valve inlet pressure is low the valve is closed, as shown in **Figure 3.5-19**. As the inlet pressure increases, the valve piston will remain closed until the force of the upstream pressure on the valve exceeds the set point forces. The set point forces are the combined forces of the piston and rod assembly weight, the valve spring, the atmospheric pressure inside the bellows, and the downstream back pressure around the outside of the bellows. Once the set point forces are exceeded, the valve piston will begin to lift. Upon opening, the upstream fluid will begin to expand through the opening into the valve ring region. This initial expansion occurs through the angle α_o, and the flow changes direction through an average angle θ_o, as shown in **Figure 3.5-19**. As the flow accelerates, the momentum effects of the expansion and change in flow direction exert a thrust on the valve piston, causing the valve to open further. As the valve partially opens, the angle of expansion decreases to α_1 and the change in flow direction increases to θ_1, as shown in **Figure 3.5-20**. This effect, in turn, further increases the thrust on the valve piston, causing it to fully open, as shown in **Figure 3.5-21**. As these processes occur, the valve reaction forces and fluid momentum forces vary in such a manner that the valve will not close until the upstream pressure decreases significantly below the valve set point pressure. In this respect, a hysteresis effect is observed that is characteristic of relief valves.

The relief valve model consists of a set of equations designed to approximate the behavior described above. In implementing the model, the dynamic behavior of the fluid is calculated at each time step by the ATHENA hydrodynamic solution scheme. The resultant phasic velocities and thermodynamic properties are then used to solve a quasi-steady equation approximating the fluid forces on the valve piston. The valve
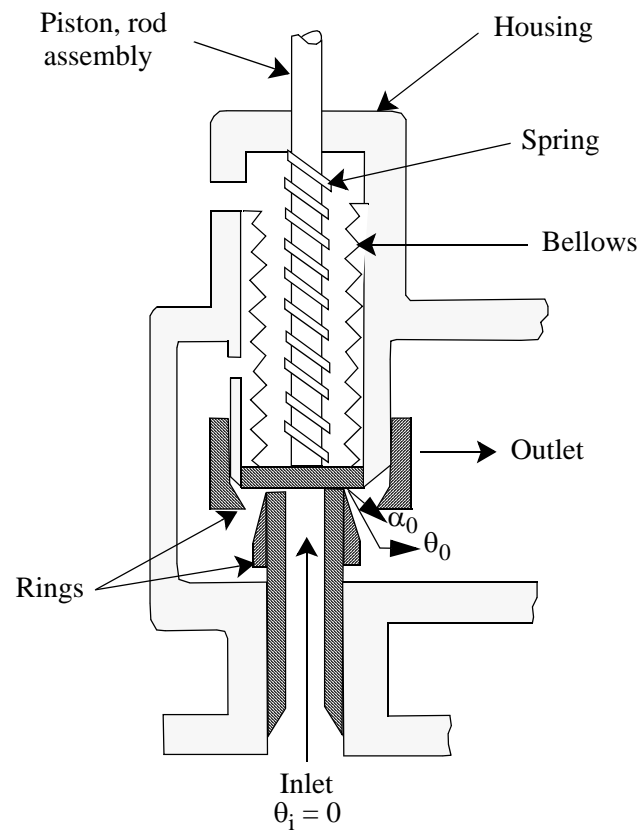
Figure 3.5-19 Schematic of a typical relief valve in the closed position.

dynamic reaction forces are then calculated, and the new time valve piston speed and position are estimated.

The relief valve model is formulated, applying D'Alembert's principle in which the forces acting on the face of the valve piston are balanced, for which the valve reaction forces can be written as

$$\text{(reaction forces)} = F_R = m_v a_{v,x} + B\,(v_{v,x} - v_{housing}) + K_s x \tag{3.5-122}$$

where

m_v =   mass of the valve mechanism that is in motion (i.e., the valve piston, rod assembly combined with the spring and bellows)

$a_{v,x}$ =   valve assembly acceleration in the x-direction

Figure 3.5-20 Schematic of a typical relief valve in the partially open position.

B	=	damping coefficient
$v_{v,x}$	=	velocity of the valve mechanism in the x-direction
$v_{housing}$	=	velocity of the valve housing = 0
K_s	=	spring constant
x	=	piston position (i.e., x-coordinate).

The positive x-direction is assumed to be in the direction of fluid flow at the valve inlet. The fluid forces, F_F, can be formulated by summing the forces acting over the surfaces of the fluid flow channel such that

$$F_F = (P_iA_D)_x - (P_aA_{Ba})_x - (P_oA_{Bo}) - (P_eA_e)_x - F_R \qquad (3.5\text{-}123)$$

Figure 3.5-21 Schematic of a typical relief valve in the fully open position.

where

F_R = reaction forces

P_i = valve inlet pressure

A_D = valve piston face area exposed to the inlet flow stream

P_a = atmospheric pressure inside the bellows

A_{Ba} = valve piston area inside the bellows

P_o = valve back pressure outside the bellows

A_{Bo} = valve piston area outside the bellows

A_e = valve ring exit area

P_e = valve ring exit pressure

and where the subscript x denotes that the force component is in the x-direction.

The valve back pressure outside the bellows (P_o) and valve ring exit pressure (P_e) are calculated from the density change from the throat to the outlet and to the ring exit respectively. Since the homogeneous sound speed (a) can be expressed by

$$a^2 = \left(\frac{\partial P}{\partial \rho}\right)_S , \tag{3.5-124}$$

the density variation is related to the pressure variation as

$$dP = a^2 \bullet d\rho . \tag{3.5-125}$$

Since the isentropic compressibility can be expressed by

$$\kappa_S = \frac{1}{\rho}\left(\frac{\partial \rho}{\partial P}\right)_S , \tag{3.5-126}$$

the pressure variation is related to the density variation as

$$d\rho = \kappa_S \rho dP . \tag{3.5-127}$$

The Bernoulli equation gives

$$dP = -\frac{\rho}{2}dv^2 . \tag{3.5-128}$$

The mass flux is expressed as

$$G = \rho v . \tag{3.5-129}$$

Consequently,

$$dG^2 = \rho^2 dv^2 + v^2 d\rho^2 . \tag{3.5-130}$$

ATHENA/2.3

Algebraic manipulations result in

$$d\rho = -\frac{\kappa_S}{2}(dG^2 - 2v^2\rho d\rho) \ . \tag{3.5-131}$$

Thus, we obtain

$$d\rho = -\left(\frac{\kappa_S}{1.0 - \kappa_S\rho v^2}\right)\frac{dG^2}{2} \ . \tag{3.5-132}$$

From Equations (3.5-129) and (3.5-132), the variations of density from the throat to the outlet and to the ring exit can be calculated as

$$\Delta\rho_o = -\left(\frac{\kappa_S}{1.0 - \kappa_S G_{th}v_{th}}\right)\frac{(G_o^2 - G_{th}^2)}{2} \tag{3.5-133}$$

and

$$\Delta\rho_e = -\left(\frac{\kappa_S}{1.0 - \kappa_S G_{th}v_{th}}\right)\frac{(G_e^2 - G_{th}^2)}{2} \tag{3.5-134}$$

where G_o is the outlet mass flux, G_e is the ring exit mass flux, G_{th} is the throat mass flux, and v_{th} is the throat velocity. The pressures at the outlet and ring exit can be obtained as

$$P_o = P_{th} - a^2\left(\frac{\kappa_S}{1.0 - \kappa_S G_{th}v_{th}}\right)\frac{(G_o^2 - G_{th}^2)}{2} \tag{3.5-135}$$

and

$$P_e = P_{th} - a^2\left(\frac{\kappa_S}{1.0 - \kappa_S G_{th}v_{th}}\right)\frac{(G_e^2 - G_{th}^2)}{2} \tag{3.5-136}$$

where the pressure at the throat (P_{th}) is obtained from the Bernoulli equation using the inlet pressure and flow conditions. The isentropic compressibility (κ_s) is obtained from standard thermodynamic relations.

Since the fluid is flowing through a channel that both expands and changes direction, the fluid undergoes a change in momentum expressed by the impulse momentum principle as

$$F_F = \Delta(mv) = \dot{m}_F(v_{e,x} - v_{i,x}) \tag{3.5-137}$$

where

$$\dot{m}_F \quad = \quad \text{mass flow rate of the fluid through the valve}$$

$$v_{e,x} \quad = \quad \text{fluid velocity exiting through the rings}$$

$$v_{i,x} \quad = \quad \text{fluid velocity entering the valve inlet.}$$

Balancing the forces by combining Equations (3.5-121), (3.5-122), and (3.5-137) gives

$$m_v a_{v,x} + B v_{v,x} + K_s x = -(P_a A_{Ba}) - (P_o A_{Bo}) - (P_e A_e)\cos\theta - \dot{m}_f(v_e \cos\theta - v_i) + P_i A_D \quad . \tag{3.5-138}$$

The valve acceleration can be expressed in terms of the valve velocity as

$$a_{v,x} = \frac{dv_{v,x}}{dt} + g \tag{3.5-139}$$

where g is the acceleration of gravity.

Combining Equations (3.5-138) and (3.5-139), treating the velocity damping term and spring force position terms implicitly, and integrating over the time step gives

$$m_v(v_{v,x}^{n+1} - v_{v,x}^n) + B v_{v,x}^{n+1}dt + K_s x^{n+1}dt + m_v g dt = [(P_i^n A_D) - (P_a A_{Ba}) - (P_o^n A_{BO})]$$
$$- (P_e^n A_e)\cos\theta_e^n - \dot{m}_f^n(v_c^n \cos\theta_e^n - v_i^n)dt \tag{3.5-140}$$

where n and n+1 represent the old and new time terms, respectively.

The position term, x^{n+1}, can be written in terms of the valve velocity by considering that

$$v_{v,x} = \frac{dx}{dt} \quad . \tag{3.5-141}$$

If Equation (3.5-141) is integrated over the time step, then

$$x^{n+1} = x^n + v_{v,x}^{n+1}dt \ .$$

(3.5-142)

If the valve set point pressure is equated to $K_s x_o$, then combining Equations (3.5-140) and (3.5-142) and both adding and subtracting the term $K_s x_o$ gives the numerical form of the relief valve model,

$$m_v(v_{v,x}^{n+1} - v_{v,x}^n) + [(B + K_s dt)v_{v,x}^{n+1} + K_s(x^n - x_o) + m_v g]dt$$
$$= -K_s x_o dt + [(P_i^n A_D) - (P_a A_{Ba}) - (P_o^n A_{Bo}) - (P_e^n A_e)\cos\theta_e^n - \dot{m}_F^n(v_e^n \cos\theta_e^n - v_i^n)]dt$$

(3.5-143)

where the sign of the gravity term, g, is dependent on the valve orientation. For example, if the valve is oriented upward (i.e., +x is upward), then the gravity term is expressed as $g = -|g|$.

In the numerical scheme, Equation (3.5-143) is solved for the new time valve piston velocity, v_v^{n+1}, in terms of the current time terms with superscript n. The terms required to model the valve geometry and the valve damping, spring, and back pressure forces are input to the code as described in Volume II, Appendix A, of this report.

The characteristic relief valve hysteresis effects are inherent in the formulation of Equation (3.5-143). For example, if the valve is closed, then all velocity terms are zero and $x = x_o$. Therefore, acceleration of the valve piston in the positive x-direction cannot occur until the upstream force $P_i A_D$ exceeds the spring set point and valve weight. Once the valve opens and the fluid accelerates, the forces due to the change in fluid momentum aid in holding the valve open. Therefore, the valve cannot close until the combined fluid pressure and momentum terms decrease significantly below the set point forces. Hence, the desired hysteresis is incorporated in the model.

3.5.7 Accumulator

An accumulator model is included that features mechanistic relationships for the hydrodynamics, heat transfer from the tank wall and liquid surface, condensation in the vapor/gas dome, and vaporization from the liquid surface to the vapor/gas dome. The geometry of the tank may be cylindrical or spherical. The accumulator model also includes the surge line and an outlet check valve junction.

3.5.7.1 Hydrodynamic Model. An accumulator is modeled in ATHENA as a lumped-parameter component. This model was chosen for two reasons; the spatial gradients in the accumulator tank are expected to be small, and a simple ideal gas equation of state can be used.

The accumulator model and associated notations are shown in **Figure 3.5-22** for the case of a cylindrical tank, and **Figure 3.5-23** for the case of a spherical tank. The basic model assumptions are:
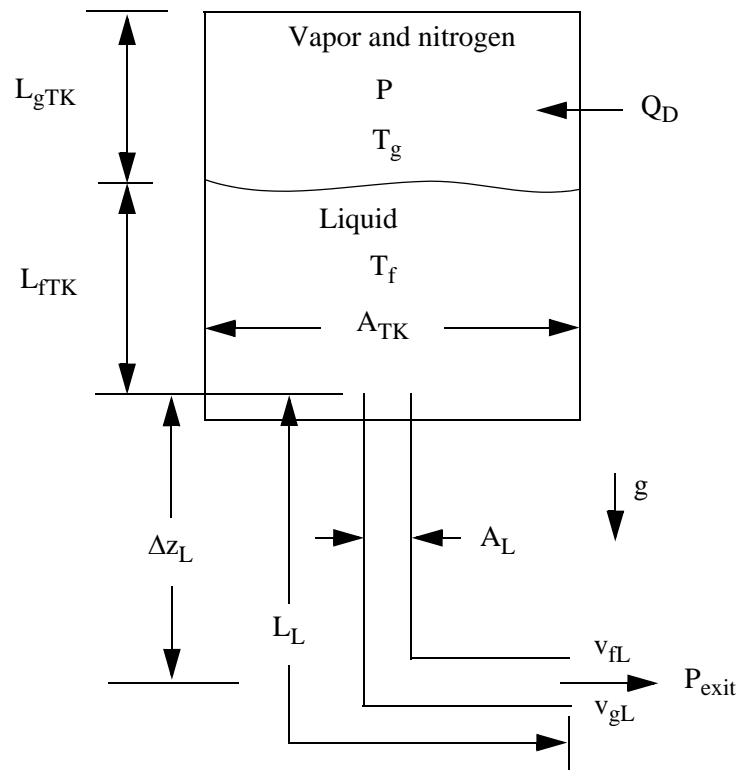
Figure 3.5-22 Typical cylindrical accumulator.

- Heat transfer from the accumulator walls and heat and mass transfer from the liquid are modeled using natural convection correlations, assuming similarity between heat and mass transfer from the liquid surface.

- The vapor/gas in the vapor/gas dome is modeled as a closed expanding system composed of an ideal gas with constant specific heat. The vapor in the dome exists at a very low partial pressure; hence, its effect on the nitrogen state is neglected. However, energy transport to the vapor/gas dome as a result of vaporization/condensation is included.

- Because of the high heat capacity and large mass of liquid below the interface, the liquid is modeled as an isothermal system.

- The model for liquid flow includes inertia, wall friction, form loss, and gravity effects.

Using these assumptions, the basic equations governing the thermal-hydraulics of the tank and discharge line are as follows:
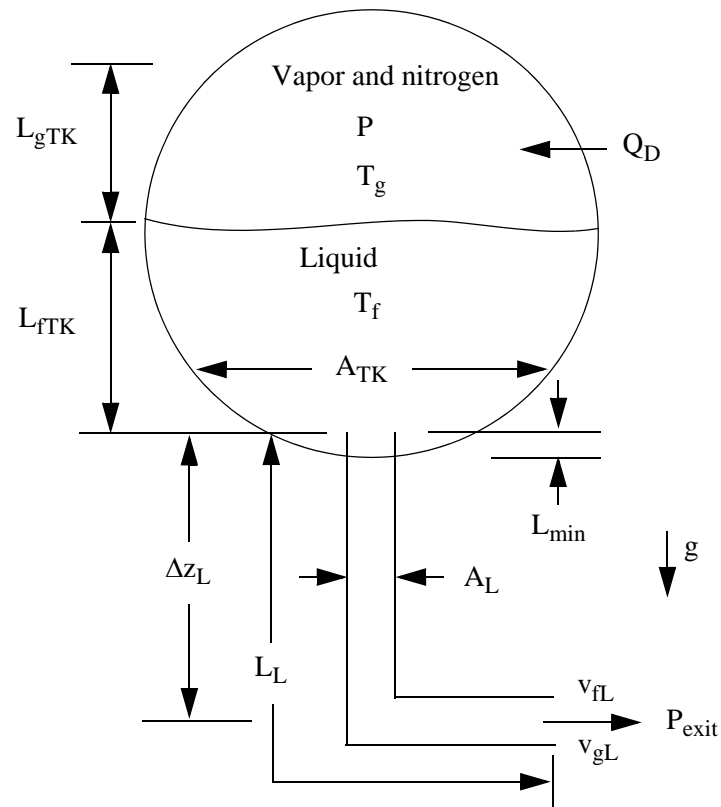
Figure 3.5-23 Typical spherical accumulator.

The conservation of mass for the nitrogen dome is

$$M_n = \text{constant} = \rho_n V_D \tag{3.5-144}$$

where

M_n = nitrogen gas mass

ρ_n = nitrogen gas density

V_D = vapor/gas dome volume.

The conservation of energy for the nitrogen gas in the dome is

$$M_n\left(\frac{dU_n}{dt}\right) = -P\left(\frac{dV_D}{dt}\right) + \dot{Q}_D \qquad (3.5\text{-}145)$$

where

U_n = nitrogen specific internal energy

P = vapor/gas dome pressure

$\dot{Q}_D$ = net heat transfer rate to the vapor/gas dome from all sources.

The conservation of energy for the tank wall is

$$M_{wall}C_{v,\,wall}\frac{dT_{wall}}{dt} = -\dot{Q}_{wall} \qquad (3.5\text{-}146)$$

where

M_{wall} = metal mass in the tank wall

$C_{v,wall}$ = metal specific heat

T_{wall} = mean metal temperature

$\dot{Q}_{wall}$ = heat transfer rate to the wall.

The conservation of momentum,[a] for the accumulator tank and surge line is

$$\rho A\left(L\frac{dv}{dt} + \frac{1}{2}v^2\right) + Fv = A(P - P_{exit}) + A\Delta P_z \qquad (3.5-147)$$

where

A = flow channel cross-sectional area

L = discharge line flow channel length

---

a. Equation (3.5-147) is the combined tank and discharge line momentum equation. The wall drag coefficient, F, is given as $\frac{1}{2}\rho_f\lambda_{wf}\frac{L}{D}A|v|$, where D = surge line diameter and λ_{wf} is the Darcy friction factor.

| v | = | velocity in discharge line |

| F | = | frictional loss coefficient |

| P_{exit} | = | pressure at exit of surge line |

| ΔP_z | = | elevation pressure differential between discharge line entrance and liquid surface. |

The equations of state for the nitrogen gas in the dome are

$$PV_D = M_n R_n T_g \tag{3.5-148}$$

$$U_n = M_n C_{v,n} T_g \ . \tag{3.5-149}$$

Using Equation (3.5-149), Equation (3.5-145), the nitrogen energy equation, can be rewritten as

$$M_n C_{v,n} \frac{dT_g}{dt} = -P\frac{dV_D}{dt} + \dot{Q}_D \ . \tag{3.5-150}$$

Differentiating Equation (3.5-148), eliminating the constant term $M_n R_n$, and substituting the result into Equation (3.5-150) yields

$$P\left(1 + \frac{R_n}{C_{v,n}}\right)\frac{dV_D}{dt} + V_D\frac{dP}{dt} = \frac{R_n}{C_{v,n}}\dot{Q}_D \ . \tag{3.5-151}$$

Equations (3.5-147), (3.5-150), and (3.5-151) comprise the system of three differential equations used in the accumulator hydrodynamic model. They are used to numerically advance T_g, V_D, and P in time.

3.5.7.2 Heat Transfer to the Vapor/Gas Dome. In the accumulator, energy transport by convective heat transfer to the vapor/gas dome from the walls and fluid surface is modeled using an empirical Newton cooling law formulation

$$Q_i = \bar{h}_i A_i (T_i - T_g) \tag{3.5-152}$$

where

| i | = | thermal transport surface |

$\bar{h}_i$ = convective heat transfer coefficient (averaged)

A_i = surface area

$T_i - T_g$ = surface to vapor/gas dome temperature difference.

It should be noted that heat and mass transfer in the accumulator discharge line are neglected.

Two turbulent natural convection heat transfer models are used and combined by superposition. First, heat transfer with the cylindrical walls of the tank is considered, using a turbulent natural convection correlation[3.5-11] for heat transfer within a vertical cylinder with closed ends for which

$$\bar{h}_1 = 0.1 \frac{k_D}{\frac{1}{2} D_{TK}} (GrPr)^{\frac{1}{3}} \left(\frac{L}{\delta}\right) \tag{3.5-153}$$

and

$$A_1 = \pi D_{TK} L \tag{3.5-154}$$

where

$\bar{h}_1$ = vapor/gas dome to cylinder heat transfer coefficient

L = vapor/gas dome cylinder length

δ = vapor/gas dome characteristic diameter

k_n = nitrogen gas thermal conductivity

D_{TK} = tank diameter

Gr = vapor/gas dome Grashof number

Pr = vapor/gas dome Prandtl number.

Second, heat transfer from the disk-shaped ends of the cylinder is considered, where the top disk is the metal top of the tank and the bottom disk is the liquid-vapor/gas interface. For this model, a turbulent natural convection correlation[3.5-11] is used for heat transfer between two horizontal disks separated vertically where, for each disk,

$$\bar{h}_2 = 0.15\frac{k_n}{L}(GrPr)^{\frac{1}{3}}\left(\frac{L}{\delta}\right) \quad\quad\quad (3.5\text{-}155)$$

and

$$A_2 = \frac{\pi D_{TK}^2}{4} \quad . \quad\quad\quad (3.5\text{-}156)$$

In the case of a spherical tank, Equation (3.5-153) is used with A_1 replaced by the surface area of the tank in contact with the vapor/gas, i.e.,

$$A_1 = 2\pi LR \quad\quad\quad (3.5\text{-}157)$$

where L is the height of the vapor/gas dome and R is the radius of the sphere. The characteristic diameter of a spherical vapor/gas dome is defined as the ratio of volume to surface area. The correlation given by Equation (3.5-155) is not used for a spherical tank, hence h_2 is set equal to zero.

In the correlations given by Equations (3.5-153) and (3.5-155), the product of the Grashof and Prandtl numbers represents the convective thermal circulation in the vapor/gas dome, where the Grashof number represents the ratio of circulation potential to viscous stress and the Prandtl number represents the ratio of viscous stress to thermal diffusion. Only the Grashof number is a function of the vapor/gas dome dimensions and temperature difference for which

$$Gr = \frac{g\beta_n|T_i - T_g|\delta^3}{v_n^2} \qu\quad\quad\quad (3.5\text{-}158)$$

where

$$g \quad = \quad \text{acceleration due to gravity}$$

$$\beta_n \quad = \quad \text{nitrogen gas isobaric coefficient of thermal expansion}$$

$$T_i - T_g \quad = \quad \text{magnitude of the interface, vapor/gas dome difference}$$

$$v_n \quad = \quad \text{nitrogen gas kinematic viscosity}$$

$$\delta \quad = \quad \text{characteristic overall diameter of the vapor/gas dome.}$$

If the Prandtl number is written in terms of the nitrogen gas thermal diffusivity, then

$$Pr = \frac{\mu_n}{\rho_n \alpha_n} \tag{3.5-159}$$

where

ρ_n =   nitrogen gas density

α_n =   nitrogen gas thermal diffusivity.

The characteristic diameter is defined in terms of the typical volume-to-surface-area ratio as

$$\delta = \frac{4V_D}{A_i} \tag{3.5-160}$$

where A_i is the combined vapor/gas dome cylinder, disk top, and bottom surface areas. In the case of a spherical vapor/gas dome, $A_s = A_1 + A_i$, where A_1 is given by Equation (3.5-157) and A_i is the surface area of liquid-vapor/gas interface, i.e.,

$$A_i = \pi L(2R - L) \tag{3.5-161}$$

where L is the height of the vapor/gas dome and R is the radius of the sphere.

3.5.7.3 Mass Transfer to the Vapor/Gas Dome. When the accumulator is in its stagnant initial condition, the vapor/gas dome and liquid are in thermal equilibrium and the vapor/gas dome is saturated with vapor. However, as the accumulator blows down, the vapor/gas dome temperature decreases due to expansion, while the liquid remains essentially isothermal. As a result, there is simultaneous vaporization at the liquid-vapor/gas interface and condensation in the vapor/gas dome. This mechanism transports a large amount of energy to the vapor/gas dome as a result of the heat of vaporization of the liquid.

At the liquid-vapor/gas interface, as vaporization occurs, the relatively warm vapor rapidly diffuses due to buoyancy into the vapor/gas dome. Assuming that the process can be approximated by a quasi-steady formulation, then for diffusion in a stagnant vapor/gas, the mass transfer for the process can be written as

$$\dot{M}_{vap} = -\zeta A_i \frac{dC}{dx} \tag{3.5-162}$$

where

$\dot{M}_{vap}$ =   rate of vapor diffusion

ζ =   diffusion coefficient

A_i =   surface area of the liquid-vapor/gas interface

$\dfrac{dC}{dx}$ =   vapor concentration gradient.

The concentration can be expressed in terms of partial pressure such that

$$C = \frac{P_s}{P}\rho_s \qquad\qquad (3.5\text{-}163)$$

where

C =   vapor concentration

P_s =   local vapor partial pressure

ρ_s =   vapor density (saturated vapor at P_s).

Hence, at the dome pressure, the concentration gradient can be written as

$$\frac{dC}{dx} = \frac{1}{P}\frac{d(P_s\rho_s)}{dx} \ . \qquad\qquad (3.5\text{-}164)$$

Combining Equations (3.5-162) and (3.5-164) and integrating gives

$$\dot{M}_{vap}L_D = -\frac{\zeta A_i}{P}\left(\bar{P}_s \int_{x=0}^{x=L_D} d\rho_s + \bar{\rho}\int_{x=0}^{x=L_D} dP_s\right) \qquad\qquad (3.5\text{-}165)$$

where the integration is performed by parts.

Both of the differential terms $d\rho_s$ and dP_s can be written in terms of temperature differentials if 100% relative humidity is assumed so that

$$P_s = P^s\,(T_g) \qquad\qquad (3.5\text{-}166)$$

where $P^s(T_g)$ is the saturation pressure at the temperature T_g. Hence, the density differential can be expanded as

$$d\rho_s = \left[\left(\frac{\partial\rho_s}{\partial P_s}\right)_T \frac{dP_s}{dT} + \left(\frac{\partial\rho_s}{\partial T}\right)_{P_s}\right]dT \tag{3.5-167}$$

where

$$\left(\frac{\partial\rho_s}{\partial P_s}\right)_T = \kappa_s\rho_s \tag{3.5-168}$$

$$\left(\frac{\partial\rho_s}{\partial T}\right)_{P_s} = -\beta_s\rho_s. \tag{3.5-169}$$

Combining Equations (3.5-167), (3.5-168), and (3.5-169) and substituting Clapeyron's equation for the $\frac{\partial\rho_s}{\partial T_s}$ term gives

$$d\rho_s = \bar{\rho}_g\left[\kappa_g\left(\frac{h_{fg}}{T_g^s V_{fg}}\right) - \beta_g\right]dT \tag{3.5-170}$$

where Clapeyron's equation is

$$dP^s = \left(\frac{h_{fg}}{T_g \upsilon_{fg}}\right)dT \tag{3.5-171}$$

and the term $\left(\frac{h_{fg}}{T_g \upsilon_{fg}}\right)$ is treated as a constant. Combining Equations (3.5-166), (3.5-170), and (3.5-171), the diffusion equation can be rewritten as

$$\dot{M}_{vap} = \frac{\zeta}{L_D}\frac{A_i}{P}\left\{\bar{P}_s\bar{\rho}_s\left[\kappa_s\left(\frac{h_{fg}}{T_g\upsilon_{fg}}\right) - \beta_s\right] + \bar{\rho}_s\left(\frac{h_{fg}}{T_g\upsilon_{fg}}\right)\right\}(T_f - T_g) \tag{3.5-172}$$

where the dome average terms are evaluated at the dome average temperature, T_g.

Equation (3.5-172) can be made analogous to a convective equation by expressing the mass transfer coefficient as

$$h_{2s} = \frac{\zeta}{L_D} \tag{3.5-173}$$

where h_{2s} is the mass transfer coefficient in a stagnant vapor/gas. Then, by applying Reynolds analogy, a turbulent natural convection mass transfer coefficient can be derived in terms of the heat transfer coefficient, h_2, from Equation (3.5-155) such that

$$h_{2s} = h_2\left(\frac{\zeta}{k_D}\right)\left(\frac{\alpha_D}{\zeta}\right)^{\frac{1}{3}} \tag{3.5-174}$$

where α_D is the thermal diffusivity in the vapor/gas dome.

Equation (3.5-174) can then be substituted in place of $\left(\frac{\zeta}{L}\right)$ in Equation (3.5-172) to give

$$\dot{M}_{vap} = h_2\left(\frac{\zeta}{k_n}\right)\left(\frac{\alpha_n}{\zeta}\right)^{\frac{1}{3}}\left(\frac{A_i}{P}\right)\left\{\bar{P}_s\bar{\rho}_s\left[\kappa_s\left(\frac{h_{fg}}{T_g\upsilon_{fg}}\right) - \beta_s\right] + \bar{\rho}_s\left(\frac{h_{fg}}{T_g\upsilon_{fg}}\right)\right\}(T_f - T_g) \tag{3.5-175}$$

which gives the rate at which water vapor is transported into the accumulator vapor/gas dome by turbulent diffusion.

Since the energy transported to the vapor/gas dome by the vaporization process must come from the liquid and since the energy per unit mass required for vaporization is h_{fg}, then the rate of energy transport to the vapor/gas dome by vaporization is

$$\dot{Q}_{vap} = \dot{M}_{vap}h_g(T_f) \tag{3.5-176}$$

where $\dot{M}_{vap}$ is the rate of vaporization at the liquid-vapor/gas interface.

In the vapor/gas dome, as the accumulator blows down, the vapor/gas temperature decreases and condensation of vapor occurs. The rate of condensation may be approximated by assuming that the vapor/gas dome remains at 100% humidity and by considering simple humidity relationships. The humidity ratio can be written as

$$w = \frac{M_s}{M_n} = \frac{N_sP_s}{N_nP_D} \tag{3.5-177}$$

where

M_s, M_n = vapor, nitrogen gas masses, respectively

N_s, N_n = vapor, nitrogen gas molecular weights, respectively.

Taking the derivative of Equation (3.5-177) gives

$$\frac{dM_s}{dt} = \frac{1}{P}\left(M_n\frac{N_s}{N_n}\frac{dP_s}{dt} - M_s\frac{dP}{dt}\right) \quad . \tag{3.5-178}$$

From equal Gibb's free energy, the equilibrium relationship between the vapor and liquid condensate in the dome is

$$\upsilon_s(P_s, T_g)\frac{dP_s}{dT_g} - S_s(P_s, T_g) = \upsilon_f(P, T_g)\frac{dP}{dT_g} - S_f(P, T_g) \tag{3.5-179}$$

and substituting the relationship

$$\frac{dP}{dt} = \frac{dP}{dT}\frac{dT}{dt} \tag{3.5-180}$$

into Equation (3.5-179) and rearranging gives

$$\frac{dP_s}{dt} = \frac{\upsilon_f(P, T_g)}{\upsilon_s(P_s, T_g)}\frac{dP}{dt} - \frac{h_g(P_s, T_g) - h_f(P, T_g)}{T_g\upsilon_g(P_s, T_g)}\frac{dT_g}{dt} \quad . \tag{3.5-181}$$

Combining Equations (3.5-178) and (3.5-177) with Equations (3.5-150) and (3.5-151) gives

$$\frac{dM_s}{dt} = \frac{1}{P}\left(M_n\frac{N_s}{N_n} - M_s\right)\frac{\upsilon_f(P, T_g)}{\upsilon_s(P_s, T_g)}\frac{1}{V_D}\left[Q_D\frac{R_n}{C_v} - P\left(1 + \frac{R_n}{C_v}\right)\frac{dV_D}{dt}\right]$$
$$+ \frac{1}{P}\frac{N_s}{N_n}\left[\frac{h_g(P_s, T_g) - h_f(P, T_g)}{T_g\upsilon_g(P_s, T_g)}\right]\frac{1}{C_{v,n}}\left(Q_D - P\frac{dV_D}{dt}\right) \tag{3.5-182}$$

and the rate of condensate formation is given as

$$\dot{M}_C = -\frac{dM_s}{dt} + \dot{M}_{vap} \quad . \tag{3.5-183}$$

The energy transported by the condensate to the interface is expressed as

$$\dot{Q}_{m_c} = \dot{m}_c h_f^s(T_g) \quad .$$
(3.5-184)

Also, since the condensation is taking place in the vapor/gas dome, the energy given up by the condensation process is given up to the vapor/gas dome at the rate expressed as

$$\dot{Q}_{M_c} = \dot{M}_c h_{fg}(T_g) \quad .$$
(3.5-185)

Finally, since it is assumed that the condensate is transported to the interface at the condensation rate, i.e.,

$$\dot{m}_c = \dot{M}_c \quad ,$$
(3.5-186)

the net energy given up to the vapor/gas dome by the condensation process can then be expressed as

$$\dot{Q}_c = \dot{Q}_{M_c} - \dot{Q}_{m_c} = \dot{m}_c [h_{fg}(T_g) - h_f^s(T_g)] \quad .$$
(3.5-187)

3.5.7.4 Energy Transported to the Vapor/Gas Dome by Combined Heat and Mass Transfer. The total energy transported to the vapor/gas dome can be rewritten by combining Equations (3.5-152), (3.5-153), (3.5-155), (3.5-176), and (3.5-187) and summing to give

$$\dot{Q}_D = (h_1 A_1 + h_2 A_2)(T_w - T_g) + h_2 A_2(T_f - T_g) + \dot{M}_{vap} h_g^s(T_f) + \dot{m}_c [h_{fg}(T_g) - h_f^s(T_g)] \quad .$$
(3.5-188)

3.5.7.5 Numerical Implementation. The numerical scheme used for the accumulator model includes special features for coupling the solution scheme to the main code in such a way that it is time step independent. This scheme is semi-implicit, and special considerations are employed to preserve the nitrogen energy and mass. Since a spherical accumulator has a variable cross-sectional area, the momentum equation is generalized to the case of a variable flow area.

The numerical scheme uses finite-difference techniques to solve the differential equations. The momentum equation is formulated by integrating Equation (3.5-147) over space and writing the time variation in difference form as

$$\left[\rho_f(L_{f_L} + L_{f_{TK}})\left(\frac{A_L}{A_f}\right) + F_f\Delta t + \rho_g(L_{g_L} + L_{g_{TK}})\left(\frac{A_L}{A_g}\right) + F_g\Delta t\right]v_{f_L}^{n+1}$$

$$= -(P^{n+1} - P^n)\Delta t + \Delta P_z\Delta t + \left[\rho_f L_{f_L} + L_{f_{TK}}\left(\frac{A_L}{A_f}\right)\right. \tag{3.5-189}$$

$$\left. + \rho_g(L_{g_L} + L_{g_{TK}})\left(\frac{A_L}{A_g}\right)\right]v_{f_L}^n - \text{CONVF} - \text{CONVG}$$

where P^{n+1} is the pressure downstream from the accumulator junction.

The inertia term is represented by

$$\rho_f(L_{f_L} + L_{f_{TK}})\left(\frac{A_L}{A_f}\right) + \rho_g(L_{g_L} + L_{g_{TK}})\left(\frac{A_L}{A_g}\right) \tag{3.5-190}$$

where L_{f_L}, $L_{f_{TK}}$, L_{g_L}, and $L_{g_{TK}}$ are the lengths of the liquid and vapor/gas in the discharge line and tank, respectively, A_L is the area of the discharge line, and A_f and A_g are the mean flow areas in the tank and discharge line of the liquid and vapor/gas, respectively. In the case of a spherical tank, A_g used in the vapor/gas inertia term is obtained from the relation

$$L_{g_{TK}}A_g = V_{g_{TK}} \tag{3.5-191}$$

and A_f used in the liquid inertia term is obtained from the relation

$$L_{f_{TK}}A_f = V_{f_{TK}} \tag{3.5-192}$$

where $V_{g_{TK}}$ and $V_{f_{TK}}$ are the vapor/gas and liquid volumes, respectively. The volume of vapor/gas in the tank is

$$V_{g_{TK}} = \frac{\pi}{3}L_{g_{TK}}^2(3R - L_{g_{TK}}), \tag{3.5-193}$$

and the available volume of liquid in the tank is

$$V_{f_{TK}} = \frac{4\pi}{3}R^3 - V_{g_{TK}} - \frac{\pi}{3}L_{min}^2(3R - L_{min}) \tag{3.5-194}$$

where L_{min} is the minimum liquid level that is determined by the position of the discharge line which may protrude into the tank. The inertia terms are computed at each time step and vary explicitly with time; as the accumulator blows down, the inertia term changes from a liquid-dominant to a vapor/gas-dominant term.

The liquid and vapor/gas friction terms, respectively, are formulated as

$$F_f = \frac{\rho_f}{2}\left(\lambda\frac{(L_{fL} + L_{f_{Tk}})}{D} + K_L\frac{L_{fL}}{L_L}\right)v_{f_L}^n\left(\frac{A_L}{A_f}\right)^2 \qquad (3.5\text{-}195)$$

for the liquid, and

$$F_g = \frac{\rho_g}{2}\left(\lambda\frac{(L_{gL} + L_{g_{Tk}})}{D} + K_L\frac{L_{gL}}{L_L}\right)v_{g_L}^n\left(\frac{A_L}{A_g}\right)^2 \qquad (3.5\text{-}196)$$

for the vapor/gas, where the friction is calculated for the tank and the line. The line friction factor λ is assumed to be the constant turbulent-turbulent Darcy friction factor given as

$$\lambda = \left[1.74 - 2\log_{10}\left(\frac{2\varepsilon}{D}\right)\right]^{-2} . \qquad (3.5\text{-}197)$$

The loss factor term, K_L, is assumed to be distributed over the discharge line length, L_L, and it is neglected in the tank. If the surge line length is 0, the loss factor term is not used. The term D is the average tank and surge line hydraulic diameter, and ε is the input wall roughness.

The elevation head term, ΔP_z, is formulated as

$$\Delta P_z = -\frac{g\Delta z_{TK}\left(\rho_f L_{f_{TK}} + \frac{1}{2}\rho_g L_{g_{TK}}\right)}{L_{TK}} - \frac{g\Delta z_L(\rho_f L_{f_L} + \rho_g L_{g_L})}{L_L} \qquad (3.5\text{-}198)$$

where Δz_{TK} and Δz_L are the tank and surge line elevation changes, respectively, and g is the gravitational acceleration.

The liquid and vapor/gas momentum flux terms, CONVF and CONVG, respectively, are formulated in linear implicit form as

$$\text{CONVF} = \frac{1}{2}\rho_f\left[1-\left(\frac{A_L}{A_f}\right)^2\right]\Delta t v_{f_L}^n(2v_{f_L}^{n+1} - v_{f_L}^n) \tag{3.5-199}$$

if there is liquid in the tank,

$$\text{CONVF} = 0.0 \tag{3.5-200}$$

where there is no liquid in the tank,

$$\text{CONVG} = \frac{1}{2}\rho_g\left[1-\left(\frac{A_L}{A_g}\right)^2\right]\Delta t v_{g_L}^n(2v_{g_L}^{n+1} - v_{g_L}^n) \tag{3.5-201}$$

if there is vapor/gas in the discharge line, and, finally

$$\text{CONVG} = 0.0 \tag{3.5-202}$$

where there is no vapor/gas in the discharge line. In the case of a spherical tank, the value of A_{TK} used in CONVF is the flow area at the liquid-vapor/gas interface, and the value of A_{TK} used in CONVG is the mean flow area of the tank. In this formulation, the momentum equation is solved over the pressure gradient from the centroid of the vapor/gas dome to the accumulator junction. However, the momentum of the fluid downstream from the accumulator junction is not included. Flow begins when the pressure, gravity, and friction forces result in positive flow out of the accumulator; and flow ceases when these forces result in reverse flow. Also, since fluxing of the vapor/gas through the junction is not allowed,

$$v_{g_L}^n = v_{f_L}^n \tag{3.5-203}$$

until the accumulator empties of liquid. The effect of this formulation is that as the accumulator blows down, the liquid-vapor/gas interface moves out of the accumulator tank and surge line. Thus, the centroid of the vapor/gas dome moves towards the centroid of the combined tank and surge line.

The pressure solution is obtained by combining Equations (3.5-145) and (3.5-149) and multiplying by $\frac{R_n}{C_{v,n}}$, which results in

$$M_n R_n \frac{dT}{dt} = -\frac{R_n P}{C_{v,n}}\frac{dV_D}{dt} + \frac{R_n}{C_{v,n}}\dot{Q}_D \tag{3.5-204}$$

where $\dot{Q}_D$ is given by Equation (3.5-188).

Since the liquid is incompressible, we obtain

$$\frac{dV_D}{dt} = -\frac{dV_f}{dt} = A_L v_{f_L} \; ; \tag{3.5-205}$$

substitution into Equation (3.5-151) and expanding in nonconservative finite difference form gives

$$P^n\left(1 + \frac{R_n}{C_{v_n}}\right) A_L \Delta t v_{f_L}^{n+1} + V_D^n (P^{n+1} - P^n) = \frac{R_n}{C_{v,n}} \dot{Q}_D^n \Delta t \quad . \tag{3.5-206}$$

The energy equation may then be solved directly for the new time vapor/gas temperature by combining Equations (3.5-148), (3.5-151), and (3.5-206) and integrating, which gives

$$T_g^{n+1} = T_g^n e^{\left(\frac{R_n}{C_{v,n}}\ln\frac{V_D^n}{V_D^{n+1}} + \Delta t \frac{R_n}{C_{v,n}}\frac{\dot{Q}_D^n}{P^n V_D^n}\right)} \quad . \tag{3.5-207}$$

The algorithm used to track the liquid level is based on the tank mass balance which is given by

$$A_L v_{f_L} = -A_{TK}\frac{dL_{g_{TK}}}{dt} \quad . \tag{3.5-208}$$

In the case of a spherical tank, A_{TK} is given by

$$A_{TK} = \pi L_{g_{TK}}(2R - L_{g_{TK}}) \quad . \tag{3.5-209}$$

Given $L_{g_{TK}}^n$, Equation (3.5-208) is solved by explicit numerical integration to obtain $L_{g_{TK}}^{n+1}$, which is of the form

$$L_{g_{TK}}^{n+1} = L_{g_{TK}}^n - \frac{A_L v_{f_L}^{n+1} \Delta t^{n+1}}{\pi L_{g_{TK}}^n (2R - L_{g_{TK}}^n)} \quad . \tag{3.5-210}$$

3.5.8 ECC Mixer

In order to calculate the process of mixing of a jet of cold water injected into a two-phase mixture and the resulting vapor condensation that follows, as in the case of emergency core cooling (ECC) injection in a PWR, a special component model, called ECCMIX, has been introduced into ATHENA.

3.5.8.1 ECCMIX Component. An ECC mixing component is a specialized branch that requires three junctions with a certain numbering order. The physical extent of the ECCMIX component is a length of the cold leg pipe centered around the position of the ECC injection location. The length of this segment should be about three times the inside diameter of the cold leg pipe. Junction number one is the ECC connection, junction number two is the cold leg cross-section through which flow enters this component in normal reactor operation, and junction number three is the one that leads to the reactor vessel. A schematic vertical cross-section of an ECCMIX component is shown in **Figure 3.5-24**. The geometrical description of the ECCMIX component is very similar to that of the JETMIXER component except for the specification of an angle for the ECC pipe connection.
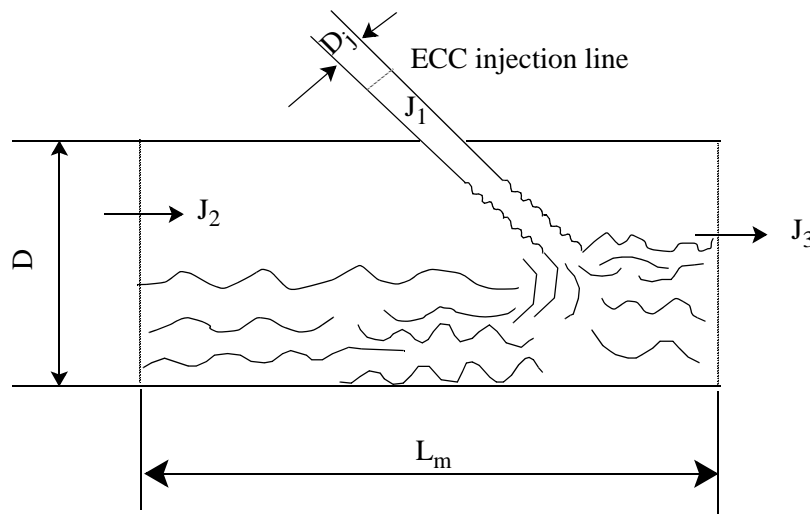
Figure 3.5-24 ECCMIX component.

The momentum effects due to the mixing for the ECCMIX component are similar to the JETMIXER component (see Section 3.5.3), except for the specification of the angle for the ECC connection. The ECCMIX component ECC connection junction is treated similarly to the JETMIXER drive junction, except that the cosine of the ECC connection junction angle is used. The ECCMIX normal flow inlet junction is treated similarly to the JETMIXER suction junction, and the ECCMIX normal flow outlet junction is treated similarly to the JETMIXER normal flow outlet junction.

The computational model for the ECCMIX component employs a particular flow regime map for condensation and, for each flow pattern, uses a different correlation for interfacial heat transfer to calculate

h_{if}, as described in detail in the following subsections. The ECCMIX component calculations are evoked only if there is subcooled ECC injection and if there is any vapor to be condensed in that component. Otherwise, the ECCMIX component is treated as an ordinary BRANCH in the ATHENA calculations.

3.5.8.2 *Flow Regimes in Condensation.* Prior to the introduction of the ECCMIX component, ATHENA included three flow regime maps, as described in the RELAP5/MOD2 manual[3.5-12] and in the RELAP5/MOD2 models and correlations report.[3.5-13] None of those, however, would apply specifically to the condensation process in a horizontal pipe near the emergency core coolant (ECC) injection point. A flow regime map for condensation inside horizontal tubes is reported by Tandon et al.,[3.5-14] and it was considered a more suitable basis for the interfacial heat transfer calculation in condensation for this geometry. A detailed description of the resultant ECC mixer volume flow regime map is found in Section 3.3.4 of this volume of the manual.

The variable names that are used in the coding for the coordinates of the condensation flow regime map are

$$\text{voider} = \frac{1 - \alpha_g}{\alpha_g} \tag{3.5--211}$$

$$\text{stargj} = v_g^* = \frac{X_{flow}G}{[gD\rho_g(\rho_f - \rho_g)]^{1/2}} \quad . \tag{3.5-212}$$

These variables are also described in more detail in Section 3.3.4.

3.5.8.3 *Vapor/Gas Mass Flux and Liquid Velocity in ECCMIX.* Before describing the calculational procedure for any of those patterns, it should be mentioned how the vapor/gas mass flux and liquid velocity inside the ECCMIX component are calculated.

3.5.8.3.1 *Vapor/Gas Mass Flux in ECCMIX--* A volume-averaged vapor mass flux ($X_{flow}G$) must be determined before the variable v_g^* can be calculated. It is given by

$$X_{flow}G = \frac{|W_{g2} + W_{g3}|}{2A} \tag{3.5-213}$$

where

$\qquad W_{g2} \qquad = \qquad$ the total vapor/gas flow rate at junction 2

$\qquad \qquad \qquad = \qquad \alpha_{gj2}\rho_{gj2}v_{gj2}A_{j2}$

W_{g3} = the total vapor/gas flow rate at junction 3

= $\alpha_{gj3}\rho_{gj3}v_{gj3}A_{j3}$

A = cross-sectional area of the ECCMIX component.

3.5.8.3.2 Liquid Velocity in ECCMIX--The liquid velocity that is used for determining the Reynolds number inside the ECCMIX component is calculated on the basis of the smallest of the absolute values of the axial liquid velocity at either end of the ECC mixer and the additional contribution of the liquid jet from the ECC connection line. The impact of the incoming ECC liquid jet is a function of the jet velocity v_{jet} and the difference between the pressure in the hydraulic cell upstream of the injection port and the pressure in the ECCMIX component, ΔP_{jet}. The equations are

$$\Delta I_{jet} = 2\frac{\Delta P_{jet}}{\rho_{fjet}}$$
(3.5–214)

and

$$v_{fres} = (\Delta I_{jet} + v_{fim}^2)^{\frac{1}{2}}$$
(3.5-215)

where

v_{fim} = $\min(|v_{fj2}|, |v_{fj3}|)$.

v_{fres} is the resultant liquid velocity that is used to determine the liquid Reynolds number in heat transfer and interfacial friction calculations.

3.5.8.4 Interfacial Heat Transfer Rates. The two-fluid model in ATHENA requires formulation of heat exchange between either phase and the interface. These are expressed as

$$Q_{ik} = H_{ik} (T^s - T_k)$$
(3.5-216)

where

k = f or g for liquid and vapor/gas, respectively

H_{ik} = volumetric interfacial heat transfer coefficient for phase k

= $h_{ik} \cdot A_i$

h_{ik} = interfacial heat transfer coefficient for phase k

A_i = interfacial area per unit volume

T^s = saturation temperature

T_k = bulk temperature of phase k.

As implied in Equation (3.5-216), the interface is assumed to be at saturation temperature, corresponding to the vapor pressure. In condensation of saturated vapor, there is almost no temperature difference between vapor and the interface, while there is a very high rate of heat transfer from the vapor to the interface (through mass transfer). For this reason, the volumetric heat transfer coefficient between vapor and the interface is set to a high constant value of 10^7 W/m^3·K.

The limiting factor is the rate of heat transfer to liquid, H_{if}. According to Equation (3.5-216), H_{if} varies with the heat transfer coefficient, h_{if}, and the interfacial area per unit volume, A_i, both of which depend on the two-phase flow pattern. The interfacial area, A_i, and the local heat transfer coefficient for the interface-to-fluid, h_{if}, are calculated with different equations for the six basic flow patterns that are identified in **Table 3.3-1**.

3.5.8.4.1 Heat Transfer to Liquid in the Six Basic Flow Patterns--The basic modes of
heat transfer to liquid are designed as:

- H_{ifb1} for wavy flow.

- H_{ifb2} for plug flow.

- H_{ifb3} for slug flow.

- H_{ifb4} for bubbly flow.

- H_{ifb5} for annular/annular-mist flow.

- H_{ifb6} for dispersed droplet flow.

Heat Transfer in Wavy Flow

<u>Interfacial Area</u>

Wavy flow inside a horizontal tube is regarded as a kind of horizontally stratified flow for the purpose of interfacial contact and exchanges between vapor/gas and liquid. With this assumption, the interfacial (contact) area between the liquid and vapor/gas is calculated from the geometrical dimensions

of the ECCMIX component, vapor/gas void fraction, and the diameter of the ECC injection pipe. **Figure 3.5-25** and **Figure 3.5-26** show schematic cross-sections of the flow topology inside the ECCMIX component in two vertical planes.
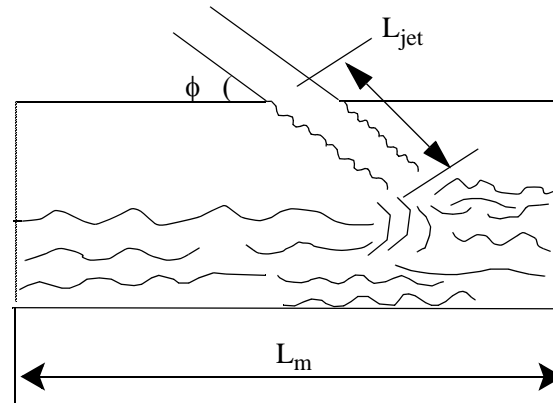
Figure 3.5-25 Schematic cross-section of stratified flow along the ECCMIX component, showing the length of interface, L_m, and the jet length, L_{jet}.
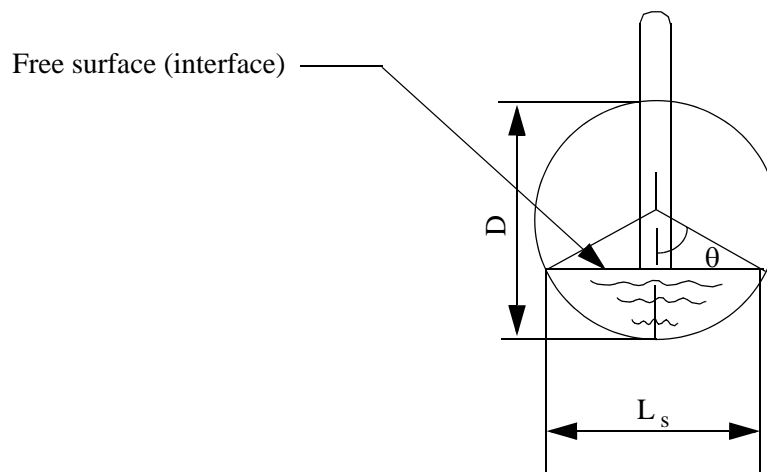
Figure 3.5-26 Schematic vertical cross-section of the ECCMIX component, showing the width of liquid surface, L_s, and the tending half-angle, θ.

The volume-average vapor/gas void fraction, α_g, is used to determine the width of the liquid surface that is a function of the half-angle, θ, facing the free surface. ATHENA uses a particular function, called HTHETA, to calculate θ for a given volume fraction that is bound by θ. If the liquid level is above the pipe center ($\alpha_g < \alpha_f$), then function HTHETA is called with α_g as an argument and θ is calculated. However, if

$\alpha_g > \alpha_f$, then α_f is used as an argument for calculating θ. For this reason, care is taken to calculate the length of the liquid jet, L_{jet}, differently for these cases, as the cylindrical surface of the liquid jet is also a part of the condensation surface. The jet surface area is given by

$$A_{jet} = \pi \, d_{jet} \bullet L_{jet} \tag{3.5-217}$$

where

$$L_{jet} \quad = \quad 0.5D \frac{(1.0 - \cos\theta)}{\sin\phi} \quad \text{if } \alpha_g < \alpha_f \tag{3.5-218}$$

$$L_{jet} \quad = \quad 0.5D \frac{(1.0 + \cos\theta)}{\sin\phi} \quad \text{if } \alpha_g \geq \alpha_f \ . \tag{3.5-219}$$

The interfacial contact area per unit volume, in this case, is the sum of the jet surface area and the rectangular horizontal interface area minus the impinging area of the jet, all divided by the component volume. It is given by

$$A_{i1} \quad = \quad \frac{A_{jet} + L_m D \sin\theta - \dfrac{S_{jet}}{\sin\theta}}{A_m L_m} \tag{3.5-220}$$

where

$$S_{jet} \quad = \quad \text{cross-sectional area of the liquid jet.}$$

A minimum value for A_{i1} that is used in the code is $(1/2)\pi \bullet d_{jet} \dfrac{L_m}{A_m \bullet L_m}$.

Heat Transfer Coefficient

The heat transfer coefficient for wavy flow is calculated according to an experimentally established correlation by Lim, Bankoff, Tankin, and Yuen,[3.5-15] based on their data from condensation in cocurrent flow of vapor/gas and liquid in a horizontally stratified flow situation. The correlation that is taken from **Reference 3.5-15** is the one that is recommended for the case of rough liquid surface, namely

$$Nu \ = \ 0.0344(Re)_g^{0.58}(Re)_f^{0.42}(Pr)_f^{0.33} \tag{3.5-221}$$

where

| Nu | = | Nusselt number |

Re = Reynolds number

Pr = Prandtl number (see nomenclature).

Using this correlation for Nusselt number, the overall heat transfer coefficient from the interface to liquid, per unit volume, in wavy flow is expressed as

$$H_{ifb1} = A_{i1} Nu\left(\frac{k_{fm}}{D}\right) \quad . \tag{3.5-222}$$

Heat Transfer in Plug Flow

Interfacial Area

According to the flow regime map (**Figure 3.3-4**), this flow pattern exists for vapor/gas void fractions between 0.25 and 0.666. It is assumed that the interfacial area changes from completely stratified at voider = 0.5 (α_g = 0.666) to a complete circular cross-section of the ECCMIX component at voider = 3.0 (for α_g = 0.25). Hence, the interface area is interpolated between these limits, using the following parameter:

$$tv1 = 0.4 \, (voider - 0.5) \quad \text{for } 0.5 < voider < 3.0 \quad . \tag{3.5-223}$$

The interfacial area for the stratified flow condition is calculated according to Equation (3.5-220), and the interpolated area for wavy flow is

$$A_{12} = (1.0 - tv1)A_{i1} + tv1\left(\frac{1}{L_m}\right) \quad . \tag{3.5-224}$$

Heat Transfer Coefficient

Since plug flow is considered an extension of the wavy flow pattern with interrupting liquid plugs, the same heat transfer coefficient that was used for wavy flow, Equation (3.5-221), has been used for plug flow. Hence, the overall heat transfer coefficient from interface to liquid, per unit volume, in plug flow is

$$H_{ifb2} = A_{i2} Nu\left(\frac{k_{fm}}{D}\right) \tag{3.5-225}$$

in which Nu is given by Equation (3.5-221).

Heat Transfer in Slug Flow

Interfacial Area

Slug flow is assumed to always include some contribution of the bubbly flow pattern; hence, there is a gradual changeover from slug flow to a pure bubbly flow. The degree of this transition depends on vapor/gas void fraction. This approach is used for all volumes in ATHENA (see Volume IV). There is only a slight modification in the application of this approach to the ECCMIX component, that is, the lower limit of vapor/gas void fraction is set at $\alpha_b = 0.20$ and the upper end void fraction is set at $\alpha_c = 0.666$. These changes had to be imposed according to the limits specified for slug flow in the modified flow regime map for condensation, as shown in **Figure 3.3-4**.

The interfacial area of slug bubbles (these are called Taylor bubbles in **Reference 3.5-13**) per unit volume is calculated as

$$A_{i3s} = 4.5\frac{\alpha_s}{D} \tag{3.5-226}$$

where

$$\alpha_s = \frac{(1-\alpha_g)-\alpha_{bb}}{1-\alpha_{bb}} \tag{3.5-227}$$

$$\alpha_{bb} = \alpha_b \exp\left\{-\left[\frac{6.778}{\alpha_c-\alpha_b}(\alpha_g-\alpha_b)\right]\right\}. \tag{3.5-228}$$

The numerical value of α_{bb} varies from 0.2 (= α_b) when $\alpha_g = \alpha_b$ to about 0.0002277 when $\alpha_g = \alpha_c$. As a result, A_{i3s} varies from 0.0 at $\alpha_g = 0.2$ to about $4.5\left(\frac{1.0-\alpha_g}{D_c}\right)$ for $\alpha_g = \alpha_c$.

The variable α_{bb} is also used to calculate the contribution of the small bubbles to the interfacial area, for both heat and shear transfer calculations. The calculation of bubble flow area, average bubble diameter and hydraulic diameter, as a function of α_g and α_{bb}, are performed in a subroutine called FIDIS. This is a part of ATHENA and is documented in Volume IV.

Heat Transfer Coefficient

For the slug part, the heat transfer coefficient is calculated for the Taylor bubbles moving through liquid. The correlation that is explained in Volume IV, is

$$Nu_{tb} = 1.18942\ (Re_{tb}Pr)^{0.5} \tag{3.5-229}$$

where

$$Re_{tb} \quad = \quad \frac{\rho_f \bullet [min(|v_g - v_f|,\ 0.8\,m/s)]D}{\mu_f}\ . \tag{3.5-230}$$

The overall heat transfer coefficient from the interface to the liquid, per unit volume, in slug flow is

$$H_{ifb3}\ =\ A_{i3s}Nu_{tb}\left(\frac{k_{fm}}{D}\right) + H_{ifb4} \tag{3.5-231}$$

in which H_{ifb4} is the contribution of the heat transfer by small bubbles in slug flow, and is calculated by consecutive calls to two of the existing subroutines in ATHENA, namely subroutines FIDIS and HIFBUB, according to the procedure that is described in the following section.

Heat Transfer in Bubbly Flow

Interfacial Area

The interfacial area per unit volume for bubbly flow in the ECCMIX component is calculated in the same manner that is done for all other components in ATHENA, as documented in Volume IV. The interfacial area per unit volume for bubbles is

$$A_{i4}\ =\ \frac{0.72\alpha_g\rho_f(v_g - v_f)^2}{\sigma}\ . \tag{3.5-232}$$

The derivation of this equation and the assumptions used in its derivation are given in Volume IV of this manual. Among other things, it is assumed that the average bubble diameter is 0.5 d_{max} and that d_{max} is determined by using a critical Weber number of Wec = 10. Computation of A_{i4} is done by using the FIDIS subroutine in ATHENA.

Heat Transfer Coefficient

For the bubbly flow regime, the heat transfer coefficient between the interface and liquid is calculated with a model based on the modified Unal bubble collapse model[3.5-16,3.5-17] and the Lahey model.[3.5-18] This is the same model that is used in non-ECCMIX volumes.

The heat transfer coefficient between the interface and liquid, per unit volume, in bubbly flow that is calculated in the HIFBUB subroutine is according to the following equation:

$$H_{ifb4} = \frac{F_5 \alpha_g h_{fg} \rho_f \rho_g}{\rho_f - \rho_g}$$
(3.5-233)

where

F_5 $=$ $0.075 \dfrac{1}{K \cdot s}$ $\quad$ for $\alpha_{bub} \geq 0.25$ (3.5-234)

F_5 $=$ $1.8\phi C \exp(-45\alpha_{bub}) + 0.075 \dfrac{1}{K \cdot s}$ $\quad$ for $\alpha_{bub} < 0.25$ (3.5-235)

C $=$ $65.0 - 5.69 \times 10^{-5} (P - 1.0 \times 10^5) \dfrac{1}{K \cdot s}$ $\quad$ for $P \leq 1.1272 \times 10^6$ Pa (3.5-236)

C $=$ $\dfrac{2.5 \times 10^9}{P^{1.418}} \dfrac{1}{K \cdot s}$ $\quad$ for $P > 1.1272 \times 10^6$ Pa (3.5-237)

ϕ $=$ 1.0 $\quad$ for $|v_f| \leq 0.61$ m/s (3.5-238)

ϕ $=$ $(1.639344 \, |v_f|)^{0.47}$ $\quad$ for $|v_f| > 0.61$ m/s (3.5-239)

α_{bub} $=$ $\max(\alpha_g, 10^{-5})$. (3.5-240)

Heat Transfer in Annular/Annular-Mist Flow

Heat transfer between interface and liquid in the annular and annular-mist flow regimes is calculated according to the procedures that are used in TRAC-BF1.[3.5-19,3.5-21,3.5-21] According to this model, the interfacial exchanges of heat and momentum at the interface have two components, one at the interface between the vapor/gas core and the liquid film on the walls and another one at the interface between the vapor/gas and the entrained liquid droplets. The contribution of the entrained droplets is minimal at the start of the annular flow, but the entrained liquid fraction increases with increasing vapor/gas velocity and it becomes 100% at the end of the annular flow, that is the start of dispersed droplet (mist) flow. Variations of the entrainment fraction serve as an interpolation mechanism in the calculation of interfacial exchanges between the annular and droplet flows.

<u>Liquid Droplet Entrainment Fraction</u>

The fraction of liquid flow entrained as droplets is calculated with the equation recommended by Andersen et al.[3.5-21,3.5-22] It is given by

$$E_f = \frac{X_e - 0.03}{[1.0 + (X_e + 0.1)^2]^{0.5}}$$ (3.5-241)

in which

$$X_e = 1.0^{-6} \bullet j_g^{*\ 2.5} D^{*\ 1.25} Re_{rel}^{0.25}$$ (3.5-242)

where

$$D^* = D \left[\frac{g(\rho_f - \rho_g)}{\sigma} \right]^{1/2}$$ (3.5-243)

$$j_g^* = \frac{\alpha_g v_g}{\left[\frac{\sigma g(\rho_f - \rho_g)}{\rho_g^2} \left(\frac{\rho_g}{\rho_f - \rho_g} \right)^{0.667} \right]^{0.25}}$$ (3.5-244)

$$Re_{rel} = \frac{\alpha_f \rho_f v_f D}{\mu_f} .$$ (3.5-245)

A vapor/gas void fraction for the vapor/gas droplet mixture of the core is calculated as

$$\alpha_{dc} = 1.0 - (1.0 - \alpha_g) E_f$$ (3.5-246)

and a vapor/gas void fraction corresponding to the liquid in the film alone is calculated as

$$\alpha_f = 1.0 - (1.0 - \alpha_g)(1 - E_f) .$$ (3.5-247)

With these definitions, the two components of interfacial area and heat transfer are calculated in the following way:

Film Interfacial Area

The average film thickness is

$$\delta_f = 0.5 D(1.0 - \alpha_f)^{0.5} .$$ (3.5-248)

A minimum film thickness is calculated as[3.5-21,3.5-22]

$$\delta_{fmin} = \left(\frac{18\mu_f^2 \sigma}{g^2 \rho_f^3} \right)^{0.2} .$$

(3.5-249)

The average film thickness is selected as

$$\delta_{fa} = \max \left(\delta_f, \delta_{fmin} \right) .$$

(3.5-250)

A void fraction corresponding to δ_{fmin} is calculated as

$$\alpha_{min} = \left(1.0 - \frac{2\delta_{fmin}}{D} \right)^2 .$$

(3.5-251)

Since the inside diameter of the liquid film is related to the inside diameter of the channel, D_c, through α_f by the relationship $D_i = D_c(\alpha_f)^{1/2}$, the interfacial area per unit volume for the liquid film is then

$$A_{i5f} = 4.0 \frac{(\alpha_f)^{1/2}}{D} .$$

(3.5-252)

If $\alpha_{min} < \alpha_g$, then

$$A_{i5f} = 4 \frac{(\alpha_f)^{1/2}}{D} \frac{1.0 - \alpha_f}{1.0 - \alpha_{min}} .$$

(3.5-253)

Droplet Interfacial Area

According to **Reference 3.5-22**, an average droplet diameter is calculated based on the total mass flux, j_{mt}, given by

$$j_{mt} = |\alpha_g v_g + (1 - \alpha_g) v_f| .$$

(3.5-254)

The relative droplet velocity is

$$v_{drop} = 1.414 \left[\frac{g\sigma(\rho_f - \rho_g)}{\rho_g^2} \right]^{0.25} .$$

(3.5-255)

However, if

$$j_{mt} > 1.456 \left[\frac{g\sigma(\rho_f - \rho_g)}{\rho_g^2} \right]^{0.25} \left[\frac{\mu_g^2}{\sigma\rho_g \sqrt{\frac{\sigma}{g(\rho_f - \rho_g)}}} \right]^{-1/12}$$ (3.5-256)

then

$$v_{drop} = \frac{3\sigma}{\rho_g} \left[\frac{g^2(\rho_f - \rho_g)^2}{\mu_g\rho_g} \right]^{0.33} j_{mt}^{-2} \ .$$ (3.5-257)

These are based on Ishii's work.[3.5-23] The droplet velocity is used to calculate the average droplet diameter, based on a critical Weber number of 2.7. The average droplet diameter is given by

$$D_{drop} = \frac{2.7\sigma}{\rho_g \bullet \max(v_{drop}^2, j_{mt}^2)} \ .$$ (3.5-258)

In order to avoid physically unrealistic values for D_{drop}, it is compared to some limiting values and adjusted if necessary. These are:

• If $D_{drop} < 2.0 \times 10^{-4}$ m, then $D_{drop} = 2.0 \times 10^{-4}$ m.

• If $D_{drop} > 0.25 \ D_c$, then $D_{drop} = 0.25 \ D_c$.

Another limit on D_{drop} is that of no more than 10^6 droplets per cubic meter, which gives

$$D_{drop} \leq D_{dropl} = \left(6\frac{1 - \alpha_g}{10^6 \pi + 1} \right)^{0.333} \ .$$ (3.5-259)

The adjusted droplet diameter is then used to calculate the droplet interfacial area per unit volume, that is

$$A_{i6} = 6\frac{1.0 - \alpha_{dc}}{D_{drop}} \ .$$ (3.5-260)

<u>Film Interfacial Heat Transfer Coefficient</u>

The heat transfer coefficient at the film interface is calculated according to **Reference 3.5-21** with the following equation that is based on Megahed's work.[3.5-24]

$$h_{iff} = \frac{0.0771 C_{pf} \dot{m}_f}{\pi D_{if} (j_{ax} Re_{ff})^{2/3}} \left(\frac{g \rho_f^2}{\mu_f^2} \right)^{1/3} \qquad (3.5\text{-}261)$$

in which $\dot{m}_f$ is the film mass flow rate and Re_{ff} is the Reynolds number based on that flow. These variables and j_{ax} are given below:

$$\dot{m}_f = (1 - E_f)(1 - \alpha_g) \rho_f v_f A_m \qquad (3.5\text{-}262)$$

$$j_{ax} = \frac{C_{pf}(T^s - T_f)}{h_{fg}} \left(\frac{\rho_f}{\rho_g} \right)^{1/2} \qquad (3.5\text{-}263)$$

$$Re_{ff} = \frac{4 \dot{m}_f}{\mu_f \pi D} \quad . \qquad (3.5\text{-}264)$$

The inside film diameter, D_{if}, that is used in Equation (3.5-261) is considered to be more relevant to the interface than D that has been used in TRAC-BF1 coding of this equation.

<u>Droplet Interfacial Heat Transfer Coefficient</u>

The heat transfer coefficient for interface to droplets based on the works of Andersen et al.[3.5-25] is

$$h_{id} = 1.8 \pi^2 \frac{k_f}{D_{drop}} \quad . \qquad (3.5\text{-}265)$$

Hence, for annular-mist flow, including droplet entrainment, the overall rate of heat transfer to liquid, per unit volume, is

$$H_{ifb5} = A_{i5f} h_{iff} + A_{i6} h_{id} \quad . \qquad (3.5\text{-}266)$$

Heat Transfer in Dispersed Droplet Flow

The interfacial area per unit volume and the heat transfer coefficient for droplets were described above. The overall heat transfer rate to liquid in this flow regime is

$$H_{ifb6} = A_{i6}h_{id} \tag{3.5-267}$$

where A_{i6} and h_{id} are given by Equations (3.5-260) and (3.5-265), respectively.

3.5.8.4.2 Heat Transfer to Liquid in Transition Zones--As shown in **Table 3.3-1**, there are five transition zones in the modified condensation flow regime map. The numerical values of the heat transfer rates, H_{if}, in the adjacent zones of the basic mode may vary considerably, and a linear interpolation over the boundary zones would not be adequate to produce a smooth transition. For this reason, an exponential interpolation is employed, as detailed in the following.

For transition between wavy and annular-mist flows,

$$H_{ift1} = H_{ifb5}^{(1-van)}H_{ifb1}^{van} \tag{3.5-268}$$

where

$$van \quad = \quad 9 - 8\,v_g^* \qquad \text{for } 1 \le v_g^* \le 1.125.$$

For transition between wavy and slug flows,

$$H_{ift2} = H_{ifb3}^{psw}H_{ifb1}^{(1-psw)} \tag{3.5-269}$$

where

$$psw \quad = \quad 8\frac{1-\alpha_g}{\alpha_g} - 4 \qquad \text{for } 0.5 \le \frac{1-\alpha_g}{\alpha_g} \le 0.625. \tag{3.5-270}$$

For transition between wavy, plug, and slug flows (double interpolation, first an interpolation is made in terms of v_g^* and then another one in terms of $\frac{1-\alpha_g}{\alpha_g}$),

$$H_{ift3} = H_{iftsp}^{p2}H_{ifb1}^{(1-p2)} \tag{3.5-271}$$

where

$$H_{iftsp} \quad = \quad H_{ifb2}^{(1-p1)}H_{ifb3}^{p1} \tag{3.5-272}$$

$$p1 \quad = \quad 400v_g^* - 4 \qquad \text{for } 0.01 \le v_g^* \le 0.0125 \tag{3.5-273}$$

$$p2 \quad = \quad 8\frac{1-\alpha_g}{\alpha_g} - 4 \qquad \text{for } 0.5 \leq \frac{1-\alpha_g}{\alpha_g} \leq 0.625 . \tag{3.5-274}$$

For transition between plug and slug flows,

$$H_{ift4} = H_{ifb2}^{(1-pp)}H_{ifb3}^{(1-pp)} \tag{3.5-275}$$

where

$$pp \quad = \quad 400v_g^* - 4 \qquad \text{for } 0.01 \leq v_g^* \leq 0.0125 . \tag{3.5-276}$$

Finally, for transition between bubbly and plug flows,

$$H_{ift5} = H_{ifb4}^{pb}H_{ifb2}^{(1-pb)} \tag{3.5-277}$$

where

$$pb \quad = \quad \frac{1-\alpha_g}{\alpha_g} - 3.0 \qquad \text{for } 3.0 \leq \frac{1-\alpha_g}{\alpha_g} \leq 4.0 . \tag{3.5-278}$$

Computation of the interfacial heat transfer according to these equations is done in the ECCMXV subroutine, that is called within subroutine PHANTV, whenever the ECCMIX component is encountered and specific logical tests indicate that there is some vapor/gas in this component and a flow of subcooled liquid is entering through the ECC injection line. Otherwise, the ECCMIX component is treated just as a regular BRANCH component in the ATHENA calculations.

3.5.8.5 Effect of Noncondensable Gases. It is known that the presence of noncondensable gases, such as air or pure nitrogen, reduces the rate of condensation. An experimental study of the effect of noncondensable gases at different partial pressures on the rate of condensation heat transfer is reported by DeVuono and Christensen.[3.5-26] According to their findings, the degradation in the condensation heat transfer with concentration of noncondensible can be correlated with the following:

$$f_r = (1.0 - y)^{4.31} \qquad \text{for } 0 < y < 0.14 \tag{3.5-279}$$

where

f_r = reduction factor in condensation heat transfer

y = noncondensible concentration (noncondensible volume at prevailing pressure and time divided by total volume).

The reduction factor, f_r, of Equation (3.5-279) is applied to H_{if} as calculated in the ECCMXV subroutine. It should be noted that the actual plots of measured data reported in **Reference 3.5-26** indicate a much stronger sensitivity to noncondensible concentration as compared to what can be calculated with their correlation.

3.5.8.6 Interfacial Friction. Calculation of the interfacial friction for different flow patterns in the ECCMIX component is done with the same correlations that are used for similar flow patterns in all other horizontal components in ATHENA. The only remarks to be made on the interfacial friction calculations in the ECCMIX components are the following:

- Transition between different flow patterns is according to the modified condensation flow regime map.

- Linear interpolation is used between the friction values of the basic pattern around each interpolation zone, employing the same interpolation variables that were used for interfacial heat transfer in those boundary zones.

- For plug flow, it is assumed that the two phases are locked into each other; hence, the interfacial friction factor is set to 1.

Computation of the interfacial friction factors is performed in a separate subroutine called ECCMXJ, whenever the ECCMIX component is encountered and specific logical tests indicate that there is some vapor/gas in the ECCMIX component and that a flow of subcooled liquid is entering through the ECC injection line. Otherwise, the ECCMIX component is treated just as a regular BRANCH in the ATHENA calculations.

3.5.8.7 Wall Friction. The two-fluid model of ATHENA requires that each phase should have its own fraction of the wall friction for momentum balance. The distribution of the total wall friction between vapor/gas and liquid varies with flow regimes. Calculations of the fractions of wall friction for each phase in different flow regimes are done according to the same procedures that are used in other components. However, transition between different flow regimes is determined in the same way that is used for the interfacial heat and momentum transfer calculations. The only differences that are introduced for wall friction in the ECCMIX component are the following:

- In bubbly flow, 100% of the wall friction is assigned to the liquid phase and nothing to the vapor/gas phase.

- In droplet flow, 100% of the wall friction is assigned to the vapor/gas phase and nothing to the liquid phase.

- Linear interpolation is used for wall friction over the transition zones, employing the same interpolation variables that were defined for the interfacial heat transfer.

Computations of wall friction fractions for vapor/gas and liquid are performed in parallel with the H_{if} calculations in the ECCMXV subroutine.

3.5.9 Annulus

For an annulus component in the annular-mist regime for both the junction and volume flow regimes, the code assumes that all the liquid is in the film and that there are no drops. Thus, $\alpha_{ff} = \alpha_f$ and $\alpha_{fd} = 0$. This was based on work by Schneider[3.5-27] on ATHENA calculations for UPTF Test 6, who showed that this was necessary in order to get downcomer penetration following a cold leg break. In addition, the Bharanthan[3.5-28] correlation used in RELAP5/MOD2 was replaced by a standard laminar correlation and the modified Wallis[3.5-29] correlation in the turbulent region for the interfacial drag when in the annular-mist flow regime (for either an annulus or any other component). Schneider found this was also necessary in order to get downcomer penetration in UPTF Test 6. This interphase drag approach for an annulus component was also used in RELAP5/MOD1.

3.5.10 Pressurizer

For a pressurizer component, the surgeline connection junction number of the junction connecting the bottom volume of the pressurizer to the surgeline volume is required input. As liquid drains out of the bottom volume through this junction, the code will donor out just liquid (rather than two-phase as is done with the pipe or annulus). For the pressurizer component, a pressurizer liquid level is calculated and is available for the major edits and the minor edits/plots. In addition for the pressurizer, the user is allowed to input a constant interfacial heat transfer coefficient for liquid in the vertically stratified flow regime and the level tracking flow regime, a constant interfacial heat transfer coefficient for vapor/gas in the vertically stratified flow regime and the level tracking flow regime, a multiplier on the film thickness in the annular-mist flow regime, a multiplier on the interfacial heat transfer coefficients for both liquid and vapor/gas in the vertically stratified flow regime and the level tracking flow regime, the pressurizer spray droplet diameter, the pressurizer spray junction identifier, and the pressurizer spray mixing coefficient. These are discussed in more detail in the next sections.

When the bottom volume of the pressurizer (volume I) is in the vertically stratified flow regime or the level tracking flow regime, a downwind donor-cell process is used for calculating the junction volume fractions at the surge line junction if a criterion is met. The criterion used is

$$\alpha_{fI} > 0.05 \tag{3.5-280}$$

where α_{fI} is the liquid volume fraction in the bottom pressurizer volume (volume I). For this situation, the volume fractions at the surge line junction (junction j) are given by

$$\dot{\alpha}_{fj} = \alpha_{fK} \tag{3.5-281}$$

$$\dot{\alpha}_{gj} = \alpha_{gK} \qquad\qquad (3.5\text{-}282)$$

where volume K is downstream of volume I. For all other situations, the normal upwind donor cell process is used for calculating the junction volume fractions at the surge line junction.

The pressurizer liquid level is calculated using the equation

$$level = \sum_{k=1}^{k_1} \alpha_{fk}dl_k + \sum_{k=1}^{k_2} dl_k \qquad\qquad (3.5\text{-}283)$$

where k_1 is the number of volumes in the pressurizer with a liquid volume fraction less than or equal to 0.99 (i.e., $\alpha_{fk} \leq 0.99$), k_2 is the number of volumes in the pressurizer with a liquid volume fraction greater than 0.99, α_{fk} is the liquid volume fraction of pressurizer volume k, and dl_k is the length of pressurizer volume k.

There are several other models that are specific to the pressurizer component. The user may specify the interfacial heat transfer coefficients to liquid and vapor/gas for the volume containing a stratified liquid level (either a liquid level created by the vertical stratification model or by the two-phase level tracking model). The user may also specify a general table or control variable whose output value is used as a multiplier on both the liquid and vapor/gas interfacial heat transfer coefficients for the volume in the pressurizer containing the stratified liquid level. The user may specify a general table or control variable whose output value multiplies the fraction of the available liquid in the annular-mist flow regime that resides in the liquid film. The user may specify the size of the droplets in the annular-mist and mist flow regimes. Finally, the user may activate a spray induced, enhanced condensation model. All of these options are provided so that the user may adjust the condensation rate between the liquid and vapor/gas phases in the pressurizer. The first three options may be used to adjust the condensation on the stratified liquid interface. The last two options may be used to adjust the condensation rate when the pressurizer spray is activated. The film fraction is the annular-mist flow regime is normally computed from an entrainment correlation. The correlation is appropriate for co-current or counter-current upflow in which the droplets are produced by entrainment from the film. This correlation is not appropriate for situations where the droplets are produced by spray nozzles. Because the production of droplets depends on the goemetry of the spray nozzle, the user may input the size of the droplets for a particular geometric arrangement. The last option provides for the enhancement of the condensation on the stratified liquid inferface due to the impingement of spray droplets. Impingement of the spray droplets on the surface of the liquid pool causes mixing of the upper layers of the pool. If the liquid in the pool is subcooled, this mixing lowers the temperature at the interface causing enhanced condensation. The model postulates that the enhanced condensation is function of the spray impingement rate and the subcooling in the pool.

The spray induced, enhanced pool condensation rate is given by

$$\dot{m}_{c,\,sp} = C\,\dot{m}_s \left(\frac{h_f^s - h_f}{h_g - h_f^s} \right) \qquad (3.5\text{-}284)$$

where

$\dot{m}_{c,\,sp}$ = spray induced, enhanced pool condenation rate (kg/sec)

C = user input mixing coefficient (-)

$\dot{m}_s$ = spray flow rate into liquid pool (kg/sec)

h_f^s = saturated liquid specific enthalpy (J/kg)

h_f = bulk liquid specific enthalpy in volume containing the liquid-vapor interface (J/kg)

h_g = vapor specific enthalpy at pool surface (J/kg).

The spray flow rate into the liquid pool consists of the total flow rate of liquid into the pool minus the flow rate of liquid into the pool along the walls of the pressurizer due to wall condensation. This flow consists of the flow through the spray junction plus any condensate on the spray droplets as they fall through the vapor space before impinging on the pool surface. This flow rate is computed in ATHENA as the flow rate of liquid into the liquid pool through the junction above the pool minus the summation of the wall condensation rates on the heat structures attached to volumes in the vapor space above the volume containing the liquid pool. This flow rate is given by

$$\dot{m}_s = \dot{m}_{f,\,j} - \sum_{i=j}^{N} \Gamma_{w,\,i} \qquad (3.5\text{-}285)$$

where

$\dot{m}_{f,\,j}$ = liquid flow rate in junction j (kg/sec)

j = index of volume containing liquid-vapor interface

$\Gamma_{w,\,i}$ = wall condensation rate in volume i (kg/sec),

N = total number of volumes in pressurizer component.

The spray induced, enhanced pool condensation rate is only computed if there is flow into the pressurizer through the spray junction.

3.5.11 Feedwater Heater

For a feedwater heater (FWHTR) component (**Figure 3.5-27**), a variation on the branch component is used to represent the shell and one or more pipes represent a tube bundle within the shell. Feedwater heaters transfer heat from the shell to the tubes primarily by condensing steam on the outside of the tubes.

.
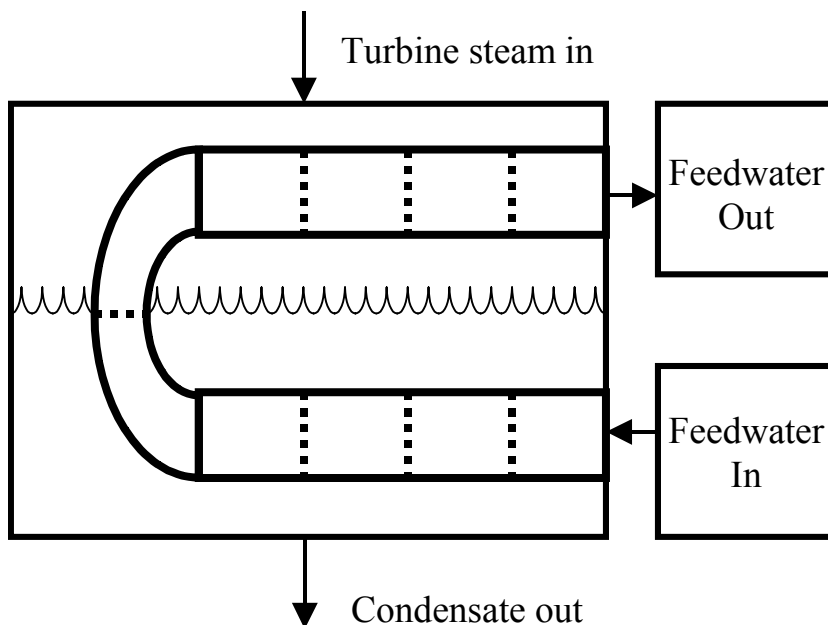
Figure 3.5-27 Schematic of feedwater heater component

It is required that the shell and pipes be defined as horizontal, that the number of junctions connected to the shell be two or three (one for vapor inlet, one for a condensatate output and an optional third junction for condensate inlet), and that the stratification entrainment/pullthrough option should be specified for all junctions connected to the feedwater heater shell. Optional data may be entered vis a table that relates the water level in the shell to the shell void fraction. Data for the right side (i.e., outside surface) of the heat slabs representing the tube walls in a FWHTR includes a specification of the top and bottom elevation of the tube bundle relative to the bottom of the shell.

When the flow regime in the FWHTR is horizontally stratified, heat transfer from the shell side to the tubes (right side of heat slabs) is computed using a condensation heat transfer correlation for the portion of the tubes exposed to steam and a convection correlation for the portion of the tubes exposed to liquid.

3.5.12 Compressor

The compressor model is similar to the existing pump model in ATHENA. It performs the same function on a gas as the pump performs on single-phase and two-phase fluids. It is anticipated that the compressor will usually be driven by a turbine on the same shaft, although the other capabilities presently available in the pump, i.e. the speed table, the motor torque table, and the coastdown feature are also

available in the compressor. The compressor head curve is specified differently than that of the pump homologous curves, and the compressor torque is calculated based on the characteristic curves and the stage efficiency. The compressor consists of an inlet junction and a control volume, and optionally, an outlet junction. The outlet connection can also be an ordinary junction or another compressor component.

3.5.12.1 *Compressor Model Description.* In a compressor, a change in angular momentum of the working fluid is caused by forces acting in the tangential direction only. Radial and axial forces are constrained by the physical design. Therefore, the total torque applied to a compressor can be thought of as being composed of two parts, one which changes the angular momentum of the fluid, and the other which results in reactive forces in the journal and thrust bearings. In principle, then, the isentropic torque can be calculated by considering an isentropic compression of the fluid and then applying an efficiency factor to get the total torque.

The compressor model begins with the conservation of angular momentum for the compressor rotor. A mass of fluid enters with an initial azimuthal velocity $v_{\theta 1}$ at a radius r_1 and exits with azimuthal velocity $v_{\theta 2}$ at a radius r_2. The torque, τ, required for this angular acceleration is[3.5-30] :

$$\tau = \dot{m}(r_1 \cdot v_{\theta 1} - r_2 \cdot v_{\theta 2}) \tag{3.5-286}$$

The rate of energy transfer (N-m/sec or ft-lb$_f$/sec) is the product of the torque and the angular velocity (ω)

$$\tau \cdot \omega = \dot{m}(r_1 \cdot \omega \cdot v_{\theta 1} - r_2 \cdot \omega \cdot v_{\theta 2}) \tag{3.5-287}$$

We can also write the steady state, steady-flow energy equation for the control volume that contains the compressor rotor[3.5-31] :

$$\dot{Q}_{c.v.} + \dot{m}\left(h_1 + \frac{v_1^2}{2} + z_1 g\right) = \dot{m}\left(h_2 + \frac{v_2^2}{2} + z_2 g\right) + \dot{W}_{c.v.} \tag{3.5-288}$$

The stagnation, or total, specific enthalpy is defined as

$$h^T = h + \frac{v^2}{2}$$

Assume that the azimuthal angular acceleration associated with the torque in Equation (3.5-286) is isentropic and neglect changes in potential energy. Combining Equations (3.5-287) and (3.5-288),

$$\dot{W}_{c.v.} = \tau_S \cdot \omega = \dot{m}(h_1^T - h_{2'}^T) \tag{3.5-289}$$

where s denotes that the process is isentropic, and $h_{2'}^T$ refers to the isentropic specific enthalpy at State 2. Equation (3.5-289) represents the isentropic work performed on the fluid by accelerating the fluid in the tangential direction. State 1, at the inlet of the compressor, is given by the upstream conditions. The specific entropy can be found as a function of total specific enthalpy and density,

$$S_1 = S(h_1^T, \rho_1) \ .$$

The total pressure at State 2 is determined from the tables of pressure ratio versus rotational velocity and flow rate. Pressure ratio is defined as

$$R_p = R_p(\omega, \dot{m}) = \frac{P_2^T}{P_1^T} \tag{3.5-290}$$

Therefore, P_2^T is

$$P_2^T = P_1^T \cdot R_p \tag{3.5-291}$$

Because the work between States 1 and 2 is isentropic, the conditions at State 2 are determined as follows:

$$S_2 = S_1$$
$$h_{2'}^T = h(P_2^T, S_2) \tag{3.5-292}$$

and the torque corresponding to the isentropic work is

$$\tau_S = \frac{\dot{m}}{\omega}(h_{2'}^T - h_1^T) \tag{3.5-293}$$

Note the sign is reversed compared to Equation (3.5-289), which indicates that work is done on the fluid. This is consistent with the sign convention within the ATHENA pump component. The adiabatic efficiency is defined as

$$\eta_{ad} = \frac{\text{Isentropic work}}{\text{Actual work}} = \frac{h_{2'}^T - h_1^T}{h_2^T - h_1^T} \tag{3.5-294}$$

from which we can obtain the actual state

$$h_2^T = \frac{h_{2'}^T - (1 - \eta_{ad})h_1^T}{\eta_{ad}} \tag{3.5-295}$$

The irreversible, or dissipative, torque is

$$\tau_d = \frac{\dot{m}}{\omega}(h_2^T - h_{2'}^T) \tag{3.5-296}$$

The compressor dissipation is the energy associated with the work due to friction,

$$\dot{W}_d = \tau_d \cdot \omega \tag{3.5-297}$$

and is added to the energy equation in the same manner as the corresponding pump dissipation is added. The above derivation assumes isentropic compression to obtain the conditions at State 2, and requires entropy-based property table look-up calls, which are not presently in the code. However, torque can be calculated from the work input to the fluid without the isentropic condition if an assumption is made regarding the conditions at State 2. The momentum equation for the compressor can be written in the form[3.5-32]

$$\int_{P_1}^{P_2} \frac{dP}{\rho} + \frac{v_2^2 - v_1^2}{2} = g \cdot H \tag{3.5-298}$$

where g is gravitational acceleration, and H is the head added to the fluid by the compressor. Assuming a mean density that is independent of pressure,

$$\rho_m = \frac{\rho_1 + \rho_2}{2} \, ,$$

Equation (3.5-298) can be integrated to give

$$P_2 + \frac{\rho_m v_1^2}{2} = P_1 + \frac{\rho_m v_1^2}{2} + \rho \cdot g \cdot H \tag{3.5-299}$$

and can be written in terms of total pressure

$$P_2^T = P_1^T + \rho_m \cdot g \cdot H = P_1^T + P_1^T(R_p - 1) \tag{3.5-300}$$

where the pressure ratio is obtained as shown by Equation (3.5-290). The compressor head that is added to the momentum equation is therefore

$$\Delta P \;=\; \rho \cdot g \cdot H \;=\; P_1^T (R_p - 1) \;=\; P_2^T \frac{R_p - 1}{R_p} \tag{3.5-301}$$

By assumption, the heat into the system is zero, so the total work input to the fluid is

$$\dot{W}_{c.v.} \;=\; \dot{m}(h_2^T - h_1^T) \;=\; \dot{m}(h_{2'}^T - h_1^T) + \dot{m}(h_2^T - h_{2'}^T) \;=\; \dot{W}_s + \dot{W}_d \tag{3.5-302}$$

again using the sign convention where work on the fluid is positive. The isentropic work is calculated from the increase in potential energy in the control volume

$$\dot{W}_s \;=\; \dot{m} \cdot g \cdot H \;=\; \frac{\dot{m}\Delta P}{\rho_m} \tag{3.5-303}$$

The torque corresponding to the isentropic work is obtained by combining Equations (3.5-293), (3.5-301) and (3.5-303):

$$\tau_s \;=\; \frac{\dot{m}}{\omega}(h_{2'}^T - h_1^T) \;=\; \frac{\dot{m}}{\omega}\frac{P_1^T (R_p - 1)}{\rho_m} \tag{3.5-304}$$

and the irreversible, or dissipitave, torque is obtained by substituting Equation (3.5-295) into Equation (3.5-296) and combining with Equations (3.5-301) and (3.5-303)

$$\tau_d \;=\; \frac{\dot{m}}{\omega}\frac{1 - \eta_{ad}}{\eta_{ad}}(h_{2'}^T - h_1^T) \;=\; \frac{\dot{m}}{\omega}\frac{1 - \eta_{ad}}{\eta_{ad}}\frac{P_1^T (R_p - 1)}{\rho_m} \tag{3.5-305}$$

The total torque is the sum of the isentropic torque and the dissipative torque

$$\tau_t \;=\; \tau_s + \tau_d \;=\; \frac{\dot{m}}{\omega}\frac{1}{\eta_{ad}}(h_{2'}^T - h_1^T) \;=\; \frac{\dot{m}}{\omega}\frac{P_1^T (R_p - 1)}{\rho_m \eta_{ad}} \;=\; \frac{\dot{m}}{\omega}\left(\frac{P_2 - P_1}{\rho_m \eta_{ad}}\right) \tag{3.5-306}$$

and can be input to the shaft rotational velocity equation. As with the pump model, the user has the option to input motor torque as a function of rotational velocity.

As with the pump model, a quasi-static model for compressor performance is imposed on the ATHENA volume-junction flow path representation. The compressor is a volume-oriented component, and the head developed by the compressor is added to the junction that connects the suction of the compressor volume to the system. The compressor model is interfaced with the two-fluid hydrodynamic model by assuming the head developed by the compressor is similar to a body force. Thus, the head term appears in the mixture momentum equation; but, like the gravity body force, it does not appear in the difference momentum equation used in ATHENA. The head term is added to both the liquid and vapor phase terms of the mixture momentum equation although it is recognized that the compressor will only be operated in a system containing single-phase vapor. The term that is added to the mixture momentum equation is $\rho_m g H$, where H is the total head rise of the compressor (m), ρ_m is the volume fluid density (kg/m^3), and g is the acceleration due to gravity (m/s^2).

The compressor model has been implemented only in the semi-implicit numerical scheme. The compressor head is coupled implicitly to the velocities through its dependence on the volumetric flow rate, Q. The volumetric flow rate is defined as the volume mass flow rate divided by the volume density. It is assumed that the head depends on the volumetric flow rate, and can be approximated by a two-term Taylor series expansion given by

$$H^{n+1} = H^n + \left(\frac{dH}{dQ}\right)^n (Q^{n+1} - Q^n) \tag{3.5-307}$$

Thus, the numerical equivalent of the term $\rho g H$ is

$$\rho^n g H^n \Delta t + \rho^n g \left(\frac{dH}{dQ}\right)^n (Q^{n+1} - Q^n)\Delta t \ . \tag{3.5-308}$$

This term is added to the right side of the mixture momentum Equation (3.1-103). The junction velocity is made implicit.

The compressor energy dissipation, $\dot{Q}$, is calculated for the compressor volume in a manner similar to that derived for the turbine. Neglecting the kinetic energy term because stagnation pressures are given in Equation (3.5-290), Equation (3.5-86) becomes

$$\dot{Q} = \dot{m}\left(\frac{P_1 - P_2}{\rho_1}\right) - \dot{W} \tag{3.5-309}$$

Computing the rate of work from Equation (3.5-305) and accounting for the different sign convention yields

$$\dot{Q} = \frac{\dot{m}(P_2 - P_1)}{\rho_m \eta_{ad}}\left(1 - \frac{\rho_m \eta_{ad}}{\rho_1}\right) = \tau_t \omega \left(1 - \frac{\rho_m \eta_{ad}}{\rho_1}\right) \tag{3.5-310}$$

If the fluid is assumed to be incompressible, the density is constant and the compressor dissipation is consistent with that obtained for the pump in Equation (3.5-62).

The energy dissipation term is evaluated explicitly in the semi-implicit scheme, and it is partitioned between the liquid and vapor thermal energy equations in such a way that the rise in temperature due to dissipation is equal in each phase. (The details of the dissipation mechanism in a two-phase system are unknown, so the assumption is made that the mechanism acts in such a way that thermal equilibrium between the phases is maintained without phase change.) Thus, the terms that are added to the right sides of the liquid and vapor/gas thermal energy equations, Equations (3.1-91) and (3.1-92), for the compressor volumes are

$$\text{DISS}_f = \tau^n \omega^n \left(1 - \eta_{ad}\frac{\rho_m}{\rho_1}\right)\Delta t \left(\frac{\alpha_f^n \rho_f^n C_{pf}^n}{\alpha_g^n \rho_g^n C_{pg}^n + \alpha_f^n \rho_f^n C_{pf}^n}\right) \tag{3.5-311}$$

and

$$\text{DISS}_f = \tau^n \omega^n \left(1 - \eta_{ad}\frac{\rho_m}{\rho_1}\right)\Delta t \left(\frac{\alpha_g^n \rho_g^n C_{pg}^n}{\alpha_g^n \rho_g^n C_{pg}^n + \alpha_f^n \rho_f^n C_{pf}^n}\right) \tag{3.5-312}$$

The compressor head H is defined by Equation (3.5-301), and torque by Equation (3.5-306). Values are obtained by means of an empirical compressor performance map, input to the code with the independent variables based on mass flow rate and speed and the dependent variables of pressure ratio and efficiency.

The mass flow rate and speed tables should be entered as relative corrected values. The general forms of independent dimensionless parameters are[3.5-33]

$$\dot{m}_C = \frac{\dot{m}}{\rho_{0,\,in} a_{0,\,in} D^2} \tag{3.5-313}$$

for the corrected mass flow and

$$N_C = \frac{ND}{a_{0,\,in}} \tag{3.5-314}$$

for the corrected speed, where subscript '0' designates total or stagnation, 'in' designates the inlet station, 'a' is the sound speed, and 'D' represents the turbomachine size. The relative corrected mass flow rate, v, is given as

$$v = \left(\frac{\dot{m}}{\rho_{0,in}a_{0,in}}\right) \bigg/ \left(\frac{\dot{m}}{\rho_{0,in}a_{0,in}}\right)_{Rated}$$

(3.5-315)

and the relative corrected speed, α, is given as

$$\alpha = \frac{N}{a_{0,in}} \bigg/ \left(\frac{N}{a_{0,in}}\right)_{Rated}$$

(3.5-316)

where D cancels from the numerator and the denominator. Equations (3.5-315) and (3.5-316) should be used to correct mass flow rate and speed entries in the performance table. If the fluid is an ideal gas, then the equations for corrected mass flow and speed are reduced to functions of pressure and temperature:

$$\dot{m}_C = \frac{\dot{m}}{\rho_{0,in}a_{0,in}} = \frac{RT_{0,in}}{P_{0,in}}\left(\frac{\dot{m}}{\sqrt{\gamma RT_{0,in}}}\right) = \frac{\dot{m}\sqrt{RT_{0,in}}}{P_{0,in}\sqrt{\gamma}}$$

(3.5-317)

and

$$N_C = \frac{N}{a_{0,in}} = \frac{N}{\sqrt{\gamma RT_{0,in}}}$$

(3.5-318)

If the fluid species does not change, R and γ can be omitted leaving

$$\dot{m}_C = \frac{\dot{m}\sqrt{T_{0,in}}}{P_{0,in}}$$

(3.5-319)

and

$$N_C = \frac{N}{\sqrt{T_{0,in}}} \, ,$$

(3.5-320)

respectively. It is most general to require input of rated fluid density and rated sonic speed as the input variables. Therefore, the ideal gas form, if desired, should be converted to rated fluid density and rated sonic speed for input to the compressor model.

3.5.13 References

3.5-1.   Y. K. Cheung, V. Parameswaran, and J. C. Shaug, *BWR Refill-Reflood Program, Task 4.7-Model Development, TRAC-BWR Component Models,* NUREG/CR-2574, EPRI NP-2376, GEAP-22052, April 1983.

3.5-2.   R. H. Moen et al., "Advances in Boiling Water Reactor Steam Separator Systems," *ASME-60-WA/NE-5, November 1969.*

3.5-3.   E. L. Burley, "Performance of Internal Steam Separator System in Boiling Water Reactors," *ASME-69-WA/NE-24, November 1969.*

3.5-4.   S. Wolf and R. H. Moen, "Advances in Steam-Water Separators for Boiling Water Reactors," *ASME-73-WA/PWR-4, November 1973.*

3.5-5.   V. H. Ransom et al., *RELAP5/MOD1 Code Manual,* NUREG/CR-4312, EGG-2070, Idaho National Engineering Laboratory, March 1982.

3.5-6.   EG&G Idaho, Inc., *RELAP4/MOD6: A Computer Program for Transient Thermal-Hydraulic Analysis of Nuclear Reactors and Related Systems, Users Manual,* CDAP-TR-003, Idaho National Engineering Laboratory, May 1978.

3.5-7.   R. F. Farman and N. R. Anderson, "A Pump Model for Loss-of-Coolant Analysis," *Topical Meeting on Water Reactor Safety*, CONF-730304, March 1973, pp. 569-580.

3.5-8.   R. B. Bird, W. E. Stewart, and E. N. Lightfoot, *Transport Phenomena*, New York: Wiley, 1960, p. 458.

3.5-9.   J. K. Salisbury, *Steam Turbines and Their Cycles,* New York: Kreiger, 1950.

3.5-10.   J. K. Vennard and R. L. Street, *Elementary Fluid Mechanics,* 6th Edition, New York: Wiley, 1982.

3.5-11.   J. P. Holman, *Heat Transfer,* 4th Edition, New York: McGraw-Hill, 1976, pp. 244-245, 280.

3.5-12.   V. H. Ransom et al., *RELAP5/MOD2 Code Manual,* NUREG/CR-4312, EGG-2396, Idaho National Engineering Laboratory, August 1985 and December 1985, revised March 1987.

3.5-13.   R. A. Dimenna et al., *RELAP5/MOD2 Models and Correlations,* NUREG/CR-5194, EGG-2531, Idaho National Engineering Laboratory, August 1988.

3.5-14.   T. N. Tandon, H. K. Varma, and C. P. Gupta, "A New Flow Regime Map for Condensation Inside Horizontal Tubes," *Journal of Heat Transfer, 104,* November 1982, pp. 763-768.

3.5-15.   I. S. Lim, S. G. Bankoff, R. S. Tankin, and M. C. Yeun, *Co-current Steam/Water Flow in a Horizontal Channel,* NUREG/CR-2289, August 1981.

3.5-16.   H. C. Unal, "Maximum Bubble Diameter, Maximum Bubble-Growth Time and Bubble-Growth Rate During the Subcooled Nucleate Flow Boiling of Water up to 17.7 MN/m^2," *International Journal of Heat and Mass Transfer, 19,* 1976, pp. 643-649.

3.5-17.   R. A. Riemke, "Modification to Unal's Subcooled Flow Boiling Bubble Model," *Nuclear Technology, 102,* 1993, pp. 416-417.

3.5-18.   R. T. Lahey, "A Mechanistic Subcooled Boiling Model," *Proceedings from Sixth International Heat Transfer Conference, Toronto, Canada, 1978,* Volume 1, pp. 293-297.

3.5-19.   W. L. Weaver et al., *TRAC-BF1 Manual: Extensions to TRAC-BD1/MOD1,* NUREG/CR-4391, EGG-2417, Idaho National Engineering Laboratory, August 1986.

3.5-20.   M. M. Giles et al., *TRAC-BF1/MOD1: An Advanced Best Estimate Computer Program for BWR Accident Analysis*, NUREG/CR-4356, EGG-2626, Idaho National Engineering Laboratory, June 1992 and August 1992.

3.5-21.   S. Z. Rouhani et al., *TRAC-BF1/MOD1 Models and Correlations,* NUREG/CR-4391, EGG-2680, Idaho National Engineering Laboratory, August 1992.

3.5-22.   J. M. G. Andersen, K. H. Chu, and J. C. Shaug, *BWR Refill-Reflood Program, Task 4.7--Model Development, Basic Models for the BWR Version of TRAC,* NUREG/CR-2573, EPRI NP-2375, GEAP-22051, September 1983.

3.5-23.   M. Ishii, *One-dimensional Drift-flux Model and Constitutive Equations for Relative Motion Between Phases in Various Two-phase Flow Regimes,* ANL-77-47, Argonne National Laboratory, September 1977.

3.5-24.   M. M. Megahed, *Interfacial Heat Transfer Countercurrent Flows of Steam and Water,* EGG-RTH-2495, Idaho National Engineering Laboratory, January 1987.

3.5-25.   J. G. M. Andersen and H. Abel-Larsen, *CORECOOL-Model Description of the Program,* RISO-M-21380, November 1980.

3.5-26.   A. C. DeVuono and R. N. Christensen, "Experimental Investigation of the Pressure Effect on Film Condensation of Steam-Air Mixture at Pressure Above Atmospheric," *Fundamentals of Phase Change: Boiling and Condensation,* ASME-HTD Vol. 38, 1984, pp. 73-80.

3.5-27.   K. Schneider, "Siemens Contributions to RCP Modeling and Evaluation of UPTF Test 6," *ICAP Meeting, Bethesda, MD, October 18-20, 1989.*

3.5-28.   D. Bharanthan, G. B. Wallis, and H. T. Richter, *Air-Water Counter-Current Annular Flow,* EPRI NP-1165, 1979.

3.5-29.   G. B. Wallis, *One-dimensional Two-phase Flow,* New York: McGraw-Hill, 1969.

3.5-30. M. P. Boyce, *Gas Turbine Engineering Handbook,* 2nd Edition, Houston: Gulf Professional Publishing, 1982.

3.5-31. G. J. Van Wylen and R. E. Sonntag, *Fundamentals of Classical Thermodynamics*, 2nd Edition, New York: Wiley, 1973.

3.5-32. J. K. Vennard and R. L. Street, *Elementary Fluid Mechanics*, 5th Edition, New York: Wiley, 1975.

3.5-33. S. L. Dixon, *Fluid Mechanics and Thermodynamics of Turbomachinery*, 4th Edition, Burlington, MA: Butterworth Heinmann (Elsevier Science), 1998.

4 Heat Structure Models

4.1 Heat Conduction Numerical Techniques

Heat structures provided in ATHENA permit calculation of the heat transferred across solid boundaries of hydrodynamic volumes. Modeling capabilities of heat structures are general and include fuel pins or plates with nuclear or electrical heating, heat transfer across steam generator tubes, and heat transfer from pipe and vessel walls. Temperatures and heat transfer rates are computed from the one-dimensional form of the transient heat conduction equation for non-reflood and from the two-dimensional form of the transient heat condution equation for reflood. The one-dimensional form is discussed first. The two-dimensional form is discussed in Section 4.9.

For one-dimensional heat conduction, heat structures are represented using rectangular, cylindrical, or spherical geometry. Surface multipliers are used to convert the unit surface of the one-dimensional calculation to the actual surface of the heat structure. Temperature-dependent and space-dependent thermal conductivities and volumetric heat capacities are provided in tabular or functional form either from built-in or user-supplied data.

The one-dimensional heat conduction model is based on the one-dimensional time dependent or steady state heat conduction code HEAT 1[4.1-1] developed at the INEEL [previously called the NRTS (National Reactor Testing Station)]. The HEAT-1 code was first converted to the HEAT-1 subcode[4.1-2] and later incorporated into RELAP5. Finite differences are used to advance the heat conduction solutions. Each mesh interval may contain a different mesh spacing, a different material, or both. The spatial dependence of the internal heat source may vary over each mesh interval. The time-dependence of the heat source can be obtained from reactor kinetics, one of several tables of power versus time, or a control system variable. Boundary conditions include symmetry or insulated conditions, a correlation package, tables of surface temperature versus time, heat flux versus time, and heat transfer coefficient versus time or surface temperature. The heat transfer correlation package can be used for heat structure surfaces connected to hydrodynamic volumes, and contains correlations for convective, nucleate boiling, transition boiling, and film boiling heat transfer from the wall to the fluid and reverse heat transfer from the fluid to the wall including condensation.

The following describes the numerical techniques for heat conduction. The integral form of the heat conduction equation is

$$\iiint_V \rho C_p(T, \bar{x}) \frac{\partial T}{\partial t}(\bar{x}, t) dV = \iint_S k(T, \bar{x}) \bar{\nabla} T(\bar{x}, t) \bullet d\bar{s} + \iiint_V S(\bar{x}, t) dV \qquad (4.1\text{-}1)$$

where

      k   =   thermal conductivity

s	=	surface
S	=	internal volumetric heat source
t	=	time
T	=	temperature
V	=	volume
$\bar{x}$	=	space coordinates
ρC_p	=	volumetric heat capacity.

The boundary conditions applied to the exterior surface have the form

$$A(T)T(t) + B(T)\frac{\partial T(t)}{\partial n} = D(T, t) \quad . \tag{4.1-2}$$

The n denotes the unit normal vector away from the boundary surface. Thus, if the desired boundary condition is that the heat transferred out of the surface equals a heat transfer coefficient, h, times the difference between the surface temperature, T, and the sink temperature, T_{sk}, i.e.,

$$-k\frac{\partial T}{\partial n} = h(T - T_{sk}) \tag{4.1-3}$$

then the correspondence between the above expression and Equation (4.1-2) yields

$$A = h, B = k, \text{ and } D = h\, T_{sk} \quad . \tag{4.1-4}$$

In one-dimensional problems, boundary conditions are applied on the left and right surfaces. ATHENA uses the terms "left" and "right" to describe the opposite sides of a heat structure. This has no particular geometric interpretation for rectangular goemetry heat structures but does for cylindrical and spherical heat structures. By convention, the right surface represents the outside diameter and the left surface represents the inside diameter. For solid cylinders and spheres, therefore, the left surface is actually a point (a cylinder or sphere with zero inside diameter). For all three geometries (rectangular, cylindrical, and spherical), the left boundary coordinate must be less than the right boundary coordinate because the mesh increments are positive. In steady-state problems, a valid physical problem requires that A be nonzero on at least one of the two boundary surfaces. If a transient or steady-state problem has cylindrical or spherical geometry and a zero radius for the left surface (that is, a solid cylinder or sphere), the left

boundary condition is normally the symmetry condition, $\dfrac{\partial T}{\partial \bar{n}} = 0$. Under these conditions, if B is nonzero,

the numerical technique forces the symmetry boundary condition, even if it is not specified.

4.1.1 References

4.1-1.   R. J. Wagner, *HEAT-1 A One-Dimensional Time Dependent or Steady State Heat Conduction Code for the IBM-650*, IDO-16867, National Reactor Testing Station, April 1963.

4.1-2.   J. A. McClure, *Guide to the HEAT-1 Subcode*, Aerojet Nuclear Company, National Reactor Testing Station, October 1972.

4.2 Mesh Point and Thermal Property Layout

Figure 4.2-1 illustrates the placement of mesh points at which temperatures are to be calculated. The mesh point spacing for a rectangular problem is taken in the positive x-direction. For cylindrical and spherical problems, the mesh point spacing is in the positive radial direction. Mesh points are placed on the external boundaries of the problem, at the interfaces between different materials, and at desired intervals between the interfaces, boundaries, or both.
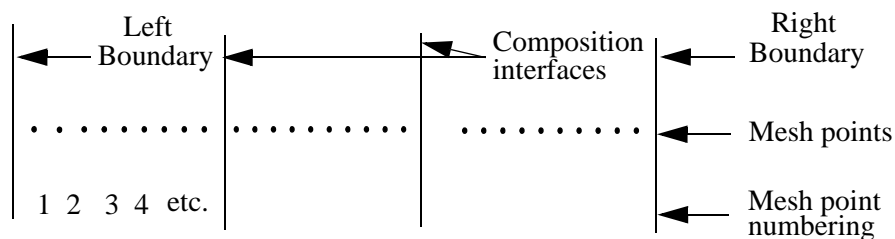
Figure 4.2-1 Mesh point layout.

Figure 4.2-2 represents three typical mesh points. The subscripts are space indexes indicating the mesh point number; and l and r (if present) designate quantities to the left and right, respectively, of the mesh point. The δ's indicate mesh point spacings that are not necessarily equal. Between mesh points, the thermal properties, k and ρC_p, and the volumetric source term, S, are assumed spatially constant; but k_{lm} is not necessarily equal to k_{rm} and similarly for ρC_p and S.

To obtain the spatial-difference approximation for the m-th interior mesh point, Equation (4.1-1) is applied to the volume and surfaces indicated by the dashed line shown in **Figure 4.2-2**. For the spatial difference approximation at the boundaries, Equation (4.1-1) is applied to the volumes and interior surfaces indicated by the dashed lines shown in **Figure 4.2-3**, and Equation (4.1-2) is used to define the gradient along the exterior surfaces. If the coefficient of the gradient in the boundary equation is zero, the
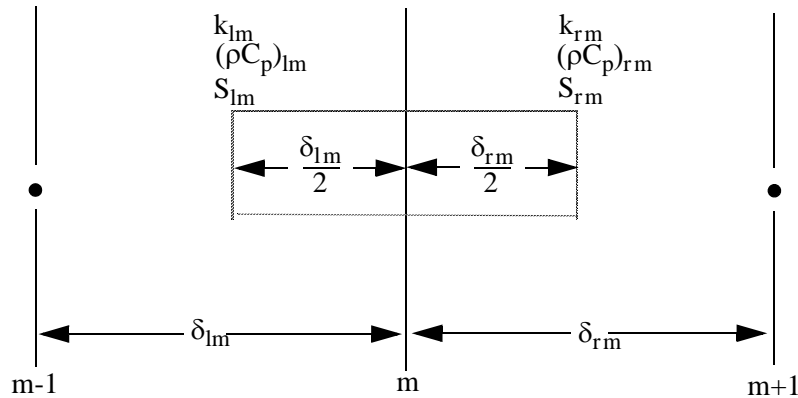
Figure 4.2-2 Typical mesh points.

surface temperature is given directly from Equation (4.1-2). Since the code is one-dimensional, the dimensions of the volume for other than the x or r coordinate are set to one. For rectangular geometry, the volume is a rectangular solid. For cylindrical geometry, the volume is a cylindrical annulus; and for spherical geometry, the volume is a spherical shell.
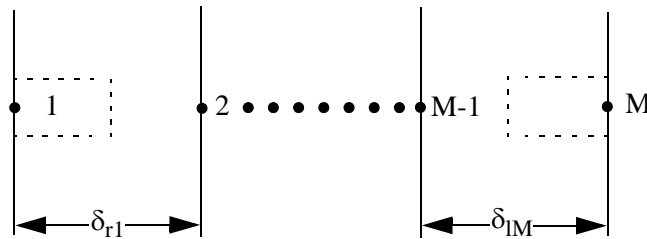
Figure 4.2-3 Boundary mesh points.

The spatial finite-difference approximations use exact expressions for the space and volume factors and simple differences for the gradient terms. To condense the expressions defining the numerical approximations and to avoid writing expressions unique to each geometry, the following quantities are defined:

For rectangular geometry,

$$\delta^v_{lm} = \frac{\delta_{lm}}{2} \ , \ \ \delta^v_{rm} = \frac{\delta_{rm}}{2} \ , \ \ \delta^s_{lm} = \frac{1}{\delta_{lm}} \ , \ \ \delta^s_{rm} = \frac{1}{\delta_{rm}} \ , \ \ \delta^b_m = 1 \ \ .$$

(4.2-1)

For cylindrical geometry,

$$\delta^v_{lm} = 2\pi \frac{\delta_{lm}}{2} \left(x_m - \frac{\delta_{lm}}{4} \right) \ , \ \ \delta^v_{rm} = 2\pi \frac{\delta_{rm}}{2} \left(x_m + \frac{\delta_{rm}}{4} \right) \ ,$$

$$\delta^s_{lm} = \frac{2\pi}{\delta_{lm}} \left(x_m - \frac{\delta_{lm}}{2} \right) \ , \ \ \delta^s_{rm} = \frac{2\pi}{\delta_{rm}} \left(x_m + \frac{\delta_{rm}}{2} \right) \ ,$$

$$\delta^b_m = 2\pi x_m \ \ .$$

(4.2-2)

For spherical geometry,

$$\delta^v_{lm} = \frac{4\pi}{3} \left[x_m^3 - \left(x_m - \frac{\delta_{lm}}{2} \right)^3 \right] \ , \ \ \delta^v_{rm} = \frac{4\pi}{3} \left[\left(x_m + \frac{\delta_{rm}}{2} \right)^3 - x_m^3 \right] \ ,$$

$$\delta^s_{lm} = \frac{4\pi}{\delta_{lm}} \left(x_m - \frac{\delta_{lm}}{2} \right)^2 \ , \ \ \delta^s_{rm} = \frac{4\pi}{\delta_{rm}} \left(x_m + \frac{\delta_{rm}}{2} \right)^2 \ ,$$

$$\delta^b_m = 4\pi x_m^2 \ \ .$$

(4.2-3)

For all geometries,

$$G_m = (\rho C_p)_{lm} \delta^v_{lm} + (\rho C_p)_{rm} \delta^v_{rm} \ \ .$$

(4.2-4)

The superscripts, v and s, refer to volume and surface-gradient weights. The δ^b_m is a surface weight used at exterior boundaries and in heat transfer rate equations.

4.3 Difference Approximation at Internal Mesh Points

Using a forward difference for the time derivative, the first term of Equation (4.1-1) for the volume of **Figure 4.2-1** is approximated by

$$\iiint\limits_V \rho C_p(T, \bar{x}) \frac{\partial T}{\partial t}(\bar{x}, t) dV \ \approx \ (T_m^{n+1} - T_m^n) \frac{G_m}{\Delta t} \ \ .$$

(4.3-1)

The superscript n refers to time; thus, T_m^n indicates the temperature at mesh point m at time t^n, and T_m^{n+1} indicates the temperature at mesh point m at time $t^{n+1} = t^n + \Delta t$.

The second term of Equation (4.1-1) for the surfaces of **Figure 4.2-2** is approximated by

$$\iint\limits_{S} k(T, \bar{x}) \overline{\nabla} T(\bar{x}, t) d\bar{s} \approx (T_{m-1} - T_m) k_{lm} \delta_{lm}^s + (T_{m+1} - T_m) k_{rm} \delta_{rm}^s \quad . \tag{4.3-2}$$

Note that the above expression includes the standard interface conditions of continuity of temperature and heat flow. The surface integral of Equation (4.1-1) is usually evaluated by integrating only along the exterior surfaces of the volume indicated by the dashed line in **Figure 4.2-2**. If, however, the volume is divided into two sub-volumes by the interface line and the surface integrals of these sub-volumes are added, the surface integrals along the common interface cancel because of the continuity of heat flow. The continuity of temperature is implied by use of a single-valued temperature at the interface.

A contact-resistance interface condition cannot be specified directly since the temperature, instead of being continuous at the interface, is given by $q = h_c \Delta T$, where q is the heat transfer rate across the interface, h_c is the contact conductivity, and ΔT is the temperature change across the interface. This condition can be specified by defining a small mesh interval with thermal properties of $k = h_c \delta$ and $\rho = 0$. The size of the mesh interval, δ, is arbitrary except in cylindrical or spherical geometry, where the surface and volume weights are dependent on the radius. This mesh interval is usually chosen very small with respect to the dimensions of the problem. Experience has shown that too small a δ can result in oscillations.

The space and time-dependence of the volumetric source term in Equation (4.1-1) is assumed to be separable into functions of space and time,

$$S(\bar{x}, t) = P_f P(t) Q(x) \tag{4.3-3}$$

where P_f is the factor that relates the reactor power (or power from a table or control variable) to the heat generation rate for a particular heat structure; $P(t)$ is the time-varying function and may be reactor power, power from a table, or a control variable; and $Q(x)$ is the space-dependent function. For this one-dimensional model, $Q(x)$ is assumed to vary only in the x direction. The value of $Q(x)$ is assumed constant over a mesh interval, but each interval can have a different value. The third term of Equation (4.1-1) is then approximated as

$$\iiint\limits_{V} S(\bar{x}, t) dV \approx P_f P(t)(Q_{lm} \delta_{lm}^v + Q_{rm} \delta_{rm}^v) \quad . \tag{4.3-4}$$

Gathering the approximations of terms in Equation (4.1-1), the basic difference equation for the m-th mesh point is

$$\frac{(T_m^{n+1} - T_m)G_m}{\Delta t} = -\ (T_m - T_{m-1})k_{lm}\delta_{lm}^s + (T_{m+1} - T_m)k_{rm}\delta_{rm}^s$$

$$+\ P_f P(t)(Q_{lm}\delta_{lm}^v + Q_{rm}\delta_{rm}^v)\ .$$

(4.3-5)

Using the symbol, ζ_m, to represent the right side, Equation (4.3-5) can be written as

$$\frac{(T_m^{n+1} - T_m^n)G_m}{\Delta t} = \zeta_m\ .$$

(4.3-6)

Thus far, the time superscripts for G_m and ζ_m have been omitted, and the procedure for approximating the temperature-dependence of the thermal properties has not been mentioned. The procedures for temperature-dependent thermal properties are discussed later. However, superscripts for thermal properties are written here even though their significance is not explained until later. For steady-state, the difference approximation becomes

$$\zeta_m = 0$$

(4.3-7)

and no time superscripts are needed. For the time-dependent case, an equation of the type

$$\frac{(T_m^{n+1} - T_m^n)G_m}{\Delta t} = w\zeta_m^{n+1} + (1-w)\zeta_m^n$$

(4.3-8)

is an explicit formula if w is zero and is an implicit formula when w is nonzero. ATHENA uses the implicit formulation with w = 1/2, sometimes called the Crank-Nicolson method.[4.3-1]

Writing Equation (4.3-8) in full, the difference approximation for the m-th interior mesh point for transient and steady-state cases is

$$a_m^n T_{m-1}^{n+1} + b_m^n T_m^{n+1} + c_m^n T_{m+1}^{n+1} = d_m$$

(4.3-9)

$$a_m^n = -\ \frac{k_{lm}^n \delta_{lm}^s \Delta t}{\sigma + 1}$$

(4.3-10)

$$b_m^n = \sigma G_m^n - a_m^n - c_m^n$$

(4.3-11)

$$c_m^n = -\frac{k_{rm}^n \delta_{rm}^s \Delta t}{\sigma + 1} \tag{4.3-12}$$

$$d_m = -\sigma a_m^n T_{m-1}^n + \sigma(G_m^n + a_m^n + c_m^n)T_m^n - \sigma c_m^n T_{m+1}^n$$
$$+ \Delta t P_f\left(\frac{P^{n+1} + \sigma P^n}{\sigma + 1}\right)(Q_{lm}\delta_{lm}^v + Q_{rm}\delta_{rm}^v) , \tag{4.3-13}$$

where σ is 1 for transient cases, and σ is 0 and Δt is 1.0 for steady-state cases. Separate subroutines are used for steady-state and transient cases, and σ and Δt do not appear in the steady-state coding.

4.3.1 References

4.3-1. J. Crank and P. Nicolson, "A Practical Method for Numerical Evaluation of Solutions to Partial Differential Equations of the Heat Conduction Type," *Proceedings of the Cambridge Philosophical Society*, *43*, 1947, pp. 50-67.

4.4 Difference Approximation at Boundaries and Boundary Condition Parameters.

To obtain the difference approximations for the mesh points at the boundaries, Equation (4.1-1) is applied to the volumes of **Figure 4.2-3** with Equation (4.1-2) used to define the gradient at the surface. The second term of Equation (4.1-1) at $x = x_1$ is approximated by

$$\iint_S k(T, \bar{x})\bar{\nabla}T(\bar{x}, t) \bullet d\bar{s} = -\frac{k_{rl}}{B_1}(A_1 T_1 - D_1)\delta_1^b + k_{rl}(T_2 - T_1)\delta_{rl}^s . \tag{4.4-1}$$

The complete basic expression for the left boundary mesh point becomes

$$\frac{(T_1^{n+1} - T_1^n)}{\Delta t}(\rho C_p)_{rl}\delta_{rl}^v = -\frac{k_{rl}}{B_1}(A_1 T_1 - D_1)\delta_1^b + k_{rl}(T_2 - T_1)\delta_{rl}^s + P_f P(t)Q_{rl}\delta_{rl}^v . \tag{4.4-2}$$

If B in the boundary condition equation is zero, the above equation is not used, since the boundary condition alone determines the temperature. Also in that case, a divide by zero would be indicated if Equation (4.4-2) were used. Approximations for the boundary at $x = x_m$ are derived in a similar fashion. These equations for the boundary mesh points are converted to the implicit formulas in the same manner as for the interior mesh points, except that the boundary condition information is evaluated completely at the n+1 time level. Thus, for the left boundary

$$b_1^n T_1^{n+1} + c_1^n T_2^{n+1} = d_1 \tag{4.4-3}$$

$$b_1^n = \sigma(\rho C_p)_{r1}^n \delta_{r1}^v + \frac{k_{r1}^n A_1^n \delta_1^b \Delta t}{B_1^n} - c_1^n \tag{4.4-4}$$

$$c_1^n = -\frac{k_{r1}^n \delta_{r1}^s \Delta t}{\sigma + 1} \tag{4.4-5}$$

$$d_1 = -\sigma c_1^n T_2^n + \sigma[(\rho C_p)_{r1}^n \delta_{r1}^v + c_1^n]T_1^n + \frac{k_{r1}^n \delta_1^b D_1^n \Delta t}{B_1^n} + P_f \frac{(\sigma P^n + P^{n+1})Q_{r1}\delta_{r1}^v \Delta t}{\sigma + 1} \quad . \tag{4.4-6}$$

For the right boundary,

$$a_M^n T_{M-1}^{n+1} + b_M^n T_M^{n+1} = d_M \tag{4.4-7}$$

$$a_M^n = -\frac{k_{lM}^n \delta_{lM}^s \Delta t}{\sigma + 1} \tag{4.4-8}$$

$$b_M^n = \sigma(\rho C_p)_{lM}^n \delta_{lM}^v + \frac{k_{lM}^n A_M^n \delta_M^b \Delta t}{B_M^n} - a_M^n \tag{4.4-9}$$

$$d_M = -\sigma a_M^n T_{M-1}^n + \sigma \cdot [(\rho C_p)_{lM}^n \delta_{lM}^v + a_M^n] \cdot T_M^n + \frac{k_{lM}^n \delta_M^b D_M^n \Delta t}{B_M^n} + P_f \frac{(\sigma P^n + P^{n+1})Q_{lM}\delta_{lM}^v \Delta t}{\sigma + 1} \quad . \tag{4.4-10}$$

The boundary condition parameters, A, B, and D, are considered functions of temperature and time.

4.5 Thermal Properties

The thermal conductivity, k, and the volumetric heat capacity, ρC_p, are considered functions of temperature and space. These thermal properties are obtained for each interval by using the average of the mesh point temperatures bounding the interval. The thermal conductivity is obtained from

$$k_{l,m} = k\left(\frac{T_{m-1} + T_m}{2}\right) = k_{r,m-1} \tag{4.5-1}$$

$$k_{r,m} = k\left(\frac{T_m + T_{m+1}}{2}\right) = k_{l,m+1} \quad . \tag{4.5-2}$$

The volumetric heat capacity is treated in the same manner.

Thermal properties for five materials are stored internally in the code: fuel rod gap gas, carbon steel, stainless steel, uranium dioxide, and zircaloy. The data in the code are consistent with those in MATPRO[4.5-1] where possible. Constant room-temperature densities (ρ) are multiplied by temperature-dependent specific heat capacities (C_P) to generate the volumetric heat capacities. For all of the properties, constant values are assumed beyond the specified temperature ranges. Arbitrary low and high values of 5 and 5,000 K are included to prevent code failures with out-of-range material property data.

Representative gap gas properties are developed for a combination of fill and fission product gases. A 0.1066/0.1340/0.7594 mole fraction He/Kr/Xe mixture is modeled.

From Section 12.1.1 of the MATPRO manual[4.5-1], the gas mixture thermal conductivity is given by

$$k_{mix} = \sum_i^n \left[\frac{k_i x_i}{x_i + \sum_{j=1}^n (1 - \delta_{ij}) \Psi_{ij} x_i} \right] \tag{4.5-3}$$

where

$$\Psi_{ij} = \phi_{ij} \left[1 + 2.41 \frac{(M_i - M_j)(M_i - 0.142 M_j)}{(M_i - M_j)^2} \right] \tag{4.5-4}$$

and

$$\phi_{ij} = \frac{\left[1 + \left(\frac{k_i}{k_j} \right)^{\frac{1}{2}} \left(\frac{M_i}{M_j} \right)^{\frac{1}{4}} \right]^2}{2^{\frac{2}{3}} \left(1 + \frac{M_i}{M_j} \right)^{\frac{1}{2}}} \tag{4.5-5}$$

and

$$\delta_{ij} = \begin{cases} 1 & \text{for } i = j \\ 0 & \text{otherwise} \end{cases}$$

$$n \quad = \quad \text{number of components in mixture (dimensionless)}$$

M_i = molecular weight of component i (kg)

x_i = mole fraction of component i (dimensionless), and

k_i = thermal conductivity of component i (W/m·K).

The thermal conductivities of the three elements are given by

$$
\begin{aligned}
k_{He} &= 2.639 \times 10^{-3} T^{0.7085} \\
k_{Kr} &= 8.247 \times 10^{-5} T^{0.8363} \\
k_{Xe} &= 4.351 \times 10^{-5} T^{0.8616} .
\end{aligned}
$$
(4.5-6)

Using these equations, thermal conductivity values as a function of the mixture temperature are provided for temperatures from 300 to 3,000 K.

For the gap gases, the perfect gas relation is used to determine the specific heat capacity (Section 13.1.1 of **Reference 4.5-2**). It is given by

$$
C_p = 2.5 \times R_o = 2.5 \times 8.3143 \times 10^3 = 2.0786 \times 10^4 \frac{J}{kmol \cdot K}
$$
(4.5-7)

The molecular weight (MW) of the mixture is

$$
MW = 4.003 \times 0.1066 + 83.3 \times 0.1340 + 131.3 \times 0.7594 = 111.37 \frac{kg}{kmol} .
$$
(4.5-8)

Using the mixture molecular weight of 111.37 kg/kmol,

$$
C_p = 2.0786 \times 10^4 / 111.37 = 186.65 \frac{J}{kg \cdot K} .
$$
(4.5-9)

A representative fuel rod internal pressure of 4.1 MPa is assumed to determine the gap gas density. Using the perfect gas relation and a temperature of 300 K yields

$$
\rho = \frac{P \cdot MW}{R_o T} = \frac{4.1 \times 10^6}{8.3143 \times 10^3 \cdot 300} \frac{kmol}{m^3} \times 111.37 \frac{kg}{kmol} = 183.06 \frac{kg}{m^3}
$$
(4.5-10)

Since both the specific heat capacity and the density are constant, a constant value is entered for the gap volumetric heat capacity. It is given by

$$\rho C_p = 183.06 \times 186.65 = 3.417 \times 10^4 \frac{J}{m^3 \cdot K} \qquad (4.5\text{-}11)$$

The Nuclear Systems Materials Handbook[4.5-3] contains data for a range of medium carbon steels (0.18-0.35% carbon), in which there are some fairly large differences in material properties. Data for C-Mn steel (>1.0% Mn, ≤0.10% Si) will be used, as its thermal conductivity was in between the values for the two other alloys presented in the handbook.

The thermal conductivity is given by

$$k = 27.975 - 3.1432 \times 10^{-3} T + 3.6548 \times 10^{-6} T^2 - 1.3289 \times 10^{-8} T^3 + 5.6749 \times 10^{-12} T^4 \qquad (4.5\text{-}12)$$

where k is in Btu/hr·ft·°F and T is in °F. The range of the presented data is from 70 to 1,650 °F (294 to 1,172 K).

The carbon steel specific heat capacity is given by

$$C_p = 8.7306 \times 10^{-2} + 1.7812 \times 10^{-4} T - 2.6758 \times 10^{-7} T^2 + 1.6445 \times 10^{-1} T^3 \qquad (4.5\text{-}13)$$

for 70 < T < 1,350 °F and

$$C_p = 4.1612 - 5.0480 \times 10^{-3} T + 1.6000 \times 10^{-6} T^2 \qquad (4.5\text{-}14)$$

for 1,450 < T < 1,600 °F. Linear interpolation is used between the boundaries (1,350 °F and 1,450 °F) of the two equations.

The reference density is 7,856 kg/m^3.

The thermal conductivity of type 304 stainless steel is provided in Section 6.3 of the MATPRO manual. The equations are

$$k = \begin{cases} 7.58 + 0.0189 T & \text{for } 300 \le T < 1,671 \text{ K} \\ 610.9393 - 0.342176 T & \text{for } 1,671 \le T < 1,727 \text{ K} \\ 20 & \text{for } T \ge 1,727 \text{ K} \end{cases} \qquad (4.5\text{-}15)$$

The stainless steel specific heat capacity is given in Section 6.2 of the MATPRO manual. The equations are

$$C_p = \begin{cases} 326 - 0.242\,T + 3.71\,T^{0.719} & \text{for } 300 \le T < 1{,}771 \text{ K} \\ 691.98 & \text{for } T \ge 1{,}771 \text{ K} \end{cases} \tag{4.5-16}$$

The reference density is 7,800 kg/m^3.

The uranium dioxide thermal conductivity data are taken from Section 2.3 of the MATPRO manual. The general equation for the thermal conductivity of solid fuel is

$$k = \left[\frac{D}{1 + T'(1-D)}\right]\left[\frac{C_v}{(A + BT'')(1 + 3e_{th})}\right] + \tag{4.5-17}$$

$$5.2997 \times 10^{-3}\,T e^{\left(\frac{-13,358}{T}\right)}\left\{1 + 0.169\left[\left(\frac{13,358}{T}\right) + 2\right]^2\right\}$$

where

k	=	thermal conductivity (W/m·K)
D	=	fraction of theoretical density (dimensionless); a value of 0.95 is assumed
C_V	=	phonon contribution to the specific heat at constant volume (J/kg·K). For pure UO_2, this is given by

$$C_v = \frac{296.7 \times 535.285^2 \times e^{\left(\frac{535.285}{T}\right)}}{T^2\left[e^{\left(\frac{535.285}{T}\right)} - 1\right]^2} \tag{4.5-18}$$

e_{th}	=	linear strain term for temperatures above 300 K (dimensionless), which is given by
e_{th}	=	$\Delta L/L_0$
	=	1.0 x 10^{-5}T $-$ 3.0 x 10^{-3} + 4.0 x 10^{-2} exp (-6.9 x 10^{-20}/1.38 x 10^{-23}T).
T	=	fuel temperature (K)

| T' | = | 6.5-0.00469 T if fuel temperature < 1,364 K. For temperatures > 1,834 K, T' = -1. Values are interpolated between these two temperatures. |

| T" | = | fuel temperature if < 1,800 K. For temperatures > 2,300 K, T" = 2,050 K. Values are interpolated between these two temperatures. |

| A | = | a factor proportional to the point defect contribution to the phonon mean free path. Assuming an oxygen-to-metal ratio of 2.0, this factor is 0.339 m·s/kg·K. |

| B | = | a factor proportional to the phonon-phonon scattering contribution to the phonon mean free path. Assuming no plutonium, this factor is 0.06867 m·s/kg·K. |

For liquid UO_2, a constant value is used. It is given by

$$k = 11.5 \text{ W/m} \cdot \text{K} . \tag{4.5-19}$$

The melting of pure UO_2 is an isothermal process. For the code input, the transition from solid to liquid is modeled to occur between 3,113.15 and 3,114 K. The lower limit on the calculated values is 300 K.

The specific heat capacity information is provided in Section 2.2 of the MATPRO manual. Assuming that the material is pure UO_2 (no PuO_2), and that the oxygen-to-metal ratio is 2.0,

$$C_p = \frac{296.7 \times 535.285^2 \times e^{\left(\frac{535.285}{T}\right)}}{T^2 \left[e^{\left(\frac{535.285}{T}\right)} - 1\right]^2} + 2.43 \times 10^{-2}T + \tag{4.5-20}$$

$$\frac{2 \times 8.745 \times 10^7 \times 1.577 \times 10^5}{2 \times 8.3143 \times T^2} e^{\left(-\frac{1.577 \times 10^5}{8.3143\,T}\right)}$$

for solid material, and

$$C_p = 503 \text{ J/kg} \cdot \text{K}$$

for liquid.

The reference density is 10,980 kg/m^3. A lower temperature limit of 300 K is calculated.

The zircaloy thermal conductivity is taken from Section 4.4 of the MATPRO manual. The equations used are

$$k = \begin{cases} 7.51 + 2.09 \times 10^{-2}T - 1.45 \times 10^{-5}T^2 + 7.67 \times 10^{-9}T^3 & \text{for } 300 \leq T < 2,089 \text{ K} \\ 36 & \text{for } T \geq 2,089 \text{ K} \end{cases}$$

The transition from solid to liquid, with the accompanying reduction in thermal conductivity, occurs between 2,098 and 2,125 K; these are the solidus and liquidus temperatures for zircaloy with a zero oxidation concentration (MATPRO manual, Section 4.1.1).

The specific heat capacity for zircaloy is a table lookup (see Table 4-2 in the MATPRO manual) with a temperature range of 300-1,248 K.

The reference density is 6,551 kg/m^3.

4.5.1 References

4.5-1. L. J. Siefken, E. W. Coryell, E. A. Harvego, and J. K. Hohorst, *SCDAP/RELAP5/MOD3.3 Code Manual, Volume 4: MATPRO – A Library of Material Properties for Light-Water-Reactor Accident Analysis*, NUREG/CR-6150, INEL-96/0422, Vol. 4, Rev. 2, Idaho National Engineering and Environmental Laboratory, January 2001.

4.5-2. J. K. Hohorst, ed., *SCDAP/RELAP5/MOD2 Code Manual, Volume 4: MATPRO – A Library of Material Properties for Light-Water-Reactor Accident Analysis*, NUREG/CR-5273, EGG-2555, Vol. 4, Idaho National Engineering Laboratory, February 1990.

4.5-3. *Nuclear Systems Materials Handbook – Volume 1, Design Data*, TID-26666, Revision 37, Oak Ridge National Laboratory, September 1988.

4.6 ATHENA Specific Boundary Conditions

The development of the difference equations uses a general form for the boundary conditions and the specific conditions implemented in ATHENA are expressed in that form. For heat structure boundaries attached to hydrodynamic volumes, a convective package is typically used to define the boundary conditions. In addition, symmetry or insulated conditions are provided, and for special situations, tabular based conditions or control variable based conditions can be specified.

4.6.1 Correlation Package Conditions

The correlation package partitions the total heat flux at the heat structure surface into heat fluxes from or to the liquid and vapor/gas phases. The heat fluxes are defined using five heat transfer coefficients and four fluid/saturation temperatures. They are given by

$$q_{wf} = h_{wff}[T_{sr} - T_f] + h_{wfT}[T_{sr} - T^s(P)] \tag{4.6-1}$$

$$q_{wg} = h_{wgg}[T_{sr} - T_g] + h_{wgT}[T_{sr} - T^s(P)] + h_{wgp}[T_{sr} - T^s(P_s)] \tag{4.6-2}$$

$$q_b = q_{wf} + q_{wg} \tag{4.6-3}$$

where

q_{wf} =   heat flux to liquid

q_{wg} =   heat flux to vapor/gas

q_b =   total heat flux

T_{sr} =   surface temperature

T_f =   liquid temperature

T_g =   vapor/gas temperature

$T^s(P)$ =   saturation temperature based on total pressure

$T^s(P_s)$ =   saturation temperature based on partial pressure of vapor

h_{wff} =   heat transfer coefficient for difference of surface temperature and liquid temperature for heat transfer to liquid

h_{wfT} =   heat transfer coefficient for difference of surface temperature and saturation temperature corresponding to total pressure for heat transfer to liquid

h_{wgg} =   heat transfer coefficient for difference of surface temperature and vapor/gas temperature for heat transfer to vapor/gas

h_{wgT} =   heat transfer coefficient for difference of surface temperature and saturation temperature corresponding to total pressure for heat transfer to vapor/gas

h_{wgp} =   heat transfer coefficient for difference of surface temperature and saturation temperature corresponding to partial pressure of vapor for transfer to vapor/gas.

Using first order Taylor series approximations,

$$q_{wf}^{n+1} = q_{wf}^0 + \frac{\partial q_{wf}}{\partial T_{sr}}\Delta T_{sr} + \frac{\partial q_{wf}}{\partial T_f}\Delta T_f + \frac{\partial q_{wf}}{\partial T^s(P)}\Delta T^s(P) \tag{4.6-4}$$

$$q_{wg}^{n+1} = q_{wg}^0 + \frac{\partial q_{wg}}{\partial T_{sr}}\Delta T_{sr} + \frac{\partial q_{wg}}{\partial T_g}\Delta T_g + \frac{\partial q_{wg}}{\partial T^s(P)}\Delta T^s(P) + \frac{\partial q_{wg}}{\partial T^s(P_s)}\Delta T^s(P_s) \qquad (4.6\text{-}5)$$

where Δ is an operator, $\Delta F = F^{n+1} - F^n$.

Note that q_{wf}^0 and q_{wg}^0 are not old-time values of heat fluxes but instead are the heat fluxes obtained from the correlations using old-time surface temperature and fluid conditions. Because only new-time boundary condition information is used in the difference equations, the old-time heat fluxes do not appear in the difference equations.

Assuming the heat transfer coefficients are constant over a time step,

$$\frac{\partial q_{wf}}{\partial T_{sr}} = h_{wff} + h_{wfT} \qquad (4.6\text{-}6)$$

$$\frac{\partial q_{wf}}{\partial T_f} = -h_{wff} \qquad (4.6\text{-}7)$$

$$\frac{\partial q_{wf}}{\partial T_T} = -h_{wfT} \qquad (4.6\text{-}8)$$

$$\frac{\partial q_{wg}}{\partial T_{sr}} = h_{wgg} + h_{wgT} + h_{wgp} \qquad (4.6\text{-}9)$$

$$\frac{\partial q_{wg}}{\partial T_g} = -h_{wgg} \qquad (4.6\text{-}10)$$

$$\frac{\partial q_{wg}}{\partial T^s(P)} = -h_{wgT} \qquad (4.6\text{-}11)$$

$$\frac{\partial q_{wg}}{\partial T^s(P)} = -h_{wgp} \;. \qquad (4.6\text{-}12)$$

Then,

$$q_{wf}^{n+1} = q_{wf}^0 + [h_{wff} + h_{wfT}]\Delta T_{sr} - h_{wff}\Delta T_f - h_{wfT}\Delta T^s(P) \qquad (4.6\text{-}13)$$

$$q_{wg}^{n+1} = q_{wg}^0 + [h_{wgg} + h_{wgT} + h_{wgp}]\Delta T_{sr} - h_{wgg}\Delta T_g - h_{wgT}\Delta T^s(P) - h_{wgp}\Delta T^s(P_s) \tag{4.6-14}$$

$$q_b^{n+1} = q_{wf}^0 + q_{wg}^0 + h_b\Delta T_{sr} - h_{wff}\Delta T_f - h_{wgg}\Delta T_g - [h_{wfT} + h_{wgT}]\Delta T^s(P) - h_{wgp}\Delta T^s(P_s) \tag{4.6-15}$$

where

$$h_b = h_{wff} + h_{wfT} + h_{wgg} + h_{wgT} + h_{wgp} \quad . \tag{4.6-16}$$

Expressing Equation (4.6-15) in terms of the general boundary condition Equation (4.1-2),

$$A = -h_b \tag{4.6-17}$$

$$B = -k \tag{4.6-18}$$

$$D = q_{wf}^0 + q_{wg}^0 - h_b T_{sr}^{n+1} - h_{wff}\Delta T_f - h_{wgg}\Delta T_g - [h_{wfT} + h_{wgT}]\Delta T^s(P) - h_{wgp}\Delta T^s(P_s) \quad . \tag{4.6-19}$$

4.6.2 Insulated and Tabular Boundary Conditions

The other boundary conditions implemented in ATHENA are given below. The first two conditions are flux-specified conditions; the first condition is a symmetry or insulated condition and is just a special case of the second condition. The third condition is a convection condition similar to that used with the correlation package except that only a total heat transfer coefficient which is a tabular function of time or surface temperature is used. The fourth condition directly specifies the surface temperature. The four conditions are

$$-k\frac{\partial T}{\partial x} = 0 \tag{4.6-20}$$

$$-k\frac{\partial T}{\partial x} = q_{TA}(t) \tag{4.6-21}$$

$$-k\frac{\partial T}{\partial x} = h_{TA}(T - T_{TA}) \tag{4.6-22}$$

$$T = T_{TA}(t) \tag{4.6-23}$$

where

q_{TA} = the total heat flux as a function of time obtained from input tables

h_{TA} = the total heat transfer coefficient as an input tabular function of either time or surface temperature

T_{TA} = an input general temperature table tabular function of time, an input control variable that calculates the temperature, or the volume fraction weighted average of the liquid and vapor/gas temperatures of the hydrodynamic volume attached to the boundary.

4.7 Solution of Simultaneous Equations

The difference approximation for the mesh points [Equations (4.3-9), (4.4-3), and (4.4-7)] lead to a tri-diagonal set of M equations.

$$\begin{bmatrix} b_1 & c_1 & & & & \\ a_2 & b_2 & c_2 & & & \\ & \bullet & \bullet & \bullet & & \\ & & \bullet & \bullet & \bullet & \\ & & & a_{M-1} & b_{M-1} & c_{M-1} \\ & & & & a_M & b_M \end{bmatrix} \begin{bmatrix} T_1 \\ T_2 \\ \bullet \\ \bullet \\ T_{M-1} \\ T_M \end{bmatrix} = \begin{bmatrix} d_1 \\ d_2 \\ \bullet \\ \bullet \\ d_{M-1} \\ d_M \end{bmatrix} . \tag{4.7-1}$$

Equations 1 and M correspond to the left and right boundary mesh points respectively, and equations 2 through M-1 correspond to the interior mesh points. The terms in d_2 through d_{M-1} do not include any of the fluid or saturation temperatures, T_f, T_g, $T^s(P)$, and $T^s(P_s)$. The terms in d_1 and d_M do include the fluid or saturation temperatures, and d_1 and d_M can be expressed as

$$d_1 = d_{10} + d_{1f}\Delta T_{1f} + d_{1g}\Delta T_{1g} + d_{1T}\Delta T_1^s(P) + d_{1p}\Delta T_1^s(P_s) \tag{4.7-2}$$

$$d_M = d_{M0} + d_{Mf}\Delta T_{Mf} + d_{Mg}\Delta T_{Mg} + d_{MT} \Delta T_M^s(P) + d_{Mp}\Delta T_M^s(P_s) \tag{4.7-3}$$

where the first subscript, 1 or M, has been introduced to indicate the left or right boundary. The coefficient matrix is symmetric unless a boundary condition specifies the surface temperature. In that case, the corresponding off-diagonal element is zero and thus symmetry may not exist in the first and/or last rows. The solution to the above equation is obtained by

$$E_1 = \frac{c_1}{b_1} \text{ and } F_1 = \frac{d_1}{b_1} \tag{4.7-4}$$

$$E_j = \frac{c_j}{b_j - a_j E_{j-1}} \quad \text{and} \quad F_j = \frac{d_j - a_j F_{j-1}}{b_j - a_j E_{j-1}} \quad \text{for } j = 2, 3, ..., M\text{-}1 \tag{4.7-5}$$

$$g_M = \frac{d_M - a_M F_{M-1}}{b_M - a_M E_{M-1}} \tag{4.7-6}$$

$$g_j = - E_j g_{j+1} + F_j \quad \text{for } j = M\text{-}1, M\text{-}2, ..., 3, 2, 1 \tag{4.7-7}$$

$$T_j^{n+1} = g_j \quad \text{for all } j \; . \tag{4.7-8}$$

These procedures can be derived by applying the rules for Gaussian elimination. This method of solution introduces little roundoff error if the off-diagonal elements are negative and the diagonal is greater than the sum of the magnitudes of the off-diagonal elements. From the form of the difference equations, these conditions are satisfied for any values of the mesh point spacing, time step, and thermal properties.

Expanding the expression for g_j in Equation(4.7-8) using Equations (4.7-4) through (4.7-7), gives

$$
\begin{aligned}
T_j^{n+1} = g_j = \; & g_{j0} + g_{j1f}\Delta T_{1f} + g_{j1g}\Delta T_{1g} + g_{j1T}\Delta T_1^s(P) + g_{j1p}\Delta T_1^s(P_s) + \\
& g_{jMf}\Delta T_{Mf} + g_{jMg}\Delta T_{Mg} + g_{jMT}\Delta T_M^s(P) + g_{jMp}\Delta T_M^s(P_s) \; .
\end{aligned}
\tag{4.7-9}
$$

The nine g factors in Equation (4.7-9) are functions of the terms a_j, b_j, c_j (j=1, ...,M), d_{10}, d_{1f}, d_{1g}, d_{1T}, d_{1p}, d_j (j=2, ..., M-1), and d_{M0}, d_{Mf}, d_{Mg}, d_{MT}, d_{Mp} in Equations (4.7-1), (4.7-2), and (4.7-3). For the first g factor (g_{j0}), the first subscript, j, indicates the mesh point number, and the second subscript, 0, indicates that no particular fluid/saturation temperatures are used for this term. For the remaining eight g factors (g_{j1f}, g_{j1g}, g_{j1T}, g_{j1p}, g_{jMf}, g_{jMg}, g_{jMT}, g_{jMp}), the first subscript indicates the mesh point number, the second subscript indicates the boundary (1 for the left boundary and M for the right boundary), and the third subscript indicates the particular fluid/saturation temperature (f, g,T, p).

In passing information to the hydrodynamics advancement, the effect of fluid/saturation temperature changes on one boundary are ignored on the other boundary. Thus, the left and right boundary surface temperatures are given by

$$T_1^{n+1} = g_{10} + g_{11f}\Delta T_{1f} + g_{11g}\Delta T_{1g} + g_{11T}\Delta T_1^s(P) + g_{11p}\Delta T_1^s(P_s) \tag{4.7-10}$$

$$T_M^{n+1} = g_{M0} + g_{MMf}\Delta T_{Mf} + g_{MMg}\Delta T_{Mg} + g_{MMT}\Delta T_M^s(P) + g_{MMp}\Delta T_M^s(P_s) \; . \tag{4.7-11}$$

A user option allows an explicit or an implicit coupling between the heat conduction-transfer and hydrodynamic time advancements. With the explicit option, the changes in hydrodynamic temperatures are assumed zero at this point and the new-time temperatures are given by the first term, g_{j0}, of Equation (4.7-9). If the implicit advancement is used, the new time temperatures are computed using all the terms in Equation (4.7-9) after the fluid temperatures are computed.

4.8 Computation of Heat Fluxes

When the correlation boundary condition package is used, the new-time heat fluxes to the liquid and vapor/gas phases are computed by substituting the Equation (4.7-9) for the surface temperature into the boundary conditions given in Equation (4.6-1) and (4.6-2). The expression for any temperature could involve the fluid/saturation temperatures from both the left and right boundary volumes. If only one side of the heat structure is attached to a hydrodynamic volume, that boundary condition would involve only those volume conditions. That fits in well with the numerical approximations in the hydrodynamic solution which assume the conservation equations for each volume include new time values only from that volume. Most heat structures such as fuel pins, plates, or piping have only one side connected to a hydrodynamic volume. An important case where the two sides are connected to two different volumes is a heat structure representing heat exchanger tubing. This situation would involve unknown temperatures from more than one volume in the energy equations for each attached volume and thus would not be compatible with the hydrodynamic advancement scheme. To avoid this problem, the heat flux for one boundary ignores the effects of fluid/saturation temperature changes in the other volume. This is a reasonable approximation since the effects of fluid/saturation temperature changes on one side of the heat structure has a highly attenuated effect on the heat flux on the other side.

Dropping the subscript for the particular surface, the expressions for heat fluxes are

$$
\begin{aligned}
q_{wf}^{n+1} &= q_{wf}^0 + [h_{wff} + h_{wfT}][g_0 - T_{sr}^n] + [h_{wff} + h_{wfT}][g_f \Delta T_f + g_g \Delta T_g + g_T \Delta T^s(P) + g_p \Delta T^s(P_s)] \\
&\quad - h_{wff}\Delta T_f - h_{wfT}\Delta T^s(P) \\
&= q_{wf0} + q_{wff}\Delta T_f + q_{wfg}\Delta T_g + q_{wfT}\Delta T^s(P) + q_{wfp}\Delta T^s(P_s)
\end{aligned}
\tag{4.8-1}
$$

$$
\begin{aligned}
q_{wg}^{n+1} &= q_{wg}^0 + [h_{wgg} + h_{wgT} + h_{wgp}][g_0 - T_{sr}^n] \\
&\quad + [h_{wgg} + h_{wgT} + h_{wgp}][g_f \Delta T_f + g_g \Delta T_g + g_T \Delta T^s(P) + g_p \Delta T^s(P_s)] \\
&\quad - h_{wgg}\Delta T_g - h_{wgT}\Delta T^s(P) - h_{wgp}\Delta T^s(P_s) \\
&= q_{wg0} + q_{wgf}\Delta T_f + q_{wgg}\Delta T_g + q_{wgT}\Delta T^s(P) + q_{wgp}\Delta T^s(P_s) \ .
\end{aligned}
\tag{4.8-2}
$$

The expression following the second equal sign in the equations above is a convenient gathering of terms for passing heat flux information to the hydrodynamic advancement. The coefficients of the fluid temperature changes are zero if the explicit coupling between the heat conduction-transfer and hydrodynamics is used.

For heat fluxes from boundaries not using the correlation package, a total heat flux is computed and distributed to the liquid and vapor/gas phases in direct proportion to their volume fractions. The heat fluxes are returned in q_{wf0} and q_{wg0}, and the coefficients of the fluid/saturation temperature changes are set to zero. For flux specified conditions, the total heat flux is given directly by the boundary condition. For a convection boundary, the total heat flux is obtained by substituting in the surface temperature. If the other boundary uses the convective package, the surface temperature is that assuming the fluid/saturation temperature changes are zero. For the temperature-specified boundary, the heat flux is computed from the boundary difference equation (even though it was not used to compute the temperature). The expression for the right boundary (the left is similar) is

$$
\begin{aligned}
q_M^{n+1}\delta_{1M}^n &= \frac{k_{1M}^n}{\sigma+1}(T_{M-1}^{n+1}-T_M^{n+1})\delta_{1M}^s + \frac{\sigma k_{1M}^n}{\sigma+1}(T_{M-1}^n-T_M^n)\delta_{1M}^s \\
&+ P_f\frac{(\sigma P^n + P^{n+1})}{\sigma+1}Q_{1M}\delta_{1M}^v - \frac{\sigma(\rho C_p)_{1M}^n}{\Delta t}(T_M^{n+1}-T_M^n)\delta_{1M}^v \quad .
\end{aligned}
$$

(4.8-3)

4.9 Two-Dimensional Conduction Solution/Reflood

A two-dimensional conduction scheme is used in the reflood model for cylindrical or rectangular heat structures. **Figure 4.9-1** shows an elemental cell around the mesh point. For a cylindrical geometry, the volume elements are

$$
V_1 = \pi\delta_t\delta_1\left(\frac{r_i - \frac{\delta_1}{4}}{2}\right)
$$

(4.9-1)

$$
V_2 = \pi\delta_t\delta_r\left(\frac{r_i + \frac{\delta_r}{4}}{2}\right)
$$

(4.9-2)

$$
V_3 = \pi\delta_b\delta_1\left(\frac{r_i - \frac{\delta_1}{4}}{2}\right)
$$

(4.9-3)

$$
V_4 = \pi\delta_b\delta_r\left(\frac{r_i + \frac{\delta_r}{4}}{2}\right)
$$

(4.9-4)
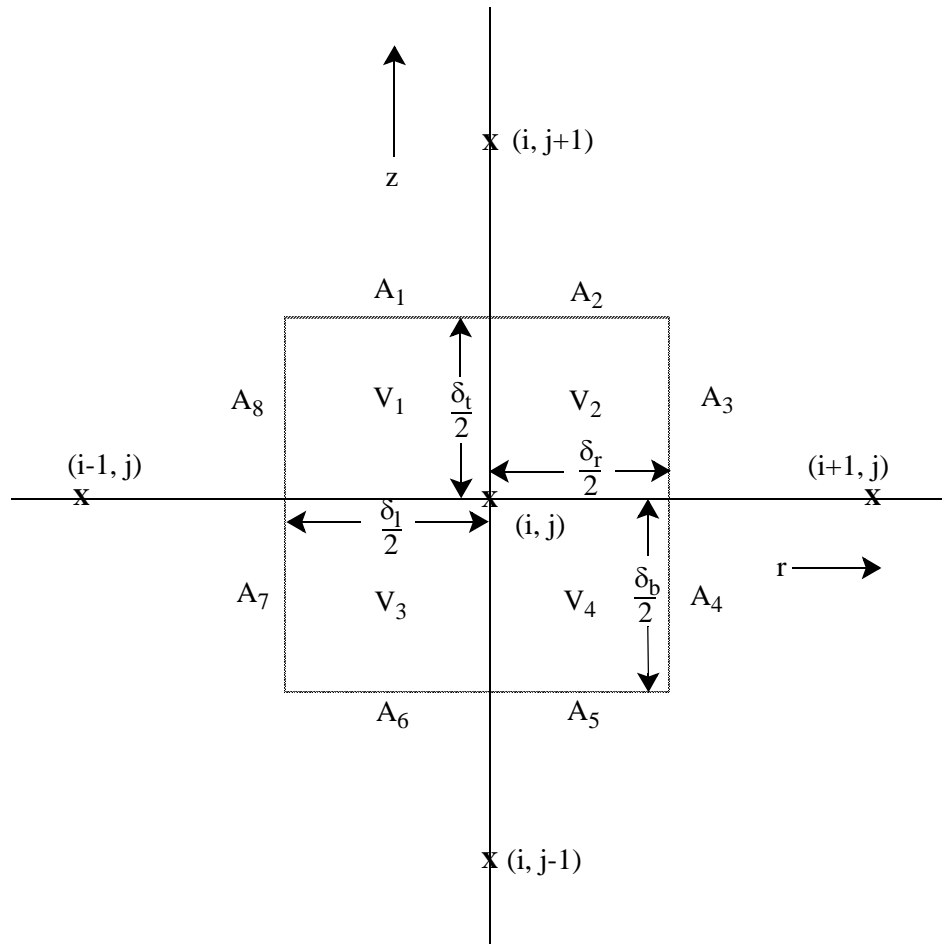
Figure 4.9-1 Volume and surface elements around a mesh point (i, j).

and the surface elements are

$$A_1 \;=\; \pi\delta_1\!\left(r_i - \frac{\delta_1}{4}\right) \tag{4.9-5}$$

$$A_2 \;=\; \pi\delta_r\!\left(r_i + \frac{\delta_r}{4}\right) \tag{4.9-6}$$

$$A_3 \;=\; \pi\delta_t\!\left(r_i + \frac{\delta_r}{2}\right) \tag{4.9-7}$$

$$A_4 \;=\; \pi\delta_b\!\left(r_i + \frac{\delta_r}{2}\right) \tag{4.9-8}$$

$$A_5 = A_2 \tag{4.9-9}$$

$$A_6 = A_1 \tag{4.9-10}$$

$$A_7 = \pi \delta_b \left(r_i - \frac{\delta_l}{2} \right) \tag{4.9-11}$$

$$A_8 = \pi \delta_t \left(r_i - \frac{\delta_l}{2} \right) \quad . \tag{4.9-12}$$

Integration of the heat conduction Equation (4.1-1) over the elemental cell yields the following form of finite difference equation

$$G_{ij} \left(\frac{T_{i,j}^{n+1} - T_{i,j}^{n}}{\Delta t} \right) = a_{ij}^L T_{i-1,j} + a_{ij}^R T_{i+1,j} + a_{ij}^T T_{i,j+1} + a_{ij}^B T_{i,j-1}$$
$$- (a_{ij}^L + a_{ij}^R + a_{ij}^T + a_{ij}^B) T_{ij} + S_{ij} \quad . \tag{4.9-13}$$

By defining the material properties, $(\rho C_p)_{ij}$ and k_{ij}, at the center of the r-direction interval between mesh points (i,j) and (i + 1,j), the coefficients G_{ij}, a_{ij}^R, and a_{ij}^T of Equation (4.9-13) can be written as

$$G_{ij} = (\rho C_p)_{i-1,j} (V_1 + V_3) + (\rho C_p)_{ij} (V_2 + V_4) \tag{4.9-14}$$

$$a_{ij}^R = \frac{k_{ij}(A_3 + A_4)}{\delta_r} \tag{4.9-15}$$

$$a_{ij}^T = \frac{\left[(k_{ij} + k_{i,j+1})\dfrac{A_2}{2} + (k_{i-1,j} + k_{i-1,j+1})\dfrac{A_1}{2} \right]}{\delta_t} \quad . \tag{4.9-16}$$

The other two coefficients, a_{ij}^L and a_{ij}^B, are obtained by the symmetry relations

$$a_{ij}^L = a_{i-1,j}^R \tag{4.9-17}$$

$$a_{ij}^B = a_{i,j-1}^T \quad . \tag{4.9-18}$$

The space and time-dependence of the volumetric source term, S, described in Equation (4.3-3) are extended to the two-dimensional cases as

$$S(\bar{x},t) = P_f P(t) Q(r,z) \tag{4.9-19}$$

with the assumption that Q is independent of z within a heat structure. For this two-dimensional model, Q(r,z) is assumed to vary only in the r and z directions. Accordingly, the volumetric heat source term S_{ij} of Equation (4.9-13) is

$$S_{ij} = P_f P(t)(Q_l^T V_1 + Q_l^B V_3 + Q_r^T V_2 + Q_r^B V_4) \quad . \tag{4.9-20}$$

Here, $Q_l^T = Q_l^B$ and $Q_r^T = Q_r^B$ if the entire cell is within the same heat structure.

Equation (4.9-13) is written for an interior point (i,j). For a point on the boundary, some of the coefficients a_{ij}^L, a_{ij}^R, a_{ij}^B, and a_{ij}^T should vanish. For example, at the bottom left corner, a_{ij}^L and a_{ij}^B are zero. Also some of the terms in Equations (4.9-16) and (4.9-20) disappear. Furthermore, the boundary condition must be added. To be consistent with the one-dimensional heat conduction scheme, an assumption is made that no heat is fluxed across the top and bottom ends. For the right and left boundaries, the boundary condition can be represented by one of the forms described in Equations (4.6-1), (4.6-2), and (4.6-20) through (4.6-22). The boundary condition specifying the surface temperature as a function of time, Equation (4.6-23), has been dropped in the two-dimensional scheme for computational efficiency.

The two-dimensional capability allows explicit or implicit coupling between the heat conduction-transfer and hydrodynamics.

The difference Equation (4.9-13) is solved using the alternating direction implicit (ADI) method. The scheme is represented by two steps as follows:

1. Column Inversion:

$$\frac{(T_{ij}^{n+1/2} - T_{ij}^n)G_{ij}}{\left(\dfrac{\Delta t}{2}\right)} = a_{ij}^L T_{i-1,j}^n + a_{ij}^R T_{i+1,j}^n + a_{ij}^T T_{i,j+1}^{n+1/2} + a_{ij}^B T_{i,j-1}^{n+1/2}$$

$$- (a_{ij}^L + a_{ij}^R)T_{ij}^n - (a_{ij}^T + a_{ij}^B)T_{ij}^{n+1/2} + S_{ij} \quad . \tag{4.9-21}$$

2. Row Inversion:

$$\frac{(T_{ij}^{n+1} - T_{ij}^{n+1/2})G_{ij}}{\left(\frac{\Delta t}{2}\right)} = a_{ij}^L T_{i-1,j}^{n+1} + a_{ij}^R T_{i+1,j}^{n+1} + a_{ij}^T T_{i,j+1}^{n+1/2} + a_{ij}^B T_{i,j-1}^{n+1/2}$$

(4.9-22)

$$- (a_{ij}^L + a_{ij}^R)T_{ij}^{n+1} - (a_{ij}^T + a_{ij}^B)T_{ij}^{n+1/2} + S_{ij} \quad .$$

Here the superscripts n, $n + \frac{1}{2}$, and n + 1 denote the values at times t, $t + \frac{\Delta t}{2}$, and t + Δt, respectively.

4.10 Fine Mesh Rezoning Scheme

A fine mesh-rezoning scheme is implemented to efficiently use the two-dimensional conduction solution for reflood calculations. The scheme is similar to the one used in COBRA-TF[4.10-1] and is intended to resolve the large axial variation of wall temperatures and heat fluxes. The number of axial nodes in the heat structures is varied in such a way that the fine nodes exist only in the nucleate boiling and transition boiling regions.

A heat-structure geometry, which is composed of 1 to 99 heat structures as specified by users, is selected as an elementary unit for the reflood model. **Figure 4.10-1**a shows a typical heat structure geometry with one fluid-control volume connected to each heat structure. The dots are radial mesh points. At the initiation of the reflood model, each heat structure is subdivided into two axial intervals (**Figure 4.10-2**b). A two-dimensional array of mesh points is thus formed. Thereafter, the number of axial intervals may be doubled, halved, or unchanged at each time step according to a set of rules to be discussed in the next paragraph. **Figure 4.10-2** also shows an example of a heat structure going through a cycle of axial nodalization variation.

The number of axial mesh intervals in a heat structure depends on the heat-transfer regimes in the heat structures. At each time step, all heat structures in a heat-structure geometry are searched to find the positions of T_{IB}, the wall temperature at the incipience of boiling, and T_{CHF}, the wall temperature where critical heat flux occurs, and T_Q, the quench or rewetting temperature. Let us assume that T_{IB}, T_{CHF}, and T_Q are at the i-, j-, and k-th heat structures and $i \le j \le k$. Also, let N be the maximum number of axial mesh intervals specified by the user and α_g be the void fraction in the connected control volume. The number of axial mesh intervals in a heat structure is determined according to the following rules:

- For $\alpha_g > 0.999$ or $\alpha_g = 0$, the number is halved but not less than 2.

- For the (k + 1)-th heat structure, the number is doubled but not greater than N/2.

- For the (i - 1)-th heat structure, the number is halved but not less than N/2.

- The number is doubled up to N for the heat structures between max (j + 1, k) and min (j-1, i) and in the region of maximum wall temperature gradient.
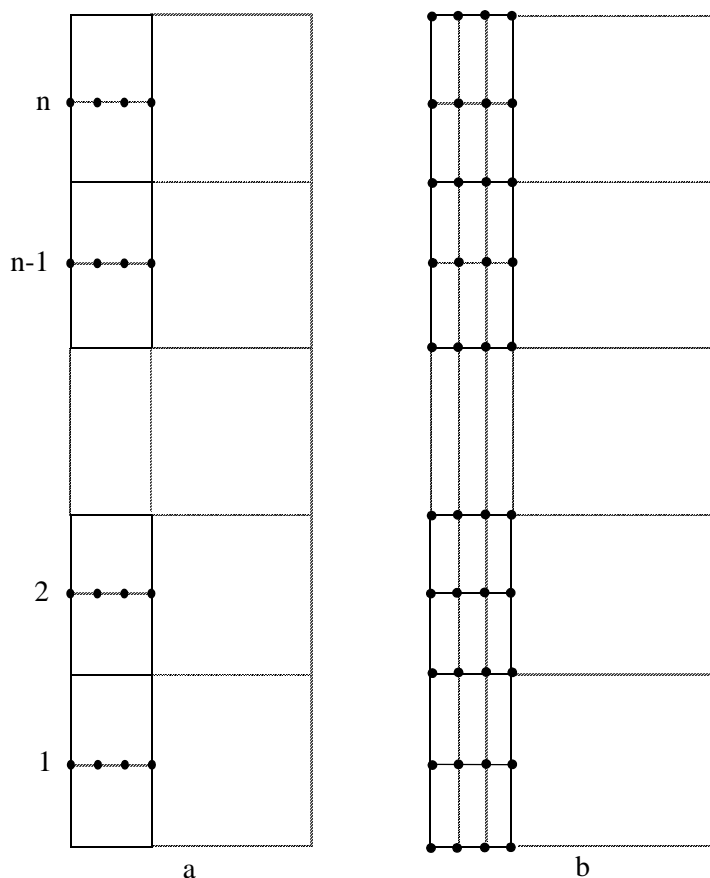
Figure 4.10-1 An elementary heat structure unit for reflood.

- For all other heat structures, the number is unchanged.

4.10.1 Reference

4.10-1. J. M. Kelly, "Quench Front Modeling and Reflood Heat Transfer in COBRA-TF," *ASME Winter Annual Meeting, New York, NY, 1979,* 79-WA/HT-63.

4.11 Gap Conductance Model

The ATHENA dynamic gap conductance model defines an effective gap conductivity based on a simplified deformation model generated from FRAP-T6.[4.11-1] The model employs three assumptions as follows: (a) the fuel-to-cladding radiation heat transfer, which only contributes significantly to the gap conductivity under the conditions of cladding ballooning, is neglected unless the cladding deformation model is activated (see Section 4.15); (b) the minimum gap size is limited such that the maximum effective
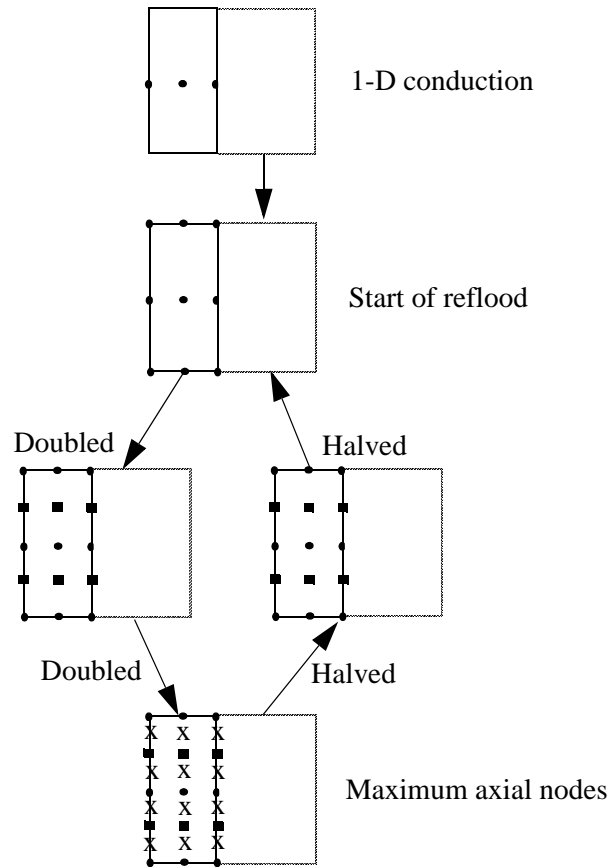
Figure 4.10-2 An example of the fine mesh-rezoning process.

gap conductivity is about the same order as that of metals; (c) the direct contact of the fuel pellet and the cladding is not explicitly considered.

The gap conductance through the gas is inversely proportional to the size of the gap. Since the longitudinal axis of the fuel pellets is usually offset from the longitudinal axis of the cladding, the width of the fuel-cladding gap varies with circumferential position. This variation causes the conductance through the gas in the fuel-cladding gap to vary with circumferential position. The circumferential variation of the conductance is taken into account by dividing the gap into several equal length segments, as shown in **Figure 4.11-1**. The conductance for each segment is calculated and then an average conductance, h_g, is computed in the FRAP-T6 model by the equation

$$h_g = \frac{k_g}{N} \sum_{n=1}^{N} \frac{1}{t_n + 3.2(R_F + R_c) + (g_1 + g_2)} \qquad (4.11\text{-}1)$$

INEEL-EXT-98-00834-V1   4-28
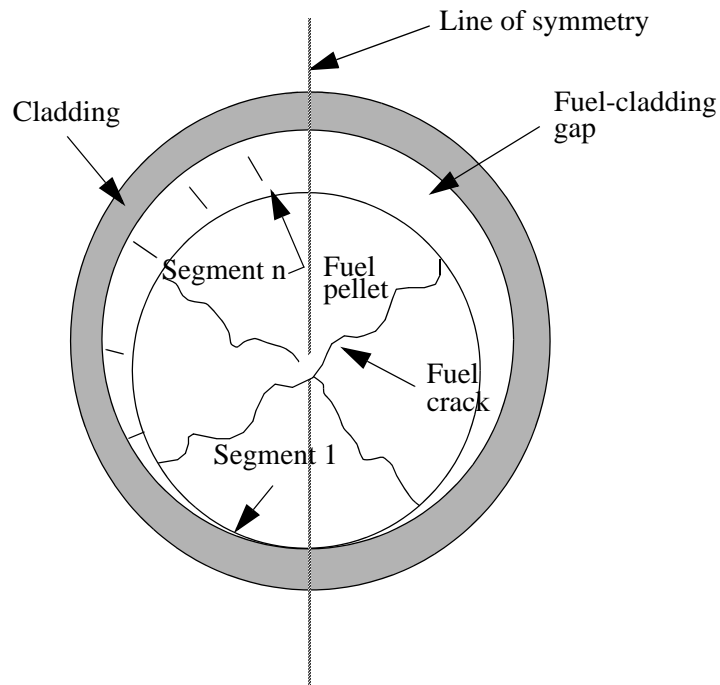
Figure 4.11-1 Segmentation at the fuel-cladding gap.

where

h_g = conductance through the gas in the gap (W/m^2•K)

n = number of a circumferential segment

N = total number of circumferential segments = 8

k_g = thermal conductivity of gas (W/m•K)

t_n = width of fuel-cladding gap at the midpoint of the n-th circumferential segment (m)

R_F = surface roughness of the fuel (m)

R_c = surface roughness of the cladding (m)

g_1, g_2 = temperature jump distance terms for fuel and cladding (m).

The width of the fuel-cladding gap at any given circumferential segment is calculated by the equation

$$t_n = t_g + \left[-1 + \left(\frac{2n-1}{N} \right) \right] t_o \tag{4.11-2}$$

where

t_g =   circumferentially averaged fuel-cladding gap width (m)

t_o =   as-fabricated fuel-cladding gap width (m).

The value of t_n in Equation (4.11-2) is limited between zero and $2t_g$.

The temperature jump distance terms account for the temperature discontinuity caused by incomplete thermal accommodation of gas molecules to the surface temperature. The terms also account for the inability of gas molecules leaving the fuel and cladding surfaces to completely exchange their energy with neighboring gas molecules, which produces a nonlinear temperature gradient near the fuel and cladding surfaces. The terms are calculated by

$$g_1 + g_2 = \frac{0.024688 k_g T_g^{1/2}}{P_g \sum_i f_i a_i M_i^{-1/2}} \tag{4.11-3}$$

where

T_g =   temperature of gas in the fuel-cladding gap (K)

P_g =   gas pressure (Pa)

f_i =   mole fractions of i-th component of gas

a_i =   accommodation coefficient of the i-th component of gas

M_i =   molecular weight of the i-th component of gas.

The accommodation coefficients for helium and xenon are obtained by using curve fits to the data of Ullman:[4.11-2]

$$a_{He} = 0.425 - 2.3 \times 10^{-4} T_g \text{ (helium)} \tag{4.11-4}$$

$$a_{Xe} = 0.740 - 2.5 \times 10^{-4} \, T_g \quad \text{(xenon)} \;. \tag{4.11-5}$$

If T_g is > 1,000 K, T_g is set to 1,000 K. The accommodation coefficients for other gases are determined by interpolation and written as

$$a_i = a_{He} + \frac{(M_i - M_{He})}{(M_{Xe} - M_{He})}(a_{Xe} - a_{He}) \;. \tag{4.11-6}$$

The circumferential averaged width of the fuel cladding gap, t_g, in Equation (4.11-2) is determined by the expression

$$t_g = t_o - u_F + u_C \tag{4.11-7}$$

where

$\quad u_F \quad = \quad$ radial displacement of the fuel pellet surface (m)

$\quad u_C \quad = \quad$ radial displacement of cladding inner surface (m).

The radial displacements, u_F and u_C, are primarily due to thermal expansion. The radial displacement, of the fuel pellet surface, u_F, is calculated by the equation

$$u_F = u_{TF} + u_r + u_s \tag{4.11-8}$$

where

$\quad u_{TF} \quad = \quad$ radial displacement due to thermal expansion (m)

$\quad u_r \quad = \quad$ radial displacement due to uniform fuel relocation (m)

$\quad u_s \quad = \quad$ radial displacement due to fission gas induced fuel swelling and densification (m).

The fuel thermal expansion displacement, u_{TF}, is obtained from

$$u_{TF} = \sum_{n=2}^{N} (r_n - r_{n-1}) \varepsilon_{TF}\left(T_{n+\frac{1}{2}}\right) \tag{4.11-9}$$

where

n	=	radial mesh point number
N	=	total number of mesh points in the fuel
r_n	=	radius of radial mesh point n
ε_{TF}	=	fuel thermal expansion strain (function of temperature)
$T_{n+\frac{1}{2}}$	=	average fuel temperature at the center on the node between mesh points n and n+1(K).

The uniform fuel relocation displacement, u_r is assumed to be zero. The fission gas induced swelling and densification, u_s is supplied by the user. The radial displacement of the inner surface of the cladding is calculated by

$$u_C = u_{TC} + u_{cc} + u_e \qquad (4.11\text{-}10)$$

where

u_{TC}	=	radial displacement due to thermal expansion (m)
u_{cc}	=	radial displacement due to cladding creepdown (m)
u_e	=	radial displacement due to elastic deformation (m).

The cladding thermal expansion displacement, u_{TC}, is obtained from

$$u_{TC} = r_{cm}\, \varepsilon_{TC}\, (T_c) \qquad (4.11\text{-}11)$$

where

r_{cm}	=	radius of midplane of cladding (m)
ε_{TC}	=	cladding thermal expansion strain (function of temperature)
T_c	=	temperature of cladding at midplane (K).

The value of the cladding creepdown displacement, u_{cc} must be supplied by the user. For beginning-of-life fuel rods, u_{cc}, is equal to zero. For fuel rods with a significant amount of burnup, a FRAPCON-2[4.11-3] analysis is required to determine the value of u_{cc}. The cladding creepdown strain is given by the cladding creepdown displacement divided by r_m.

The cladding elastic deformation displacement, u_e, is calculated by

$$u_e = r_m \varepsilon_e = r_{cm}\left(\frac{\sigma_h - \nu\sigma_z}{E}\right)$$ (4.11-12)

where

ε_e = cladding elastic deformation strain

E = Young's modulus for the cladding (Pa)

σ_h = cladding hoop stress (Pa)

σ_z = cladding axial stress (Pa)

ν = Poisson's ratio for the cladding.

The cladding hoop and axial stress are given by

$$\sigma_h = \frac{P_g r_i - P_f r_o}{r_o - r_i}$$ (4.11-13)

$$\sigma_z = \frac{P_g r_i^2 - P_f r_o^2}{r_o^2 - r_i^2}$$ (4.11-14)

where

P_f = coolant pressure (Pa)

r_i = inner radius of cladding (m)

r_o = outer radius of cladding (m).

The Poisson's ratio used is

$$\nu = 0.3 \ . \tag{4.11-15}$$

The internal gas pressure P_g is determined in FRAP-T6[4.11-1] by a detailed plenum model. Since a plenum model is not included in the simplified approach, a static-ideal gas approximation for a fixed-plenum volume is used to calculate P_g, i.e.,

$$P_g = P_{g,i} \frac{T_f}{T_{f,i}} \tag{4.11-16}$$

where

$P_{g,i}$ =   initial gas pressure in the gap (Pa)

$T_{f,i}$ =   initial coolant temperature at the top of the core (K)

T_f =   current coolant temperature at the top of the core (K).

The initial internal gas pressure must be supplied by the user.

The volumetric heat capacity and thermal conductivity of the fuel rod materials, except for the thermal conductivity of the gap gas, must be supplied by the user. For the computation of the gas thermal conductivity, the user is required to provide the gas composition in terms of the mole fractions of seven common gases included in the model. The properties for determining material thermal expansion and elastic deformation are calculated from permanent data within the code, and no user-input is needed. The user, however, should be aware that these properties are computed under the assumption that the fuel material is uranium oxide and the cladding material is zircaloy. The properties of UO_2 and zircaloy along with gas conductivity are taken from MATPRO-11 (Revision 2)[4.11-4] and are described below.

The conductivity as a function of temperature for a pure noble or diatomic gas is calculated using

$$k_g = A T_g^B \ . \tag{4.11-17}$$

The constants A and B for seven common gases are given in **Table 4.11-1**. The thermal conductivity of a gas mixture is calculated from the expression

Table 4.11-1 Constants used in gas thermal conductivity correlation.

Gas	Constant	
	A (W/m·K^{1+B})	B (-)
Helium	2.639×10^{-3}	0.7085
Argon	2.986×10^{-4}	0.7224
Krypton	8.247×10^{-5}	0.8363
Xenon	4.351×10^{-5}	0.8616
H_2	1.097×10^{-3}	0.8785
N_2	5.314×10^{-4}	0.6898
O_2	1.853×10^{-4}	0.8729

$$k_g = \sum_{i=1}^{N} \frac{k_i X_i}{X_i + \sum_{j=1}^{N} \Phi_{ij} X_j} \tag{4.11-18}$$

where

$$\Phi_{ij} = \frac{\left[1 + \left(\frac{k_i}{k_j}\right)^{1/2}\left(\frac{M_i}{M_j}\right)^{1/4}\right]^2}{\left[8\left(1 + \frac{M_i}{M_j}\right)\right]^{1/2}} \tag{4.11-19}$$

N = number of components in the mixture

M_i = molecular weight of component i

X_i = mole fraction of the component i

k_i = thermal conductivity of the component i (W/m·K).

The strain function, ε_{TF} in Equation (4.11-9), of the UO_2 fuel due to thermal expansion is described by

$$\varepsilon_{TF} = 1.0 \times 10^{-5} T - 3.0 \times 10^{-3} + 4.0 \times 10^{-2} \exp\left(\frac{-6.9 \times 10^{-20}}{k_B T}\right) \tag{4.11-20}$$

where

T = fuel pellet temperature

k_B = Boltzmann constant (1.38×10^{-23} J/K).

The radial strain function, ε_{TC} in Equation (4.11-11), for the cladding thermal expansion is given by

$$\varepsilon_{TC} = 1.5985 \times 10^{-3} + 6.721 \times 10^{-6} \, T \tag{4.11-21}$$

for T < 1,073.15 K (α phase) and

$$\varepsilon_{TC} = -4.150 \times 10^{-3} + 9.7 \times 10^{-6} \, T \tag{4.11-22}$$

for T > 1,273.15 K (β phase), where T = cladding temperature (K). In the α to β phase transition zone (1,073.15 K $\leq$ T $\leq$ 1,273.15 K), a table lookup is used. Some selected values are listed in **Table 4.11-2**.

Table 4.11-2 Radial thermal strain of zircaloy for 1083 K < T < 1273 K.

Temperature (K)	ε_{TC}
1,083	5.22×10^{-3}
1,093	5.25×10^{-3}
1,103	5.28×10^{-3}
1,123	5.24×10^{-3}
1,143	5.15×10^{-3}
1,183	4.45×10^{-3}
1,223	2.97×10^{-3}
1,273	2.90×10^{-3}

Young's modulus, E, for zircaloy cladding is approximated by neglecting the effects of oxidation, cold work, and irradiation. Young's modulus is given by

$$E = 1.088 \times 10^{11} - 5.475 \times 10^7 \text{ T} \qquad (4.11\text{-}23)$$

for T $<$ 1,090 K (α phase) and

$$E = \max (1.0 \times 10^{10} \text{Pa}, 9.21 \times 10^{10} - 4.05 \times 10^7 \text{ T}) \qquad (4.11\text{-}24)$$

for T $>$ 1,240 K (β phase), where T is the cladding temperature (K). In the α to β phase transfer zone, 1,090 K $\leq$ T $\leq$ 1,240 K, Young's modulus is given by

$$E = 4.912 \times 10^{10} - 4.827 \times 10^7 (\text{T} - 1,090 \text{ K}) \ . \qquad (4.11\text{-}25)$$

4.11.1 References

4.11-1.   L. J. Siefken et al., *FRAP-T6: A Computer Code for the Transient Analysis of Oxide Fuel Rods,* EGG-CDAP-5410, Idaho National Engineering Laboratory, April 1981.

4.11-2.   A. Ullman, R. Acharya, and D. R. Olander, "Thermal Accommodation Coefficients of Inert Gases on Stainless Steel and UO_2," *Journal of Nuclear Materials, 51,* 1974, pp. 277-279.

4.11-3.   G. A. Berna et al., *FRAPCON-2 Developmental Assessment,* NUREG/CR-1949, PNL-3849, Pacific Northwest Laboratory, July 1981.

4.11-4.   D. L. Hagrman, G. A. Reyman, and R. E. Mason, *MATPRO-Version 11 (Revision 2), A Handbook of Materials Properties for Use in the Analysis of Light Water Reactor Fuel Rod Behavior,* NUREG/CR-0479, TREE-1280, Revision 2, Idaho National Engineering Laboratory, August 1981.

4.12   Radiation Enclosure Model

Several radiation text books (**Reference 4.12-1** and **Reference 4.12-2**) describe the approach used here to compute the rate of radiation exchange between surfaces. The surfaces that have a line-of-sight or a reflection path through which they can communicate with each other are in the same enclosure. The computation method is a lumped-system approximation for gray diffuse surfaces contained in an enclosure. The assumptions of this method are that:

•   The fluid in the enclosure neither emits nor absorbs radiant thermal energy.

- • Reflectance from a surface is neither a function of incident nor reflected direction nor of radiation frequency.

- • Temperature, reflectance, and radiosity are constant over each surface.

The radiosity of a surface is the total radiant energy leaving a surface (i.e., the emitted energy plus the reflected energy). Mathematically this is written for the i-th surface as

$$R_i = \varepsilon_i \sigma T_i^4 + \rho_i \sum_{j=1}^{n} R_j F_{ji} \qquad (4.12\text{-}1)$$

where

R	=	radiosity
ε	=	emissivity
σ	=	Stefan-Boltzmann constant
T	=	temperature
ρ	=	1 - ε; reflectivity
F_{ji}	=	view factor from surface j to surface i.

The net heat flux, Q_i, at surface i is the difference between the radiosity for i and the radiosity of all surfaces times their view factor to surface i, and it is given by

$$Q_i = R_i - \sum_{j=1}^{n} R_j F_{ji} \quad . \qquad (4.12\text{-}2)$$

The above two equations can be combined to yield

$$Q_i = \frac{\varepsilon_i}{\rho_i} (\sigma T_i^4 - R_i) \quad . \qquad (4.12\text{-}3)$$

Thus, the only problem in obtaining the heat flux at surface i is to solve for R_i. Equation (4.12-3) represents a set of n simultaneous linear algebraic equations, which can be written in a matrix form as

$$(\delta_{ij} - \rho_i F_{ji})R_i \ = \ \varepsilon_i \sigma T_i^4 \tag{4.12–4}$$

where the Kronecker delta is defined as

$$\delta_{ij} \ = \ 0 \quad i \ne j$$

$$\delta_{ij} \ = \ 1 \quad i = j.$$

The solution of Equation (4.12-4) involves a matrix inversion written as

$$R_i \ = \ (\delta_{ij} - \rho_i F_{ji})^{-1} \varepsilon_i \sigma T_i^4 \ . \tag{4.12-5}$$

Fortunately, the matrix inversion need only be performed once during initialization since it does not involve variables that change with time.

Radiation changes the heat conduction solution boundary condition [Equation (4.12-3)] at surface i to the form

$$- k\frac{\partial T}{\partial n}\bigg|_i \ = \ h_i(T_i - T_{sk}) + Q_i \tag{4.12-6}$$

where

k	=	surface conductivity
n	=	unit normal vextor away from the boundary surface
h	=	convective heat transfer coefficient
T_{sk}	=	sink temperature
Q_i	=	net heat flux at surface i [Equation (4.12-3)].

Note that the radiation term is not implicit in surface temperature. This can cause solution instabilities for thin surfaces and large time steps unless convection dominates radiation.

The tedious part of performing a radiation calculation in an enclosure with surfaces having arbitrary shapes is finding the view factors. Text books describe integral, graphical, and mechanical methods of doing this. For many types of surfaces, formulas, tables, or charts are available. Naturally, the view factors from each surface to all other surfaces must sum to 1. Also, to conserve energy, the area of surface i times

the view factor for each surface i to any other surface j must equal the area of surface j times the view factor from j to i. These two restrictions are written as

$$\sum_{i=1}^{n} F_{ij} = 1.0 \tag{4.12-7}$$

$$A_i F_{ij} = A_j F_{ji} \ . \tag{4.12-8}$$

The latter restriction is known as the reciprocity rule. ATHENA has a built in check that if the above two equations are not satisfied within a relative error of 0.001, a message is printed and the calculation will not go beyond input checking, because energy conservation errors will be too large.

4.12.1 References

4.12-1.   T. J. Love, *Radiative Heat Transfer,* Columbus, OH: Merrill, 1968.

4.12-2.   E. M. Sparrow and R. D. Cess, *Radiation Heat Transfer,* Belmont, CA: Brooks-Cole, 1966.

4.13 Conduction Enclosure Model

The ATHENA conduction enclosure model is an adaptation of the thermal radiation model described in Section 4.12. The model can be used to simulate multidimensional heat conduction in a lumped parameter fashion. As is the case with the radiation enclosure model, the conduction enclosure model permits thermal "connections" between an arbitrary number of heat structures. The only difference is the nature of the connection. In the conduction enclosure model, a gap conductance (κ) is used to characterize the thermal connection between heat structures. This represents the ability to transfer heat via physical contact between heat structure surfaces. Consider the surface node i of a heat structure thermally coupled to the surfaces of a set of M other heat structures. The conduction enclosure surface heat flux is given by

$$Q_i^{n+1} = \sum_{m=1}^{M} \kappa_{im} F_{im}(T_i^n - T_m^n) \qquad [m \neq i] \tag{4.13-1}$$

where

κ_{im}	=	gap conductance between adjacent surfaces of heat structures i and m
F_{im}	=	fraction of surface area (area factor) of heat structure i in contact with heat structure m
T_i	=	temperature of surface node of heat structure i.

The solution for the surface heat fluxes is carried out in the same fashion as the surface-to-surface radiation enclosure model. Input data cards for the model are also shared with the surface-to-surface radiation enclosure model. The model has been used for an RBMK reactor application[4.13-1].

The conduction enclosure model does not require the area factors from a surface to all other surfaces to sum to 1. However, to conserve energy, the area of surface i times the area factor for surface i to any other surface m must equal the area of surface m times the area factor from m to i. This reciprosity rule has a built in check so that if the rule is not satisfied to within a relative error of 0.001, a message is printed and the calculation will not go beyond input chacking, because energy conservation errors will be too large.

4.13.1 References

4.13-1.   S. Paik, "RELAP5-3D Multidimensional Heat Conduction Enclosure Model for RBMK Reactor Applications," *Nuclear Technology, 128*, 1999, pp. 87-102.

4.14 Metal-Water Reaction Model

The reaction of zirconium and steam is treated using the correlation developed by Cathcart.[4.14-1] The metal-water reaction model is coupled with the fuel rod deformation model so that if a rod ruptures, the inside of the cladding can react. The metal-water reaction heat source term for the cladding surface mesh point is added into the total heat source term for the heat structure.

The metal-water reaction model calculates the thickness of the cladding annulus converted to oxide; however, it does not alter the thermal-physical properties of the cladding as the oxide layers develop. Similarly, although the model calculates the amount of hydrogen freed from each surface undergoing metal-water reaction, this hydrogen does not get included into the ATHENA hydraulic equations, nor does the steam being consumed by the metal-water reaction get withdrawn from the hydraulic equations.

The metal-water reaction assumes there is always sufficient steam to allow the reaction to proceed. The model does not recognize the possibility of a reduced reaction rate due to insufficient available steam. The model does, however, recognize that the reaction is limited by the amount of cladding available. When all the cladding for a heat structure has been consumed the model terminates the metal-water reaction for that heat structure.

The chemical equation being modeled is

$$Zr + 2H_2O \rightarrow ZrO_2 + 2H_2 + 5.94 \text{ x } 10^8 \text{ J/(kg-mole)} \ . \qquad (4.14\text{-}1)$$
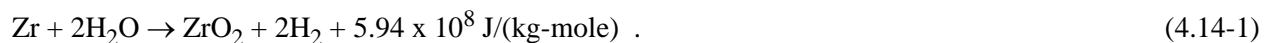
The thickness of the cladding annulus converted to oxide at time-point n is given by

$$dr_n = \left[dr_{n-1}^2 + (K\Delta t)\exp\left(-\frac{A}{RT}\right) \right]^{\frac{1}{2}} \qquad (4.14-2)$$

where

dr_n = thickness of the cladding annulus converted to oxide at time-point n (m)

dr_{n-1} = thickness of the cladding annulus converted to oxide at time-point n-1 (m)

K = 2.252×10^{-6} m^2/s

Δt = time step size (t^{n+1} - t^n) (s)

A = 35,889 mole/cal

R = 1.987 cal/(K-mole)

T = cladding temperature (K).

The amount of heat added to the cladding's outer surface between time-point n and n-1 is given by multiplying the volume of cladding undergoing reaction by the density of zirconium and the reaction heat release, and it is given by

$$Q = \rho\pi[(r_o - dr_{n-1})^2 - (r_o - dr_n)^2]\frac{H}{W} \qquad (4.14-3)$$

where

Q = heat addition per unit length (J/m)

ρ = density of zirconium = 6,500 kg/m3

r_o = cladding outer radius (m)

H = reaction heat release = 5.94×10^8 J/(kg-mole)

W = molecular weight of zirconium = 91.22 kg/(kg-mole).

Similar equations are used for the cladding's inner surface if cladding rupture occurs.

The total hydrogen mass generated by the metal-water reaction is calculated by multiplying the mass of zirconium reacted by the ratio of the molecular weight of 4 hydrogen atoms to 1 zirconium atom.

4.14.1 Reference

4.14-1.   J. V. Cathcart et al., *Reaction Rate Studies, IV, Zirconium Metal-Water Oxidation Kinetics,* ORNL/NUREG-17, Oak Ridge National Laboratory, August 1977.

4.15 Cladding Deformation Model

An empirical cladding deformation model from FRAP-T6[4.15-1] has been incorporated into ATHENA. The model may be invoked only in conjunction with the dynamic gap conductance model. The purpose of the model is to allow plastic deformation of the cladding to be accounted for in the calculation of fuel rod's cladding temperature during LOCA simulations; and to inform a user of the possible occurrence of rod rupture and flow blockage and hence the necessity of conducting more detailed simulations of the fuel rods' behavior.

With the deformation model modifications, an additional term is included in the gap conductance [Equation (4.11-1)] to account for radiation across the gap

$$h_r = \sigma F(T_f^2 + T_c^2)(T_f + T_c) \qquad\qquad (4.15\text{-}1)$$

$$F = \cfrac{1}{\left\{ \cfrac{1}{\varepsilon_f} + \left(\cfrac{R_f}{R_c}\right)\left[\cfrac{1}{(\varepsilon_c - 1)}\right] \right\}} \qquad\qquad (4.15\text{-}2)$$

where

h_r	=	radiation gap conductance
σ	=	Stefan-Boltzmann constant $= 5.67 \times 10^{-8}\ \mathrm{W/(m^2\ K^4)}$
F	=	emissivity factor
ε_f	=	emissivity of fuel
ε_c	=	emissivity of cladding
R_f	=	outer radius of fuel (m)
R_c	=	inner radius of cladding (m)
T_f	=	temperature of fuel's outer surface (K)

T_c =   temperature of cladding's inner surface (K).

When the deformation model is active, the total cladding strain used in the gap conductance model is the sum of the thermal strain, the creepdown strain, the elastic strain, and the plastic strain. The cladding thermal strain, creepdown strain, and elastic strain are given in Section 4.11. The plastic strain is given by

$$\varepsilon_p = 0.25\ \varepsilon_{rup}\ \exp\ [-0.0153(T_r - T_c)] \qquad (4.15\text{-}3)$$

where

ε_p =   plastic hoop strain before rupture

ε_{rup} =   cladding strain at rupture

T_r =   rupture temperature (°C)

T_c =   average cladding temperature (°C).

The rupture temperature is

$$T_r = 3{,}960\ ^\circ C - \left(\frac{20.4 \bullet S}{1 + H}\right) - \left[\frac{8.51 \times 10^6 S}{100(1 + H) + 2{,}790 \bullet S}\right] \qquad (4.15\text{-}4)$$

where

S   =   cladding hoop stress (KPSI)

H   =   max [(heating rate)/(28 °C/s), 1.0].

The rupture temperature correlation is depicted in **Figure 4.15-1**.

Plastic strain is calculated only if the average cladding temperature exceeds T_{plas}, the temperature at which plastic strain begins

$$T_{plas} = T_r - 70°C \qquad\qquad ; \qquad T_r < 700\ ^\circ C$$

$$= T_r - 70\ ^\circ C - 0.14\ (T_r - 700\ ^\circ C);\ \ 700\ ^\circ C < T_r < 1{,}300\ ^\circ C$$

$$= T_r - 155\ ^\circ C \qquad\qquad ;\ 1{,}300\ ^\circ C < T_r \qquad (4.15\text{-}5)$$
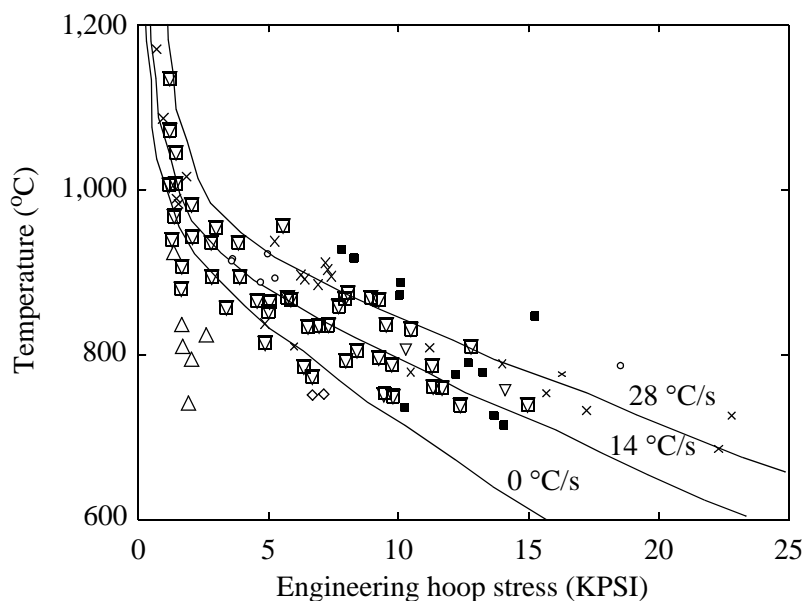
Figure 4.15-1 ORNL correlation of rupture temperature as a function of engineering hoop stress and temperature-ramp rate with data from internally heated zircaloy cladding in aqueous atmospheres.

If the average cladding temperature exceeds the value of T_{plas}, then the rupture temperature is used together with the heating rate to determine the rupture strain E_{rup}, via a table lookup. When rupture occurs, a similar table lookup is used to obtain the flow blockage. The rupture strain and blockage tables are from **Reference 4.15-2**. The correlations used for cladding strain and rupture are given in **Table 4.15-1** and illustrated in **Figure 4.15-2** through **Figure 4.15-4**. Linear interpolation is used between 10 °C/s and 25 °C/s .

Table 4.15-1 Tabulation of cladding correlations.

Rupture temperature (°C)	Slow-ramp correlations (≤ 10 °C/s)		Fast-ramp correlations (≥ 25 °C/s)	
	Burst strain (%)	Flow blockage (%)	Burst strain (%)	Flow blockage (%)
600	10	6.5	10	6.5
625	11	7.0	10	6.5

Table 4.15-1 Tabulation of cladding correlations. (Continued)

Rupture temperature (°C)	Slow-ramp correlations (≤ 10 °C/s)		Fast-ramp correlations (≥ 25 °C/s)	
	Burst strain (%)	Flow blockage (%)	Burst strain (%)	Flow blockage (%)
650	13	8.4	12	7.5
675	20	13.8	15	10.0
700	45	33.5	20	13.8
725	67	52.5	28	20.0
750	82	65.8	38	27.5
775	89	71.0	48	35.7
800	90	71.5	57	43.3
825	89	71.0	60	46.0
850	82	65.8	60	46.0
875	67	52.5	57	43.3
900	48	35.7	45	33.5
925	28	20.0	28	20.0
950	25	18.0	25	18.0
975	28	20.0	28	20.0
1,000	33	24.1	35	25.7
1,025	35	25.7	48	35.7
1,050	33	24.1	77	61.6
1,075	25	18.0	80	64.5
1,100	14	9.2	77	61.6
1,125	11	7.0	39	28.5
1,150	10	6.5	26	18.3
1,175	10	6.5	26	18.3
1,200	10	6.5	36	26.2

If a fuel rod ruptures (i.e., one of the heat structure segments ruptures in one of the heat structure geometries connected to a fluid volume), the rod's (i.e., the heat structure geometry's) internal gap
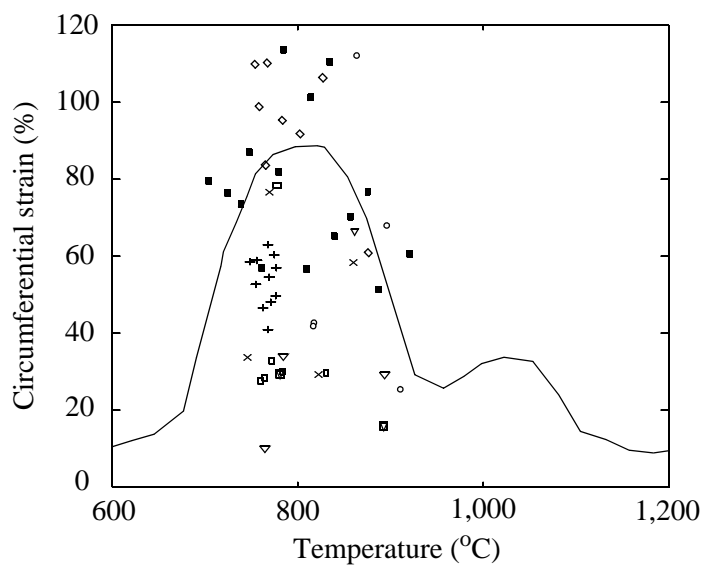
Figure 4.15-2 Maximum circumferential strain as a function of rupture temperature for internally heated zircaloy cladding in aqueous atmospheres at heating rates less than or equal to 10 °C/s.
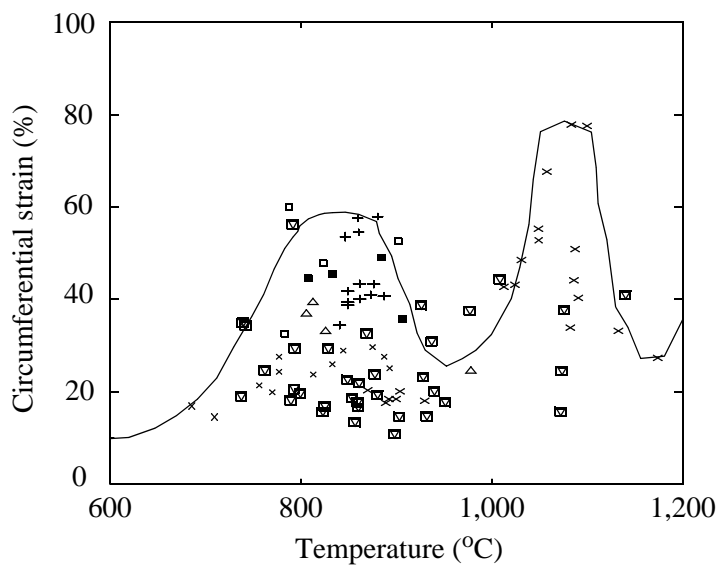
Figure 4.15-3 Maximum circumferential strain as a function of rupture temperature for internally heated zircaloy cladding in aqueous atmospheres at heating rates greater than or equal to 25 °C/s.
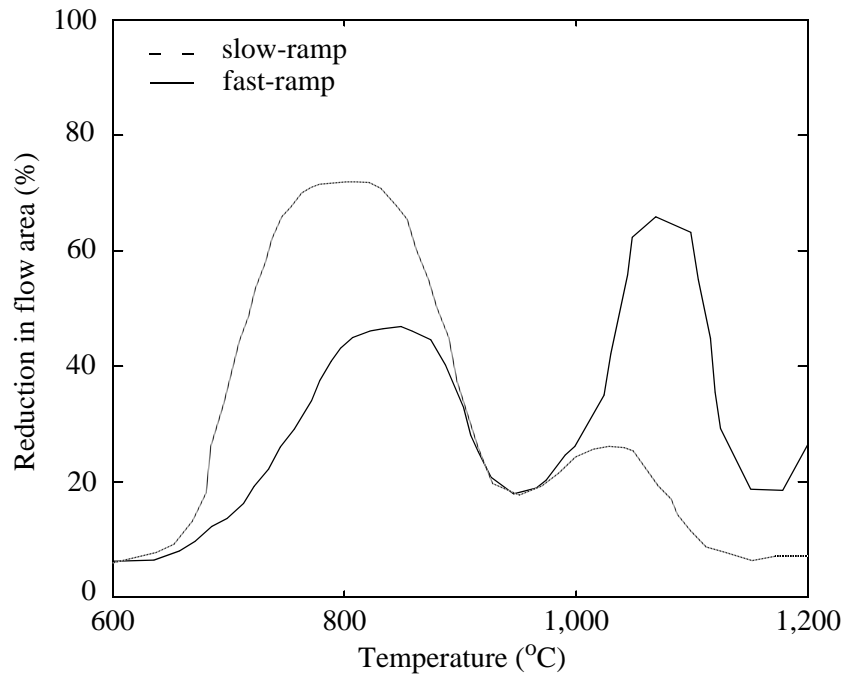
Figure 4.15-4 Reduction in PWR assembly flow area as a function of rupture temperature and ramp.

pressure is set equal to the external fluid volume's pressure; metal-water reaction is initiated on the inner surface of the cladding for the structure where rupture occurs if the metal-water reaction model is active; and additional form loss coefficients are (optionally) computed for the junctions just below and just above the rupture location. They are

$$K_e = (1-B)^2, \text{ expansion loss coefficient} \tag{4.15-6}$$

$$K_c = 0.45(1-B), \text{ contraction loss coefficient} \tag{4.15-7}$$

$$B = (\text{flow area after blockage})/(\text{flow area before blockage}) \ . \tag{4.15-8}$$

The cladding deformation model also alters other parameters affecting the ATHENA hydraulic solution. The approach is similar to that used in SCDAP/RELAP5-3D[4.15-3]. In particular, it alters the flow area, volume, and volume hydraulic diameter of the fluid cell containing a deformed or ruptured heat structure. It also alters the heat transfer hydraulic diameter (heated equivalent diameter) for the volume, as well as the junction area, the junction hydraulic diameter, and the junction throat ratio connecting the volumes. The cladding deformation model is shown in **Figure 4.15-5**, where R_o is the clad outer radius.
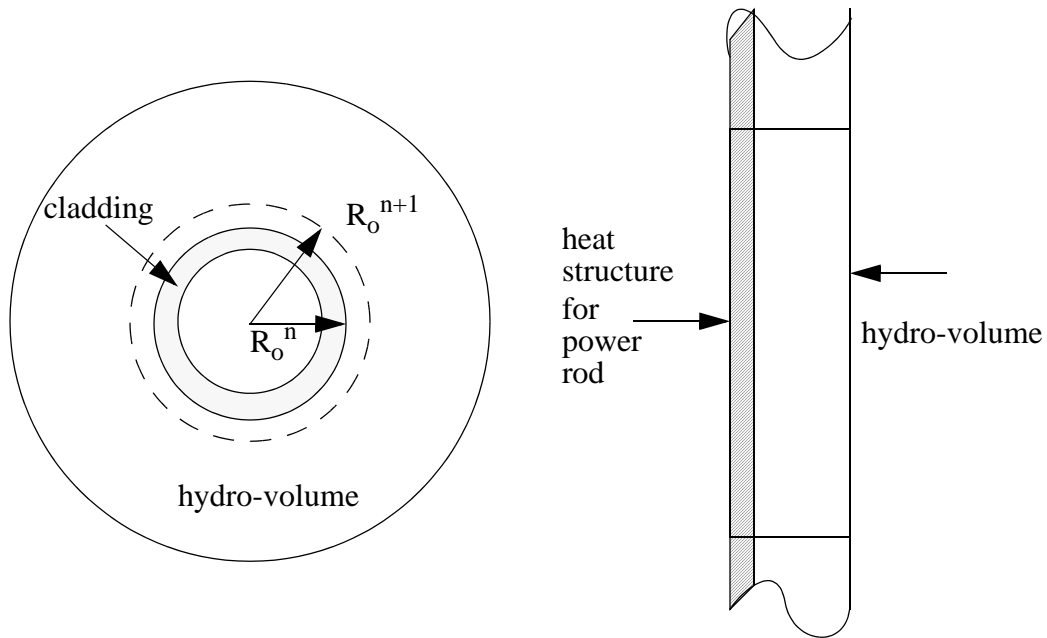
Figure 4.15-5 Cladding deformation model

The cladding deformation model is restricted to cylindrical geometry. The model uses the feature that the time step (Δt) for advancing the hydrodynamics may be different than the time step (Δt_{ht}) for advancing the heat structures. The new time hydrodynamic flow area of the volume (A^{n+1}) is calculated by

$$A^{n+1} = A^n - \Delta A \tag{4.15-9}$$

The change of the hydrodynamic flow area (ΔA) is determined as follows:

1.   If the cladding swells, the change of area is calculated by

$$\Delta A = \{\pi[(R_o^{n+1})^2 - (R_o^n)^2]\} \cdot \frac{\Delta t}{\Delta t_{ht}} \cdot \frac{L_{ht_j}}{L_h} \, , \tag{4.15-10}$$

where L_{ht_j} is the length of the j-th heat structure segment of the fuel rod and L_h is the length of the volume. The last two terms in the preceding equation deserve explanation. The time step ratio term $\Delta t/\Delta t_{ht}$ serves to extrapolate the clad deformation that occurred during the last heat transfer advancement time step, Δt_{ht}, into the future hydrodynamic advancements, Δt, that are smaller than Δt_{ht}. In other words, the assumption is made that the rate of deformation will remain constant whenever there are multiple hydrodynamic time steps between each heat transfer advancement.

The length ratio L_{ht_j}/L_h serves the following purposes: (1) for a volume representing a core volume with fuel pins, it represents the number of pins; (b) it limits the area change in those instances in which there are multiple heat structures stacked on one another in a volume; (c) it limits the area change in those instances in which the heat structure length is less than the volume length.

2. If the cladding ruptures, the change of area is calculated by

$$\Delta A = A^n (1 - B) \frac{\Delta t}{\Delta t_{ht}} \frac{L_{ht_j}}{\sum\limits_{i=1}^{N} L_{ht_i}} \qquad (4.15\text{-}11)$$

where variable B is defined by Equation (4.15-8) and N is the number of heat structure segments attached to the volume (either stacked on one another in the same heat strucrure geometry or in separate heat structure geometries).

The other variables are calculated from the ratio of new and old areas of the volume as

$$V^{n+1} = V^n \cdot \text{ratio} \qquad (4.15\text{-}12)$$

$$D_h^{n+1} = D_h^n \cdot \sqrt{\text{ratio}} \qquad (4.15\text{-}13)$$

$$D_{he}^{n+1} = D_{he}^n \cdot \sqrt{\text{ratio}} \qquad (4.15\text{-}14)$$

where the variable ratio is

$$\text{ratio} = \frac{A^{n+1}}{A^n} , \qquad (4.15\text{-}15)$$

V is the volume, D_h is the volume hydraulic diameter, and D_{he} is the volume heat transfer hydraulic diameter (heated equivalent diameter). The junction area, junction hydraulic diameter, and junction throat ratio are also changed accordingly.

The geometric changes in a heat structure experiencing plastic deformation are not coupled to the geometry seen by the heat structures heat conduction solution. The geometry changes enter the conduction solution only by affecting the value being calculated for gap conductance.

When the reflood fine mesh rezoning algorithm is active, the deformation model sees only the coarse zones. Deformation calculations are not done for each of the fine mesh points in a axial set of heat structures. Rather, the deformation calculation is done once for each of the axial heat structures and all of the fine mesh nodes within a particular heat structure having the same gap conductance value.

4.15.1 References

4.15-1.   S. C. Resch et al., *FRAP-T6: The Transient Fuel Rod Behavior Code,* NUREG/CR-2950, Idaho National Engineering Laboratory, September 1982.

4.15-2.   D. A. Powers and R. O. Meyer, *Cladding Swelling and Rupture Models for LOCA Analysis,* NUREG-0630, U. S. Nuclear Regulatory Commission, April 1980.

4.15-3.   The SCDAP/RELAP5-3D$^{©}$ Development Team, *SCDAP/RELAP5-3D$^{©}$ Code Manual*, INEEL-EXT-02-00589, Idaho National Engineering and Environmental Laboratory, Rev. 2.2, October 2003.

5 Trip System

The trip system consists of the evaluation of logical statements. Each trip statement is a simple logical statement that has a true or false result and an associated variable, TIMEOF. The TIMEOF variable is -1.0 whenever the trip is false, and contains the time the trip was last set true whenever the trip is true. Linear interpolation, along with limits, between the current time step and the previous time step, is used to obtain a more accurate time when the trip was last set true. This variable allows for time delays and unit step functions based on events during the transient.

Within the structure of ATHENA, the trip system is considered to be only the evaluation of the logical statements. The decision of what action is needed, based on trip status, resides within other models. For example, valve models are provided that open or close the valve based on trip values; pump models test trip status to determine whether a pump electrical breaker has tripped.

Two types of trip statements are provided--variable and logical trips. Since logical trips involve variable trips and other logical trips, complex logical expressions can be constructed from simple logical statements. Both types of trips can be latched or unlatched. A latched trip, once set true, is no longer tested and remains true for the remainder of the problem or until reset at a restart. An unlatched trip is evaluated every time step.

5.1 Variable Trips

A variable trip evaluates the statement

$$T_{ri} \ = \ V_1 \ OP \ (V_2 + C) \ . \tag{5.1-1}$$

The value T_{ri} is the i-th trip variable that may be true or false. Values V_1 and V_2 are quantities from the heat structures, hydrodynamics, reactor kinetics, control systems, or may be a TIMEOF quantity. The value C is a constant. The operation OP is one of the following arithmetic relational operations: EQ is equal, NE is not equal, GT is greater than, GE is greater than or equal, LT is less than, and LE is less than or equal.

Trips are evaluated at the beginning of the overall ATHENA time advancement and are evaluated in numerical order. Except for TIMEOF variables, all other V quantities have beginning of time step values; and the results of the trip evaluation are independent of the evaluation order. But when a variable trip statement references TIMEOF (T_{rk}), the new value of TIMEOF is used if k < i. When a variable trip statement references a TIMEOF variable whose value is -1.0 (i.e., the trip is false), the evaluation of the variable trip is bypassed. Thus, the value of the variable trip remains the same as its value on the previous time step.

5.2 Logical Trips

A logical trip evaluates

$$T_{ri} = \pm T_{rj} \text{ OP} \pm T_{rl} \ . \tag{5.2-1}$$

The values T_{rj} and T_{rl} are variable or logical trips, and the minus sign, if present, denotes the complement of the trip value. The operation OP is one of the logical operations AND, OR (inclusive or), or XOR (exclusive or).

Logical trips are evaluated following the evaluation of variable trips and are evaluated in numerical order. When T_{rj} (or T_{rl}) is a variable trip, new trip values are used; when T_{rj} is a logical trip used in logical trip expression i, new values are used when $j < i$ and old values are used when $j \geq i$.

6 Control System

The control system provides the capability to evaluate simultaneous algebraic and ordinary differential equations. The capability is primarily intended to simulate control systems typically used in hydrodynamic systems, but it can also model other phenomena described by algebraic and ordinary differential equations (see Section 8.4.5 for a description of special controllers for use in steady-state initialization). Another use is to define auxiliary output quantities, such as differential pressures, so they can be printed in major and minor edits and be plotted.

The control system consists of several types of control components. Each component defines a control variable as a specific function of time-advanced quantities. The time-advanced quantities include hydrodynamic volume, junction, pump, valve, heat structure, reactor kinetics, trip quantities, and the control variables themselves (including the control variable being defined). This permits control variables to be developed from components that perform simple, basic operations.

In the following equations that define the control components and associated numerical techniques, Y_i is the control variable defined by the i-th control component, A_j, R, and S are real constants input by the user, I is an integer constant input by the user, V_j is a quantity advanced in time by ATHENA and can include Y_i, t is time, and s is the Laplace transform variable. Superscripts involving the index n denote time levels. The name in parentheses to the right of the definition is used in input data to specify the component.

6.1 Arithmetic Control Components

6.1.1 Constant

$$Y_i = S \qquad (\text{CONSTANT}) \ . \tag{6.1-1}$$

6.1.2 Addition-Subtraction

$$Y = S (A_0 + A_1 V_1 + A_2 V_2 + ...) \qquad (\text{SUM}) \ . \tag{6.1-2}$$

6.1.3 Multiplication

$$Y_i = S V_1 V_2 ... \qquad (\text{MULT}) \ . \tag{6.1-3}$$

6.1.4 Division

$$Y_i = \frac{S}{V_1} \text{ or } Y_i = \frac{S V_2}{V_1} \qquad (\text{DIV}) \ . \tag{6.1-4}$$

6.1.5 Exponentiation

$$Y_i \ = \ SV_1^I \qquad \text{(POWERI)} \tag{6.1-5}$$

$$Y_i \ = \ SV_1^R \qquad \text{(POWERR)} \tag{6.1-6}$$

$$Y_i \ = \ SV_1^{V_2} \qquad \text{(POWERX)} \ . \tag{6.1-7}$$

6.1.6 Table Lookup Function

$$Y_i \ = \ S \, F(V_1) \qquad \text{(FUNCTION)} \tag{6.1-8}$$

where F is a function defined by table lookup and interpolation.

6.1.7 Standard Functions

$$Y \ = \ S \, F(V_1, V_2, V_3, ...) \qquad \text{(STDFNCTN)} \tag{6.1-9}$$

where F can be $|V_1|$, $\exp(V_1)$, $\ln(V_1)$, $\sin(V_1)$, $\cos(V_1)$, $\tan(V_1)$, $\tan^{-1}(V_1)$, $(V_1)^{1/2}$, $MAX(V_1, V_2, V_3, ...)$, and $MIN(V_1, V_2, V_3, ...)$. Only MAX and MIN may have multiple arguments and must have at least two arguments.

6.1.8 Delay

$$Y_i \ = \ S \, V_1(t - t_d) \qquad \text{(DELAY)} \tag{6.1-10}$$

where t_d is the delay time. A user-input, h, determines the number of pairs of data used to store past values of V_1. The maximum number of time-function pairs is h + 2. The delay table time increment is $\frac{t_d}{h}$. The delayed function is obtained by linear interpolation using the stored past history. As time is advanced, new time values are added to the table. Once the table fills, new values replace values that are older than the delay time.

6.1.9 Unit Trip

$$Y_i \ = \ SU \, (\pm t_r) \qquad \text{(TRIPUNIT)} \ . \tag{6.1-11}$$

6.1.10 Trip Delay

$$Y_i = ST_r(t_r) \qquad (\text{TRIPDLAY}) \ . \tag{6.1-12}$$

In the above two trip-related components, t_r is a trip number and, if negative (TRIPUNIT only), indicates that the complement of the trip is to be used; U is 0.0 or 1.0, depending on trip t_r (or its complement if t_r is negative) being false or true; and T_r is -1.0 if the trip is false and the time the trip was last set true if the trip is true.

No numerical approximations are involved in evaluating the algebraic components. Evaluation is by simply performing the indicated operations. In the sequence of operations that perform a time advancement of the trip, heat conduction, hydrodynamic, reactor kinetic, and control systems of ATHENA, the control system is processed last. Thus, the end of time step (n + 1) values for trip variables t_r and all V_1 variables except control variables Y_i are available. The control components are evaluated in component number order. As the first control variable Y_1 is being evaluated, only old-time values are available for all control component variables. Once Y_1 is evaluated, the new-time value for Y_1 is available for the remaining control variable evaluations of Y_i. In general, while Y_i is being evaluated, new-time values are available for Y_k, k < i, and only old-time values are available for Y_k, k ≥ i.

In the example,

$$Y_{10}^{n+1} = A_0 + A_1 T^{n+1} + A_2 P^{n+1} + A_3 Y_8^{n+1} + A_4 Y_{10}^n + A_5 Y_{15}^n \tag{6.1-13}$$

T and P, which represent a temperature and pressure from the heat structure or hydrodynamic systems, are new-time values. The value Y_8 is also a new-time value because it was advanced before control component 10, and Y_{10} and Y_{15} are old-time values.

Initialization of the algebraic control components is very similar to a time advancement. At the start of control component initialization, all other time-advanced quantities have been initialized. Control component input includes an initial value and a flag that indicates if initialization is to be performed. The initialization proceeds in the order of component numbers. The initial value entered becomes the initial value if no initialization is specified. If initialization is specified, it is simply the specified computation using the available data. If component i references Y_k, k < i, the initialized value of Y_k is used; if k ≥ i, the entered initial value is used.

6.2 Integration Control Component

The integration component evaluates

$$Y_i = S \int_{t_1}^{t} V_1 dt \qquad \text{(INTEGRAL)} \tag{6.2-1}$$

where t_1 is the simulation time when the component is added to the system, and the initial value at t_1 is the input item regardless of the initialization flag.

The integral is advanced by trapezoidal approximation,

$$Y_1^{n+1} = Y_1^n + S[V_1^n + V_1^{n+1}]\frac{\Delta t}{2} \quad . \tag{6.2-2}$$

Both new-time (n+1) and old-time (n) values are available for V_1 except when it is a control variable Y_k, $k > i$. For the case when $V_1 = Y_k$, $k \geq i$, the V^n and V^{n+1} are instead V^{n-1} and V^n. Use of the integral component when old-time values will be used should be avoided. Consider the example

$$a = P_1 - P_2 - Bv - kd \tag{6.2-3}$$

$$v = \int a \, dt \tag{6.2-4}$$

$$d = \int v \, dt \quad . \tag{6.2-5}$$

This acceleration-velocity-distance system cannot be advanced without use of old values. As a general rule, it is considered better to use the old value in the algebraic expression and not in the integral expressions.

Thus, using $Y_1 = a$, $Y_2 = v$, and $Y_3 = d$,

$$Y_1 = P_1 - P_2 - BY_2 - kY_3 \tag{6.2-6}$$

$$Y_2 = \text{INTEGRAL} (Y_1) \tag{6.2-7}$$

$$Y_3 = \text{INTEGRAL} (Y_2) \quad . \tag{6.2-8}$$

6.3 Differentiation Control Components

Two components provide for differentiation

$$Y_i = \frac{dV_1}{dt} \quad . \tag{6.3-1}$$

One component evaluates the derivative by the inverse of the integration technique,

$$Y_i = \frac{2S}{\Delta t}(V_1^{n+1} - V_1^n) - Y_i^n \qquad \text{(DIFFERNI)} \quad . \tag{6.3-2}$$

This component is not recommended, since it can be unstable, requires an accurate initial value, and does not recover from a bad initial value. Deletion of this component is being considered. The recommended derivative component uses a simple difference expression,

$$Y_i = S\frac{(V_1^{n+1} - V_1^n)}{\Delta t} \qquad \text{(DIFFERND)} \quad . \tag{6.3-3}$$

Differentiation is a <u>noisy</u> process and should be avoided. Differentiation of control system variables can almost always be avoided. Filtering the result of differentiation of other variables should be considered. Similar to the case of the integral component, old-time values are used when advancement of Y_i involves $V_1 = Y_k$, $k \geq i$.

6.4 Proportional-Integral Component

This component evaluates

$$Y_i = S\left(A_1 V_1 + A_2 \int_{t_1}^{t} V_1 dt\right) \qquad \text{(PROP-INT)} \tag{6.4-1}$$

or, in Laplace transform notation,

$$Y_i(s) = S\left(A_1 + \frac{A_2}{s}\right)V_1(s) \quad . \tag{6.4-2}$$

This component is advanced in time by

$$I^{n+1} = I^n + (V_1^n + V_1^{n+1})\frac{\Delta t}{2} \tag{6.4-3}$$

$$Y_i^{n+1} = S(A_1 V_1^{n+1} + A_2 I^{n+1}) \quad . \tag{6.4-4}$$

The comments in the previous section concerning integration with $V_1 = Y_k$ hold for this component. If the initialization control flag is off, $Y°$ is the entered initial value and

$$I° = \frac{1}{A_2}\left(\frac{\overset{\circ}{Y_i}}{S} - A_1 \overset{\circ}{V_1}\right) \quad . \tag{6.4-5}$$

If the initialization control flag is on,

$$I° = 0 \tag{6.4-6}$$

$$\overset{\circ}{Y_i} = SA_1 \overset{\circ}{V_1} \quad . \tag{6.4-7}$$

6.5 Lag Control Component

The lag component is defined in Laplace transform notation as

$$Y_i(s) = S\left(\frac{1}{1 + A_1 s}\right) V_1(s) \qquad (LAG) \ . \tag{6.5-1}$$

Through algebraic rearrangement,

$$Y_i(s) + A_1 s Y_i(s) = S\ V_1(s) \tag{6.5-2}$$

$$\frac{Y_i(s)}{s} + A_1 Y_i(s) = \frac{S V_1(s)}{s} \tag{6.5-3}$$

$$Y_i(s) = \frac{S V_1(s) - Y_i(s)}{A_1 s} \quad . \tag{6.5-4}$$

Transforming to the time domain gives

$$Y_i = \int_o^t \frac{(S V_1 - Y_i)dt}{A_1} \quad . \tag{6.5-5}$$

The above expression is advanced numerically by

$$Y_i^{n+1} = Y_i^n + [S(V_1^n + V_1^{n+1}) - Y_i^n - Y_i^{n+1}]\frac{\Delta t}{2A_1} \qquad (6.5\text{-}6)$$

or

$$Y_i^{n+1} = \frac{Y_i^n\left(1 - \frac{\Delta t}{2A_1}\right) + S(V_1^n + V_1^{n+1})\frac{\Delta t}{2A_1}}{1 + \frac{\Delta t}{2A_1}} \qquad . \qquad (6.5\text{-}7)$$

If the initialization control flag is off or on,

$$Y_i^\circ = SV_1^\circ \quad . \qquad (6.5\text{-}8)$$

6.6 Lead-Lag Control Component

The lead-lag component is defined in Laplace transform notation as

$$Y_i(s) = S\left(\frac{1 + A_1 s}{1 + A_2 s}\right)V_1(s) \qquad \text{(LEAD-LAG)} \quad . \qquad (6.6\text{-}1)$$

Rearranging algebraically, this yields

$$Y_i(s) + A_2 s Y_i(s) = SV_1(s) + A_1 s \, SV_1(s) \qquad (6.6\text{-}2)$$

or

$$Y_i(s) = \frac{A_1 SV_1(s)}{A_2} + \frac{SV_1(s) - Y_i(s)}{A_2 s} \qquad . \qquad (6.6\text{-}3)$$

Transforming to the time domain gives

$$Y_i = \frac{A_1 SV_1}{A_2} + \int_o^t\left(\frac{SV_1 - Y_i}{A_2}dt\right) \quad . \qquad (6.6\text{-}4)$$

Note that the differentiation implied by the $sV_1(s)$ term has been avoided. The above expression is advanced numerically by

$$Y_i^{n+1} = \frac{A_1}{A_2}SV_1^{n+1} + I^n + [S(V_1^n + V_1^{n+1}) - Y_i^n - Y_i^{n+1}]\frac{\Delta t}{2A_2} \tag{6.6-5}$$

or

$$Y_i^{n+1} = \frac{\frac{A_1}{A_2}SV_1^{n+1} + I^n + [S(V_1^n + V_1^{n+1}) - Y_1^n]\frac{\Delta t}{2A_2}}{1 + \frac{\Delta t}{2A_2}} \tag{6.6-6}$$

and finally

$$I^{n+1} = I^n + [S(V_1^n + V_1^{n+1}) - Y_i^n - Y_i^{n+1}]\frac{\Delta t}{2A_2} \quad . \tag{6.6-7}$$

If the initialization control flag is off, then $I^0 = 0$ and Y_i^0 is the entered initial value. If the initialization control flag is on, then

$$Y_i^0 = SV_i^0$$
$$I^0 = \left(1 - \frac{A_1}{A_2}\right)SV_i^0 \quad . \tag{6.6-8}$$

For both lag and lead-lag components, if $V_1 = Y_k$: $k = i$ is an error; when $k < i$, old and new values are used as indicated; if $k > i$, V_1^n and V_1^{n+1} are really Y_k^{n-1} and Y_k^n.

6.7 Shaft Component

The shaft component is a special control component that advances the rotational velocity,

$$\sum_i I_i \frac{d\omega}{dt} = \sum_i \tau_i - \sum_i f_i\omega + \tau_c \qquad \text{(SHAFT)} \tag{6.7-1}$$

where I_i is the moment of inertia from component i, τ_i is the torque from component i, f_i is the friction from component i, and τ_c is an optional torque from a control component. The summations are over the pump,

generator, motor, or turbine components that are connected to the shaft and the shaft itself. The shaft and each associated component contains its own model, data, and storage for inertia, friction, and torque and has storage for its rotational velocity. Each associated component also has a disconnect trip number. If zero (no trip), the component is always connected to the shaft. If a trip is specified, the component is connected when false and disconnected when true. Any disconnected component is advanced separately and thus can have a different rotational velocity than the shaft. All connected components have the same rotational velocity.

The shaft equation is advanced explicitly by

$$\sum_i I_i^n \frac{(\omega^{n+1} - \omega^n)}{\Delta t} = \sum_i \tau_i^n - \sum_i f_i^n \omega^n + \tau_c \quad . \tag{6.7-2}$$

Inertias, torques, and frictions are evaluated using old-time information. The torque from the control system, τ_c, would be in terms of new-time values for quantities other than control variables and would use new or old-time values for control variables depending on their component numbers relative to the shaft component number. Except when a generator component is involved, the shaft component calculations consist of solving Equation (6.7-2) for ω^{n+1} separately for each component disconnected from the shaft (if any) and for the shaft and the connected components as one system. For separated components, the new rotational velocity is stored with the component data, and the summations are only over terms within the component. For the shaft and the connected components, the summations are over the shaft and the connected components; and the new rotational velocity is stored as the shaft's and each connected component's rotational velocity. A tripped generator, attached or connected, is treated as described above. An untripped generator rotates at the input synchronous speed; and, if connected to the shaft, the shaft and all connected components are forced to the synchronous speed.

6.8 Inverse Kinetics Component

The inverse kinetics component solves the point reactor kinetics equations for the reactivity rather than for the neutron density.

$$Y = S \left(\frac{\frac{\Lambda}{\bar{\beta}} \left(\frac{dV_1}{dt} \right) + \sum_{i=1}^{N_d} D_i(t_o + \Delta t)}{V_1} \right) \qquad \text{(INVKIN)} \tag{6.8-1}$$

where

$$D_i(t_o + \Delta t) = e^{-\lambda_i \Delta t} D_i(t_o) + \frac{\beta_i}{\beta \lambda_i} (1 - e^{-\lambda_i \Delta t}) \frac{dV_1}{dt} \qquad (6.8\text{-}2)$$

The input to the inverse kinetics control block should be the total fission power computed by the point kinetics model, the total fission power computed by the nodal neutron kinetics model, the fission power in one of the nodal neutron kinetics zones, or the response of a neutron detector that senses the neutron flux computed by either of the two neutron kinetics models.

The inverse kinetics reactivity algorithm utilizes a finite differencing procedure to compute reactivity based upon the time rate of change of the delayed neutron precursor concentration and the neutron density in the point reactor kinetics equations. Equation (7.1-1) is solved for ρ, where it is assumed that the neutron source S is zero.

$$\rho = \frac{\Lambda}{n} \left(\frac{dn}{dt} + \frac{\beta}{\Lambda} n - \sum_{i=1}^{N_d} \lambda_i C_i \right). \qquad (6.8\text{-}3)$$

The terms in Equation (6.8-3) are defined in Section 7.1. Substituting Equation (7.1-2) into Equation (6.8-3) gives

$$\rho = \frac{\Lambda}{n} \left(\frac{dn}{dt} + \sum_{i=1}^{N_d} \frac{dC_i}{dt} \right). \qquad (6.8\text{-}4)$$

Next, the variable D_i is defined as

$$D_i = \frac{\Lambda}{\beta} \frac{dC_i}{dt}. \qquad (6.8\text{-}5)$$

Substituting D_i into Equation (6.8-4) gives

$$\rho = \frac{\Lambda}{n} \frac{dn}{dt} + \frac{\beta}{n} \sum_{i=1}^{N_d} D_i \qquad (6.8\text{-}6)$$

The equation for D_i is derived by differentiating Equation (7.1-2) with respect to time and eliminating the delayed neutron precursor concentration using Equation (6.8-5) to obtain

$$\frac{dD_i}{dt} + \lambda_i D_i = \frac{\beta_i}{\beta}\frac{dn}{dt}.$$ (6.8-7)

Assuming that the neutron density n varies linearly over a time step interval (i.e., $\frac{dn}{dt}$ is constant), Equation (6.8-7) can be integrated over the time step interval Δt using standard methods (i.e., Laplace transforms) to give,

$$D_i(t_o + \Delta t) = e^{-\lambda_i \Delta t}D_i(t_o) + \frac{\beta_i}{\beta\lambda_i}(1 - e^{-\lambda_i \Delta t})\frac{dn}{dt}$$ (6.8-8)

where t_o is the time at the beginning of the time step interval.

Evaluating Equation (6.8-6) at the end of the time step interval and dividing by β to convert the units of reactivity into dollars, we obtain

$$\frac{\rho(t_o + \Delta t)}{\beta} = \frac{\Lambda}{\beta n(t_o + \Delta t)}\left(\frac{dn}{dt}\right)\Big|_{t_o}^{t_o + \Delta t} + \frac{1}{n(t_o + \Delta t)}\sum_{i=1}^{N_d}D_i(t_o + \Delta t)$$ (6.8-9)

where the derivative of the neutron density with respect to time is given by

$$\left(\frac{dn}{dt}\right)\Big|_{t_o}^{t_o + \Delta t} = \frac{n(t_o + \Delta t) - n(t_o)}{\Delta t}$$ (6.8-10)

For this control component, the output Y is the reactivity $\rho(t_o + dt)/\beta$ computed from Equation (6.8-9) where the neutron density n in Equation (6.8-9) is replaced by the control block input V_1.

7 Reactor Kinetics Model

There is one option for the computation of the reactor power in the ATHENA code. The option is the point reactor kinetics model based on the IREKIN[7.0-1] program developed at the INEEL [previously called NRTS (National Reactor Testing Station)]; this option was implemented in previous versions of RELAP5.

7.0.1 References

7.0-1.   R. J. Wagner, *IREKIN -- Program for the Numerical Solution of the Reactor Kinetics Equations*, IDO-17114, National Reactor Testing Station, January 1966.

7.1 Point Reactor Kinetics Model

The point reactor kinetics model in the ATHENA code is the simplest model that can be used to compute the transient behavior of the neutron fission power in a nuclear reactor. The model is based ion the IREKIN[7.1-1] program developed at the INEEL (previously call the NRTS). The power is computed using the space-independent or point kinetics approximation which assumes that power can be separated into space and time functions. This approximation is adequate for cases in which the space distribution remains nearly constant.

The point reactor kinetics model computes both the immediate (prompt and delayed neutrons) fission power and the power from decay of fission products. The immediate (prompt and delayed neutrons) power is that released at the time of fission and includes power from kinetic energy of the fission products and neutron moderation. Decay power is generated as the fission products undergo radioactive decay. The user can select the decay power model based on either the ATHENA approximate implementation of the 1973 ANS Proposed Standard[7.1-2],   the ATHENA exact implementation of the 1979 ANSI/ANS Standard,[7.1-3,7.1-4,7.1-5] or the ATHENA exact implemetation of the 1994 ANSI/ANS Standard[7.1-6].

7.1.1   Point Reactor Kinetics Equations

The point kinetics equations are (see Glasstone and Sesonske[7.1-7])

$$\frac{dn(t)}{dt} = \frac{[\rho(t)-\beta]}{\Lambda}n(t) + \sum_{i=1}^{N_d}\lambda_i C_i(t) + S \tag{7.1-1}$$

$$\frac{dC_i(t)}{dt} = \frac{\beta f_i}{\Lambda}n(t) - \lambda_i C_i(t) \quad i = 1, 2, ..., N_d \tag{7.1-2}$$

$$\varphi(t) = n(t)v \tag{7.1-3}$$

$$\psi(t) = V\Sigma_f\varphi(t) \qquad\qquad\qquad\qquad\qquad\qquad\qquad\qquad\qquad (7.1\text{-}4)$$

$$P_f(t) = Q_f\psi(t) \qquad\qquad\qquad\qquad\qquad\qquad\qquad\qquad\qquad (7.1\text{-}5)$$

where

t	$=$	time (s)
n	$=$	neutron density (neutrons/m^3)
φ	$=$	neutron flux (neutrons/m$^2\cdot$s)
v	$=$	neutron velocity (m/s)
C_i	$=$	delayed neutron precursor concentration in group i (nuclei/m^3)
β	$=$	effective delayed neutron fraction
	$=$	$\displaystyle\sum_{i=1}^{N_d}\beta_i$
Λ	$=$	prompt neutron generation time (s)
ρ	$=$	reactivity (only the time-dependence has been indicated; however, the reactivity is dependent on other variables)
f_i	$=$	fraction of delayed neutrons of group i
	$=$	β_i/β
β_i	$=$	effective delayed neutron precursor yield of group i
λ_i	$=$	decay constant of group i (1/s)
S	$=$	source rate density (neutrons/m$^3\cdot$s)
ψ	$=$	fission rate (fissions/s)
Σ_f	$=$	macroscopic fission cross-section (1/m)

P_f = immediate (prompt and delayed neutron) fission power (MeV/s)

Q_f = immediate (prompt and delayed neutron) fission energy per fission (MeV/fission).

V = volume (m^3).

N_d = number of delayed neutron precursor groups.

7.1.2 Fission Product Decay Model

The 1979 and the 1994 Standards express the power $P_{s\alpha}$ (t) in MeV/s as a function of time t resulting from one fission of isotope α at t = 0 as

$$P_{s\alpha}(t) = \sum_{j=1}^{N_\alpha} a_{\alpha j} \exp(-\lambda_{\alpha j} t) \ . \tag{7.1-6}$$

Data are presented for three isotopes, ^{235}U, ^{238}U, and ^{239}Pu for the 1979 Standard. Data are presented for four isotopes, ^{235}U, ^{238}U, ^{239}Pu, and ^{241}Pu for the 1994 Standard. The parameters a and λ were obtained by fitting to fission decay power data. The fitting for each isotope used 23 groups ($N_\alpha = 23$). The above expression is an impulse response to one fission and can be extended to an arbitrary fission rate ψ_α(t) through the convolution integral

$$P_\alpha(t) = P_{s\alpha}(t) * \psi_\alpha(t) = \sum_{j=1}^{N_\alpha} a_{\alpha j} \exp(-\lambda_{\alpha j} t) * \psi_\alpha(t) \tag{7.1-7}$$

where the convolution operation is defined by

$$A(t) * B(t) = \int_0^t A(t-\tau) B(\tau) d\tau = \int_0^t A(\tau) B(t-\tau) d\tau \ . \tag{7.1-8}$$

Since numerical evaluation of convolution integrals is cumbersome, a set of differential equations equivalent to the convolution integral is derived.

Assume that the power from each group is from radioactive decay of a fission fragment i. Then

$$P_{\alpha j}(t) = \lambda_{\alpha j} \gamma_{\alpha j}(t) = a_{\alpha j} \exp(-\lambda_{\alpha j} t) \ . \tag{7.1-9}$$

For simplification in the following derivation, the α and j subscripts are dropped and the following expressions represent an equation for one group for one isotope. From Equation (7.1-9) we have

$$\gamma(t) = \frac{a}{\lambda}\exp(-\lambda t) \ . \tag{7.1-10}$$

Laplace transforming Equation (7.1-10) gives

$$\gamma(s) = \frac{a}{\lambda(s+\lambda)} \ . \tag{7.1-11}$$

Rearranging Equation (7.1-11) gives

$$s\gamma(s) = \frac{a}{\lambda} - \lambda\gamma(s) \ . \tag{7.1-12}$$

Transforming to real time yields

$$\frac{d\gamma(t)}{dt} = \frac{a}{\lambda}\delta(0) - \lambda\gamma(t) \tag{7.1-13}$$

where $\delta(0)$ is the impulse function. Applying a time-dependent fission rate $\psi(t)$ in place of the single fission (impulse response), Equations (7.1-12) and (7.1-13) become

$$s\gamma(s) = \frac{a}{\lambda}\psi(s) - \lambda\gamma(s) \tag{7.1-14}$$

$$\frac{d\gamma(t)}{dt} = \frac{a}{\lambda}\psi(t) - \lambda\gamma(t) \ . \tag{7.1-15}$$

Solution of Equations (7.1-14) or (7.1-15) (remembering that $P = \lambda\gamma$) for an impulse yields Equation (7.1-6) and a similar expression in the 1979 and 1994 Standards. Solution of Equations (7.1-14) or (7.1-15) for an arbitrary fission source yields Equation (7.1-7). When specifying

$$\psi(t) = \begin{cases} 1, & 0 \le t \le T \\ 0, & t > T \end{cases} \tag{7.1-16}$$

Equations (7.1-14) and (7.1-15) yield another solution given in the 1979 and 1994 Standards. (Note that the Standard defines t as starting at 0 after fissioning for T s.)

A physical model can be attached to the terms in Equation (7.1-15). The first term on the right represents production of the isotope during fission; the last term is the loss of the isotope due to decay. A more mechanistic model would also provide for production of one isotope due to the decay of another (see Section 7.1.3).

The 1979 and 1994 Standards for decay power can be implemented by advancing the differential equations, which become

$$\frac{d\gamma_{\alpha j}(t)}{dt} = \frac{F_\gamma a_{\alpha j}}{\lambda_{\alpha j}} F_\alpha \psi(t) - \lambda_{\alpha j}\gamma_{\alpha j}(t) \quad j = 1, 2, \ldots, N_\alpha, \tag{7.1-17}$$

where $\alpha = 1, 2, 3$ for the 1979 Standard and $\alpha = 1, 2, 3, 4$ for the 1994 Standard,

$$P'_\gamma(t) = \sum_{\alpha=1}^{N_I} \sum_{j=1}^{N_\alpha} \lambda_{\alpha j}\gamma_{\alpha j}(t), \tag{7.1-18}$$

where $N_I = 3$ for the 1979 Standard and $N_I = 4$ for the 1994 Standard, and where ψ is the fission rate from all isotopes, F_α is the fraction of fissions from isotope α, and P'_γ is the uncorrected decay power. Summation of F_α over α is 1.0. The value F_γ is a input factor to allow easy specification of a conservative calculation. It is usually 1.0 for best-estimate calculations, and 1.2 was recommended for a conservative calculation with the 1973 Proposed Standard. The 1979 and 1994 Standards should allow consistent use of 1.0 for F_γ.

The 1979 and 1994 Standards use a correction factor to the energy from fission product decay to account for the effects of neutron absorption. Both an equation and a table for the correction factor are provided. The table is a maximum value for the G factor. The equation is

$$G(t) = 1.0 + (3.24 \cdot 10^{-6} + 5.23 \cdot 10^{-10}t)\, T^{0.4}\psi_g \tag{7.1-19}$$

where ψ_g is the number of fissions per initial fissile atom, T is the reactor operating time including any periods of shutdown, and t is the time since shutdown. Limits on the quantities are $1.0 \le \psi_g \le 3.0$, $T < 1.2614 \cdot 10^8$ seconds, and $t < 10^4$ seconds. The table is used for $t \ge 10^4$. Note that there is a discontinuity in G(t) when switching from the equation to the table. The standard allows the table to be used in place of the equation and the code through user input allows the same. The corrected decay power is given by

$$P_\gamma = G(t)P'_\gamma \quad . \tag{7.1-20}$$

The 1973 Proposed Standard[7.1-2] is presented in terms of the Shure[7.1-8] curve and tabular data. The ATHENA implementation of the 1973 Proposed Standard is the same as the RELAP4[7.1-9] implementation, where differential equations for one isotope and 11 groups are fitted to the Shure curve (the 1973 Proposed Standard). The ATHENA and RELAP4 implementations of the 1973 Proposed Standard are within 4% of the tabular values of the 1973 Proposed Standard. The 1979 Standard[7.1-3,7.1-4,7.1-5] lists data for three isotopes, ^{235}U, ^{238}U, and ^{239}Pu, and uses 23 groups for each isotope. The ATHENA implementation of the 1979 Standard is exact (i.e., not a curve fit). A user option also allows only the 1979 Standard data for ^{235}U to be used. The 1994 Standard[7.1-6] lists data for four isotopes, ^{235}U, ^{238}U, ^{239}Pu, and ^{241}Pu, and uses 23 groups for each isotope. The ATHENA implemetation of the 1994 Standard is exact (i.e., not a curve fit). A user option also allows only the 1994 Standard data for ^{235}U to be used. The data for all standards are built into the code as default data, but the user may enter different data.

7.1.3 Actinide Decay Model

The actinide model describes the production of ^{239}U, ^{239}Np, and ^{239}Pu from neutron capture by ^{238}U.

$$\frac{d\gamma_U(t)}{dt} = F_U\psi(t) - \lambda_U\gamma_U(t) \tag{7.1-21}$$

$$\frac{d\gamma_N(t)}{dt} = \lambda_U\gamma_U(t) - \lambda_N\gamma_N(t) \tag{7.1-22}$$

$$P_\alpha(t) = \eta_U\lambda_U\gamma_U(t) + \eta_N\lambda_N\gamma_N(t) \quad . \tag{7.1-23}$$

The quantity F_U is user-specified and is the number of atoms of ^{239}U produced by neutron capture in ^{238}U per fission from all isotopes. A conservative factor if desired should be factored into F_U. The λ and η values can be user-specified, or default values equal to those stated in the 1979 ANS Standard and the 1994 Standard can be used.

The first equation describes the rate of change of atoms of ^{239}U. The first term on the right represents the production of ^{239}U; the last term is the loss of ^{239}U due to beta decay. The second equation describes the rate of change of ^{239}Np. The production of ^{239}Np is from the beta decay of ^{239}U, and ^{239}Pu is formed from the decay of ^{239}Np. Solution of the actinide Equations, (7.1-21) and (7.1-22), for the fission source given in Equation (7.1-16) yields the result quoted in the 1979 Standard and the 1994 Standard.

7.1.4 Transformation of Equations for Solution

The differential equations to be advanced in time are Equations (7.1-1), (7.1-2), (7.1-17), (7.1-21), and (7.1-22). Multiplying by $V\Sigma_f$ and X which is the conversion factor from MeV/s to watts, the equations become

$$\frac{d}{dt}\left[\frac{X\psi(t)}{v}\right] = \frac{[\rho(t)-\beta]X\psi(t)}{\Lambda v} + \sum_{i=1}^{N_d}\lambda_i XV\Sigma_f C_i(t) + XV\Sigma_f S \qquad (7.1\text{-}24)$$

$$\frac{d}{dt}[X\Sigma_f C_i(t)] = \frac{\beta f_i X\psi(t)}{\Lambda v} - \lambda_i XV\Sigma_f C_i(t) \qquad i = 1, 2, ..., N_d \qquad (7.1\text{-}25)$$

$$\frac{d}{dt}[X\gamma_{\alpha j}(t)] = \frac{F_\gamma a_{\alpha j} F_\alpha X\psi(t)}{\lambda_{\alpha j}} - \lambda_{\alpha j} X\gamma_{\alpha j}(t) \qquad j = 1, 2, ..., N_\alpha \qquad (7.1\text{-}26)$$

where $\alpha = 1, 2, 3$ for the 1979 Standard and $\alpha = 1, 2, 3, 4$ for the 1994 Standard,

$$\frac{d}{dt}[X\gamma_U(t)] = F_U X\psi(t) - \lambda_U X\gamma_U(t) \qquad (7.1\text{-}27)$$

$$\frac{d}{dt}[X\gamma_N(t)] = \lambda_U X\gamma_U(t) - \lambda_N X\gamma_N(t) \ . \qquad (7.1\text{-}28)$$

The total power P_T is the sum of immediate fission power, corrected fission product decay, and actinide decay power, and now in units of watts is

$$P_T(t) = Q_f X\psi(t) + G(t)\sum_{\alpha=1}^{N_I}\sum_{j=1}^{N_\alpha}\lambda_{\alpha j}X\gamma_{\alpha j}(t) + \eta_U\lambda_U X\gamma_U(t) + \eta_N\lambda_N X\gamma_N(t) \qquad (7.1\text{-}29)$$

where $N_I = 3$ for the 1979 Standard and $N_I = 4$ for the 1994 Standard.

For solution convenience, the following substitutions are made:

$$\rho(t) = \beta r(t) \qquad (7.1\text{-}30)$$

$$X\psi(t) = \psi'(t) \qquad (7.1\text{-}31)$$

$$\frac{XV\Sigma_f \Lambda v S}{\beta} = S' \tag{7.1-32}$$

$$XV\Sigma_f v C_i(t) = \frac{\beta f_i}{\Lambda \lambda_i} W_i(t) \qquad i = 1, 2, ..., N_d \tag{7.1-33}$$

$$X\gamma_{\alpha j}(t) = \frac{F_\gamma a_{\alpha j} F_\alpha}{\lambda_{\alpha j}^2} Z_{\alpha j}(t) \qquad j = 1, 2, ..., N_\alpha \tag{7.1-34}$$

where $\alpha = 1, 2, 3$ for the 1979 Standard and $\alpha = 1, 2, 3, 4$ for the 1994 Standard,

$$X\gamma_U(t) = \frac{F_U}{\lambda_U} Z_U(t) \tag{7.1-35}$$

$$X\gamma_N(t) = Z_N(t) . \tag{7.1-36}$$

The equations to be advanced are now

$$\frac{d}{dt}\psi'(t) = \frac{\beta}{\Lambda}\left\{[r(t) - 1]\psi'(t) + \sum_{i=1}^{N_d} f_i W_i(t) + S'\right\} \tag{7.1-37}$$

$$\frac{d}{dt}W_i(t) = \lambda_i \psi'(t) - \lambda_i W_i(t) \qquad i = 1, 2, ..., N_d \tag{7.1-38}$$

$$\frac{d}{dt}Z_{\alpha j} t = \lambda_{\alpha j} \psi'(t) - \lambda_{\alpha j} Z_{\alpha j}(t) \qquad i = 1, 2, ..., N_d \tag{7.1-39}$$

where $\alpha = 1, 2, 3$ for the 1979 standard and $\alpha = 1, 2, 3, 4$ for the 1994 Standard,

$$\frac{d}{dt}Z_U(t) = \lambda_U \psi'(t) - \lambda_U Z_U(t) \tag{7.1-40}$$

$$\frac{d}{dt}Z_N(t) = F_U Z_U(t) - \lambda_N Z_N(t) \tag{7.1-41}$$

$$P_T(t) = Q_f\psi'(t) + G(t) \sum_{\alpha=1}^{N_I} \sum_{j=1}^{N_\alpha} \frac{F_\gamma a_{\alpha j} F_\alpha Z_{\alpha j}(t)}{\lambda_{\alpha j}} + F_U \eta_U Z_U(t) + \eta_N \lambda_N Z_N(t) \ ,$$ (7.1-42)

where $N_I = 3$ for the 1979 Standard and $N_I = 4$ for the 1994 Standard.

These equations are advanced using the modified Runge-Kutta method described in Section 7.1.7.

7.1.5 Initialization

Two initialization options are provided. In both options, the fission rate and delayed neutrons are in steady-state or equilibrium conditions, that is, their time derivatives are zero. With $r(0)$ an input quantity,

$$W_i(0) = \psi'(0) \qquad j = 1, 2, \dots, N_d$$ (7.1-43)

$$S' = -r(0)\psi'(0) \ .$$ (7.1-44)

The first option assumes that the fission product decay and actinides are also in equilibrium. This is equivalent to assuming that the reactor has been operating at a constant total power for an infinite period of time. The initial conditions are

$$Z_{\alpha j}(0) = \psi'(0) \qquad i = 1, 2, \dots, N_\alpha$$ (7.1-45)

where $\alpha = 1, 2, 3$ for the 1979 Standard and $\alpha = 1, 2, 3, 4$ for the 1994 Standard,

$$Z_U(0) = \psi'(0)$$ (7.1-46)

$$Z_N(0) = \frac{F_U}{\lambda_N}\psi'(0)$$ (7.1-47)

$$P_T(0) = \left[Q_f v + G(0) \sum_{\alpha=1}^{N_I} \sum_{j=1}^{N_\alpha} \frac{F_\gamma a_{\alpha j} F_\alpha}{\lambda_{\alpha j}} + F_U \eta_U + \eta_N \lambda_N \right] \psi'(0)$$ (7.1-48)

$$Q = Q_f + \sum_{\alpha=1}^{N_I} \sum_{j=1}^{N_\alpha} \frac{F_\gamma a_{\alpha j} F_\alpha}{\lambda_{\alpha j}} + F_U \eta_U + F_U \eta_N$$ (7.1-49)

where $N_I = 3$ for the 1979 Standard and $N_I = 4$ for the 1994 Standard.

The quantity Q, which is the total energy in MeV generated per fission, is either an input value or can be defaulted to 200 MeV. The quantity Q_f is defined from Equation (7.1-49) and the user-specified or defaulted data, even if the second initialization option is used. The total power is an input quantity, and $\psi'(0)$ is determined from Equation (7.1-48). The remaining quantities are computed from $\psi'(0)$ using Equations (7.1-43) through (7.1-47). Depending on a user option, the G factor is evaluated from Equation (7.1-19) with the reactor operating time T set to the user input and the operating time t set to zero or from the first value in the G factor table in the standard (1.020).

The second option uses a power history to determine the initial values of the fission product and actinide quantities. The power history consists of one or more periods of constant total power. For each period, the input consists of the total power, the time duration at that power, and, in the case of three isotopes, the fraction of power from each isotope. The fission product and actinide differential Equations, (7.1-39), (7.1-40), and (7.1-41), are advanced in time starting with initial values of zero. The fission rate, ψ, is defined from Equation (7.1-49). Depending on a user option, the G factor during this advancement is obtained from Equation (7.1-19) with the reactor operating time T advanced in time and the shutdown time t equal to zero or using the first value in the G factor table in the standard (1.020).The fission rate is reset to zero whenever a negative value is computed. This would occur whenever the user-entered total power is less than the current fission product and actinide decay power. Thus, for shutdown periods, the user may conveniently enter zero total power even though significant decay power remains. The fission product and actinide values at the end of the power history become the initial values for the transient. The initial fission rate is computed from Equation (7.1-49), using the total reactor power at the start of the transient (which may be different from the last power history value). If this fission rate is negative or zero, it is reset such that the immediate fission power is 10^{-12} times the decay power.

The differential equations for the power history calculation are advanced using the same numerical technique as for the transient advancement except for a simplified time step control. Time step control consists of starting the advancement of each history period with a time step of 1 second. The time step is doubled after each advancement. When the next advancement would exceed the time duration, the last advancement is with the remaining time. This scheme was selected since, with each different power value, the solution moves toward a new equilibrium condition asymptotically; and the most rapid change is at the beginning of a power change.

7.1.6 Reactivity Feedback

Either separable or tabular models can be selected for reactivity feedback in point reactor kinetics.

7.1.6.1 Separable Feedback Model

The separable model, which is similar to the RELAP4[7.1-10] model, defines reactivity as

$$r(t) \; = \; r_o - r_B + \sum_{i=1}^{n_s} r_{si}(t) + \sum_{i=1}^{n_c} V_{ci} + \sum_{i=1}^{n_\rho} [W_{\rho i} \bullet R_\rho(\rho_i(t)) + a_{Wi} \bullet T_{Wi}(t)] +$$

$$\sum_{i=1}^{n_F} [W_{Fi} \bullet R_F(T_{Fi}(t)) + a_{Fi} \bullet T_{Fi}(t)] \; . \tag{7.1-50}$$

The quantity r_o is an input quantity that represents the reactivity corresponding to assumed steady-state reactor power at t = 0. The quantity r_B is the bias reactivity which is calculated during input processing such that $r(0) = r_o$ and is printed in the input level printout. Should the user check the bias reactivity computation using Equation (7.1-50), the temperature used in the $a_{Wi} T_{Wi}(t)$ and $a_{Fi} T_{Fi}(t)$ terms should use absolute temperature, i.e., Kelvin in SI units and Rankine in British units. The temperature used in the table lookup term $W_{Fi} R_F[T_{Fi}(t)]$, however, should still use Kelvin in SI units and Fahrenheit in British units.

The quantities r_{si} are obtained from input tables defining n_s reactivity (or scram) curves as a function of time. The quantities V_{ci} are n_c control variables that can be user-defined as reactivity contributions. R_ρ is a table defining reactivity as a function of the current moderator density of fluid $\rho_i(t)$ in the hydrodynamic volume i (density reactivity table); $W_{\rho i}$ is the density weighting factor for volume i; $T_{Wi}(t)$ is the spatial density averaged moderator fluid temperature of volume i; a_{Wi} is the temperature coefficient (not including density changes) for volume i; and n_ρ is the number of hydrodynamic volumes in the reactor core. The quantity R_F is a table defining reactivity as a function of the heat structure volume average fuel temperature $T_{Fi}(t)$ in heat structure i (Doppler reactivity table); W_{Fi} and a_{Fi} are the fuel temperature weighting factor and the fuel temperature coefficient, respectively, for heat structure i; and n_F is the number of heat structures in the reactor core.

The model assumes nonlinear feedback effects from moderator density and fuel temperature changes and linear feedback from moderator and fuel temperature changes. It is called the separable model because each effect is assumed to be independent of the other effects. Boron feedback is not provided, but a user-defined boron feedback can be implemented with the control system. The separable model can be used if boron changes are quite small and the reactor is near critical about only one state point.

7.1.6.2 Tabular Feedback Model

A postulated BWR anticipated transient without scram (ATWS) accident is an example where the reactor could be nearly critical for two different state points. One point is at normal power operating conditions--high moderator and fuel temperatures, highly voided, and no boron. During accident recovery, the reactor might approach a critical condition with relatively cold moderator and fuel temperatures, with no voids, but with some boron concentration. The reactivity could be nearly critical for both states, but the

contributions from the different feedback effects are vastly different. The assumptions of no interactions among the different feedback mechanisms, especially boron, cannot be justified.

The tabular feedback model computes reactivity from multi-dimensional table lookup and linear interpolation. The tabular model overcomes the objections of the separable model since all feedback mechanisms can be nonlinear and interactions among the mechanisms are included. The penalty for the expanded modeling capability is greatly increased input data requirements.

Two different sets of variables within the tabular feedback option are available. Both sets of variables allow a boron related variable as one of the four variables. Both sets of variables allow the boron related variable to be omitted when only three variables are used.

7.1.6.2.1 Standard Variables. With standard independent variables, the tabular model defines reactivity as

$$r(t) \ = \ r_o - r_B + \sum_{i=1}^{n_s} r_{si}(t) + \sum_{i=1}^{n_c} V_{ci} + R(\bar{\rho}(t), \bar{T}_W(t), \bar{T}_F(t), \bar{\rho}_b(t)) \tag{7.1-51}$$

$$\bar{\rho}(t) \ = \ \sum_{i=1}^{n_\rho} W_{\rho i} \rho_i(t) \tag{7.1-52}$$

$$\bar{T}_W(t) \ = \ \sum_{i=1}^{n_\rho} W_{\rho i} T_{Wi}(t) \ = \ \sum_{i=1}^{n_\rho} W_{\rho i} \left[\frac{\alpha_{fi} \rho_{fi} T_{fi}(t) + \alpha_{gi} \rho_{gi} T_{gi}(t)}{\alpha_{fi} \rho_{fi} + \alpha_{gi} \rho_{gi}} \right] \tag{7.1-53}$$

$$\bar{T}_F(t) \ = \ \sum_{i=1}^{n_F} W_{Fi} T_{Fi}(t) \tag{7.1-54}$$

$$\bar{\rho}_b(t) \ = \ \sum_{i=1}^{n_\rho} W_{\rho i} \rho_{bi}(t) \ . \tag{7.1-55}$$

The variables, r_o, r_B, r_{si}, and V_{ci} are the same as for separable feedback, $\rho_i(t)$ is the moderator fluid density in volume i (mass of liquid, vapor, and noncondensable gas divided by volume of volume), $T_{Wi}(t)$ is the spatial density averaged moderator fluid temperature of volume i, $T_{fi}(t)$ and $T_{gi}(t)$ are the liquid and vapor/gas temperatures of volume i, α_{fi} and α_{gi} are liquid and vapor volume fractions in volume i, $T_{Fi}(t)$ is the heat structure volume averaged fuel temperature for heat structure i, and $\rho_{bi}(t)$ is the spatial boron

density (mass of boron divided by volume of volume). The average quantities are obtained with the use of one weighting factor for each hydrodynamic volume $W_{\rho i}$ contributing to reactivity feedback and one weighting factor for each heat structure W_{Fi} contributing to reactivity feedback. The reactivity function R is defined by a table input by the user. In the Input Requirements, Volume II of these manuals, TABLE3 and TABLE4 options refer to the above set of independent variables; TABLE4 option specifies a four-dimensional table, TABLE3 option assumes no boron dependence and the table is then three-dimensional.

7.1.6.2.2 Alternate Variables. With alternate independent variables, the tabular model defines reactivity as

$$r(t) = r_o - r_B + \sum_{i=1}^{n_s} r_{si}(t) + \sum_{i=1}^{n_c} V_{ci} + R(\bar{\alpha}_g(t), \overline{T}_f(t), \overline{T}_F(t), \overline{C}_b(t)) \qquad (7.1\text{-}56)$$

$$\bar{\alpha}_g(t) = \sum_{i=1}^{n_\rho} W_{\rho i} \alpha_{gi}(t) \qquad (7.1\text{-}57)$$

$$\overline{T}_f(t) = \sum_{i=1}^{n_\rho} W_{\rho i} T_{fi}(t) \qquad (7.1\text{-}58)$$

$$\overline{T}_F(t) = \sum_{i=1}^{n_F} W_{Fi} T_{Fi}(t) \qquad (7.1\text{-}59)$$

$$\overline{C}_b(t) = \sum_{i=1}^{n_\rho} W_{\rho i} \frac{\rho_{bi}}{\alpha_{fi}\rho_{fi}}(t) \quad . \qquad (7.1\text{-}60)$$

The quantity $C_b(= \dfrac{\rho_b}{\alpha_f\rho_f})$ is the boron concentration in mass of boron per mass of liquid and the other quantities are the same as for the standard variables. Input options TABLE3A and TABLE4A specify the alternate set of independent variables; TABLE4A selects four independent variables and TABLE3A selects only three independent variables with the boron concentration being omitted.

7.1.6.2.3 Interpolation Procedures. The reactivity function R is evaluated by a direct extension of the one-dimensional table lookup and linear interpolation scheme to multiple dimensions. One-dimensional table lookup and interpolation of the function $V = F(W)$ uses an ordered set of N_w

independent variable values W_i, with the corresponding values of the dependent variable V_i, to determine the value of V corresponding to a search argument W. The independent variable is searched such that W_i and W_{i+1} bracket W; an equation for a straight line is fitted to the points W_i, V_i, and W_{i+1}, V_{i+1}; and the straight line equation is evaluated for the given W.

Using subscripts 0 and 1 for the bracketing independent values and corresponding dependent values and defining $w = \left(\dfrac{W - W_0}{W_1 - W_0}\right)$ so that w varies from 0 through 1 as W varies from W_0 through W_1, the interpolation equations are

$$V = \sum_{i=0}^{1} a_i w^i \qquad (7.1\text{-}61)$$

$$a_0 = V_0 \qquad (7.1\text{-}62)$$

$$a_1 = V_1 - V_0 \qquad (7.1\text{-}63)$$

For two-dimensional interpolation of V = F(W,X), two sets of independent variables are used; N_w values of W_i and N_x values of X_j. A total of $N_w N_x$ dependent values of V_{ij} are entered, one value for each combination of variables from the two sets of independent variables. Graphically, the two sets of independent variables form a rectangular grid when the W_i and X_j variables are plotted on horizontal and vertical coordinates, respectively. The dependent variables are entered corresponding to the intersections of the mesh lines. The search for bracketing values in each independent set locates a mesh rectangle, and the dependent values at the four corners are used to form an interpolation equation which is the product of two straight line functions, one for each independent variable. Using 0 and 1 subscripts for the bracketing values,

$$V = \sum_{i=0}^{1} \sum_{j=0}^{1} a_{ij} w^i x^j \qquad (7.1\text{-}64)$$

$$x = \frac{X - X_0}{X_1 - X_0} \qquad (7.1\text{-}65)$$

$$a_{00} = V_{00} \qquad (7.1\text{-}66)$$

$$a_{01} = V_{01} - V_{00} \qquad (7.1\text{-}67)$$

$$a_{10} = V_{10} - V_{00} \tag{7.1-68}$$

$$a_{11} = V_{11} - V_{01} - V_{10} + V_{00} \; . \tag{7.1-69}$$

This process is simply extended to three- and four-dimensions. Three sets of independent variables define a three-dimensional rectangular grid; and eight dependent quantities corresponding to the corners of a rectangular solid are used to define the interpolation equation, which is the product of three straight line functions. In four-dimensions, four sets of independent variables are defined; and 16 dependent values are used to define the interpolation equation, which is the product of four straight line functions.

For three-dimensional interpolation,

$$V = F(W, X, Y) \tag{7.1-70}$$

$$y = \frac{Y - Y_0}{Y_1 - Y_0} \tag{7.1-71}$$

$$V = \sum_{i=0}^{1} \sum_{j=0}^{1} \sum_{k=0}^{1} a_{ijk} w^i x^j y^k \tag{7.1-72}$$

$$a_{000} = V_{000} \tag{7.1-73}$$

$$a_{001} = V_{001} - V_{000} \tag{7.1-74}$$

$$a_{010} = V_{010} - V_{000} \tag{7.1-75}$$

$$a_{100} = V_{100} - V_{000} \tag{7.1-76}$$

$$a_{011} = V_{011} - V_{001} - V_{010} + V_{000} \tag{7.1-77}$$

$$a_{101} = V_{101} - V_{001} - V_{100} + V_{000} \tag{7.1-78}$$

$$a_{110} = V_{110} - V_{010} - V_{100} + V_{000} \tag{7.1-79}$$

$$a_{111} = V_{111} - V_{011} - V_{101} - V_{110} + V_{001} + V_{010} + V_{100} - V_{000} \; . \tag{7.1-80}$$

For four-dimensional interpolation,

$$V = F(W, X, Y, Z) \tag{7.1-81}$$

$$z = \frac{Z - Z_0}{Z_1 - Z_0} \tag{7.1-82}$$

$$V = \sum_{i=0}^{1} \sum_{j=0}^{1} \sum_{k=0}^{1} \sum_{m=0}^{1} a_{ijkm} w^i x^j y^k z^m \tag{7.1-83}$$

$$a_{0000} = V_{0000} \tag{7.1-84}$$

$$a_{0001} = V_{0001} - V_{0000} \tag{7.1-85}$$

$$a_{0010} = V_{0010} - V_{0000} \tag{7.1-86}$$

$$a_{0100} = V_{0100} - V_{0000} \tag{7.1-87}$$

$$a_{1000} = V_{1000} - V_{0000} \tag{7.1-88}$$

$$a_{0011} = V_{0011} - V_{0001} - V_{0010} + V_{0000} \tag{7.1-89}$$

$$a_{0101} = V_{0101} - V_{0001} - V_{0100} + V_{0000} \tag{7.1-90}$$

$$a_{0110} = V_{0110} - V_{0010} - V_{0100} + V_{0000} \tag{7.1-91}$$

$$a_{1001} = V_{1001} - V_{0001} - V_{1000} + V_{0000} \tag{7.1-92}$$

$$a_{1010} = V_{1010} - V_{0010} - V_{1000} + V_{0000} \tag{7.1-93}$$

$$a_{1100} = V_{1100} - V_{0100} - V_{1000} + V_{0000} \tag{7.1-94}$$

$$a_{0111} = V_{0111} - V_{0011} - V_{0101} + V_{0110} + V_{0001} + V_{0010} + V_{0100} - V_{0000} \tag{7.1-95}$$

$$a_{1011} = V_{1011} - V_{0011} - V_{1001} + V_{1010} + V_{0001} + V_{0010} + V_{1000} - V_{0000} \tag{7.1-96}$$

$$a_{1101} = V_{1101} - V_{0101} - V_{1001} + V_{1100} + V_{0001} + V_{0100} + V_{1000} - V_{0000} \tag{7.1-97}$$

$$a_{1110} = V_{1110} - V_{0110} - V_{1010} + V_{1100} + V_{0010} + V_{0100} + V_{1000} - V_{0000} \qquad (7.1\text{-}98)$$

$$\begin{aligned} a_{1111} = &\; V_{1111} - V_{0111} - V_{1011} - V_{1101} - V_{1110} + V_{0011} + V_{0101} + V_{0110} + V_{1101} \\ &+ V_{1001} + V_{0001} - V_{0010} - V_{1010} + V_{1100} - V_{0100} - V_{1000} + V_{0000} \; . \end{aligned} \qquad (7.1\text{-}99)$$

The interpolating equations define a continuous function. There is no discontinuity in the dependent quantity as any one or combination of dependent variables pass to the next bracketing pair of values.

Using N_W, N_X, N_Y, and N_Z as the number of values in the four sets of independent variables, the number of data points for a three-dimensional table is $N_W\,N_X\,N_Y$ and is $N_W\,N_X\,N_Y\,N_Z$ for a four-dimensional table. Using only four values for each independent variable, a four-dimensional table requires 256 data points.

7.1.7 Reactor Kinetics Numerical Procedures

The reactor kinetics equations are advanced in time using the modified Runge-Kutta method of Cohen.[7.1-11] A first-order differential equation is written as

$$\dot{n}(t) = \alpha n(t) + R(n,t) \qquad (7.1\text{-}100)$$

where α is constant over the time step, and $R(n, t)$ contains the remaining terms of the differential equation, including the non-constant portion of any coefficient of $n(t)$. If the coefficient of $n(t)$ is $\beta(n, t)$, α would be $\beta[n(0), 0]$; and $R(n, t)$ would contain a term of the form $\beta[n(t), t] - \alpha\, n(t)$. Multiplying Equation (7.1-100) by the integrating factor $e^{-\alpha t}$ and integrating gives

$$n(t) = n(0)e^{\alpha t} + \int_0^t e^{\alpha(t-\lambda)} R(n, \lambda)\,d\lambda \; . \qquad (7.1\text{-}101)$$

Since

$$n(0)e^{\alpha t} = n(0) + \int_0^t \alpha n(0) e^{\alpha(t-\lambda)}\,d\lambda , \qquad (7.1\text{-}102)$$

$$n(t) = n(0) + \int_0^t [\alpha n(0) + R(n, \lambda)] e^{(t-\lambda)}\,d\lambda \; . \qquad (7.1\text{-}103)$$

Letting $\lambda = ut$, then $d\lambda = t\,du$, and

$$n(t) = n(0) + t \int_0^1 [\alpha n(0) + R(n, u)] e^{\alpha t (1 - u)} du \quad . \tag{7.1-104}$$

The numerical technique for advancing the solution over the time step consists of making approximations to the behavior of R(n,u) over the time step. For convenience in the following expressions, the following function is defined,

$$C_m(x) = \int_0^1 u^{m-1} e^{x(1-u)} du \quad . \tag{7.1-105}$$

Stage 1:

Assume $R(n, \lambda) = R[n(0), 0] = R_0$ and write $n(0)$ as n_0; then compute $n\left(\dfrac{h}{2}\right)$ by

$$n_1 = n\left(\frac{h}{2}\right) = n_0 + \frac{h}{2}(\alpha n_0 + R_0) C_1\left(\alpha \frac{h}{2}\right) \quad . \tag{7.1-106}$$

Stage 2:

Assume straight line variation of $R(n, \lambda)$ between R_0 and $R_1 = R\left(n_1, \dfrac{h}{2}\right)$ and compute $n\left(\dfrac{h}{2}\right)$ by

$$R(n, \lambda) = R_0 + \frac{2(R_1 - R_0)\lambda}{h} \tag{7.1-107}$$

$$R(n, \lambda) = R_0 + (R_1 - R_0) u \tag{7.1-108}$$

$$n_2 = n\left(\frac{h}{2}\right) = n_1 + \frac{h}{2}(R_1 - R_0) C_2\left(\alpha \frac{h}{2}\right) \quad . \tag{7.1-109}$$

Stage 3:

Assume straight line variation of $R(n, \lambda)$ between R_0 and $R_2 = R\left(n_2, \dfrac{h}{2}\right)$ and compute $n(h)$ by

$$R(n, \lambda) = R_0 + \frac{2}{h}[R_2 - R_0]\lambda \tag{7.1-110}$$

$$R(n, u) = R_0 + 2 [R_2 - R_0] u \tag{7.1-111}$$

$$n_3 = n(h) = n_0 + h(\alpha n_0 + R_0) C_1(\alpha h) + 2h(R_2 - R_0) C_2(\alpha h) \ . \tag{7.1-112}$$

Stage 4:

Assume quadratic through points R_0, R_2, and $R_3 = R(n_3, h)$, then compute n(h) by

$$R(n, u) = (2R_0 + 4R_2 + 2R_3) u_2 + (-3R_0 + 4R_2 - R_3) u + R_0 \tag{7.1-113}$$

$$n_4 = n(h) = n_3 + h (R_4 - R_3) [2C_3 (\alpha h) - C_2(\alpha h)] \ . \tag{7.1-114}$$

Stage 5:

Assume quadratic through points R_0, R_2, and $R_4 = R(n_4, h)$, then compute n(h) by

$$n_5 = n(h) = n_4 + h (R_4 - R_3) [2C_3 (\alpha h) - C_2 (\alpha h)] \ . \tag{7.1-115}$$

Third-, fourth-, and fifth-order approximations are obtained by terminating the process at the end of the third-, fourth-, and fifth-stages, respectively. ATHENA uses only the fifth-order approximation.

By direct integration, the function $C_1(x)$ is given by

$$C_1(x) = \frac{e^x - 1}{x} \ . \tag{7.1-116}$$

Using integration by parts, a recursion relation for $C_m(x)$ is

$$C_{m+1}(x) = \frac{mC_m(x) - 1}{x} \ . \tag{7.1-117}$$

During machine calculations of the $C_m(x)$ functions for $x \le 1$, excessive loss of significance occurs. For this range, $C_3(x)$ is computed from its MacLaurin series expansion

$$C_3(x) = 2\left(\frac{1}{3!} + \frac{x}{4!} + \frac{x^2}{5!} + \frac{x^3}{6!} + \frac{x^4}{7!} + \frac{x^5}{8!} + \frac{x^6}{9!} + \frac{x^7}{10!}\right) \ . \tag{7.1-118}$$

C$_2$ and C$_1$ are evaluated by solving Equation (7.1-117) for C$_m$ (x).

During the advancement in time of the solution, the time increment is automatically increased or decreased to maintain a specified degree of accuracy. After the calculations for a reactor kinetics time advancement, an empirical formula is used to estimate the error. If he error is excessive, the time increment is halved; and the advancement calculation is redone. If the error is sufficiently small, the time interval is doubled for the next time step. If the estimated error is between limits, the same interval is used for the next time advancement. These procedures for time step control, taken from the AIREK code[7.1-12] are as follows:

$$\omega_1 = \frac{\psi'(0)}{\psi'(0)} \qquad\qquad\qquad (7.1\text{-}119)$$

$$\omega_3 = \frac{\psi'(h)}{\psi'(h)} \quad . \qquad\qquad\qquad (7.1\text{-}120)$$

$\overline{\omega}$ is defined by

$$\psi'(h) = \psi'(0)e^{\overline{\omega}h} \qquad\qquad\qquad (7.1\text{-}121)$$

$$Q = \frac{hC_2(\alpha h)}{1 + C_1(\alpha h)}(\omega_1 - 2\overline{\omega} + \omega_3) \quad . \qquad\qquad\qquad (7.1\text{-}122)$$

The α in Equation (7.1-117) is that of the neutron flux Equation (7.1-37)

$$\delta = \max\left(\frac{n_{1i} - n_{0i}}{n_{1i}}\right) \quad . \qquad\qquad\qquad (7.1\text{-}123)$$

The Q$_L$ and Q$_H$ appearing below are 0.0001 and 0.001 respectively.

1.   If $\delta < 2^{-15}$ and $Q \geq Q_L$, the program continues with the same time step.

2.   If $\delta < 2^{-15}$ and $Q < Q_L$, the program doubles the time step for the next advancement.

3.   If $\delta \geq 2^{-15}$ and

            a. $Q < Q_L$, the time step is doubled for the next advancement.

        b. $Q \leq Q_H$, the same time step is used for the next advancement.

        c. $Q > Q_H$, the time advancement is recalculated with half the time step.

    4.   The time advancement is also recomputed with the time step halved if

        a. αh of any equation > 88.0.

        b.   negative or zero power is computed.

If the coefficient of the neutron flux in Equation (7.1-37) is negative, a subtraction is involved in determination of the derivative and a loss of significant digits can occur. If this coefficient is negative, a check is made of the number of bits lost in the subtraction. If more than nine bits are lost, the value of neutron flux computed by the current stage of the advancement procedure is discarded; instead, neutron flux is determined from the expression obtained by setting the neutron flux derivative to zero

$$\psi(t) = \frac{-\sum_{i=1}^{N_d} f_i W_i(t) - S'}{r(t) - 1} \quad . \tag{7.1-124}$$

The transfer of information between the reactor kinetics calculation and the other calculations is explicit. Hydrodynamic and heat conduction/transfer calculation precede reactor kinetics, and the control system calculation follows reactor kinetics. The reactor power used in hydrodynamics and heat conduction is the value at the beginning of the time step. The reactivity used as the end of time step value in the kinetics advancement is computed from end of time step values from hydrodynamics and heat conduction and beginning of time step values from the control system.

The reactor kinetics equations are advanced at the same time step as the hydrodynamics, and reactivity is assumed to vary linearly between time step values. The maximum time step for the reactor kinetics advancement is the hydrodynamic time step. That time step is reduced, if necessary, as described above.

7.1.8 References

7.1-1.   R. J. Wagner, *IREKIN -- Program for the Numerical Solution of the Reactor Kinetics Equations*, IDO-17114, National Reactor Testing Station, January 1966.

7.1-2.   *American Nuclear Society Proposed Standard, ANS 5.1, Decay Energy Release Rate Following Shutdown of Uranium-Fueled Thermal Reactors,* October 1971, revised October 1973.

7.1-3.   *American National Standard for Decay Heat Power in Light Water Reactors,* ANSI/ANS-5.1-1979, August 1979.

7.1-4.   V. E. Schrock, "A Revised ANS Standard for Decay Heat from Fission Products," *Nuclear Technology, 46*, 1979, pp. 323-331.

7.1-5.   V. E. Schrock, "Evaluation of Decay Heating in Shutdown Reactors," *Progress in Nuclear Energy, 3,* 1979, pp. 125-156.

7.1-6.   *American National Standard for Decay Heat Power in Light Water Reactors*, ANSI/ANS-5.1-1994, August 1994.

7.1-7.   S. Glasstone and A. Sesonske, *Nuclear Reactor Engineering*, New York: Von Nostrand Reinhold, 1981.

7.1-8.   K. Shure, *Fission-Product Decay Energy,* WAPD-BT-24, Westinghouse Atomic Division, Bettis, December 1961.

7.1-9.   *RELAP4/MOD5 Users Manual,* ANCR-NUREG-1335, Idaho National Engineering Laboratory, September 1976.

7.1-10.   EG&G Idaho, Inc., *RELAP4/MOD6: A Computer Program for Transient Thermal-Hydraulic Analysis of Nuclear Reactors and Related Systems, Users Manual,* CDAP-TR-003, Idaho National Engineering Laboratory, May 1978.

7.1-11.   E. R. Cohen, "Some Topics In Reactor Kinetics," *A/CONF, 15,* 1958, p. 629.

7.1-12.   A. Schwartz, *Generalized Reactor Kinetics Code AIREK II,* NAA-SR-Memo-4980, 1960.

7.2 Multi-Dimensional Neutron Kinetics

The multi-dimensional neutron kinetics model in the ATHENA code was developed to allow the user to model reactor transients where the spatial distribution of the neutron flux changes with time. The model is based on the NESTLE[7.2-1] code developed at North Carolina State University. The model solves the few-group neutron diffusion equation utilizing the Nodal Expansion Method (NEM). It can solve the steady state eigenvalue (criticality) and/or eigenvalue initiated transient problems. The subroutines used to solve the steady state eigenvalue and the eigenvalue initiated transient problems were taken from the NESTLE code source, were modified to be compatible with the coding standards and data storage methodology used in ATHENA, and were inserted into ATHENA. ATHENA was modified to call the appropriate NESTLE subroutines depending upon the options chosen by the user.

The neutron kinetics model in NESTLE and ATHENA uses the few-group neutron diffusion equations. Two or four energy groups can be utilized, with all groups being thermal groups (i.e. upscatter exits) if desired. Core geometries modeled include Cartesian and hexagonal. Three, two and one dimensional models can be utilized. Various core symmetry options are available, including quarter, half and full core for Cartesian geometry and one-sixth, one-third and full core for hexagonal geometry. Zero flux, non-reentrant current, reflective and cyclic boundary conditions are treated

The few-group neutron diffusion equations are spatially discretized utilizing the Nodal Expansion Method (NEM). Quartic or quadratic polynomial expansions for the transverse integrated fluxes are employed for Cartesian or hexagonal geometries, respectively. Transverse leakage terms are represented by a quadratic polynomial or constant for Cartesian or hexagonal geometry, respectively. Discontinuity Factors (DFs) are utilized to correct for homogenization errors. Transient problems utilize a user specified number of delayed neutron precursor groups. Time discretization is done in a fully implicit manner utilizing a first-order difference operator for the diffusion equation. The precursor equations are analytically solved assuming the fission rate behaves linearly over a time-step.

Independent of problem type, an outer-inner iterative strategy is employed to solve the resulting matrix system. Outer iterations can employ Chebyshev acceleration and the Fixed Source Scaling Technique to accelerate convergence. Inner iterations employ either color line or point SOR iteration schemes, dependent upon problem geometry. Values of the energy group dependent optimum relaxation parameter and the number of inner iterations per outer iteration to achieve a specified L_2 relative errorreduction are determined a priori. The non-linear iterative strategy associated with the NEM method is utilized. This has advantages in regard to reducing FLOP count and memory size requirements versus the more conventional linear iterative strategy utilized in the surface response formulation. In addition, by electing to not update the coupling coefficients in the nonlinear iterative strategy, the Finite Difference Method (FDM) representation, utilizing the box scheme, of the few-group neutron diffusion equation results. The implication is that the model can be utilized to solve either the nodal or FDM representation of the few-group neutron diffusion equation.

The neutron kinetics subroutines require as input the neutron cross sections in the computational nodes of the kinetics mesh. A neutron cross section model has been implemented that allows the neutron cross sections to be parameterized as functions of ATHENA heat structure temperatures, fluid void fraction or fluid density, poison concentration, and fluid temperatures. A flexible coupling scheme between the neutron kinetics mesh and the thermal hydraulics mesh has been developed to minimize the input data needed to specify the neutron cross sections in terms of ATHENA thermal hydraulic variables. A control rod model has been implemented so that the effect of the initial position and subsequent movement of the control rods during transients may be taken into account in the computation of the neutron cross sections. The control system has been modified to allow the movement of control rods by control variables.

7.2.1 Nodal Model - Cartesian Geometry

The nodal model for the solution of the steady state multi-group diffusion equations in Cartesian geometry is described in the following sections.

7.2.1.1 Steady State Eigenvalue Problem

The following section describes the standard NEM formulation for the solution of the three-dimensional, Cartesian geometry, multi-group, eigenvalue neutron diffusion equation[7.2-2,7.2-3]. The

ATHENA/2.3

principal characteristics of the polynomial nodal method are its quartic expansions of the one-dimensional transverse-integrated flux and quadratic leakage model for the transverse leakage.

Consider the general form of the steady-state multi-group neutron diffusion equation, written in standard form and with the group constants (i.e., properly weighted cross-sections and discontinuity factors) already available from a lattice physics calculation for g = 1, 2, ..., G. It is given by

$$\vec{\nabla} \cdot D_g \vec{\nabla} \phi_g + \Sigma_{tg} \phi_g = \sum_{g'=1}^{G} \Sigma_{sgg'} \phi_{g'} + \frac{\chi_g}{k} \sum_{g'=1}^{G} v_{g'} \Sigma_{fg'} \phi_{g'}$$ (7.2-1)

where the dependence of each quantity on the spatial coordinate $\vec{r}$ has been suppressed, and

D_g = diffusion coefficient (cm)

ϕ_g = neutron flux (cm^{-2}sec^{-1})

Σ_{tg} = total macroscopic cross section (cm^{-1})

$\Sigma_{sgg'}$ = group-to-group scattering cross section (cm^{-1})

χ_g = fission neutrons yield

k = multiplication factor (i.e., critical eigenvalue)

v_g = average number of neutrons created per fission

Σ_{fg} = macroscopic fission cross section (cm^{-1}).

As with most modern nodal methods, we begin by integrating the multi-group neutron diffusion equation over a material-centered spatial node which has homogenized properties. For Cartesian geometry we rewrite Equation (7.2-1) for the arbitrary spatial node l as

$$-D_g^l \frac{\partial^2}{\partial x^2} \phi_g^l(\vec{r}) - D_g^l \frac{\partial^2}{\partial y^2} \phi_g^l(\vec{r}) - D_g^l \frac{\partial^2}{\partial z^2} \phi_g^l(\vec{r}) + A_g^l \phi_g^l(\vec{r}) = Q_g^l(\vec{r}),$$ (7.2-2)

where $g \in (1, G)$

$(\vec{r}) \equiv (x, y, z) \in V^l = \Delta x \Delta y \Delta z \equiv \text{Volume of node l}$ (7.2-3)

$$A_g^l = \Sigma_{tg}^l - \Sigma_{sgg}^l - \frac{x_g^l}{k} v_g \Sigma_{fg}^l \tag{7.2-4}$$

$$Q_g^l(\dot{r}) = \sum_{g' \neq g}^{G} Q_{gg'}^l \phi_{g'}^l(\dot{r}) = \sum_{g' \neq g}^{G} \Sigma_{sgg'}^l \phi_{g'}^l(\dot{r}) + \frac{x_g^l}{k} \sum_{g' \neq g}^{G} v_{g'} \Sigma_{fg'}^l \phi_{g'}^l(\dot{r}) . \tag{7.2-5}$$

For simplicity, in cases where redundant equations exist in all three directions, the illustrating equations will be only given in the x-direction. Using Fick's Law, which in the x-direction can be expressed as,

$$j_{gx}^l(\dot{r}) = - D_g^l \frac{\partial}{\partial x} \phi_g^l(\dot{r}) \tag{7.2-6}$$

where, $j_{gx}^l(\dot{r})$ is the x-component of the net neutron current which allows Equation (7.2-2) to be rewritten as

$$\tag{7.2-7}$$

Integration of Equation (7.2-7) over the volume of node l generates a local neutron balance equation in terms of the face-averaged net currents and the node volume average flux. It is given by

$$\frac{1}{\Delta x^l}(\bar{L}_{gx}^l) + \frac{1}{\Delta y^l}(\bar{L}_{gy}^l) + \frac{1}{\Delta z^l}(\bar{L}_{gz}^l) + A_g^l \bar{\phi}_g^l = \bar{Q}_g^l \tag{7.2-8}$$

where, assuming node l is centered around the coordinate's origin, the volume integrated quantities are defined as

$$\bar{\phi}_g^l = \frac{1}{V^l} \int_{-\frac{\Delta x^l}{2}}^{\frac{\Delta x^l}{2}} \int_{-\frac{\Delta y^l}{2}}^{\frac{\Delta y^l}{2}} \int_{-\frac{\Delta z^l}{2}}^{\frac{\Delta z^l}{2}} \phi_g^l(\dot{r}) dx\, dy\, dz \equiv \text{Node volume average flux} \tag{7.2-9}$$

$$\bar{Q}_g^l = \frac{1}{V^l} \int_{-\frac{\Delta x^l}{2}}^{\frac{\Delta x^l}{2}} \int_{-\frac{\Delta y^l}{2}}^{\frac{\Delta y^l}{2}} \int_{-\frac{\Delta z^l}{2}}^{\frac{\Delta z^l}{2}} Q_g^l(\dot{r}) dx\, dy\, dz \equiv \text{Node volume average source} \tag{7.2-10}$$

$$\frac{1}{\Delta x^l}\bar{L}_{gx}^l \;=\; \frac{1}{\Delta x^l}(\bar{J}_{gx+}^l - \bar{J}_{gx-}^l) \;=\; \frac{1}{V^l}\int_{-\frac{\Delta x^l}{2}}^{\frac{\Delta x^l}{2}}\int_{-\frac{\Delta y^l}{2}}^{\frac{\Delta y^l}{2}}\int_{-\frac{\Delta z^l}{2}}^{\frac{\Delta z^l}{2}}\frac{\partial}{\partial x}j_{gx}^l(\hat{r})dxdydz \qquad (7.2\text{-}11)$$

where $\bar{J}_{gx\pm}^l$ is the average x-directed net current on node faces $\pm\dfrac{\Delta x^l}{2}$.

Equation. (7.2-8) is known as the nodal balance equation. Now for the neutron diffusion equation written in this form, in order to obtain the spatial neutron flux distribution, one must devise some relationship between the node average flux and the face-averaged net (surface) currents. It is the equations used to compute the surface currents in Equation (7.2-8) which distinguish one nodal formulation from another. In NEM, the widely used method of transverse-integration is used, where the three-dimensional diffusion equation is integrated over the two directions transverse to each axis. This generates three one-dimensional equations, one for each direction in Cartesian coordinates, of the following form:

$$(7.2\text{-}12)$$

where $\bar{L}_{gy}^l(x)$ is the average y-direction transverse leakage given by

$$\bar{L}_{gy}^l(x) \;=\; \frac{1}{\Delta z^l}\int_{-\frac{\Delta z^l}{2}}^{\frac{\Delta z^l}{2}}\int_{-\frac{\Delta y^l}{2}}^{\frac{\Delta y^l}{2}}\frac{\partial}{\partial y}\,j_{gy}^l(\hat{r})dydz \qquad (7.2\text{-}13)$$

and $\bar{L}_{gz}^l(x)$ is the average z-direction transverse leakage given by

$$\bar{L}_{gz}^l(x) \;=\; \frac{1}{\Delta y^l}\int_{-\frac{\Delta y^l}{2}}^{\frac{\Delta y^l}{2}}\int_{-\frac{\Delta z^l}{2}}^{\frac{\Delta z^l}{2}}\frac{\partial}{\partial z}\,j_{gz}^l(\hat{r})dzdy \,. \qquad (7.2\text{-}14)$$

In NEM, the one-dimensional averaged flux that appears in Equation. (7.2-12), is expanded as a general polynomial given by

$$\bar{\phi}_{gx}^l(x) \;=\; \bar{\phi}_g^l + \sum_{n=1}^{N} a_{gxn}^l\, f_n(x) \qquad (7.2\text{-}15)$$

where $\bar{\phi}_g^1$ is the node average flux, implying for Equation (7.2-15) to be true that $f_n(x)$ must be chosen such that the basis functions satisfy

$$\int_{-\frac{\Delta x^1}{2}}^{\frac{\Delta x^1}{2}} f_n(x)dx \; = \; 0 \text{ for } n \; = \; 1, 2, ..., N. \tag{7.2-16}$$

Note that for quartic NEM, the method used in ATHENA, the summation extends to N = 4. The first four basis functions in NEM can be expressed as follows[7.2-2],

$$\tag{7.2-17}$$

which can be shown to also satisfy

$$f_n\left(\pm\frac{\Delta x^1}{2}\right) \; = \; 0 \qquad \text{for} \qquad n \; = \; 3, 4 \quad . \tag{7.2-18}$$

At this point it is appropriate to consider the elementary concept of accounting for the total number of equations and that of unknowns. For a three-dimensional Cartesian geometry, the node average and N expansion coefficients in each direction appear per node per energy group, implying a total of 3N+1 equations are required. The nodal balance equation, Equation (7.2-8), provides one equation, where now Equations (7.2-6) and (7.2-15) are used to eliminate face-averaged net currents from this equation. Surface current and flux continuity provide 6 more equations per node per energy group. So for N = 2, there would be an equal number of equations and unknowns without any further development. However, for N = 4, two additional unknowns are introduced for each direction per node per energy group. This is addressed by using a weighted residual scheme[7.2-4] applied to Equation (7.2-12), which in essence provides the additional equations (referred to as the moment equations) needed,

$$<\omega_n(x), \frac{d}{dx} j_{gx}^1(x)> + A_g^1\bar{\phi}_{gxn}^1 \; = \; \bar{Q}_{gxn}^1 - \frac{1}{\Delta y^1}\bar{L}_{gyxn}^1 - \frac{1}{\Delta z^1}\bar{L}_{gzxn}^1 \tag{7.2-19}$$

where the two weighting functions for n = 1,2 are chosen to be the same as the basic functions, namely $\omega_n(x) = f_n(x)$, as those used in the one-dimensional flux expansion[a]. Here, the first and second (actually linear combination of zeroth and second) moments of the flux, source, and leakage for each group g are defined by

$$\underbrace{\bar{\phi}_{gxn}^l}_{<\omega_n(x),\bar{\phi}_{gx}^l(x)>} \qquad \underbrace{\bar{Q}_{gxn}^l}_{<\omega_n(x),\bar{Q}_{gx}^l(x)>} \qquad \underbrace{\bar{L}_{gyxn}^l}_{<\omega_n(x),\bar{L}_{gy}^l(x)>} \qquad \underbrace{\bar{L}_{gzxn}^l}_{<\omega_n(x),\bar{L}_{gz}^l(x)>} \; . \tag{7.2-20}$$

The first term in Equation (7.2-19) is evaluated by using Equations (7.2-6) and (7.2-15) and the definition of the expansion coefficients, and completing the integration (i.e. inner product) analytically.

One last point which needs to be addressed before Equation (7.2-19) can be solved is the transverse leakage terms appearing on the right hand side. Their spatial dependency is unknown, so their "shape" must be approximated. The most popular approximation in NEM is the quadratic transverse leakage approximation. For example, the x-direction spatial dependence of the y-direction transverse leakage is approximated by

$$\bar{L}_{gy}^l(x) \cong \bar{L}_{gy}^l + \rho_{gy1}^l f_1(x) + \rho_{gy2}^l f_2(x) \tag{7.2-21}$$

where $\bar{L}_{gy}^l$ is the average y-directed leakage in node l, and the coefficients ρ_{gy1}^l and ρ_{gy2}^l can be expressed in terms of average y-directed leakages of the two nearest-neighbor nodes along the x-direction (i.e. nodes l-1 and l+1) so as to preserve the node average leakages of these three nodes. The quadratic expansion coefficients can be shown to be given by

$$\rho_{gy1}^l = g^l(\Delta x^l)[(\bar{L}_g^{l+1} - \bar{L}_g^l)(\Delta x^l + 2\Delta x^{l-1})(\Delta x^l + \Delta x^{l-1})$$
$$+ (\bar{L}_{gy}^l - \bar{L}_{gy}^{l-1})(\Delta x^l + 2\Delta x^{l+1})(\Delta x^l + \Delta x^{l+1})] \tag{7.2-22}$$

$$\rho_{gy2}^l = g^l(\Delta x^l)^2[(\bar{L}_{gy}^{l+1} - \bar{L}_{gy}^l)(\Delta x^l + \Delta x^{l-1}) + (\bar{L}_{gy}^{l-1} - \bar{L}_{gy}^l)(\Delta x^l + \Delta x^{l+1})] \tag{7.2-23}$$

where

$$g^l = [(\Delta x^l + \Delta x^{l+1})(\Delta x^l + \Delta x^{l-1})(\Delta x^{l-1} + \Delta x^l + \Delta x^{l+1})]^{-1} \; . \tag{7.2-24}$$

7.2.1.2 Non-Linear Iterative Strategy

The most common manner of solving the matrix system associated with NEM is the response-matrix formulation. To minimize computer run time and memory requirements, and to facilitate the capability to

---

a. This constitutes a moments weighting scheme; if one uses $\omega_n(x) = f_{n+2}(x)$ for n = 1,2 it is known as Galerkin weighting. Numerical experiments favor moments weighting.

solve either the NEM or Finite Difference Method (FDM) formulation, the non-linear iterative strategy is employed in ATHENA. This technique was developed by Smith[7.2-5,7.2-6,7.2-7] and successfully implemented into the Studsvik QPANDA and SIMULATE code packages. The documentation available on this technique is scarce, but it turns out to be rather simplistic and almost trivial to implement in a FDM code which utilizes the box-scheme (i.e. material-centered).

The basic idea is applicable to the standard FDM solution algorithm of the multi-group diffusion equation. Solving the FDM based equation utilizing an outer-inner iterative strategy, every ΔN_0 outer iterations (where ΔN_0 is somewhat arbitrary but can be optimized) the so-called "two-node problem" calculation (a spatially-decoupled NEM calculation spanning two adjoining nodes) is performed for every interface (for all nodes and in all directions) to provide an improved estimate of the net surface current at that particular interface. Subsequently, the NEM estimated net surface currents are used to update (i.e. change) the original FDM diffusion coupling coefficients. Outer iterations of the FDM based equation are then continued utilizing the updated FDM coupling coefficients for ΔN_0 outer iterations. The entire process is then repeated. This procedure of updating the FDM couplings is a convergent technique which progressively forces the FDM equation to yield the higher-order NEM predicted values of the net surface currents while satisfying the nodal balance Equation (7.2-8), thus yielding the NEM results for the node-average flux and fundamental mode eigenvalue. The advantages of this technique come in many forms; the storage requirements are minimal because the two-node problem arrays are re-usable (disposable) at each interface, the rate of convergence is nearly comparable to that of the base FDM algorithm being used, the number of iteratively determined unknowns is reduced by a factor of 6 (node flux vs. partial surface current), and the simplicity of the algorithm and ease of implementation, compared to any other nodal technique, is far superior.

The two-node problem produces an 8G x 8G linear system of equations which can be constructed by applying the standard NEM relations to two adjoining nodes. For simplicity, consider two arbitrary adjoining nodes in the x-direction. Denote these notes as l and l+1:
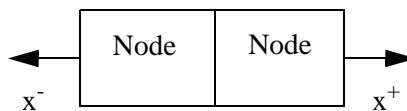
Substitution of the one-dimensional expansion, Equation (7.2-15), into Fick's law yields expressions for the average x-direction net surface currents at the left(-) and right(+) interfaces of node l gives

$$j_{gx\pm}^{:l} \equiv \frac{-D_g^l}{\Delta x^l}\left[a_{gx1}^l \pm 3a_{gx2}^l + \frac{1}{2}a_{gx3}^l \pm \frac{1}{5}a_{gx4}^l\right]. \tag{7.2-25}$$

Now, assume the node average flux, criticality constant, and all transverse direction terms are known from a previous iteration; then, the total number of unknowns associated with the x-direction two node

problem is 8G, which corresponds to the 4 expansion coefficients/group/node (x) G groups (x) two nodes. The 8G constraint equations are obtained as follows. We begin with the substitution of Equation (7.2-25) into the nodal balance equation for node l, to yield the zeroth moment constraints (G equations/node) given by

$$-\frac{D_g^l}{\Delta x^l}\left[6a_{gx2}^l + \frac{2}{5}a_{gx4}^l\right] = -\frac{1}{\Delta y^l}\bar{L}_{gy}^l - \frac{1}{\Delta z^l}\bar{L}_{gz}^l - A_g^l\bar{\phi}_g^l + \sum_{g'\neq g}^{G} Q_{gg'}^l\bar{\phi}_{g'}^l. \tag{7.2-26}$$

A similar substitution into the moment-weighted equation, Equation (7.2-19), yields the first and second moment constraints (2G equations/node) given by

$$\tag{7.2-27}$$

$$\left[\frac{140}{\Delta x^l}\frac{D_g^l}{\Delta x^l} + A_g^l\right]a_{gx4}^l - \sum_{g'\neq g}^{G} Q_{gg'}^l a_{g'x4}^l - 35 A_g^l a_{gx2}^l + 35\sum_{g'\neq g}^{G} Q_{gg'}^l a_{g'x2}^l = 35\left(\frac{1}{\Delta y^l}\rho_{gy2}^l + \frac{1}{\Delta z^l}\rho_{gz2}^l\right). \tag{7.2-28}$$

Similar equations can be written for node l + 1, producing a total of 6G equations. The continuity of net surface current constraints at the interface (G equations) are obtained by using Equation (7.2-25) at the adjoining interface of the two nodes. The result is

$$-\frac{D_g^l}{\Delta x^l}\left[a_{gx1}^l + 3a_{gx2}^l + \frac{a_{gx3}^l}{2} + \frac{a_{gx4}^l}{5}\right] = -\frac{D_g^l}{\Delta x^{l+1}}\left[a_{gx1}^{l+1} - 3a_{gx2}^{l+1} + \frac{a_{gx3}^{l+1}}{2} - \frac{a_{gx4}^{l+1}}{5}\right]. \tag{7.2-29}$$

Last, the continuity (or discontinuity) of surface-averaged flux constraints (G equations) are obtained by equating the surface-averaged fluxes of the two adjoining nodes by using Equation (7.2-15). The result is

$$d_{gx+}^l\left[\phi_g^l + \frac{a_{gx1}^l}{2} + \frac{a_{gx2}^l}{2}\right] = d_{gx-}^{l+1}\left[\phi_g^{l+1} - \frac{a_{gx1}^{l+1}}{2} + \frac{a_{gx2}^{l+1}}{2}\right] \tag{7.2-30}$$

where $d_{gx\pm}^l$ and $d_{gx\pm}^{l+1}$ are the Discontinuity Factors (DFs) obtained from lattice physics calculations. Do note that continuity conditions are never imposed on the outside surfaces of the two-node problem, since the two-node problem is deliberately formulated to be spatially decoupled. Continuity is assured in the formulation of the FDM based equations.

Equations (7.2-15) through (7.2-30) constitute the 8G system of equations needed to be solved at each interface. This matrix system, after taking advantage of its reducability and by noting that the even-moment expansion coefficients don't change whether the node is on the left or right of a two-node problem, can be reduced to smaller systems which can be solved quite efficiently[7.2-8]. Table 7.2-1 illustrates this more efficient arrangement of unknowns for the case of $G = 2$.

Table 7.2-1 Non Zero entries in the 16 by 16 two-node NEM Problem.

Eqn	Grp	Nod	a	b	c	d	e	f	g	h	i	j	k	l	m	n	o	p
0th Moment	1	l	x		x													
0th Moment	2	l		x		x												
2nd Moment	1	l	x	x	x	x												
2nd Moment	2	l	x	x	x	x												
0th Moment	1	l+1					x		x									
0th Moment	2	l+1						x		x								
2nd Moment	1	l+1					x	x	x	x								
2nd Moment	2	l+1					x	x	x	x								
1st Moment	1	l									x	x	x	x				
1st Moment	2	l									x	x	x	x				
1st Moment	1	l+1													x	x	x	x
1st Moment	2	l+1													x	x	x	x
Cur Con	1		x		x		x		x		x		x		x		x	
Cur Con	2			x		x		x		x		x		x		x		x
Fix Dis	1		x				x				x				x			
Fix Dis	2			x				x				x				x		

Unknown	Node	Group	Exp. Coef.*
a	l	1	2
b	l	2	2
c	l	1	4
d	l	2	4
e	l+1	1	2
f	l+1	2	2
g	l+1	1	4
h	l+1	2	4
i	l	1	1
j	l	2	1
k	l	1	3
l	l	2	3
m	l+1	1	1
n	l+1	2	1
o	l+1	1	3
p	l+1	2	3

* Refers to order of polynomial that transverse integrated flux expansion coefficient is associated with.

In ATHENA, the two-node problems are solved by utilizing the analytic solution to the 8G x 8G matrix system. This was accomplished by employing symbolic manipulator software to produce the FORTRAN code segment used in ATHENA. This approach is computationally more efficient than utilizing a direct matrix solver (e.g., LU decomposition); however, it limits the values of G to those directly programmed for. Also note that on boundaries special treatments of the two-node problems are required. Depending upon the specified boundary condition (BC), one-node problems may originate (e.g., zero flux BC), or on interior axis geometry unfolding may be required to create a two-node problem (e.g., cyclic BC).

Solutions of the two-node problems provide NEM evaluated values of the currents on all surfaces for specified values of the node average fluxes (recall they were assumed known in solving the two-node problems). To correct the FDM based expression for the surface current, the following approach is utilized. The coupling coefficient update to the FDM equation can be implemented by simply expressing the FDM net surface current at the *x+* face of node l as follows:

$$\bar{J}_{gx+}^{l,\,FDM} \;\; = \;\; -\frac{D_{gx+}^{l,\,FDM}}{\dfrac{\Delta x^{l} + \Delta x^{l+1}}{2}}(\bar{\phi}_{g}^{l+1} - \bar{\phi}_{g}^{l}) - \frac{\tilde{D}_{gx+}^{l,\,NEM}}{\dfrac{\Delta x^{l} + \Delta x^{l+1}}{2}}(\bar{\phi}_{g}^{l+1} + \bar{\phi}_{g}^{l}). \tag{7.2-31}$$

The first term on the RHS is the normal FDM approximation for a box scheme, where $D_{gx+}^{l,\,FDM}$ is the actual FDM diffusion coupling coefficient between nodes l and l+1. It is given by

$$D_{gx+}^{l,\,FDM} \;=\; \frac{D_{g}^{l}D_{g}^{l+1}(\Delta x^{l} + \Delta x^{l+1})}{D_{g}^{l}\Delta x^{l} + D_{g}^{l+1}\Delta x^{l+1}}. \tag{7.2-32}$$

The second term on the RHS represents the nonlinear NEM correction applied to the FDM scheme. The (+) sign between the flux values in the second term of Equation (7.2-31) is purposely there to improve the convergence behavior of the nonlinear iterative method[a]. Note that if $\tilde{D}_{gx+}^{l,\,NEM}$ is zero, which it initially is in ATHENA's implementation, then Equation (7.2-31) corresponds to the standard FDM definition of the net surface current. This is the basis for the FDM option within ATHENA, where now two-node problem solves and coupling coefficients updates are never completed. The value of $\tilde{D}_{gx+}^{l,\,NEM}$ is determined by setting Equation (7.2-31) equal to the NEM two-node predicted surface current value, using the associated node average flux values in Equation (7.2-31)and solving for this quantity.

Summarizing, to apply a NEM update after ΔN_0 outer iterations of the FDM routine, one solves the two-node problem at a given interface, then (with the expansion coefficients known for that interface) one calculates the NEM estimate of the net surface current using Equation (7.2-25). Finally, one equates this result to Equation (7.2-31), and solves for the value of $\tilde{D}_{gx+}^{l,\,NEM}$ which will be used in the subsequent set of FDM iterations.

7.2.2 Nodal Model - Hexagonal Geometry

The nodal method for the solution of the multi-group diffusion equations in hexagonal geometry is described in the following sections.

7.2.2.1 Steady State Eigenvalue Problem

Utilization of NEM for hexagonal (hex) geometry introduces several complications not encountered for Cartesian geometry, originating because the surfaces of the hex do not all align with the Cartesian axis. This can be seen in **Figure 7.2-1**. The axes are placed so that the positive x axis is perpendicular to one of the faces of the hexagonal node and proceeds to the right (East), and the positive y axis passes through the

---

a. Personal communication, G. H. Hobson to P. J. Turinsky, 1991.
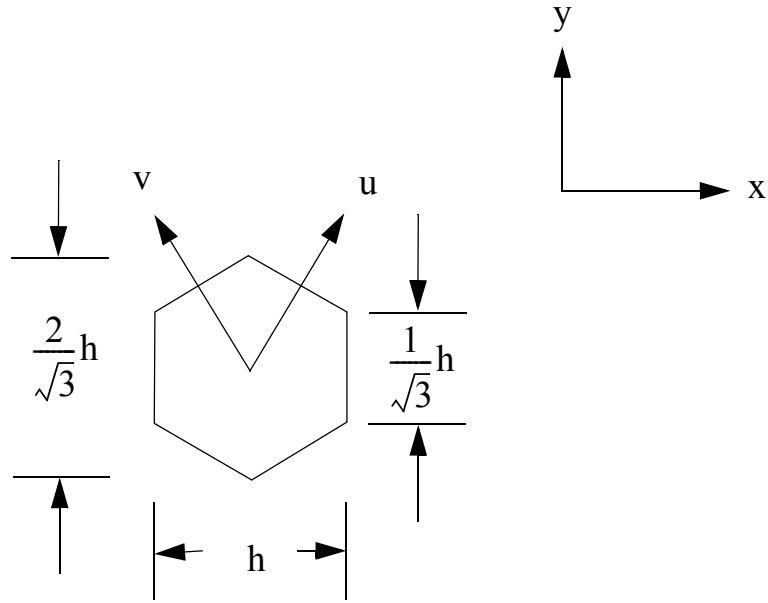
Figure 7.2-1 Hexagonal geometry dimensions and axis orientations

point of intersection of the next two adjacent faces of the hexagon when proceeding around the hexagonal node in the counterclockwise direction (North).

Lawrence addressed these difficulties in implementing the hex NEM option in DIF3D[7.2-9]. ATHENA utilizes this earlier work, now adapting it for implementation within the context of the non-linear iterative method which facilitates utilization of a higher order transverse leakage treatment.

The derivation of the governing equations for hex-Z geometry follows the same general approach as for Cartesian geometry. Introducing the transverse directions u and v noted in Figure 7.2-1, the nodal balance equation over a hex is given by

$$\left(\frac{2}{3h}\right)[\bar{L}^1_{g_x} + \bar{L}^1_{g_u} + \bar{L}^1_{g_v}] + \left(\frac{1}{\Delta z^1}\right)\bar{L}^1_{g_z} + A^1_g \bar{\phi}^1_g = \bar{Q}^1_g \qquad (7.2\text{-}33)$$

where the $\bar{L}$'s denote as before face-averaged net leakages. Let us first consider the radial plane. By transverse-integration of the diffusion equation over z and y, the one-dimensional balance equation in direction x is

$$\frac{dj_{g_x}^l}{dx} + A_g^l \phi_{g_x}^l(x) = Q_{g_x}^l(x) - \frac{2}{\sqrt{3}} j_{g_{xy}}(x,y) \Big|_{-y_s(x)}^{y_s(x)} - \int\limits_{-y_s(x)}^{y_s(x)} dy L_{g_z}^l(x,y)$$ (7.2-34)

where $\pm y_s(x)$ denote the upper and lower boundaries of the hex for a given x value; that is,

$$y_s(x) \equiv \frac{1}{\sqrt{3}}(h - |x|) \qquad \text{for } x \in \left[-\frac{h}{2}, \frac{h}{2}\right],$$ (7.2-35)

$j_{g_x}^l(x)$ denotes the transverse-integrated current in the x direction,

$$j_{g_x}^l(x) = \int\limits_{\frac{-\Delta z^l}{2}}^{\frac{\Delta z^l}{2}} dz \int\limits_{-y_s(x)}^{y_s(x)} dy - D_g^l \frac{\partial}{\partial x} \phi_g^l(x,y,z),$$ (7.2-36)

$j_{g_{xy}}^l(x, \pm y_s(x))$ denotes the z-integrated, surface-normal components of the net current across the u and v directed surfaces,

$$j_{g_{xy}}^l(x, \pm y_s(x)) = \mp \int\limits_{\frac{-\Delta z^l}{2}}^{\frac{\Delta z^l}{2}} dz D_g^l \hat{n}_\pm \cdot \vec{\nabla} \phi_g^l(x,y,z) \Big|_{\pm y_s(x)},$$ (7.2-37)

and $L_{g_z}^l(x,y)$ denotes axial leakage defined by

$$L_{g_z}^l(x,y) = -D_g^l \frac{\partial}{\partial z} \phi_g^l(x,y,z) \Big|_{\frac{-\Delta z^l}{2}}^{\frac{\Delta z^l}{2}}.$$ (7.2-38)

Two additional equations can be defined in a similar manner for the u and v directions. Note that these quantities are neither volume nor surface averaged, which differs from the earlier derivation for Cartesian coordinates. This difference arises since taking the derivation of the surface-averaged x-directed current appearing in Equation (7.2-34) would involve derivatives of $y_s(x)$, which introduces algebraic complexity as now discussed.

To solve Equation (7.2-34) using NEM the one-dimensional surface-averaged flux is expanded in terms of a polynomial expressed as indicated in Equation (7.2-15) with N = 4. The expansion functions $f_n(x)$ for n = 1 and 2 are selected as before, indicated in Equation (7.2-17). However, due to the behavior of $\phi_{g_x}(x)$ with x, the functions $f_n(x)$ for n = 3 and 4 must be selected differently for hexagonal geometry. To see this need, evaluate the transverse-integrated current in terms of the transverse-integrated flux, utilizing their definitions and Fick's Law to obtain

$$j_{g_x}^l(x) = -D_g^l \frac{d\phi_g^l}{dx} + D_g^l y'_s(x)[\phi_{g_{xy}}^l(x, y_s(x)) + \phi_{g_{xy}}^l(x, -y_s(x))] \tag{7.2-39}$$

where

$$\phi_{g_{xy}}^l(x, y) = \int_{\frac{-\Delta z^l}{2}}^{\frac{\Delta z^l}{2}} dz \phi_g^l(x, y, z). \tag{7.2-40}$$

Now

$$y_s'(x) = -\frac{1}{\sqrt{3}} \text{sign}(x) \tag{7.2-41}$$

is discontinuous at x = 0, the node's center-line perpendicular to the x-direction. Since the transverse-integrated current and flux must be continuous everywhere, Equation (7.2-39) implies that the first derivative of the transverse-integrated flux must be discontinuous at x = 0; in particular,

$$\lim_{\varepsilon \to 0} \left(-D_g^l \frac{d\phi_{g_x}^l}{dx} \right) \Bigg|_{-\varepsilon}^{\varepsilon} = \frac{2D_g^l}{\sqrt{3}}[\phi_g^l(x, y_s(x)) + \phi_g^l(x, -y_s(x))]. \tag{7.2-42}$$

To capture this discontinuity and satisfy Equations (7.2-16) and (7.2-18), the functions $f_n(x)$ for n = 3 and 4 are selected as follows:

$$\overbrace{\frac{10}{13}\left(\frac{x}{h}\right)^2 - \frac{1}{2}\left|\frac{x}{h}\right| + \frac{3}{52}}^{f_3} \qquad \overbrace{\left(\frac{x}{h}\right)\left(\left|\frac{x}{h}\right| - \frac{1}{2}\right)}^{f_4}. \tag{7.2-43}$$

We again have a problem with five unknowns per node and group. Continuity of transverse-integrated current, discontinuity of surface-averaged flux, and the nodal balance equation provide three of the required five equations. The jump discontinuity condition given by Equation (7.2-42) provides an additional equation, which can be shown to produce[7.2-9]

$$(7.2\text{-}44)$$

where

$$E_{g_x}^l(x) \ = \ \phi_g^l(x, y_s(x)) + \phi_g^l(x, -y_s(x)) - 2\bar{\phi}_{g_x}^l(x) . \qquad (7.2\text{-}45)$$

Assuming expressions for $\phi_g^l(x, \pm y_s(s))$ in terms of node average flux and expansion coefficients can be obtained, one then has five unknowns and four equations implying one additional equation is required. This is provided by a Weighted Residual Method, where the weight $\omega_1(x)$ is defined as

$$\omega_1(x) \ = \ \text{sign}(x) . \qquad (7.2\text{-}46)$$

Using this weight in a Weighted Residual Method in conjunction with the nodal balance equation can be shown equivalent to preserving half-node nodal balance on each half of the hexagonal node. The Weighted Residual Method equation that results is

$$\left[A_g^l + 32\frac{D_g^l}{h^2} \right]\bar{\phi}_{g_{x1}}^l \ = \ \bar{Q}_{g_{x1}}^l - \frac{2}{3h}[\bar{T}_{gx}^l + \bar{T}_{gu}^l - \bar{T}_{gv}^l] - \frac{1}{\Delta z^l}\bar{L}_{g_{zx1}}^l + \frac{40}{9}\frac{D_g^l}{h^2}a_{g_{x1}}^l \qquad (7.2\text{-}47)$$

where the following definitions have been introduced

$$
\overset{\displaystyle \bar{\phi}_{g_{x1}}^l}{\overbrace{\frac{1}{\Delta V^l}\langle \omega_1(x), \phi_{g_x}^l(x)\rangle}} \qquad
\overset{\displaystyle \bar{Q}_{g_{x1}}^l}{\overbrace{\frac{1}{\Delta V^l}\langle \omega_1(x), Q_{g_x}^l(x)\rangle}} \qquad
\overset{\displaystyle \bar{L}_{g_{zx1}}^l}{\overbrace{\frac{\Delta z^l}{\Delta V^l}\langle \omega_1(x), \int\limits_{-y_s(x)}^{y_s(x)} dy L_{g_z}^l(x, y)\rangle}} \qquad (7.2\text{-}48)
$$

$$\overline{T}^1_{g_u} = \frac{\sqrt{3}h}{\Delta V^1}\langle \omega_1(x), j^1_{g_{xy}}(x,y)|^{y_s(x)}_{-y_s(x)}[u \text{ directed component}]\rangle$$

$$= \left(\frac{1}{\Delta z^1 \cdot \frac{h}{2}}\right)\left[\int_{-h/2}^{0} dx j^1_{g_{xy}}(x,-y_s(x)) + \int_{0}^{h/2} dx j^1_{g_{xy}}(x,y_s(x))\right]\text{Substitution} \quad \text{of} \quad \text{the} \quad \text{polynomial}$$

$$= j^{:1}_{gu}\left(-\frac{h}{2}\right) + j^{:1}_{gu}\left(-\frac{h}{2}\right) \quad .$$

expansion for the transverse integrated flux into Equation (7.2-48) gives $\overline{\phi}^1_{gx1}$ and $\overline{Q}^1_{gx1}$ in terms of the expansion coefficients.

To solve the above equations, we require expressions for $E^1_{gx}(0)$ and $\overline{L}^1_{gzx1}$ in terms of the node average flux and expansion coefficients. As with Cartesian geometry, the transverse leakage in the z-direction will be approximated by a quadratic polynomial. Specifically, following Equation (7.2-21) one makes the following approximation:

$$\overline{L}_{gz}(x) = \frac{1}{2y_s(x)}\int_{-y_s(x)}^{y_s(x)} dy L^1_{gz}(x,y) = \overline{L}^1_{gzx} + \rho^1_{gzx1}f_1(x) + \rho^1_{gzx2}f_2(x) \tag{7.2-49}$$

where $f_1(x)$ and $f_2(x)$ are defined as previously for Cartesian geometry.

To obtain the expression for $E^1_{gx}(0)$ it can be shown that via a Taylor series expansion about $y = 0$ that

$$E^1_{gx}(x) = -\frac{1}{6D^1_g}[2y_s(x)]^2 L^1_{gy}(x) + 0(h^4) \tag{7.2-50}$$

where the y-directed leakage is defined as

$$L^1_{gy}(x) = \frac{1}{2y_s(x)}\left[-D^1_g\frac{\partial}{\partial y}\phi^1_{g_{xy}}(x,y)\right]\Bigg|_{-y_s(x)}^{y_s(x)} . \tag{7.2-51}$$

Using the "two-step" approximation (i.e., assuming constant transverse leakage over each half-node) produces

$$L^1_{gy}(x) = \begin{cases} L^1_{gy-} & \text{for } x \in [-h/2, 0) \\ L^1_{gy+} & \text{for } x \in (0, h/2] \end{cases}$$
(7.2-52)

where

$$L^1_{gy-} = \frac{2}{V^1} \int_{-h/2}^{0} dx - D^1_g \frac{\partial}{\partial y} \phi^1_{gxy}(x, y)\Big|_{-y_s(x)}^{y_s(x)}$$
(7.2-53)

and

$$L^1_{gy+} = \frac{2}{V^1} \int_{0}^{h/2} dx - D^1_g \frac{\partial}{\partial y} \phi^1_{gxy}(x, y)\Big|_{-y_s(x)}^{y_s(x)}.$$
(7.2-54)

Using this approximation and ignoring the $0(h^4)$ term in Equation (7.2-50) gives

$$E^1_{gx}(0) = \frac{1}{2}[E^1_{gx}(0^-) + E^1_{gx}(0^+)]$$
(7.2-55)

$$E^1_{gx}(0) = \frac{-h^2}{9D^1_g}[L^1_{gy-} + L^1_{gy+}].$$
(7.2-56)

To complete the evaluation, expressions for L^1_{gy-} and L^1_{gy+} in terms of node average flux and expansion coefficients must be determined. This is done via manipulation of previously introduced equations and definitions resulting in the following expression, recalling Equation (7.2-44):

$$a^1_{gx3} = E^1_{gx}(0) = -\frac{26}{189}\frac{h}{D^1_g}[\bar{L}^1_{gu} + \bar{L}^1_{gv}] - \frac{8}{21}[\bar{\phi}^1_{g_x}(h/2) + \bar{\phi}^1_{g_x}(-h/2) - 2\bar{\phi}^1_g].$$
(7.2-57)

Since the transverse integrated flux is a function of node average flux and expansion coefficients, Equation (7.2-57) involves only the unknowns being sought except for the leakage terms.

To complete the formulation of the hexagonal problem, from Equation (7.2-39) one recognizes that expressions for $\phi^1_{g_x}(x, \pm y_s(x))$ at $x = \pm h/2$ in terms of the working unknowns is required to evaluate the surface currents. From Equation (7.2-39) the expression for the face-averaged transverse-integrated current can be obtained. It is given by

$$\overset{:1}{j}_{gx} = -D_g^l \frac{d}{dx} \overline{\phi}_{gx}^1(x) + D_g^l \frac{y_s'(x)}{2y_s(x)} E_{gx}^1(x). \tag{7.2-58}$$

Again an expression for $E_{gx}^1(x)$ in terms of the working unknowns is required, this time evaluated at $x = \pm \frac{h}{2}$. Using the "two-step" approximation produces

$$\tag{7.2-59}$$

and substituting in the expression for $L_{gy\pm}^1$ gives

$$E_{gx}^1\left(\frac{h}{2}\right) = -\frac{1}{285}\frac{h}{D_g^l}\left\{17\left[\overset{:1}{j}_{gu}\left(\frac{h}{2}\right) - \overset{:1}{j}_{gv}\left(-\frac{h}{2}\right)\right] + 2\left[\overset{:1}{j}_{gv}\left(\frac{h}{2}\right) - \overset{:1}{j}_{gu}\left(-\frac{h}{2}\right)\right]\right\}$$
$$-\frac{1}{1,235}\left[179\overline{\phi}_{gx}^1\left(\frac{h}{2}\right) + 49\overline{\phi}_{gx}^1\left(-\frac{h}{2}\right) - 228\overline{\phi}_g^1\right] + \frac{1}{130}a_{gx3}^1 \tag{7.2-60}$$

$$E_{gx}^1\left(-\frac{h}{2}\right) = -\frac{1}{285}\frac{h}{D_g^l}\left\{2\left[\overset{:1}{j}_{gu}\left(\frac{h}{2}\right) - \overset{:1}{j}_{gv}\left(-\frac{h}{2}\right)\right] + 17\left[\overset{:1}{j}_{gv}\left(\frac{h}{2}\right) - \overset{:1}{j}_{gu}\left(-\frac{h}{2}\right)\right]\right\}$$
$$-\frac{1}{1,235}\left[49\overline{\phi}_{gx}^1\left(\frac{h}{2}\right) + 179\overline{\phi}_{gx}^1\left(-\frac{h}{2}\right) - 228\overline{\phi}_g^1\right] + \frac{1}{130}a_{gx3}^1 \ . \tag{7.2-61}$$

By combining Equation (7.2-58) and either Equation (7.2-60) or (7.2-61) we obtain an expression for the surface-averaged transverse current in one direction in terms of currents in the other hex directions. This does not succeed in eliminating current as an unknown as we desire. This can be addressed as follows:

Since $E_{gx}^1(x)$ at $x = \pm \frac{h}{2}$ are truly continuous since the fluxes defining it via Equation (7.2-45) are continuous, and the surface averaged transverse-integrated current is continuous everywhere, Equation (7.2-58) implies that the flux derivative appearing in this equation must be discontinuous at $x = \pm \frac{h}{2}$. Employing the above noted properties, the current continuity condition produces

$$\overset{:1}{j}_{gx}\left(\frac{h}{2}\right) = -\frac{D_g^l D_g^{l+1}}{D_g^l + D_g^{l+1}}\left[\frac{d\overline{\phi}_g^1}{dx}\bigg|_{h/2} + \frac{d\overline{\phi}_g^{l+1}}{dx}\bigg|_{-h/2}\right]. \tag{7.2-62}$$

This expression for current is in terms of the expansion coefficients as desired.

Utilizing Equations (7.2-33), (7.2-47), (7.2-57), and (7.2-58) through (7.2-61) in the surface-averaged current continuity equation, surface-averaged flux discontinuity equation, and various auxiliary equations relating currents and leakages to flux, we arrive at 13 equations for the 13 unknowns per node per energy groups when considering the x, u, and v directions. Deferring the two-node problem formulation, the z-direction transverse integrated equations will be now developed.

The z-direction transverse integrated equations development follows that for Cartesian geometry except for the transverse leakage terms in the radial plane. The transverse balance equation is given by

$$\frac{d}{dz}\bar{j}_{gz}^1(z) + A_g^1\bar{\phi}_{gz}^1(z) = \bar{Q}_{gz}^1(z) - \frac{\Delta z^1}{V^1}L_{gxy}^1(z) \tag{7.2-63}$$

where the radial plane transverse leakage is defined as

$$L_{gxy}^1(z) = \int_{-\frac{h}{2}}^{\frac{h}{2}} dx \int_{-y_s(x)}^{y_s(x)} dy\left[\frac{\partial}{\partial x}\bar{j}_{gx}^1(x, y, z) + \frac{\partial}{\partial y}\bar{j}_{gy}^1(x, y, z)\right]. \tag{7.2-64}$$

This equation is solved assuming a quartic expansion for the transverse integrated flux as used in Cartesian geometry. The nodal balance [Equation (7.2-33)], first and second moment Weighted Residual, surface-averaged flux discontinuity, and surface-averaged current continuity equations provide the required number of equations.

The moments of the radial plane transverse leakage that enter the Weighted Residual equations are evaluated utilizing the quadratic approximation to obtain the within node shape; that is,

$$\bar{L}_{gxy}^1(z) \cong \bar{L}_{gxy}^1 + \rho_{gxy1}^1 f_1(z) + \rho_{gxyz}^1 f_2(z) \tag{7.2-65}$$

where

$$\bar{L}_{gxy}^1 = \frac{3h}{2}\frac{1}{V^1}\int_{\frac{-\Delta z^1}{2}}^{\frac{\Delta z^1}{2}} dzL_{gxy}^1(z) \tag{7.2-66}$$

and hence

$$\bar{L}^l_{gxy} = \bar{L}^l_{gx} + \bar{L}^l_{gu} + \bar{L}^l_{gv} .$$ (7.2-67)

The expansion coefficients in Equation (7.2-65) are defined as before [see Equations (7.2-22)-(7.2-24)]. Since the derivation of the Weighted Balance equations is identical to that presented for Cartesian geometry except as noted above in regard to transverse leakages, the interested reader is referred to the earlier presentation.

7.2.2.2 Non-Linear Iterative Strategy

For hex-Z geometry, the non-linear iterative strategy is applied the same as for Cartesian geometry. For each surface of a node, a two-node problem is solved to obtain the NEM predicted surface-averaged current based upon the FDM flux solution utilizing corrected coupling coefficients. The corrected coupling coefficients are determined demanding that the FDM and NEM predicted currents agree. In the radial plane for hexagonal geometry, Equation (7.2-32) is modified to read as

$$D^{l,\,FDM}_{gx+} = \frac{2D^l_g D^{l+1}_g}{D^l_g + D^{l+1}_g} .$$ (7.2-68)

Hex Directions (Example - x direction):

Flux Discontinuity,

$$d^l_{gx+}\ (a^l_{gx1} + a^l_{gx2}) + d^{l+1}_{gx-}\ (a^{l+1}_{gx1} - a^{l+1}_{gx2}) = 2(d^{l+1}_{gx-}\ \phi^{l+1}_g - d^l_{gx+}\ \phi^l_g) ;$$ (7.2-69)

Current Continuity,

$$
\begin{aligned}
&-D^l_g \Bigg[\left(\frac{234}{247}\right) a^l_{gx1} + \left(\frac{3306}{1235}\right) a^l_{gx2} + \left(\frac{18}{65}\right) a^l_{gx3} + \left(\frac{1}{2}\right) a^l_{gx4} \Bigg] \\
&+ D^{l+1}_g \Bigg[\left(\frac{234}{247}\right) a^{l+1}_{gx1} - \left(\frac{3306}{1235}\right) a^{l+1}_{gx2} - \left(\frac{18}{65}\right) a^{l+1}_{gx3} + \left(\frac{1}{2}\right) a^{l+1}_{gx4} \Bigg] = \\
&- \left(\frac{h}{285}\right) \Big\{ 17 \Big[\overset{:}{j}{}^l_{gv}\!\left(\frac{h}{2}\right) - \overset{:}{j}{}^l_{gu}\!\left(-\frac{h}{2}\right) + \overset{:}{j}{}^{l+1}_{gu}\!\left(\frac{h}{2}\right) - \overset{:}{j}{}^{l+1}_{gv}\!\left(-\frac{h}{2}\right) \Big] \\
&\qquad + 2\Big[\overset{:}{j}{}^l_{gu}\!\left(\frac{h}{2}\right) - \overset{:}{j}{}^l_{gv}\!\left(-\frac{h}{2}\right) + \overset{:}{j}{}^{l+1}_{gv}\!\left(\frac{h}{2}\right) - \overset{:}{j}{}^{l+1}_{gu}\!\left(-\frac{h}{2}\right) \Big] \Big\};
\end{aligned}
$$ (7.2-70)

Center Node Jump Condition,

$$\left(\frac{8}{21}\right)a^l_{gx2} + a^l_{gx3} = -\left(\frac{26}{189}\right)\left(\frac{h}{D^l_g}\right)(\bar{L}^l_{gu} + \bar{L}^l_{gv}) ;$$

(7.2-71)

Nodal Balance,

(7.2-72)

Odd Moment Balance,

$$\left[\left(\frac{2}{9}\right)A^l_g + \left(\frac{240}{171}\right)\left(\frac{D^l_g}{h}\right)\left(\frac{1}{h}\right)\right]a^l_{gx1} - \left[\left(\frac{1}{24}\right)A^l_g + 2\left(\frac{D^l_g}{h}\right)\left(\frac{1}{h}\right)\right]a^l_{gx4}$$

$$. \qquad -\sum_{g' \neq g}^{G} Q^l_{gg'}\left[\left(\frac{2}{9}\right)a^l_{g'x1} - \left(\frac{1}{24}\right)a^l_{g'x4}\right] =$$

(7.2-73)

$$-\left(\frac{2}{9}\right)\left(\frac{1}{\Delta z^l}\right)\rho^l_{gz1} - \left(\frac{2}{3h}\right)\left(\frac{20}{19}\right)[\bar{T}^l_{gv} - \bar{T}^l_{gu}] .$$

These equations are supplemented by the following auxiliary equation obtained from Equation (7.2-62),

$$j^{:l}_{gx}\left(\frac{h}{2}\right) = -\left(\frac{D^l_g D^{l+1}_g}{D^l_g + D^{l+1}_g}\right)\left(\frac{1}{h}\right)\left[(a^l_{gx1} + a^l_{gx2}) + \left(\frac{36}{13}\right)(a^l_{gx2} - a^{l+1}_{gx2})\right] +$$

$$. \qquad\qquad\qquad\qquad\qquad\qquad\qquad\qquad\qquad\qquad\qquad . $$

(7.2-74)

$$\left(\frac{7}{26}\right)(a^l_{gx3} - a^{l+1}_{gx3}) + \left(\frac{1}{4}\right)(a^l_{gx4} + 3a^{l+1}_{gx4}).$$

Do note that for the u and v directions, the following mappings of surface currents occur, which impacts the signs of the leakage terms on the RHS of the current continuity and odd moment balance equations:

u direction: $x \rightarrow u, v \rightarrow -x, u \rightarrow -v$

v direction: $x \rightarrow v, u \rightarrow -x, v \rightarrow u$

(7.2-75)

Axial Direction:

Flux Discontinuity,

$$d^l_{gz+} [a^l_{gz1} + a^l_{gz2}] + d^{l+1}_{gz-} [a^{l+1}_{gz1} - a^{l+1}_{gz2}] = 2[d^{l+1}_{gz-} \bar{\phi}^{l+1}_g - d^l_{gz+} \bar{\phi}^l_g];$$

(7.2-76)

Current Continuity,

$$(7.2\text{-}77)$$

Nodal Balance,

$$-\left(\frac{D_g^l}{\Delta z^l}\right)\left(\frac{1}{\Delta z^l}\right)\left[6a_{gz2}^l + \left(\frac{2}{5}\right)a_{gz4}^l\right] = -\left(\frac{2}{3h}\right)(\overline{L}_{gx}^l + \overline{L}_{gu}^l + \overline{L}_{gv}^l) - A_g^l\overline{\phi}_g^l + \sum_{g'\neq g}^G Q_{gg'}^l\overline{\phi}_{g'}^l; \qquad (7.2\text{-}78)$$

First Moment,

$$\left[\left(\frac{60}{\Delta z^l}\right)\left(\frac{D_g^l}{\Delta z^l}\right) + A_g^l\right]a_{gz3}^l - \sum_{g'\neq g}^G Q_{gg'}^l a_{g'z3}^l - 10A_g^l a_{gz1}^l + 10\sum_{g'\neq g}^G Q_{gg'}^l a_{g'z1}^l = 10\left(\frac{2}{3h}\right)\rho_{gxy1}^l; \qquad (7.2\text{-}79)$$

Second Moment,

$$\left[\left(\frac{140}{\Delta z^l}\right)\left(\frac{D_g^l}{\Delta z^l}\right) + A_g^l\right]a_{gz4}^l - \sum_{g'\neq g}^G Q_{gg'}^l a_{g'z4}^l - 35A_g^l a_{gz2}^l + 35\sum_{g'\neq g}^G Q_{gg'}^l a_{g'z2}^l = 35\left(\frac{2}{3h}\right)\rho_{gxy2}^l. \qquad (7.2\text{-}80)$$

For the z-direction, the same matrix structure as for Cartesian geometry results allowing rearrangement of the associated two-node problem coefficient matrix to achieve reducibility. For the x, u, and v-directions, the two-node problem for two groups can be reduced from a 16 x 16 matrix problem to four 2 x 2 matrix problems and one 8 x 8 matrix problem. For four groups the 32 x 32 matrix problem can be reduced to eight 2 x 2 matrix problems and one 16 x 16 matrix problem. The associated matrix problems are solved analytically to reduce floating point operations required. Having solved the two-node problems, the corrections to the coupling coefficients can be obtained as previously indicated in Equation (7.2-31).

7.2.3 Outer-Inner Solution Method for FDM Equations

The only large matrix that requires solution for the non-linear iterative method is the FDM representation of the multi-group diffusion equation. Much work has been done on formulating, understanding and implementing the iterative solution of this large, sparse matrix system. ATHAENA takes advantage of this wealth of knowledge in its iterative solution implementation, utilizing an outer-inner iterative strategy.

The "Outer-Inner Method" refers to outer iterations to update the fission source term and inner iteration to approximately solve the resulting fixed source problem. The outer iterations correspond to a

"Power Method." This method can be applied to both Fixed Source Problems (FSP) and the Associated Eigenvalue Problem (AEVP). Shortly it will be shown that both the fixed source steady-state and transient problems are representable as FSP in ATHENA's formulation. Although the AEVP involves additional calculations for the eigenvalue, basically the iteration schemes for both problems are similar. We will discuss the AEVP first.

Returning to Equation (7.2-8), the FDM representation of this equation in three-dimensional Cartesian geometry within homogenous mode l can be expressed as

$$\sum_{l'=1}^{L} C_g^{l,l'} \overline{\phi}_g^{l'} + A_g^l \overline{\phi}_g^l = \overline{Q}_g^l \tag{7.2-81}$$

where the non-zero values of the coupling coefficients $\{C_g^{l,l'}\}$ are obtained via Equations (7.2-31) and (7.2-32) and L denotes the total number of nodes. Substituting in the definitions for A_g^l and $\overline{Q}_g^l$ into Equation (7.2-81) and rearranging terms we obtain

$$\sum_{l'\neq l}^{L} C_g^{l,l'} \overline{\phi}_g^{l'} + (\Sigma_{t_g}^l - \Sigma_{s_{gg}}^l + C_g^{l,l})\overline{\phi}_g^l - \sum_{g'\neq g}^{G} \Sigma_{s_{gg'}}^l \overline{\phi}_{g'}^l = \frac{x_g^l}{k}\sum_{g'=1}^{G} \upsilon_{g'}\Sigma_{fg'}^l \overline{\phi}_{g'}^l . \tag{7.2-82}$$

This equation can be written in terms of matrix notation spanning the spatial domain as

$$\overline{\overline{A}}_g \overline{\phi}_g - \sum_{g'\neq g}^{G} \overline{\overline{\Sigma}}_{s_{gg'}} \overline{\phi}_{g'} = \frac{1}{k}\overline{\overline{x}}_g \sum_{g'=1}^{G} \overline{\overline{\upsilon_{g'}\Sigma_{fg'}^l}} \overline{\phi}_{g'} \tag{7.2-83}$$

where the "bar" over the node average flux value now denotes a column vector. Matrix $\overline{\overline{A}}_g$ has a seven-banded matrix structure for three-dimensional Cartesian geometry. In turn, the G (L x L) matrix systems expressed by Equation (7.2-83) can be collected to write the following single (GL x GL) matrix system

$$\overline{\overline{A}}\overline{\phi} = \frac{1}{k}\overline{\overline{F}}\overline{\phi}. \tag{7.2-84}$$

The matrix $\overline{\overline{A}}$ is block lower triangular in structure for that portion applicable to the fast groups.

The outer-inner iteration process is summarized as follows: For the AEVP specified by Equation (7.2-84), given an arbitrary initial vector $\bar{\phi}^{(0)}$, the outer iterations generate successive estimates for the flux vector $\bar{\phi}$ by the process

$$\bar{\phi}^{(q)} = \frac{1}{k^{(q-1)}} \bar{\bar{A}}^{-1} (\bar{\bar{F}} \bar{\phi}^{q-1}) \tag{7.2-85}$$

where how the criticality constant (i.e., eigenvalue) is updated will be discussed later. The iterative matrix associated with the outer iterations is

$$\bar{\bar{Q}} = \bar{\bar{A}}^{-1} \bar{\bar{F}}. \tag{7.2-86}$$

The properties of the iterative matrix $\bar{\bar{Q}}$ has a significant role in determining the convergence rate of the power iterations[7.2-10,7.2-11].

In solving Equation (7.2-85), advantage is taken of the structure of the $\bar{\bar{A}}$ matrix. For the fast groups, solving from low to high energy group number results in energy group decoupling. This implies that we may solve a system of linear equations of the form

$$\bar{\bar{A}}_g \bar{\phi}_g^{(q)} = \bar{S}_g^{(q)} \tag{7.2-87}$$

where

$$\bar{S}_g^{(q)} = \sum_{g' \neq g}^{G} \bar{\bar{\Sigma}}_{sgg'} \bar{\phi}_{g'}^{(q)} + \frac{1}{k^{(q-1)}} \bar{\bar{\chi}}_g \sum_{g'=1}^{G} \overline{\overline{\nu_{g'} \Sigma_{fg'}}} \bar{\phi}_{g'}^{(q-1)}. \tag{7.2-88}$$

For the thermal groups, ATHENA assumes the group fluxes for all other thermal groups except the one being updated are known. This produces energy group decoupling, allowing Equation (7.2-87) to be utilized. So called "scattering" iterations are then completed after all thermal groups' fluxes are updated. Stationary acceleration is employed to accelerate convergence of the scattering iterations.

7.2.3.1 Inner Iteration Acceleration

To solve Equation (7.2-87) we introduce the inner iterations. In this work we employ a Multi-Color Point or Line SOR Method, depending upon problem geometry, for the inner iterations. Specifically, a Red-Black Point or Line SOR method is used in ATHENA for two or three-dimensional Cartesian

geometry, respectively. For one-dimensional Cartesian geometry, a direct matrix solve is utilized since the group-wise A matrix is triangular allowing employment of Gaussian elimination.

Mathematically, this approach is a multi-splitting method and can be expressed as

$$\bar{\phi} = \oplus \bar{\phi}_p \tag{7.2-89}$$

where $\bar{\phi}_p$ vector spans nodes of color "p",

$$\bar{\phi}_p^{(m+1)} = \bar{\bar{B}}_p^{-1}\left[\bar{S} + \sum_{p'=1}^{p-1}\bar{\bar{C}}_{pp'}\bar{\phi}_{p'}^{(m+1)} + \sum_{p'=p+1}^{P}\bar{\bar{C}}_{pp'}\bar{\phi}_{p'}^{(m)}\right] \qquad \text{for} \qquad p = 1, 2, ..., P \tag{7.2-90}$$

where

$$\bar{\bar{A}} = \otimes \bar{\bar{A}}_p \tag{7.2-91}$$

and non-square matrix $\bar{\bar{A}}_p$ equals rows of $\bar{\bar{A}}$ that span nodes of color "p",

$$\bar{\bar{A}}_p = \bar{\bar{B}}_p - \sum_{p'\neq p}^{P}\bar{\bar{C}}_{pp'} \qquad \text{for} \qquad p = 1, 2, ..., P, \tag{7.2-92}$$

and

$$\bar{\phi}_p^{(m+1)} = \bar{\phi}_p^{(m)} + \omega(\bar{\phi}_p^{(m+1)} - \bar{\phi}_p^{(m)}). \tag{7.2-93}$$

Note that the group g and outer iteration count (q) indices have been suppressed for clarity in the above equations. The matrix $\bar{\bar{B}}_p$ is square and has either a diagonal structure for the point scheme or block diagonal structure composed of tridiagonal blocks for the line scheme. This implies that the action of $\bar{\bar{B}}_p^{-1}$ indicated in Equations (7.2-90) is simple to evaluate. A total of ΔN_I inner iterations per outer iterations are completed, this value determined such that the specified relative error reduction from the 0th iterative error for the inner iterations is achieved.

To a priori determine the value of the optimum relaxation parameter, ω and ΔN_I [which are energy group dependent but dependence notation has been suppressed], it is assumed that the iterative matrix associated with this inner iterative method is symmetrizable. This is not true since the NEM corrections to the FDM coupling coefficients invalidate symmetry; however, these corrections have been found to be relatively small so the symmetrizable assumption is acceptable. Making this assumption, we can express ω in terms of the spectral radius of the associated Gauss-Seidel iteration matrix, $\rho(\overline{\overline{L}}^{\text{G-S}})$, as

$$\omega = \frac{2}{1 + [1 - \rho(L^{\text{G-S}})]^{1/2}} .$$

(7.2-94)

Clearly $\overline{\overline{L}}^{\text{G-S}} = \overline{\overline{L}}^{\text{SOR}}(\omega)$ with $\omega = 1$. Therefore, calculation of the spectral radius of the associated Gauss-Seidel iterative matrix is the heart of this procedure. The following summarizes the details of the computational procedure used in ATHENA to obtain an estimate of the value of ω, which is based upon the DIF3D methodology[7.2-11]. The following steps are completed for each energy group:

Step 1.

Starting with an arbitrary non-negative initial guess vector $\overline{x}^{(0)}$, complete at least ten Gauss-Seidel iterations in solving

$$\overline{\overline{A}}\overline{x} = \overline{0} .$$

(7.2-95)

Step 2.

Following each iteration with m >10, estimate the upper and lower bounds of the spectral radii using

$$\lambda^{(m)} \equiv \frac{\left\langle \overline{x}^{(m)}, \overline{x}^{(m)} \right\rangle}{\left\langle \overline{x}^{(m)}, \overline{x}^{(m-1)} \right\rangle}$$

(7.2-96)

$$\overline{\lambda}^{(m)} \equiv \max_i \left| \frac{x_i^{(m)}}{x_i^{(m-1)}} \right|$$

(7.2-97)

$$\underline{\lambda}^{(m)} \equiv \min_i \left| \frac{x_i^{(m)}}{x_i^{(m-1)}} \right| .$$

(7.2-98)

Compute the corresponding relaxation factors given by

$$(7.2\text{-}99)$$

$$\bar{\omega}^{(m)} \equiv \frac{2}{1 + [1 - \bar{\lambda}^{(m)}]^{1/2}} \qquad (7.2\text{-}100)$$

$$\underline{\omega}^{(m)} \equiv \frac{2}{1 + [1 - \underline{\lambda}^{(m)}]^{1/2}} . \qquad (7.2\text{-}101)$$

Step 3.

  Terminate iteration when either

$$\left| \bar{\omega}^{(m)} - \underline{\omega}^{(m)} \right| < \frac{2 - \omega^{(m)}}{5} \qquad (7.2\text{-}102)$$

or m equals a specified upper limit[7.2-11,7.2-12]. The optimum factor ω is then set to $\omega^{(m)}$. This test forces tighter convergence of ω when $\rho(L^{\text{G-S}})$ is close to unity to ensure the required numerical accuracy is achieved.

Step 4.

  Determine the number of inner iterations required for each outer iteration ΔN_I, such that the value of ΔN_I satisfies the following equation:

$$\left\| (\bar{\bar{L}}^{\text{SOR}}(\omega))^{\Delta N_{I-1}} \cdot \bar{\bar{L}}^{\text{G-S}} \right\| = [t^2_{2\Delta N_I - 1} + t^2_{2\Delta N_I}]^{\frac{1}{2}} \leq \varepsilon_{\text{in}} \qquad (7.2\text{-}103)$$

where

$$t_{\Delta N_I} = [\omega - 1]^{\frac{\Delta N_I - 1}{2}} [\rho(\bar{\bar{L}}^{\text{G-S}})]^{\frac{1}{2}} \left[1 + (\Delta N_I - 1)(1 - \rho(\bar{\bar{L}}^{\text{G-S}}))^{\frac{1}{2}} \right] \qquad (7.2\text{-}104)$$

and ε_{in} denotes the desired relative error reduction from the initial iteration to the end of ΔN_I-th iteration. It is suggested that a very small number for ε_{in} not be used since it may force excessive inner iterations[7.2-11].

The advantages of these accelerations strategies are clear. The automated determination of the optimum overrelaxation factors relieves users of the burden of the trial and error manner of specifying optimum parameters for a large class of reactor models. In addition, substantial computational time can be saved since the need to check the convergence of inner iterations has been removed by using a fixed number of predetermined inner iterations for each energy group.

The outer iterations defined by Equation (7.2-85) are slow to converge, since the dominance ratio of the iterative matrix, Equation (7.2-86), is close to one. Two complementary acceleration techniques are utilized in ATHENANA to accelerate the outer iterations of the AEVP.

7.2.3.2 Outer Iteration Acceleration

The outer iterations for the AEVP are accelerated by using linear combinations of the previous iterative vectors as now described. The Chebyshev polynomials are used to obtain the best linear combinations when there is no knowledge of higher eigenvalues[7.2-13]. The method implemented is the Chebyshev Semi-Iterative method[7.2-10,7.2-11,7.2-12,7.2-14]. In this method, the error vector associated with the acceleration method is expressed in terms of a linear combination of the error vectors of the underlying interactive method. Acceleration of the iteration is achieved by minimizing the error vector by appropriate selection of the expansion coefficients, which is determined to be those associated with Chebyshev polynomials. Further details of the mathematical background of this method can be found in the related references[7.2-10,7.2-11].

Since the rate of convergence in the AEVP is dependent on the dominance ratio $\sigma(\overline{\overline{Q}})$, the Chebyshev acceleration method[7.2-10,7.2-11,7.2-12,7.2-14] can therefore be applied to iterations. It is given by

$$\bar{\phi}^{(q)} = \frac{1}{k^{(q-1)}} \overline{\overline{Q}} \bar{\phi}^{(q-1)} \tag{7.2-105}$$

provided that a suitable estimate of $\sigma(\overline{\overline{Q}})$ is obtained. ATHENA follows the DIF3D approach to solve the AEVP in which we accelerate the fission source $\overline{\Psi}$[7.2-14], where $\overline{\Psi}$ is defined as

$$\overline{\Psi} = \sum_{g'=1}^{G} \overline{\overline{v_{g'}\Sigma_{fg'}}} \bar{\phi}_{g'} = \overline{\overline{v\Sigma_f}} \bar{\phi} . \tag{7.2-106}$$

The accelerated iterative procedure can then be expressed as

$$\tag{7.2-107}$$

where

$$\bar{\bar{Q}} = \overline{\overline{\nu\Sigma_f}}(\bar{\bar{A}})^{-1}\bar{\bar{\chi}} \qquad\qquad (7.2\text{-}108)$$

$$\overline{\tilde{\Psi}}^{n^*+p} = \overline{\tilde{\Psi}}^{(n^*+p-1)} + \alpha_p\left[\overline{\Psi}^{(n^*+p)} - \overline{\tilde{\Psi}}^{(n^*+p-1)}\right] + \beta_p\left[\overline{\tilde{\Psi}}^{(n^*+p-1)} - \overline{\tilde{\Psi}}^{(n^*+p-2)}\right] \qquad (7.2\text{-}109)$$

$$k^{(n^*+p)} = k^{(n^*+p-1)}\left(\frac{\left\|\overline{\Psi}^{(n^*+p)}\right\|_2^2}{(\overline{\Psi}^{(n^*+p)}, \overline{\tilde{\Psi}}^{(n^*+p-1)})}\right) \qquad (7.2\text{-}110)$$

$$\alpha_1 = \frac{2}{2 - \sigma(\bar{\bar{Q}})} \qquad\qquad (7.2\text{-}111)$$

$$\beta_1 = 0 \qquad\qquad (7.2\text{-}112)$$

$$\alpha_p = \frac{4}{\sigma(Q)}\left\{\frac{\cosh[(p-1)\gamma]}{\cosh[p\gamma]}\right\} \qquad\qquad (7.2\text{-}113)$$

$$\beta_p = \left(1 - \frac{\sigma(\bar{\bar{Q}})}{2}\right)\alpha_p - 1 \qquad\qquad (7.2\text{-}114)$$

$$\gamma = \text{arccosh}\left(\frac{2}{\sigma(\bar{\bar{Q}})} - 1\right) \qquad\qquad (7.2\text{-}115)$$

where n^* is the outer iteration index where acceleration begins and p denotes the successive fission source iterations employed $(p \geq 1)$ within a Chebyshev cycle (i.e., since last updating the estimate of $\sigma(\bar{\bar{Q}})$). Note the dominance ratio $\sigma(\bar{\bar{Q}})$ needs to be estimated in order for the scheme to work. This is accomplished using the procedure implemented in DIF3D[7.2-11] as now outlined.

Since an accurate estimate of $\sigma(\bar{\bar{Q}})$ is not known when the outer iterations are commenced, a "boot-strap" process is required. By performing a limited number of power iterations, a reasonable initial estimate of $\sigma(\bar{\bar{Q}})$ is obtained. Only when all but the first overtone mode are essentially damped out,

high-order cycles based on accurate estimates of $\sigma(\overline{\overline{Q}})$ are utilized[7.2-11,7.2-15]. More precisely, the algorithm can be described in terms of four basic steps:

Step 1.

A minimum of three power iterations are performed initially. The first Chebyshev acceleration cycle is begun on outer iteration $(n^* + 1)$, where $(n^* + 1)$ is the smallest integer such that $n^* \geq 3$ for which the dominance ratio estimate, $\hat{\sigma}$ satisfies the following criterion;

$$0.4 \leq \hat{\sigma} \leq 1.0$$

where

$$\hat{\sigma} = \left\{ \frac{\langle \overline{R}^{(n^*)}, \overline{R}^{(n^*)} \rangle}{\langle \overline{R}^{(n^*-1)}, \overline{R}^{(n^*-1)} \rangle} \right\}^{1/2} \qquad (7.2\text{-}116)$$

$$\overline{R}^{(n^*)} \equiv \overline{\Psi}^{(n^*)} - \overline{\overline{\Psi}}^{(n^*-1)}. \qquad (7.2\text{-}117)$$

Step 2.

Using $\hat{\sigma}$ as the dominance ratio estimate for $\sigma(\overline{\overline{Q}})$, the accelerated iterative sequence given by Equations (7.2-108) and (7.2-109) is carried out for iterations $(n^* + p)$ with $p \geq 1$. At first low degree polynomials are applied repeatedly with estimates of the dominance ratio being updated continuously according to

$$\hat{\sigma}' = \frac{\hat{\sigma}}{2} \cosh\left\{ \left[\frac{\cosh^{-1}(\gamma)}{p-1} \right] + 1 \right\} \qquad (7.2\text{-}118)$$

where

$$\gamma = C_{p-1}\left(\frac{2-\hat{\sigma}}{\hat{\sigma}} \right) E_{n^*,p\text{-}1} \qquad (7.2\text{-}119)$$

$$(7.2\text{-}120)$$

and $C_{p-1}(y)$ is the Chebyshev polynomial of degree p-1 given by

$$C_{p-1}(y) = \cosh[(p-1)\arccosh(y)], \; y > 1 .$$ (7.2-121)

The polynomials are at least of degree 3 and are terminated when the error reduction factor $E_{n^*, p-1}$ is greater than the theoretical error reduction factor

$$E_{n^*,p-1} > \left[C_{p-1}\left(\frac{2-\hat{\sigma}}{\hat{\sigma}}\right)\right]^{-1} .$$ (7.2-122)

The theoretical error reduction factor is the error reduction which would have been achieved if $\hat{\sigma}$ were equal to $\sigma(\overline{\overline{Q}})$, the true dominance ratio. If $E_{n^*, p-1}$ is greater than this, the acceleration cycle has not been as effective as it should have been, so a new cycle is started using the updated dominance ratio estimate, $\hat{\sigma}'$. Alternately, the polynomial degree will be terminated if the reduction in the L_2 relative residual of the diffusion equation

$$\frac{\dfrac{\left\|\overline{\overline{A}}\,\overline{\phi}^{(n^*+p)} - \dfrac{1}{k^{(n)}}\overline{\overline{F}}\,\overline{\phi}^{(n^*+p)}\right\|_2}{\left\|\dfrac{1}{k^{(n^*+p)}}\overline{\overline{F}}\,\overline{\phi}^{(n^*+p)}\right\|_2}}{\dfrac{\left\|\overline{\overline{A}}\,\overline{\phi}^{(n^*)} - \dfrac{1}{k^{(n)}}\overline{\overline{F}}\,\overline{\phi}^{(n^*)}\right\|_2}{\left\|\dfrac{1}{k^{(n^*)}}\overline{\overline{F}}\,\overline{\phi}^{(n^*)}\right\|_2}}$$ (7.2-123)

falls below a specified value.

Step 3.

After the estimates for $\sigma(\overline{\overline{Q}})$ have converged higher degree polynomials are applied.

Step 4.

The outer iterations are terminated at outer iteration n if the following four criteria are met:

(7.2-124)

$$\frac{\left\|\overline{\overline{\Psi}}^{(n)} - \overline{\overline{\Psi}}^{(n-1)}\right\|_2}{\langle \overline{\overline{\Psi}}^{(n)}, \overline{\overline{\Psi}}^{(n-1)} \rangle^{1/2}} \leq \varepsilon_{\Psi_2} \tag{7.2-125}$$

$$\left(\frac{1}{1 - \hat{\sigma}}\right) \max_i \left|\frac{\Psi_i^{(n)} - \tilde{\Psi}_i^{(n-1)}}{\Psi_i^{(n)}}\right| < \varepsilon_{\Psi_\infty} \tag{7.2-126}$$

$$\frac{\left\|\overline{\overline{A}}\,\overline{\phi}^{(n)} - \frac{1}{k^{(n)}}\overline{\overline{F}}\,\overline{\phi}^{(n)}\right\|_2}{\left\|\frac{1}{k^{(n)}}\overline{\overline{F}}\,\overline{\phi}^{(n)}\right\|_2} < \varepsilon_\phi \tag{7.2-127}$$

where ε_k, ε_{Ψ_2}, $\varepsilon_{\Psi_\infty}$ and ε_ϕ are input parameters. The following meanings of the "normed" stopping criteria should be noted: ε_{Ψ_2} is the L_2 norm of the relative residual of the outer iterative equation, $\varepsilon_{\Psi_\infty}$ is the L_∞ norm of the true error of the fission source, and ε_ϕ is the L_2 norm of the relative residual of the diffusion equation. (Note that for the fixed source problem associated with a transient problem, the normalization shown in the denominator of the expression bounded by ε_ϕ is changed to the L_2 norm of the source.)

It should be noted that a modification to this basic scheme is made in the actual implementation in ATHENA of the Chebyshev polynomial acceleration. That is, since the NEM corrections to the coupling coefficients are dependent upon the flux solution, our matrix problem is truly non-linear since $\overline{\overline{A}}$ and $\overline{\overline{F}}$ depend upon the flux solution. Since the non-linearity is weak, one can guess a flux solution, determine the corrections to the coupling coefficients and appropriately modify $\overline{\overline{A}}$ and $\overline{\overline{F}}$, and solve for the flux. This updated flux solution can then be used to reinitiate the cycle until both the NEM corrections to the coupling coefficients and flux solutions converge. One way to handle these effects is to update the $\overline{\overline{A}}$ and $\overline{\overline{F}}$ matrices after complete termination of the outer iteration process. This approach has a clear disadvantage in that it requires large computational time to obtain converged solutions for NEM corrections to the coupling coefficients and flux. An alternate approach is to update the coefficient matrix with the corrections to the coupling coefficients during the Chebyshev acceleration process. In doing so, a substantial reduction in computation time can be realized. The latter approach can be justified by observing that the corrections to the coupling coefficients are relatively small perturbations to the original system from a reactor physics point of view and hence, the entire Chebyshev acceleration scheme is not jeopardized. This modified scheme is incorporated in our work in such a manner that the matrices are updated just before a new Chebyshev polynomial acceleration cycle begins. **Figure 7.2-2** summarizes the overall nested iterative solution strategy used within the ATHENA code for each attempted advancement.

This strategy has been demonstrated to be efficient and robust. A NEM non-linear iteration is completed when specified maximum number of outer iterations is reached,.
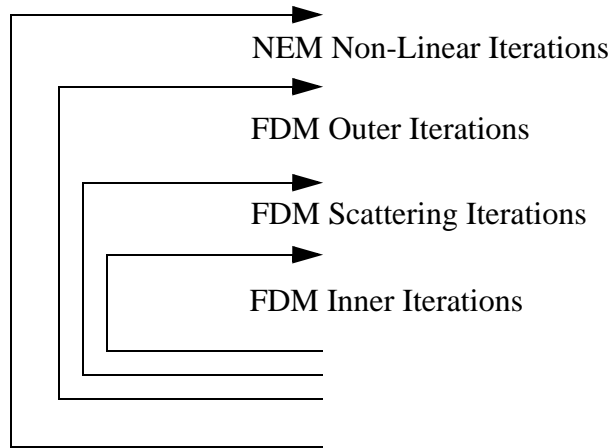
Figure 7.2-2 Overview of nested iterative solution strategy.

7.2.4 Transient Problem

Under transient conditions, both the multi-group diffusion equation and delayed neutron precursor equations must be solved. These equations, accounting for an external neutron source and utilizing six precursor groups, are given by (suppressing $\vec{r}$ and t dependences for clarity)

$$\frac{1}{v_g}\frac{\partial \phi_g}{\partial t} = \sum_{g'=1}^{G} \Sigma_{S_{gg'}}\phi_{g'} + (1-\beta)\chi_g^{(P)}\sum_{g'=1}^{G}\nu_{g'}\Sigma_{fg'}\phi_{g'} + \sum_{i=1}^{I^{(D)}}\chi_{gi}^{(D)}\lambda_i C_i + \vec{\nabla}\cdot D_g\vec{\nabla}\phi_g - \Sigma_{tg}\phi_g + S_{ext_g} \qquad (7.2\text{-}128)$$

$$\frac{\partial C_i}{\partial t} = \beta_i\sum_{g=1}^{G}\nu_g\Sigma_{fg}\phi_g - \lambda_i C_i \qquad \text{for} \qquad i = 1, 2, ..., I^{(D)} \qquad (7.2\text{-}129)$$

where the notation is identical as before except as now noted

v_g $\qquad$ = $\qquad$ neutron speed for energy group g

$\chi_g^{(P)}$ $\qquad$ = $\qquad$ fraction of prompt neutrons born into energy group g

$\qquad$ = $\qquad$ fraction of delayed neutrons for precursor group i born into energy group g

C_i =   neutron precursor concentration in precursor group i

λ_i =   decay constant for precursor group i

β_i =   fraction of all fission neutrons emitted per fission in precursor group i

β =   total fraction of fission neutrons which are delayed.

Alternately, the 'eigenvalue initiated' transient equations can be obtained from Equations (7.2-128) and (7.2-129) by setting $S_{ext_g} = 0$ and by replacing $\nu_g \Sigma_{fg}$ with $(\nu_g \Sigma_{fg})/k$ everywhere.

The neutron kinetics equations, Equations (7.2-128) and (7.2-129), involve differentials in space and time. The time dependence is a difficult problem to treat in neutronics modeling due to the stiffness of the associated equations. The time constants range from very small, associated with prompt neutrons, to very long, associated with the longer lived precursors. ATHENA numerically treats the temporal dependence in a manner that results in a FSP, which can be solved utilizing the methodology developed for the steady-state FSP.

The first step in this conversion to a FSP is to discretize the time domain into discrete times $\{t_n\}$ and to approximate the time derivative of the flux at time t_{n+1} by a backward difference

$$\left. \frac{\partial \phi_g}{\partial t} \right|_{t_{n+1}} = \frac{\phi_g(t_{n+1}) - \phi_g(t_n)}{\Delta t_n} . \tag{7.2-130}$$

This assures unconditional stability. Do note that spatial dependence notation has been and will continue to be suppressed in the equations.

To develop an expression for the precursors' concentrations at time t_{n+1} in terms of the flux $\phi_g(t_{n+1})$, Equation (7.2-129) is solved utilizing the Integrating Factor method over time span $[t_n, t_{n+1}]$ to obtain

$$C_i(t_{n+1}) = C_i(t_n) e^{-\lambda_i \Delta t_n} + \beta_i \int_{t_n}^{t_{n+1}} \sum_{g=1}^{G} \upsilon_g \Sigma_{fg} \phi_g(t') e^{-\lambda_i(t_{n+1} - t')} dt' . \tag{7.2-131}$$

To solve the above integral, a functional form for the time dependent neutron fission source must be assumed over time span $[t_n, t_{n+1}]$. Consistent with the backward difference operator approximation for the time derivative of the flux, the fission source is assumed to vary linearly between time-steps and is given by

$$v_g \Sigma_{fg} \phi_g(t) = v_g \Sigma_{fg} \phi_g(t_n) + \frac{v_g \Sigma_{fg} \phi_g(t_{n+1}) - v_g \Sigma_{fg} \phi_g(t_n)}{\Delta t_n}(t - t_n) . \tag{7.2-132}$$

Incorporating this approximation into Equation (7.2-131) and rearranging terms, we obtain

$$C_i(t_{n+1}) = C_i(t_n)e^{-\lambda_i \Delta t_n} + F^0_{i_n} \sum_{g=1}^{G} v_g \Sigma_{fg} \phi_g(t_n) + F^1_{i_n} \sum_{g=1}^{G} v_g \Sigma_{fg} \phi_g(t_{n+1}) \tag{7.2-133}$$

where

$$F^1_{i_n} = \frac{\beta_i}{\lambda_i \Delta t_n}\left[\Delta t_n - \frac{1}{\lambda_i}(1 - e^{-\lambda_i \Delta t_n})\right] \tag{7.2-134}$$

$$F^0_{i_n} = -F^1_{i_n} + \frac{\beta_i}{\lambda_i}(1 - e^{-\lambda_i \Delta t_n}) . \tag{7.2-135}$$

Now substituting Equations (7.2-130) and (7.2-133) into Equation (7.2-128) one obtains

$$\frac{1}{\Delta t_n v_g}\phi_g(t_{n+1}) - \vec{\nabla} \cdot D_g \vec{\nabla}\phi_g(t_{n+1}) + \Sigma_{t_g}\phi_g(t_{n+1}) = \sum_{g'=1}^{G} \Sigma_{sgg'}\phi_{g'}(t_{n+1})$$
$$+ \left[(1-\beta)\chi_g^{(P)} + \sum_{i=1}^{I^{(D)}} \chi_{gi}^{(D)}\lambda_i F^1_{i_n}\right]\sum_{g'=1}^{G} v_{g'}\Sigma_{fg'}\phi_{g'}(t_{n+1}) + S_{eff_g}(t_{n+1}) \tag{7.2-136}$$

where

$$S_{eff_g}(t_{n+1}) = \left[\sum_{i=1}^{I^{(D)}} \chi_{gi}^{(D)}\lambda_i F^0_{i_n} \sum_{g'=1}^{G} v_{g'}\Sigma_{fg'}\phi_{g'}(t_n) + \sum_{i=1}^{I^{(D)}} \chi_{gi}^{(D)}\lambda_i C_i(t_n)e^{-\lambda_i \Delta t_n}\right]$$
$$+ \frac{1}{\Delta t_n v_g}\phi_g(t_n) + S_{ext_g}(t_{n+1}) . \tag{7.2-137}$$

In Equation (7.2-136) all cross-sections are evaluated at time t_{n+1}. Inspection of Equation (7.2-136) indicates it to be a FSP, with modified operators and source from the steady-state FSP. We refer to Equation (7.2-136) as the transient FSP. Hence the application of NEM to the transient FSP and the iterative solution of the resulting coupled equations can proceed exactly the same as for the steady-state

FSP. As would be expected, the values of flux and adjusted FDM coupling coefficients at time t_{n+1} for the 0th outer iterative step are based upon their values at time t_n.

If we proceed in this manner, in the two-node problems spatial moments of $S_{eff_g}(t_{n+1})$ would appear. As Equation (7.2-137) indicates, $S_{eff_g}(t_{n+1})$ is dependent upon $\{\phi_g(t_n)\}$ and $\{C_i(t_n)\}$. The implication is that the expansion coefficients associated with the transverse integrated fluxes, obtained from solution of the two-node problems, at the previous time t_n must be saved. The same is true for the precursor concentrations, which are treated like the flux for time dependent problems solved by NEM. This would substantially increase the computer memory requirements.

To overcome this difficulty, further approximations are required in formulating the two-node problems. Recognizing that the within node spatial dependence of $S_{eff_g}(t_{n+1})$ is associated with the contributions from the delay neutrons and the external neutron source, that the external neutron source is assumed to be constant within a node, and that these contributions of neutrons are small, one would expect $S_{eff_g}(t_{n+1})$ within node spatial shape to have little impact on the solution. This justifies treating $S_{eff_g}(t_{n+1})$ spatial dependence approximately. In ATHENA this approximate treatment is done in the same manner as for the transverse leakages; that is, using a quadratic polynomial as indicated in Equation (7.2-21). Now only node average values of the flux and precursor concentrations at time t_n must be saved. The node average precursor values are solved for via back substitution using Equation (7.2-133) after the node average flux has been computed.

This implementation does create one problem that must be addressed. Since different spatial treatments are used at times t_n and t_{n+1}, the solution of the steady-state FSP and the transient FSP, now for steady-state conditions, will not agree. The practical consequence is that when one utilizes the steady-state FSP solution to determine initial conditions for the transient FSP, the flux will undergo a very mild transient with time even when the initial steady-state conditions are preserved. This annoyance can be avoided by regrouping terms in Equations (7.2-136) and (7.2-137) as

$$
-\vec{\nabla} \cdot D_g \vec{\nabla} \phi_g(t_{n+1}) + \Sigma_{tg} \phi_g(t_{n+1}) =
$$
$$
\sum_{g'=1}^{G} \Sigma_{sgg'} \phi_{g'}(t_{n+1}) + \chi_g \sum_{g'=1}^{G} \nu_{g'} \Sigma_{fg'} \phi_{g'}(t_{n+1}) + \tilde{S}_{eff_g}(t_{n+1})
$$

(7.2-138)

where

(7.2-139)

$$\tilde{S}_{eff_g}(t_{n+1}) = \left[\sum_{i=1}^{I^{(D)}} \chi_{gi}^{(D)} \lambda_i F_{i_n}^1 - \beta_i \chi_{gi}^{(D)}\right] \sum_{g'=1}^{G} \nu_{g'} \Sigma_{fg'} \phi_{g'}(t_{n+1})$$

$$- \frac{1}{\Delta t_n v_g} \phi_g(t_{n+1}) + S_{eff_g}(t_{n+1}) \ . \tag{7.2-140}$$

Equation (7.2-138) is recognized to be identical to the steady-state FSP except for the replacement of S_{ext_g} with the modified effective source $\tilde{S}_{eff_g}$. Under steady-state conditions, $\tilde{S}_{eff_g}$ equals S_{ext_g} since all the additional terms in Equation (7.2-140) cancel. This is true even for the moments of $\tilde{S}_{eff_g}(t_{n+1})$ that appear in the two-node problems provided the within node spatial dependence is treated consistently for the variables appearing in Equation (7.2-140) at times t_n and t_{n+1}; in particular, when they are all treated by a quadratic polynomial as previously indicated by Equation (7.2-21) for the transverse leakages. The implication is that the transient FSP under steady-state conditions will produce the same solution as produced by the steady-state FSP. This approach has been implemented in ATHENA.

Since the values of node average flux at time t_{n+1}, the unknowns, now appear in the modified effective source, an iterative approach is required. This is easily accomplished within the context of the non-linear iterative method of solving the NEM equations. Recall when solving the two-node problems, node average fluxes are assumed known based upon the latest outer iterative values available for the FDM equation's solution. For transient problems, this corresponds to node averaged flux values at time t_{n+1}, which are precisely the values requires to evaluate the moments of $\tilde{S}_{eff_g}$ that appear in the two-node problems. This approach is utilized within ATHENA to assure the steady-state FSP solution does not "drift" when used as an initial condition in the transient FSP.

To improve upon the initial iterative estimate of the fission source and flux, thereby hopefully minimizing the number of outer and inner iterations required to achieve convergence, the 0th outer iterative estimates of both are determined utilizing a time extrapolated flux. Specifically, assuming an exponential time dependence, the 0th iterative flux at time step n+1 is given by

$$\phi_g(t_{n+1}) = \phi_g(t_n) e^{\omega_{g_n} \Delta t_n} \tag{7.2-141}$$

where

$$\omega_{g_n} = \frac{1}{\Delta t_{n-1}} \ln\left[\frac{\phi_g(t_n)}{\phi_g(t_{n-1})}\right] \tag{7.2-142}$$

7.2.5 Neutron Cross Section Model

The inputs to the kinetics modules in ATHENA consist of neutron cross sections, boundary conditions, control flags, control data, etc. Neutron cross sections are needed for each neutron energy group and kinetics node and consist of the diffusion coefficient (D), absorption cross section (Σ_a), fission cross section (Σ_f), the product of the mean number of secondary neutrons per fission and the fission cross section ($\nu\Sigma_f$), and the scattering cross section for scattering <u>into</u> the neutron energy group from the other neutron energy groups ($\Sigma_{sg \cdot g}$). Discontinuity factors for each face of the kinetics nodes are also needed for each energy group. The user supplies the control information and the boundary conditions as part of the required input data. The neutron cross sections are computed from a function selected from a set of built-in functions or a user supplied function whose independent variables are weighted averages of ATHENA hydraulic or heat structure variables. There are four built-in neutron cross section functions from which the user can select or the user may supply his own function in the form of an external subroutine. The same user specified function is used for the computation of the neutron cross sections for all kinetics nodes. The coefficients in the first three built-in cross section functions for each of the cross sections are supplied through user input and a set of coefficients for the neutron cross sections is called a composition. The user defines a number of compositions and specifies which composition is to be used for the computation of the neutron cross sections in each kinetics node in the reactor core model. The mapping of compositions to nodes is accomplished through the use of composition figures. A composition figure specifies the composition for all of the kinetics nodes in a single axial plane in the reactor model and composition figures are required for each axial plane in the reactor model. The user may specify as many composition figures as needed to describe the reactor and a composition figure may be assigned to more than one axial plane in the reactor model. The user specifies the volumes and heat structures to be used in computing the weighted averages of thermal-hydraulic variables as well as the values of the weighting factors. A set of volume averaged properties consists of an average fluid density (or fluid vapor fraction depending on which neutron cross section function is selected by the user), an average fluid temperature, and an average poison density, while the average heat structure property is simply the average heat structure temperature. The group of volumes and heat structures used to define sets of average thermal-hydraulic properties is called a zone. One of the built-in cross section functions uses a single set of average properties in a zone while the other two built-in neutron cross section functions use multiple sets of average volume and average heat structure properties in a zone. The user defines a number of zones and specifies which set of zone average thermal-hydraulic properties is to be used for the computation of the neutron cross sections in each node of the reactor core through the use of zone figures. A zone figure specifies which zone is to be used for the computation of the neutron cross sections for each node in an axial plane of the reactor. Zone figures are required for each axial plane in the reactor model and the same zone figure may be specified for more than one axial level. In addition to the weighted averages of hydraulic and heat structure variables, the neutron cross section function uses the position of the control rods as another independent variable. A control rod model is used to determine the positions of the control rods and to compute the control rod variable needed by the neutron cross section function on each axial level in the reactor core. The three neutron cross section functions that the user may select to compute the neutron cross sections and the control rod model are described in the following section.

7.2.5.1 RAMONA Neutron Cross Section Model

The first built-in cross section model is the RAMONA model. The RAMONA neutron cross section model uses the neutron cross section parameterization from the RAMONA-3B[7.2-16] code. The functional form for the computation of cross sections is

$$
\begin{aligned}
\Sigma_l^x \;=\; & Cf_l(a_{1n}^x + a_{2n}^x \bar{\alpha}_k + a_{3n}^x \bar{\alpha}_k^2) + (1 - Cf_l)(a_{4n}^x + a_{5n}^x \bar{\alpha}_k + a_{6n}^x \bar{\alpha}_k^2) \\
& + a_{7n}^x(\sqrt{\bar{T}_{sk}} - \sqrt{T_{sn}^{ref}}) + a_{8n}^x(\bar{T}_{mk} - T_{mn}^{ref}) + a_{9n}^x \bar{B}_k
\end{aligned}
\tag{7.2-143}
$$

where

$\bar{\alpha}_k$	=	average void fraction in zone k
$\bar{T}_{sk}$	=	average heat structure temperature in zone k
T_{sn}^{ref}	=	heat structure reference temperature for composition n
$\bar{T}_{mk}$	=	average moderator temperature in zone k
T_{mn}^{ref}	=	moderator reference temperature for composition n
$\bar{B}_k$	=	average poison concentration in zone k

and zone k and composition n have been specified for kinetics node l and a set of coefficients a_{jn}^x , j = 1, 2, ..., 9, have been specified for cross section x. Each of the cross sections for each node is computed using Equation (7.2-143). The nodal discontinuity factors are computed as

$$
DF_l^x \;=\; Cf_l(DF_l^x)_{controlled} + (1 - Cf_l)(DF_l^x)_{uncontrolled}
\tag{7.2-144}
$$

for each face x of node l where $(DF_l^x)_{controlled}$ and $(DF_l^x)_{uncontrolled}$ are user input quantities.

7.2.5.2 HWR Neutron Cross Section Model

The second built-in cross section model is the HWR model[a] that was developed at Argonne National Laboratory as part of the Heavy Water New Production Reactor project. The HWR feedback option uses a different function to compute the neutron cross sections. Each cross section consists of two parts, a base cross section that only depends on the control fraction, and a variable part that depends upon changes in the

thermal-hydraulic properties from those defined for the base state. The base portion of the cross section x in node l is computed from

$$\Sigma_{xl}^{base} = Cf_l(\Sigma_{xn}^{base})_{controlled} + (1 - Cf_l)(\Sigma_{xn}^{base})_{uncontrolled} \quad . \tag{7.2-145}$$

where composition n has been specified for node l. The controlled base cross section is computed by the neutronics simulator for a control fraction of one and the uncontrolled cross section is computed with a control fraction of zero. The variable portion of the cross section is computed from

$$\frac{\delta\Sigma_{xl}}{\Sigma_{xl}^{base}} = \sum_{i \in N_v} a_{xin}\Delta\bar{T}_{mik} + \sum_{i \in N_v} b_{xin}\Delta\bar{\rho}_{mik} + \sum_{i \in N_v} c_{xin}(\Delta\bar{\rho}_{mik})^2$$
$$+ \sum_{i \in N_v} d_{xin}\Delta\bar{B}_{ik} + \sum_{i \in N_s} e_{xin}\Delta\bar{T}_{sik} \tag{7.2-146}$$

where the neutron cross section is the sum of the base cross section and the change in the cross section

$$\Sigma_{xl} = \Sigma_{xl}^{base} + \delta\Sigma_{xl} \tag{7.2-147}$$

where

Σ_{xl}^{base} =   base cross section of type x in node l

$\delta\Sigma_{xl}$ =   change in cross section x in node l due to changes in the thermal-hydraulic state of the zone to which node l corresponds

Cf_l =   control fraction in node l

    =   coefficient for change in cross section x of composition n due to changes in average moderator temperature of volume region i

$\Delta\bar{T}_{mik}$ =   change in average moderator temperature in volume region i of zone k

---

a. W. Yang, "Representation of Temperature Effects on HWR Nodal Neutron Cross Sections," Intra-Laboratory Memo, to H. Khalil, Argonne National Laboratory, May 3, 1991.

$$= \quad \overline{T}_{mik} - \overline{T}_{min}^{base}$$

$\overline{T}_{mik}$ = average moderator temperature in volume region i of zone k

$\overline{T}_{min}^{base}$ = average moderator temperature in volume region i for composition n at base thermal-hydraulic conditions, e.g. full power steady state

N_v = number of volume regions in each zone

b_{xin} = linear coefficient in change of cross section x of composition n due to changes in average moderator density in volume region i

$\Delta\overline{\rho}_{mik}$ = change in average moderator density in volume region i of zone k

$$= \quad \overline{\rho}_{mik} - \overline{\rho}_{min}^{base}$$

$\overline{\rho}_{min}^{base}$ = average moderator density in volume region i for composition n at base thermal-hydraulic state

c_{xin} = quadratic coefficient in change of cross section x of composition n due to changes in average moderator density in volume region i

d_{xin} = coefficient for change in cross section x of composition n due to changes in average poison density in volume region i

$\Delta\overline{B}_{ik}$ = change in average poison concentration in volume region i of zone k,

$$= \quad \overline{B}_{ik} - \overline{B}_{in}^{base}$$

$\overline{B}_{in}^{base}$ = average poison concentration in volume region i for composition n at base thermal-hydraulic condition

= coefficient for change in cross section x of composition n due to changes in average structure temperature of structure region i

$\Delta\overline{T}_{sik}$ = change in the average structure temperature in structure region i of zone k

$$= \overline{T}_{sik} - \overline{T}_{sin}^{base}$$

$$\overline{T}_{sin}^{base} = \text{average structure temperature in structure region i of composition n for base thermal-hydraulic state}$$

$$N_s = \text{number of structure regions in each zone.}$$

The nodal discontinuity factors for the HWR feedback option are computed using Equation (7.2-144). The HWR cross section model allows the user to specify more than one set the averaged thermal hydraulic properties per zone.

7.2.5.3 GEN Neutron Cross Section Model

The last built-in cross section model is the most general built-in cross section model and was developed[7.2-17] as part of the ATHENA code development project. The GEN cross section function uses a form similar to the HWR formulation except that the variable portion of the cross section is defined for three control states, active controlled, driver controlled and uncontrolled states. The GEN cross section function is given by

$$\Sigma_l^x = C_{fl}^a \Sigma_{xc}^a \left(1 + \frac{\delta \Sigma_{xc}^a}{\Sigma_{xc}^a} \right) + (1 - C_{fl}^a - C_{fl}^d) \Sigma_{xc}^u \left(1 + \frac{\delta \Sigma_{xc}^u}{\Sigma_{xc}^u} \right) + C_{fl}^d \Sigma_{xc}^d \left(1 + \frac{\delta \Sigma_{xc}^d}{\Sigma_{xc}^d} \right) \tag{7.2-148}$$

where

$$C_{fl}^{a,d} = \text{control fraction for active and driver portions of the control rods in node l}$$

$$\Sigma_{xc}^{a,d,u} = \text{base cross section of reaction type x for composition c for active controlled, driver controlled, or uncontrolled states}$$

$$\delta \Sigma_{xc}^{a,d,u} = \text{variation of cross section for reaction type x for composition c due the changes in the thermal-hydraulic variables from the base thermal-hydraulic state for active controlled, driver controlled, and uncontrolled state}$$

and composition c has been specified for node l.

The variations for the active controlled, driver controlled, and uncontrolled states are given by Equation (7.2-146) where the coefficients a, b, c, d, and e are input separately for the active controlled,

driver controlled, and uncontrolled states. The other differences between to HWR and the GEN formulation are that the density variable in the variation of the cross section may be either the fluid mixture density or the fluid void fraction and the variation of the structure temperature may be the difference of the structure temperature and the reference temperature or the difference of the square roots of the structure temperature and the reference temperature as in the RAMONA formulation. The RAMONA and HWR formulations of the neutron cross sections may be manipulated into the GEN form. The nodal discontinuity factors are also computed from Equation (7.2-148) except that the thermal-hydraulic variations are identically zero and are therefore not included.

7.2.5.4 RBMK Neutron Cross Section Model

This neutron cross section model is intended for modeling of RBMK reactors. The cross sections are computed by a subroutine supplied by the Russian Research Centre - Kurchatov Institute in Moscow. No information is currently available as to how the neutron cross sections are computed in this subroutine.

7.2.5.5 USER Neutron Cross Section Model

The last neutron cross section model is the USER option. In this option, the user supplies an external subroutine which computes the set of neutron cross sections and optional discontinuity factors for a single node given the material type in the node determined from the composition maps, the region average properties in the zone specified in the zone maps for the node, and the control fractions and insertion directions for any control rods associated with the node. The user may also specify the values of up to four additional variables in each node through the use of additional input data. These additional variables are passed to the external subroutine and may be used by the user to represent the values of any variables that may affect the neutron cross sections that are not computed by ATHENA (e.g., fuel burnup, xenon and samarium concentration, etc.).

7.2.5.6 Computation of Zone Average Properties

All three neutron cross section models use averages of ATHENA thermal hydraulic variables, volume quantities and heat structure quantities, as the independent variables in the neutron cross section functions. The RAMONA model uses a set of three volume average properties in each zone, the zone average vapor fraction, $\overline{\alpha}_{gk}$, the zone average moderator temperature, $\overline{T}_{mk}$, and a zone average poison concentration, $\overline{B}_k$, and a single average of heat structure quantities, the zone average heat structure temperature, $\overline{T}_{sk}$. The subscript k denotes the zone. These quantities are defined by

$$\overline{\alpha}_{gk} = \frac{\sum_{i \in M_k} W_{ik}^{\alpha} \alpha_{gi}}{\sum_{i \in M_k} W_{ik}^{\alpha}} \qquad (7.2\text{-}149)$$

$$\overline{T}_{mk} = \frac{\sum\limits_{i \in M_k} W_{ik}^m T_{mi}}{\sum\limits_{i \in M_k} W_{ik}^m}$$ (7.2-150)

$$\overline{B}_k = \frac{\sum\limits_{i \in M_k} W_{ik}^B B_i}{\sum\limits_{i \in M_k} W_{ik}^B}$$ (7.2-151)

$$\overline{T}_{sk} = \frac{\sum\limits_{i \in S_k} W_{ik}^s \overline{T}_{si}}{\sum\limits_{i \in S_k} W_{ik}^s}$$ (7.2-152)

where

$\overline{\alpha}_{gk}$ = average vapor/gas fraction in zone k

α_{gi} = vapor/gas fraction in volume i

W_{ik}^{α} = vapor/gas fraction weight factor for volume i in zone k

M_k = list of volumes for volume averages in zone k

$\overline{T}_{mk}$ = average moderator temperature in zone k

  = moderator temperature weighting factor for volume i in zone k,

T_{mi} = moderator temperature in volume i

  = $\dfrac{\alpha_{fi}\rho_{fi}T_{fi} + \alpha_{gi}\rho_{gi}T_{gi}}{\alpha_{fi}\rho_{fi} + \alpha_{gi}\rho_{gi}}$

α_{ki}	$=$	volume fraction of phase k in volume i (k = f for liquid and k = g for vapor/gas)
ρ_{ki}	$=$	density of phase k in volume i
T_{ki}	$=$	temperature of phase k in volume i
$\overline{B}_k$	$=$	average poison concentration in zone k
W_{ik}^B	$=$	poison concentration weighting factor for volume i in zone k
B_i	$=$	poison concentration in volume i
	$=$	10^6 times poison density in volume i divided by liquid density in volume i
$\overline{T}_{sk}$	$=$	average structure temperature in zone k
$\overline{T}_{si}$	$=$	average temperature in structure i
W_{ik}^s	$=$	structure temperature weighting factor for structure i in zone k
S_k	$=$	list of structures for structure averages in zone k.

The user supplies the lists of volumes and heat structures to be used for the averages in each zone and ATHENA computes the thermal-hydraulic variables needed to determine the zone average properties. The same list of volumes is used for the three volume averaged quantities in each zone but different weighting factors are used for each of the three averages.

The other two built-in cross section models, the HWR cross section model and the GEN model, as well as the user supplied external subroutine model, subdivide each zone into a number of regions and define averages of volume and heat structure quantities for each region of a zone. The number of regions in a zone for the computation of volume average properties may be different from the number of regions in a zone for the computation of the heat structure average properties, but the number of volume regions and the number of heat structure regions is the same for each zone. The region average moderator temperature, the region average moderator density, the region average poison density, and the region structure temperature are computed using equations like Equations (7.2-150), (7.2-151), and (7.2-152) respectively except that the summations and weighting fractions are defined for a region in a zone rather than for the entire zone. The HWR cross section model uses the average moderator density instead of the average vapor fraction in the set of volume average properties while the GEN cross section model uses either the

moderator density or the moderator void fraction depending upon which option the user specifies. The average void fraction in each region is computed using Equation (7.2-149). The region average properties are computed as

$$\bar{T}_{mik} = \frac{\sum\limits_{j \in M_{ik}} W^m_{jik} T_{mj}}{\sum\limits_{j \in M_{ik}} W^m_{jik}} \qquad (7.2\text{-}153)$$

$$\bar{\rho}_{mik} = \frac{\sum\limits_{j \in M_{ik}} W^\rho_{jik} \rho_{mj}}{\sum\limits_{j \in M_{ik}} W^\rho_{jik}} \qquad (7.2\text{-}154)$$

$$\bar{B}_{fik} = \frac{\sum\limits_{j \in M_{ik}} W^B_{jik} B_j}{\sum\limits_{j \in M_{ik}} W^B_{jik}} \qquad (7.2\text{-}155)$$

$$\bar{T}_{sik} = \frac{\sum\limits_{j \in S_{ik}} W^s_{jik} \bar{T}_{sj}}{\sum\limits_{j \in S_{ik}} W^s_{jik}} \qquad (7.2\text{-}156)$$

where

	=	average moderator temperature in volume region i of zone k
W^m_{jik}	=	moderator temperature weighting factor for volume j in volume region i of zone k
T_{mj}	=	moderator temperature in volume j
M_{ik}	=	list of volumes for volume averages in volume region i of zone k
$\bar{\rho}_{mik}$	=	average moderator density in volume region i of zone k

ρ_{mj}　　　　$=$　　　　　　fluid mixture density in volume j

　　　　　　　　$=$　　　　　　　　$\alpha_{fj}\rho_{fj} + \alpha_{gj}\rho_{gj}$

W^{ρ}_{jik}　　　　$=$　　　　　　fluid density weighting factor for volume j in volume region i of zone k

$\overline{B}_{ik}$　　　　$=$　　　　　　average poison concentration in volume region i of zone k

W^{B}_{jik}　　　　$=$　　　　　　poison weighting factor for volume j in volume region i of zone k

B_j　　　　$=$　　　　　　poison concentration in volume j

　　　　　　　　$=$　　　　　　10^6 times poison density in kg/m^3 divided by mixture density ρ_{mj} in volume j

$\overline{T}_{sik}$　　　　$=$　　　　　　average structure temperature in structure region i of zone k

W^{s}_{jik}　　　　$=$　　　　　　structure temperature weighting factor for structure j in structure region i of zone k

$\overline{T}_{sj}$　　　　$=$　　　　　　average temperature in structure j

S_{ik}　　　　$=$　　　　　　list of structures for structure averages in structure region i of zone k.

7.2.6 Control Rod Model

Zero or more control rods may be associated with each axial stack of neutronics nodes The insertion depth of the individual control rods is determined as the sum of the user input initial insertion depth and the value returned by the control component (i.e., either a general table or a control block) associated with the control rod. If no control component is associated with the control rod, it remains at its user specified initial insertion depth. Control rods may be inserted from either the top or bottom faces of the reactor.

7.2.6.1 Computation of Control Fractions

The control fractions for the kinetics nodes on each axial level is computed from the insertion depths of the control rods. The control rods are sorted by the user into control rod groups where the rods in a group have the same insertion depth, move at the same velocity, are controlled by the same control variable or general table and have the same neutronics worth. The control rods may be inserted from either the top or bottom of the reactor core. Each rod group may also represent full length or partial length rods and this

must be taken into account when computing the control fractions. The control fraction for node n on axial level l is given by

$$Cf_{n,1} = \frac{\sum\limits_{r \in R_n} Cf^r_{n,1}}{N_n} \tag{7.2-157}$$

where

$Cf_{n,1}$ = control fraction for node n on axial level l

$Cf^r_{n,1}$ = control fraction for control rod group r in node n on level l

N_n = number of control rods associated with node n

R_n = list of rod groups to be used for node n.

The control fraction for a full length control rod inserted from the bottom of the reactor core for axial level l is computed from

$$Cf^r_1 = \min\left\{1.0, \max\left[0.0, \frac{h_r - h_{l-1}}{h_1 - h_{l-1}}\right]\right\} \tag{7.2-158}$$

where

h_r = insertion depth of the tip of the control rod group r measured from the end of the reactor core through which the rod in inserted

h_1 = height of top of level l measured from the bottom of the reactor core,

h_{l-1} = height of bottom of level l measured from the bottom of the reactor core.

The control fraction for the rod inserted the same depth from the top of the reactor core is given by,

$$Cf^r_1 = \min\left\{1.0, \max\left[0.0, \frac{h_r - (h_N - h_1)}{h_1 - h_{l-1}}\right]\right\} \tag{7.2-159}$$

where

h_N = height of top of level N measured from the bottom of the reactor core, i.e., height of reactor core

and the other variables are as defined above.

The computation of the control fractions for partial length control rods is similar to the computation for the full length rods except that the partial rod consists of two pieces, a neutronically active portion adjacent to the tip of the rod and a neutronically inactive or driver portion below the active portion. The control fraction for the active potion of a partial length rod is computed by subtracting the control fraction for the driver portion from the control fraction for the active portion. The control fractions for the two pieces of the rod are computed from Equations (7.2-158) and (7.2-159) except that the insertion depth of the driver portion is the insertion depth of the rod minus the active length of the rod. The formulas are

$$Cf_l^{r,a} = Cf_l^r - Cf_l^{r,d} \tag{7.2-160}$$

where

Cf_l^r = control fraction for control rod r on level l, based on the position of the tip of the control rod computed from either Equation (7.2-158) or Equation (7.2-159)

$Cf_l^{r,a}$ = control fraction for active portion of control rod group r,

$Cf_l^{r,d}$ = control fraction for driver portion of control rod group r.

The control fraction for the driver portion of the rod group inserted from the bottom of the reactor core is computed as

$$Cf_l^{r,d} = \min\left\{1.0, \max\left[0.0, \frac{(h_r - l_r) - h_{l-1}}{h_l - h_{l-1}}\right]\right\} \tag{7.2-161}$$

and from

$$Cf_l^{r,d} = \min\left\{1.0, \max\left[0.0, \frac{(h_r - l_r) - (h_N - h_l)}{h_l - h_{l-1}}\right]\right\} \tag{7.2-162}$$

for a partial rod inserted from the top of the reactor core where

l_r = active length of control rod group r.

7.2.7 References

7.2-1.   P. J. Turinsky et al., *NESTLE: A Few-Group Neutron Diffusion Equation Solver Utilizing the Nodal Expansion Method for Eigenvalue, Adjoint, Fixed-Source Steady State and Transient Problems*, EGG-NRE-11406, Idaho National Engineering Laboratory, June 1994.

7.2-2.   B. R. Bandini, *A Three-Dimensional Transient Neutronics Routine for the TRAC-PF1 Reactor Thermal Hydraulic Computer Code*, Ph. D. Dissertation, Pennsylvania State University, 1990.

7.2-3.   R. D. Lawrence, "Progress in Nodal Methods for the Solution of the Neutron Diffusion and Transport Equations," *Progress in Nuclear Energy, 17,* 3, 1986, pp. 271.

7.2-4.   B. A. Finlayson and L. E. Scrivin, "The Method of Weighted Residuals - A Review," *Applied Mechanics Review, 19,* 9, 1966, pp. 735.

7.2-5.   K. S. Smith, "Nodal Method Storage Reduction By Non-Linear Iteration," *Transactions of the American Nuclear Society*, *Detroit, MI, June 1983,* 44, pp. 265.

7.2-6.   K. S. Smith, "QPANDA: An Advanced Nodal Method for LWR Analyses," *Transactions of the American Nuclear Society*, *June 1985*, pp. 265.

7.2-7.   K. S. Smith and K. R. Rempe, "Testing and Applications of the QPANDA Nodal Method," *Proceedings of the International Topical Meeting on Advances in Reactor Physics, Pittsburgh, PA, 1987,* 2*,* pp. 861.

7.2-8.   P. R. Engrand, G. I. Maldanado, R. Al-Chalabi, and P. J. Turinsky, "Non-Linear Iterative Strategy for NEM: Refinement and Extension," *Transactions of the American Nuclear Society, Boston, MA, June 1992*, 65, pp. 221.

7.2-9.   R. D. Lawrence, *The DIF3D Nodal Neutronics Option for Two- and Three-Dimensional Diffusion-Theory Calculations in Hexagonal Geometry*, ANL-83-1, Argonne National Laboratory, 1983.

7.2-10.   L. A. Hageman and D. M. Young, "Applied Iterative Methods," *Computer Science and Applied Mathematics*, Orlando: Academic Press, 1981.

7.2-11.   K. I. Derstine, *DIF3D: A Code to Solve One-, Two-, and Three-Dimensional Finite Difference Diffusion Theory Problems*, ANL-82-84, Argonne National Laboratory, 1984.

7.2-12.   R. S. Varga, *Matirx Iterative Analysis*, Englewood Cliffs, NJ: Prentice-Hall, 1962.

7.2-13.   S. Nakamura, *Computational Methods in Engineering and Science*, New York: Wiley, 1977.

7.2-14.   S. K. Zee, *Numerical Algorithms for Parallel Processors Computer Architectures with Applications to a Few-Group Neutron Diffusion Equations*, Ph. D. Dissertation, North Carolina State University, 1987.

7.2-15.   L. A. Hageman and C. J. Pfeifer, *The Utilization of the Neutron Diffusion Program PDQ-5*, WAPD-TM-385, Bettis Atomic Power Laboratory, Westinghouse Power Corporation, 1965.

7.2-16.   W. Wulff, H. S. Cheng, D. J. Diamond, and M. Khatib-Rahbar, *A Description and Assessment of RAMONA-3B MOD.0 CYCLE 4: A Computer Code with Three-Dimensional Neutron Kinetics for BWR System Transients*, NUREG/CR-3664, BNL-NUREG-51746, Brookhaven National Laboratory, January 1984.

7.2-17.   W. L. Weaver, *Software Design and Implementation Document; Three Dimensional Neutron Kinetics for RELAP5/MOD3*, EGG-NRE-11021, Idaho National Engineering Laboratory, November 1993.

7.3 Nuclear Detector Model

A nuclear detector model is needed to provide kinetics input to the control systems model. A detector model can be built by the user using the capabilities of the control systems model but this method uses a large number of control blocks and depletes the pool of control blocks that can be used to model the actual control system. The detector model mimics the thermal radiation model in that the dectector 'sees' a user specified region of the reactor core and responds (i.e., generates a signal) to the radiation emitted from that region of the reactor. The model accounts for the fact that the radiation emanating from the source region is attenuated by the material between the source and the detector and that the attenuation is a function of the properties of the material between the source and the detector. These properties may be constant in time such as for solid materials or may be time-varying such as for fluids. Nuclear detectors respond to several types of radiation (i.e., neutrons and gamma rays), and the detector model allows the user to specify the type of radiation from each source region and the source region can consist of several kinetics nodes.

7.3.1 The Model

The detector model is based on a ray-tracing algorithm, The contribution of each source node in the source region to the detector response is described by a contribution factor CF_i for source S_i in kinetics node i. The detector response is the sum of the responses from each source node in the source region,

$$\text{response} = SF \sum_{i=1}^{N_S} CF_i \times S_i \qquad (7.3\text{-}1)$$

where N_S is the number of source nodes 'seen' by the detector. The contribution factors CF_i should be normalized so that they sum to one,

$$\sum_{i=1}^{N_S} CF_i = 1.0 \; . \tag{7.3-2}$$

The multiplier SF is a scale factor that can be used to convert the source units (usually watts) to the detector response units (usually amps).

The contribution factors are determined assuming some distribution of material between a source node and the detector and by assuming that the materials between the source node and detector attenuate the response. The attenuation is affected by changes in the properties of these materials (e.g., density or temperature). For this model, it is assumed that the change in attenuation for each material region between a source node and detector can be modelled by an exponential based on the material property.

$$attenuation = \exp\left[\sum_{j=1}^{N_M} \mu_j (X^j - X_{ref}^j)\right] \tag{7.3-3}$$

where N_M is the number of material regions between the source node and detector, μ_j is the attenuation coefficient for the material in material region j, X^j is the instantaneous value of the material property in material region j, and X_{ref}^j is the reference value (i.e., the condition where CF_i was evaluated) of the material in material region j. The detector response for all source nodes becomes,

$$response = SF \sum_{i=1}^{N_S} CF_i \times S_i \times \exp\left[\sum_{j=1}^{N_{M,i}} \mu_{i,j}(X_i^j - X_{i,ref}^j)\right] \tag{7.3-4}$$

where there may be a different number of material regions between the source node and detector for each source node.

8 Special Techniques

The mass from the state relationship is compared to the mass from the continuity equation, and the difference is a measure of the truncation error inherent in the numerical solution. This is the main method used to control the time step and thus control the truncation error. Other methods are also used.

Special techniques are also used to mitigate mass and energy errors. These are (1) a second evaluation of the semi-implicit scheme equations using non-linearized time derivatives, (2) velocity flip-flop situations, and (3) noncondensable gas appearance situations.

Special methods are provided in the code for use in obtaining initial conditions. These methods are based on the transient solution algorithm but make use of an accelerated thermal transient solution technique in order to shorten the computer time required to achieve steady-state. Generic control component options are available to allow the user to minimize the time, effort, and cost to achieve steady-state.

8.1 Time Step Control

A variety of checks on solution acceptability are used to control the time step. These include material Courant limit checks, mass error checks, material properties out of defined ranges, thermodynamic fluid property errors, excessive extrapolation of state (thermodynamic fluid) properties in the metastable regimes, phase appearance/disappearance checks, or large pressure changes in a volume when noncondensable appears.

The material Courant limit check is made before a hydrodynamic advancement takes place. Thus, it may reduce the time step, but it does not cause a time step to be repeated. All of the other checks may cause all or part of the time advancement to be repeated at a smaller time step. The material Courant limit is evaluated for each hydrodynamic volume using the phasic volume velocities and the phasic volume fractions, and it is given by

$$(\Delta t_c)_i \ = \ \Delta x_i \ \frac{\max(\alpha_{fi}^n, \alpha_{gi}^n)}{\max(\left|\alpha_{fi}^n v_{fi}^n\right|, \left|\alpha_{gi}^n v_{gi}^n\right|)} \qquad i = 1, 2, ..., N \ . \tag{8.1-1}$$

The N volumes are divided into five subsets, i.e., the 1st, 6th, 11th, ... volumes belong to the first subset, the 2nd, 7th, 12th, ... volumes belong to the second subset, etc. The minimum Courant limits for each of the five subsets are rearranged in ascending order, i.e.,

$$\Delta t_c^1 \ \leq \ \Delta t_c^2 \ \leq \ \Delta t_c^3 \ \leq \ \Delta t_c^4 \ \leq \ \Delta t_c^5 \ . \tag{8.1-2}$$

Thus, Δt_c^1 is the minimum Courant limit for all the volumes. This is the number printed at each major edit under "CRNT. DT =". For the semi-implicit scheme, Δt_c^2 is used for limiting the time step size. Thus, partial violation of the material Courant limit is allowed for this scheme. For the nearly-implicit scheme, 20 times Δt_c^2 is used for limiting the time step size for the transient mode, and 40 times Δt_c^2 is used for limiting the time step size for the steady-state mode.

The mass error check is made when the time step solution is nearly complete. If excessive mass error is detected, the time step is repeated at a reduced interval. Two types of mass error measures are computed. The first one is designed to check the validity of the density linearization and is defined as

$$\varepsilon_m = \max\left(\frac{|\rho_{mi} - \rho_i|}{\rho_i}\right) \qquad i = 1, \ 2, \ ..., \ N \tag{8.1-3}$$

where ρ_{mi} is the total density of the i-th volume obtained from the mass continuity equation, and ρ_i is the total density of the i-th volume computed from the state relationship. The second one is a measure of overall system mass error and is given by

$$\varepsilon_{rms} = \frac{2\sum_{i=1}^{N}[V_i(\rho_i - \rho_{mi})]^2}{\sum_{i=1}^{N}(V_i\rho_i)^2} \quad . \tag{8.1-4}$$

If either ε_m or ε_{rms} is $> 8 \times 10^{-3}$, the time step is rejected and repeated with one half of the time step size. Otherwise, the time step is accepted, and the next time step size is doubled if both ε_m and ε_{rms} are $< 8 \times 10^{-4}$. The value of ε_m for each system is shown in the individual system major edits (ERR.EST). The maximum of ε_m for all systems and ε_{rms} is shown in the major edits Time Step Summary (ERR.EST) and minor edits/plots (ERRMAX).

The first type of mass error measure $[(\rho_{mi} - \rho_i)V_i]$ is added for each volume at each time step. This is the same as computing the mass flowing in through junctions connected to time-dependent volumes, subtracting the mass flowing out through junctions connected to time-dependent volumes, and adding the difference between the previous time step mass and the current mass. This mass error is accumulated for each system and is shown in the system major edits (MASS ERROR) and minor edits/plots (SYSMER). This mass error is accumulated for all the systems and is shown in the Time Step Summary (MS.RED) and minor edits/plots (EMASS). The total mass in each system is shown in the system major edits (MASS) and minor edits/plots (SYSTMS). The total mass for all systems is shown in the Time Step Summary (TOT.MS) and minor edits/plots (TMASS). At any given time, the following equation holds:

$$\begin{array}{c}
\text{mass at} \\
\text{start of} \\
\text{calculation}
\end{array}
\quad + \quad
\begin{array}{c}
\text{mass flowing in} \\
\text{through junctions} \\
\text{connected to} \\
\text{time dependent} \\
\text{volumes}
\end{array}
\quad - \quad
\begin{array}{c}
\text{mass flowing out} \\
\text{through junctions} \\
\text{connected to} \\
\text{time dependent} \\
\text{volumes}
\end{array}
\qquad \qquad (8.1\text{-}5)$$

$$= \quad
\begin{array}{c}
\text{mass at} \\
\text{current} \\
\text{time} \\
\text{(TMASS)}
\end{array}
\quad + \quad
\begin{array}{c}
\text{cumulative} \\
\text{mass error} \\
\text{at current} \\
\text{time} \\
\text{(EMASS)}
\end{array}$$

At any point in the solution flow, if a thermodynamic fluid property is found to lie outside the defined range, the time step is halved and repeated. This halving process proceeds until the property is within range or the user-specified minimum time step is reached. If the minimum time step is reached without obtaining a valid solution, the code calculation is terminated; the last time step is repeated with a diagnostic dump printed, and the program stops at the completion of the advancement. This same procedure is applied for all thermodynamic fluid property or extrapolation failures. The liquid metastable checks used are specific volume less than or equal to 0 and liquid temperature greater than 50 K above saturation temperature. The vapor metastable checks are vapor specific volume less than or equal to 0 and the vapor temperature less than 50 K below saturation temperature. The vapor 50 K limit is used for the vapor only case, but not for the noncondensable/vapor case which uses iteration. There is also time step control based on problems with void fraction (α_g), noncondensable quality (X_n), and mixture density from the phasic continuity equations (ρ_m). Advancements that result in α_g and X_n being slightly less than 0.0 or slightly greater than 1.0 are allowed, and the variable is reset to 0.0 or 1.0. Advancements that result in values much less than 0.0 or much greater than 1.0 are considered an error, and the time step is repeated. The cutoff points are based on a functional relationship. This relation is tied to the mass error upper limit (8 x 10^{-3}). Advancements that result in ρ_m being ≤ 0 are also considered an error and the time step is repeated. In addition, if too much of one-phase appears (more than a typical thermal boundary layer thickness) starting from a single phase state, an error is assumed to have occurred, and the time step is repeated. In addition, there is a time step control based on the change in the pressure in a volume during an advancement, which is used whenever noncondensable gas first appears in a volume. This time step control algorithm causes the code to repeat a time step if the change in pressure during a time step exceeds the old-time value, the new-time value, or 50,000 Pa. This time step control has the effect of allowing the pressure to change by no more than a factor of two during a time step.

8.2 Mass/Energy Error Mitigation

The semi-implicit numerical scheme described in Section 3.1.3 and Section 3.1.4 has two calculations of the new-time variables α_g, U_g, U_f, and X_n. These variables are first calculated in connection with a linearization of all the product terms involved in the time derivatives and are referred to as tentative new-time variables [see Equations (3.1-88) through (3.1-92)]. They are denoted by a tilde in Section 3.1.3 and Section 3.1.4. This first calculation uses a numerically conservative form for all flux calculations of mass and energy, but because the products in the time derivatives are linearized, the quantities $\alpha_g \rho_g$, $\alpha_f \rho_f$, $\alpha_g \rho_g U_g$, $\alpha_f \rho_f U_f$, and $\alpha_g \rho_g X_n$ are not numerically conserved. These tentative new-time values are only used to evaluate the interphase heat and mass transfer terms to be used in the second evaluation of the basic equations. In this second evaluation of the basic equations [see Equations (3.1-110), (3.1-112), (3.1-113), (3.1-115), and (3.1-116)], the products appearing in the time derivatives are not linearized. This second step also uses the numerically conservative form for the flux terms. Hence, the final end of time step values have been calculated using a consistent and numerically conservative form of differencing. The truncation errors in the linearization procedure may produce errors in the solution for pressure, phasic specific internal energies, and void fraction. Since the state is computed from these basic variables, the resultant density may have some error. This error is used in the time step control presented in Section 8.1.

There are mass and energy errors that the numerically conservative form of differencing cannot remove. The convective terms in the field equations are computed with donored properties determined by the direction of phasic velocities. There are times that the final velocities may differ in directions from the explicit velocities used to define the donored properties. This may result in mass/energy errors due to incorrect properties used in the numerical scheme. The term *velocity flip-flop* refers to the situation in which the final velocities and the explicit velocities differ in sign. In the ATHENA numerical scheme, the pressures and final velocities are calculated using the donor properties based on the explicit velocities (see Section 3.1.3 for the semi-implicit and Section 3.1.5 for the nearly-implicit). The velocity flip-flop implies that inconsistent donor properties were used for the pressure computation and the final mass/energy computation. This may result in bad velocity and energy solutions and large mass errors. Thus, a mitigation scheme is employed to detect errors of this type. Let $\alpha_{fj}^{n,\,exp}$, $\rho_{fj}^{n,\,exp}$, $U_{fj}^{n,\,exp}$, $\alpha_{gj}^{n,\,exp}$, $\rho_{gj}^{n,\,exp}$, and $U_{gj}^{n,\,exp}$ be the junction liquid fraction, liquid density, liquid specific internal energy, void fraction, vapor/gas density, and vapor/gas specific internal energy, respectively, based on the explicit velocities, and let α_{fj}^{n+1}, ρ_{fj}^{n+1}, U_{fj}^{n+1}, α_{gj}^{n+1}, ρ_{gj}^{n+1} and U_{gj}^{n+1} be the same variables based on the final velocities. A velocity flip-flop has occurred when one of the junctions in a system satisfies the following condition:

$$
\frac{\left| \begin{array}{l} \alpha_{fj}^{n,\,exp} \min(\rho_{fj}^{n,\,exp}, 5\rho_{gj}^{n,\,exp}) U_{fj}^{n,\,exp} + \alpha_{gj}^{n,\,exp} \rho_{gj}^{n,\,exp} U_{gj}^{n,\,exp} - \\ \alpha_{fj}^{n+1} \min(\rho_{fj}^{n+1}, 5\rho_{gj}^{n+1}) U_{fj}^{n+1} + \alpha_{gj}^{n+1} \rho_{gj}^{n+1} U_{gj}^{n+1} \end{array} \right|}{0.20 [\alpha_{fj}^{n,\,exp} \min(\rho_{fj}^{n,\,exp}, 5\rho_{gj}^{n,\,exp}) U_{fj}^{n,\,exp} + \alpha_{gj}^{n,\,exp} \rho_{gj}^{n,\,exp} U_{gj}^{n,\,exp}]} > .
\tag{8.2-1}
$$

Under such circumstances, the time step is repeated with the same time step size using the donor properties based on the previously calculated final velocities.

Another situation that may cause excessive mass and/or energy errors is when a noncondensable gas first appears in a volume. Because the linearized phasic properties are evaluated at the state existing at the beginning of an advancement, the derivatives of the phasic properties with respect to the noncondensable gas quality will be zero since there is no noncondensable gas in the volume at the beginning of the advancement. The convection of noncondensable gas into the volume during the advancement will result in an inconsistent state at the end of the advancement because the derivatives needed for the computation of a consistent state are identically zero. The inconsistency may be manifested as a large mass error where the noncondensable gas fails to appear in the volume even though the flux of noncondensable gas into the volume is positive. The inconsistency may also be manifested as an unphysically high vapor temperature when noncondensable gas first appears in a volume. This inconsistency is corrected by repeating the time step advancement with the same time step size when noncondensable gas first appears in a volume. This is done for both the semi-implicit scheme and the nearly-implicit scheme. The code checks for this situation at the end of every advancement if the noncondensable gas model has been activated by the user. The situation is detected whenever the noncondensable quality in a volume is zero at the beginning of the advancement and the flux of noncondensable gas into the volume during the advancement is greater than a small noncondensable source term. This term (can be zero) was determined from tests of thought problems, separate effects calculations, integral effects calculations, and plant calculations. The noncondensable quality and vapor fraction that would result from the flux of noncondensable gas into the volume is estimated from an explicit mass balance on the vapor phase in the volume. The estimated noncondensable gas quality is then used in the computation of the derivatives of the phasic properties. The estimated noncondensable gas quality and vapor fraction are also used in the construction of the linearized conservation equations instead of the beginning of advancement quantities. The modified linearized conservation equations are then used to compute the end of advancement quantities as described previously. The time step size used for the repeated advancement is the same as that used for the original attempted advancement unless the pressure change in the cell is too large. The time step control based on the change in the pressure described in Section 8.1 is activated for volumes in which noncondensable gas is first appearing. The time step control based on pressure may result in multiple time step repeats with smaller and smaller time steps when a noncondensable gas first appears in a volume.

8.3 Steady-State

A steady-state initialization capability is included in ATHENA. With this capability, the transient solution algorithm is continually monitored to determine the achievement of a steady-state. During this process, convergence criteria are calculated and used in the steady-state testing scheme. These convergence criteria are related to an overall calculational precision. This overall precision is the result of combining both the precision of the transient solution algorithm and the standard tolerance of the thermodynamic state algorithm. The following discussion describes the fundamental concepts of tests to detect steady-state during transient calculations.

8.3.1   Fundamental Concepts for Detecting Hydrodynamic Steady-State During

Transient Calculations

The fundamental concept of steady-state is that the state of a reactor system being modeled does not change with respect to time. In the hydrodynamic solution scheme, three terms can be monitored whose variation in time include the variation of all of the other terms. These three terms are the thermodynamic density, internal energy, and pressure. Furthermore, these three terms can be combined into a single-term, enthalpy. Hence, monitoring the time variation of enthalpy is equivalent to monitoring the time variation of all of the other variables in the solution scheme. For each volume cell in the system model, the enthalpy can be written as

$$V_i \rho_i^n h_i^n = V_i (\rho_i^n U_i^n + P_i^n) \qquad (8.3\text{-}1)$$

where subscript i denotes the i-th volume element, h_i is the volume element specific enthalpy in units of energy per unit mass, and V_i is the element volume. Since volume is constant, Equation (8.3-1) can be simplified as

$$\rho_i^n h_i^n = \rho_i^n U_i^n + P_i^n \quad . \qquad (8.3\text{--}2)$$

The rate of variation with respect to time of Equation (8.3-2) can be expressed numerically as

$$\left(\frac{d(\rho h)}{dt} \right)_i^n = \frac{(\rho_i^{n+1} U_i^{n+1} + P_i^{n+1}) - (\rho_i^n U_i^n + P_i^n)}{\Delta t^n} \quad . \qquad (8.3\text{-}3)$$

Absolute hydrodynamic steady-state occurs when Equation (8.3-3) is zero for each of the volume elements in the modeled system.

In order to simplify the task of detecting steady-state, a system mean enthalpy can be expressed as

$$\overline{(\rho h)}^n = \frac{\displaystyle\sum_{i=1}^{NVOLS} V_i (\rho_i^n U_i^n + P_i^n)}{\displaystyle\sum_{i=1}^{NVOLS} V_i} \quad . \qquad (8.3\text{-}4)$$

A system mean rate of change can also be formulated as

$$\overline{\frac{d}{dt}(\rho h)}^{\,n} = \frac{1}{\Delta t^n} \frac{\sum_{i=1}^{NVOLS} V_i[(\rho_i^{n+1} U_i^{n+1} + P_i^{n+1}) - (\rho_i^n U_i^n + P_i^n)]}{\sum_{i=1}^{NVOLS} V_i} \quad . \tag{8.3-5}$$

However, since the rate of change in any volume element can be positive or negative, these terms would tend to cancel. Hence, a better formulation for the mean rate of change is a mean square summation that can be written as

$$\left[\overline{\left(\frac{d}{dt}(\rho h)\right)^2}\right]^n = \frac{1}{(\Delta t^n)^2} \frac{\sum_{i=1}^{NVOLS} V_i^2[(\rho_i^{n+1} U_i^{n+1} + P_i^{n+1}) - (\rho_i^n U_i^n + P_i^n)]^2}{\sum_{i=1}^{NVOLS} V_i^2} \quad . \tag{8.3-6}$$

During the course of the problem solution, Equation (8.3-6) can be used to monitor the system approach to steady-state because, as each volume element approaches steady-state, its rate of change goes to zero and drops out of the summation. The detection of absolute steady-state is therefore relatively simple, since the calculations need only be monitored until Equation (8.3-6) becomes zero. However, another property of Equation (8.3-6) is that it will fluctuate wildly, varying between small and large magnitudes. These fluctuations decrease in magnitude as the calculations proceed toward steady-state. Hence, Equation (8.3-6) is not a well-behaved function, and it is therefore difficult to monitor its behavior. However, a well-behaved function can be curve-fitted to the results of Equation (8.3-6) over reasonable time intervals. An exponential function is of this type; and if

$$\left[\overline{\left(\frac{d}{dt}(\rho h)\right)^2}\right]^n = y = e^{\alpha + \beta t^n + \gamma (t^n)^2 + \phi (t^n)^3}, \ (t_o \le t^n \le t) \tag{8.3-7}$$

the coefficients α, β, γ, and ϕ may be computed by the method of least squares over any reasonable time interval greater than four time steps. Equation (8.3-7) has the property that it can increase to large values at small values of time and then decrease to small values as time increases and the system approaches steady-state. Equation (8.3-7) represents the time-smoothed root mean square (RMS) rate of change in system enthalpy.

Because the user must provide boundary conditions, controls, or trips to guide the transient solution to steady-state, it may not be possible to achieve an absolute steady-state. For example, a steam generator water level control may be modeled so that the water level oscillates between high and low set points. In addition, since numerical schemes are inexact, it may only be possible to calculate absolute steady-state within a small limit of precision. For this kind of fluctuating average steady-state, the RMS $\frac{d(\rho h)}{dt}$ will

approach a constant, positive, nonzero value. As a result, an additional method must be used to detect an average steady-state over limited time intervals.

If the system $\overline{(\rho h)}^{n}$ is varying with time over the interval $t_1 \leq t^n \leq t_2$, its variation can be expressed approximately in the form of a straight line such that

$$H^n = b + at^n \approx \overline{(\rho h)}^{n} \quad . \tag{8.3-8}$$

If the system is approaching an absolute steady-state, then the line rate of change will be zero and Equation (8.3-8) will give the system time average (ρh) such that

$$\overline{(\rho h)}\Big|_{t_1}^{t_2} = b, \quad (t_1 \leq t^n \leq t_2) \tag{8.3-9}$$

where the averaging is over the interval $t_1 \leq t^n \leq t_2$.

The second testing method consists of monitoring the system $(\rho h)^n$ at the completion of each successful time step and, at reasonable time intervals, solving for the straight line coefficients a and b using the method of least squares.

In performing the method of least squares, the mean system enthalpy is computed at the successful completion of each time step in the interval $t_1 \leq t^n \leq t_2$, and an equation expressing the sum of the squares of the differences between ρh^n and Equation (8.3-8) can be written as

$$\xi_{\rho h}^2\Big|_{t_1}^{t_2} = \sum_{n=n_1}^{n_2} \left(\overline{(\rho h)}^{n} - b - at^n\right)^2 \quad . \tag{8.3-10}$$

The coefficients a and b can then be calculated by the method of least squares.

A measure of the RMS fluctuation of $(\rho h)^n$ with respect to the line of Equation (8.3-8) can also be computed using the mean square form of Equation (8.3-10), where

$$\overline{(\rho h)}_{RMS}\Big|_{t_1}^{t_2} = \left[\frac{1}{(n_2 - n_1)}\xi_{\rho h}^2\Big|_{t_1}^{t_2}\right]^{1/2} \quad . \tag{8.3-11}$$

The RMS fluctuation then represents a measure of the typical difference between the mean system enthalpy and the line of Equation (8.3-8). However, the coefficients a and b cannot be calculated with any better precision than the overall precision of the solution scheme for the entire system.

8.3.2 Calculational Precision and the Steady-State Convergence Criteria

In the ATHENA solution scheme, at the successful completion of calculations over a time step, three fundamental variables are computed for each volume element in the system modeled. These variables are

1. ρ_{mi}^{n+1}, the thermodynamic density of the volume substance, where subscript m denotes the solution by conservation of mass.

2. U_i^{n+1}, the thermodynamic specific internal energy of the volume substance resulting from conservation of energy.

3. P_i^{n+1}, the thermodynamic pressure of the volume substance resulting from the combined solution conserving momentum, mass, and energy.

The thermodynamic pressure, phasic specific internal energies, and vapor/gas volume fraction are used to compute the state using a set of properties tables. In the resulting calculations, a thermodynamic density ρ^{n+1} is calculated corresponding to the solution results. If the pressure and overall specific internal energy are preserved, then the precision of the calculations can be defined as

$$\varepsilon_{\rho,i}^{n+1} = \rho_i^{n+1} - \rho_{mi}^{n+1} \tag{8.3-12}$$

for each volume element in the system. If the calculations were exact, then Equation (8.3-12) would be zero. However, the properties tables are limited in precision to a tolerance of ± 1 in the fifth significant figure. In statistical terminology, the mean expected precision would be approximately ± 5 in the sixth significant figure. If the mean expected precision is considered to be a *standard* precision, an approximate expression can be written in terms of the properties table density as

$$\varepsilon_{std,\rho,i}^{n+1} \sim \pm(5\times10^{-6})\rho_i^{n+1} \tag{8.3-13}$$

which is approximately ± 5 in the density sixth significant figure and which represents the best expected precision for the calculational scheme.

In the steady-state testing scheme, the precision of the volume enthalpy can be written as

$$\varepsilon_{\rho h,i}^{n+1} = (\rho_i^{n+1}U_i^{n+1} + P_i^{n+1}) - (\rho_{mi}^{n+1}U_i^{n+1} + P_i^{n+1}) \tag{8.3-14}$$

or

$$\varepsilon_{\rho h, i}^{n+1} = (\rho_i^{n+1} - \rho_{mi}^{n+1}{}_i)U_i^{n+1} \quad . \tag{8.3-15}$$

Similarly, the precision of the rate of change in volume enthalpy can be written as

$$\varepsilon_{\frac{d}{dt}(\rho h), i}^{n+1} = \frac{1}{\Delta t^n}\{[(\rho_i^{n+1}U_i^{n+1} + P_i^{n+1}) - (\rho_i^n U_i^n + P_i^n)]\}$$
$$- [(\rho_{mi}^{n+1}U_i^{n+1} + P_i^{n+1}) - (\rho_{mi}^n U_i^n + P_i^n)] \tag{8.3-16}$$

which simplifies to

$$\varepsilon_{\frac{d}{dt}(\rho h), i}^{n+1} = \frac{1}{\Delta t^n}\varepsilon_{\rho h, i}^{n+1} \quad . \tag{8.3-17}$$

For the entire system at the current time step, a statistical precision can be defined where

$$\varepsilon_{\rho h}^{n+1} = \left\{ \frac{\displaystyle\sum_{i=1}^{NVOLS} V_i^2[(\rho_i^{n+1} - \rho_{mi}^{n+1})U_i^{n+1}]^2}{\displaystyle\sum_{i=1}^{NVOLS} V_i^2} \right\}^{1/2} \tag{8.3-18}$$

for the system mean enthalpy and where

$$\varepsilon_{\frac{d}{dt}(\rho h)}^{n+1} = \left[\frac{1}{(\Delta t^n)^2}(\varepsilon_{\rho h}^2)^{n+1} \right]^{1/2} \tag{8.3-19}$$

for the system rate of change in enthalpy.

Simple mean differences for the entire system can also be written as

$$\bar{\delta}_{\rho h}^{n+1} = \frac{\displaystyle\sum_{i=1}^{NVOLS} V_i(\rho_i^{n+1} - \rho_{mi}^{n+1})U_i^{n+1}}{\displaystyle\sum_{i=1}^{NVOLS} V_i} \tag{8.3-20}$$

for the system mean enthalpy and as

$$\bar{\delta}_{\frac{d}{dt}(\rho h)}^{n+1} = \frac{1}{\Delta t^n}\bar{\delta}_{\rho h}^{n+1} \tag{8.3-21}$$

for the system rate of change in enthalpy.

The relationship between the mean difference and precision terms defines the uncertainty characteristics of the overall solution scheme. From Equations (8.3-18) through (8.3-21), it is obvious that

$$-\varepsilon_\eta \le \delta_\eta \le \varepsilon_\eta \tag{8.3-22}$$

where subscript η denotes the particular term, ρh or $\frac{d}{dt}(\rho h)$, being considered. In particular, if ε_η is small, it can be concluded that calculations are made with a high degree of precision throughout the entire system modeled. If the mean difference term is such that $\delta_\eta \sim 0$, then the overall system solution is said to be unbiased. This means that the overall system mass, energy, and momentum are precisely conserved. However, if $\delta_\eta \sim \varepsilon_\eta$, then the overall system solution is said to be biased. This means that if Equation (8.3-22) is true and $\delta_\eta < 0$, then the overall system solution behaves as if it were losing mass, energy, or momentum. If $\delta_\eta > 0$, then the system solution behaves as if it were gaining mass, energy, or momentum. In ATHENA, the size of the calculational time steps are controlled to maintain a high degree of precision which, in turn, limits the system bias. However, the characteristics just described can have an effect in determining time-average steady-state.

Since the time-average straight line test defined by Equation (8.3-6) is conducted over a time interval, time-average precision and mean difference terms must be calculated over the same time interval using the relationships

$$\overline{(\varepsilon_{\rho h})^2}\Big|_{t_1}^{t_2} = \frac{\displaystyle\sum_{n=n_1}^{n_2} \Delta t^n (\varepsilon_{\rho h}^n)^2}{\displaystyle\sum_{n=n_1}^{n_2} \Delta t^n} \qquad (8.3\text{-}23)$$

$$\left(\overline{\varepsilon_{\frac{d}{dt}(\rho h)}}\right)^2\Bigg|_{t_1}^{t_2} = \frac{\displaystyle\sum_{n=n_1}^{n_2} \Delta t^n \left[\left(\varepsilon_{\frac{d}{dt}(\rho h)}\right)^2\right]^n}{\displaystyle\sum_{n=n_1}^{n_2} \Delta t^n} \qquad (8.3\text{-}24)$$

$$\overline{\bar{\delta}_{\frac{d}{dt}(\rho h)}}\Big|_{t_1}^{t_2} = \frac{\displaystyle\sum_{n=n_1}^{n_2} \Delta t^n \delta_{\rho h}^n}{\displaystyle\sum_{n=n_1}^{n_2} \Delta t^n} \qquad (8.3\text{-}25)$$

$$\bar{\delta}_{\frac{d}{dt}(\rho h)}\Big|_{t_1}^{t_2} = \frac{\displaystyle\sum_{n=n_1}^{n_2} \Delta t^n \delta_{\frac{d}{dt}(\rho h)}^n}{\displaystyle\sum_{n=n_1}^{n_2} \Delta t^n} \qquad (8.3\text{-}26)$$

where the averaging is over the time interval, $t_2 - t_1$, and the summation terms n_1 and n_2 denote the number of time steps taken over the interval.

Equations (8.3-23) through (8.3-26) represent the precision of the actual calculations relative to the thermodynamic state algorithm. These equations have the characteristic that if the system approaches absolute steady-state, both Equations (8.3-23) and (8.3-24) will become very small. Since the property tables are limited in precision, it is useless in a practical sense to continue calculations if absolute steady-state is achieved with a precision better than that for the properties tables. This criterion can be defined by considering equations similar to Equations (8.3-23) and (8.3-24) but written in terms of the properties tables *standard* precision. These equations can be derived by simply substituting Equation (8.3-24) for the density difference term in the equations leading to Equations (8.3-23) and (8.3-24).

The steady-state convergence criteria can then be defined by combining the calculational and standard precisions such that

$$\left.(\varepsilon_{c,\,\rho h})^2\right|_{t_1}^{t_2} = \left\{\frac{1}{2}\left[\left(\left.\varepsilon_{std,\,\rho h}\right|_{t_1}^{t_2}\right)^2 + \left(\left.\varepsilon_{\rho h}\right|_{t_1}^{t_2}\right)^2\right]\right\}^{1/2} \tag{8.3-27}$$

for the system mean enthalpy, and

$$\left.\varepsilon_{c,\,\frac{d}{dt}(\rho h)}\right|_{t_2}^{t_2} = \left\{\frac{1}{2}\left[\left(\left.\varepsilon_{std,\,\frac{d}{dt}(\rho h)}\right|_{t_1}^{t_2}\right)^2 + \left(\left.\varepsilon_{\frac{d}{dt}(\rho h)}\right|_{t_1}^{t_2}\right)^2\right]\right\}^{1/2} \tag{8.3-28}$$

for the system rate of change in enthalpy.

Equations (8.3-27) and (8.3-28) represent the steady-state convergence criterion. It can be said that, within the limits of calculational and properties precision, time-average steady-state is achieved when the mean rate of change in system enthalpy is within the limits of

$$-\left.\varepsilon_{c,\,\frac{d}{dt}(\rho h)}\right|_{t_1}^{t_2} \le a \le \left.\varepsilon_{c,\,\frac{d}{dt}(\rho h)}\right|_{t_2}^{t_2} \tag{8.3-29}$$

where "a" is the mean rate of change in system enthalpy given by Equation (8.3-8). If Equation (8.3-29) is true and if Equation (8.3-7) is such that

$$y \le \left.\varepsilon_{c,\,\frac{d}{dt}(\rho h)}\right|_{t_1}^{t_2} \tag{8.3-30}$$

then absolute steady-state is achieved. If Equation (8.3-29) is true and

$$y > \left.\bar{\varepsilon}_{c,\,\frac{d}{dt}(\rho h)}\right|_{t_1}^{t_2} \tag{8.3-31}$$

then the system is fluctuating and time-average steady-state is achieved.

8.3.3 Steady-State Testing Scheme, Time Interval Control, and Output

In the steady-state testing scheme, the concepts discussed for detecting steady-state are used, and calculations are performed over time intervals composed of a number of time steps. Because the *nature* of each problem is different, a systematic method of varying the test time intervals is performed.

These tests are performed in two parts. First, the system model overall state and rate of change in state are monitored by evaluating Equations (8.3-1) through (8.3-5) and including these results in the least-square terms for Equation (8.3-6). At time intervals computed internally, Equation (8.3-6) is evaluated; and the current system rate of change is determined. If the rate of change in state is increasing, then a *divergent* condition is indicated. If the rate of change in state is decreasing or zero, then a *convergent* condition is indicated. Second, if a *convergent* condition is indicated, then calculations are performed to determine the system average state and average rate of change in state over the internally computed time intervals. These time-averages are formed by obtaining successive overlapping least-square solutions for Equation (8.3-7). These successive time-average values are compared, and the achievement or nonachievement of a time-average steady-state is determined. In performing these tests, the calculational precision is accounted for by using Equations (8.3-12) through (8.3-29).

In the steady-state scheme, each time a solution for Equation (8.3-6) is obtained, the overall-state and steady-state convergence test results are printed. This printout is composed of current time results and time smoothed results integrated over the test time interval. The current time results are (a) the state and rates of change in state resulting from Equations (8.3-4), (8.3-5), and (8.3-6); (b) the current time uncertainties resulting from Equations (8.3-18) through (8.3-21); and (c) the current time mean and root mean square (RMS) mass errors. The time-smoothed results that are printed are the current time evaluation of Equation (8.3-7) and the resultant coefficients of Equation (8.3-7) determined by the least-squares solution over the time interval from t_1 to the current time TIMEHY. The time, t_1, corresponds to the time at the successful completion of calculations for the first time step after problem initiation. For example, if the problem is a <u>NEW</u> problem, then t_1 corresponds to

$$t_1 = 0 + \Delta t_1 \tag{8.3-32}$$

where Δt_1 is the first successful time step. If the problem is a <u>RESTART</u> problem, then t_1 corresponds to

$$t_1 = TREST + \Delta t \tag{8.3-33}$$

where TREST is the time of restart and Δt is the first successful time step after restart. If the results of the overall state tests indicate a *convergent* condition, then time-average tests are initiated.

The time-average tests consist of approximating the overall state with a set of three straight lines where each test line is fitted to the calculational results over successive test intervals. The time rates of change of these test lines are then monitored to determine time-average steady-state. In the testing scheme,

when the time-average tests are initiated, calculations continue until the successive test time interval is exceeded. At this time, the first test line, Line A, is defined and its results are printed. Calculations then continue until the next successive test time interval is exceeded. At this time, the second test line, Line B, is defined for the second test interval and the third test line, Line C, is defined for the combined first and second test intervals. The results for the three test lines are then printed, and tests are performed to determine the achievement of time-average steady-state. If steady-state has not been achieved, then test <u>Line A</u> is reset to <u>Line B</u>, and the process is repeated until steady-state is achieved.

In the printed edit for time-average steady-state tests, the results for each of the three test lines are printed. The test line results are obtained by curve fitting Equation (8.3-8) over each of the line test intervals. The results printed are the endpoints of Equation (8.3-8) evaluated at the test interval start and end times and the time rate of change of Equation (8.3-8). Also printed are the time-average uncertainties from Equations (8.3-23) through (8.3-26), the RMS fluctuation of system mean ρh about the line from Equation (8.3-11), and the mass error integrated over the line test interval.

In performing both the overall and time-average sets of tests, calculations proceed through a logic scheme to perform tests that monitor the solution scheme's approach to steady-state. After completing the logic scheme calculations, the steady-state conclusions and next course of action are printed. This printout is composed of statements of the mode of convergence and the state of the system in alphanumeric terms. These statements are defined as the calculations proceed through the logic scheme. To prevent excessive printout during the overall state convergence tests, the first test for overall convergence is not performed until the completion of ten successful time steps. At this time, a current test time interval is initialized as $\Delta t_{cur} = \text{TIMEHY} - t_1$. If this test indicates a *divergent* condition, then the test time interval is increased and the test procedure is repeated. To increase the test time interval, three tests are performed. First, the current test time interval is halved and the time t_2 is estimated as

$$t_2 \ = \ \text{TIMEHY} + \frac{1}{2}\Delta t_{cur} \quad . \tag{8.3-34}$$

Then, Equation (8.3-7) is evaluated as $y(t_2)$. If $y(t_2)$ is greater than the current value of y, then the time t_2 is reset to

$$t_2 \ = \ \text{TIMEHY} + \Delta t_{cur} \tag{8.3-35}$$

and Equation (8.3-7) is reevaluated, which results in resetting $y(t_2)$. If $y(t_2)$ is again $> y$, then the time t_2 is again reset to

$$t_2 \ = \ \text{TIMEHY} + 2\Delta t_{cur} \quad . \tag{8.3-36}$$

In any case, the test time interval is expanded by either maintaining, halving, or doubling the current test time interval based on a projected estimate of the current time-smoothed convergence function. This test procedure is then successively repeated until a *convergent* condition is calculated.

To provide efficiency for the time-average testing scheme, upon the first occurrence of an overall state *convergent* condition, the time-average testing scheme is activated and the test time interval is redefined by estimating the time interval over which a 10% change in state will occur. This time interval is approximately

$$\Delta t_c \sim \frac{0.1(\overline{\rho h})^n}{y} \quad .$$

(8.3-37)

However, to prevent excessively small or large intervals, the time interval is limited such that $10 \Delta t \leq \Delta t_c \leq 100 \Delta t$, where Δt is the current calculational time step. The calculations for the time-average scheme then proceed with each successive test time interval specified 10% larger than the time interval just completed. As the calculations progress and approach steady-state, the line segments approach a constant value within the steady-state convergence criteria. When this condition is met, the test time interval is doubled. If this condition is recursively maintained for two more successive test intervals, then a final steady-state has been achieved and the calculations are terminated. If the line segment tests indicate the solution is diverging from steady-state, the results of the time-average tests are discarded. When the conditions of Equation (8.3-7) again become true, the time-average tests are reinitiated, and the procedure is continued until steady-state is achieved.

A user-control over termination of advancements toward steady-state is available as part of the time step control options. The control can be set to force continued advancements regardless of the steady-state termination algorithm up to a specified time, then allow automatic termination during a following time period.

8.3.4 Heat Structure Heat Conductance Scheme for Steady-State

In both the steady-state and transient solution schemes, the same transient heat transfer algorithm is used. However, in the steady-state scheme, the heat structure heat capacity data input by the user are ignored, and this term is evaluated as an artificially small number such that

$$\frac{\rho C_p (\Delta x)^2}{k \Delta t_{hc}} \geq 2$$

(8.3-38)

where ρC_p is the volumetric heat capacity, Δx is the heat structure mesh interval, k is the heat structure thermal conductivity, and Δt_{hc} is the heat conduction scheme calculational time step. Equation (8.3-38) corresponds to the explicit stability criteria for a transient numerical heat conduction scheme.

In a transient solution scheme, the volumetric heat capacity is treated analogously to a *thermal* inertia, and its magnitude determines the characteristic response time of the conduction solution. For example, ρC_p is typically quite large, on the order of 10^5 J/m^{3}K or larger. Hence, a large value of ρC_p results in a characteristic response time much greater than the hydrodynamic response time. Indeed, hydrodynamic steady-state can be approximately achieved in reasonably short calculational times before large heat structures have even begun to respond.

By making the value of the volumetric heat capacity small, the characteristic response time is made small and on the order of or less than the hydrodynamic calculational time step. The resultant solution would therefore be equivalent to a steady-state solution that is damped and stabilized by a small thermal inertia. Hence, fluctuations of the heat structure rate of change in state are on the order of or less than the fluctuations of its hydrodynamic boundary conditions. As a result, the heat structure solution scheme will achieve time-average steady-state at approximately the same time as time-average hydrodynamic steady-state.

8.3.5 Interrelationship of Steady-State and Transient Restart-Plot Records

During the course of the calculations, restart-plot records are written at the frequency specified by the user. When the code determines that steady-state has been achieved, a restart-plot record is written unconditionally. Subsequent problems can then be run as restarts using any of these restart records. However, the code will treat the restart records differently, depending on the type of problem using the restart record.

If a transient problem is being run by restarting from a steady-state restart record or, conversely, if a steady-state problem is being run restarting from a transient restart record, the restart is treated as a new problem. In this case, only the restart record at which the problem restarts is written and used for initial conditions. The code time step counters, statistics, and problem simulation time are reset to zero, and additional restart-plot records are written as the problem progresses.

If a steady-state problem is being run restarting from a steady-state restart record or, conversely, if a transient problem is being run restarting from a transient restart record, then the restart is treated as a continuation of the problem. In the continuation case, the previous restart-plot records up to the point of restart are preserved; and additional records are written as the problem progresses.

8.3.6 Energy Discrepancy

The default code contains a discrepancy when checking the steady state by means of an energy balance. The default code should add the form loss (code calculated abrupt area change loss and user-supplied loss) dissipation to the phasic energies. This dissipation was removed in RELAP5/MOD2 because of temperature problems (i.e., overheating), and thus it is not present in ATHENA. The dissipation can be activated by the user in the input deck, however the user is cautioned that temperature problems may occur.

8.4 Self-Initialization

8.4.1 General Description

Obtaining a desired, steady-state condition for a ATHENA plant model often requires considerable time and effort on the part of the analyst. Typically, this process involves successive calculations involving a trial-and-error approach in adjusting various input data. While the ATHENA code can compute a steady-state condition for a particular set of boundary conditions, this steady-state may not match all parameters measured in the plant due to the particular nodalization chosen by the analyst, inherent inaccuracies in code models of the physical processes, inability to model geometric details, etc. The self-initialization option is designed to reduce the time, effort, and cost to achieve a steady-state for a given ATHENA plant model to more nearly match plant data if necessary.

The strategy of the scheme is to automate the control aspects of the problem and to significantly reduce the computational time needed to reach a steady-state. The concept retains the conventional approach of conducting a transient calculation that is driven to a desired steady-state condition.

Automation of plant model control is effected by a generic set of controllers that mimic an actual plant control system. These controllers are control components defined by the user. Four suboptions are permitted with respect to the definition of independent and dependent plant model parameters. The choice of suboptions affords the user flexibility in meeting particular analysis objectives. Moreover, the overall scheme has been designed such that the user may invoke a standard control package or opt to custom-tailor the new control components to suit a particular plant model.

A reduction in calculational computer time to perform the initialization is accomplished by using the steady-state and nearly-implicit solution scheme options (see Section 8.3 and Section 3.1.5, respectively). The steady-state option diminishes thermal capacitance terms to lower stability limits, thereby significantly reducing thermal relaxation of the model. It also monitors for a steady-state condition. The nearly-implicit solution scheme permits time steps larger than those implied by the material Courant limit.

The self-initialization option is described for PWR-type models employing either U-tube or once-through steam generators and of single- or multiple-loop design. However, the principles illustrated can be applied to other systems.

8.4.2 Required Plant Model Characteristics

The option accommodates plant models representing all domestically produced PWR designs, i.e., those of Westinghouse, Combustion Engineering, and Babcock & Wilcox. More specifically, single-loop, two-loop, three-loop, four-loop, and 2 x 4 loop representations are accommodated, using either U-tube or once-through steam generators. Other assumptions and restrictions related to the plant model are as follows:

- The model must have at least one coolant loop consisting of a core region, pump, steam generator, and pressurizer.

- The core power must be constant or it too must be driven by a control system to constant power. The reactor kinetics model may be used and held to constant input power by not entering feedback data. Reactor kinetics data with feedback needed for the transient can be entered at the restart starting the transient.

- User-specified makeup and letdown flow modeling should be suppressed during the null transient. The same applies to pressurizer heater and spray modeling. They may be introduced into the model as a renodalization at transient initiation. Volume and pressure control during the null transient must be effected through a time-dependent volume that serves to replace the pressurizer.

- Self-initialization of the plant model encompasses the primary coolant system and steam generators under the standard approach described subsequently. That is, no provisions have been made to include the balance-of-plant components in the testing for a steady-state, though this is possible and is not incompatible with the self-initialization option. However, if the plant model includes a balance-of-plant representation (e.g., turbine, condensers, feedwater pumps, feedwater heaters, etc.), appropriate controllers would have to be supplied by the user to govern the operation of these components.

- The option is executable from either a new problem data deck or the restart of an old problem.

8.4.3 Standard Suboptions

Four standard suboptions are available in terms of specifying the independent parameter data set. This flexibility allows the user to select the suboption that best suits the situation at hand. Here it should be noted that the term standard refers to the employment of the control components in a standardized way that will subsequently be described. The nature of the control components, however, allows them to be used in other ways (i.e., with respect to sensed variable and controlled variable).

Recognize that the state of the plant model cannot be totally dictated by the analyst, since this would represent an overspecification of the problem. Certain interdependencies are implied by the plant model geometry and the mathematical models in the code. For example, one cannot simultaneously specify the thermal power, cold leg temperature, primary coolant flow rate, secondary pressure, and coolant level. This is an overspecification, since the overall heat transfer characteristics of the steam generator(s) have been implied by its (their) geometrical description and the heat transfer models in the code. Either the secondary pressure (and temperature) or cold leg temperature would have to be dependent in this example.

Each of the four standard suboptions has a common set of fixed parameters. These, and the remaining independent and dependent parameters for each suboption, are listed in **Table 8.4-1**. These

suboptions are derived from the four logical combinations that result from selecting two of four variables, allowing the other two to be dependent. These four are primary flow, reactor coolant pump (RCP) speed, cold leg temperature, and secondary pressure. Each of the suboptions is described below.

Table 8.4-1 Independent/dependent data set suboptions.

Always fixed	Core thermal power Pressurizer pressure Feedwater temperatures Secondary coolant level	
Suboption	**Independent**	**Dependent**
A	Loop flow Cold leg temperature	RCP speed Secondary pressure Secondary flow
B	RCP speed Cold leg temperature	Loop flow Secondary pressure Secondary flow
C	Loop flow Secondary pressure	RCP speed Cold leg temperature Secondary flow
D	RCP speed Secondary pressure	Loop flow Cold leg temperature Secondary flow

8.4.3.1 Suboption A. Loop flow and cold leg temperature are specified. (Note that specification of primary flow, core thermal power, and primary pressure fixes the differential temperature across the vessel.[a]) This suboption requires that the pump speed, secondary pressure, and secondary feedwater flow be dependent variables.

The pump speed (ω) is determined based on loop flow ($\dot{m}$), loop pressure drop (ΔP), and the pump characteristics, as determined from pump model input. That is,

$$\omega = f(\dot{m}, \Delta P) \quad . \tag{8.4-1}$$

---

a. This takes into account the total pump power and heat losses as well.

Here it should be noted that the resulting pump speed may be different than an observed value (in the case of an experimental facility) or the synchronous speed (in the case of a full-scale plant). This merely implies that a mismatch is present in the input data. For example, the user-specified geometry and/or loss coefficients for the primary coolant system (PCS) may be inaccurate, and/or the pump model may be inaccurate. The analyst must resolve such inconsistencies. The code will not alter either the pump model or loss coefficients to arrive at a flow/speed combination that matches facility data.

Analogously, specifying the cold leg temperature (along with power and loop flow) requires that the secondary pressure and flow must be dependent. The secondary pressure dictates the secondary sink temperature and, therefore, the primary-to-secondary heat transfer potential and cold leg temperature. Here again, it should be noted that the resulting secondary pressure may not match that observed in the plant or test facility. This may mean one of two things. Either the plant model representation of the steam generator is inadequate (e.g., inaccurately modeled, improperly nodalized, etc.), or the physical models in the code are imprecise. For example, the failure to match a measured value of secondary pressure might be due to the fact that the tube fouling was not accounted for in the input model.

8.4.3.2   Suboption B. RCP speed and cold leg temperature are specified, while loop flow, secondary pressure, and secondary flow are dependent. This suboption is similar to suboption A except that the roles of RCP speed and loop flow as dependent and independent variables are reversed. This suboption would be desirable when modeling a plant for which no data exist but the synchronous pump speed is known.

8.4.3.3 Suboption C. Loop flow and secondary pressure are specified, while RCP speed, cold leg temperature, and secondary flow are dependent. This suboption is desirable when secondary pressure matching (to data) would play an important role in the transient.

8.4.3.4 Suboption D. RCP speed and secondary pressure are specified, while loop flow, cold leg temperature, and secondary flow are dependent. This suboption is similar to suboption C, except that the independent/dependent roles of loop flow and pump speed are reversed.

8.4.4 Inherent Model Incompatibilities

With such generality possible in defining a plant model with ATHENA, it is clearly possible that a desired steady-state condition is impossible to achieve given the input data supplied. Several types of incompatibilities will not be readily apparent until a null transient is attempted. For example, the overall heat transfer capacity of the steam generator(s) may be insufficient to transfer the total core thermal power without causing the hot leg temperature to exceed T_{SAT}. Such anomalies will be obvious as the null transient proceeds but cannot be readily identified from the input data stream.

Another problem is that the default code contains a discrepancy when checking the steady-state by means of an energy balance. The default code should add the form loss (code calculated abrupt area change and user-supplied loss) dissipation to the phasic energies. This dissipation was removed in RELAP5/MOD2 because of temperature problems (i.e., overheating), and thus it is not present in

ATHENA. The dissipation can be activated by the user in the input deck, however the user is cautioned that temperature problems may occur.

8.4.5 Description of Standard Controllers

To effect overall control of the model during the null transient, three generic control components are available and are used to invoke any one of the four suboptions just described. These control components are identified as PUMPCTL, STEAMCTL, and FEEDCTL. For all suboptions, both STEAMCTL and FEEDCTL are needed; whereas, PUMPCTL is used only for suboptions A and C where loop flow control is desired. The following subsections describe the design and operation of the controllers.

8.4.5.1 PUMPCTL Controller. The standard use of the PUMPCTL component is to sense loop flow and control pump speed to achieve the desired flow rate. As is the case with the other controllers, it uses proportional and integral control. Through input, the user specifies (among other things) the desired flow rate, where the flow is to be sensed, and which pump is to be controlled. The mathematical expressions representing the operation of the controller are next described.

An error signal (E_1) is generated by subtracting the actual (V_2) from desired (V_1) flow rate and dividing the result by a user-supplied constant (S_i). It is given by

$$E_1 = \frac{V_1 - V_2}{S_1} \quad . \tag{8.4-2}$$

This error signal is used to compute a new output signal (pump speed = Y_1) for the next time advancement in accordance with the relationship

$$Y_1^{n+1} = G_1 \left(\frac{E_1}{T_1} + \frac{\int_{t_0}^{t_n} E_1 dt}{T_2} \right) + (Y_1)_0 \tag{8.4-3}$$

where G_1 equals the gain, T_1 is a constant applied to the proportional part, T_2 is the time constant for the integral part, and $(Y_1)_0$ is the initial value of the pump speed.

8.4.5.2 STEAMCTL Controller. The standard employment of the STEAMCTL component is to sense either cold leg temperature (suboptions A and B) or secondary pressure (suboptions C and D) and control steam flow (through adjustment of the steam valve flow area) to achieve the desired set point. It functions in exactly the same way as the PUMPCTL component just described, except that the definition of sensed and controlled variables is changed. For the STEAMCTL component,

$$E_2 = \frac{V_3 - V_4}{S_j} \tag{8.4-4}$$

where V_3 is the desired temperature (or pressure), V_4 is the actual value, and S_j is a constant supplied by the user. Likewise, the output signal (normalized steam valve area) for each new advancement is given as

$$Y_2^{n+1} = G_2 \left(\frac{E_2}{T_3} + \frac{\int_{t_0}^{t_n} E_2 dt}{T_4} \right) + (Y_2)_0 \tag{8.4-5}$$

where the terms are analogous to those for the PUMPCTL component.

8.4.5.3 FEEDCTL Controller. The standard employment of the FEEDCTL component is to sense steam flow and steam generator secondary coolant level (or coolant mass) and control feedwater flow (through adjustment of the feedwater valve flow area) to achieve a match between feedwater flow and steam flow and to achieve the desired coolant level (or mass). It is also a proportional/integral controller but uses a summed error signal made up of the individual flow and level (mass) errors. It is given by

$$E_3 = \frac{V_5 - V_6}{S_k} + \frac{V_7 - V_8}{S_m} \tag{8.4-6}$$

where

V_5 = desired level (mass)

V_6 = actual level (mass)

S_k = user-supplied constant

V_7 = actual steam flow

V_8 = actual feedwater flow

S_m = user-supplied constant.

The output signal (feedwater valve flow area) is computed analogously to the PUMPCTL and STEAMCTL components. It is given by

$$Y_3^{n+1} = G_3 \left(\frac{E_3}{T_5} + \frac{\int\limits_{t_0}^{t_n} E_3 dt}{T_6} \right) + (Y_3)_0 \quad .$$

(8.4-7)

8.4.5.4 Pressure and Volume Control. The self-initialization option requires that a constant pressure boundary condition be imposed on the primary coolant system during the null transient. The user supplies this condition by adding a time-dependent volume as a replacement for the pressurizer. This time-dependent volume should be defined as containing liquid at the desired primary system pressure and at a temperature near that estimated to be the final hot leg temperature. During the null transient, liquid will either flow into or out of the time-dependent volume to accommodate expansion and shrinkage, with no attendant change in primary pressure. When the self-initialization option is invoked, the code will check to determine if the time-dependent volume has been included.